université PARIS-SACLAY

Living colloidal crystals: Tunable and photoswitchable assemblies of metal nanoparticles via depletion

Cristaux colloïdaux vivants: Assemblages réglables et photocommutables de nanoparticules métalliques par déplétion

Thèse de doctorat de l'université Paris-Saclay

École doctorale n° 571, Sciences Chimiques :
Molécules, Matériaux, Instrumentation et Biosystèmes (2MIB)
Spécialité de doctorat : Physique
Graduate School : Chimie. Référent : Faculté des Sciences d'Orsay

Thèse préparée dans le **Laboratoire de Physique des Solides (Université Paris-Saclay, CNRS)**,
sous la direction de **Marianne IMPEROR-CLERC**, Directrice de Recherche,
et la co-direction de **Cyrille HAMON**, Chargé de Recherche

Thèse soutenue à Paris-Saclay, le 14 octobre 2026, par

Jaime Gabriel TRAZO

Composition du Jury

Membres du jury avec voix délibérative

Jongwook KIM Professeur, École Polytechnique Palaiseau	Président
Mona TRÉGUER-DELAPIERRE Professeur, Université de Bordeaux	Rapporteur & Examinatrice
Sandrine ITHURRIA-LHUILLIER Professeur, ESPCI Paris, Université Paris Sciences et Lettres	Rapporteur & Examinatrice
Leonardo SCARABELLI Associate Professor, Universidad de Cantabria	Examinateur

THÈSE DE DOCTORAT

NNT : 2026UPASF035

université PARIS-SACLAY

ÉCOLE DOCTORALE
Sciences Chimiques : Molécules, Matériaux, Instrumentation et Biosystèmes (2MIB)

Titre : Cristaux colloïdaux vivants: Assemblages réglables et photocommutables de nanoparticules métalliques par déplétion

Mots clés : nanoparticules, auto-assemblage, déplétion, métamatériaux, photoswitch

Résumé : Les métamatériaux dynamiques présentent des propriétés fonctionnelles ajustables qui sont absentes dans la nature ou dans les dispositifs conventionnels. Les métamatériaux optiques et électroniques, utilisés pour manipuler la propagation de la lumière, sont souvent réalisés par la création de réseaux nanostructurés de métaux et de diélectriques via des techniques de nanofabrication top-down, telles que la lithographie ou l'utilisation de moules. Toutefois, ces méthodes aboutissent à des systèmes statiques et non reconfigurables. Afin de reproduire des fonctionnalités actives inspirées du vivant, l'auto-assemblage colloïdal bottom-up de nanoparticules (NPs) a été proposé comme une nouvelle voie d'élaboration de métamatériaux.

L'auto-assemblage induit par déplétion (DISA) repose sur une attraction directionnelle, entropique et ajustable entre les plus grandes faces de NPs en interaction, en présence de particules plus petites dites « déplétants » telles que des micelles de tensioactifs. Dans cette thèse, nous avons étudié comment l'anisotropie et la frustration peuvent être transférées à plus grande échelle des NPs vers leurs assemblages en supercristaux via le procédé DISA; cela permet d'obtenir des structures chirales ou de basse dimensionnalité, ouvertes et reconfigurables, dotées de métapropriétés particulièrement intéressantes pour l'optoélectronique, la détection et la catalyse.

Après l'introduction et la présentation de la méthodologie, le chapitre 3 décrit l'élaboration de notre système DISA, constitué d'une part de nanobâtonnets (NRs) métalliques anisotropes servant d'unités élémentaires et d'autre part de micelles de tensioactif agissant comme agents de déplétion. Nous abordons les avancées obtenues pour la synthèse de NRs à forte anisotropie, le comportement de phase du tensioactif CTAC, les techniques de microscopie in situ et de diffusion de rayons X aux petits angles (SAXS) pour le suivi dynamique des assemblages colloïdaux de NRs, ainsi que la modélisation et l'ajustement des données SAXS pour comprendre la dimensionnalité, la taille et la cristallinité des assemblages.

Viennent ensuite les trois chapitres principaux. Le chapitre 4 se concentre sur l'obtention par DISA en milieu liquide de « métasurfaces colloïdales » 2D s'étendant sur des dizaines à des centaines de micromètres. En effet, la diffusion lente de l'agent de déplétion CTAC permet d'obtenir des métasurfaces ouvertes avec une compacité ajustable (de 21 % à 80 %) et qui peuvent être assemblées et désassemblées de manière réversible sur de nombreux cycles. Ce résultat est ensuite utilisé pour la diffusion Raman exaltée de surface (SERS) accordable afin de détecter des analytes dilués tels que le 4-aminothiophénol.

Dans le chapitre 5, nous montrons comment la méthode DISA s'applique à des nanobâtonnets d'or chiraux torsadés (cGNRs). L'effet de déplétion induit la formation d'agrégats torsadés de cGNRs par transfert de chiralité, ce qui conduit à une exaltation réversible du dichroïsme circulaire plasmonique (PCD), avec une augmentation du facteur g pouvant atteindre deux ordres de grandeur dans le proche infrarouge (NIR). L'exaltation du PCD dépend fortement de la concentration en déplétant et du degré de torsion des cGNR.

Enfin, dans le chapitre 6, nous explorons l'utilisation de tensioactifs photosensibles comment agent de déplétion à la place du CTAC afin de contrôler directement par la lumière le processus d'auto-assemblage. En combinant des NRs métalliques passifs avec un tensioactif photosensible actif (azoTAB), l'assemblage par DISA est rendu commutable par la lumière car elle modifie la forme et la taille des micelles, et donc leur concentration, ce qui par conséquent change l'intensité des forces de déplétion entre les NRs. Cela permet un assemblage-désassemblage ou une expansion-contraction réversibles des assemblages de nanobâtonnets (en 1D ou 2D) par irradiation lumineuse dans l'UV ou le bleu, avec une durée de cycle complète de seulement quelques minutes. Ce contrôle lumineux permet une détection SERS photo-modulable ainsi que la stabilisation d'états d'assemblage hors d'équilibre lors d'une commutation ultra-rapide de la lumière.

Ce projet positionne le DISA comme une méthode «valence-free» permettant d'obtenir des suprastructures dynamiques et anisotropes (1D, 2D et chirales) de NRs, ajustables en jouant sur l'anisotropie des NRs et sur la concentration en déplétant, que ce soit de manière passive ou active par la lumière. Cette étude a apporté de nouveaux éclairages sur le transfert hiérarchique d'anisotropie, les mécanismes d'auto-assemblage, la réversibilité et l'hystérésis des processus induits par déplétion, ainsi que sur la SERS colloïdale in situ.

université PARIS-SACLAY

ÉCOLE DOCTORALE
Sciences Chimiques : Molécules, Matériaux, Instrumentation et Biosystèmes (2MIB)

Title : Living colloidal crystals: Tunable and photoswitchable assemblies of metal nanoparticles via depletion

Keywords : nanoparticles, self-assembly, depletion, metamaterials, photoswitch

Abstract : Dynamic metamaterials exhibit tunable functional properties not found in nature or conventional devices. Optical and electronic metamaterials, used to play with the propagation of light, are often made by creating nanostructured arrays of metals and dielectrics using top-down nanofabrication like lithography or templates. However, these techniques result in static and non-reconfigurable systems. To mimic active bio-inspired functionality, colloidal bottom-up self-assembly of nanoparticles (NPs) has been proposed as a new way of making metamaterials.

Depletion-induced self-assembly (DISA) works via a tunable, entropic, and directional attraction between the largest faces of interacting NPs in the presence of smaller 'depletant' particles like micelles. In this thesis, we studied how anisotropy and frustration can be transfered from NPs to their supercrystal assemblies via DISA using surfactant as depletant, resulting in open and reconfigurable low-dimensional or chiral structures with metaproperties – desirable for optoelectronics, sensing, and catalysis.

After the introduction and methodology, Chapter 3 briefly goes through the development of our DISA system, composed of anisotropic metal nanorods (NRs) as building blocks, and surfactant micelles as depletants. We touch on new developments in the synthesis of highly anisotropic NRs, on the preparation and phase behavior of CTAC as depletant, on in situ microscopy and small-angle X-ray scattering (SAXS) techniques to monitor dynamic colloidal NR assemblies, and on SAXS modelling and fitting to understand assembly dimensionality, size, and crystallinity.

The three main chapters then follow. In Chapter 4, we focus on the formation of 2D 'colloidal metasurfaces' in liquid from tens to hundreds of microns wide, via controlled DISA of long gold core – silver shell NRs using slow diffusion of CTAC depletant. These open metasurfaces exhibit tunable compacity from 21% to 80%, can be reversibly assembled and disassembled over many cycles, and can be used for tunable surface-enhanced Raman scattering (SERS) to detect dilute analytes like 4-aminothiphenol.

In Chapter 5, we consider the case of DISA with twisted chiral gold nanorods (cGNRs). Depletion induces the formation of twisting clusters of cGNRs due to chirality transfer, leading to a reversible enhancement of plasmonic circular dichroism (PCD), with the g-factor increasing up to two orders of magnitude in the NIR range. PCD enhancement depended strongly on the depletant concentration and on the degree of twist in the cGNRs.

In Chapter 6, we then explore the possibility of using photosensitive surfactants to achieve direct light-control of DISA. By combining passive metal NRs with active azoTAB photosurfactant as depletant, DISA was rendered photoswitchable due to changing micelle shape and thus depletion strength. This allows for reversible assembly-disassembly or expansion-contraction of 1D/2D NR assemblies by UV or blue light irradiation, with full cycling time as fast as 3 min. Such light control also allowed for photo-modulable SERS detection, and the stabilization of intermediate assembly states by rapid UV-blue switching.

This doctoral project advances DISA as a valence-free method towards attaining dynamic and anisotropic 1D, 2D, and chiral superstructures of NRs that can be tuned by playing with NP anisotropy and with depletion strength, passively or actively by light. New insights into hierarchical anisotropy transfer, self-assembly mechanisms, reversibility and hysteresis of depletion-induced processes, and in situ colloidal SERS have been uncovered in the course of this study.

TABLE OF CONTENTS

TABLE OF CONTENTS **4**
ACKNOWLEDGMENTS **5**
RÉSUMÉ EN FRANÇAIS (Summary in French) **6**
1 GENERAL INTRODUCTION: METAMATERIALS, SELF-ASSEMBLY, AND DEPLETION **13**
1.1. Towards Functional Metamaterials: Advances and Trends 13
1.2. Current State of Plasmonic Nanomaterials 19
1.3. Nanoscale Self-Assembly: Models, Methods, Probing, and Outlook 29
1.4. The Depletion Interaction, Entropy, and Soft Matter 36
1.5. Summary points and challenges 42
1.6. Scope of the thesis 43
1.7. References 45
2 METHODOLOGY **53**
2.1. General scheme of methods and components 53
2.2. Nanoparticle synthesis 54
2.3. Depletion-induced shape purification of NPs 61
2.4. Conventional depletion-induced self-assembly (DISA) 62
2.5. Phototunable depletion-induced self-assembly (Photo-DISA) 64
2.6. Characterization of NPs and their assemblies 67
2.7. Functional properties of assemblies 71
2.8. References 72
3 DEPLETION-INDUCED SELF-ASSEMBLY (DISA): DEVELOPMENT AND TIPS-AND-TRICKS **74**
3.1. Micellar depletant systems 75
3.2. Development and synthesis of anisotropic nanoparticles 82
3.3. The DISA process and the characterization of assemblies 90
3.4. Tips-and-tricks guide 102
3.5. References 111
4 TUNABLE METASURFACES VIA DEPLETION-INDUCED SELF-ASSEMBLY (DISA) OF NANORODS **114**
4.1. Introduction 114
4.2. Perspectives 121
4.3. Take-home message 130
4.4. References 132
5 CHIRALITY AND TUNING THE FRUSTRATED SELF-ASSEMBLY OF NANORODS **135**
5.1. Introduction 136
5.2. Perspectives 142
5.3. Take-home message 149
5.4. References 150
6 ACTIVE LIGHT-CONTROLLED ASSEMBLY BY PHOTOTUNABLE DEPLETION **152**
6.1. Introduction 152
6.2. Results and discussion 162
6.3. Perspectives 187
6.4. Conclusion and take-home message 190
6.5. References 192
CONCLUSION AND PERSPECTIVES **196**
ANNEX: PUBLISHED ARTICLES **200**

ACKNOWLEDGMENTS

While this PhD has been an amazing opportunity (and responsibility) for me to contribute to the development of materials science, it has also been a great gift entrusted to me: a gift that has sparked my growth not only in terms of my skills and know-how, but my growth as a full human person. To all those who have made this doctorate possible, know that you have not only shared with me your knowledge and support, but that you have also freely shared with me a real part of yourselves. For that, and for that most of all, I will be always grateful.

Firstly, I am truly grateful to my motivated and kind thesis supervisors Cyrille Hamon and Marianne Impéror-Clerc for having been good teachers and mentors to me. You have seen me grow and learn a lot these past three years. I will remember most vividly all the curious and animated team discussions we've had, where the most eye-opening ideas would come up.

Second, I wish to thank my dear colleagues in our research group, particularly Nika Kutalia, Jules Marcone, Claire Goldmann, Noemi Ghelardini, Rahul Nag, Phuong Lan Dao, Sébastien Marchand, Claire Hotton, as well as Jennifer Bodin and Stéphan Rouzière from the MORPHEUS platform, the rest of the MATRIX team in LPS, and my other friends in the lab. You have made LPS not just a laboratory but a community for me. A big shoutout as well to my friends and colleagues from U. Paris-Saclay, particularly the Filipino community and the Erasmus-Mundus alumni who have been with me through many years.

Next, I wish to thank Prof. Hynd Remita and Philipp Gotico whom I have known since my SERP master's program, for being inspiring guides during my PhD.

I am also grateful for the support and warm welcome of our many collaborators. From France, I would like to thank Thomas Bizien from the SOLEIL Synchrotron, Bruno Palpant and the LuMIn team, and Claire Boulogne from the Imagerie Gif TEM. From Spain, I am honored to have worked and learned together with Andrés Serrano-Freijeiro, Daniel García-Lojo, and Professors Isabel Pastoriza-Santos, Jorge Pérez, Luis Liz-Marzán and their whole team from U. Vigo / CICbiomaGUNE, San Sebastián. From the Netherlands, I wish to thank Sara Bals and Mikhail Mychinko from EMAT, U. Antwerp.

Finally, I wish to thank my family and close friends. To my father Jimmy and my mother Ginina, through all these years, you have taught me and shown me what love really is, have loved me unconditionally, and inspired me to love and give myself in the same way. To my friends in Paris, and especially those from the family of Abba Joseph, you have been an anchor of joy and light through the good times and the bad. To my friends from my undergrad years at Ateneo de Manila and my high school years at Seton, thank you for everything, and I hope to see you in person soon!

Inay ko, Itay ko, ako'y buong-buong inyo. Maraming salamat sa lahat!

Non è mia questa vita, è tutto un dono.

Mahal ko, ika'y nababalisa't nababagabag sa maraming mga bagay. Iisa lamang ang mahalaga at kinakailangan. Pinili niya ang nakahihigit, at hindi ito aalisin sa kanya.

RÉSUMÉ EN FRANÇAIS (Summary in French)

Dans le cadre de cette thèse, en s'appuyant sur les progrès simultanés réalisés en nanochimie et dans le domaine des matériaux fonctionnels et bio-inspirés, nous avons exploré et approfondi la méthode d'auto-assemblage de nanoparticules anisotropes induit par déplétion in situ (DISA). Cette approche constitue une stratégie universelle et accordable pour la création de métamatériaux, notamment de systèmes fortement ordonnés, de faible dimensionnalité (1D ou 2D) et sensibles à des stimuli externes. Cette méthode a été étudiée à l'aide d'un système modèle composé de nanobâtonnets (NR) métalliques colloïdaux (servant d'unités de base) et d'agents de déplétion micellaires formés de tensioactifs cationiques (CTAC passif ou azoTAB actif) en milieu aqueux. Ces travaux de thèse ont été motivés par deux grandes questions scientifiques : premièrement, comment exploiter *l'anisotropie ou la frustration géométrique* des nanoparticules pour créer des *suprastructures anisotropes*, chirales ou de faible dimensionnalité, conférant ainsi au matériau des métapropriétés anisotropes ? Comment les forces de déplétion jouent-elles le rôle d'intermédiaire pour transférer l'anisotropie et la frustration de l'échelle des nanoparticules à celle des suprastructures ? Deuxièmement, est-il possible de contrôler finement, dans l'espace et dans le temps, le processus DISA par l'utilisation de tensioactifs photo-commutables (tels que l'azoTAB) comme agents de déplétion ? Quel est le mécanisme régissant cet assemblage de nanoparticules contrôlé par la lumière ? Cet assemblage est-il réversible et la force attractive peut-elle être modulée en continu en fonction des conditions d'irradiation ?

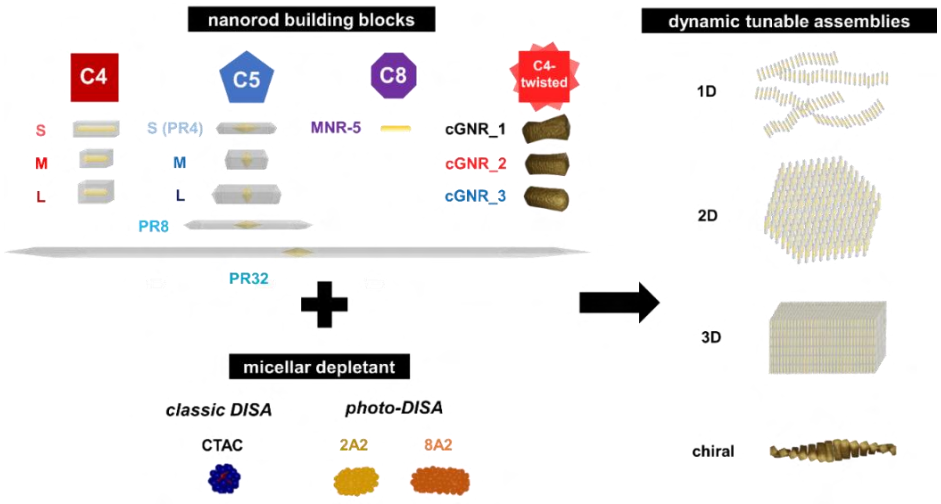

Figure 1. *Résumé de l'auto-assemblage induit par déplétion (DISA) et de ses composantes.*

Tout d'abord, nous avons conçu et étudié les deux composantes de notre système modèle d'auto-assemblage : des nanobâtonnets (NR) métalliques anisotropes (à rapport d'aspect élevé) constitués d'un cœur en or et d'une coquille en argent (core-shell Au@Ag), ainsi que des micelles de CTAC ou d'azoTAB. De nouveaux protocoles de synthèse par germination (seed-mediated growth) de tels nanobâtonnets, atteignant jusqu'à 1,1 µm de longueur, ont été mis au point, permettant l'observation directe de leur auto-assemblage par microscopie optique. Par ailleurs, nos expériences ont apporté un éclairage nouveau sur la structure ellipsoïdale des micelles de CTAC et d'azoTAB sur une large gamme de concentrations, en sondant notamment l'excentricité et la charge variable de ces micelles par diffusion de rayons X aux petits angles (SAXS).

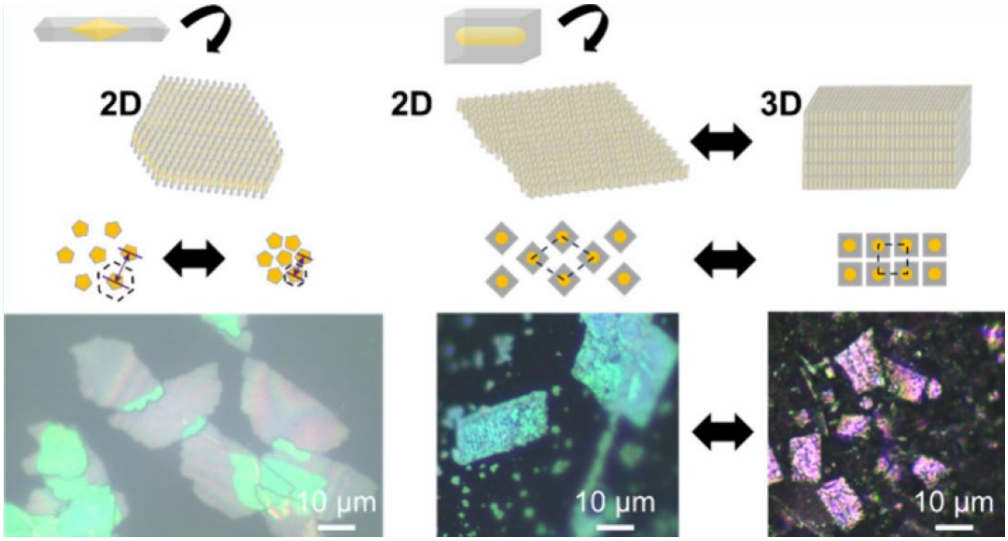

Figure 2. *Création de métasurfaces colloïdales 2D et de supercristaux 3D par auto-assemblage induit par déplétion de nanobâtonnets présentant une anisotropie de forme variable.*

À l'aide de ce système DISA à deux composantes, nous avons testé divers protocoles pour obtenir en suspension aqueuse des assemblages ordonnés de nanobâtonnets colloïdaux plasmoniques, dans le but de créer des suprastructures dynamiques et reconfigurables, par opposition aux suprastructures statiques obtenues par séchage.

Au cours de ce processus, nous avons réalisé quatre avancées notables dans le domaine du DISA :

Premièrement, nous avons observé un transfert d'anisotropie des nanobâtonnets individuels (à rapport d'aspect élevé) vers leurs assemblages. Une introduction rapide de l'agent de

déplétion conduit souvent à des assemblages unidimensionnels (1D) en forme d'aiguilles, constitués de nanobâtonnets disposés côte à côte, tandis qu'une introduction lente aboutit à des assemblages bidimensionnels (2D) de taille micrométrique — sous forme de plaquettes ou de métasurfaces — composés de nanobâtonnets côte à côte et tous parallèles entre eux, privilégiant ainsi les interactions par leurs faces latérales. Les bâtonnets nanométriques C5 (C5-NR) forment préférentiellement des métasurfaces bidimensionnelles (2D), contrairement aux C4-NR qui ont tendance à former des structures 3D ou des empilements aléatoires d'un petit nombre de suprastructures 2D. La compacité 2D de ces métasurfaces (volume occupé par les nanobâtonnets par rapport au solvant) varie entre 21 % et 80 % en fonction de la concentration en agent de déplétion et du rapport d'aspect des bâtonnets. Plus généralement, la technique DISA permet d'ajuster les espaces interparticulaires sur une large gamme de distances.

Deuxièmement, nous avons observé que la vitesse d'introduction de l'agent de déplétion dans le système colloïdal influence considérablement la réversibilité du processus DISA. Ce dernier est totalement réversible sur cinq cycles ou plus, à condition toutefois que la concentration en agent de déplétion ait le temps de s'équilibrer par diffusion lors de la durée d'un cycle.

Troisièmement, le processus DISA peut être suivi directement in situ par microscopie optique, révélant la dynamique de formation de suprastructures (régies par le mouvement brownien) de bâtonnets nanométriques, qu'elles soient 2D ou 1D. En réalisant le processus DISA avec une diffusion ultra-lente (pseudo-dialyse) de CTAC dans un capillaire long, les conditions de croissance sont proches de l'équilibre (quasi-statique), et permettent d'obtenir des assemblages cristallins atteignant 100 µm de largeur, voire davantage.

Quatrièmement, nous avons démontré que ces métasurfaces peuvent servir de substrats colloïdaux pour la détection d'analytes dilués par diffusion Raman exaltée de surface (SERS). En utilisant le 4-aminothiophénol (4ATP) comme marqueur Raman, il a été constaté que le signal SERS augmente fortement lors de l'assemblage, mais suit ensuite une évolution non monotone à mesure que la concentration en agent de déplétion continue d'augmenter. L'hypothèse avancée est que l'exaltation du signal SERS dépend fortement de la taille des domaines cristallins au sein des métasurfaces.

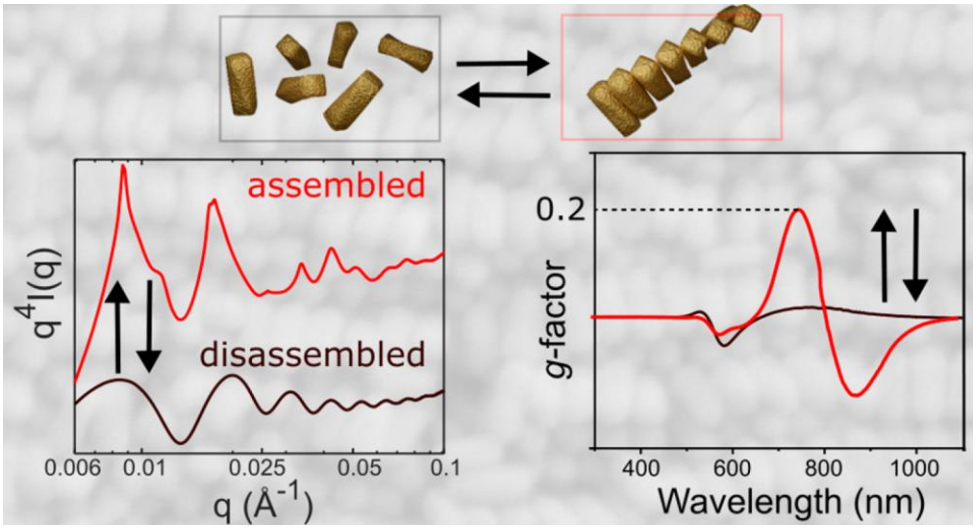

Figure 3. *Dichroïsme circulaire plasmonique (PCD) accordable dans des « métafluides » colloïdaux par auto-assemblage induit par déplétion de nanobâtonnets d'or chiraux et torsadés (cGNR).*

Dans le cas de l'assemblage de nanobâtonnets d'or (NR) chiraux et torsadés (cGNR), nous avons démontré que l'effet de déplétion peut induire leur assemblage réversible et cyclable en structures « côte à côte » frustrées, dotées d'une chiralité extrinsèque résultant de la frustration géométrique et d'un transfert de la chiralité à l'échelle nanométrique. Par l'ajout et la redilution de l'agent de déplétion CTAC, il est possible d'obtenir un dichroïsme circulaire plasmonique (PCD) modulable des cGNR en suspension, s'accompagnant d'une amplification réversible du signal chiroptique (facteur g) pouvant atteindre près de deux ordres de grandeur. La réduction du degré de torsion des cGNR par gravure oxydative contrôlée modifie la symétrie du réseau de l'assemblage correspondant — passant d'une structure 1D à une structure 2D rhombique ou hexagonale — et diminue également l'amplification maximale du facteur g. Au vu des résultats actuels, nous émettons l'hypothèse qu'il existe un rapport optimal entre la longueur des NRs et le pas hélicoïdal de leur torsade pour maximiser l'amélioration du facteur g lors de l'auto-assemblage. La cinétique de l'auto-assemblage des cGNR par DISA, en particulier en régime ultra-lent conduisant à des surfaces courbes singulières (passant de la 1D à la 3D), reste à élucider.

Enfin, en combinant des nanobâtonnets (NR) passifs (insensibles aux stimuli) avec des photosurfactants actifs à base d'azobenzène (azoTAB) agissant comme agents de déplétion, nous avons démontré un contrôle spatio-temporel de l'assemblage de nanoparticules colloïdales par irradiation lumineuse alternée avec de la lumière UV et bleue. Ainsi, à notre

connaissance, la photo-modulabilité directe de la force de déplétion a été réalisée pour la première fois, mettant en évidence plusieurs preuves d'un mécanisme d'auto-assemblage piloté par la déplétion. Cette technique « photo-DISA » peut être appliquée comme mécanisme d'auto-assemblage « valence-free », ce qui signifie qu'elle fonctionne indépendamment de la composition des particules ou de la nature chimique de leur surface et de leurs ligands. Des cycles d'assemblage-désassemblage ou d'expansion-contraction d'assemblages de NR unidimensionnels ou bidimensionnels peuvent être déclenchés par une irradiation alternée UV/bleue. Fait remarquable, des états intermédiaires ou métastables ont pu être atteints grâce à une séquence de commutations alternées UV/bleue très rapides à une échelle de temps inférieure à 10 secondes, avec une stabilisation analogue au mécanisme du pendule de Kapitza. Il a été démontré que ce procédé photo-DISA est spatialement sélectif, avec une résolution de l'ordre de 0,1 mm, permettant de créer des images par photo-structuration à partir d'une suspension de NRs et d'un masque d'image. De plus, en contrôlant la structure des assemblages de NR plasmoniques, la technique photo-DISA permet de réaliser une détection SERS in situ et modulable par la lumière d'analytes tels que le 4ATP ou le bleu de méthylène (MB).

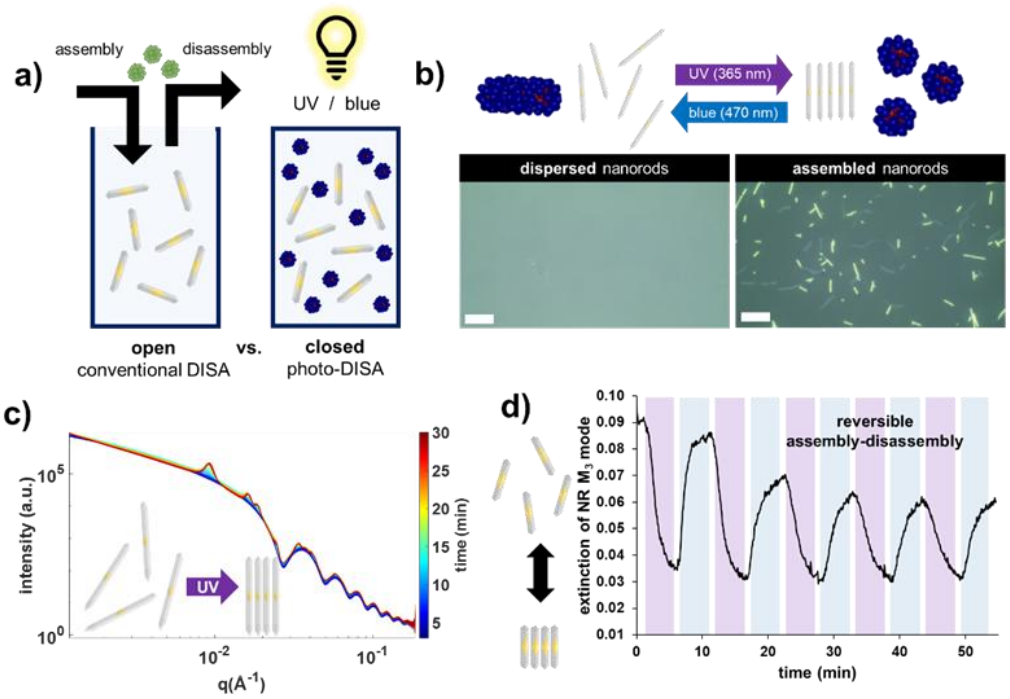

Figure 4. *Cristaux colloïdaux vivants : assemblages colloïdaux de nanobâtonnets métalliques modulables par la lumière, utilisant un tensioactif photosensible comme agent de déplétion (photo-DISA).*

Pour conclure, en jouant sur l'ingénierie précise de la forme des particules et sur l'intensité de l'interaction de déplétion, il est possible de contrôler de manière modulable et « valence-free », sous l'effet de stimuli, l'auto-assemblage de nanoparticules (NP) par DISA. Ce processus permet de propager l'anisotropie et la frustration pour créer des assemblages dynamiques, de basse dimensionnalité ou chiraux — incluant certains états métastables — capables d'agir comme des métamatériaux colloïdaux en phase liquide. Les analyses par spectroscopie SERS, UV-vis-NIR et dichroïsme circulaire (CD) ont démontré que la structure modulable de ces assemblages est corrélée à leurs propriétés plasmoniques, elles aussi ajustables. Ces travaux ouvrent de nombreuses perspectives et soulèvent de nouvelles questions, notamment concernant le transfert d'anisotropie et la dynamique de la cristallisation colloïdale. Il reste à élaborer un modèle cinétique complet ainsi qu'une description du mécanisme de DISA réversible ou de photo-DISA — en particulier pour la formation de suprastructures 1D et 2D — tout en tenant compte d'un éventuel piégeage cinétique de structures hors d'équilibre. Les méthodes d'observation directe de l'auto-assemblage de NP colloïdales par microscopie optique offrent un potentiel de développement important. Notre équipe développe actuellement des dispositifs micro- ou millifluidiques (en capillaire de verre ou en PDMS) pour réaliser des mesures in situ par SAXS et microscopie. Le procédé de DISA ultra-lent peut également être optimisé pour permettre la croissance de monocristaux dont les dimensions caractéristiques dépassent 100 µm. Concernant la photo-DISA, la stabilisation d'états d'assemblage intermédiaires, soit par photo-isomérisation partielle, soit par une séquence de commutations rapides de la longueur d'onde de type « Kapitza », mérite d'être approfondie. Une autre perspective intéressante réside dans l'utilisation d'agents de déplétion de tailles ou de charges variées (tensioactifs ou polymères, passifs ou photosensibles), afin de moduler les interactions en jeu, celles de déplétion mais aussi les répulsions électrostatiques, ceci afin de mieux comprendre comment les interactions se compensent entre elles. Enfin, les corrélations entre les signaux SERS (et leur écart-type) et les paramètres tels que le paramètre de maille moyen, la taille des domaines cristallins et la dimensionnalité de l'assemblage restent à élucider complètement.

Dans une perspective plus large, les progrès réalisés dans le domaine du DISA ouvrent la voie à trois applications notables. Premièrement, le DISA étant « valence-free », il pourrait servir à

assembler de manière réversible une vaste gamme d'autres particules, telles que des particules colloïdales minérales, polymères ou biologiques, à l'échelle nanométrique ou micrométrique. Deuxièmement, il permet de stabiliser des états de la matière molle, tels que les cristaux liquides (CL) et les gels, tels que des CL colloïdaux formés de longs nanobâtonnets (NR) bimétalliques Au@Ag, dont nous avons découvert l'existence au cours de ce projet. Troisièmement, en concevant spécifiquement les ligands des nanoparticules et en jouant sur la chimie des agents de déplétion, il est possible d'augmenter la distance entre particules au sein des assemblages induits par déplétion afin d'obtenir des métamatériaux à la fois diffractifs et photoniques avec des résonances dans le spectre allant du visible au proche infrarouge (par exemple, couleurs structurelles, résonances collectives de réseau). À ce jour, nous avons déjà confirmé l'existence de couleurs structurelles photoniques dans des CL composés de NR métalliques avec une très grande longueur/rapport d'aspect. Quatrièmement, l'utilisation combinée de plusieurs agents de déplétion (actifs ou passifs) permettrait d'obtenir des assemblages sensibles à des stimuli multiples — réagissant à plusieurs longueurs d'onde ou déclencheurs — une caractéristique recherchée pour un contrôle avancé des propriétés des matériaux.

Dans la quête de métamatériaux actifs obtenus par auto-assemblage, cette thèse a exploité des forces de déplétion ajustables et sensibles aux stimuli pour créer des « **cristaux colloïdaux vivants** » : des assemblages plasmoniques reconfigurables en milieu liquide, dotés de propriétés fonctionnelles modulables. De nouveaux développements sont toutefois nécessaires pour accroître la polyvalence et le contrôle spatio-temporel du DISA ; cela implique notamment la synthèse chimique d'agents de déplétion (en particulier des photo-agents de déplétion), des études plus approfondies sur la cinétique du DISA, ainsi que la mise au point de nouvelles techniques expérimentales pour l'auto-assemblage et son observation in situ à différentes échelles de temps.

Chapter 1

GENERAL INTRODUCTION: METAMATERIALS, SELF-ASSEMBLY, AND DEPLETION

In this introductory chapter, we will first explore the general landscape of metamaterials, particularly those with unique and collective optical-plasmonic metaproperties. We will then go through strategies of making metamaterials via top-down array fabrication versus bottom-up self-assembled superstructures of plasmonic metal nanoparticles (NPs). A brief state-of-the-art of plasmonic NPs and their applications will follow. Next, various strategies of nanoscale self-assembly will be considered in terms of making tunable and dynamic metamaterials. Finally, the depletion interaction, a well-known entropic phenomenon in colloidal science, will be explored as a novel and chemically-universal means of tunable self-assembly of NPs to achieve colloidal metamaterials. At the end, the plan and scope of this thesis will be discussed, going through each chapter, and finally noting the important challenges to be addressed in this thesis.

1.1. Towards Functional Metamaterials: Advances and Trends

Throughout history, advances in materials research have mainly been driven by the discovery of new materials like polymers or semiconductors, or by the economic demand for new devices such as in the telecommunications industry. These factors are summarized in the well-known materials science tetrahedron, where material processing, structure, property, and performance are all interconnected[1] (**Figure 1a**).

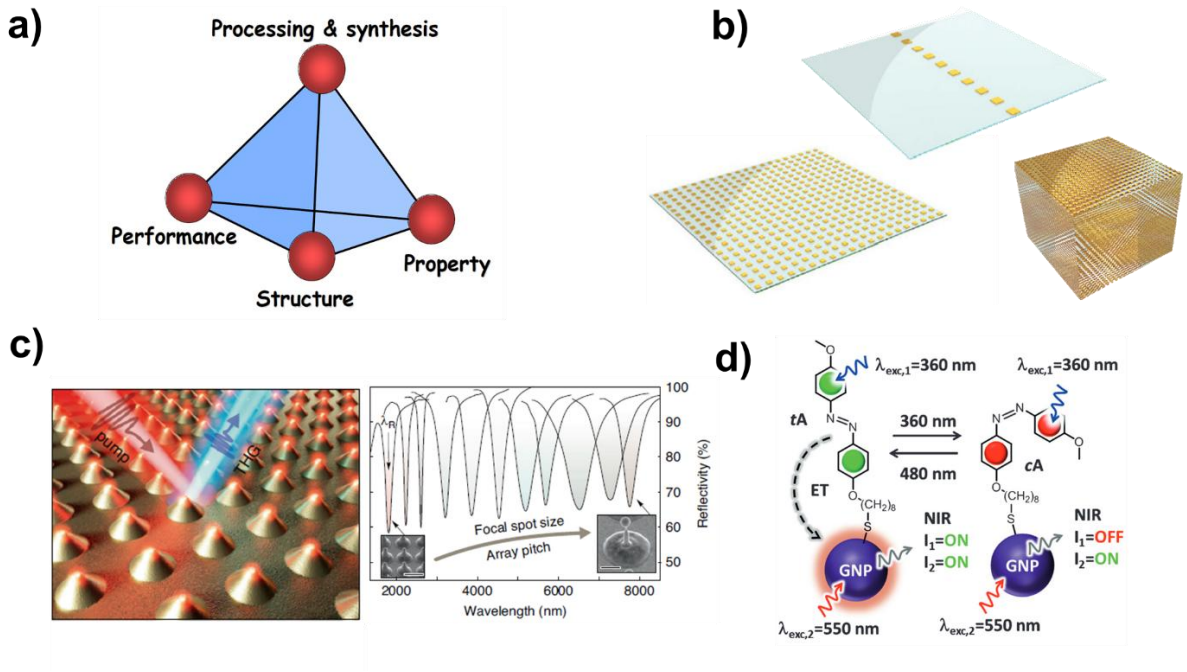

Figure 1. Concepts in metamaterials design. ***(a)*** *The materials science tetrahedron, showing the relationship between aspects of materials design*[2]. ***(b)*** *Scheme of metamaterials with collective properties by ordered arrays of 'meta-atoms' at different dimensionalities*[3], ***(c)*** *Collective optical resonant properties in plasmonic gold metasurfaces*[4], ***(d)*** *Dynamic switching of gold nanoparticle optical properties by light-sensitive azobenzene*[5].

In the past decades, there has been considerable effort in developing *metamaterials* with unique metaproperties – whether *optical, mechanical, thermal, electrical, etc.* – not found in natural or conventional materials[6]. Instead of relying on new material compositions, they rely on particular micro to nanoscale structuration of existing materials typically leading to *collective properties*. Plasmonic metals like gold or silver[3] which exhibit surface plasmon resonance (SPR), or certain semiconductors are often used to make such nanostructured materials, many times in combination with dielectrics. Such structuration enables unique properties due to quantum effects, plasmonic coupling, low dimensionality (1D/2D), or high surface-to-volume ratio and allows the miniaturization of optoelectronic devices (**Figure 1b**). Frequently, metamaterial structuration is close to or less than the wavelength of the electromagnetic (EM) radiation of interest, allowing the manipulation of light or electric fields in fascinating ways, which is desirable for energy materials, optics, electronics, catalysis, and other applications. This is the case for 2D *electromagnetic metasurfaces* which can modulate light as an ultrathin component in a device, and in certain cases exhibit sharp and collective (surface) lattice resonances (SLRs)[7,8]. Broader definitions of metamaterials can include colloidal

metal or semiconductor nanoparticles in suspension, which exhibit particular optical 'metaproperties' due to their nanometric size, and can be rendered stimuli-responsive to light or heat by coating them with appropriate ligands, thus enhancing their functionality (**Figure 1b,c**).

Early inspirations for metamaterials include natural systems exhibiting structural color and other photonic properties. Many organisms such as beetles, butterflies, birds, and fruit-bearing plants exhibit photonic structural color due to micro-structured scale-like structures[9]. Cellulose and other biopolymers can also be converted into nanocrystal particles which form chiral or cholesteric liquid crystals and gels that exhibit tunable structural color due to their pitch[10]. The challenge is achieving repeatable drying that preserves this cholesteric phase and has a pitch that leads to diffraction of visible light. These types of colors are very vivid and angle-dependent (**Figure 2a-b**). On the other hand, emergent and hierarchical 'metastructures' are also observed in biological self-assembly of macromolecules like lipids, proteins, and saccharides, leading to complex self-limited structures like vesicles or capsids. These model systems have inspired the creation of self-assembling materials exploiting anisotropy and chirality templating or transfer to greater length scales (**Figure 2c,d**).

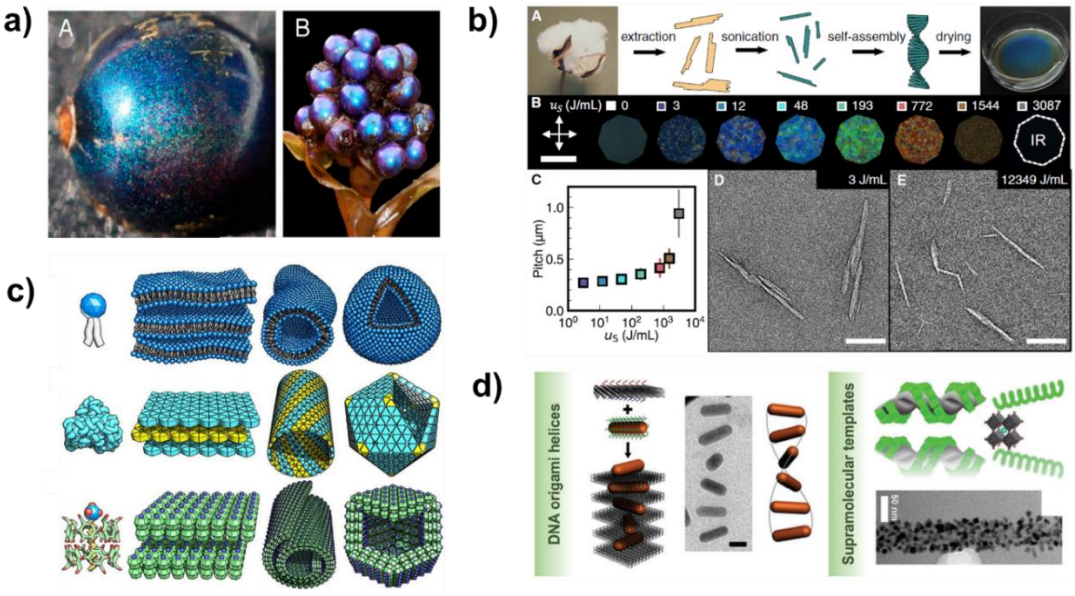

Figure 2. Biological and bio-sourced metaproperties. ***(a)*** *Vivid pointillist structural color in Pollia condensata fruit[9]* ***(b)*** *Tunable structural color via tunable pitch in cholesteric liquid crystals of processed cotton-based cellulose nanocrystals (CNCs)[10]* ***(c)*** *Biological self-assembly of lipids, proteins, or saccharides into lamellar, tubular, or vesicle structures of various geometries and curvatures[11],* ***(d)*** *Directed assembly of NPs like gold NRs and perovskite nanocrystals with DNA origami or supramolecular templates respectively[12].*

Proposals for optical metamaterials have existed since the discovery of light as a wave of EM radiation since the 19th century. As early as 1785, Rittenhouse conducted an early metasurface-like diffraction experiment with fine gratings made of hair[13]. However, it is in past fifty years where cleaner methods of metamaterial and metasurface fabrication have been developed, either by *top-down* nanofabrication, or by *bottom-up* self-assembly of plasmonic nanoparticles. In 1998, T.W. Ebbesen reported extraordinarily high transmission of light through a silver film with sub-wavelength hole arrays fabricated by a focused ion beam (FIB) system. This transmission has correctly been attributed to plasmon resonances[14]. Other developments have been driven by increased interest in bio-inspired sustainable materials and advances in nanofabrication[7]. Today's metamaterial research indeed represents a convergence of different directions of technological development from holography and diffractive optics, to micro- and nanofabrication, to plasmonic nanoparticles and their self-assembly[15].

Advances in nanofabrication, like in particle-beam, laser, or nano-imprint lithography, have enabled the realization of intricate and extended 2D electromagnetic metasurfaces with intricate and precise designs[16] (**Figure 7**). These metasurfaces use subwavelength structuration of phase-shifting elements (e.g. metal units) to control the wavefront of EM radiation by sharply tuning the phase, amplitude, and polarization of incident light, even enabling propagation with phase discontinuities[17]. This functionality using a 2D nanostructure enables the creation of flat ultrathin optics[18]. Metasurface-based optics are also now being thought of as an alternative or complement to common liquid-crystal based optics, which have some similar properties[15]. Other forms of general optical metamaterials have also come about. Metalenses like Fresnel lenses focus light in unique ways using a light and compact construction, while holography has developed to record and reconstruct wave interference, leading to a high degree of control of light. Newer printing technologies have enabled the miniaturization and higher-throughput reproducibility of these optical materials. Now, preliminary designs for 'invisibility cloaks' have also been proposed, relying on gradations of refractive indices (e.g. with negative and fractional refractive index materials, or metasurfaces wrapping around a zero-index material to guide light around an object) rendering it optically hidden from the front[19]. Similar concepts are also being employed for thermal shields and cloaks, using composite polymer layered materials[20] (**Figure 3a,b**).

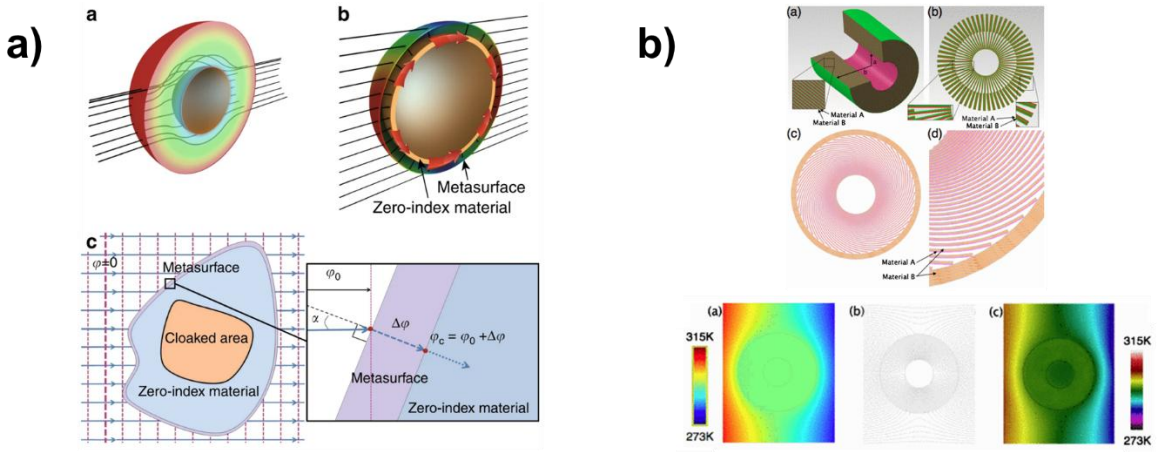

Figure 3. 'Cloaking' and other wave-playing properties using metamaterials. (a) *Hybrid invisibility cloak design using a combination of an electromagnetic metasurface and a zero-index material*[19]. ***(b)*** *Thermal/microwave heat shielding and cloaking using an anisotropic composite of latex rubber and silicone elastomer layers*[20].

While these various kinds of metamaterials are very powerful in their respective applications, their top-down nanofabrication as solid-state arrays means they have static periodic structures that usually fix their optoelectronic properties. It is true that some physico-chemical phenomena such as thermal expansion or gas ad/absorption have been exploited to render 'solid-state metamaterial' properties, including electromagnetic metasurfaces, more tunable and dynamic. For instance, the group of A. Baldi designed a palladium array metasurface with reversible hydrogen (H_2) sorption for gas detection. In this device, the collective plasmonic SLR is shifted by the gas sorption, acting as a gauge of gas concentration. Opto-thermal effects have also been used to make active wave modulation, or rewritable chalcogenide-based microprints. These and other techniques have allowed the design of optically, thermally, and electrically-tunable metasurfaces to act as beam steerers, meta-lenses, or modulators[15] (**Figure 4**, **Figure 5**).

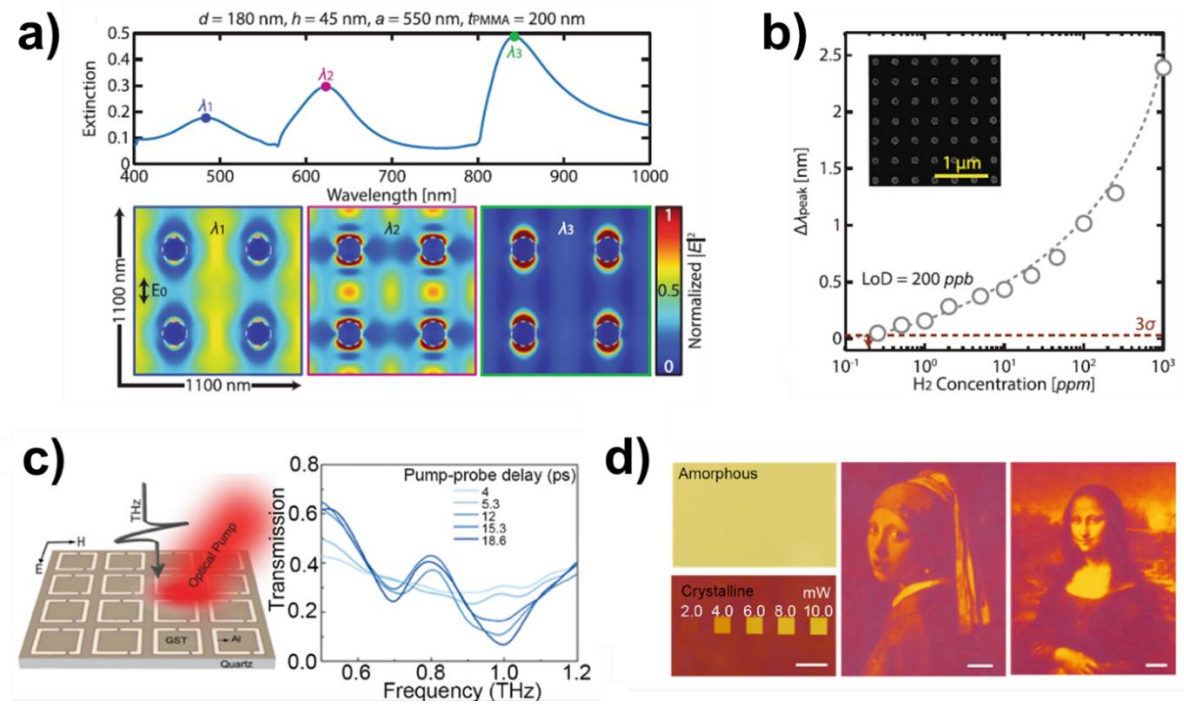

Figure 4. Tunable properties in top-down fabricated sold-state metamaterials. ***(a)*** *Ultrasensitive and low LOD ppb detection of hydrogen gas via an inverse-designed Pd array metasurface.* ***Optical*** *properties like Vis-NIR extinction and 2D normalized electric field mapping of the metasurface.* ***(b)*** *Measured shift of the surface lattice resonance in response to H_2 sorption at various gas concentrations[21].* ***(c)*** *Optically-controlled terahertz wave modulation with GST ($Ge_2Sb_2Te_5$)[22].* ***(d)*** *Chalcogenide Sb_2S_3 phase-change material (PCM) for laser-rewritable microprints[23].*

Nonetheless, in this thesis, we propose an alternative strategy of achieving dynamic properties in metamaterials. By using in situ *tunable and controlled self-assembly of plasmonic NPs* in colloidal suspension, one can conceive of *colloidal or 'liquid' metamaterials* with more dynamic metaproperties, as opposed to solid-state 2D/1D metamaterials. By broadening our vision of metamaterials in this way, we can expand the typical use cases for such systems towards liquid or colloidal media, and achieve similar extended 2D or 1D superstructures of Brownian NPs in suspension. With the increased reconfigurability of these plasmonic arrays (e.g., mechanotunable lattices, possibility of disassembly) in liquid, one can even achieve tunable, smart, or self-regulating properties in response to light, heat, or chemical environment, akin to living organisms. To create such '*living*' colloidal metamaterials via NP self-assembly, one needs plasmonic NP building blocks of the right shape and size, and a selective self-assembly method to induce the formation of well-ordered 2D or 1D colloidal superstructures or assemblies with the desired interparticle spacing.

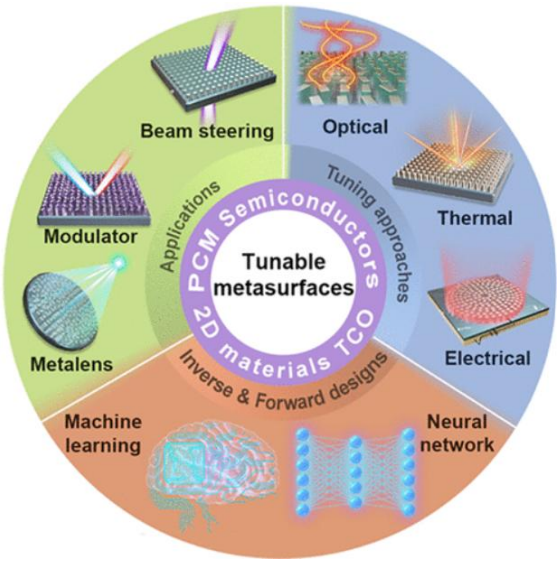

Figure 5. Diverse implementations of tunable electromagnetic metasurfaces[24].

1.2. Current State of Plasmonic Nanomaterials

When metals or semiconductors exist in the form of nanoparticles in a non-conducting or dielectric medium, they exhibit a unique phenomenon called *localized surface plasmon resonance* (LSPR or SPR), which is the resonance of coherent collective electron oscillations confined in NPs in response to electromagnetic (EM) radiation. When the NP size is smaller than the wavelength of the EM radiation, dipolar oscillation of the NP electron cloud occurs, resulting in an LSPR and an increase in the absorption and scattering cross-sections of the particle. LSPRs must not be confused with bulk plasmons or surface plasmon polaritons propagating along the metal-dielectric interface; LSPRs can strongly couple with light while the latter two cannot. Interestingly, the resonant wavelength of LSPRs can be tuned by changing the size, shape, or composition of the plasmonic NP. In particular, anisotropic rods or ellipsoids will exhibit both a longitudinal and transverse localized SPR, with tunable resonant wavelength according to the particle's aspect ratio[25]. Additionally, the EM field close to the NP surface or in the gaps between NPs in close proximity can be enhanced by several orders of magnitude, which can be leveraged for applications in spectroscopy and sending (surface-enhanced infrared spectroscopy or SEIRA, surface-enhanced Raman scattering or SERS) or in catalysis[26] (**Figure 6**).

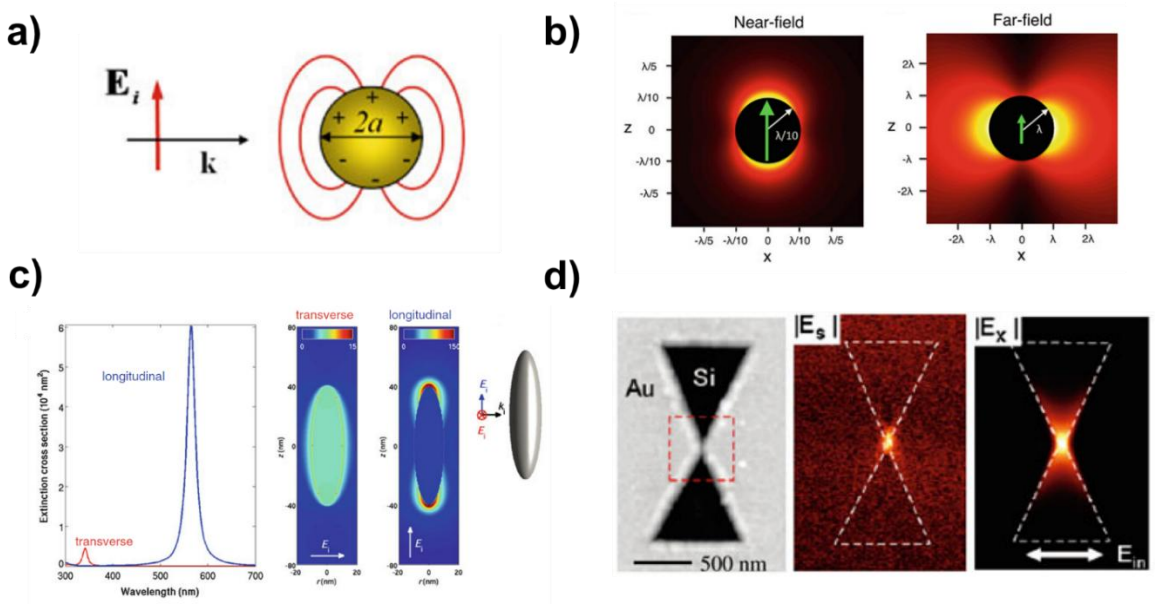

Figure 6. Plasmon resonance in metal nanoparticles. ***(a)*** *Scheme of plasmonic excitation by light and localized surface plasmon resonance (LSPR or SPR).* ***(b)*** *Modulus of the electric field amplitude for the near-field and far-field regions around a plasmonic dipole.* ***(c)*** *Extinction cross-sections for a silver nano-ellipsoid irradiated by longitudinally and transversally polarized light, showing two localized SPRs.* [26] ***(d)*** *Plasmonic near-field enhancement between tips of a 'bowtie antenna' nanocavity*[27].

As noted previously, the preparation of plasmonic materials – particularly for metamaterial applications – can be done by either a *top-down* approach starting with a bulk metal on a substrate, by a *bottom-up* approach starting from atomic or small colloidal NP precursors, or by some *hybrid* of these two approaches, for instance by using PDMS templates with a NP suspension to imprint the desired pattern on a substrate[8,16,28] (**Figure 7a**). Most top-down approaches rely on some form of particle (e.g., electron-beam), or laser beam or photolithography to directly draw a pattern onto a sensitive organic resist layer deposited on top of the substrate material (e.g., the desired metal or another material like silicon). The patterned substrate layer is then revealed by first a development step, typically immersion in a solvent to remove the unwanted resist affected by light or electrons. The pattern is then transferred or revealed by one of two methods. Via etching, a certain amount of the exposed substrate not covered by resist is chemically removed. Via lift-off, the desired metal is deposited onto the whole sample by chemical vapor deposition (CVD), and then all the resist is removed by dissolution, taking away all metal sitting on it. Working as the negative counterpart of etching, lift-off may be used to create arrays of metallic or oxide pillars, holes, nanodrums, or other shapes and patterns. Electron-beam lithography has the advantage of

accurately and flexibly drawing patterns onto the resist with resolution reaching even below 5 to 10 nm, but is very time-consuming, taking many hours to days for typical patterns on Si wafers. To increase the throughput for larger metasurfaces, *direct-write* lithography may be used to first create photomasks or imprint templates for *pattern-transfer*, akin to the stamp in traditional ink printing, which can then be repeatedly used to pattern substrates. Many variations of lithography and similar methods also exist to improve the practicability, uniformity, and resolution of fabrication. These include plasmonic lithography, nano-imprint lithography, laser ablation, and even self-assembly lithography, where the spontaneous organization of colloidal particles (e.g., polystyrene spheres into a hexagonal monolayer at an air-water interface) (**Figure 7b-d**) [16,24,29].

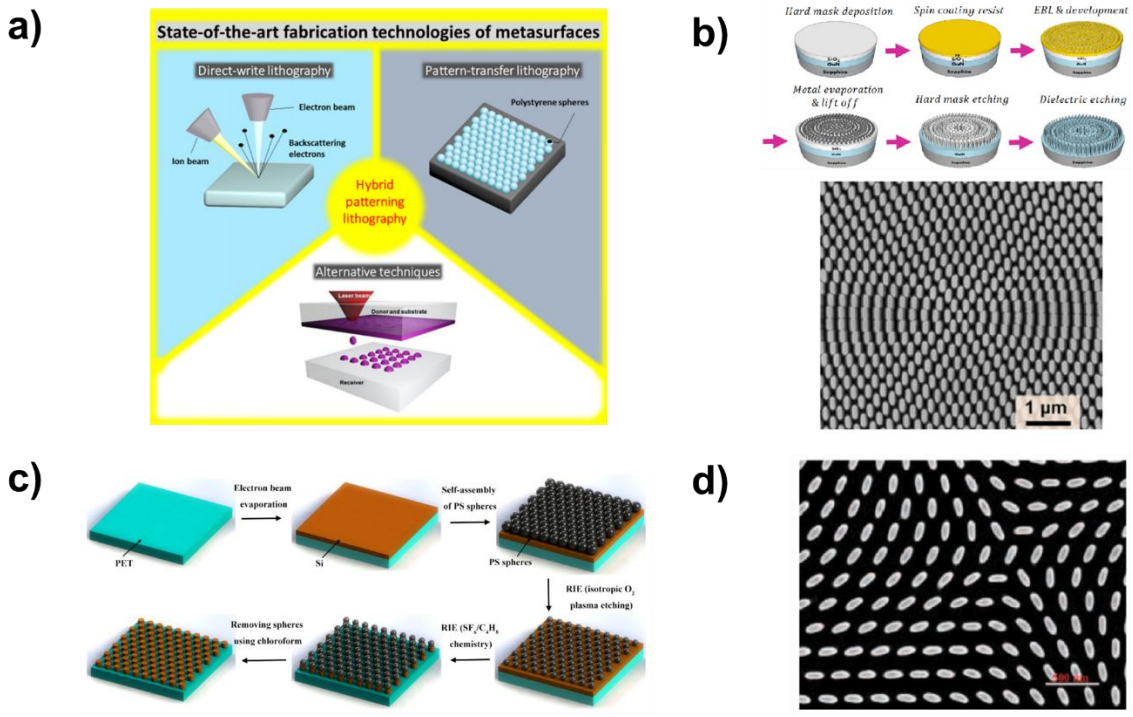

Figure 7. Top-down nanofabrication of metasurfaces. ***(a)*** *Main types of substrate-based top-down fabrication,* ***(b)*** *Steps for a typical metasurface preparation by e-beam lithography via the lift-off method, here for a GaN-based metalens[30],* ***(c)*** *Pattern-transfer lithography using the monolayer self-assembly of polystyrene spheres[29],* ***(d)*** *A chiral metasurface fabricated by focused-ion beam lithography[31].*

On the other hand, the self-assembly of individual plasmonic NPs from colloidal suspension can be used for direct bottom-up preparation of metamaterials or metasurfaces. This often requires highly monodisperse particles in terms of shape and size, and good control of self-assembly by doing NP ligand exchange, monitoring the rate of evaporation of the NP suspension, or using substrate treatments to attain a well-organized monolayer of particles[32,33].

To create free and high-quality colloidal metal nanoparticles, wet synthesis by chemical reduction of metallic precursors in solution is most often employed. Here, a combination of precursor, reducing agents, and templating or shape-directing agents are used to achieve the desired NP shape and size. In this synthesis, the formation of NPs can be described by the LaMer model, which consists of three phases. In phase I (reduction), the metal precursor is converted to reduced solute atoms, and solute concentration [M^0] increases linearly over time, but the atoms cannot yet form into particles (i.e., crystal nuclei) due to the free energy cost of forming a new solid phase. In phase II (nucleation), the [M^0] reaches a critical concentration C_{crit}, where small nuclei particles cam form from the coalescence of solute atoms and remain stable, leading to a decrease of the free energy and of the solute concentration. Then in phase III (growth), the nuclei increase in size as more solute atoms attach onto them, leading to larger NPs (**Figure 8**)[34,35].

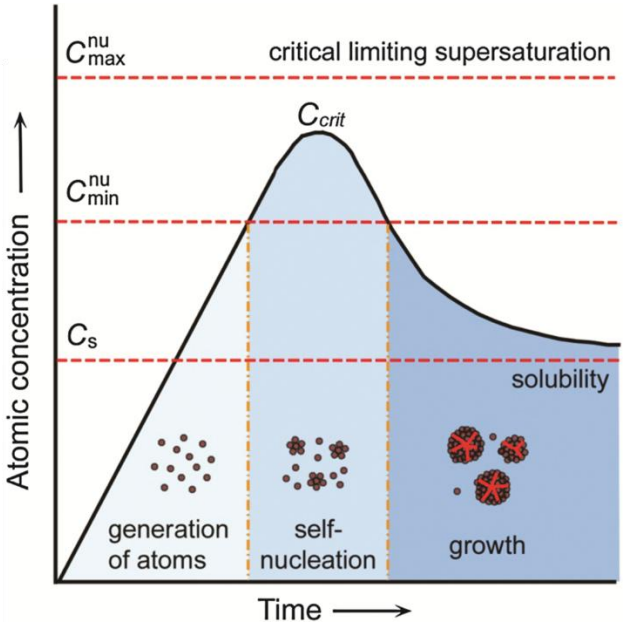

Figure 8. The LaMer model of nanoparticle formation: *Plot of changing concentration over time of reduced metal atoms at different stages of crystallization. Figure adapted from Y. Sun[35].*

During the growth step or during long-term storage of NPs, a phenomenon called Ostwald ripening also often occurs, where the average NP size can grow even without continual reduction of metal precursor, as smaller NPs get dissolved and their atoms get incorporated into larger NPs, to reduce the surface free energy of the system. This ripening phase tends to decrease the size polydispersity of the particles. On the other hand, in real synthesis protocols, the nucleation and growth phases often overlap, and the time period of nucleation can

sometimes get prolonged, leading to higher size polydispersity since the growth of newly formed nuclei lags behind the previously formed ones. Therefore, good kinetic control of NP synthesis is essential, including temperature control, to separate nucleation from growth. One must also keep the nucleation period as narrow as possible by fast, uniform addition of appropriate reducing agents[34–36].

Many NP syntheses use polyols as both solvent and reducing agent, but require quite high temperatures to have efficient throughput[37]. As an alternative, aqueous colloidal NP synthesis is also done, using reducing agents of different reducing power. As mentioned, to achieve high monodispersity of NP morphology necessary for synthesis, it is important to decouple nucleation from growth, and control any subsequent Ostwald ripening. Therefore, by the turn of the 21st century, methods of *aqueous seed-mediated growth* have been developed to increase the reproducibility of colloidal NP synthesis. For most shapes, typical seed-mediated growth proceeds in three steps: (a) seed (nuclei) formation with symmetry breaking or twinning where the seeds are NPs typically less than 10 nm in size, (b) growth step onto the seeds, typically with chemical agents like ions or organic compounds to promote growth into anisotropic shapes, and (c) subsequent growth (regrowth) steps to enlarge or modify the shape and composition of the NPs, for instance when making core-shell or heterometallic NPs (**Figure 9a**). Note that the crystallinity of the seeds is essential, as they dictate the crystallinity of the final NP after the growth steps. Monocrystalline seeds yield monocrystalline NPs, and polycrystalline seeds with twin planes yield polycrystalline NPs, for instance pentatwinned particles like pentagonal bipyramids with 5-fold symmetry. Fresh seeds should ideally be used for growth, to ensure that the seeds have good size monodispersity and preserve the correct crystallinity or twinning or lack thereof[36,38].

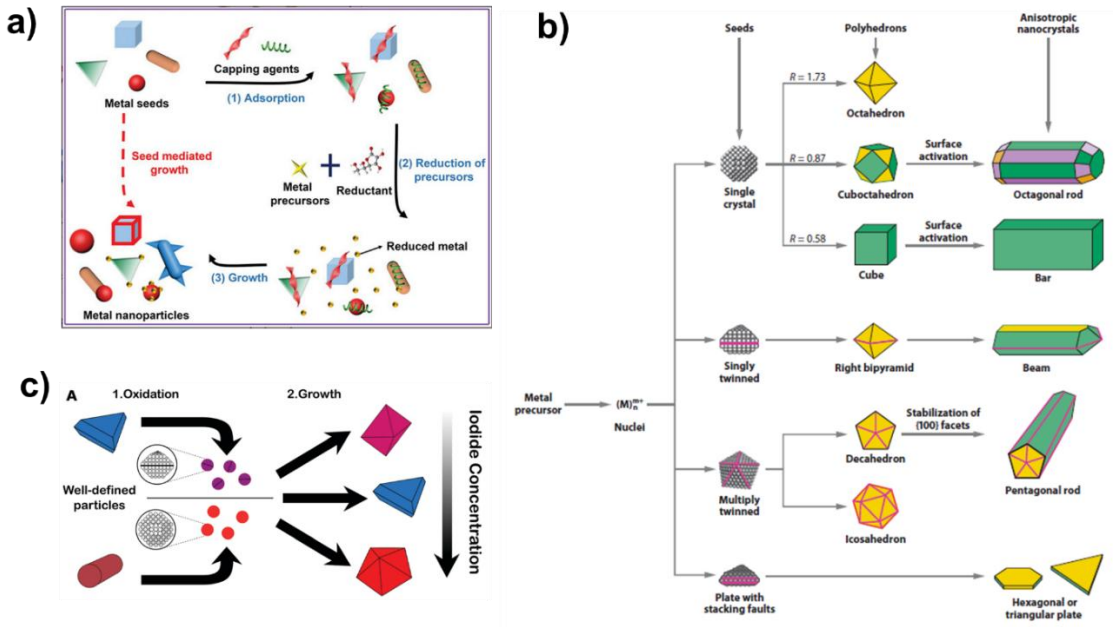

Figure 9. Advances in reproducible metal nanoparticle (NP) synthesis: (a) *General scheme of seed-mediated growth of metal nanoparticles*[39]. ***(b)*** *Pathways of synthesizing different shapes of palladium NPs by controlling seed twinning and controlling the growth on specific crystallographic planes*[40]. ***(c)*** *Metal NP synthesis using iodide as a shape-inducing agent and seeds with well-defined size and crystallinity*[41].

The key to achieving a desired anisotropic NP shape is the stabilization or passivation of certain facets (i.e., crystalline planes) of the growing NP, while promoting growth on other facets. This is done by first slowing down the growth kinetics by temperature control and by using reducing agents with the right reducing power. Various additives in solution can then be used to passivate or activate certain facets. These additives can be acid to lower pH, ions like Br^- or Cl^-, and even certain surfactants (**Figure 9b,c**)[38,39,41–43].

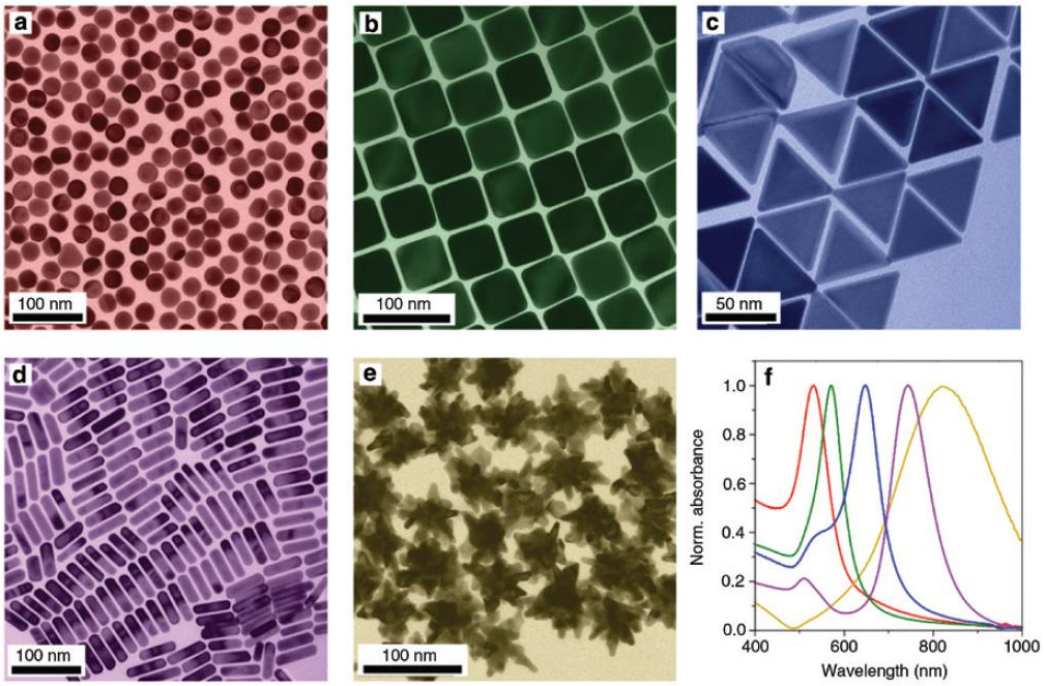

Figure 10. Diverse shapes of gold nanoparticles seen by transmission electron microscopy: (a) *spheres,* ***(b)*** *cubes/hexahedrons,* ***(c)*** *triangular platelets,* ***(d)*** *nanorods, and* ***(e)*** *nanostars, with their corresponding* ***(f)*** *color-coded UV-vis-NIR extinction spectra. Adapted from L. Scarabelli*[38].

They are often used in combination in varying ratios to stabilize different crystalline planes, leading to different shapes with variable amounts of truncation. Thus, with seed-mediated growth, a wide range of shapes can be achieved like polyhedral (cubes, octahedra, tetrahedra), platelets (nanotriangles, hexagonal plates), and elongated shapes (bipyramids, nanorods, bars), and more bizarre pointed structures (tetrapods, nanostars) in a variety of sizes and aspect ratios, depending on the crystallinity of the seed, the amount of metal precursor added, and the specific surface passivation/activation agents used (**Figure 10**). Additionally, it has been discovered that more 'trivial' parameters like stirring and water quality can also have a big impact on the quality of the synthesized NPs[38,40,44–46]. Finally, recent advances in the seed-mediated growth, such as disconnecting the symmetry breaking and growth processes, have allowed for more fine-tuned control and robust, reproducible synthesis of highly anisotropic NPs like nanorods (**Figure 11**)[41,43,46].

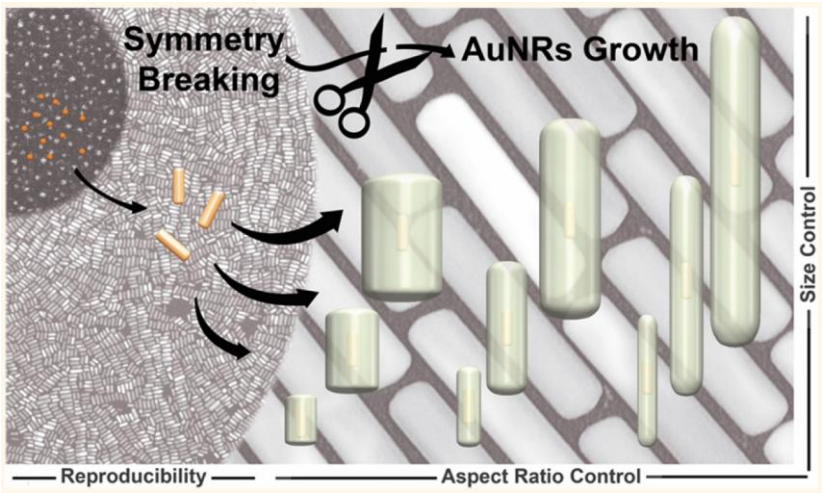

Figure 11. Separated control of nanorod (NR) aspect ratio and size by disconnecting the symmetry-breaking and growth processes during NR synthesis. *Adapted from G. González-Rubio, et al.*[46]**.**

In spite of these advances however, certain limitations and perspectives remain for colloidal metal NP synthesis. First, the synthesis of very long NRs (above 1 micron in length), or very complex shapes like twisted chiral NPs remains low yield and difficult to reproduce[47,48]. In the case of long NRs, fine control of temperature and slow of addition of reagents in large synthesis batches requires further optimization[49]. Second, our understanding of the real structure, properties, and complex role of surfactant (and other) ligands in NP synthesis, capping, and aging remains limited. Both experimental and theoretical studies, including numerical simulations will be needed to advance our knowledge in this matter[50,51]. Many synthesis protocols also remain confined to the ligand capping paradigm[52]. Additionally, ligand-exchange methods exist but can be improved due to the difficulty of removing certain ligands like CTAB for certain applications, and CTA+ and other surfactant-free synthesis have yet to be fully developed[36]. Third, the use of external factors like light, chelating agent, or templates (e.g., micelles) during synthesis to create complex NPs has much unexplored potential for creating new NP shapes – including chiral ones – with better efficiency or different pathways[39]. Fourth, high throughput and continuous NP synthesis protocols, such as with microfluidic chips, must remain a priority for development[53]. Finally, more comprehensive studies plus aid from computer modelling and machine learning could bridge the gap between practical lab synthesis and theoretical modelling of NP growth. In this regard, more efficient screening methods of reaction parameters is needed. Likewise, advanced and in situ

characterization techniques, such as advanced liquid cell TEM, will be required to probe NP growth in situ[54].

As an alternative to traditional metal NPs for plasmonics, NPs made of other materials like metal oxides and semiconductors have been developed to achieve plasmonic metaproperties. For instance, semiconductor 2D nanocrystals exhibit unique electronic properties, particularly for luminescence and other optics in the infrared range[55]. Doped metal oxide rods and platelets with variable crystalline structure and particle shape are a promising alternative to achieving tunable SPRs[56]. These nanocrystals have also been demonstrated to form designer IR metasurfaces, including for light-switching applications[57,58]. Other non-metallic plasmonic particles made from chalcogenides, nitrides, and MXenes have also been utilized for photocatalysis, energy conversion, and environmental remediation. Such NPs have the advantage of having adjustable carrier density and LSPRs over a wide optical range in the UV-vis-NIR, though more studies on their mechanisms of photocatalysis and their photothermal effects are required to optimize these systems (**Figure 12**)[59].

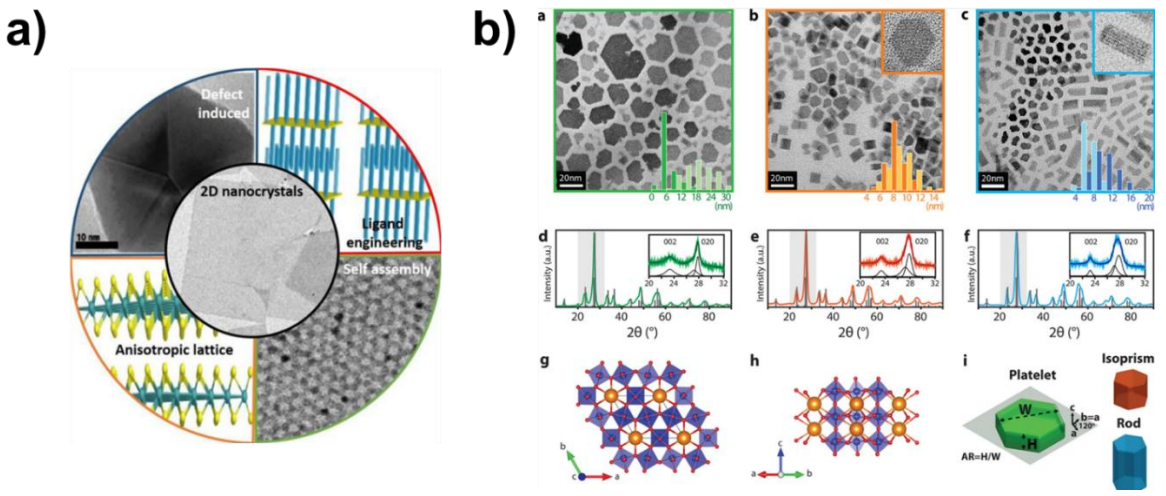

Figure 12. Non-metallic and anisotropic plasmonic nanoparticles. (a) *2D platelet nanocrystals of semiconductors, particularly cadmium chalcogenides[55] ,* ***(b)*** *Cesium-doped tungsten oxide (h-Cs:WO3) nanocrystals with different aspect ratios exhibit tunable visible to near-IR localized surface plasmon resonance due to their shape anisotropy[56].*

In the field of noble metal plasmonics, the technique of surface-enhanced Raman scattering (SERS) has emerged as a powerful and specialized tool for analyte sensing in various fields, like in the biomedical industry, chemical reaction monitoring, or environmental protection. In SERS, molecular analytes exhibit enhancement of their Raman scattering signal by several orders of

magnitude when adsorbed onto a rough metal or plasmonic surface, including individual metal NPs or their self-assembled structures[26,60]. Three notable strategies exist to optimize the detection of ultra-low concentrations of analyte adsorbed onto plasmonic NP surfaces. First is the engineering of the NP shape and composition. In particular, narrow and pointed NP shapes induce greater 'tip enhancement' of the electric field, leading to greater SERS signal. Such morphologies include nanostars or thin nanorods or pillars[60]. Second is the creation of SERS platforms that can efficiently select or confine the analytes, whether in composite nanoshells[61], encapsulation by self-assembly, 2D nanometric-confinement geometries, or superhydrophobic and high-roughness substrates that concentrate analyte solutions upon drying[62]. Third is the use of highly-ordered supercrystals or assemblies of plasmonic NPs, where electric field enhancement is heightened by plasmonic coupling in the many gaps between the nanorods, and potentially by the large-domain crystallinity and coherent orientation in the supercrystals (**Figure 13**)[63,64].

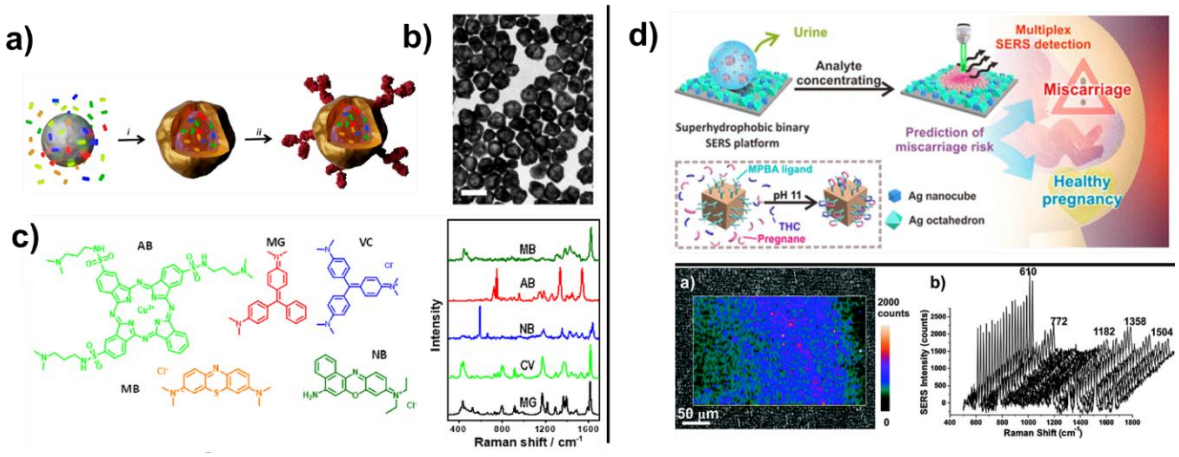

Figure 13. Sensing of analytes with plasmonic nanoparticles via surface-enhanced Raman scattering (SERS). (a-c) *Combinatorial encapsulation and detection of multiple compounds in silver core – gold shell hollow nanoshells[61]. **(d)** Reproducible and multiplex identification of urine metabolites via a superhydrophobic plasmonic SERS substrate for miscarriage risk quantification[62].*

One emerging challenge in the field of plasmonic NPs is the mimicry and exploitation of biological functions such as structural colors, selective catalysis, hierarchical structure – including chirality transfer, and stimuli-responsiveness. For example, SERS nanotags, an emerging class of labelling agents, have employed bioconjugation using antibodies or complementary oligonucleotide strands to achieve highly-specific targeting of analyte molecules[60]. Chiral templating has also been used to create unique plasmonic structures like

gold NP helices, using silica nanohelix templates whose chirality was transferred from tartrate and Gemini surfactant assembly[65], or helically-wrinkled gold nanorods by NP regrowth with adsorbed chiral wormlike micelles of CTAC with dissymmetric co-surfactants like binamine[48]. Finally, a biomimetic 'butterfly wing' micro/nanoarchitecture made of bismuth vanadate (BVO), combined with gold nanorod antennas loaded inside, has been shown to heighten red to near-infrared (NIR) light absorption for efficient solar photocatalysis (**Figure 14**)[66]. In all these emerging applications, the programmability of the induction of hierarchical structure determines the plasmonic metaproperties of the system.

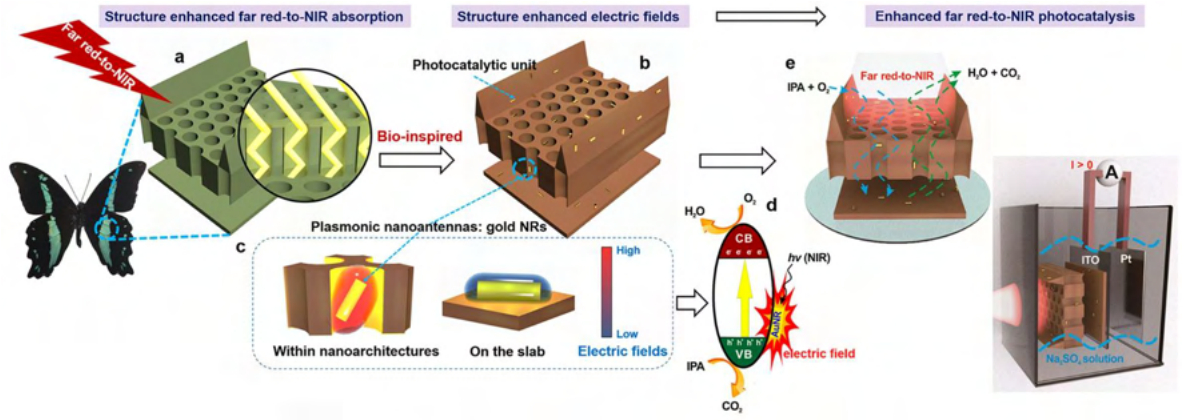

Figure 14. Bio-inspired plasmonic photocatalysis with enhanced light absorption and electric field via butterfly-wing inspired microcavities[66].

1.3. Nanoscale Self-Assembly: Models, Methods, Probing, and Outlook

This study of self-assembly processes at the nanoscale, also termed or overlapping with colloidal self-assembly, is multi-faceted. It concerns first the methods of NP self-assembly, the theoretical models of assembly, and techniques for probing the assembly process. This thesis focuses experimentally on the methods and probing techniques, but in light of theoretical predictions and questions raised by non-classical and entropy-driven crystallization/assembly models[67,68].

Self-assembly refers to the spontaneous organization of individual building blocks into well-ordered structures without direct external direction or manipulation of the blocks. Typical examples include the self-assembly of lipid molecules into micelles or membranes, or the crystallization of water into well-defined ice crystals like snowflakes. In materials and colloidal

science, stricter definitions of self-assembly often require that this organization be reversible, occur in a fluid medium (i.e., in a colloidal suspension), be mediated by weak interparticle forces, and lead to a higher degree of order than the isolated blocks. In classical *equilibrium* self-assembly (ESA), a thermodynamically stable ordered state is reached with minimum free energy in a local or global maximum of entropy. In this case, the interaction strength between particles is typically weak and close to the energy of thermal Brownian fluctuations. On the other hand, *far-from-equilibrium or dynamic self-assembly* (DSA) results from high interaction strength and fast assembly kinetics, and results from kinetic traps, or is maintained by a continuous supply of external energy, whether mechanical, light, or thermal (**Figure 15**)[67,69].

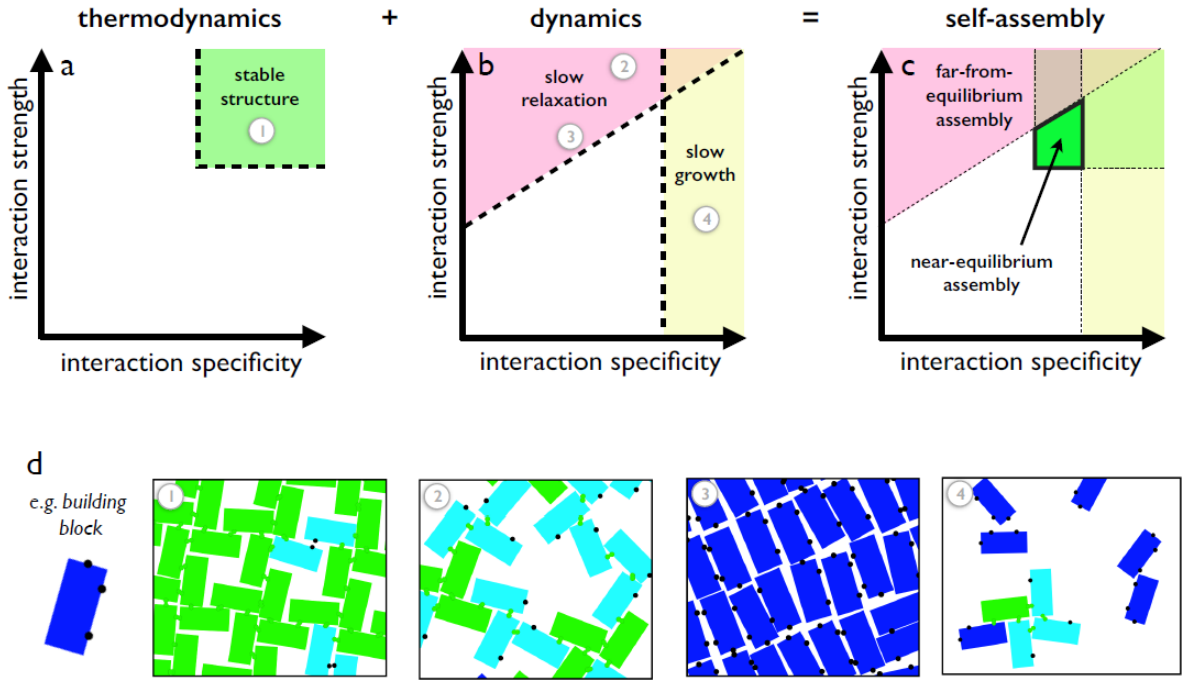

Figure 15. Conflict between thermodynamic stability and kinetic accessibility in the process of self-assembly[70].

The pathway to a self-assembled state requires a balance of thermodynamic and kinetic (i.e., dynamic) considerations. While interaction strength and specificity are both required for ESA nor near-ESA, these two factors compete. Moderate strength and specificity throughout the assembly process are required to allow both 'proper' interparticle interactions and relaxation to correct 'wrong' interactions. This is very important in the assembly of highly complex or anisotropic shapes or in multi-component systems, with soft particles or matter (partly shape-deforming), and in systems which tend to self-assemble faster and possibly aggregate, as in

nanometric versus micrometric colloids[68,71,72]. Moreover, many colloidal systems tend to self-assemble by *non-classical crystallization* with aggregative growth, as opposed to classical crystallization which proceeds only via monomer-by-monomer addition onto nuclei. Non-classical crystallization introduces complexity, frustration, and metastability to assemblies, and features in biomolecular systems like proteins[73]. Spatially and temporally controlling the emergence of order from disorder in ESA or DSA is fundamental challenge in materials science. Therefore, new theories and predictive models are required to improve our understanding of entropy and of non-classical crystallization (**Figure 16**)[68].

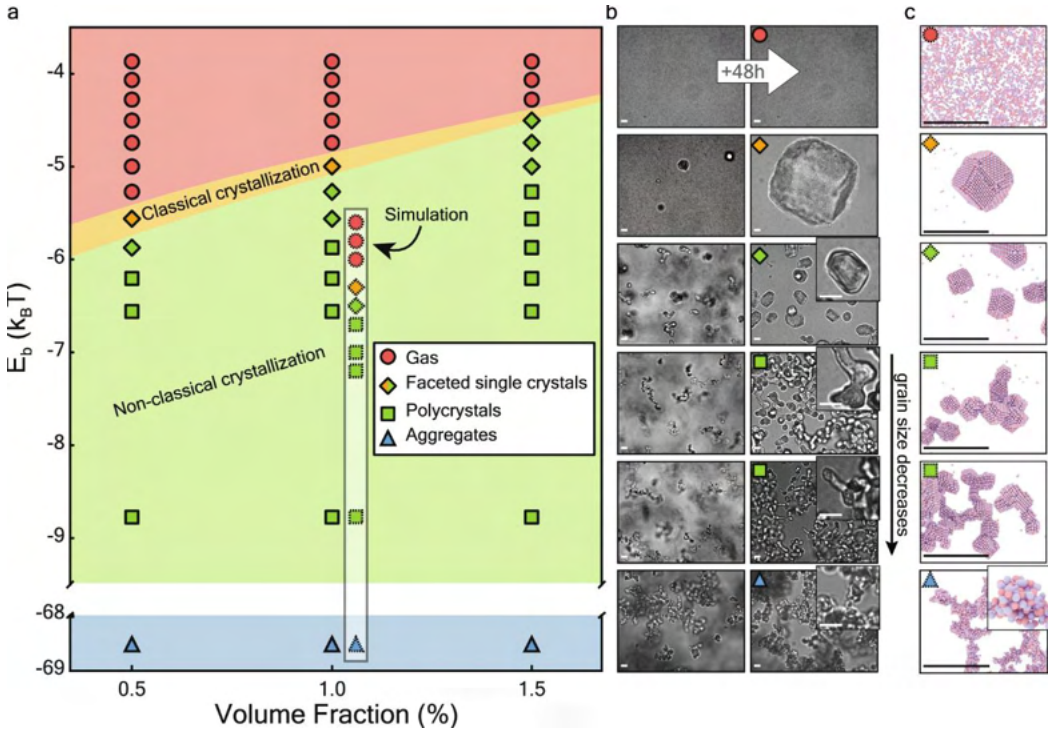

Figure 16. Non-classical crystallization and phase interconversion in the electrostatic self-assembly of colloidal particles[68].

More experiments on anisotropic particle ESA and DSA, especially kinetic experiments at a range of short to long timescales is needed to greatly improve our understanding of ESA and DSA. One such study uses water dialysis in a capillary to achieve electrostatic co-assembly of oppositely-charged colloids at different assembly rates, effectively performing many parallel kinetic experiments at the same time and accessing different states of assembly (e.g., gaseous, gel, aggregates, polycrystals, single crystals) – even those out-of-equilibrium, including previously unobserved binary supercrystal structures. These and other similar studies used optical microscopy to directly observe assembly in colloidal suspension in real time, and

supported their conclusions on kinetics and mechanisms with molecular dynamics (MD) simulations[68,74].

Second, a wider variety of self-assembly methods can be explored to extract common aspects in the mechanisms and control parameters in colloidal and stimulus-driven DSA more generally. The use of different methods could expand our view on possible types of assemblies that can be used for metamaterials. Below are listed the main types of self-assembly methods used for nano- to microscale particles, highlighting their unique advantages and drawbacks (**Table 1**). Among these, two major limitations stand out. First, many methods yield static dry structures on substrates, which are non-reconfigurable. Second, these methods have mainly been used to self-assemble spherical metal NPs, while the controlled assembly of rods and other anisotropic shapes remains quite limited, with rare observation of polymorphism[75]. Third, some of these methods require complex chemical functionalization or ligand exchange which hinders their practicability for the assembly of other NP types or compositions. Nonetheless, there exist many interesting multi-stimuli responsive ligands like pNIPAM, or co-assembling agents like spiropyran or porphyrin-based complexes, which change their physico-chemical properties in response to mechanical, light, temperature, or chemical stimulus[76–78]. Among these self-assembly methods, the depletion force is unique as a purely physical and entropic interaction. The depletion interaction strength does not rely on the NP composition nor the ligand chemistry, but on the presence of small Brownian *depletant* particles hitting the NPs which induce attractive osmotic pressure[79–81]. Therefore, depletion could be considered a 'valence-free' or universal strategy of self-assembly. Depletion will be properly introduced and surveyed in the next and final section.

Table 1. Comparison of current nanoparticle self-assembly methods in terms of creating tunable metamaterials[8,12,72,77,79,82–91].

Method	Groups / PIs	Advantages	Drawbacks
Evaporation-induced: On substrate	***X.C. Ye (Indiana)*** ***N. Kotov (Michigan)***	Very large crystalline domains 2D or 3D supercrystals	Static structures Long assembly times Typically, strong substrate effects

Evaporation-induced: Templates and confinement	***A. Mihi (Barcelona)*** ***H. Wolf (IBM Zurich)***	Facile creation of ordered arrays Integration into micro- or millifluidic chip setups Possible control of NP orientation	Static structures Reproducibility of drying
Interfacial (e.g., air-water, liquid-liquid)	***H. Duan (NTU)*** ***C.B. Murray (Pennsylvania)***	Creates thin and large-scale 2D assemblies High surface-to-volume ratio	Needs good surface chemistry / ligand control
Soft matter templates (e.g. PDMS, liquid crystals, etc.)	***A. Fery (IPF Dresden)*** ***I. Smalyukh (UC Boulder)***	Tunable in fluid / gel / colloidal suspension	Optical or chemical interference of templating medium
Freezing-induced / Directional freezing	***M. Impéror (LPS Orsay)*** ***D. Wang (Wuhan)***	Creates directional porous assembled materials	Mostly applied on polymer chain or amphiphilic molecule self-assembly
DNA / oligonucleotides (as ligands) or DNA origami (as templates)	***C. Mirkin (Northwestern, USA)*** ***A. Kuzyk (Aalto)*** ***L. Na Liu (Stuttgart)***	Programmable interparticle attraction Structural complexity and precision Partial effective shape-modification of NPs	Limited number of particles can be assembled Too strong and specific attractive forces Complex ligand / origami preparation
Solvophobic or polar interactions	***E. Kumacheva (Toronto)***	Can be coupled with thermal or light stimulus	Need for ligand exchange More difficult to obtain 2D 'metasurfaces'
Electrostatic / Coulombic	***R. Klajn (ISTA)***	Modulable by controlling ionic strength Binary and multicomponent assemblies	Too strong attractive forces
Depletion forces (DISA)	***H. Lekkerkerker (Utrecht)*** ***S. Sacanna, D.J. Pine, P.M. Chaikin (New York)***	Universal or 'valence-free' Can be induced by micelles or other Brownian particles (polymers)	Entropic effects may cause hysteresis Disassembly needs dilution of depletant suspension More reconfigurable for micrometric particles

	S. Glotzer (Michigan)		

Another important aspect of DSA is hysteresis in cyclic assembly-disassembly, which has been the focus of several recent studies on stimuli-responsive metal NP systems. For example, kinetic rate-dependent hysteresis was observed in the temperature-induced clustering of negatively-charged spherical gold NPs in an agarose gel, due to a difference in the temperature of clustering versus that of disassembly. In this case, the degree of assembly was monitored by its UV-visible extinction. Interestingly, the degree of hysteresis (i.e., area inside the assembly vs. temperature hysteresis curve) increased when assembling larger NPs, while the average degree of assembly during each cycle could be tuned by ionic strength (**Figure 17**)[92]. In the case of biomolecular self-assembly like with elastin-like polypeptides (ELPs), increasing peptide concentration and hydrophobicity generally increased the irreversibility of their temperature-induced assembly[93]. On the other hand, the contraction and expansion of colloidal depletion-induced assemblies of metal nanoplatelets did not exhibit hysteresis upon repeated heating-cooling cycles, nor by cycling between high and low salt concentration[84].

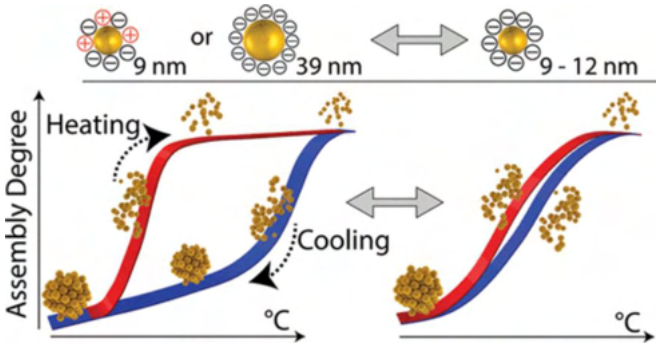

Figure 17. Kinetic and thermodynamic hysteresis in metal nanoparticle assembly-disassembly affected by particle size and charge[92].

A final outlook on nanoparticle self-assembly is the regulation of frustration (e.g., in particle packing, inability to tile space, or the need to alter NP orientation within the assembly) and self-regulation or self-limitation in growth, particularly using stimuli, mimicking behavior seen in many living organisms[94]. Here, self-regulation refers to how a self-assembling system limits or controls its own size or structure in response to its continual growth. In particular, chiral frustration and self-regulation over different length scales plays a significant role in the hierarchical structure of many living systems, such as plant tendrils, filamentous virus proteins,

and mollusk shells[95]. Understanding of the origin of this transfer of chirality, frustration, or anisotropy is critical to developing bio-inspired DSA, especially in making self-limited 1D, 2D, or chiral structures which are desirable for metamaterials. However, due to the complex shape of chiral and twisted NPs and the difficulty of their synthesis, studies on their self-assembly are more limited versus simpler particle shapes, or versus bio-sourced chiral particles which are more geometrically uniform and size-monodisperse[47,48,96]. Nonetheless, one study on the depletion-induced self-assembly of M13 bacteriophage virus rods has demonstrated the possibility of in situ tuning of chirality self-regulation through magnetic field application to change both the size and shape of assemblies (**Figure 18**)[88].

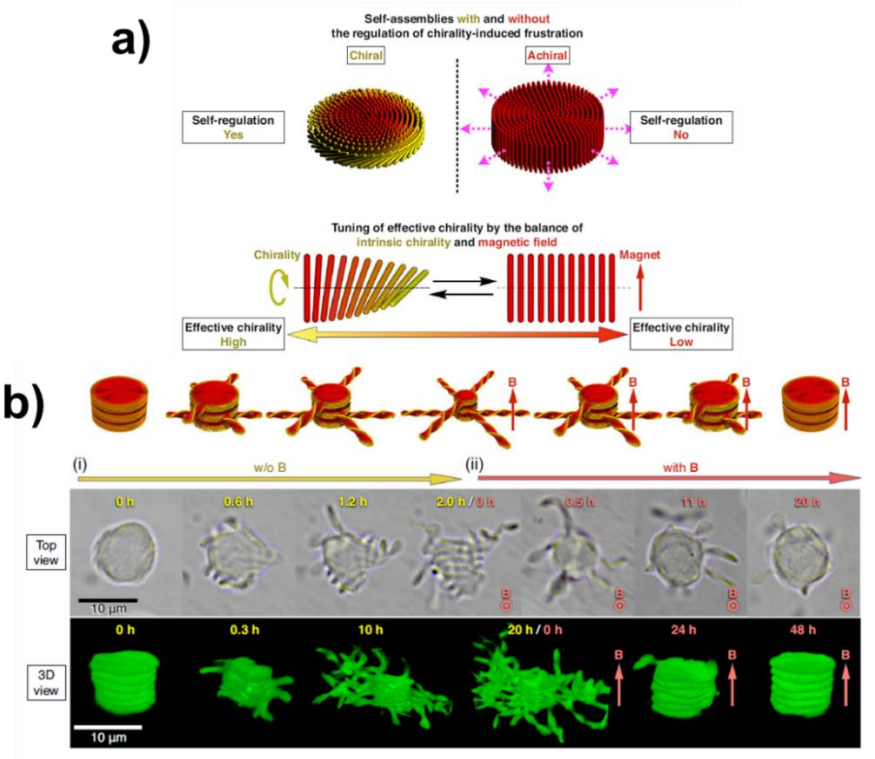

Figure 18. Magnetic tuning and self-regulation of frustration in the self-assembly of chiral virus rods[88]. (a) *Scheme of tuning effective chirality-induced frustration by magnetic field application onto magnetic chiral virus particles.* ***(b)*** *Changing magnetic field strength causes deformations in existing virus rod assemblies by tuning self-regulation.*

1.4. The Depletion Interaction, Entropy, and Soft Matter

Many properties of everyday products such as food, cosmetics, and paint are governed by their colloidal stability. These products are typically suspensions containing nano- to microscale *colloids* (e.g., NPs), and smaller *depletant* particles (e.g., suspended polymer chains, surfactant micelles, or large solvent molecules), both of which exhibit Brownian motion in the liquid medium. When the concentration of depletants exceeds a critical value, the larger colloids experience an effective attractive force when they approach such that depletants cannot enter the space between them (i.e., their depletant exclusion volumes overlap), leading to a net osmotic pressure pushing the colloids together. This depletion interaction is *entropic*, and can be described as a maximization of the depletant entropy: fractionally increasing the space occupied by depletants by fractionally decreasing the space between the colloids (**Figure 19**)[79,80].

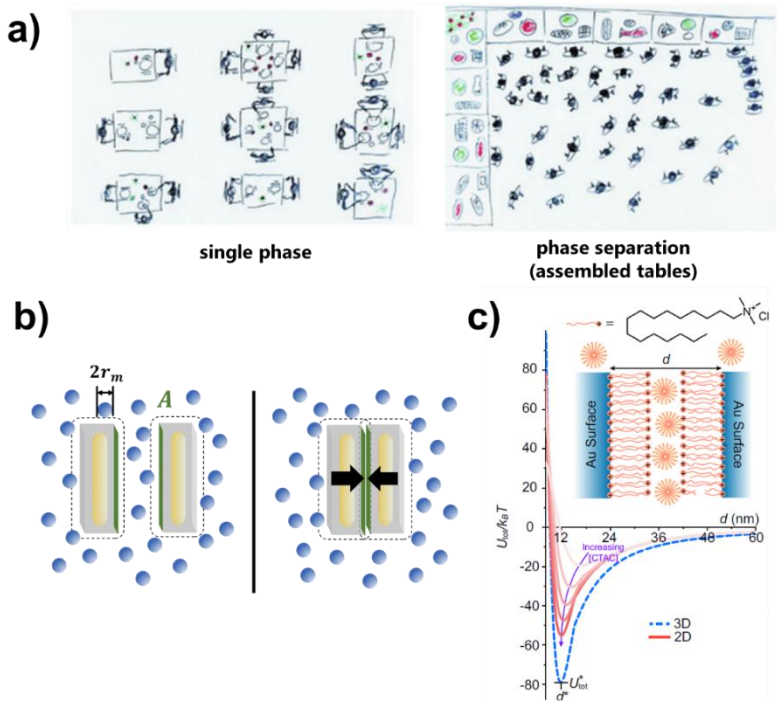

Figure 19. Depletion interaction and depletion-induced self-assembly (DISA). (a) *'Sit-down restaurant vs. buffet' illustration of depletion-induced phase separation and assembly of larger particles[79]. **(b)** Scheme of DISA described as an entropic effect of effective osmotic pressure when larger particles approach within the depletant exclusion volume. **(c)** Theoretical calculation and plot of the DLVO potential well between two nanoparticles as a sum of depletion, van der Waals, and electrostatic forces[97].*

In the case of colloidal NPs suspended in a liquid medium of quasi-spherical depletants, this attractive depletion force can be simply approximated via the Asakura-Oosawa model, taking two interacting NPs as a pair of flat sheets and the depletants as spheres. With this model, the attractive depletion potential then becomes the product of the effective *osmotic pressure* ΔΠ due to the depletant Brownian motion and the *exclusion volume* for the micelles around the NPs:

$$U = -\Pi_m V_{exc} \qquad \textbf{(Equation 1.1)}$$

$$\Pi_m = n_m kT;\ V_{exc} = 2r_m A \qquad \textbf{(Equation 1.2)}$$

$$U = -\Pi_m V_{exc} = \frac{2r_m \boldsymbol{A}\, N_0 (\boldsymbol{c} - cmc)}{Nagg} kT \qquad \textbf{(Equation 1.3)}$$

Thus, one calculates that the magnitude of the depletion force is proportional to the number of depletant particles and to the interaction area between the NPs. At a fixed depletant concentration, attractive depletion is stronger between high surface area facets of NPs[98] The depletion force can be greater when the depletants are highly asymmetric solutes like long rigid macromolecules. The depletion potential at different inter-NP distances can be determined by first calculating ΔΠ[67]. In the case of charged micellar depletants like CTAC or CTAB at relatively high concentration, ΔΠ can be approximated by the Carnahan-Sterling equation. For a system of charged colloids, the full inter-NP interaction potential is the sum of the attractive depletion and van der Waals potentials and the repulsive electrostatic potentials[69,71,97]. Colloidal self-assembly, or aggregation if depletion is poorly controlled, proceeds when the attractive depletion is greater than around 4 to 5 kT, where kT is the energy of thermal agitation of the particles. Crucially, the ionic strength and the dielectric constant of the solvent modulates the effective hydrodynamic size of charged depletants in solution, which affects the range of the depletion force apart from any Coulombic interaction. This affects the kinetics and reversibility of depletion-induced assembly, as well as the accessibility of certain metastable states[75].

In the field of nanoscience and plasmonics, depletion-induced attraction has primarily been used for the shape purification of NPs following wet colloidal synthesis, where a typical synthesis produces both the desired NPs, but also some byproduct NPs of different shapes or sizes. Such purification is done by controlled addition of depletant such as surfactant micelles

(e.g., CTAC) to the as-made (post-synthesis) product to reach the minimum *depletion threshold* of depletant concentration required to slowly flocculate and sediment the desired NPs, leaving behind smaller NPs with lower interaction surface area[71,98]. This purification method is very sensitive to the NP interaction area, and the depletion threshold can be theoretically calculated using the AO model[79,99]. To recover the sedimented particles, one simply reverses the flocculation by reduction of the surfactant concentration by one-shot redilution or by dialysis/diffusion (**Figure 20**). Importantly, this method can be applied to mixed NP systems with different compositions, like metal oxides, semiconductors, etc. Nonetheless, depletion purification is often not efficient for purifying very small NPs with a characteristic dimension less than 50 nm, as the required depletion threshold is very high when using common surfactants like CTAC, CTAB, or BDAC[71,81,98,99].

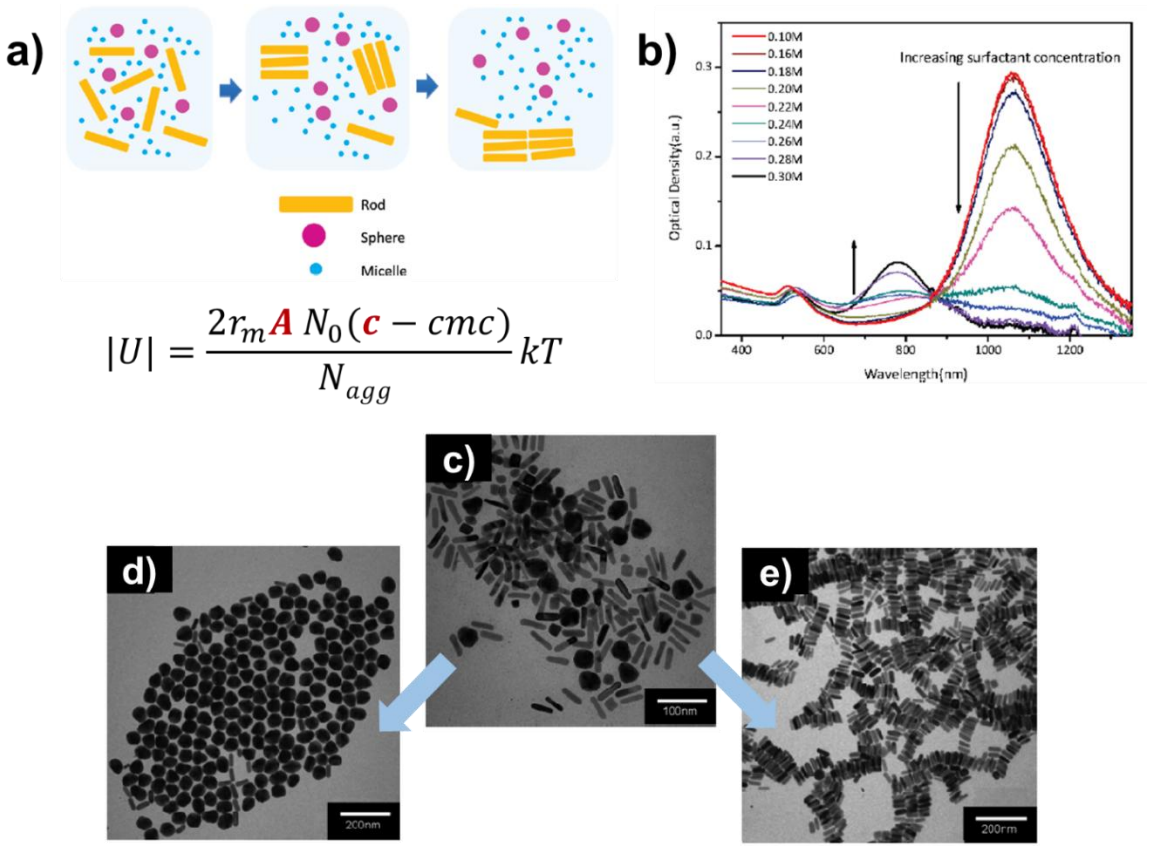

Figure 20. Size/shape purification of NPs by depletion. ***(a)*** *Scheme of depletant-induced size and shape selection of NPs post-synthesis, and* ***(b)*** *UV-vis-NIR extinction spectra for Au NRs for monitoring the depletion-induced flocculation.* ***(c)*** *Successful separation of Au NRs and AU polycrystalline spheres seen by transmission electron microscopy (TEM). Adapted from K. Park, et al.* [98]

On the other hand, given the tunable nature of depletion and its preferential action between larger facets with anisotropic NPs, depletion has started to be exploited to do self-assembly.

Such depletion-induced self-assembly (DISA) has been used in both *static* systems in the dry state and *dynamic* (in situ) systems in liquid / colloidal suspension, but more commonly in the latter. In the process of evaporation-induced self-assembly, where a sessile drop of NP suspension is allowed to dry, the small amount of initial surfactant typically present will concentrate over time, leading to some DISA effects[64,100]. In liquid, DISA can result in the formation of dynamic colloidal superstructures, with NPs assembling even in effectively 1D or 2D geometries due to anisotropy transfer from the NP shape to the assembly dimensionality by preferential depletion interaction between larger NP facets (**Figure 21**). Existing studies showed that the inter-NP gap distance (d_{gap}) can be precisely controlled by changing the depletant concentration in solution, or by changing the temperature which affects the size and shape of the micellar depletants, thus changing their number concentration and effective osmotic pressure[84,101]. DISA has been observed to induce colloidal assemblies of different metal NPs like rods, thin platelets, and polyhedra, leading to various interesting crystal structures due to 'directional entropic bonding'[102,103]. Nonetheless, the precise link between NP shape and assembly dimensionality, and the possibility of highly extended colloidal superstructures up to tens or hundreds of microns large, remains largely unexplored. More critically, reversing DISA requires opening the colloidal system by rediluting the depletant, and the commutation (assembly-disassembly) time can take hours when introducing depletant by diffusion[71,104]. Thus, an 'internal switch' to render DISA more easily cyclable is highly desired.

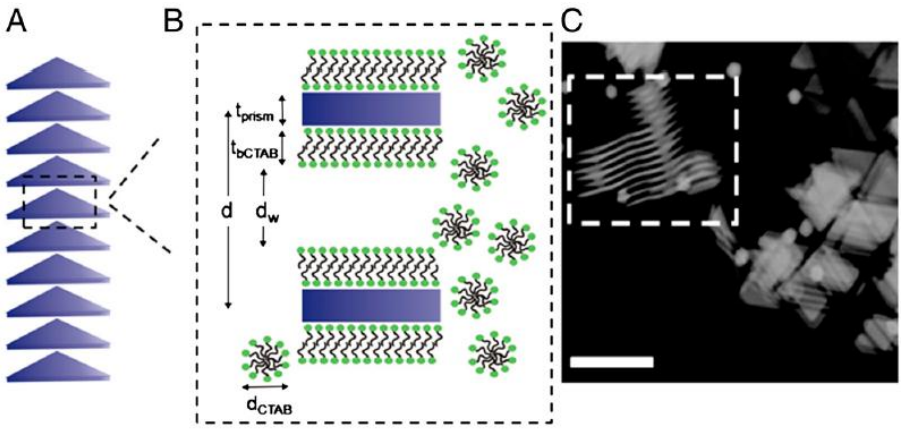

Figure 21. Formation of dynamic and anisotropic 1D superstructures of gold triangular nanoplatelets via depletion-induced self-assembly[84].

The depletion-induced assemblies of highly anisotropic nanorods (NRs) are particularly interesting, as a plethora of phases with different symmetries and dimensionalities can be

attained depending on the aspect ratio of the NRs, the NR cross-section, the concentration of depletant, and the speed of depletant addition into the system which directly influences the assembly kinetics and characteristic growth time. While this has not yet been well explored for plasmonic NRs, other particles like colloidal *fd* virus rods in the presence of PEG particles were found to self-organize into phases ranging from highly 2D platelets or stacked platelets to 1D smectic or columnar fibers, with increasing compacity and rigidity in that order, all the while maintaining a side-by-side hexagonal crystalline order between the rods. In this system, the average aspect ratio and size of the 1D fibers could be well predicted by simple thermodynamic considerations. Additionally, these fibers could be flow-aligned, which is beneficial for applications in anisotropic and stimuli-responsive materials[75]. It has been theorized that the stiffness of the rods, the degree of inter-rod electrostatic repulsion, as well as the relative size of the smaller depletant particles (e.g., PEG, Dextran, CTAC) with respect to the width of the colloidal rods influences the range and width of the inter-NP attraction potential, and whether or not certain phases like liquid crystalline phases may exist for certain systems (**Figure 22**)[101,105].

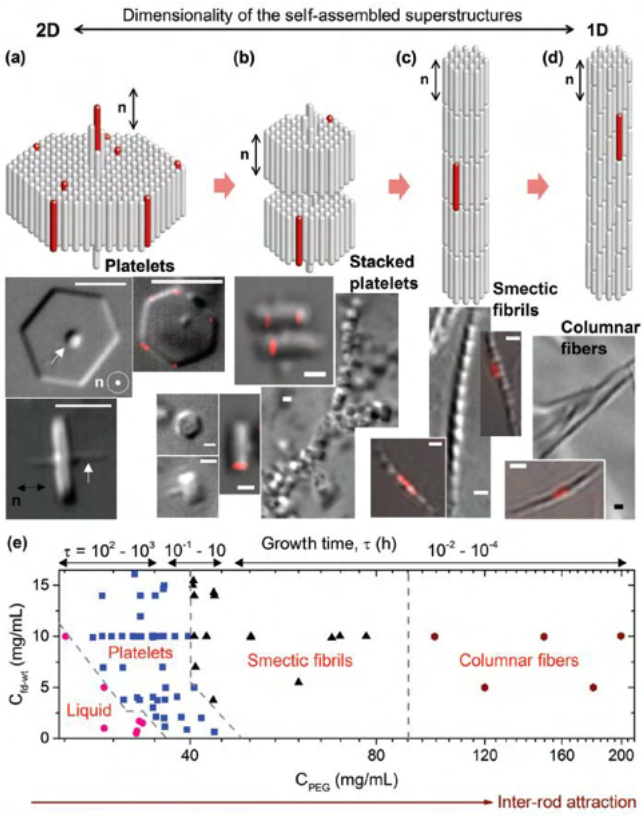

Figure 22. Control of the dimensionality and assembly timescale of colloidal superstructures by depletion force: *The case of fd virus rods using PEG particles as depletant[75].*

Zooming out further, various other entropic effects have been applied to try to achieve a wider range of anisotropic assemblies, with varying NP orientation, frustration, or polymorphism. For example, rotational entropy has been cited as a driving factor in the transition from fcc/hexagonal to rhombic to cubic lattices of superball (i.e., rounded cube) particles[106,107]. Orientational entropy is critical in how the formation of colloidal liquid crystals of nanorods formed via Onsager theory[79,101,108]. The formation of high-entropy alloys by self-assembly has also been explored experimentally and by simulations[109,110]. In certain cases of colloidal assembly, entropy maximization can lead to the formation of quasicrystals (QCs), as in the case of liquid to dodecagonal QCs of nano-tetrahedra, seen both in simulation and in experiment[72,111]. Of particular interest is the use of confinement in micrometric cells, channels, or templated holes (e.g., with PDMS templates or microfluidics), which result in tunable or multi-domain orientation and the switching of assembly dimensionality. These studies also highlight the strong substrate and interfacial effects on supercrystal growth under confinement (**Figure 23**) [81,112,113].

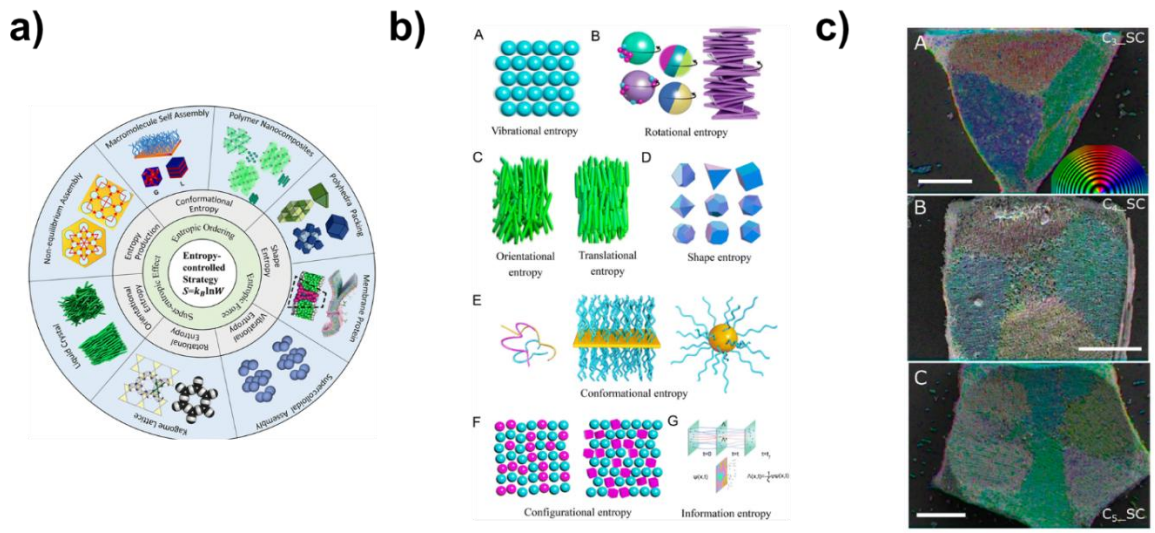

Figure 23. Crucial role of entropy in self-assembly. ***(a)*** *Various instances of entropy-driven or affected assembly and self-organization,* ***(b)*** *Different examples of entropy in nanoscale systems[114],* ***(c)*** *Prismatic confinement during the self-assembly of anisotropic gold nanorods induces tunable orientation[113].*

Lastly, there is much potential in developing dynamic reversible metamaterials to better understand the role of entropy in cyclic self-assembly and self-regulating behavior. For example, a cyclic self-regulating thermo-optical device was made by combining a gold NR plasmonic metasurface with a metal-organic framework matrix (MOFs). This device exhibited

a tunable optical density via shifting LSPR wavelength, due to laser-induced water desorption and cooling-induced water absorption in the MOF. The device thus acts like a nanoscale steam engine (**Figure 24**)[94]. Additionally, with the development of new stimuli-responsive surfactants or polymers or other organic compounds (i.e., molecular switches) following advances in chemical synthesis, there is now the possibility to test whether depletion can be rendered directly responsive to light, heat, or other stimuli, perhaps not merely as an assembly 'on-off switch' but as a control knob for continuous modulation of interparticle attraction. [74,115–117].

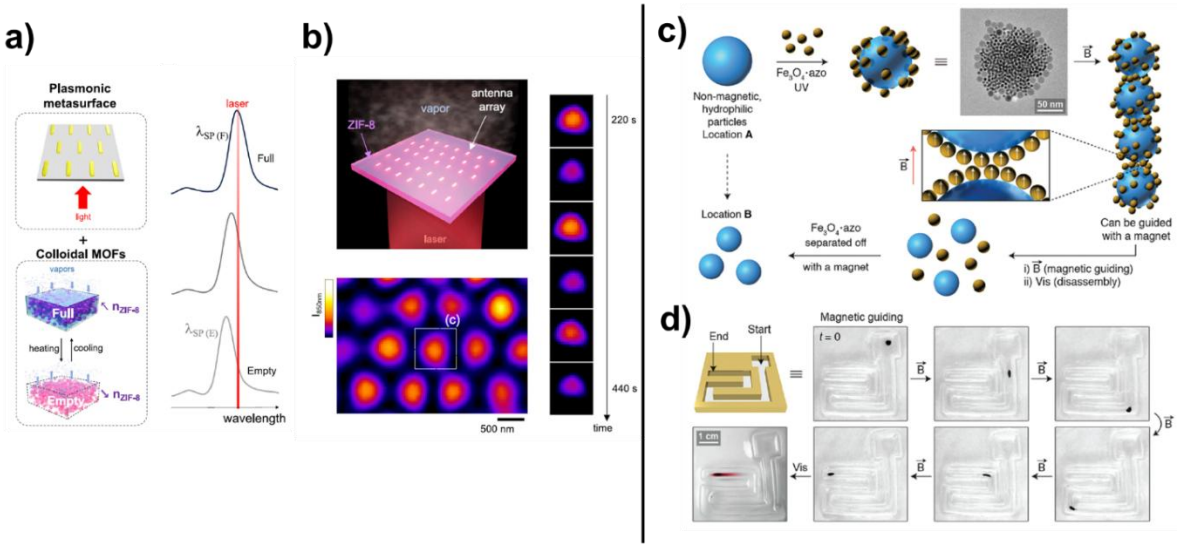

Figure 24. Programmable and multi-stimuli-responsive metamaterials. (a) *Self-regulating thermo-optical metamaterial via a composite of a plasmonic metasurface and metal-organic framework (MOF) with* ***(b)*** *capacity to act as a tunable nano-'steam engine' in response to varying intensities of laser irradiation[94].* ***(c-d)*** *Magnetic steering of light-responsive self-assembling carriers to carry non-magnetic particles[118].*

1.5. Summary points and challenges

- Metamaterials exhibit metaproperties not found in natural or conventional materials. They typically attain their metaproperties through collective behavior or nano-structuration. Interest in more *dynamic, programmable, and/or bio-inspired metamaterials* has grown in recent decades.
- Optical metamaterials, particularly 2D electromagnetic metasurfaces, are powerful devices that manipulate light by playing with the phase, amplitude, and polarization of incident light. These are typically made by top-down substrate-based nanofabrication like lithography, resulting in a *static* material with non-reconfigurable properties.
- 'Living' self-assembly of colloidal plasmonic nanoparticles (NPs) – assembly that is tunable, dynamic, and stimuli-responsive – has been proposed as a way of creating colloidal

metamaterials in liquid. To achieve dynamic and ordered 1D, 2D, or chiral plasmonic metamaterials in liquid, a combination of *anisotropic NPs* and a *directional and stimuli-responsive self-assembly method* is required.

- Our current understanding of dynamic and far-from-equilibrium self-assembly (DSA) remains limited, especially in the case of the kinetics, mechanism, and hysteresis of NP assembly and disassembly. Advances in *in-situ characterization methods* and numerical simulations are required to better understand DSA.
- The *depletion interaction* is an effective entropic attraction between colloidal particles in the presence of small Brownian depletant particles above a critical concentration. Among the common NP self-assembly methods, depletion-induced self-assembly (DISA) stands out for its reversibility and valence-free applicability to many NP compositions.
- However, the use of DISA for extended 1D, 2D, or chiral assemblies of anisotropic metal NPs remains largely unexplored. Reversing depletion time can very long and requires opening the system by depletant redilution. Likewise, DISA has not yet been rendered directly light-responsive.

1.6. Scope of the thesis

This doctoral thesis develops depletion-induced self-assembly (DISA) of metal nanoparticles (NPs) as a more active, tunable, and reversible method of creating highly-extended colloidal superstructures with modulable optical or plasmonic metaproperties. In doing so, it aims to highlight the possibility of having colloidal or 'liquid' metamaterials, as opposed to traditional static, dry, substrate-based metasurfaces. Specifically, this thesis explores two main aspects of DISA: (1) the transfer of *anisotropy and frustration* from individual NPs to spontaneously create low-dimensional, self-limited, or complex-shaped assemblies, and (2) the rendering of DISA as a *dynamic and reversible stimuli-driven process*, particularly using *light* to shorten the assembly commutation time and cycle DISA in a closed system.

To explore these two aspects, we will play with the two components of DISA: First are the nanoparticle building blocks, specifically their shape anisotropy, and second are the physico-chemical properties of the depletant. Such control of DISA will then be utilized to create dynamic and stimuli-responsive assemblies with metamaterial-like properties.

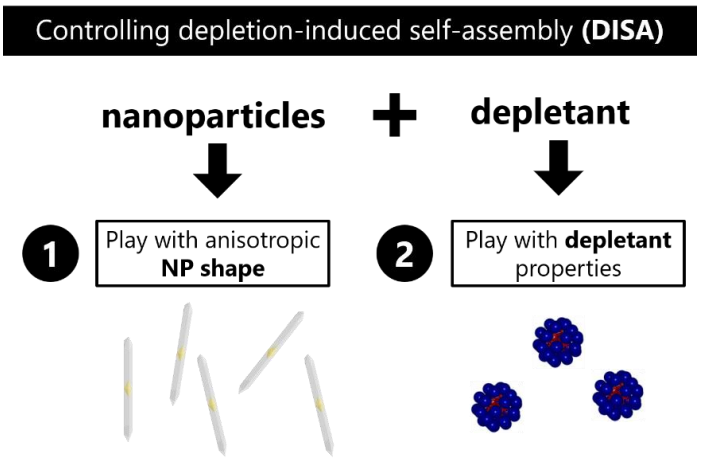

In this introductory chapter, we have gone through the current landscape of metamaterials and plasmonics, and noted how nanoparticle self-assembly is a strong method for creating dynamic colloidal superstructures with metaproperties, with behaviors inspired by biological systems. Reconfigurability, anisotropy, and frustration were identified as factors to consider in making 'living' colloidal metamaterials. Such metamaterials need two components: well-designed anisotropic metal NPs as building blocks, and a directional and tunable means of self-assembly. Among current NP self-assembly methods, the depletion interaction is a promising strategy for inducing tunable and valence-free attraction, but depletion has not yet been shown to be photo-responsive. Depletion has also been mostly limited to the self-assembly of micrometric colloids, and to shape purification of metal NPs.

Chapter 2 lays out the main methodology for the preparation of our DISA system: the nanoparticle design and synthesis, the preparation of surfactants as depletants, the DISA self-assembly process, and the characterization of the assemblies and their formation.

Chapter 3 goes more into detail on the development of the DISA system, notable insights and perspectives during this development, and a practical tips-and-tricks guide for readers.

Next are the three main Chapters 4, 5, and 6, the first two of which are based on our *published articles in peer-reviewed journals*, and the last currently in writing.

Chapter 4 explores the basic principles of DISA towards the creation of 2D metasurfaces and 1D needles via anisotropy transfer, and explores its applications in surface-enhanced Raman scattering (SERS). The main text is a published first-author article in a peer-reviewed journal.

Chapter 5 tackles the relationship between tuning frustration in NP shape and tuning chiral frustration in their NP assemblies via DISA. It is explored whether DISA can enable fast reconfigurable plasmonic circular dichroism (PCD) in colloidal suspension. The main text is likewise a published first-author article in a peer-reviewed journal.

Finally, Chapter 6 goes through the successful implementation of phototunable DISA (photo-DISA) using active azobenzene depletants, showing the modulable light control of NP assembly and disassembly into anisotropic structures with unique properties. This chapter contents will be adapted for an article in preparation. Conclusions and perspectives then follow.

This thesis focuses on depletion-induced assemblies of metal nanoparticles using micellar surfactants as depletants, and will not delve into the use of non-metallic NP building blocks. Particular attention is given to the development of the DISA and photo-DISA methods, the in situ characterization of the colloidal metamaterials, including their hierarchical structure, optical/plasmonic properties, and cyclic assembly-disassembly behavior. The detailed kinetics, mechanisms, and mathematical modelling of DISA are outside the main scope of this project.

1.7. References

(1) Sun, C. C. Materials Science Tetrahedron—A Useful Tool for Pharmaceutical Research and Development. *J. Pharm. Sci.* **2009**, *98* (5), 1671–1687. https://doi.org/10.1002/jps.21552.

(2) Diaz, J. M. Introduction to Materials Science, 2018.

(3) Meinzer, N.; Barnes, W. L.; Hooper, I. R. Plasmonic Meta-Atoms and Metasurfaces. *Nat. Photonics* **2014**, *8* (12), 889–898. https://doi.org/10.1038/nphoton.2014.247.

(4) Pavlov, D. V.; Sergeeva, K. A.; Seredin, A. A.; Cherepakhin, A. B.; Sergeev, A. A.; Sokolova, A. V.; Kulchin, Y. N.; Zhizhchenko, A. Yu.; Petrov, M. I.; Kuchmizhak, A. A.; Rogach, A. L. Nonlinear Light Conversion and Infrared Photodetection with Laser-Printed Plasmonic Metasurfaces Supporting Bound States in the Continuum. *Light Sci. Appl.* **2026**, *15* (1), 23. https://doi.org/10.1038/s41377-025-02040-4.

(5) Bonacchi, S.; Cantelli, A.; Battistelli, G.; Guidetti, G.; Calvaresi, M.; Manzi, J.; Gabrielli, L.; Ramadori, F.; Gambarin, A.; Mancin, F.; Montalti, M. Photoswitchable NIR-Emitting Gold Nanoparticles. *Angew. Chem. Int. Ed.* **2016**, *55* (37), 11064–11068. https://doi.org/10.1002/anie.201604290.

(6) Wang, P.; Nasir, M. E.; Krasavin, A. V.; Dickson, W.; Jiang, Y.; Zayats, A. V. Plasmonic Metamaterials for Nanochemistry and Sensing. *Acc. Chem. Res.* **2019**, *52* (11), 3018–3028. https://doi.org/10.1021/acs.accounts.9b00325.

(7) Kravets, V. G.; Kabashin, A. V.; Barnes, W. L.; Grigorenko, A. N. Plasmonic Surface Lattice Resonances: A Review of Properties and Applications. *Chem. Rev.* **2018**, *118* (12), 5912–5951. https://doi.org/10.1021/acs.chemrev.8b00243.

(8) Qi, X.; Pérez, L. A.; Alonso, M. I.; Mihi, A. High *Q* -Factor Plasmonic Surface Lattice Resonances in Colloidal Nanoparticle Arrays. *ACS Appl. Mater. Interfaces* **2024**, *16* (1), 1259–1267. https://doi.org/10.1021/acsami.3c08617.
(9) Vignolini, S.; Rudall, P. J.; Rowland, A. V.; Reed, A.; Moyroud, E.; Faden, R. B.; Baumberg, J. J.; Glover, B. J.; Steiner, U. Pointillist Structural Color in *Pollia* Fruit. *Proc. Natl. Acad. Sci.* **2012**, *109* (39), 15712–15715. https://doi.org/10.1073/pnas.1210105109.
(10) Parton, T. G.; Parker, R. M.; Van De Kerkhof, G. T.; Narkevicius, A.; Haataja, J. S.; Frka-Petesic, B.; Vignolini, S. Chiral Self-Assembly of Cellulose Nanocrystals Is Driven by Crystallite Bundles. *Nat. Commun.* **2022**, *13* (1), 2657. https://doi.org/10.1038/s41467-022-30226-6.
(11) Yang, S.; Yan, Y.; Huang, J.; Petukhov, A. V.; Kroon-Batenburg, L. M. J.; Drechsler, M.; Zhou, C.; Tu, M.; Granick, S.; Jiang, L. Giant Capsids from Lattice Self-Assembly of Cyclodextrin Complexes. *Nat. Commun.* **2017**, *8* (1), 15856. https://doi.org/10.1038/ncomms15856.
(12) Probst, P. T.; Dong, Y.; Zhou, Z.; Aftenieva, O.; Fery, A. Bottom-Up Assembly of Inorganic Particle-Based Chiroptical Materials. *Adv. Opt. Mater.* **2024**, *12* (5), 2301834. https://doi.org/10.1002/adom.202301834.
(13) Hopkinson, F.; Rittenhouse, D. An Optical Problem, Proposed by Mr. Hopkinson, and Solved by Mr. Rittenhouse. *Trans. Am. Philos. Soc.* **1786**, *2*, 201. https://doi.org/10.2307/1005186.
(14) Ebbesen, T. W.; Lezec, H. J.; Ghaemi, H. F.; Thio, T.; Wolff, P. A. Extraordinary Optical Transmission through Sub-Wavelength Hole Arrays. *Nature* **1998**, *391* (6668), 667–669. https://doi.org/10.1038/35570.
(15) Rubin, N. A. Introduction to Metasurfaces, 2024. https://www.kiss.caltech.edu/workshops/metasurface_optics/Presentations/Talk%201%20-%20Rubin.pdf.
(16) Su, V.-C.; Chu, C. H.; Sun, G.; Tsai, D. P. Advances in Optical Metasurfaces: Fabrication and Applications [Invited]. *Opt. Express* **2018**, *26* (10), 13148. https://doi.org/10.1364/OE.26.013148.
(17) Yu, N.; Genevet, P.; Kats, M. A.; Aieta, F.; Tetienne, J.-P.; Capasso, F.; Gaburro, Z. Light Propagation with Phase Discontinuities: Generalized Laws of Reflection and Refraction. *Science* **2011**, *334* (6054), 333–337.
(18) Yu, N.; Capasso, F. Flat Optics with Designer Metasurfaces. *Nat. Mater.* **2014**, *13* (2), 139–150. https://doi.org/10.1038/nmat3839.
(19) Chu, H.; Li, Q.; Liu, B.; Luo, J.; Sun, S.; Hang, Z. H.; Zhou, L.; Lai, Y. A Hybrid Invisibility Cloak Based on Integration of Transparent Metasurfaces and Zero-Index Materials. *Light Sci. Appl.* **2018**, *7* (1), 50. https://doi.org/10.1038/s41377-018-0052-7.
(20) Narayana, S.; Sato, Y. Heat Flux Manipulation with Engineered Thermal Materials. *Phys. Rev. Lett.* **2012**, *108* (21), 214303. https://doi.org/10.1103/PhysRevLett.108.214303.
(21) Nugroho, F. A. A.; Bai, P.; Darmadi, I.; Castellanos, G. W.; Fritzsche, J.; Langhammer, C.; Gómez Rivas, J.; Baldi, A. Inverse Designed Plasmonic Metasurface with Parts per Billion Optical Hydrogen Detection. *Nat. Commun.* **2022**, *13* (1), 5737. https://doi.org/10.1038/s41467-022-33466-8.
(22) Pitchappa, P.; Kumar, A.; Prakash, S.; Jani, H.; Venkatesan, T.; Singh, R. Chalcogenide Phase Change Material for Active Terahertz Photonics. *Adv. Mater.* **2019**, *31* (12), 1808157. https://doi.org/10.1002/adma.201808157.
(23) Liu, H.; Dong, W.; Wang, H.; Lu, L.; Ruan, Q.; Tan, Y. S.; Simpson, R. E.; Yang, J. K. W. Rewritable Color Nanoprints in Antimony Trisulfide Films. *Sci. Adv.* **2020**, *6* (51), eabb7171. https://doi.org/10.1126/sciadv.abb7171.
(24) Abdelraouf, O. A. M.; Wang, Z.; Liu, H.; Dong, Z.; Wang, Q.; Ye, M.; Wang, X. R.; Wang, Q. J.; Liu, H. Recent Advances in Tunable Metasurfaces: Materials, Design, and Applications. *ACS Nano* **2022**, *16* (9), 13339–13369. https://doi.org/10.1021/acsnano.2c04628.
(25) Bohren, C. F.; Huffman, D. R. *Absorption and Scattering of Light by Small Particles*, 1st ed.; Wiley, 1998. https://doi.org/10.1002/9783527618156.

(26) *Plasmonics: From Basics to Advanced Topics*; Enoch, S., Bonod, N., Eds.; Springer Series in Optical Sciences; Springer Berlin Heidelberg: Berlin, Heidelberg, 2012; Vol. 167. https://doi.org/10.1007/978-3-642-28079-5.
(27) Schnell, M.; Garcia-Etxarri, A.; Alkorta, J.; Aizpurua, J.; Hillenbrand, R. Phase-Resolved Mapping of the Near-Field Vector and Polarization State in Nanoscale Antenna Gaps. *Nano Lett.* **2010**, *10* (9), 3524–3528. https://doi.org/10.1021/nl101693a.
(28) Hanske, C.; González-Rubio, G.; Hamon, C.; Formentín, P.; Modin, E.; Chuvilin, A.; Guerrero-Martínez, A.; Marsal, L. F.; Liz-Marzán, L. M. Large-Scale Plasmonic Pyramidal Supercrystals via Templated Self-Assembly of Monodisperse Gold Nanospheres. *J. Phys. Chem. C* **2017**, *121* (20), 10899–10906. https://doi.org/10.1021/acs.jpcc.6b12161.
(29) Zhang, G.; Lan, C.; Bian, H.; Gao, R.; Zhou, J. Flexible, All-Dielectric Metasurface Fabricated via Nanosphere Lithography and Its Applications in Sensing. *Opt. Express* **2017**, *25* (18), 22038. https://doi.org/10.1364/OE.25.022038.
(30) Chen, B. H.; Wu, P. C.; Su, V.-C.; Lai, Y.-C.; Chu, C. H.; Lee, I. C.; Chen, J.-W.; Chen, Y. H.; Lan, Y.-C.; Kuan, C.-H.; Tsai, D. P. GaN Metalens for Pixel-Level Full-Color Routing at Visible Light. *Nano Lett.* **2017**, *17* (10), 6345–6352. https://doi.org/10.1021/acs.nanolett.7b03135.
(31) Ma, X.; Pu, M.; Li, X.; Huang, C.; Wang, Y.; Pan, W.; Zhao, B.; Cui, J.; Wang, C.; Zhao, Z.; Luo, X. A Planar Chiral Meta-Surface for Optical Vortex Generation and Focusing. *Sci. Rep.* **2015**, *5* (1), 10365. https://doi.org/10.1038/srep10365.
(32) Acunzo, A.; De Luca, M.; Marra, D.; Della Ventura, B.; Offenhäusser, A.; Mayer, D.; Velotta, R. Ultra-Uniform High-Quality Plasmonic Metasurfaces through Electrostatic Self-Assembly of Gold Nanoparticles on Chemically Unmodified Glass. *Nanoscale* **2025**, *17* (23), 14125–14133. https://doi.org/10.1039/D5NR01116G.
(33) Rozin, M. J.; Rosen, D. A.; Dill, T. J.; Tao, A. R. Colloidal Metasurfaces Displaying Near-Ideal and Tunable Light Absorbance in the Infrared. *Nat. Commun.* **2015**, *6* (1), 7325. https://doi.org/10.1038/ncomms8325.
(34) Whitehead, C. B.; Özkar, S.; Finke, R. G. LaMer's 1950 Model for Particle Formation of Instantaneous Nucleation and Diffusion-Controlled Growth: A Historical Look at the Model's Origins, Assumptions, Equations, and Underlying Sulfur Sol Formation Kinetics Data. *Chem. Mater.* **2019**, *31* (18), 7116–7132. https://doi.org/10.1021/acs.chemmater.9b01273.
(35) Sun, Y. Controlled Synthesis of Colloidal Silver Nanoparticles in Organic Solutions: Empirical Rules for Nucleation Engineering. *Chem Soc Rev* **2013**, *42* (7), 2497–2511. https://doi.org/10.1039/C2CS35289C.
(36) Scarabelli, L.; Sánchez-Iglesias, A.; Pérez-Juste, J.; Liz-Marzán, L. M. A "Tips and Tricks" Practical Guide to the Synthesis of Gold Nanorods. *J. Phys. Chem. Lett.* **2015**, *6* (21), 4270–4279. https://doi.org/10.1021/acs.jpclett.5b02123.
(37) Jiu, J.; Suganuma, K.; Nogi, M. Effect of Additives on the Morphology of Single-Crystal Au Nanosheet Synthesized Using the Polyol Process. *J. Mater. Sci.* **2011**, *46* (14), 4964–4970. https://doi.org/10.1007/s10853-011-5413-z.
(38) Scarabelli, L. Recent Advances in the Rational Synthesis and Self-Assembly of Anisotropic Plasmonic Nanoparticles. *Pure Appl. Chem.* **2018**, *90* (9).
(39) He, M.; Ai, Y.; Hu, W.; Guan, L.; Ding, M.; Liang, Q. Recent Advances of Seed-Mediated Growth of Metal Nanoparticles: From Growth to Applications. *Adv. Mater.* **2023**, *35* (46), 2211915. https://doi.org/10.1002/adma.202211915.
(40) Xiong, Y.; Xia, Y. Shape-Controlled Synthesis of Metal Nanostructures: The Case of Palladium. *Adv. Mater.* **2007**, *19* (20), 3385–3391. https://doi.org/10.1002/adma.200701301.
(41) González-Rubio, G.; De Oliveira, T. M.; Altantzis, T.; La Porta, A.; Guerrero-Martínez, A.; Bals, S.; Scarabelli, L.; Liz-Marzán, Luis. M. Disentangling the Effect of Seed Size and Crystal Habit on Gold Nanoparticle Seeded Growth. *Chem. Commun.* **2017**, *53* (82), 11360–11363. https://doi.org/10.1039/C7CC06854A.

(42) Sánchez-Iglesias, A.; Winckelmans, N.; Altantzis, T.; Bals, S.; Grzelczak, M.; Liz-Marzán, L. M. High-Yield Seeded Growth of Monodisperse Pentatwinned Gold Nanoparticles through Thermally Induced Seed Twinning. *J. Am. Chem. Soc.* **2017**, *139* (1), 107–110. https://doi.org/10.1021/jacs.6b12143.
(43) Scarabelli, L.; Grzelczak, M.; Liz-Marzán, L. M. Tuning Gold Nanorod Synthesis through Prereduction with Salicylic Acid. *Chem. Mater.* **2013**, *25* (21), 4232–4238. https://doi.org/10.1021/cm402177b.
(44) Lu, X.; Rycenga, M.; Skrabalak, S. E.; Wiley, B.; Xia, Y. Chemical Synthesis of Novel Plasmonic Nanoparticles. *Annu. Rev. Phys. Chem.* **2009**, *60* (1), 167–192. https://doi.org/10.1146/annurev.physchem.040808.090434.
(45) Aliyah, K.; Lyu, J.; Goldmann, C.; Bizien, T.; Hamon, C.; Alloyeau, D.; Constantin, D. Real-Time *In Situ* Observations Reveal a Double Role for Ascorbic Acid in the Anisotropic Growth of Silver on Gold. *J. Phys. Chem. Lett.* **2020**, *11* (8), 2830–2837. https://doi.org/10.1021/acs.jpclett.0c00121.
(46) González-Rubio, G.; Kumar, V.; Llombart, P.; Díaz-Núñez, P.; Bladt, E.; Altantzis, T.; Bals, S.; Peña-Rodríguez, O.; Noya, E. G.; MacDowell, L. G.; Guerrero-Martínez, A.; Liz-Marzán, L. M. Disconnecting Symmetry Breaking from Seeded Growth for the Reproducible Synthesis of High Quality Gold Nanorods. *ACS Nano* **2019**, *13* (4), 4424–4435. https://doi.org/10.1021/acsnano.8b09658.
(47) Ni, B.; Mychinko, M.; Gómez-Graña, S.; Morales-Vidal, J.; Obelleiro-Liz, M.; Heyvaert, W.; Vila-Liarte, D.; Zhuo, X.; Albrecht, W.; Zheng, G.; González-Rubio, G.; Taboada, J. M.; Obelleiro, F.; López, N.; Pérez-Juste, J.; Pastoriza-Santos, I.; Cölfen, H.; Bals, S.; Liz-Marzán, L. M. Chiral Seeded Growth of Gold Nanorods Into Fourfold Twisted Nanoparticles with Plasmonic Optical Activity. *Adv. Mater.* **2023**, *35* (1), 2208299. https://doi.org/10.1002/adma.202208299.
(48) González-Rubio, G.; Mosquera, J.; Kumar, V.; Pedrazo-Tardajos, A.; Llombart, P.; Solís, D. M.; Lobato, I.; Noya, E. G.; Guerrero-Martínez, A.; Taboada, J. M.; Obelleiro, F.; MacDowell, L. G.; Bals, S.; Liz-Marzán, L. M. Micelle-Directed Chiral Seeded Growth on Anisotropic Gold Nanocrystals. *Science* **2020**, *368* (6498), 1472–1477. https://doi.org/10.1126/science.aba0980.
(49) Qin, F.; Zhang, H.; Tan, T.; Wang, J.; Liu, H.; Wang, C. Three-Step, Seed-Mediated Synthesis of Ultrathin AgNWs in Aqueous Solution. *Chem. Mater.* **2022**, *34* (10), 4613–4620. https://doi.org/10.1021/acs.chemmater.2c00468.
(50) Mosquera, J.; Wang, D.; Bals, S.; Liz-Marzán, L. M. Surfactant Layers on Gold Nanorods. *Acc. Chem. Res.* **2023**, *56* (10), 1204–1212. https://doi.org/10.1021/acs.accounts.3c00101.
(51) Paz-Insua, M.; Consolaro, V. G.; Vlasov, E.; Mychinko, M.; Triviño-Sánchez, S.; Bals, S.; Criado, A.; Mosquera, J. Unraveling the Role of Surfactants in Micelle-Templated Growth of Chiral Plasmonic Nanoparticles. *Adv. Opt. Mater.* **2025**, *13* (34), e01377. https://doi.org/10.1002/adom.202501377.
(52) Yuan, H.; Janssen, K. P. F.; Franklin, T.; Lu, G.; Su, L.; Gu, X.; Uji-i, H.; Roeffaers, M. B. J.; Hofkens, J. Reshaping Anisotropic Gold Nanoparticles through Oxidative Etching: The Role of the Surfactant and Nanoparticle Surface Curvature. *RSC Adv.* **2015**, *5* (9), 6829–6833. https://doi.org/10.1039/C4RA14237C.
(53) Gimondi, S.; Ferreira, H.; Reis, R. L.; Neves, N. M. Microfluidic Devices: A Tool for Nanoparticle Synthesis and Performance Evaluation. *ACS Nano* **2023**, *17* (15), 14205–14228. https://doi.org/10.1021/acsnano.3c01117.
(54) Nguyen, Q. N.; Wang, C.; Shang, Y.; Janssen, A.; Xia, Y. Colloidal Synthesis of Metal Nanocrystals: From Asymmetrical Growth to Symmetry Breaking. *Chem. Rev.* **2023**, *123* (7), 3693–3760. https://doi.org/10.1021/acs.chemrev.2c00468.
(55) Nasilowski, M.; Mahler, B.; Lhuillier, E.; Ithurria, S.; Dubertret, B. Two-Dimensional Colloidal Nanocrystals. *Chem. Rev.* **2016**, *116* (18), 10934–10982. https://doi.org/10.1021/acs.chemrev.6b00164.
(56) Kim, J.; Agrawal, A.; Krieg, F.; Bergerud, A.; Milliron, D. J. The Interplay of Shape and Crystalline Anisotropies in Plasmonic Semiconductor Nanocrystals. *Nano Lett.* **2016**, *16* (6), 3879–3884. https://doi.org/10.1021/acs.nanolett.6b01390.

(57) Sakotic, Z.; Brown, M.; Chang, W. J.; Hurst, L. E.; Mansfield, N.; Paul, T.; Truskett, T. M.; Allen, M.; Allen, J.; Milliron, D. J.; Wasserman, D. Self-Assembled Mid-Infrared Metasurfaces for High-Contrast Femtosecond Switching. *Adv. Photonics* **2026**, *8* (02). https://doi.org/10.1117/1.AP.8.2.026001.
(58) Chang, W. J.; Green, A. M.; Sakotic, Z.; Wasserman, D.; Truskett, T. M.; Milliron, D. J. Plasmonic Metal Oxide Nanocrystals as Building Blocks for Infrared Metasurfaces. *Acc. Mater. Res.* **2025**, *6* (1), 104–113. https://doi.org/10.1021/accountsmr.4c00302.
(59) Guo, Y.; Yin, H.; Hu, J.; Yang, B.; Wang, J. Nonmetal Plasmonic Photocatalysts. *J. Phys. Chem. C* **2024**, *128* (14), 5777–5797. https://doi.org/10.1021/acs.jpcc.3c08508.
(60) Langer, J.; Jimenez De Aberasturi, D.; Aizpurua, J.; Alvarez-Puebla, R. A.; Auguié, B.; Baumberg, J. J.; Bazan, G. C.; Bell, S. E. J.; Boisen, A.; Brolo, A. G.; Choo, J.; Cialla-May, D.; Deckert, V.; Fabris, L.; Faulds, K.; García De Abajo, F. J.; Goodacre, R.; Graham, D.; Haes, A. J.; Haynes, C. L.; Huck, C.; Itoh, T.; Käll, M.; Kneipp, J.; Kotov, N. A.; Kuang, H.; Le Ru, E. C.; Lee, H. K.; Li, J.-F.; Ling, X. Y.; Maier, S. A.; Mayerhöfer, T.; Moskovits, M.; Murakoshi, K.; Nam, J.-M.; Nie, S.; Ozaki, Y.; Pastoriza-Santos, I.; Perez-Juste, J.; Popp, J.; Pucci, A.; Reich, S.; Ren, B.; Schatz, G. C.; Shegai, T.; Schlücker, S.; Tay, L.-L.; Thomas, K. G.; Tian, Z.-Q.; Van Duyne, R. P.; Vo-Dinh, T.; Wang, Y.; Willets, K. A.; Xu, C.; Xu, H.; Xu, Y.; Yamamoto, Y. S.; Zhao, B.; Liz-Marzán, L. M. Present and Future of Surface-Enhanced Raman Scattering. *ACS Nano* **2020**, *14* (1), 28–117. https://doi.org/10.1021/acsnano.9b04224.
(61) Rodal-Cedeira, S.; Vázquez-Arias, A.; Bodelón, G.; Skorikov, A.; Núñez-Sánchez, S.; Laporta, A.; Polavarapu, L.; Bals, S.; Liz-Marzán, L. M.; Pérez-Juste, J.; Pastoriza-Santos, I. An Expanded Surface-Enhanced Raman Scattering Tags Library by Combinatorial Encapsulation of Reporter Molecules in Metal Nanoshells. *ACS Nano* **2020**, *14* (11), 14655–14664. https://doi.org/10.1021/acsnano.0c04368.
(62) Kao, Y.-C.; Han, X.; Lee, Y. H.; Lee, H. K.; Phan-Quang, G. C.; Lay, C. L.; Sim, H. Y. F.; Phua, V. J. X.; Ng, L. S.; Ku, C. W.; Tan, T. C.; Phang, I. Y.; Tan, N. S.; Ling, X. Y. Multiplex Surface-Enhanced Raman Scattering Identification and Quantification of Urine Metabolites in Patient Samples within 30 Min. *ACS Nano* **2020**, *14* (2), 2542–2552. https://doi.org/10.1021/acsnano.0c00515.
(63) Lyu, J.; Chaâbani, W.; Modin, E.; Chuvilin, A.; Bizien, T.; Smallenburg, F.; Impéror-Clerc, M.; Constantin, D.; Hamon, C. Double-Lattice Packing of Pentagonal Gold Bipyramids in Supercrystals with Triclinic Symmetry. *Adv. Mater.* **2022**, *34* (21), 2200883. https://doi.org/10.1002/adma.202200883.
(64) Brissaud, C.; Chaâbani, W.; Giráldez-Martínez, J.; Mockbel, M.; Santiago, E. Y.; Trazo, J. G.; Nag, R.; Lau-Truong, S.; Blond, G.; Faustini, M.; Hamon, C.; Besteiro, L. V.; Piquemal, J.; Comesaña-Hermo, M. Faceted 3D Supercrystals for Plasmonic Photocatalysis: Design, Reactivity, and Operando Studies. *Small Struct.* **2025**, *6* (12), e202500481. https://doi.org/10.1002/sstr.202500481.
(65) Oda, R.; Anfar, Z.; Nakaya, M.; Yospanya, W.; Poly, S.; Battie, Y.; Okazaki, Y.; Baaziz, W.; Ersen, O.; Talaga, D.; Buffeteau, T.; Pauly, M.; Hano, N.; Bertuolo, M.; Fuente, P. D. L.; Nlate, S.; Pouget, E.; Murase, K.; Fukami, K. Nano-Confinement-Directed Crystallization of Morphochiral Gold Nanohelices with Kinetically Programmable Geometry. In Review April 23, 2026. https://doi.org/10.21203/rs.3.rs-9308726/v1.
(66) Yan, R.; Chen, M.; Zhou, H.; Liu, T.; Tang, X.; Zhang, K.; Zhu, H.; Ye, J.; Zhang, D.; Fan, T. Bio-Inspired Plasmonic Nanoarchitectured Hybrid System Towards Enhanced Far Red-to-Near Infrared Solar Photocatalysis. *Sci. Rep.* **2016**, *6* (1), 20001. https://doi.org/10.1038/srep20001.
(67) Bishop, K. J. M.; Wilmer, C. E.; Soh, S.; Grzybowski, B. A. Nanoscale Forces and Their Uses in Self-Assembly. *Small* **2009**, *5* (14), 1600–1630. https://doi.org/10.1002/smll.200900358.
(68) Zang, S.; Paul, S.; Leung, C. W.; Chen, M. S.; Hueckel, T.; Hocky, G. M.; Sacanna, S. Direct Observation and Control of Non-Classical Crystallization Pathways in Binary Colloidal Systems. *Nat. Commun.* **2025**, *16* (1), 3645. https://doi.org/10.1038/s41467-025-58959-0.
(69) Hunter, R. J. *Foundations of Colloid Science*, 2. ed., reprinted.; Oxford Univ. Press: Oxford, 2009.

(70) Whitelam, S.; Jack, R. L. The Statistical Mechanics of Dynamic Pathways to Self-Assembly. *Annu. Rev. Phys. Chem.* **2015**, *66* (1), 143–163. https://doi.org/10.1146/annurev-physchem-040214-121215.
(71) Nag, R.; Rouvière, N.; Trazo, J. G.; Marcone, J.; Kutalia, N.; Goldmann, C.; Impéror-Clerc, M.; Alloyeau, D.; Constantin, D.; Hamon, C. Depletion-Induced Tunable Assembly of Complementary Platonic Solids. *Nano Lett.* **2024**, *24* (51), 16368–16373. https://doi.org/10.1021/acs.nanolett.4c04923.
(72) Wang, Y.; Chen, J.; Li, R.; Götz, A.; Drobek, D.; Przybilla, T.; Hübner, S.; Pelz, P.; Yang, L.; Apeleo Zubiri, B.; Spiecker, E.; Engel, M.; Ye, X. Controlled Self-Assembly of Gold Nanotetrahedra into Quasicrystals and Complex Periodic Supracrystals. *J. Am. Chem. Soc.* **2023**, *145* (32), 17902–17911. https://doi.org/10.1021/jacs.3c05299.
(73) Du, J. S.; Bae, Y.; De Yoreo, J. J. Non-Classical Crystallization in Soft and Organic Materials. *Nat. Rev. Mater.* **2024**, *9* (4), 229–248. https://doi.org/10.1038/s41578-023-00637-y.
(74) Van Kesteren, S.; Smina, N.; Zang, S.; Leung, C. W.; Hocky, G. M.; Sacanna, S. Light-Controlled Colloidal Crystallization. *Chem* **2026**, 102917. https://doi.org/10.1016/j.chempr.2025.102917.
(75) Sung, B.; Wensink, H. H.; Grelet, E. Depletion-Driven Morphological Transitions in Hexagonal Crystallites of Virus Rods. *Soft Matter* **2019**, *15* (46), 9520–9527. https://doi.org/10.1039/C9SM01207A.
(76) Liu, D.; Chen, W.; Sun, K.; Deng, K.; Zhang, W.; Wang, Z.; Jiang, X. Resettable, Multi-Readout Logic Gates Based on Controllably Reversible Aggregation of Gold Nanoparticles. *Angew. Chem. Int. Ed.* **2011**, *50* (18), 4103–4107. https://doi.org/10.1002/anie.201008198.
(77) Fava, D.; Winnik, M. A.; Kumacheva, E. Photothermally-Triggered Self-Assembly of Gold Nanorods. *Chem. Commun.* **2009**, No. 18, 2571. https://doi.org/10.1039/b901412h.
(78) Klinkova, A.; Thérien-Aubin, H.; Choueiri, R. M.; Rubinstein, M.; Kumacheva, E. Colloidal Analogs of Molecular Chain Stoppers. *Proc. Natl. Acad. Sci.* **2013**, *110* (47), 18775–18779. https://doi.org/10.1073/pnas.1315381110.
(79) Lekkerkerker, H. N. W.; Tuinier, R. *Colloids and the Depletion Interaction*; Lecture Notes in Physics; Springer Science+Business Media B.V: Dordrecht, 2011.
(80) Miyazaki, K.; Schweizer, K. S.; Thirumalai, D.; Tuinier, R.; Zaccarelli, E. The Asakura–Oosawa Theory: Entropic Forces in Physics, Biology, and Soft Matter. *J. Chem. Phys.* **2022**, *156* (8), 080401. https://doi.org/10.1063/5.0085965.
(81) Goldmann, C.; Chaâbani, W.; Hotton, C.; Impéror-Clerc, M.; Moncomble, A.; Constantin, D.; Alloyeau, D.; Hamon, C. Confinement Effects on the Structure of Entropy-Induced Supercrystals. *Small* **2023**, 2303380. https://doi.org/10.1002/smll.202303380.
(82) Grzelczak, M.; Liz-Marzán, L. M.; Klajn, R. Stimuli-Responsive Self-Assembly of Nanoparticles. *Chem. Soc. Rev.* **2019**, *48* (5), 1342–1361. https://doi.org/10.1039/C8CS00787J.
(83) Ryssy, J.; Natarajan, A. K.; Wang, J.; Lehtonen, A. J.; Nguyen, M.; Klajn, R.; Kuzyk, A. Light-Responsive Dynamic DNA-Origami-Based Plasmonic Assemblies. *Angew. Chem. Int. Ed.* **2021**, *60* (11), 5859–5863. https://doi.org/10.1002/anie.202014963.
(84) Young, K. L.; Jones, M. R.; Zhang, J.; Macfarlane, R. J.; Esquivel-Sirvent, R.; Nap, R. J.; Wu, J.; Schatz, G. C.; Lee, B.; Mirkin, C. A. Assembly of Reconfigurable One-Dimensional Colloidal Superlattices Due to a Synergy of Fundamental Nanoscale Forces. *Proc. Natl. Acad. Sci.* **2012**, *109* (7), 2240–2245. https://doi.org/10.1073/pnas.1119301109.
(85) Hou, S.; Bai, L.; Lu, D.; Duan, H. Interfacial Colloidal Self-Assembly for Functional Materials. *Acc. Chem. Res.* **2023**, *56* (7), 740–751. https://doi.org/10.1021/acs.accounts.2c00705.
(86) Albouy, P. A.; Deville, S.; Fulkar, A.; Hakouk, K.; Impéror-Clerc, M.; Klotz, M.; Liu, Q.; Marcellini, M.; Perez, J. Freezing-Induced Self-Assembly of Amphiphilic Molecules. *Soft Matter* **2017**, *13* (9), 1759–1763. https://doi.org/10.1039/C6SM02154A.
(87) Zhou, W.; Li, Y.; Je, K.; Vo, T.; Lin, H.; Partridge, B. E.; Huang, Z.; Glotzer, S. C.; Mirkin, C. A. Space-Tiled Colloidal Crystals from DNA-Forced Shape-Complementary Polyhedra Pairing. *Science* **2024**, *383* (6680), 312–319. https://doi.org/10.1126/science.adj1021.

(88) Wang, S.; Kang, L.; Salamon, P.; Wang, X.; Uchida, N.; Araoka, F.; Aida, T.; Dogic, Z.; Ishida, Y. Stimuli-Responsive Self-Regulating Assembly of Chiral Colloids for Robust Size and Shape Control. *Nat. Commun.* **2024**, *15* (1), 9891. https://doi.org/10.1038/s41467-024-54217-x.
(89) Bian, T.; Gardin, A.; Gemen, J.; Houben, L.; Perego, C.; Lee, B.; Elad, N.; Chu, Z.; Pavan, G. M.; Klajn, R. Electrostatic Co-Assembly of Nanoparticles with Oppositely Charged Small Molecules into Static and Dynamic Superstructures. *Nat. Chem.* **2021**, *13* (10), 940–949. https://doi.org/10.1038/s41557-021-00752-9.
(90) He, M.; Gales, J. P.; Ducrot, É.; Gong, Z.; Yi, G.-R.; Sacanna, S.; Pine, D. J. Colloidal Diamond. *Nature* **2020**, *585* (7826), 524–529. https://doi.org/10.1038/s41586-020-2718-6.
(91) Liu, Q.; Kuzyk, A.; Endo, M.; Smalyukh, I. I. Colloidal Plasmonic DNA-Origami with Photo-Switchable Chirality in Liquid Crystals. *Opt. Lett.* **2019**, *44* (11), 2831. https://doi.org/10.1364/OL.44.002831.
(92) Kruse, J.; Merkens, S.; Chuvilin, A.; Grzelczak, M. Kinetic and Thermodynamic Hysteresis in Clustering of Gold Nanoparticles: Implications for Nanotransducers and Information Storage in Dynamic Systems. *ACS Appl. Nano Mater.* **2020**, *3* (9), 9520–9527. https://doi.org/10.1021/acsanm.0c02249.
(93) Bahniuk, M. S.; Alshememry, A. K.; Elgersma, S. V.; Unsworth, L. D. Self-Assembly/Disassembly Hysteresis of Nanoparticles Composed of Marginally Soluble, Short Elastin-like Polypeptides. *J. Nanobiotechnology* **2018**, *16* (1), 15. https://doi.org/10.1186/s12951-018-0342-5.
(94) Amyar, H.; Ceratti, D. R.; Benisty, H.; Cattoni, A.; Besbes, M.; Faustini, M. Self-Regulating and Self-Oscillating Metal-Organic Framework Hybrid Plasmonic Metasurfaces. *Nat. Commun.* **2025**, *16* (1), 10392. https://doi.org/10.1038/s41467-025-65338-2.
(95) Wang, J.-S.; Wang, G.; Feng, X.-Q.; Kitamura, T.; Kang, Y.-L.; Yu, S.-W.; Qin, Q.-H. Hierarchical Chirality Transfer in the Growth of Towel Gourd Tendrils. *Sci. Rep.* **2013**, *3* (1), 3102. https://doi.org/10.1038/srep03102.
(96) Grelet, E.; Tortora, M. M. C. Elucidating Chirality Transfer in Liquid Crystals of Viruses. *Nat. Mater.* **2024**, *23* (9), 1276–1282. https://doi.org/10.1038/s41563-024-01897-x.
(97) Cheng, Z.; Jones, M. R. Assembly of Planar Chiral Superlattices from Achiral Building Blocks. *Nat. Commun.* **2022**, *13* (1), 4207. https://doi.org/10.1038/s41467-022-31868-2.
(98) Park, K.; Koerner, H.; Vaia, R. A. Depletion-Induced Shape and Size Selection of Gold Nanoparticles. *Nano Lett.* **2010**, *10* (4), 1433–1439. https://doi.org/10.1021/nl100345u.
(99) Scarabelli, L.; Coronado-Puchau, M.; Giner-Casares, J. J.; Langer, J.; Liz-Marzán, L. M. Monodisperse Gold Nanotriangles: Size Control, Large-Scale Self-Assembly, and Performance in Surface-Enhanced Raman Scattering. *ACS Nano* **2014**, *8* (6), 5833–5842. https://doi.org/10.1021/nn500727w.
(100) Hotton, C.; Trazo, J. G.; Modin, E.; Bardouil, A.; Kutalia, N.; Marcone, J.; Nag, R.; Goldmann, C.; Paineau, E.; Chuvilin, A.; Impéror-Clerc, M.; Bizien, T.; Constantin, D.; Hamon, C. Evaporation-Induced Phase Transitions in Free-Standing Plasmonic Nanoparticle Assemblies. *Nano Lett.* **2026**, acs.nanolett.6c01619. https://doi.org/10.1021/acs.nanolett.6c01619.
(101) Kutalia, N.; Trazo, J. G.; Marchand, S.; Goldmann, C.; Ratel-Ramond, N.; Dozov, I.; Bizien, T.; Constantin, D.; Impéror-Clerc, M.; Davidson, P.; Hamon, C. Plasmonic Nanorods Form Reconfigurable Liquid Crystalline Assemblies. May 21, 2026. https://doi.org/10.26434/chemrxiv.15003689/v1.
(102) Young, K. L.; Personick, M. L.; Engel, M.; Damasceno, P. F.; Barnaby, S. N.; Bleher, R.; Li, T.; Glotzer, S. C.; Lee, B.; Mirkin, C. A. A Directional Entropic Force Approach to Assemble Anisotropic Nanoparticles into Superlattices. *Angew. Chem. Int. Ed.* **2013**, *52* (52), 13980–13984. https://doi.org/10.1002/anie.201306009.
(103) Vo, T.; Glotzer, S. C. A Theory of Entropic Bonding. *Proc. Natl. Acad. Sci.* **2022**, *119* (4), e2116414119. https://doi.org/10.1073/pnas.2116414119.
(104) Yang, P.-W.; Thoka, S.; Lin, P.-C.; Su, C.-J.; Sheu, H.-S.; Huang, M. H.; Jeng, U.-S. Tracing the Surfactant-Mediated Nucleation, Growth, and Superpacking of Gold Supercrystals Using Time and

Spatially Resolved X-Ray Scattering. *Langmuir* **2017**, *33* (13), 3253–3261. https://doi.org/10.1021/acs.langmuir.6b04319.

(105) Gibaud, T.; Constantin, D. Direct Liquid to Crystal Transition in a Quasi-Two-Dimensional Colloidal Membrane. *J. Phys. Chem. Lett.* **2018**, *9* (15), 4302–4307. https://doi.org/10.1021/acs.jpclett.8b01524.

(106) Meijer, J.-M.; Pal, A.; Ouhajji, S.; Lekkerkerker, H. N. W.; Philipse, A. P.; Petukhov, A. V. Observation of Solid–Solid Transitions in 3D Crystals of Colloidal Superballs. *Nat. Commun.* **2017**, *8* (1), 14352. https://doi.org/10.1038/ncomms14352.

(107) Rossi, L.; Soni, V.; Ashton, D. J.; Pine, D. J.; Philipse, A. P.; Chaikin, P. M.; Dijkstra, M.; Sacanna, S.; Irvine, W. T. M. Shape-Sensitive Crystallization in Colloidal Superball Fluids. *Proc. Natl. Acad. Sci.* **2015**, *112* (17), 5286–5290. https://doi.org/10.1073/pnas.1415467112.

(108) Kato, R.; Mikami, T.; Kato, T. 2D Photonic Colloidal Liquid Crystals Composed of Self-Assembled Rod-Shaped Particles. *Adv. Mater.* **2024**, *36* (38), 2404396. https://doi.org/10.1002/adma.202404396.

(109) Castagnède, A.; Filion, L.; Smallenburg, F. Fast Event-Driven Simulations for Soft Spheres: From Dynamics to Laves Phase Nucleation. *J. Chem. Phys.* **2024**, *161* (2), 024116. https://doi.org/10.1063/5.0209178.

(110) George, E. P.; Raabe, D.; Ritchie, R. O. High-Entropy Alloys. *Nat. Rev. Mater.* **2019**, *4* (8), 515–534. https://doi.org/10.1038/s41578-019-0121-4.

(111) Frenkel, D. Order through Entropy. *Nat. Mater.* **2015**, *14* (1), 9–12. https://doi.org/10.1038/nmat4178.

(112) García-Lojo, D.; Modin, E.; Gómez-Graña, S.; Impéror-Clerc, M.; Chuvilin, A.; Pastoriza-Santos, I.; Pérez-Juste, J.; Constantin, D.; Hamon, C. Structure and Formation Kinetics of Millimeter-Size Single Domain Supercrystals. *Adv. Funct. Mater.* **2021**, *31* (27), 2101869. https://doi.org/10.1002/adfm.202101869.

(113) Chaâbani, W.; Lyu, J.; Marcone, J.; Goldmann, C.; Ten Veen, E. J. M.; Dumesnil, C.; Bizien, T.; Smallenburg, F.; Impéror-Clerc, M.; Constantin, D.; Hamon, C. Prismatic Confinement Induces Tunable Orientation in Plasmonic Supercrystals. *ACS Nano* **2024**, *18* (13), 9566–9575. https://doi.org/10.1021/acsnano.3c12799.

(114) Zhang, X.; Dai, X.; Gao, L.; Xu, D.; Wan, H.; Wang, Y.; Yan, L.-T. The Entropy-Controlled Strategy in Self-Assembling Systems. *Chem. Soc. Rev.* **2023**, *52* (19), 6806–6837. https://doi.org/10.1039/D3CS00347G.

(115) Blayo, C.; Houston, J. E.; King, S. M.; Evans, R. C. Unlocking Structure–Self-Assembly Relationships in Cationic Azobenzene Photosurfactants. *Langmuir* **2018**, *34* (34), 10123–10134. https://doi.org/10.1021/acs.langmuir.8b02109.

(116) Blayo, C.; Kelly, E. A.; Houston, J. E.; Khunti, N.; Cowieson, N. P.; Evans, R. C. Light-Responsive Self-Assembly of a Cationic Azobenzene Surfactant at High Concentration. *Soft Matter* **2020**, *16* (40), 9183–9187. https://doi.org/10.1039/D0SM01512A.

(117) Kundu, P. K.; Samanta, D.; Leizrowice, R.; Margulis, B.; Zhao, H.; Börner, M.; Udayabhaskararao, T.; Manna, D.; Klajn, R. Light-Controlled Self-Assembly of Non-Photoresponsive Nanoparticles. *Nat. Chem.* **2015**, *7* (8), 646–652. https://doi.org/10.1038/nchem.2303.

(118) Chovnik, O.; Balgley, R.; Goldman, J. R.; Klajn, R. Dynamically Self-Assembling Carriers Enable Guiding of Diamagnetic Particles by Weak Magnets. *J. Am. Chem. Soc.* **2012**, *134* (48), 19564–19567. https://doi.org/10.1021/ja309633v.

Chapter 2

METHODOLOGY

In this thesis project, the development of 'living colloidal crystals' from plasmonic metal nanoparticles (NPs) was a multistep process that required much development and optimization. This chapter will report in detail the ***main protocols*** used in this study of depletion-induced self-assembly (DISA). Chapter 3 will then go in depth into the development of these protocols and some practical tips-and-tricks for the readers in implementing these methods.

Note that the methods detailed here for Chapters 3, 4, and 5 are also reported in the *two first-author articles (**J. Trazo, et al. ACS Appl. Mater. Interfaces. 2025** and **J. Trazo, et al. Chem. Mater. 2025**)* upon which those chapters are based[1,2], as well as *one second-author article (**C. Hotton, J. Trazo, et al. Nano Letters. 2026**)* on the characterization of micellar depletants and SAXS techniques[3].

2.1. General scheme of methods and components

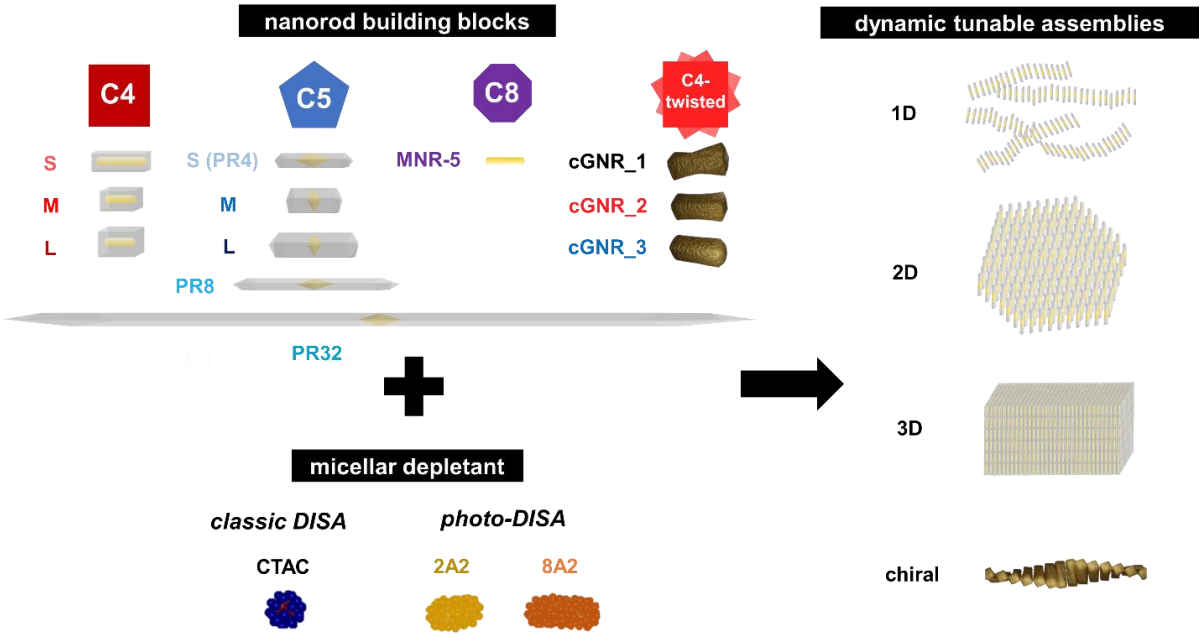

Figure 1. Depletion-induced self-assembly towards living colloidal crystals as dynamic metamaterials.

2.2. Nanoparticle synthesis

Classic achiral metal nanorods of varying anisotropy

Gold core - silver shell nanorods (Au@AgNRs) were synthesized by seed-mediated growth in aqueous solution as described previously in literature[4–8] and modified by our team in LPS according to our recent articles[9,10].

The depletion-based shape purification of the NRs after synthesis is detailed in the following section.

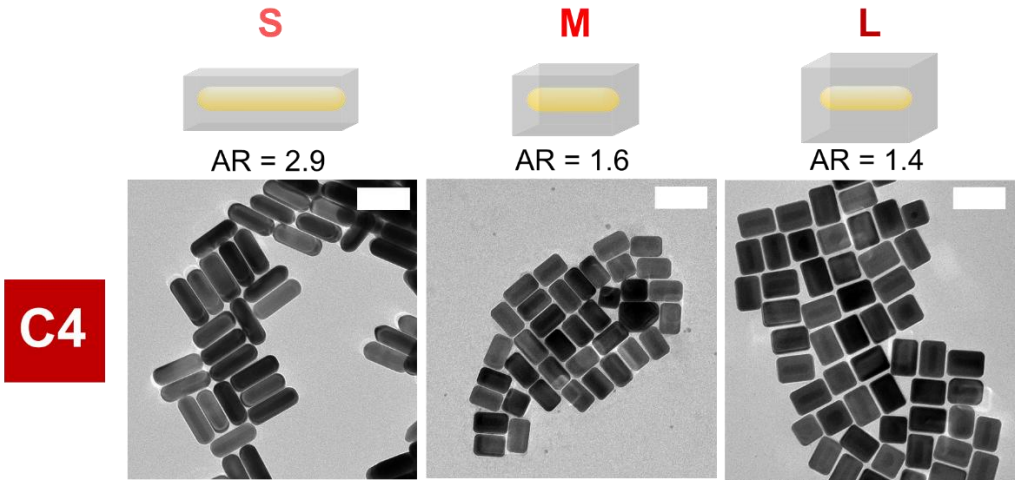

Figure 2. Size characterization of cuboid C4-NRs of different anisotropy: *TEM micrographs and corresponding illustrations of the NRs. (Scale bars are 100 nm.)*

C4 (square section) Au@Ag nanorods or cuboids. This synthesis required three steps: the fabrication of monocrystalline gold seeds, followed by a first seed-mediated growth to obtain gold nanorods, and finally a second seed-mediated growth of silver to obtain the C4-NRs. For small C4-NRs (C4-S), the gold cores were higher aspect ratio AuNRs. For medium and large C4-NRs (C4-M and C4-L), lower aspect ratio AuNRs served as the gold cores.

1) ***C4-S.*** To make long AuNRs for the C4-S gold core, first, the monocrystalline gold seeds were obtained from a solution of CTAB (50 mM) and decanol (14 mM) in H_2O (7 mL), to which was added $HAuCl_4$ (140 µL, 25 mM), AA (35 µL, 100 mM) and $NaBH_4$ (280 µL, 20 mM). The mixture was stirred at room temperature for 1 h. The gold nanorods were obtained from 100 mL of a similar CTAB/decanol/water solution, to which was added $AgNO_3$ (800 µL, 10 mM), HCl (7 mL, 1 M), $HAuCl_4$ (2 mL, 25 mM), AA (1.3 mL, 100 mM) and 6 mL of the previously prepared seeds solution. The mixture was stirred at 28°C for

4 h, before being centrifuged at 15000 rcf for 1 h and washed with water twice. Finally, the Au@Ag C4-NRs were obtained from a solution of 250 mL of a similar CTAB/decanol/water solution, to which was added $AgNO_3$ (500 µL, 100 mM), $HAuCl_4$ (5 mL, 25 mM), AA (2 mL, 100 mM), HCl (25 mL, 1 M) and the previously prepared nanorod solution (650 µL, $[Au^0]$ = 8.75 mM). The final Au@Ag C4-NRs were obtained by Ag growth onto these high AR AuNRs. Here, the AuNRs, $AgNO_3$ solution, and ascorbic acid solution were added into an aqueous CTAC solution to achieve a final gold concentration $[Au^0]$ of 0.25 mM, CTAC concentration of 10 mM, with a Ag^+:Au^0 molar ratio of 8:1 and a Ag^+:AA molar ratio of 4:1 for C4-S This mixture was stirred at 70 °C for 2h. After synthesis, the C4-NRs were collected and washed by two rounds of centrifugation at 5000 rcf for 20 min, and then purified using CTAC-induced depletion, detailed in the next section.

2) ***C4-M and C4-L.*** To obtain lower AR AuNRs as the gold core, first, monocrystalline seeds were obtained from a solution of CTAB (100 mM, 4.7 mL) mixed with $HAuCl_4$ solution (25 mM, 50 µL) at 30°C. After mixing, freshly prepared $NaBH_4$ (300 µL, 10 mM) solution was injected with vigorous stirring. This seed solution was aged at 30°C for at least 30 min before adding it into the growth solution. Next, the growth solution to synthesize AuNRs was prepared by mixing aqueous CTAB (250 mL, 100 mM), 5-bromosalicylic acid (450 mg, 5-BrSA), and water (240 mL). This mixture was sonicated until all the solids dissolved. Then, aqueous $AgNO_3$ (476 µL, 100 mM) and aqueous $HAuCl_4$ solution (10 mL, 25 mM) were added to the mixture to begin Au^{3+} prereduction. The progress of prereduction was monitored by UV-vis spectroscopy; prereduction was allowed to continue until the absorbance at 396 nm reached 0.7 (with an optical path of 1 cm), at which ascorbic acid solution (1250 µL, 100 mM) was injected under vigorous stirring, followed quickly by adding 800 µL of previously synthesized seed solution with stirring. The mixture was then kept stirring at 30°C for 4 h. After synthesis, the AuNRs were collected and washed by two rounds of centrifugation at around 13000 rcf for 15 min each time. The final Au@Ag C4-NRs were obtained by Ag growth onto these AuNRs. Here, the AuNRs, $AgNO_3$ solution, and ascorbic acid solution were added into a CTAC aqueous solution to achieve a final gold concentration $[Au^0]$ of 0.25 mM, CTAC concentration of 10 mM, with a Ag^+:Au^0 molar ratio of 8:1 and a

Ag^+:AA molar ratio of 4:1 for C4-M, and a Ag^+:Au^0 molar ratio of 12:1 and a Ag^+:AA molar ratio of 4:1 for C4-L. This mixture was stirred at 70 °C for 2h. After synthesis, the C4-NRs were collected and washed by two rounds of centrifugation at 4000 to 5000 rcf for 20 min depending on the size of the NRs, and then purified using CTAC-induced depletion, detailed in the next section.

C5 (pentagonal section) Au@Ag nanorods. This synthesis required three steps: the fabrication of pentatwinned gold seeds, followed by a first seed-mediated growth to obtain either gold pentagonal bipyramids (AuBPs) for C5-S and other thin C5-NRs or gold decahedra (AuDh) for C5-M and C5-L, and then a second seed-mediated growth of silver to obtain C5-NRs. The seeds were synthesized in a solution of CTAC (60 mM) in water (33 mL) to which was added trisodium citrate (4 mL, 50 mM) at 30°C. The mixture was left at 30°C for 30 min before adding $NaBH_4$ (1 mL, 25 mM). After stirring for 30 s, the mixture was left for 5 days in an oven at 40°C to obtain pentatwinned seeds.

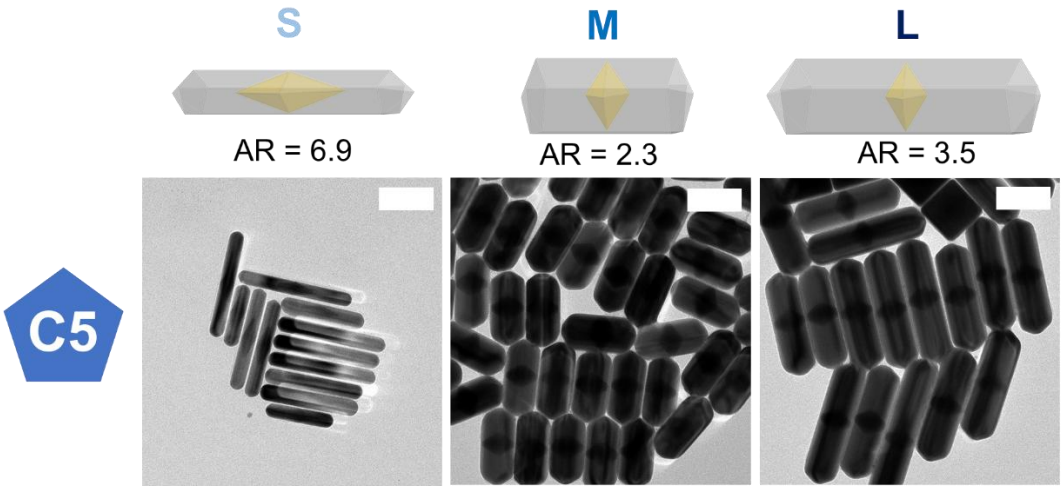

Figure 3. Size characterization of pentagonal C5-NRs of different anisotropy: *TEM micrographs and corresponding illustrations of the NRs. (Scale bars are 100 nm.)*

1) ***C5-S*** To prepare AuBPs as cores for C5-S NRs, first, a growth solution was prepared by successive addition of aqueous CTAB (200 mL, 100 mM), $AgNO_3$ (200 µL, 100 mM), $HAuCl_4$ (4 mL, 25 mM), HCl (4 mL, 1 M), and finally with vigorous stirring, first ascorbic acid solution (1600 µL, 100 mM), and then the pentatwinned seeds solution (3600 µL) after the mixture turned colorless. The mixture was left stirring at 30°C for 4 h. After synthesis, the particles were collected and washed by two rounds of centrifugation.

Further purification of the BPs was done by BDAC-induced depletion. For this, in a 15 mL tube, concentrated 450 mM BDAC surfactant solution and water was added to 1 mL of concentrated BP solution ([Au^0]=100 mM, [CTAC] = 1 mM), to achieve a total mixture volume of 10 mL and a final BDAC concentration of 350 mM. This suspension was mixed, and then allowed to stand vertically and separate overnight, with the purified PRs sedimenting as a precipitate. This BP precipitate was separated from the supernatant; then, the purified BPs were washed with 1 mM CTAC in one centrifugation step at 13000 rcf for 10 min. Finally, all the precipitate was redispersed into 1 mM CTAC for storage. The final thin Au@Ag C5-NRs were obtained by Ag growth onto these AuBPs. Here, the AuBPs, $AgNO_3$ solution, and ascorbic acid solution were added into a CTAC aqueous solution to achieve a final gold concentration [Au^0] of 0.25 mM, CTAC concentration of 10 mM, with a Ag^+:Au^0 molar ratio of 4:1 and a Ag^+:AA molar ratio of 4:1 for C5-S. For other lengths of thin C5-NRs, the Ag^+:Au^0 molar ratio can be varied from 2:1 to 8:1, keeping a Ag^+:AA molar ratio of 4:1. This mixture was stirred at 70 °C for 2h. After synthesis, the C5-NRs were collected and washed by two rounds of centrifugation at 2460 rcf for 20 min, and then purified using CTAC-induced depletion, detailed in the next section.

2) ***C5-M, C5-L.*** To prepare AuDhs as cores for C5-M and C5-L NRs, first, a growth solution was prepared from a solution of BDAC (100 mM) in water (400 mL) to which was added $HAuCl_4$ (8 mL, 25 mM) and AA (3 mL, 100 mM). A portion of the same pentatwinned seed solution (1200 µL, [Au^0] = 0.3 mM) was added under fast stirring. The mixture was subsequently left under slow stirring at 30°C for 30 min. The decahedra were then centrifuged at 7300 rcf for 10 min and washed with water, before being stored in 5 mL of 5 mM CTAC. The final Au@Ag C5-NRs were made by silver growth onto these AuDhs. Here, the AuDhs, $AgNO_3$ solution, and ascorbic acid solution were added into a CTAC aqueous solution to achieve a final gold concentration [Au^0] of 0.25 mM, CTAC concentration of 10 mM, with a Ag^+:Au^0 molar ratio of 5:1 and a Ag^+:AA molar ratio of 4:1 for C5-M, and with a Ag^+:Au^0 molar ratio of 8:1 and a Ag^+:AA molar ratio of 4:1 for C5-L. This mixture was stirred at 70 °C for 2h. After synthesis, the C5-NRs were collected

and washed by two rounds of centrifugation, and then purified using CTAC-induced depletion, detailed in the next section.

Long C8 monocrystalline Au nanorods (Au mNRs). Long Au mNRs for supplementary DISA experiments were synthesized using the protocol reported by G. González-Rubio, et al.[7] In particular, Au mNRs with a width of 15 nm and a length of 75 to 90 nm were targeted. This is the same protocol to make Au mNRs as seeds for the chiral growth to make cGNRs in the next section.

Chiral gold nanorods

Fourfold twisted gold nanorods (cGNRs). cGNRs were prepared by our collaborator Andrés Serrano-Freijeiro (CINBIO, U. Vigo, Spain) via a five-step seed mediated growth approach that can be described as followed: (1) the synthesis of 1-2 nm gold seeds, (2) synthesis of small anisotropic seeds, (3) synthesis of "minirods", (4) synthesis of larger achiral rods, (5) synthesis of the cGNRs. Steps 1-4 were adapted from González-Rubio et al.[7] with minor modifications and step 5 was described in Bing Ni et. al.[11] with slight modifications.

1) *Synthesis of 1-2 nm gold seeds:* In a 50 mL glass baker, 50 µL of NaOH 0.5 M was added to 20 mL of an aqueous solution containing 50 mM CTAB and 13.5 mM n-decanol at 27 ºC to adjust the pH to 7.6. Then, 200 µL of a 50 mM $HAuCl_4$ solution was added, obtaining a yellowish solution. Immediately after, 800 µL of fresh 20 mM $NaBH_4$ was added under strong magnetic stirring (1000-1100 rpm). The reduction was allowed to proceed under stirring for 2 min until the solution turned brownish yellow. The solution was then left undisturbed for at least 1 h at 27 ºC prior to use.

2) *Synthesis of anisotropic seeds:* In a 500 mL Erlenmeyer flask, 200 mL of an aqueous solution containing 50 mM CTAB and 13.5 mM n-decanol at 27 ºC was prepared. Subsequently, 1.6 mL of 10 mM $AgNO_3$, 14 mL of 1 M HCl, 2 mL of 50 mM $HAuCl_4$, and 2.6 mL of 0.1 M ascorbic acid were added at 25 ºC. Next, 12 mL of the previously prepared seed solution was added under stirring and the mixture was allowed to age for at least 4 h until it turned dark brown. After that time, the longitudinal LSPR

band should be centered around 730 nm. The obtained particles were centrifuged at 23140 rcf for 45 min in 2 mL tubes and redispersed in 5.5 mL of 10 mM CTAB, yielding a final Au^0 concentration of 10 mM.

3) *Synthesis of "minirods".* On a 500mL Erlenmeyer flask, 200 mL solution of CTAB 50mM and n-decanol 13.5 mM was prepared. Then, 1.6mL of $AgNO_3$ (10mM), 14mL of HCl (1M), 2mL of $HAuCl_4$ (50mM) and 2.6 mL of ascorbic acid (0.1M) were subsequently added at 25ºC. Then, 12mL of previously prepared seed solution was added under stirring and the mixture is left aging for at least 4 hours until it turns dark brown. After that time, longitudinal plasmon should peak at 730nm and the final particles are centrifuged at 45000 rcf for 45 minutes in 2mL tubes and dispersed in 5,5mL of CTAB 10 mM for a final Au^0 concentration of 10 mM.

4) *Synthesis of achiral AuNRs:* First, 174 mL of an aqueous solution containing 50 mM CTAB and 11 mM n-decanol was prepared. Then, 2 mL of 50 mM $HAuCl_4$ was added, and the resulting yellowish solution was left undisturbed for 10 min at 16 ºC. Afterwards, 3 mL of 10 mM $AgNO_3$, 20 mL of 1 M HCl, 1.6 mL of 0.1 M ascorbic acid, and 400 µL of 10 mM Au "minirods" were sequentially added. The resulting mixture was left undisturbed for 5 hours to allow complete anisotropic growth. Then, the particles were centrifuged at 5750 rcf for 20 min in 50 mL tubes and redispersed in 5 mL of 1 mM CTAB, yielding a final Au^0 concentration of 5 mM. The LSPR maximum was at 1150 nm.

5) *Chiral gold nanoparticles.* Typically, 200 µL of HAuCl4 (10 mM) was dispersed on 10 mL of 10 mM CTAC solution and incubated at 40ºC for 8-10 min. Then, for the chiral nanoparticles with larger aspect ratio, 200 µL of L-ascorbic acid (0.1 M), 40 to 60 µL of L-/D-cysteine (20 µM) and 12 µL of achiral gold nanorods with LSPR at 1150 nm (5 mM) were added sequentially. For chiral particles with smaller aspect ratio, 200 µL of L-ascorbic acid (0.1 M), 120 µL of L-/D-cysteine (20 µM) and 14 µL of achiral gold nanorods with LSPR at 1040 nm (5 mM) were added instead. The particles were then centrifuged (10 min at 3980 rcf) and dispersed in 1 mM CTAC twice.

Oxidized cGNRs. cGNRs with different degrees of oxidation were also prepared by Andrés Serrano Freijeiro (CINBIO, U. Vigo, Spain) via a procedure described in Rodríguez-Fernández

et. al.[12] with slight modifications. 2.5 mL of 2 mM cGNRs dispersed in CTAC 1 mM were added into 20 mL solution of CTAB (50 mM). Subsequently, 100 µL of $HAuCl_4$ (50 mM) was added under stirring (500 rpm). The oxidation was then stopped by centrifugation (10 min at 4700 rcf twice dispersing the particles in 1 mM CTAC) at different times to yield cGNR_2 and cGNR_3 after 3h and 24h respectively.

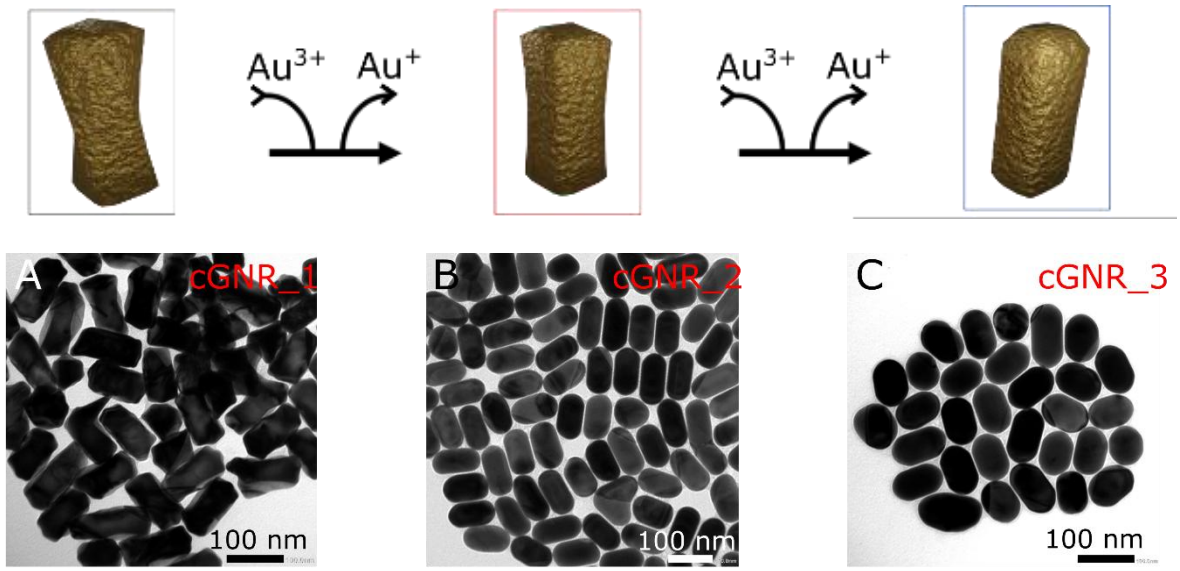

Figure 4. Tuning of twist degree in fourfold chiral Au nanorods via progressive oxidation with $HAuCl_4$, from (a) high (cGNR_1, standard), to (b) medium (cGNR_2), to (c) low chirality (cGNR_3)[2].

Chiral nanoscrews or nano-arrows. For further tests of the depletion-induced self-assembly and colloidal liquid crystal formation of high aspect ratio chiral NPs, gold nanoscrews (or nanoarrows) were prepared by our collaborators Jinyi Dong and Tsz-Him (Kevin) Chow from CICbiomaGUNE, San Sebastián, Spain by micelle-directed chiral growth of gold onto gold nanorods, using the procedure from González-Rubio, et al[13].

Nanorod functionalization or ligand exchange

Raman analyte 4ATP functionalization. This functionalization step was inspired by other protocols in the literature[14,15]. NRs were functionalized with 4-aminothiophenol (4ATP). Into a round bottom flask, an aqueous 40 mL solution of CTAC (2.5 mM), hydrochloric acid (3.3 mM, targeting a pH of 2.5 to 3.0), 4ATP (15 µM by adding 60 µL of 10 mM 4ATP ethanol solution), and C5-S NRs (0.5 mM in total M^0 = Au^0 + Ag^0) was prepared. The mixture was stirred at 60 °C

for 3 h. Afterwards, the functionalized NRs were collected and washed by two rounds of centrifugation, and stored in aqueous 2.5 mM CTAC.

MUTAB functionalization of NRs for passivation. The MUTAB functionalization protocol was inspired by other methods found in literature[16,17]. C5-NRs were functionalized with (11-mercaptoundecyl)-N,N,N-trimethylammonium bromide (MUTAB), a shorter thiol analog of CTAB surfactant in order to passivate and protect the NR surfaces. In an Erlenmeyer flask, an aqueous 100 mL suspension was made of the C5-NRs (10 mM Ag^0) in 1 mM CTAC and the appropriate concentration of MUTAB to have 10x excess coverage of the NR surface, approximating the NR as a pentagonal prism and ignoring the contribution of the end faces. This mixture was then stirred gently overnight at room temperature. After this, the MUTAB-functionalized NRs by multiple centrifugation and washing steps with MUTAB solutions of progressively lower concentration (from 1 mM to 1 µM MUTAB) to not shock the NRs with pure water. The functionalized NRs are then stored in 1 µM MUTAB.

2.3. Depletion-induced shape purification of NPs

After synthesis and centrifugation of the NPs into a concentrated aqueous stock suspension, the stock is then transferred into a 15 mL centrifuge tube, and diluted as needed to around 20 to 100 mM total M^0 (Au^0 + Ag^0) and in 1 mM CTAC. Into this stock, concentrated aqueous CTAC (100 mM or 756 mM) is added stepwise by micropipette, with homogenization by rapid vortexing each time, to slowly increase the CTAC concentration.

Addition is stopped once a notable change of color or turbidity occurs within 15 min of addition. This change signals the start of the depletion-induced flocculation and sedimentation of the larger desired NPs, leaving behind smaller NP impurities. The tube is then stored vertically undisturbed for at least 3 h to overnight to complete the separation and sedimentation. The supernatant is then carefully separated from the desired precipitate, and the latter is redispersed, and its UV-vis-NIR absorbance spectrum checked. The precipitate stock is rediluted and washed with 1 mM CTAC, and recentrifuged and concentrated for storage.

2.4. Conventional depletion-induced self-assembly (DISA)

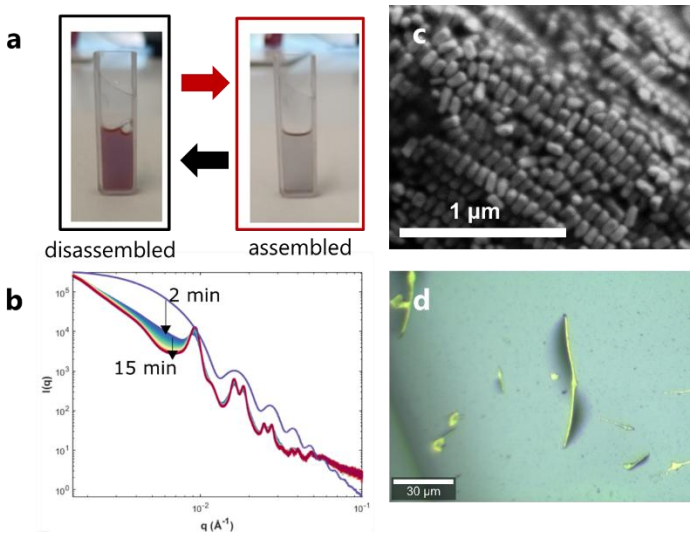

Figure 5. Typical steps and characterizations in studying DISA of nanorods: (a) *Preparation of (chiral) Au NR-depletant mixtures for visual observation and UV-vis-NIR extinction spectroscopy.* ***(b)*** *SAXS kinetics of progressive assembly of (chiral) Au NRs.* ***(c)*** *Scanning electron micrographs showing the internal structure of a (chiral) Au NR assembly by EISA.* ***(d)*** *In situ optical microscopy (reflection) of similar assemblies in liquid made by DISA, showing the large-scale shape of the superstructure.*

Main self-assembly protocols

Two procedures were tested for DISA, resulting in slow or fast self-assembly kinetics, as described below. More details and explanations on the method are found in **Chapter 3**.

1) *Slow kinetics:* This procedure is adapted from P. Yang, et al[18]. Into a round glass capillary (diameter = 1.5 mm), 10 µL of aqueous NR suspension (at 1 mM CTAC) is injected with a syringe near the bottom of the capillary, leaving a 1 cm deep air pocket below. Then, 20 µL of aqueous CTAC solution of the selected concentration was slowly deposited on top of the NR phase with a syringe, ensuring a sharp and well-defined interface between the two phases. Finally, the capillaries were sealed using a glue gun and left undisturbed for at least 24 h to allow diffusion, self-assembly, and equilibration before characterization of the colloidal sample by SAXS or optical microscopy.
2) *Fast kinetics:* Into a 0.5 mL Eppendorf tube, 10 µL of aqueous NR suspension (at 1 mM CTAC) was rapidly and evenly mixed within a few seconds with 20 µL of aqueous CTAC solution of the selected concentration. The mixture was allowed to stand, self-

assemble, and equilibrate for either 1 h or 24 h before characterization by SAXS or optical microscopy. The colloidal one-shot sample is transferred to a glass capillary prior to SAXS characterization.

Either slow or fast kinetics may be used to determine or screen the *minimum depletion threshold* in CTAC (or other depletant) needed for NP self-assembly, which is commonly detected by a sharp change in color or turbidity of the NP suspension, or by in situ optical microscopy to check for micron-sized colloidal assemblies.

Comparison with EISA: Evaporation of a sessile droplet

A 10 µL drop of NPs (variable NP concentration in $M^0 = A^0 + Ag^0$, 2.5 mM CTAC) is first drop casted onto a substrate (either a silicon wafer or a glass coverslip). The substrate is placed in a covered container with added water droplets to maintain saturated humidity, thereby slowing down evaporation. The sample is allowed to slowly dry in around 48 h. While Si wafers were preferred for SEM characterization, glass coverslips were preferred for SAXS characterization. Note that during this process, some concentration of the initial surfactant in the droplet also causes some depletion-induced self-assembly (DISA) prior to complete drying.

Ultra-slow DISA: immersion or pseud-dialysis method

The ultra-slow DISA method was developed by trial-and-error, following inspiration from several microfluidic and capillary dialysis experiments[19,20].

First, a glass optical capillary (0.05 mm × 0.1 mm section) was filled with a suspension of the selected NR (around 20-50 mM M^0), leaving a short air gap of a few millimeters at one end. The whole capillary is then immersed and laid flat in a bath of depletant (e.g. in a Petri dish) at a chosen concentration. Here effectively, only one end of the capillary suspension is open to the depletant bath, as the other has an air gap. The whole bath is then covered tightly with a watch glass and left for anywhere from a few days to a few weeks, to allow the depletant concentration to equilibrate within the capillary, or until the NRs are assembled. To characterize

the sample, the capillary is removed from the bath, sealed either by a glue gun or by flame, and washed to remove excess depletant outside.

Cyclic DISA on cGNRs: Reconfigurable PCD

On a 10 mL centrifuge tube 2 mL of CTAC 87.5 mM and 500 µL of cGNRs were added for a final concentration of 70 mM CTAC. The CD and extinction spectra were immediately measured one after another in order to calculate the *g*-factor at the optimal assemble stage. Then, the sample was either let undisturbed until total sedimentation of the nanoparticles or centrifuged at 2240 rcf for 5 minutes to accelerate the sedimentation process, yielding the same result. The supernatant was then carefully removed and the remaining NPs were dispersed in 2.5 mL of 1 mM CTAC. The CD and extinction spectra were then measured again, followed by another centrifugation at 3980 rcf for 10 minutes. The supernatant was discarded and precipitates at the bottom of the tube were dispersed with CTAC 70 mM completing one cycle. Please see **Chapter 5** for more details, as well as **Article Figure 4** for the scheme[2].

2.5. Phototunable depletion-induced self-assembly (Photo-DISA)



Figure 6. Typical methods in optimizing photo-DISA methodology: ***(a)*** *Series of NR-AzoTAB depletant mixtures at increasing depletant concentration to screen depletion threshold.* ***(b)*** *Combined UV/blue irradiation and in situ SAXS setup to study assembly-disassembly kinetics.*

Synthesis of azoTAB photosurfactants

Four types of azoTAB compounds (C_2AzoOC_2TAB / 2A2, C_8AzoOC_2TAB / 8A2, C_6AzoOC_4TAB / 6A4, C_4AzoOC_6TAB / 4A6) were synthesized according to the protocol in Blayo, et al. and Cheng, et al.[21,22]. More on the synthesis development, purity, and other analyses of the azoTABs are detailed in **Chapter 3.1**.

Main self-assembly protocols

Preparation of NR – azoTAB mixtures. Into an Eppendorf tube, appropriate volumes of aqueous NR suspension, of azoTAB stock solution (8A2 or 2A2), and optionally of NaCl solution are quickly mixed and homogenized by vortexing to achieve the desired concentrations of each component. The typically total sample volume was anywhere from 10 to 100 µL. If the AzoTAB concentration is above 'UV depletion threshold' but below the 'dark depletion threshold', the mixture first needs to be irradiated before colloidal assemblies appear. If [AzoTAB] is above the 'dark depletion' threshold, then assemblies should already be present uniformly in the liquid without UV irradiation. In this case, UV irradiation will just decrease the inter-NR gaps due to further increase of depletion forces. More information on these thresholds is found in **Chapter 6**.

Sample irradiation / LED cycling. Photo-DISA samples to be irradiated are typically placed in either a thin quartz cuvette (1 mm path length) or in a glass optical capillary (0.05 mm × 1 mm section), keeping a thin path length to ensure efficient and uniform irradiation of the whole sample volume. This cyclic irradiation may be used to either repeatedly assemble/disassemble NRs, or to repeatedly expand/contract existing assemblies, depending on the specific NR size and AzoTAB depletant concentration. The light sources used were mounted ThorLABs LEDs for three different wavelengths (see **Table 1**), operated with a T-Cube LED power, at the maximum power setting in continuous current (i.e., continuous illumination) mode, with the LED source placed 5 cm away (unless otherwise stated). The specific power and irradiances for each LED wavelength are detailed below:

Table 1. *Irradiation parameters for LED sources used for photo-DISA.*

Color and center wavelength	**Power setting**	**Irradiance (mW / mm^2) at 5 cm lamp-to-sample distance (driven at 1 A)**
UV (365 nm)	6 (max)	0.2304 mW / mm^2
Blue (470 nm)	6 (max)	0.2115 mW / mm^2
Red (660 nm)	6 (max)	0.2035 mW / mm^2

These LEDs can be manually set up directly into measurement setups like a UV-vis-NIR extinction spectrometer or in a small-angle X-ray scattering (SAXS) setup (**Figure 7**). Depending on nature and duration of the experiment, the capillary or cuvette may need to be inverted and/or gentle agitated to redisperse any sedimented nanoparticles or assemblies, in order to properly characterize them in situ, e.g. by optical microscopy or UV-vis-NIR extinction.

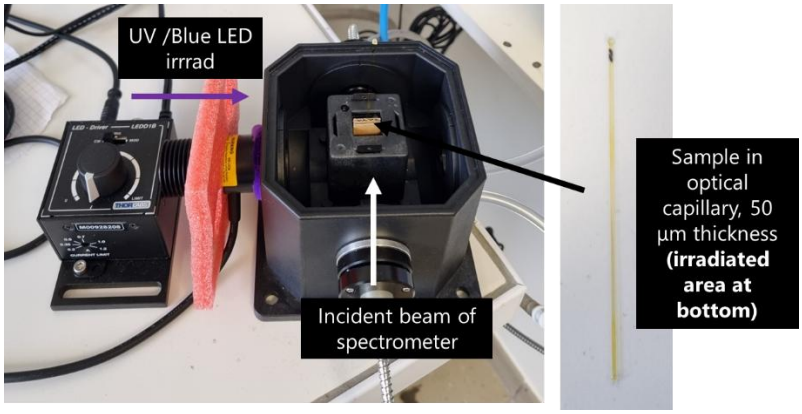

Figure 7. *In house* ***manual*** *photo-DISA UV-vis-NIR (absorption) spectrometer setup for studying assembly-disassembly kinetics, integrated with UV/blue LED source.*

For finer and automated control of illumination, in collaboration with the instrumentation service of LPS, we developed a remote-controlled illumination setup named PhotoSwitch (**Figure 8**). This device connects to both the UV and blue LEDs, turns them on/off, controls each one's power separately, collimates the light, and directs it to an exit hole toward the sample. The exit is fitted with an optical fiber so that the light can be optionally directed to any position on the sample. The PhotoSwitch setup can be controlled via PC connected through an ethernet

cable. In the graphic user interface, various modes of illumination can be chosen, such as simple on-off control of each LED, UV-blue cycles, and rapid pulses of UV, blue, or alternate illumination, all with the option to change duration and cycling time.

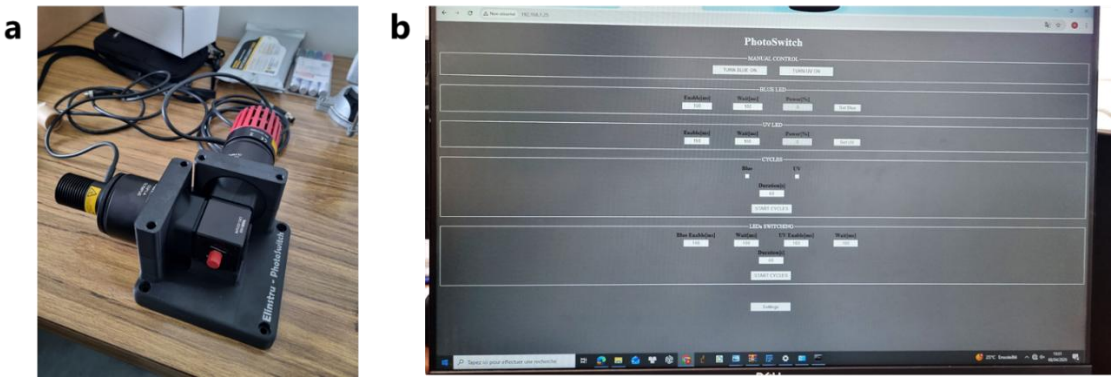

Figure 8. PhotoSwitch setup. (a) *In house* ***automated*** *photo-DISA UV/blue irradiation setup with optical fiber for studying assembly-disassembly kinetics and cycling, with ethernet remote control and* ***(b)*** *computer interface.*

Photoswitchable image imprinting

A concentrated NP suspension (about 100-200 mM M^0) with the appropriate AzoTAB concentration is placed into a wide glass optical capillary, typically around 0.1 mm thick and 3 to 6 mm wide. The appropriate photomask is then placed directly on top of the capillary, and the capillary is then irradiated (directly incident) for 5 min with a UV or blue LED placed 5 cm above. The sample is then characterized after each irradiation as needed. The photomask may either be a clear cellulose acetate photomask with an inkjet-printed pattern, or a flat cardboard or thick bond paper with the pattern manually cut out.

2.6. Characterization of NPs and their assemblies

UV-visible-NIR extinction spectroscopy. Extinction spectra of the NR suspensions were obtained by a Cary 5000 UV-vis-NIR spectrophotometer (Agilent) in polystyrene (PS) cuvettes with an optical path length of 1 cm. Au^0 concentrations of pure Au NR suspensions were estimated using their measured extinction at 400 nm, taking a NP concentration of 0.5 mM in Au^0 for a sample absorbance of 1.2.[70, 71] In the case of bimetallic gold core – silver shell (Au@Ag) NPs, the NP concentration is determined by SAXS, by fitting its form factor diffractogram to first determine its volume fraction. More on this method is discussed in **Chapter 3.2**.

Kinetic measurements of the DISA process were performed using an Avantes UV-vis-NIR spectrophotometer operated in kinetic absorbance mode and controlled by AvaSoft software. Samples were loaded into either PS cuvettes or in a quartz optical capillary with a 0.05 mm × 1 mm section, and absorbance changes were recorded as a function of time. UV-vis-NIR kinetics could also be done at various temperatures, using a Peltier module to heat and cool the sample.

Transmission electron microscopy. TEM was performed at Imagerie-Gif (I2BC CNRS, Gif-sur-Yvette, France) using a JEOL JEM-1400 microscope operating at 120 kV with a filament current of ≈55 µA.

Scanning electron microscopy. SEM images were obtained with a Zeiss Supra55VP, operating at an acceleration voltage of 3 kV. We used two strategies, yielding similar results, to retrieve assemblies for SEM, both aimed at minimizing evaporation-induced self-assembly:

1) Fast drying: The suspension is dried under a gentle air flow.

2) Quenching with ethanol: The suspension is prepared in a vial with a Si wafer at the bottom where the assemblies sediment. After at least 12 h of DISA, most of the supernatant is removed, and the pellet is washed with ethanol to limit further self-assembly.

Optical microscopy. Optical microscopy images were obtained by a WITec Alpha300 Access microscope in reflection mode.

Polarized optical microscopy. Transmission optical microscopy in both bright field and dark field was done with a polarized-light optical microscope (POM, Olympus BX51) equipped with Olympus LED light sources (BX3M-LEDT, transmission and reflection) and different Olympus objectives (with magnifications of 5x, 10x, 20x, 50x, and 100x). The images were recorded using a CCD color camera (Euromex, s-CMEX20), either between crossed polarizers or without the polarizer and analyzer (natural light). An Instec HCS302XY heating stage controlled by software (mK2000B) was used to investigate temperature-dependent behavior in the sample under POM observation.

Small-angle x-ray scattering (SAXS). SAXS measurements were performed on the SWING beamline of the SOLEIL synchrotron (Saint-Aubin, France) at a beam energy of 16 keV with a sample-to-detector distance of 6.22 m, resulting in a q range of 0.001 to 0.24 $Å^{-1}$. Exposure

times were either 500 ms or 1000 ms per measurement. The beam size was approximately 500 × 200 μm^2 (horizontal × vertical). All measurements were performed at room temperature (295 K). The scattered signal was recorded by an Eiger 4M detector (Dectris Ltd, Switzerland) with a pixel size of 75 μm. Preliminary data treatment (angular averaging and normalization) was done using the software Foxtrot developed at the beamline (https://www.synchrotron-soleil.fr/fr/lignes-de-lumiere/swing), which yielded the intensity as a function of the scattering vector magnitude I(q) in absolute units. Subsequent SAXS data modeling and analysis was done either with homemade Python codes (https://pypi.org/project/prismformfactors/) or with SasView 6.0.0 (https://www.sasview.org/).[1,10]

Wide-angle x-ray scattering (WAXS). Additionally, WAXS was performed on the same SWING beamline of the SOLEIL synchrotron, with a sample-to-detector distance of 0.52 m, and all other parameters such as beam energy, exposure time, and beam size the same as in SAXS.

SAXS analysis: Colloidal NR assemblies. More detailed explanation of the SAXS analysis of the assemblies is found in **Chapter 3.3**.

Lattice symmetry, parameters, and compacity

The positions (q-values) of the Bragg peaks in the 1D SAXS radial profiles of each sample were manually fitted using a homemade Python code to determine the lattice symmetry and parameters of the different NR colloidal metasurfaces.

Compacity in 2D and 3D

3D compacities of the colloidal assemblies were calculated by dividing the volume of one metallic NR with the volume of the corresponding 3D primitive unit cell of the assembly at the specific CTAC concentration. Similarly, 2D compacities of colloidal metasurfaces were calculated by dividing the cross-sectional area of one NR with the area of the corresponding 2D primitive unit cell of the assembly at the specific CTAC concentration. Note that only the metallic volume or area of the NR is considered in this calculation, and not the CTAC ligand bilayer around the NR.

Crystalline domain size, D_{corr}

The shapes of the Bragg peaks in the 1D SAXS radial profiles of each sample were fitted in SasView Version 6.0.0 using a pseudo-Voigt model

(https://marketplace.sasview.org/models/127/), which is a weighted sum of a Gaussian and a Lorentzian peak model. The full width at half maximum (FWHM) value from the fit is taken to calculate the Debye-Scherrer correlation length (D_{corr}) in either the xy plane or the z-axis of the NR assemblies with the z-axis taken along the normal of a metasurface, as follows:

$$D_{corr} = \frac{2\pi\, n}{FWHM}$$

where n is a constant, equal to 1.05 for $D_{corr,\,xy}$, and 0.89 for $D_{corr,\,z}$, different from unity due to the anisotropy of the shapes of the NR assemblies, which causes elongations of the Bragg spots in different directions depending on which *hkl* reflection they correspond to.

SAXS analysis: Structures of micellar depletants. More detailed explanation of the SAXS analysis of the micellar depletants is found in **Chapter 3.1-3.2**. To model the structure of surfactant (CTAC or azoTAB) micelles, either a prolate or ellipsoid core-shell model form factor was used depending on the known geometry in literature. The core contains the hydrophobic carbon chains, and the head contains the polar trimethylammonium head and any condensed counterions. In the case of concentrated surfactant solutions, correlation between micelle positions was modelled by the Hayter-Penfold Rescaled Mean Spherical Approximation (Hayter MSA) structural factor model was employed, which applies for charged colloidal spheres in a dielectric medium[23,24]. The fitting was done in SasView 6.0.0, with SAXS data in absolute scaling, with the background signal of the capillary and water subtracted. To increase the accuracy of the fitting, certain parameters like the electron scattering length density (SLD) for the core and shell were kept within a narrow range.

Theoretical depletion model. The interaction potentials experienced by pairs of colloidal NRs were calculated by modelling a pair of NRs as flat silver plates experiencing a sum of van der Waals, electrostatic, and depletion forces. Equations were taken from Cheng, et al[22]. A Hamaker constant $H = 9 \times 10^{-20}$ J was used for the Ag-water-Ag geometry, within the range determined by Jiang and Pinchuk[25,26]**.** The interaction area *A* is the surface area of a NR lateral facet. For C4-NRs, $A = l_{TEM} \times w_{TEM}$. For C5-NRs, $A = l_{TEM} \times a$, where a is the edge length of the pentagonal section, and l_{TEM} and w_{TEM} are the lengths and widths of the NRs measured by TEM. Here, a is approximated as $\pi\, w_{TEM} / 5$. The constant potential at the CTAC-modified NR surface is taken

to be ϕ = 30 mV, adapted from Walker, et al[27]. The theoretical equilibrium d_{gap} is taken to be inter-NR gap at the minima of the total potential well U_{tot} where depletion force is non-zero.

2.7. Functional properties of assemblies

Surface enhanced Raman scattering. SERS microscopy was done using a WITec Alpha300 Access microscope and C5-S functionalized with 4-ATP. For each batch of metasurfaces made at a specific CTAC concentration, the Eppendorf tube containing NR metasurfaces was gently agitated, and 5 µL of suspension was taken up into an optical capillary (0.05 mm × 1 mm section). The capillary is then sealed and set on the microscope stage for SERS. For each capillary, measurements are taken on 15 metasurfaces randomly chosen along the whole length of the capillary. For each metasurface measurement, an average of 10 spectrum acquisitions each acquired in 1 s, with the 100x objective and at optimal focus for maximum SERS counts. Measurements are done with either red laser (633 nm) and green laser (532 nm) excitation, with 0.1 mW laser power with a beam width of approximately 1 µm, using the 100x objective. For light-controlled SERS with photo-DISA, the SERS setup remains the same, except that the samples in optical capillaries are irradiated prior to SERS measurement to induce tunable plasmonic enhancement. The samples are irradiated with UV or blue light at a 5 cm sample-to-LED distance for the desired duration, at the maximum power setting; the exact irradiances are detailed in **Table 1**.

Circular dichroism (CD) spectroscopy. Circular dichroism spectra were recorded using a Jasco V-1700 CD-spectrophotometer. For the characterization of colloidal dispersions, quartz cuvettes with an optical path of 5mm were used for the extinction and CD equipment[2].

Electric field application and alignment of colloidal assemblies. A suspension of the colloidal NP assemblies was placed into an optical capillary through capillary suction. This capillary was then inserted perpendicularly between two electrodes, with the electrodes between a space of around 5 mm between them. An alternate electric current was then applied to the sample using a programmable AC power supply ((ITECH IT-M7700, MB Electronique). A sinusoidal AC voltage (f = 500 kHz) of variable amplitude was applied, ramping up and down between E = 0 to 200 $V_{peak\text{-}to\text{-}peak}$ / mm.

2.8. References

(1) Trazo, J. G.; Marcone, J.; Nag, R.; Goldmann, C.; Kutalia, N.; Bizien, T.; Pansu, B.; Impéror-Clerc, M.; Hamon, C. Colloidal Tunable Metasurfaces via Depletion-Induced Self-Assembly of Plasmonic Nanorods. *ACS Appl. Mater. Interfaces* **2025**, *17* (45), 62349–62359. https://doi.org/10.1021/acsami.5c17436.

(2) Trazo, J. G.; Serrano Freijeiro, A.; Mychinko, M.; Kutalia, N.; Impéror-Clerc, M.; Bals, S.; Liz-Marzán, L. M.; Pérez-Juste, J.; Pastoriza-Santos, I.; Hamon, C. Tunable Plasmonic Circular Dichroism of Hierarchical Chiral Assemblies. *Chem. Mater.* **2025**, *37* (16), 6237–6245. https://doi.org/10.1021/acs.chemmater.5c00909.

(3) Hotton, C.; Trazo, J. G.; Modin, E.; Bardouil, A.; Kutalia, N.; Marcone, J.; Nag, R.; Goldmann, C.; Paineau, E.; Chuvilin, A.; Impéror-Clerc, M.; Bizien, T.; Constantin, D.; Hamon, C. Evaporation-Induced Phase Transitions in Free-Standing Plasmonic Nanoparticle Assemblies. *Nano Lett.* **2026**, acs.nanolett.6c01619. https://doi.org/10.1021/acs.nanolett.6c01619.

(4) Sánchez-Iglesias, A.; Winckelmans, N.; Altantzis, T.; Bals, S.; Grzelczak, M.; Liz-Marzán, L. M. High-Yield Seeded Growth of Monodisperse Pentatwinned Gold Nanoparticles through Thermally Induced Seed Twinning. *J. Am. Chem. Soc.* **2017**, *139* (1), 107–110. https://doi.org/10.1021/jacs.6b12143.

(5) Scarabelli, L.; Grzelczak, M.; Liz-Marzán, L. M. Tuning Gold Nanorod Synthesis through Prereduction with Salicylic Acid. *Chem. Mater.* **2013**, *25* (21), 4232–4238. https://doi.org/10.1021/cm402177b.

(6) Aliyah, K.; Lyu, J.; Goldmann, C.; Bizien, T.; Hamon, C.; Alloyeau, D.; Constantin, D. Real-Time *In Situ* Observations Reveal a Double Role for Ascorbic Acid in the Anisotropic Growth of Silver on Gold. *J. Phys. Chem. Lett.* **2020**, *11* (8), 2830–2837. https://doi.org/10.1021/acs.jpclett.0c00121.

(7) González-Rubio, G.; Kumar, V.; Llombart, P.; Díaz-Núñez, P.; Bladt, E.; Altantzis, T.; Bals, S.; Peña-Rodríguez, O.; Noya, E. G.; MacDowell, L. G.; Guerrero-Martínez, A.; Liz-Marzán, L. M. Disconnecting Symmetry Breaking from Seeded Growth for the Reproducible Synthesis of High Quality Gold Nanorods. *ACS Nano* **2019**, *13* (4), 4424–4435. https://doi.org/10.1021/acsnano.8b09658.

(8) Gómez-Graña, S.; Goris, B.; Altantzis, T.; Fernández-López, C.; Carbó-Argibay, E.; Guerrero-Martínez, A.; Almora-Barrios, N.; López, N.; Pastoriza-Santos, I.; Pérez-Juste, J.; Bals, S.; Van Tendeloo, G.; Liz-Marzán, L. M. Au@Ag Nanoparticles: Halides Stabilize {100} Facets. *J. Phys. Chem. Lett.* **2013**, *4* (13), 2209–2216. https://doi.org/10.1021/jz401269w.

(9) Goldmann, C.; Chaâbani, W.; Hotton, C.; Impéror-Clerc, M.; Moncomble, A.; Constantin, D.; Alloyeau, D.; Hamon, C. Confinement Effects on the Structure of Entropy-Induced Supercrystals. *Small* **2023**, 2303380. https://doi.org/10.1002/smll.202303380.

(10) Marcone, J.; Trazo, J. G.; Nag, R.; Goldmann, C.; Ratel-Ramond, N.; Hamon, C.; Impéror-Clerc, M. Form Factor of Prismatic Particles for Small-Angle Scattering Analysis. *J Appl Crystallogr* **2025**, *58* (2), 543–552. https://doi.org/10.1107/S1600576725000676.

(11) Ni, B.; Mychinko, M.; Gómez-Graña, S.; Morales-Vidal, J.; Obelleiro-Liz, M.; Heyvaert, W.; Vila-Liarte, D.; Zhuo, X.; Albrecht, W.; Zheng, G.; González-Rubio, G.; Taboada, J. M.; Obelleiro, F.; López, N.; Pérez-Juste, J.; Pastoriza-Santos, I.; Cölfen, H.; Bals, S.; Liz-Marzán, L. M. Chiral Seeded Growth of Gold Nanorods Into Fourfold Twisted Nanoparticles with Plasmonic Optical Activity. *Advanced Materials* **2023**, *35* (1), 2208299. https://doi.org/10.1002/adma.202208299.

(12) Rodríguez-Fernández, J.; Pérez-Juste, J.; Mulvaney, P.; Liz-Marzán, L. M. Spatially-Directed Oxidation of Gold Nanoparticles by Au(III)−CTAB Complexes. *J. Phys. Chem. B* **2005**, *109* (30), 14257–14261. https://doi.org/10.1021/jp052516g.

(13) González-Rubio, G.; Mosquera, J.; Kumar, V.; Pedrazo-Tardajos, A.; Llombart, P.; Solís, D. M.; Lobato, I.; Noya, E. G.; Guerrero-Martínez, A.; Taboada, J. M.; Obelleiro, F.; MacDowell, L. G.; Bals, S.; Liz-Marzán, L. M. Micelle-Directed Chiral Seeded Growth on Anisotropic Gold Nanocrystals. *Science* **2020**, *368* (6498), 1472–1477. https://doi.org/10.1126/science.aba0980.

(14) Üzer, A.; Can, Z.; Akın, İ.; Erçağ, E.; Apak, R. 4-Aminothiophenol Functionalized Gold Nanoparticle-Based Colorimetric Sensor for the Determination of Nitramine Energetic Materials. *Anal. Chem.* **2014**, *86* (1), 351–356. https://doi.org/10.1021/ac4032725.
(15) Patel, U. B.; Mehta, V. N.; Kumar, M. A.; Kailasa, S. K. 4-Aminothiophenol Functionalized Gold Nanoparticles as Colorimetric Sensors for the Detection of Cobalt Using UV–Visible Spectrometry. *Res Chem Intermed* **2013**, *39* (2), 771–779. https://doi.org/10.1007/s11164-012-0773-9.
(16) Wedler, V.; Strauß, F.; Sudhakar, S.; Hermsdorf, G. L.; Stierhof, Y.-D.; Schäffer, E. Polycationic Gold Nanorods as Multipurpose *in Vitro* Microtubule Markers. *Nanoscale Adv.* **2020**, *2* (9), 4003–4010. https://doi.org/10.1039/D0NA00406E.
(17) Goßler, F. R.; Steiner, A. M.; Stroyuk, O.; Raevskaya, A.; König, T. A. F. Active Plasmonic Colloid-to-Film-Coupled Cavities for Tailored Light–Matter Interactions. *J. Phys. Chem. C* **2019**, *123* (11), 6745–6752. https://doi.org/10.1021/acs.jpcc.8b12566.
(18) Yang, P.-W.; Thoka, S.; Lin, P.-C.; Su, C.-J.; Sheu, H.-S.; Huang, M. H.; Jeng, U.-S. Tracing the Surfactant-Mediated Nucleation, Growth, and Superpacking of Gold Supercrystals Using Time and Spatially Resolved X-Ray Scattering. *Langmuir* **2017**, *33* (13), 3253–3261. https://doi.org/10.1021/acs.langmuir.6b04319.
(19) Zang, S.; Paul, S.; Leung, C. W.; Chen, M. S.; Hueckel, T.; Hocky, G. M.; Sacanna, S. Direct Observation and Control of Non-Classical Crystallization Pathways in Binary Colloidal Systems. *Nat Commun* **2025**, *16* (1), 3645. https://doi.org/10.1038/s41467-025-58959-0.
(20) García-Lojo, D.; Modin, E.; Gómez-Graña, S.; Impéror-Clerc, M.; Chuvilin, A.; Pastoriza-Santos, I.; Pérez-Juste, J.; Constantin, D.; Hamon, C. Structure and Formation Kinetics of Millimeter-Size Single Domain Supercrystals. *Adv. Funct. Mater.* **2021**, *31* (27), 2101869. https://doi.org/10.1002/adfm.202101869.
(21) Blayo, C.; Houston, J. E.; King, S. M.; Evans, R. C. Unlocking Structure–Self-Assembly Relationships in Cationic Azobenzene Photosurfactants. *Langmuir* **2018**, *34* (34), 10123–10134. https://doi.org/10.1021/acs.langmuir.8b02109.
(22) Cheng, Z.; Jones, M. R. Assembly of Planar Chiral Superlattices from Achiral Building Blocks. *Nat Commun* **2022**, *13* (1), 4207. https://doi.org/10.1038/s41467-022-31868-2.
(23) Hansen, J.-P.; Hayter, J. B. A Rescaled MSA Structure Factor for Dilute Charged Colloidal Dispersions. *Molecular Physics* **1982**, *46* (3), 651–656. https://doi.org/10.1080/00268978200101471.
(24) Hayter, J. B.; Penfold, J. An Analytic Structure Factor for Macroion Solutions. *Molecular Physics* **1981**, *42* (1), 109–118. https://doi.org/10.1080/00268978100100091.
(25) Pinchuk, A. O. Size-Dependent Hamaker Constant for Silver Nanoparticles. *J. Phys. Chem. C* **2012**, *116* (37), 20099–20102. https://doi.org/10.1021/jp3061784.
(26) Jiang, K.; Pinchuk, P. Temperature and Size-Dependent Hamaker Constants for Metal Nanoparticles. *Nanotechnology* **2016**, *27* (34), 345710. https://doi.org/10.1088/0957-4484/27/34/345710.
(27) Walker, D. A.; Browne, K. P.; Kowalczyk, B.; Grzybowski, B. A. Self-Assembly of Nanotriangle Superlattices Facilitated by Repulsive Electrostatic Interactions. *Angew Chem Int Ed* **2010**, *49* (38), 6760–6763. https://doi.org/10.1002/anie.201002558.

Chapter 3

DEPLETION-INDUCED SELF-ASSEMBLY (DISA): DEVELOPMENT AND TIPS-AND-TRICKS

In this thesis project, the development of 'living colloidal crystals' from plasmonic metal nanoparticles (NPs) was a multistep process that required much development and optimization. As noted in the Introduction, the big idea of this is to *control depletion-induced self-assembly (DISA) by playing with its two components:* first, the nanoparticle building blocks, specifically their shape anisotropy, and second, the physico-chemical properties of the depletant. Such control of DISA will then be utilized to create dynamic and stimuli-responsive assemblies with metamaterial-like properties.

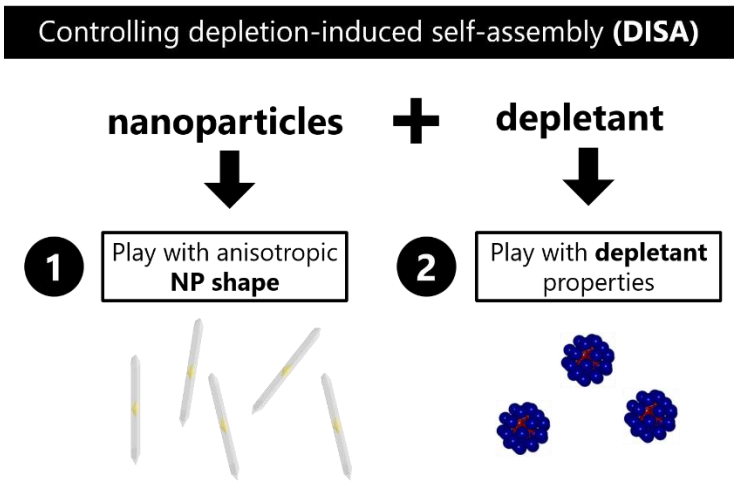

This chapter will talk about the ***development*** of our protocols for depletion-induced self-assembly (DISA), including some ***new results and insights*** from this development phase, and finally a ***'tips-and-tricks' section*** for the readers in implementing these methods. This discussion section is divided into three parts on: micellar depletants, the synthesis of anisotropic metal nanorod (NR) building blocks, and the development of DISA protocols and characterization of the resulting assemblies.

3.1. Micellar depletant systems

Preparation of depletant solutions and mixtures

In this project, the first component of the DISA system is the colloidal depletant, particularly aqueous micelles of surfactants. For classic *passive* DISA, cetyltrimethyammonium chloride (CTAC) was used, as it does not crystallize around room temperature, unlike other similar surfactants like CTAB, its bromide analog. Aqueous stock solutions of CTAC were prepared either from commercial solutions (25 wt.%) or from dissolution of commercial solid CTAC powder. These solutions were then used for performing DISA, either by fast one-shot addition of depletant (fast DISA), or by slow diffusion of depletant (slow DISA). When used for DISA, it was ensured that these depletant solutions were at around 20 °C. These solutions were characterized by small-angle X-ray scattering (SAXS) to probe the structures and their concentrations formed by the self-assembly of the CTAC molecules in water, both in the micellar phase and more concentrated mesophases (**Figure 1**), and to connect the micelle structure and concentration to the corresponding depletion forces that they can exert.

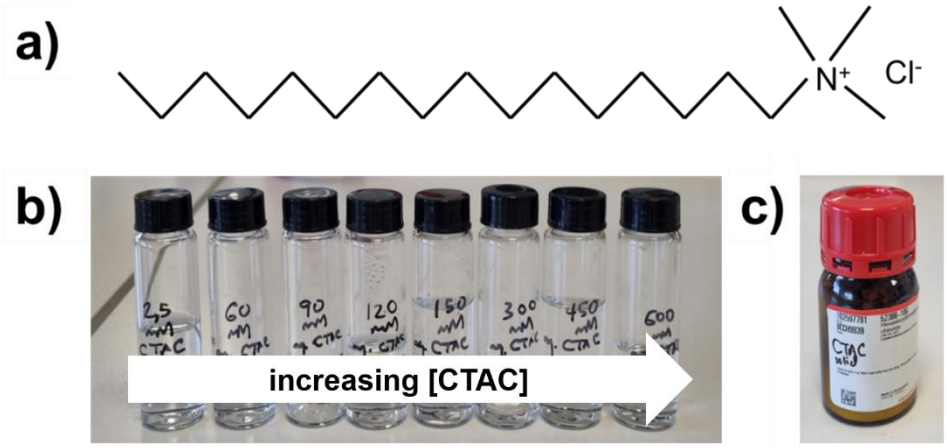

Figure 1. (a) *Molecular structure of cetyltrimethyammonium chloride (CTAC).* ***(b)*** *Series of aqueous CTAC solutions of increasing concentration.* ***(c)*** *Commercial anhydrous CTAC powder used to make concentrated depletant mixtures (> 25 wt. %).*

For *active* photo-DISA, four different azoTAB compounds were synthesized in-house by our colleague Claire Goldmann of the LPS chemistry service, and then characterized and screened for use. These surfactants have a general form of C_xAzoOC_yTAB, having the same trimethylammonium bromide head as CTAB, but also having an azobenzene moiety in the hydrophobic portion of the molecule, with a tail (C_x) and a spacer (C_y) aliphatic carbon chain on either side. More details on the tail and spacer lengths will be discussed in Chapter 6, in

relation the effect of these lengths on the change in micelle shape upon UV or blue illumination. These azoTABs were then characterized by UV-vis absorption spectroscopy, ^{1}H-NMR, SAXS, and water solubility tests to assess their purity and their phase behavior (**Figure 2**). Two major concerns on the azoTAB properties were noted. First, the azoTABs exhibited a tendency to crystallize at high concentrations, particularly the 6A4 and 4A6 varieties above 100 mM, leading to precipitation of a large fraction of the surfactant as fine white to yellow solids, leaving a strongly yellow to orange supernatant; this precipitation persisted in the temperature range of 10 to 50 °C. Therefore, to minimize the difference between the known depletant concentration and the concentration existing as dispersed micelles, only 2A2 and 8A2 were used as depletants. Second, purity of the azoTABs lied in the range of 80-90% as determined by ^{1}H-NMR, which may partially impact the micellar self-organization of the surfactant molecules versus what is reported in other literature[1,2] (**Figure 3**).

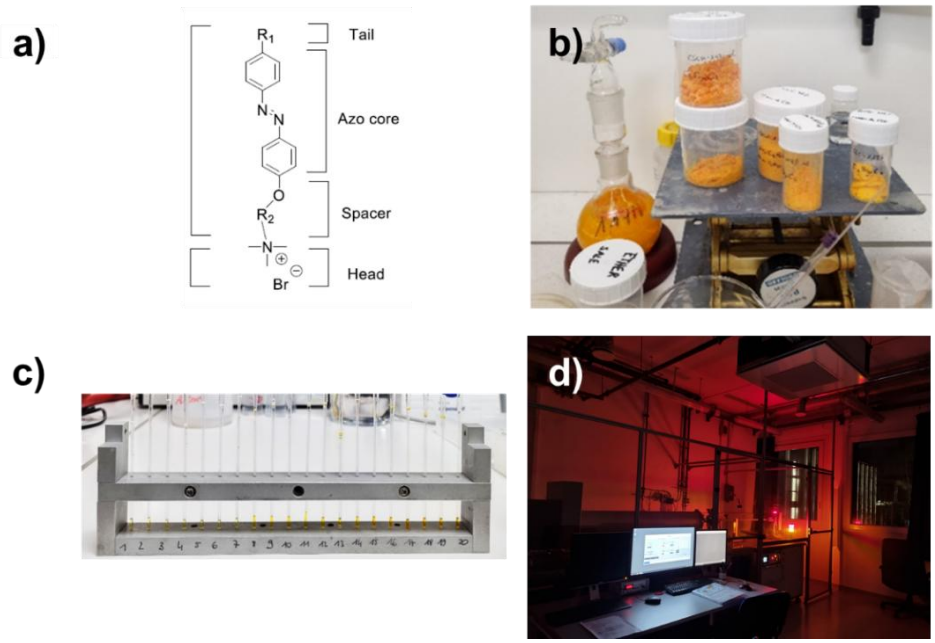

Figure 2. (a) *General molecular structure of azoTABs with variable tail and spacer lengths[1]. **(b)** Various batches of synthesized AzoTABs. **(c)** Series of aqueous AzoTAB solutions (2A2 and 8A2) at varying [Azo] concentration for SAXS. **(d)** In-house SAXS-Cu setup at LPS Orsay.*

Impurities may act as co-surfactants and modify the shape and size of the azoTAB micelles, thus slightly affecting the depletion strength[3]. However, both SAXS analysis of the azoTAB solutions and the comparison of experimental versus theoretical depletion strength (discussed in Chapter 6) reveal only a minimal effect of possible co-surfactants on the micelle shape and

size. One must note that in the case of 8A2, only a 1.57% of the surfactant was in the precipitate. Additionally, no detectable difference was seen in the ^{1}H-NMR spectra of the 2A2 and 8A2 precipitate versus supernatant, suggesting that the precipitation does not separate a substantial fraction of any impurities in the azoTAB (**Figure 3**). More on micelle characterization is discussed in the next sections.

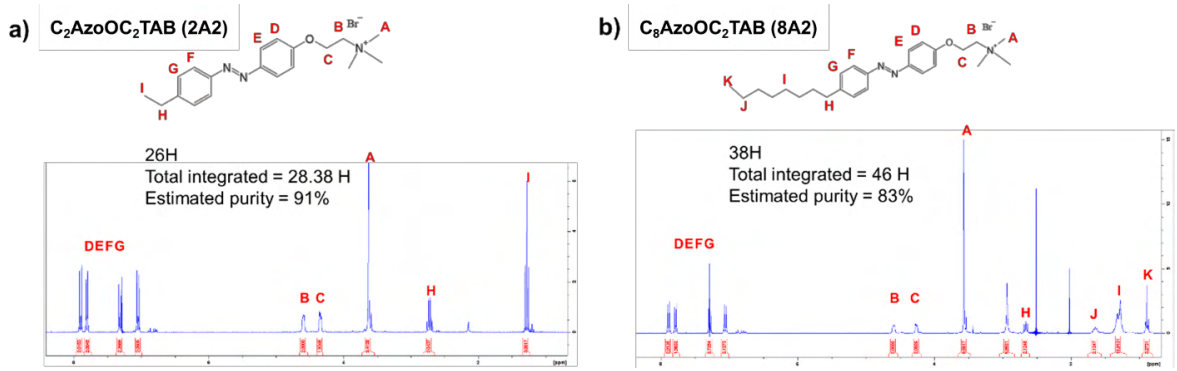

***Figure 3. ^{1}H-NMR characterization of synthesized azoTABs and estimated purity: (a)** 2A2, **(b)** 8A2.*

Control of depletant concentration and phase behavior

To address the concerns of purity and to verify the micelle shape and phase behavior for both CTAC and the azoTABs, gravimetric measurements (i.e., weight fraction of solids) and structural characterization by SAXS were performed. For CTAC, both SAXS and WAXS (wide-angle X-ray scattering) were performed on a series of aqueous solutions of increasing surfactant concentration, up to the gel mesophases and pure solid powder. With this set of SAXS/WAXS data, a robust calibration curve for determining the true CTAC concentration via SAXS peak positions was prepared, particularly for the fluid micellar region where depletion occurs. To make this calibration curve from the SAXS data, first, the q-position of the fundamental Bragg correlation peak (structure factor) was converted to the interplanar spacing $d = 2\pi/q$, and the evolution of d was fitted using a dilution law with the assumption that micelle number concentration would linearly scale by $1/d^3$ in the fluid micellar phase where micelles can move in three dimensions, and $1/d^2$ in the 2D-symmetry hexagonal mesophase (**Figure 4**). This curve was then used in several kinetics experiments conducted later in this thesis, particularly the real-time monitoring of DISA by ultra-slow diffusion of depletant in capillaries, and in monitoring evaporation-induced self-assembly (EISA) of NPs in a freely levitating droplet via

SAXS (i.e., lev-SAXS) to know the actual CTAC concentration. With this lev-SAXS technique, both the full phase behavior of CTAC in water , as well as the depletion-induced self-assembly of NPs in concentrating CTAC were also elucidated in a single experiment[4].

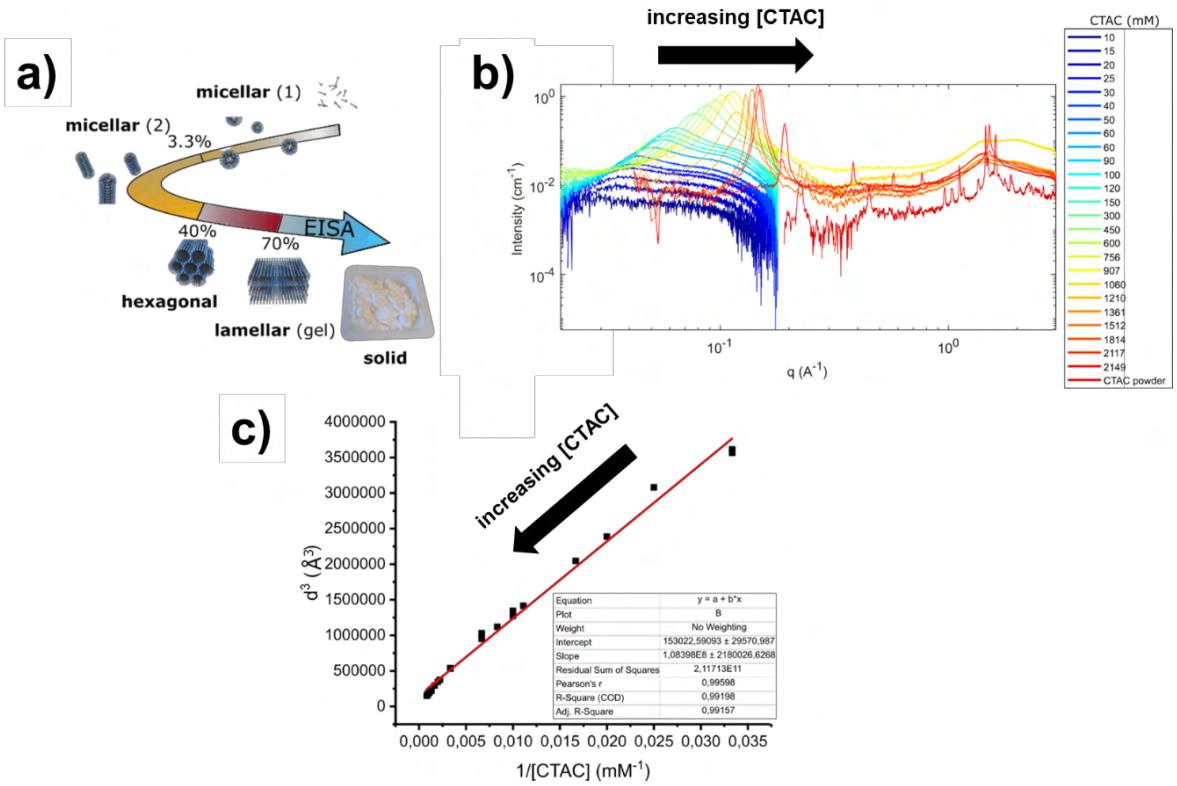

Figure 4. (a) *Scheme of the phase behavior of CTAC in H_2O with increasing surfactant concentration, noted here in weight fraction.* ***(b)*** *1D SAXS radial profiles of aqueous CTAC at increasing concentration, elucidating different phase transitions.* ***(c)*** *CTAC concentration calibration curve via SAXS data: Fitting of primary SAXS structure factor peak position vs. CTAC molar concentration with a $1/d^3$ dilution law. Adapted from our article[4].*

It is important to note that for CTAC, only the concentration range of 1 mM to 1210 mM – the micellar phase – is usable for DISA; it is in this range where freely moving, Brownian micelles exist to induce the depletion interaction between NPs. Beyond this threshold of around 40 wt. %, CTAC exists in a gel mesophase where any dispersed NPs are highly immobilized and the surfactant molecules organize into long-range structures which do not induce appreciable depletion. In fact, it was discovered that metal NRs remain individually dispersed (i.e., not assembled nor aggregated) when in a gel of the CTAC hexagonal phase, as evidenced by the absence of a structure factor or of Bragg peaks in SAXS, and by the retention of the strong color of the dispersed NRs. Similar SAXS analysis for the azoTABs is currently ongoing in our team, and a full phase diagram is yet to be prepared. Highly viscous and gel-like phases, likely

the same liquid crystal phases noted in literature, have been observed[5,6]. However, the long-term stability and the concentration range in which these phases occurred appear to differ from what has been previously reported. It is inferred that effects of impurities may shift the phase boundaries for the azoTABs.

Analysis of the micelle structure

By analyzing and fitting the same 1D SAXS radial profiles, we investigated the evolution of the shape and number concentration of the CTAC micelles as a function of surfactant concentration. Following previous publications on CTAB and CTAC[7], a prolate ellipsoid core-shell model was used to model the micelles, where the core contains the hydrophobic carbon chains, and the head contains the polar trimethylammonium head and any condensed counterions. To model the structure factor which accounts for inter-micellar order or packing, the Hayter-Penfold Rescaled Mean Spherical Approximation (Hayter MSA) model was employed, which applies for charged colloidal spheres in a dielectric medium[8,9]. The fitting was done in SasView 6.0.0, with SAXS data in absolute scaling, with the background signal of the capillary and water subtracted. To increase the accuracy of the fitting, certain parameters like the electron scattering length density (SLD) for the core and shell were kept within a narrow range (**Figure 5**). Doing this, a comprehensive data set of the anisotropic CTAC micelle structure at a wide concentration range (30 mM to 1060 mM) was reported for the first time. Specifically, the fitting allowed the determination of the micellar core and shell dimensions, the charge of one micelle, the aggregation number N_{agg}, and the effective radius and volume fraction of interaction. N_{agg} was taken to be the volume of the whole ellipsoidal micelle, core and shell, divided by the mean volume of one CTAC molecule ν, including both the core (carbon chain) and the polar head with one condensed Cl^- ion. N_{agg} was calculated via the equation:

$$N_{agg} = \frac{4\pi(a+t)(b+t)^2}{3\nu} \qquad \text{(Equation 3.1)}.$$

where a and b are the polar and equatorial radii of the core of the prolate ellipsoid micelles, t is the uniform shell thickness, and ν is the mean volume of one CTAC molecule including core and polar head with condensed Cl^-, calculated to be 618 $Å^3$ via data from literature[10].

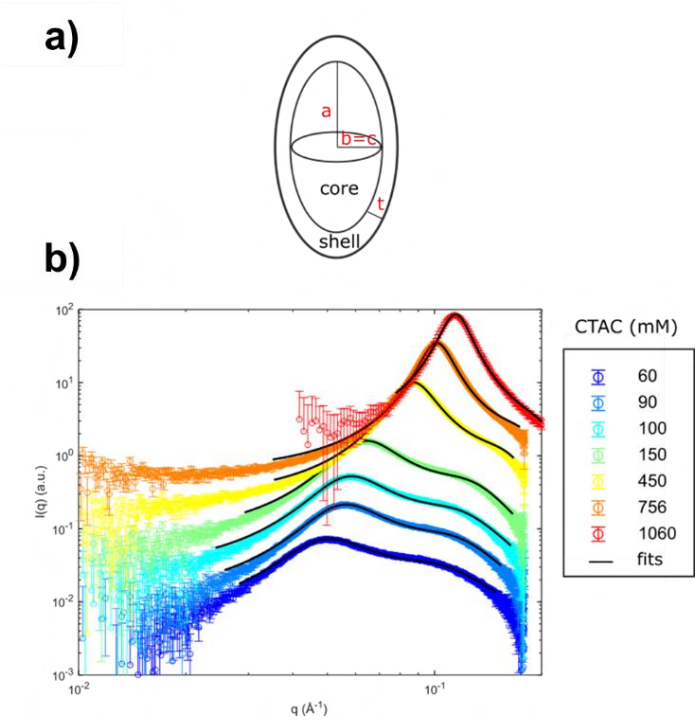

Figure 5. (a) *Illustration of a typical prolate ellipsoid CTAC micelle structure in water, with its hydrophobic core (carbon chains) and hydrophilic shell (polar head and condensed counterions)* ***(b)*** *Fitting of 1D SAXS radial profiles of CTAC with the aforementioned prolate ellipsoid core-shell model form factor and Hayter MSA structure factor. Adapted from our article[4].*

It was found that the ellipticity of the micelles increases with increasing surfactant concentration, with a *transition from spherical to prolate ellipsoid geometry* in the range of 50 to 90 mM. Interestingly, this transition corresponds to a sharp increase in fractional charge of the micelles, followed by a slow decline in charge beyond 200 mM CTAC, hinting at a possible connection between counterion condensation and change in micelle geometry. Both the aggregation number and counterion shell thickness of the micelles also slowly increase past this spherical to ellipsoidal transition (**Figure 6, Table 1**). As CTAC concentration increases, the intensity of the Hayter MSA structure factor peak increases, dominates the SAXS curve, and shifts to higher q values, corresponding to a decreasing average distance between micelles in the medium. It was also found that adding NaCl to the CTAC solutions screens the electrostatic repulsions between the charged micelles, which destroys the correlation between them, causing the broadening and weakening of the structure factor peak. Note however that salt addition also changes the shape and size of the individual micelles. All these data support the hypothesis that the micelles become increasingly elongated just prior to the transition to the hexagonal mesophase, where the surfactant self-organizes into long 'tubes' with 2D hexagonal

packing. The data also supports the strong effect of salt and electrostatics on the shape of the micellar depletant. More details on the CTAC phase behavior, SAXS data fitting method, and determined micelle shape are found in our recent article on Lev-SAXS (C. Hotton, J. G. Trazo, et al. 2026[4])

Table 1. Fitting parameters for aqueous CTAC micelles at increasing surfactant concentration, *using a prolate ellipsoid form factor model and the Hayter MSA structure factor model.*

[CTAC], mM	a_{core} (polar), Å	$b_{core} = c_{core}$ (equatorial), Å	a_{core}/b_{core}	t_{shell}, Å	$\Phi_{interaction}$, Hayter MSA	$V_{micelle}$, nm^3	N_{agg}	SLD_{shell} (10^{-6} $Å^{-2}$)	micelle charge (e)	fractional charge α
30	18.2	18.0	1.01	4.98	0.010	51.42	83.2	9.5	20.1	0.24
50	19.3	19.1	1.01	5.08	0.049	59.82	96.8	9.5	39.2	0.41
60	21.4	18.5	1.16	5.32	0.030	63.68	103.0	9.5	26.7	0.26
90	22.7	17.0	1.34	5.08	0.030	57.00	92.2	9.5	31.9	0.35
100	24.3	16.2	1.50	4.85	0.032	54.35	87.9	9.5	34.7	0.39
150	25.0	16.4	1.53	4.81	0.047	56.06	90.7	9.5	42.5	0.47
450	27.2	17.3	1.57	7.76	0.171	92.17	149.1	9.5	43.5	0.29
756	27.5	16.9	1.63	7.60	0.255	88.24	142.8	9.5	46.9	0.33
1060	27.9	17.1	1.63	8.25	0.418	97.42	157.6	9.5	26.5	0.17

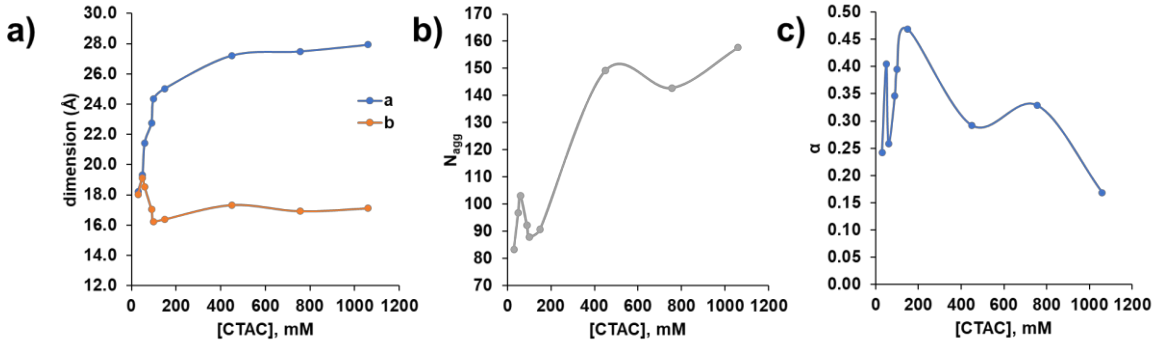

Figure 6. Evolution of CTAC micelle structure and properties at increasing surfactant concentration. (a) *micelle dimensions with changing ellipticity,* ***(b)*** *aggregation number,* ***(c)*** *fractional charge of one micelle.*

Meanwhile, full fitting of the 2A2 and 8A2 azoTAB micelle SAXS data, under dark, UV, and blue illumination, is still ongoing as of writing. However, some successful fitting results by our collaborator, Jérôme Combet from ICS Strasbourg, already revealed a typical oblate ellipsoid geometry for 8A2 in the trans isomer, and a typical spherical geometry in the cis isomer, corroborating with known literature on this azoTAB[1]. This supports the approximately three times increase in depletion force from the trans to cis isomerization of 8A2 experimentally

observed during our photo-DISA experiments. Again, more data and details about the azoTAB micelle fitting are laid out in Chapter 6.

3.2. Development and synthesis of anisotropic nanoparticles

The second component of our DISA system is anisotropic metal nanorods (NRs), primarily gold core – silver shell (Au@Ag) NRs with varying aspect ratio and cross section symmetry *synthesized by ourselves in LPS* and used in Chapters 4 and 6, while chiral fourfold twisted gold NRs (cGNRs) used in Chapter 5 were *synthesized by our collaborator Andrés Serrano-Freijeiro from CINBIO, U. Vigo, Spain*.

Control of nanorod width, length, and symmetry

These NRs were synthesized by controlled seed-mediated growth of silver onto gold cores with the required symmetry, i.e. monocrystalline versus pentatwinned. This was done for precise and separated control of their length and width, to properly study the effect of aspect ratio on the dimensionality, general shape, and internal lattice symmetry of the colloidal NR assemblies. In the development of the NP synthesis protocols, screening was done by doing a series of increasing molar equivalents of silver grown onto the gold cores, adapting the synthesis protocols from our team's previous recent publications[11,12]. For C4-NRs, monocrystalline Au C8-NRs acted as seeds, and the silver shell grows perpendicular to the NR long axis, with the final equilibrium NP shape being a cube. This results in a series of C4-NRs with constant length and varying width. For C5-NRs, pentatwinned Au bipyramids acted as seeds, and the silver shell grows along the NR long axis, to minimize the strain induced by the presence of twin planes, and also due to the use of chloride as a capping agent (**Figure 7**). Typically, the main NRs used in this thesis exhibited strong scattering in the visible range due to one of their dimensions being close to or greater than 100 nm. Additionally, many of the NRs exhibit multipolar longitudinal localized surface plasmon resonances (LSPRs), as well as multiple transverse SPRs (TSPRs) due to them being bimetallic. These resonances were one way of monitoring the extent of NR assembly or disassembly via UV-vis-NIR extinction.

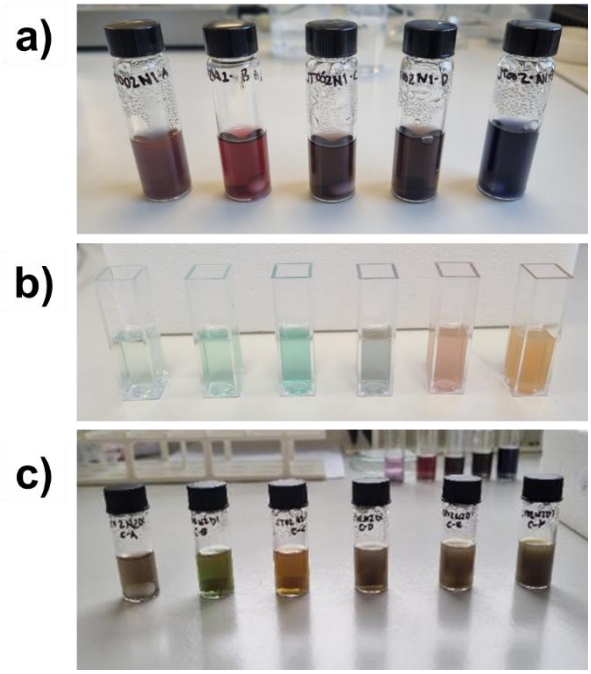

Figure 7. (a) *Screening of Au bipyramids of increasing aspect ratio (left to right) in order to make Au@Ag nanorods of controlled widths.* ***(b)*** *Screening of Au@Ag cuboid nanorods of different width by growing increasing amounts of silver (left to right).* ***(c)*** *Screening of Au@Ag pentagonal nanorods of different length by growing increasing amounts of silver (left to right).*

For all these screening experiments, UV-vis-NIR extinction spectra and TEM images of the NRs were taken for optical and size characterization respectively. Overnight depletion with CTAC was also used to purify the synthesized NRs (**Figure 8**)[13]. The minimum CTAC threshold to induce depletion was also compared to the theoretical threshold determined via the Asakura-Oosawa model[14,15], and used as a starting point for testing DISA with a given NR type. Nonetheless, for very long NRs (length > 200 nm), it was typically not necessary to perform depletion purification prior to self-assembly, as the side products of the silver growth were much smaller than the desired NRs and easily separated during centrifugation.

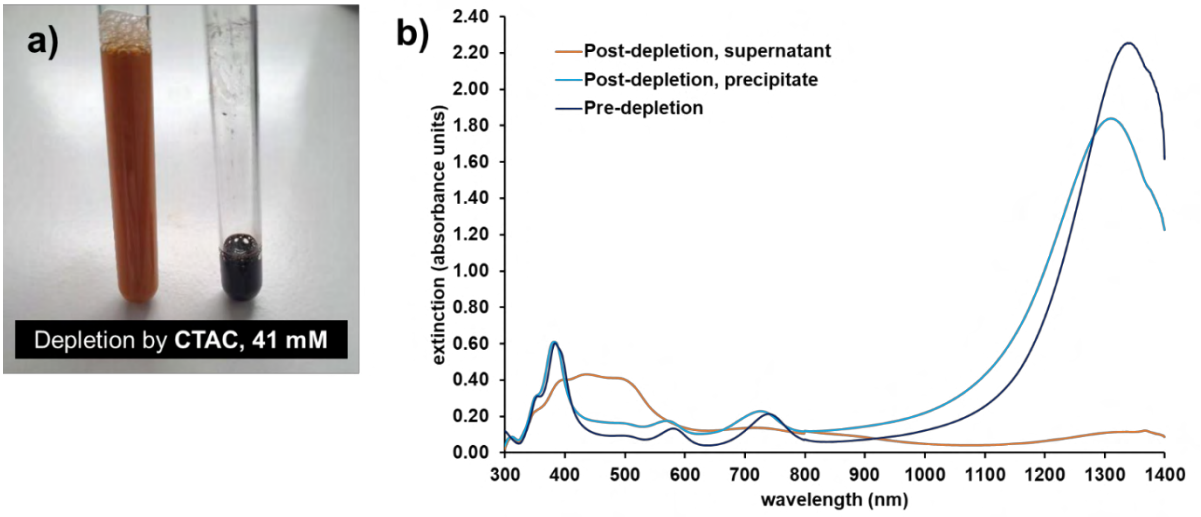

Figure 8. Testing CTAC-induced depletion purification of long Au@Ag C5-NRs: (a) *Separated supernatant (left) and precipitate with desired long C5-S NRs (right); length = 190 nm, width = 27 nm.* ***(b)*** *UV-vis-NIR extinction spectra for pre-depletion and post-depletion supernatant and precipitate for the same C5-S NRs. The supernatant spectrum was rescaled to highlight its features.*

Finally, as a second way of verifying the NR dimensions at very high statistics apart from TEM, we fitted 1D SAXS data of dilute suspensions of our NRs using a new method of fast form factor calculation. This method was developed with the leadership of Jules Marcone, a fellow PhD student in LPS. The calculation method utilizes a numerically stable formula from J. Wuttke to calculate the form factor of a general nanoprism[16], and employs the Lebedev quadrature in averaging the form factor over all possible NR orientations for free particles in colloidal suspension. With the implementation of this method in an interactive widget, in the Python library 'prismformfactors', one can easily determine via SAXS the symmetry and dimensions of any prismatic nanoparticle with fast computation times of less than one second, versus fitting with the Debye equation from atomic coordinates which can take minutes to hours[17] (**Figure 9**, **Figure 10**, **Table 2**). Additionally, our model is now incorporated in the next SASView software release (6.2.0) to come in July 2026, called prism model, where the quadrature used is now the Fibonacci instead of the Lebedev method. More information on our form factor fitting method and its application is found in our recent article (J. Marcone, J.G. Trazo, et al., 2025)[17].

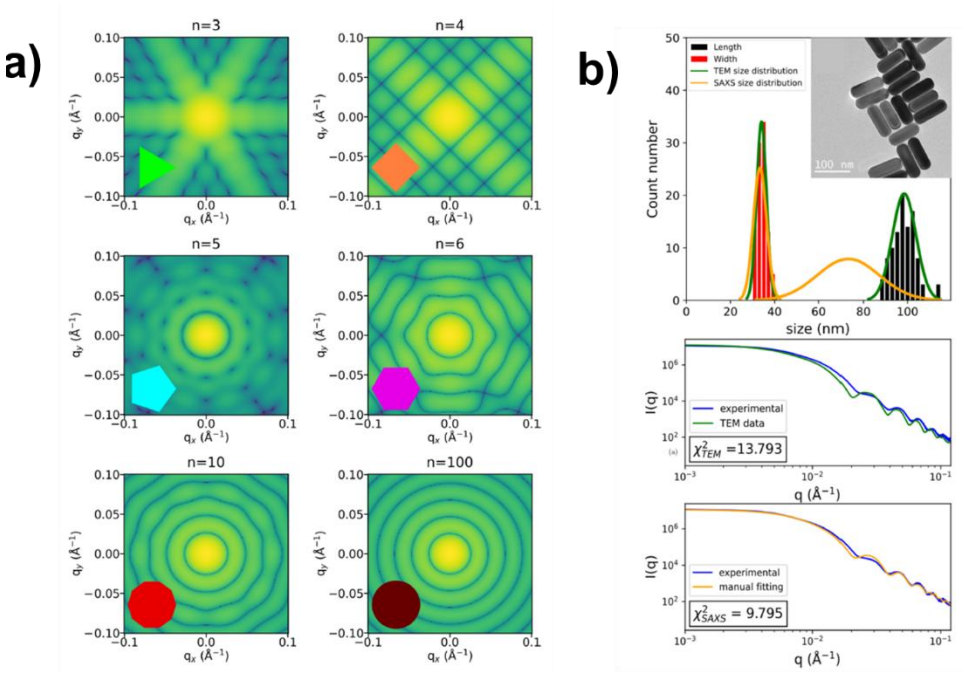

Figure 9. (a) *Fast form factor modelling of 2D SAXS diffractograms for nanoprisms of different cross-sections.* ***(b)*** *Comparison of C4-NR sizes obtained by TEM versus manual SAXS fast form factor fitting. Adapted from our recent paper*[17].

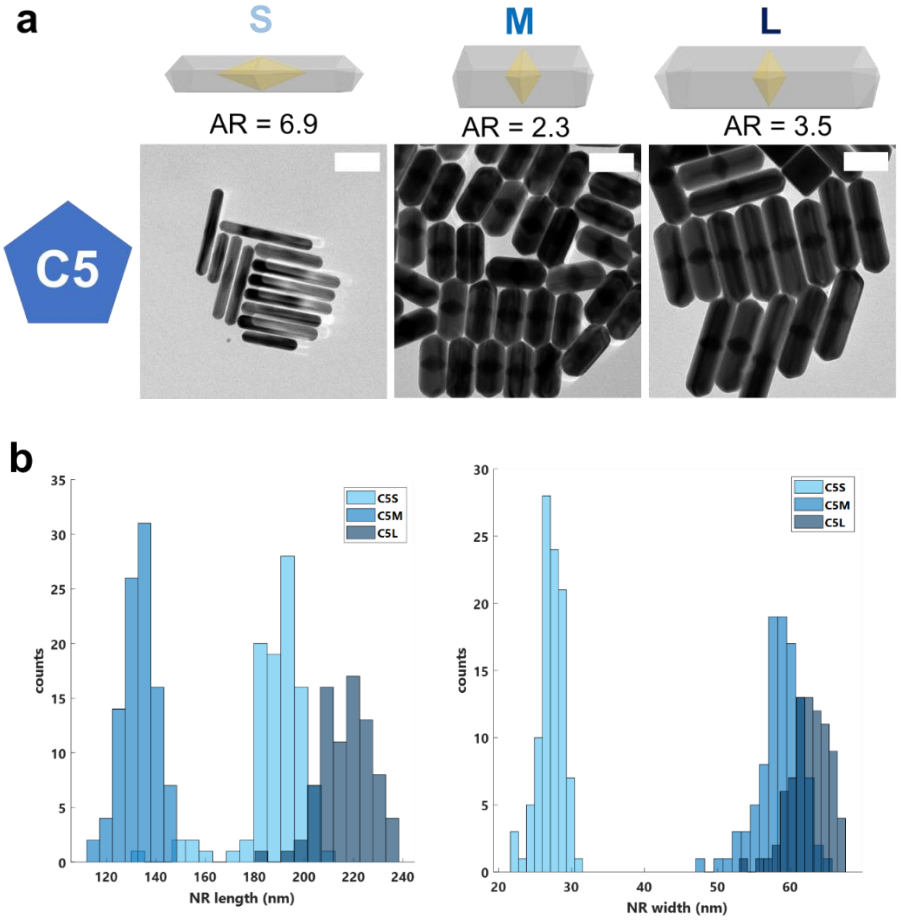

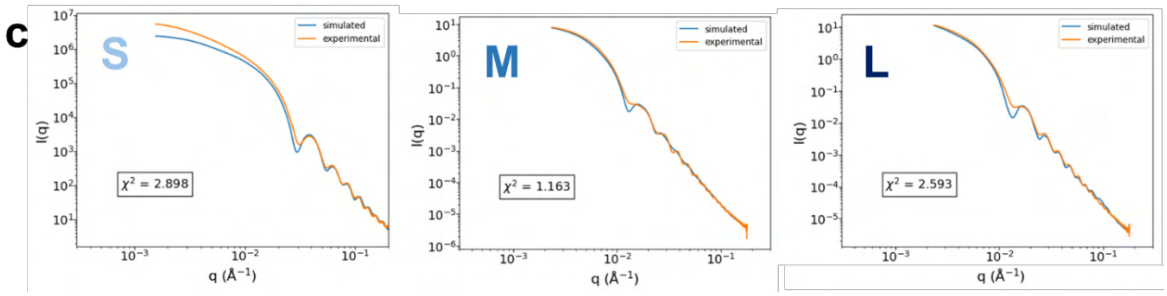

Figure 10. Size characterization of Au@Ag C5-NRs: TEM vs. SAXS. a) *TEM micrographs and corresponding illustrations of the NRs (Scale bars are 100 nm.)* ***b)*** *Histograms of length and width distributions by TEM image analysis.* ***c)*** *NR size analysis by SAXS form factor fitting. Adapted from our paper[18].*

Table 2. Size distribution analysis of the Au@Ag C5-NRs of varying anisotropy, and their minimum DISA threshold. *Adapted from our paper[18].*

	l_{TEM} (nm)	w_{TEM} (nm)	l_{SAXS} (nm)	w_{SAXS} (nm)	aspect ratio (AR_{TEM})	facet interaction area (A_{TEM}, 1000 nm^2)	experimental self-assembly threshold (mM CTAC)	theoretical self-assembly threshold (mM CTAC)
C5-S	**188.9 ± 12.5**	**27.2 ± 1.8**	121.8 ± 7.3	26.4 ± 1.3	6.9 ± 0.6	3.2 ± 0.3	35 ± 5	55 ± 5
C5-M	**133.2 ± 6.6**	**58.6 ± 3.0**	111.7 ± 7.8	61.2 ± 6.1	2.3 ± 0.2	4.9 ± 0.4	35 ± 5	36 ± 3
C5-L	**217.1 ± 10.2**	**62.6 ± 2.7**	182.7 ± 7.3	60.0 ± 3.0	3.5 ± 0.2	8.5 ± 0.6	20 ± 5	22 ± 1

Synthesis of ultra-long metal nanorods

One notable contribution of this thesis is in development of synthesis protocols for ultra-long Au@Ag C5-NRs (or AgNRs, as they are predominantly silver due to high extent of growth), up to one to two microns long, that remain straight and rigid in suspension. These NRs are targeted particularly for their very high anisotropy and strong plasmon resonance in the near-IR. In this thesis, our ultra-long NRs were synthesized by controlled silver growth onto pentatwinned Au bipyramid seeds, but with pre-heating of the bipyramid suspension prior to the addition of the silver precursor ($AgNO_3$ solution) and reducing agent (ascorbic acid), and with temperature control of the reaction mixture by insulation with aluminum foil (**Figure 11a,b**). More on the synthesis and behavior of these NRs is discussed in our recent preprint (N. Kutalia, J. G. Trazo, et al. 2026)[19]. With the help of the LPS chemistry service, even longer NRs

from 2 to 6 µm long could be synthesized, but these syntheses required the use of nitric acid to slow down the silver growth kinetics, or the use of a syringe pump for the $AgNO_3$ and/or reducing agent to limit the formation of Ag NP side products[20]. For these ultra-long NRs, depletion purification after synthesis was not necessary as the desired particles were much denser than any side products, and in fact, the NRs would already exist in the form of depletion-induced assemblies in the as-synthesized mixture, due to the presence of free CTAC (usually 10 mM) in solution which is added to control the NR growth, but can also act as a depletant.

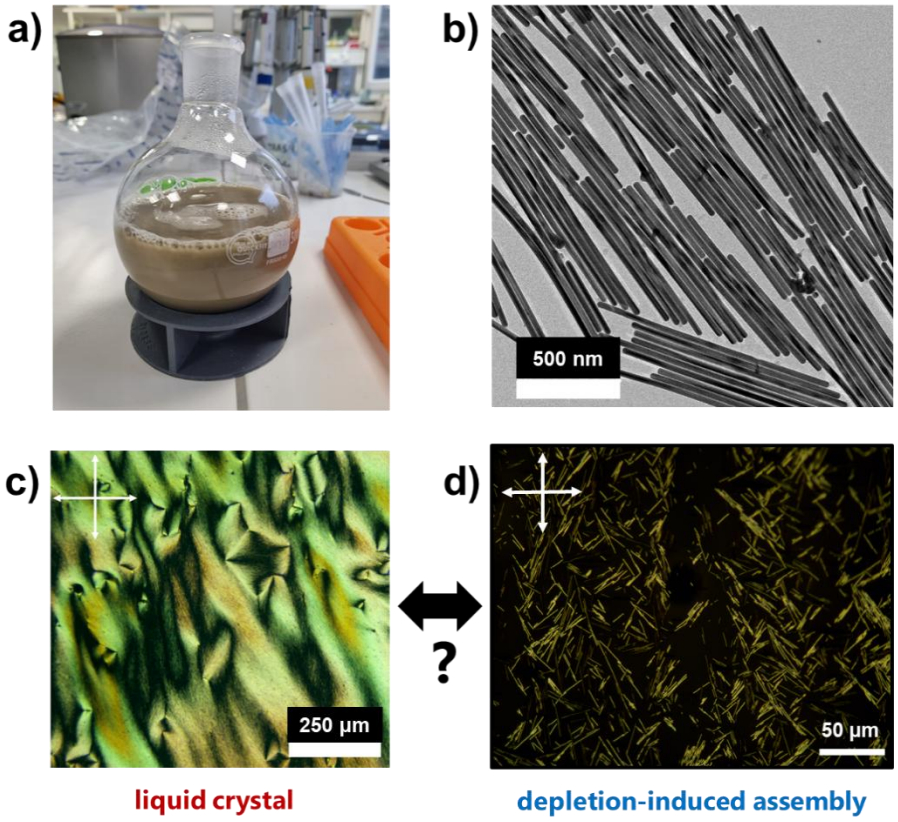

Figure 11. (a) *As-synthesized suspension of micron-long silver nanorods (AgNRs) by silver growth onto purified Au NPs as seeds.* ***(b)*** *Tranmission electron micrographs (TEM) of the micron-long AgNRs.* ***(c)*** *Colloidal liquid crystals of ultra-long AgNRs with dominant interparticle repulsion, versus* ***(d)*** *depletion-induced colloidal assemblies of the same AgNRs with dominant interparticle attraction.*

Unlike the other main NRs in this project, these ultra-long NRs exhibit unique phases – particularly either colloidal liquid crystals in the absence of any substantial depletion interaction, or 1D 'needle' assemblies made of side-by-side NRs in the presence of depletant (**Figure 11c,d**). The remarkable phase behavior of these very anisotropic rods is detailed further in the perspectives of Chapters 4 and 6.

Determination of NP concentration for non-Au or bimetallic composition

One notable challenge in this project is the determination of NP concentration, which tends to influence the size and dimensionality of colloidal assemblies, whether they are induced by depletion or other nanoscale forces in general. For a suspension of pure Au NPs, a robust and reliable approximation is to measure its extinction at 400 nm, where the extinction is mainly due to the Au interband transitions, without overlap with the Au NP SPRs, signifying the molar amount of reduced gold independent of the size and shape of the NPs. For example, an absorbance of 1.2 corresponds to a total Au^0 concentration of 0.5 mM[21]. However, this approximation cannot be used in the case of bimetallic gold core – silver shell (Au@Ag) NPs – the main particles used in this project. Even in the case of pure Ag NPs, the interband transition is deeper in the UV range, and there has been more limited work on using UV absorbance as a measure of Ag^0 concentration whether for spheres or rods[22]. As a result, we resorted to a combination of SAXS analysis and weight fraction determination to control the real concentration of the Au@Ag NRs which we self-assembled. Two methods were employed. The first method uses volume fraction determination by fitting 1D SAXS radial profiles of the dispersed NRs (i.e., form factors) with an appropriate prism or cylinder model. When the experimental data is rescaled in absolute units (cm^{-1}), the fit will return a scale parameter that corresponds exactly to the volume fraction of NRs in suspension, assuming the particle has a uniform scattering length density (SLD), meaning uniform composition. The method can still be applied to bimetallic core-shell particles, but proper modelling with different SLDs for the particle's core and shell is required[23]. By geometric calculations and given the known dimensions of a single NR, this volume fraction can then be converted to the molar concentration of reduced metal ($M^0 = Au^0 + Ag^0$), and also the number concentration of NRs. To ensure that our SAXS data is correctly rescaled in absolute units, one must utilize a calibrant or standard reference for intensity; in our team, we utilized a glassy carbon sample from the Argonne National Laboratory, USA[24] (**Figure 12**). The full equation for the rescaling is detailed in Figure 10 below (**Equation 3.2**):

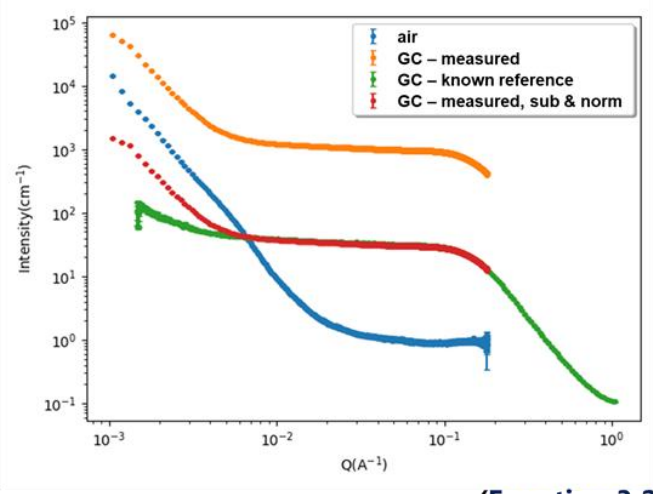

$$I_{sample,\,norm}\,(cm^{-1}) = K\frac{I_{sample} - I_{cap,solvent}}{l_{cap}\,(mm)}$$ **(Equation 3.2)**

K = 0.036, from GC calibration

Figure 12. Determination of NR concentration via absolute intensity calibration with a glassy carbon reference.

where $I_{sample,\,norm}$ is the SAXS intensity of a sample normalized in absolute units, I_{sample} and $I_{cap,solvent}$ are the non-normalized intensities of the sample and of a capillary (container) with solvent as background respectively, l_{cap} is the thickness of the capillary in the direction of incident X-rays, and K is the calibration constant for absolute scaling, determined by renormalizing the experimentally-measured SAXS intensity of the glassy carbon standard in comparison to a reference SAXS intensity.

The second method uses X-ray transmission measured during SAXS to determine the NR volume fraction, from which again one can calculate the molar concentration of reduced metal and NR number concentration. This method requires knowing the correct linear X-ray attenuation coefficient for the metal, solvent, and sample container. In this case, no numerical fitting of the SAXS form factor data is needed, but a precise calibration of the X-ray transmission is required, as well as reference measurements of the sample container and solvent as 'background', typically glass and water for samples stored in capillaries. The transmission method is convenient and more accurate and robust when samples exceed about 50 mM in total reduced metal concentration (M^0), especially when high brilliance synchrotron X-rays are used. Finally, this method has the advantage of being applicable to more complex NP shapes. The full equations for NR volume fraction (φ) determination are laid below, specifically for the case of Au@Ag NRs (**Equations 3.3-3.6**):

$$\ln\left(\frac{T_{total}}{T_{SiO_2}}\right) = -l_{sample}[\mu_{H_2O}(1-\varphi) + \mu_{rod}\,\varphi] \quad \textbf{(Equation 3.3)}$$

$$\mu_{rod} = \frac{\mu_{Au}+n\mu_{Ag}}{n+1} \quad \textbf{(Equation 3.4)}$$

$$V_{Ag-shell} = nV_{Au-core} \quad \textbf{(Equation 3.5)}$$

$$\ln\left(\frac{T_{total}}{T_{SiO_2}}\right) = -l_{sample}\left[\mu_{H_2O}(1-\varphi) + \mu_{Ag}\varphi\frac{n}{n+1} + \mu_{Au}\varphi\frac{1}{n+1}\right] \quad \textbf{(Equation 3.6)}$$

where T is the X-ray transmission, l_{sample} is the thickness of the sample in the direction of the incident X-rays, μ is the linear X-ray attenuation coefficient of a material for the specific X-ray wavelength used, φ is the volume fraction of the NRs, and n is the silver-to-gold molar ratio in the Au@AgNRs. Note that Equations 3.4 and 3.5 are valid given that silver and gold atoms occupy almost the same volume in their fcc lattices (a = 0.41 nm).

The molar or number concentrations of NRs determined by either the form factor fitting and or the X-ray transmission method were also compared in light of the weight fraction of metal of the NR suspensions, determined by simple weighing of the suspensions before and after complete drying. All these concentration data, plus the known size of the Au@AgNRs, also allowed the determination of the typical reaction yields of the silver growth step.

3.3. The DISA process and the characterization of assemblies

Development of DISA methods: Fast, slow, and ultra-slow

Recent literature over the past ten years have reported various methods of performing depletion-induced self-assembly (DISA) of colloids or of NPs. These methods differ primarily in the manner of introducing the depletant into the NP suspension, or in the sample container or substrate used[25–28]. In this project, glass capillaries were the primarily containers for DISA, given their transparency to visible, near UV, and near IR radiation for optical and plasmonic characterization, as well as to X-rays for structural characterization. When sealed by glue or flame-sealing, they are also easy to handle and transport. The thin nature of the capillaries (0.05 to 0.1 mm sample width for our optical capillaries) allows for easy access to viewing the colloidal assemblies, and decreases NP or assembly concentration due to sedimentation when the capillaries are stored flat and horizontally (**Figure 13**).

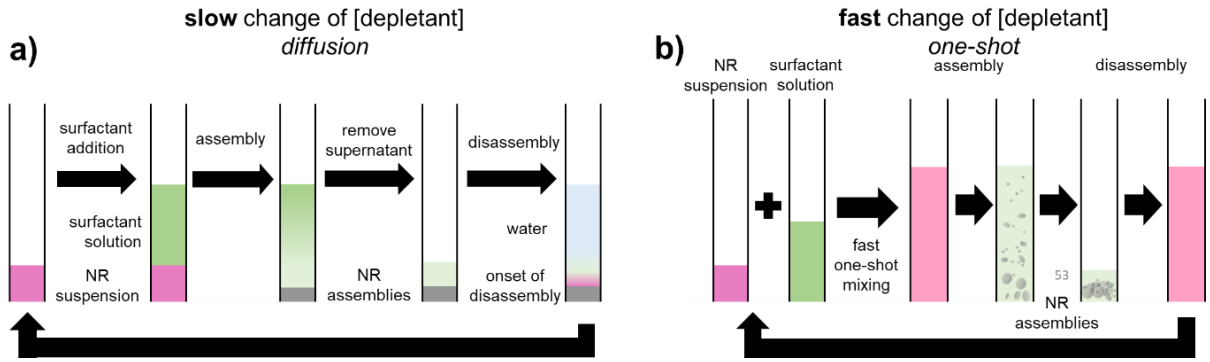

Figure 13. Schemes of cyclic depletion-induced assembly and disassembly (DISA) of NPs by (a) *slow or* ***(b)*** *fast change of depletant concentration.*

DISA was then performed either by *fast one-shot mixing* of the NP suspension and depletant solution (e.g., in an Eppendorf tube), or by *slow diffusion* between a depletant phase in contact with a separate NP phase in the capillary, keeping a defined interface between the two, and waiting for depletant concentration to equilibrate over hours to days. To perform fast disassembly, the suspension of assemblies is simply diluted by fast one-shot addition of deionized water of the appropriate concentration to go below the assembly threshold of depletant. To perform slow disassembly, the suspension is first gently centrifuged or allowed to sediment – isolating the assemblies at the bottom, then an appropriate amount of the supernatant is removed carefully by micropipette, and then replaced with a certain amount of deionized water, keeping a defined interface between the water and the remaining sample, to again go below the assembly threshold after letting the depletant concentration equilibrate by diffusion (**Figure 13**).

For slow DISA, the length of the capillary controls the lengths occupied by the depletant and the NP phases, and thus controls the characteristic diffusion time which is proportional to the square of the characteristic length by Fick's laws of diffusion[29]. The speed of DISA also depends on the gradients in NP and in depletant concentrations, which are determined by the concentration of NPs and of depletant in each phase. For most depletant concentrations and the majority of NPs studied in this project, slow DISA requires around 2 h to 12 h to complete in round capillaries (thickness = 1.0 to 1.8 mm) or even flat optical capillaries (thickness = 0.05 to 0.10 mm), for a total sample height (total length of NP and depletant volume) of 1 to 2 cm, where the sample has reached its steady state in both surfactant concentration and in the size

and structure (e.g., inter-NP distances) of the colloidal assemblies. For rapid screening of assembly parameters or for many cycles of assembly-disassembly, Eppendorf tubes were used instead as they can easily be opened and resealed. In this case, characterizations such as UV-vis-NIR extinction spectroscopy were done by first transferring the sample mixture into a UV-vis cuvette of either 1 cm path length, or 1 mm path length if the NR concentration is very high (**Figure 14**). Note that the thickness of the sample container affects the clear definition of the interface between the NR and depletant phases, and it was desirable to have a thickness of around 1 to 2 mm or less, and any thicker would induce too much partial mixing of the phases, leading to fast premature crystallization of the NRs.

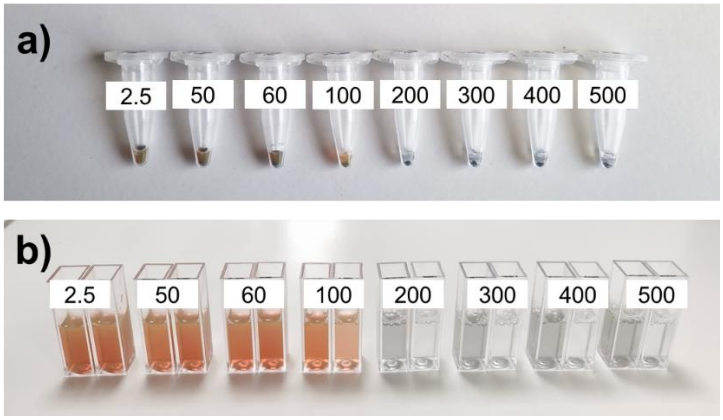

Figure 14. (a) *Slow DISA with Au@Ag C4-M NRs (length = 63 nm, width = 38 nm), 24 h after depletant addition: CTAC depletant concentration (in millimolar) series for screening the self-assembly* ***(b)*** *Comparing the reversibility of fast (left) vs. slow (right) DISA with the same Au@Ag NRs at different CTAC depletant concentrations in millimolar.*

Inspired by various microfluidic platforms for the preparation of NP supercrystals, as well as diffusion, dialysis, or annealing methods for electrostatic self-assembly[30–33], we also tried to develop our own PDMS milli- and microfluidic chips to conduct ultra-slow DISA by diffusion – to allow depletant diffusion and NR crystallization to proceed over a period of one to several weeks. The original chip design involved a millimetric channel with two reservoirs at either end, one for the NR suspension and one for the depletant solution. Here, the two phases are allowed to meet in the middle of the channel with a defined interface, where NR crystallization is triggered and then proceeds as the phases equilibrate by diffusion. However, due to time constraints and technical challenges in introducing liquids into the channels, the PDMS chip project was temporarily set aside. On the other hand, some experiments on pervaporation-induced self-assembly were done, using microfluidic chips designed by our collaborators in

CINBIO, U. Vigo, Spain[31]. Here, slow evaporation of solvent from the NP suspension out of the channel, together with slow refilling from a reservoir of NPs, causes the slow formation of large NP supercrystals, with single domain sizes up to the millimeter range (**Figure 15**). While this method was promising – in particular for assembling chiral or high aspect ratio NRs, they were not the focus of this thesis and was not yet well developed for our specific particles.

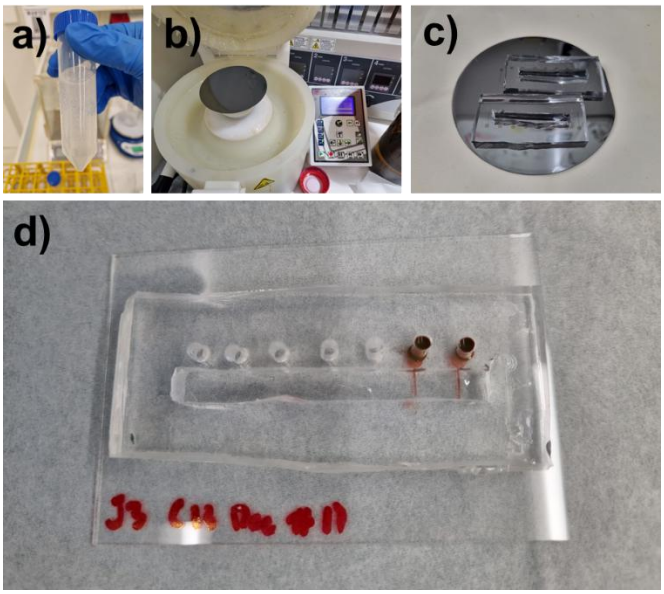

Figure 15. Preparation of PDMS microfluidic platforms for NP self-assembly by pervaporation. ***(a)*** *Fluid PDMS pre-mix prior to curing.* ***(b)*** *Preparation for spin coating PDMS onto a Si wafer with well patterns.* ***(c)*** *Cured PDMS chips ready for final cutting and removal.* ***(d)*** *PDMS chips loaded with twisted chiral Au NRs (cGNRs) for pervaporation.*

Instead of using PDMS channels, we opted to use thin optical capillaries (typically 0.05 mm × 1 mm in cross section, 100 mm in length) as the container for conducting ultra-slow DISA. Here, a capillary is first filled with a NR suspension, but keeping a small amount of air at one end to block the movement of liquid. Then, this capillary is fully immersed lying horizontally in a bath of depletant (e.g., aqueous CTAC in a Petri dish) of appropriate concentration, and the bath is sealed to prevent evaporation. The depletant is allowed to slowly enter, diffuse, and equilibrate inside the capillary but only from the one open end, akin to a 'pseudo-reverse dialysis' (**Figure 16**).

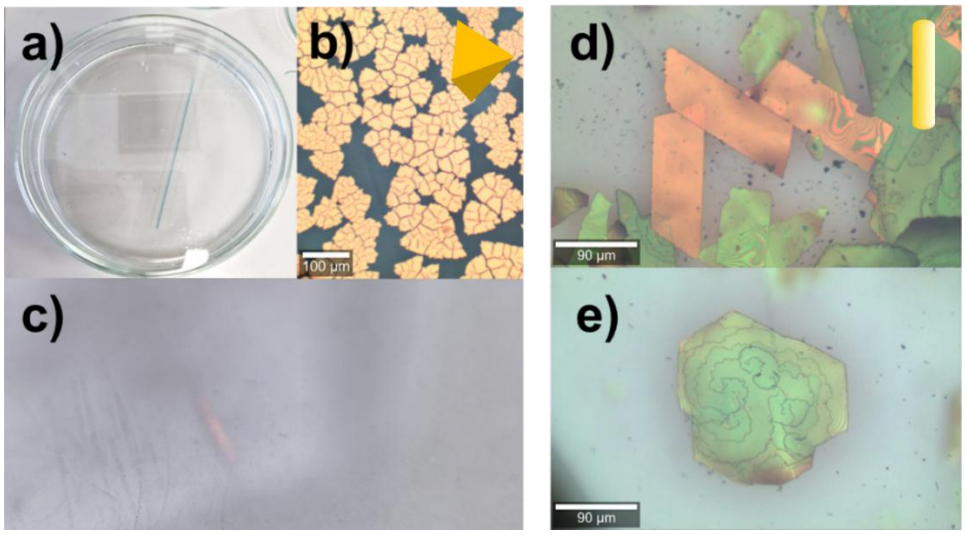

Figure 16. Ultra-slow DISA for growing highly-extended NP supercrystals in liquid. ***(a)*** *Ultra-DISA by slow diffusion of CTAC in a 'pseudo-dialysis' capillary immersion setup* ***(b)*** *2D supercrystals of Au nano-tetrahedra by ultra-slow DISA.* ***(c)*** *Strong luster of these supercrystals visible by eye upon turning the capillary.* ***(d)*** *Large trapezoidal and* ***(e)*** *hexagonal 2D 'metasurfaces' or supercrystals of Au NRs by the same method.*

With this method and this size of capillary, the timescale of DISA can be extended from seven to twenty days. With the help of our colleague Brigitte Pansu in LPS, we also adapted this method by connecting one end of a filled optical capillary to a reservoir of depletant in a syringe via plastic tubing, to avoid having to immerse a whole capillary in a depletant bath. With this syringe/tubing method, DISA can be slowed down further to one to two months, with full equilibration of depletant concentration possibly lasting even longer (**Figure 17d**). Both the immersion and the syringe methods yield highly-extended assemblies or supercrystals up to 100 µm across, with variable dimensionality, though typically yielding 2D or 1D structures in the case of anisotropic rod-like metal NPs. Depending on the speed of depletant diffusion, varying sizes, crystallinities, and types of crystallographic defects can be observed within these assemblies (**Figure 16**). More details on these ultra-slow DISA methods are found in the perspectives of Chapter 4.

In situ assembly characterization: Microscopy and X-ray scattering

As noted earlier, the use of glass capillaries, particularly flat optical capillaries, was particularly advantageous for our in situ characterization of colloidal NP assemblies by optical microscopy and small-angle or wide-angle X-ray scattering (SAXS/WAXS). The real time dynamic behavior of depletion-induced assemblies, including their nucleation, growth, breaking and

reconnecting, and disassembly, can easily be monitored with a conventional optical microscope in either transmission or reflection mode, with the possibility of using polarizers (in POM) to reveal interesting optical properties like birefringence as a clue of NP orientation, or changing colors revealing plasmonic resonances or coupling. Likewise, in situ SAXS in capillaries reveals the true structure of the assemblies in their native state, without collapsing their shape or changing the inter-NP spacing when drying by evaporation or lyophilization. While SAXS was done with both flat optical capillaries and round capillaries, optical microscopy was only done with the former, as in microscopy, the samples need to remain flat and stable on the stage, with minimum optical path length to avoid too high absorbances. Examples of in situ microscopy and SAXS are shown below. Note that during SAXS measurements, the capillaries are typically set vertically, while for optical microscopy, there are set flat and lying down horizontally (**Figure 17**).

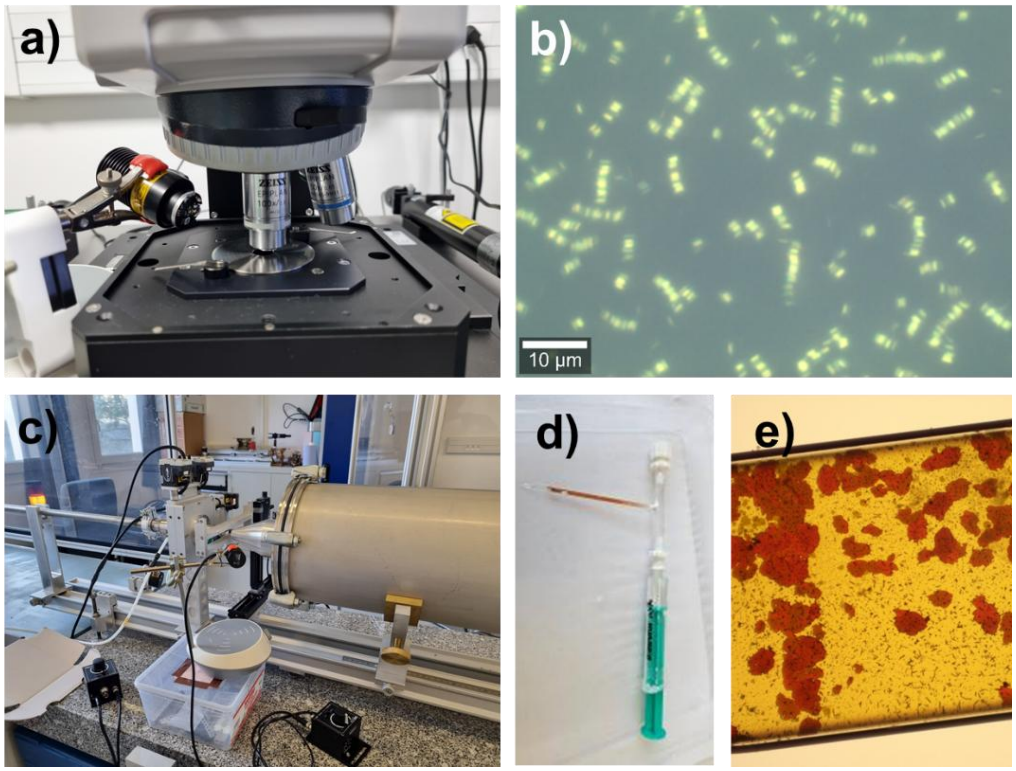

Figure 17. Colloidal depletion-induced assemblies in glass optical capillaries for characterization: ***(a)*** *A capillary for observation via optical microscopy (reflection mode) with optional UV lamp for irradiation for photoswitchable DISA, containing* ***(b)*** *dynamic needle assemblies of side-by-side long Au@Ag C5-NRs.* ***(c)*** *In-house SAXS setup for structural characterization of assemblies in round or flat glass capillaries.* ***(d)*** *Custom T-shaped syringe setup for ultra-slow DISA, with connection to tubing and a reservoir for the slow diffusion or exchange of depletant over weeks to months.* ***(e)*** *2D to 3D supercrystals of Au@Ag C4-NRs grown in a T-shaped syringe setup for ultra-slow DISA over several weeks.*

SAXS analysis of assemblies: Lattice, domain size, and dimensionality

The 2D SAXS diffractograms obtained for depletion-induced assemblies of NRs are very rich, revealing information about the assembly's internal lattice, its dimensionality, crystallinity, and orientation. In this project, some initial analyses have been successfully done in fitting these 2D diffractograms, particularly to check the uni- or bi-dimensionality of our NR assemblies and their orientation, using a Python code developed by our collaborator Nicolas Ratel-Ramond from INSA Toulouse, France, as well as an in-house Python code already in development by Marianne Impéror-Clerc. However, this thesis focused primarily on the analysis of 1D radial profiles integrated from the 2D analysis, which forms the bulk of the structural characterization of the depletion-induced assemblies. To this end, three main tools were developed.

First, an interactive Python widget was developed, originally by our fellow PhD student Jules Marcone, and subsequently improved and expanded during this thesis, to check the lattice symmetry of our assemblies. This widget takes one's experimental 1D SAXS data and, for each possible supercrystal lattice symmetry, plots this data together with lines corresponding to all possible Bragg peak positions using an initial guess for the lattice parameters. The lattice parameters and then be adjusted by sliders. The experimental data can thus be fitted by simply adjusting these sliders for each lattice parameter, and then checking which symmetry has the best match for all the peaks in the 1D profile (**Figure 18**). Various locations of the lattice points can be specified to account for possible extinctions of peaks (e.g., body-centered, face-centered lattice). One can also impose limits to the numbers of peak positions being superimposed (i.e., max h, k or l values), or completely remove one or more dimensions to account for 1D or 2D order. In this thesis, particular focus was given to fitting with 2D hexagonal (hp) symmetry, 1D symmetry, and centered rectangular (2D oc) or body-centered orthorhombic (3D oI), the latter two being transitional symmetries between hexagonal and square/cubic symmetries, which featured in the assemblies of cuboid (C4) NRs or of chiral NRs with twisting square cross-sections.

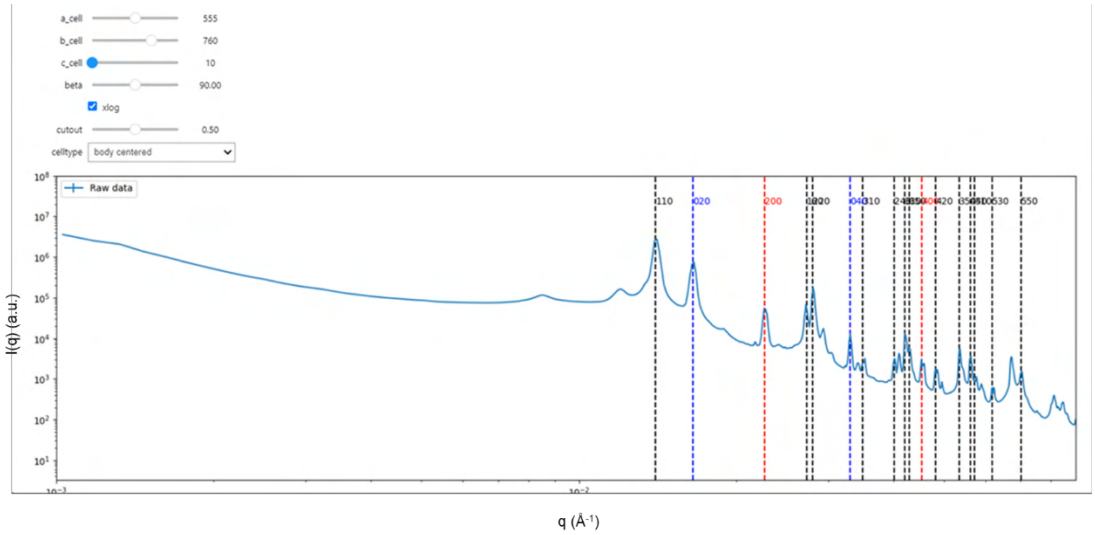

Figure 18. Python modelling widget for matching SAXS 1D radial profiles to supercrystal lattice symmetries. *Case of Au@Ag C4-M NRs (cuboids, length = 63 nm, width = 38 nm) in 200 mM CTAC, self-assembled into stacked sheets of standing NRs, with each sheet having 2D rhombic (centered rectangular) symmetry.*

Second, to have a fuller understanding of the hierarchical structure of the depletion-induced assemblies, more complete fitting of the 1D SAXS data was also performed in SasView 6.0.0 by combining several models. First, a Porod model was used to account of the general shape and background of the SAXS profile which follows a q^{-4} power law by Porod's laws, particularly the asymptotic high-q region as a consequence of flat interfaces in the scattering sample. Second is the form factor of the individual NRs – modelled as prisms via projection of a regular polygon normal to its plane. Third, the sharp Bragg peaks corresponding to long-range inter-NR order were modelled by multiple pseudo-Voigt peaks, that is, by a weighted average between a Gaussian and a Lorentzian curve to account for a variety of peak shapes in a sample – with an adjustable weight controlling the character of the peak towards Gaussian or Lorentzian shape (**Figure 19a**)[23]. In our model, the standard deviation of the Gaussian model is related to the full-width half-maximum (HFHM) for the Lorentzian model as:

$$\sigma = \frac{FWHM}{2\sqrt{2}\ \ln 2} \qquad \textbf{(Equation 3.7)}$$

The Debye-Scherrer correlation length of the assembly along a certain crystallographic direction can then be calculated as:

$$D_{corr} = \frac{2\pi n}{FWHM} \qquad \textbf{(Equation 3.8)}$$

where n is a direction-dependent constant close to but deviating from unity due to the anisotropic shape of the assembly, causing distortions of the Bragg spots in SAXS[34].

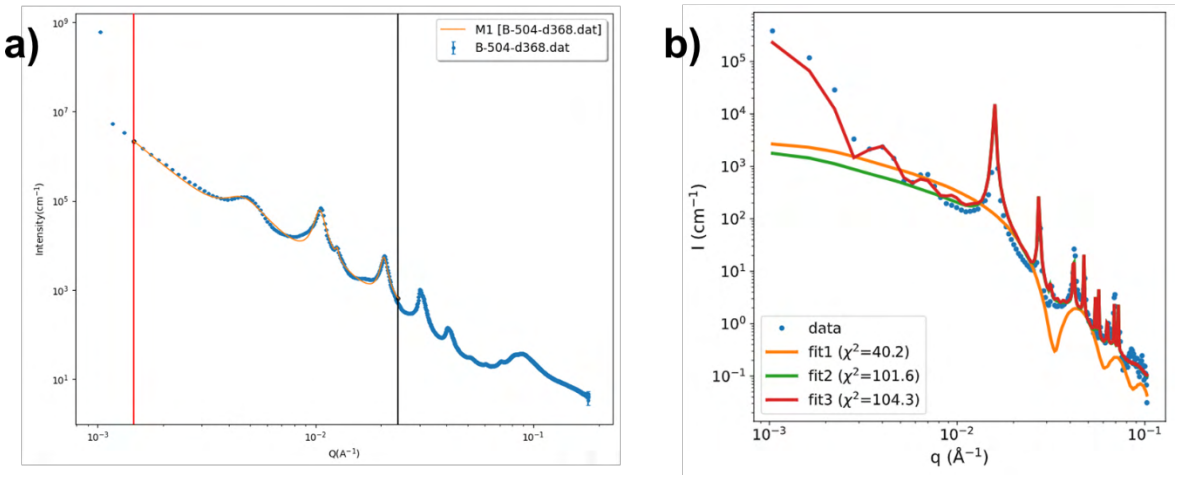

Figure 19. Complete fitting of SAXS 1D radial profiles with a combination of the NR form factor, pseudo-Voigt-based supercrystal Bragg peaks, the supercrystal form factor, and a Porod background. (a) *Assembly of oxidized chiral Au NRs (cGNR_2 used in Chapter 5) by DISA: Fitted model with using Porod plus pseudo-Voigt Bragg peaks.* ***(b)*** *Assembly of long C5-NRs (PR32 used in Chapters 4 and 6) by photo-DISA: Multiple fitted models, with 'fit3' containing all model components: Porod, NR and supercrystal form factors, and pseudo-Voigt Bragg peaks.*

Lastly, to account for the shape of the colloidal micron-sized assemblies, a form factor for the assemblies was introduced which accounts for oscillations in the low-q region. This form factor was especially prominent in the case of long C5-NR assemblies, which are either 2D platelets or 'metasurfaces', or 1D needle-like objects extending at least a few microns wide. A rectangular prism model was used for the form factor, as an approximation of these thin 2D or 1D objects (**Figure 19b**). This combined model was designed as a central project of this thesis, while the implementation of the assembly form factor and the elaboration of a sum model from SasView library in Python code was now accomplished by our master's intern Anirban Mandal from U. Paris-Cité, who is applying the combined model to analyze several data from Chapter 6 on the photo-DISA project.

The third and final tool used to analyze and check SAXS data of the assemblies was an inter-NP interaction potential well model calculated using simplified DLVO (Derjaguin–Landau–Verwey–Overbeek) theory. This model was used to compare the experimental inter-NR gaps

known by SAXS versus the theoretical gaps obtained by the calculated potential well minima. The DLVO model was a sum of van der Waals, electrostatic, and depletion potentials acting on a pair of parallel metallic plates covered with a CTAC surfactant bilayer, and with free spherical changed CTAC micelles acting as depletant in suspension[35,36] (**Figure 20a**). More details on the results from using this model are found in Chapter 4. However, in terms of methods and bigger picture findings, there were two notable results. First, the model was able to accurately predict the inter-NR gaps in the depletion-induced assemblies, in agreement with SAXS to within 2 nm for the major NRs used in this project at a wide range of CTAC depletant concentrations. Second, the model revealed an apparently strong role of electrostatic repulsion and the effect of added salt in the DISA process, which can control the accessibility and depth of the overall potential well, and thus affect both the kinetic and thermodynamic stability of the assemblies, and perhaps the ease of disassembly (**Figure 20b,c**). Nonetheless, more rigorous numerical simulations of our assemblies using the DLVO model need to be performed to more confidently conclude on these points. Initial work on these simulations is being done by our collaborators in the Theory Group of LPS, particularly by our fellow PhD student Numa Zorzi.

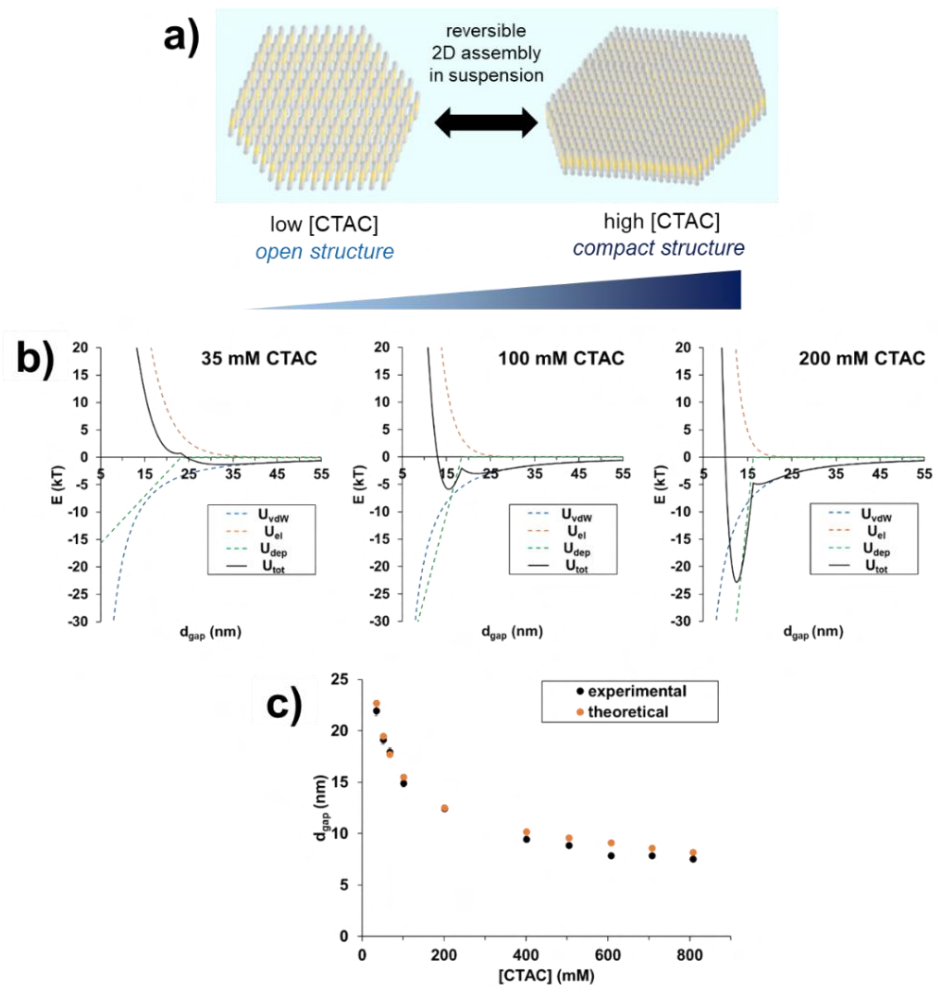

Figure 20. Inter-NP interaction potential modelled by DLVO theory. ***(a)*** *Scheme of open vs. closed dynamic assemblies at low versus high depletant concentration.* ***(b)*** *Changing interaction potentials for Au@Ag C5-NRs at increasing depletant concentration.* ***(c)*** *Comparison of experimental inter-NR gaps and the theoretical gaps taken as the minima of the primary DLVO potential well. Adapted from our article*[18].

Development of the photo-DISA process and PhotoSwitch setup

In the case of photoswitchable DISA (photo-DISA) using active photosurfactants as depletants, a third component of the self-assembly system was added, namely light illumination of the sample. As this form of DISA is dynamic and time-sensitive, the illumination system needs to be directly integrable (i.e., usable in situ) into the characterization methods for the photo-DISA assemblies, namely optical microscopy, UV-vis-NIR extinction spectroscopy, and SAXS. The initial light sources employed were uncollimated UV (365 nm) and blue (470 nm) LEDs. These LEDs were simply positioned close to the sample mounted on whichever instrument was being used. In the early stages of the photo-DISA project, these LEDs had to be manually turned on

and off using the power knob, and the UV and blue LEDs swapped, costing a delay of around 5 s up to 20 s during sensitive kinetics experiments. For this reason, in collaboration with the instrumentation service of LPS, we developed a remote-controlled illumination setup named 'PhotoSwitch', which connects to both the UV and blue LEDs, turns them on/off, controls each one's power separately, collimates the light, and directs it to an exit hole toward the sample. The exit is also fitted with an optical fiber so that the incident light can be optionally directed to any position on the sample. The PhotoSwitch setup can be controlled via PC connected through an ethernet cable. In the graphic user interface, various modes of illumination can be chosen, such as simple on-off control of each LED, UV-blue cycles, and rapid pulses of UV, blue, or alternate illumination, all with the option to change duration and cycling time (**Figure 21**). The development of this PhotoSwitch setup and its use for photo-DISA under rapid UV-blue switching was done with Phuong-Lan Dao, a masters intern whom we supervised during the later stages of this thesis.

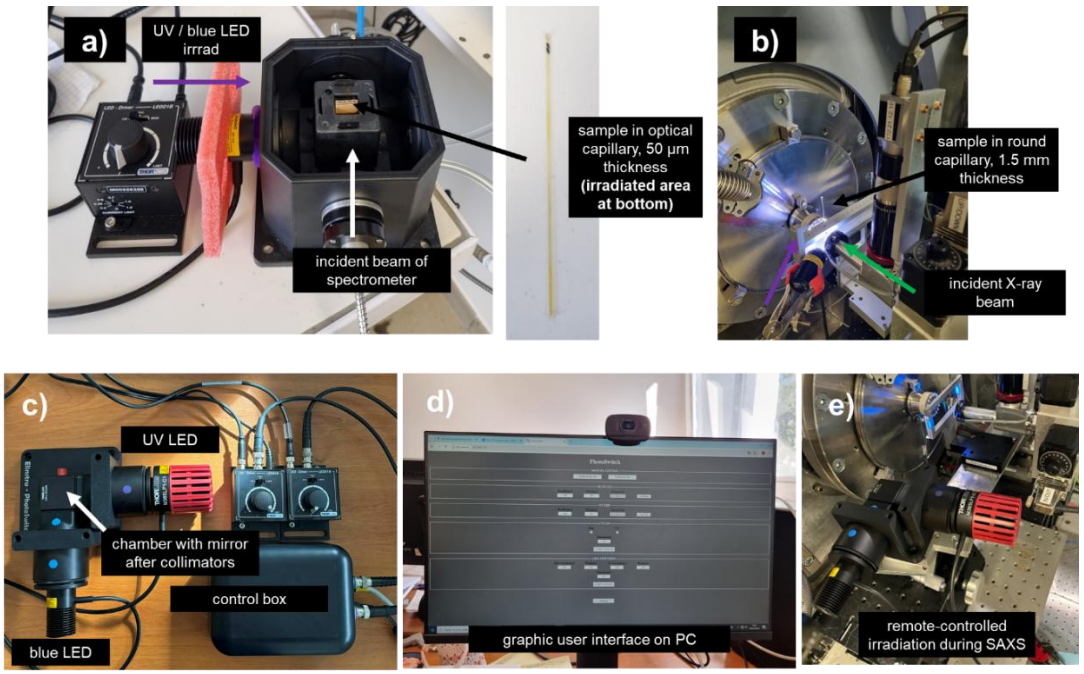

Figure 21. Implementation of the photo-DISA setups: ***(a)*** *Initial LED irradiation and spectrometry setup for UV-vis-NIR kinetics for in situ study of the photo-DISA process.* ***(b)*** *In situ LED irradiation during SAXS characterization of photo-DISA samples.* ***(c)*** *Completed remote-controlled 'PhotoSwitch' illumination setup with its* ***(d)*** *graphic user interface on a PC connected via ethernet cable.* ***(e)*** *PhotoSwitch used for real-time illumination and switching during SAXS.*

3.4. Tips-and-tricks guide

1. Synthesis of very long nanorods: What to know

The synthesis of very long Au@Ag pentatwinned nanorods (C5-NRs), typically longer than 500 nm, brings new difficulties that shorter rods do not. First, as the silver growth is done in a 10 mM CTAC solution, the rods generally exist in the form of side-by-side '1D needle' assembles in suspension after the reaction. This will cause some *scintillation* that varies when the reaction flask is gently shaken. The presence of these 'needles' can be directly verified via optical microscopy of the reaction mixture in a capillary, and if the rods are nearly 1 µm long or more, the thickness of the needles can be used to approximate the length of the individual rods. The absence of scintillation, strong turbidity, and needle assemblies when making micron long rods indicates some type of failure in the synthesis, which must then be repeated. Typically, the failure is in improper *temperature control* at 70 °C, due to either inadequate preheating of the reaction mixture prior to seeds and silver nitrate addition, or improper insulation of the reaction flask with aluminum foil (**Figure 22**). Improper temperature control often leads to high length polydispersity or lower average length of the NRs.

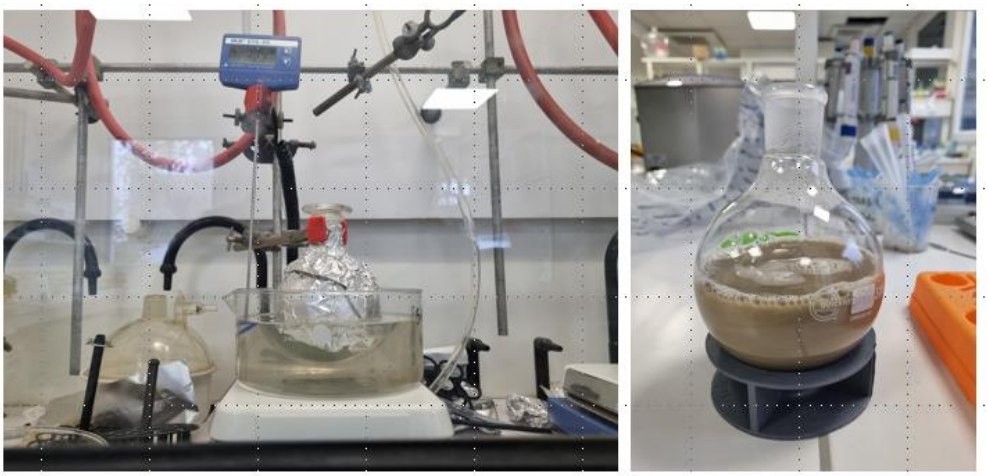

Figure 22. *Synthesis of micron-long Au@Ag C5-NRs by aqueous seed-mediated growth onto Au bipyramid cores.*

Second, when making nanorods with one-shot addition of silver nitrate precursor, there will typically be *two populations* of rods with slightly different lengths, which can be separated when centrifuging at gentle speed, around 500-600 rcf. In terms of [Ag^0], the two populations might be anywhere from a 50:50 to a 70:30 ratio. Separating these populations is desirable if

length monodispersity is important for one's particular application, whether in making 1D/2D colloidal assemblies or supercrystals, or in making liquid crystals. If the size polydispersity is still too large among fractionated populations, one may try adding the silver nitrate solution using a syringe pump overnight instead of by one-shot addition, or add small amounts of nitric acid to slow the growth kinetics, depending on the success of the synthesis.

2. Nanorod sedimentation, aging, and sonication

The seed-mediated growth method of nanoparticle (NP) synthesis produces generally very monodisperse particles which keep their shape and plasmonic properties for at least a few months, which is important when making assemblies with functional plasmonic properties. *NPs stored in 1 mM to 2.5 mM aqueous CTAC* are ideally used within two months of synthesis. Storing the NPs in less than 1 mM CTAC risks destabilizing the NP colloidal stability, leading to aggregation and/or reshaping sooner. It is always advised to vortex the NP suspensions and sonicate for 5 to 10 min prior to use, to ensure homogeneity of the NP concentration and reverse any sedimentation. When using NPs a month or more after synthesis, it is worth retaking their UV-vis-NIR extinction spectrum to check for any NP degradation such as reshaping, aggregation, etc.

3. Optimal concentration of nanoparticles for assembly

For the typical DISA superstructures explored in this thesis, and for the typical NP sizes mentioned (length = 60 to 400 nm, width = 15 to 40 nm), it is recommended to perform DISA with a stock solution of NPs of around *20 mM to 100 mM* Au^0 (or the total amount of metal M^0 regardless of the composition), at 1 to 2.5 mM CTAC. This works for both slow (diffusion) or fast (one-shot) DISA. This is equivalent to an optimal concentration of around 10^{12} NPs / mL. Above 100 mM M^0 (total metal), the dynamics and final form of the assemblies, as well as the depletion threshold for NP self-assembly, become very sensitive to small changes in NP concentration; this regime, while interesting, is far more complex kinetically speaking, and is not yet well explored in this thesis. Nonetheless for DISA, it must be emphasized that the effect of depletant concentration is always much greater than that of NP concentration.

4. How to determine the depletion threshold

The depletion threshold (i.e. minimum depletant concentration to induce self-assembly of a specific NP) is a very important number to keep in mind for each NP – depletant system. It can be approximated using the simplified Asakura-Oosawa (AO) model-based equation noted previously in the Introduction. However, for each new NP, it is always recommended to experimentally determine the depletion threshold in both slow and fast DISA conditions, as the thresholds are close but slightly different. Typically, the threshold in fast (one-shot mixing) DISA is slightly higher than that for slow diffusion (**Figure 23**).

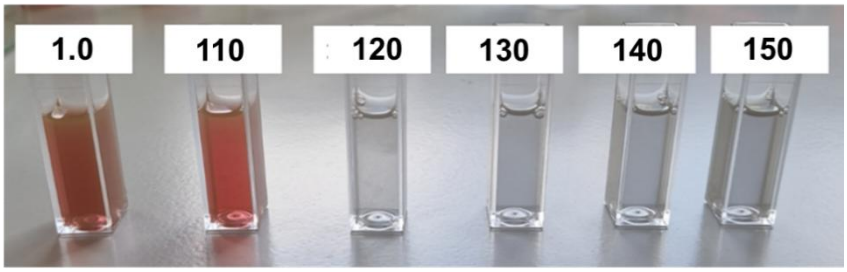

Figure 23. Depletion-threshold screening of Au@Ag C4-NR self-assembly *at different CTAC depletant concentrations by fast one-shot mixing. Labels are the concentration of CTAC in millimolar (mM).*

Practically speaking, one determines the threshold by making a series of NP-depletant samples in increasing depletant concentration. One needs to wait for at least 10 min before checking for signs of DISA, either by a notable change in *color* or *turbidity* of the initial NP suspension, or by directly observing the mixture for micron-sized assemblies under an optical microscope.

5. Choice of container: width and length matters

While DISA can be performed in a wide variety of containers (e.g. glass capillaries, Eppendorf tubes, vials), it must be noted that for slow (diffusion) DISA, the specific width and length of the container strongly affect the growth process of the NP assemblies. For samples with a depletant gradient along the length, a longer container slows down further the assembly growth, yielding larger and more well-faceted supercrystals. Meanwhile, gradients on a short length yield smaller and more polycrystalline supercrystals. Therefore, the speed of DISA can be easily controlled by changing the length of the capillary with its depletant gradient. If the capillary sample is stored lying flat and horizontal, and if the capillary is much thicker (i.e., higher) than 0.05 mm, there will generally be multiple populations of different sized or shaped

assemblies across different heights along the sample, due to differential sedimentation during the DISA process.

6. Slow DISA: How to add depletant well

When making assemblies in a wider container such as an Eppendorf tube or a round X-ray capillary, it is recommended to slowly add the depletant (e.g. CTAC or other surfactant) with a micropipette or a syringe needle, gently touching the tip just at the surface or slightly above the air-NP phase meniscus. Do not let any air get into the depletant or NP phase, as the depletant can form and trap air bubbles which will affect the assembly nucleation and growth. One may also let the depletant solution flow on the sides of the tube or capillary. Be careful when handling and closing the Eppendorf tube or the capillary, as sudden agitation can mix the NP and depletant phases and cause premature and rapid NP self-assembly. Finally, in case you accidentally get air bubbles into your sample, use a syringe needle or micropipette tip (without pushing the micropipette or sucking air) to touch and 'pull out' the bubble from the liquid to the top.

When performing DISA with an optical capillary, the depletant and NP phases can be sequentially introduced into by slow capillary action (i.e., dipping an open capillary into the liquid to suck it in), keeping the capillary flat and horizontal. Otherwise, if one has a thin enough syringe needle, one can directly and carefully inject the separate phases similar to how it is done with wider round capillaries (**Figure 24**).

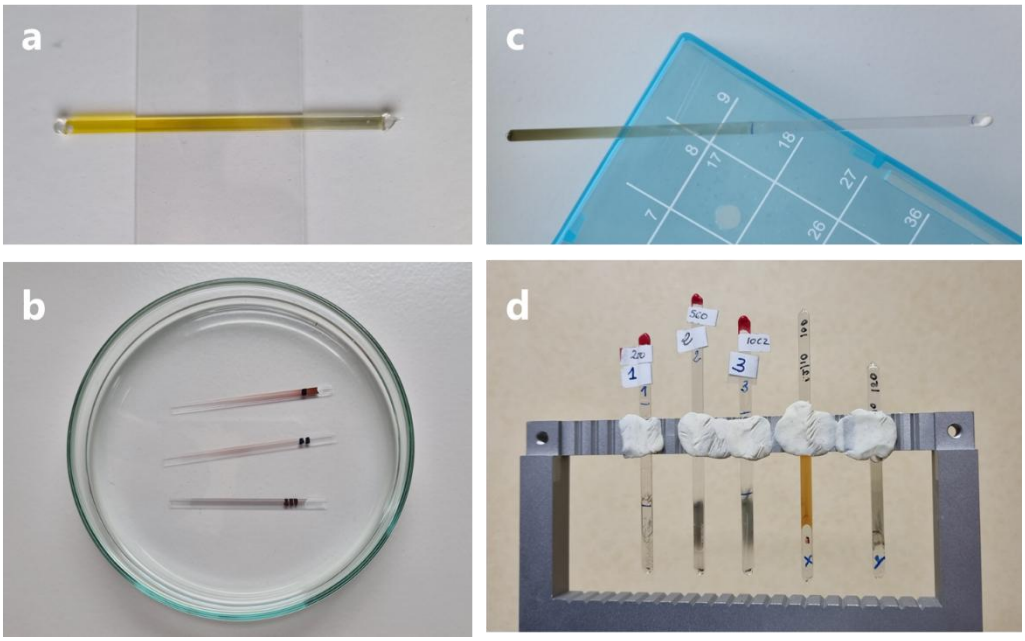

Figure 24. Various methods of ultra-slow DISA by diffusion of depletant into glass capillaries: (a) *Sequential aspiration of NR suspension and then AzoTAB depletant solution.* ***(b)*** *Immersion of a capillary with NR suspension in a bath of CTAC depletant for 'pseudo reverse dialysis'.* ***(c-d)*** *Sequential injection by syringe of NR suspension and CTAC depletant into a wide glass capillary for ultra-slow diffusion.*

7. Storage of assembly samples

For slow DISA, to prevent any sedimentation of NPs or to prevent disturbing too much the NP-depletant interface (that will hasten the growth and affect the assembly size), one must avoid any tilting, agitation, or shaking of the capillaries, especially prior to characterization (e.g. by optical microscopy, SAXS, electron microscopy). Flat optical capillaries must be stored lying down, horizontally, while wide round capillaries must be stored vertically, to preserve the NP-depletant interface. It is also very important to ensure that the ends of the capillary are sealed very well, particularly with ultra-slow DISA, as any evaporation will interfere with the expected kinetics. If stored well, the colloidal NP supercrystals can last for several months.

8. *In situ* optical microscopy of assemblies in liquid: locations, populations, z-positions

When using an optical microscopy, it is often difficult in the beginning to recognize different objects in one's DISA assembly samples. Here are some fundamental things to consider when viewing a sample. First, ensure that your capillary sample is well-sealed and flat on the

microscope stage. Otherwise, the assemblies can sediment towards one side, or be disturbed by flows within the liquid, making it more difficult to focus the image. Second, there will typically be multiple populations of objects (including your NP assemblies) at different heights/z-positions in the capillary, each group slightly differing in size, number, and shape of objects. Third, check very well whether you are imaging the real image of the object/assembly, or simply its shadow. For colloidal assemblies of metal NPs, the real image of the sample is often brighter and more colored and detailed. Fourth, be sure to check the whole length or area of the sample to have a representative view of (or see variation in) the sample (e.g. presence of assemblies, their size and shape, color). Finally, it is important to know whether an object you are looking at is really a colloidal NP assembly, and not some form of dust, impurity, or unknown object. NP assemblies are usually quite bright and shiny, and exhibit at least some Brownian motion. For fresh samples less than a day old made by fast DISA, most of them will exist floating in the middle z-position of the capillary, rather than being stuck to or sedimented onto one of the walls (**Figure 25**). Of course, the best way to learn and apply these tips know your assemblies is to prepare many of them and get more and more experience with the microscope.

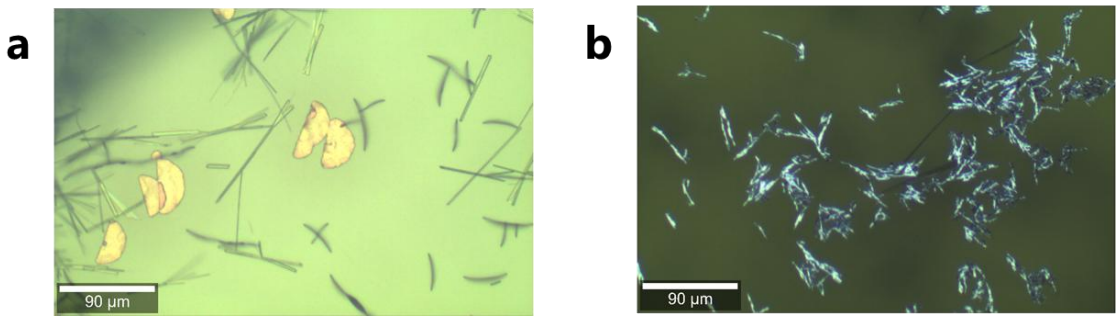

Figure 25. *Typical in situ optical microscopy (reflection) images of Au@Ag C5-NR assemblies using azoTAB as depletant:* ***(a)*** *2D platelets of assembled NRs and heavier AzoTAB crystals at lower z-positions,* ***(b)*** *1D needles and bundles of assembled NRs at higher z-positions.*

9. Raman SERS microscopy on assemblies: Making good measurements

General principles and tips in optical microscopy also apply to Raman microscopy. Additionally, it is always good practice to measure the laser power and take the Raman spectrum of reference sample before every experimental session.

Here, we present three tips for making good Raman measurements. First, avoid biases regarding where to measure in a NP assembly or in choosing which assemblies to irradiate with the laser. When making a statistically meaningful set of measurements, take as random a sample of locations as possible on different assemblies (e.g. thin and thick regions, different orientations and shapes of assemblies, different heights/z-positions in the liquid). Second, be very careful with high laser power: exposing assemblies to high power above 1 mW for more than a few seconds can partially or fully disassemble them if made by CTAC depletant, and thus alter the plasmonic properties being probed. For AzoTABs, this power threshold can be even lower, as exposure to 0.10 to 0.20 mW for a few seconds can cause disassembly. However, for laser power less than 1 mW, it was observed by optical microscopy that the disassembly is temporary, as colloidal assembles tend to reform anywhere from a few seconds to half an hour after intense laser exposure. In this case, there is probably negligible NP aggregation, and minimal NP reshaping. The strength of this laser disassembly effect likely depends on the excitation laser wavelength, with green lasers being more destructive than red ones due to more overlap of green light with the metal NP SPRs. For more 'fragile' assemblies, wait until the very last moment before opening the laser shutter just before the Raman spectrum acquisition, but always use a consistent waiting time for the sample. Third, take measurements on as a fresh a sample as possible, meaning, do not let the assemblies and the Raman analyte/reporter hang out together in the sample capillary for a day or longer. Rather, measure them immediately or within a few hours, as certain analytes may irreversibly attach/detach to the NP assemblies.

10. Using AzoTAB solutions

AzoTAB solutions can be a bit difficult to work with, depending on the specific compound, particularly those with longer tail or spacer carbon chains. Be sure to store both solid powders and liquid solutions of AzoTAB away from light in a dark bottle, or a glass container covered with foil, to ensure the compound is fully in the *trans* isomer.

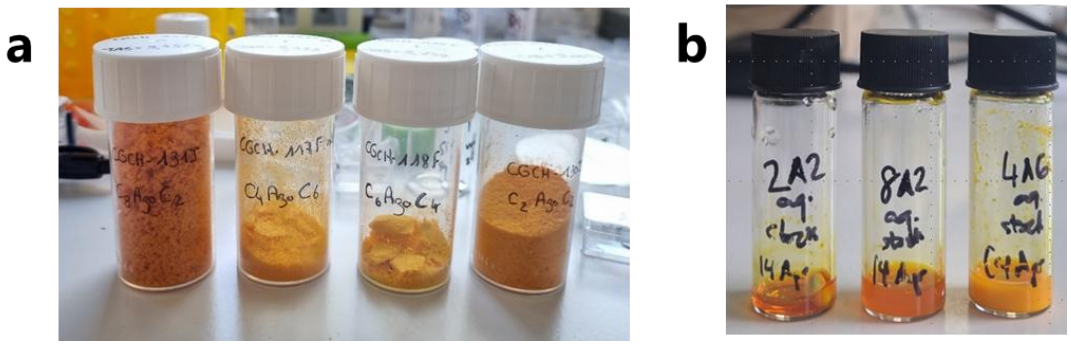

Figure 26. (a) *Purified solid powders of AzoTABs with different tail and spacer carbon chain lengths* ***(b)*** *Concentrated AzoTAB-H_2O mixtures showing varying amounts of suspended precipitate.*

When preparing aqueous AzoTAB solutions, it is recommended to stir them for several hours to overnight with a magnetic stirrer as some AzoTABs have poor solubility. After maximum dissolution, allow all undissolved solids to settle completely, if any. The mixture can be gently sonicated if necessary. Use only the clear supernatant as the depletant for photo-DISA; try to carefully separate it from the sediment. Afterwards, determine the molar or weight fraction of AzoTAB in the supernatant versus the sediment, to ensure that you know the real concentration of depletant in your system (**Figure 26**).

11. Correct mixing of DISA or photo-DISA samples: Order matters

As with regular DISA, it is important to note the order of addition and the relative volume of depletant versus NP suspension, especially if one is adding additional salt into the system. In general, contact between the NPs and depletant should be delayed to the last mixing or addition. If adding salt, one must first mix the depletant and salt first, and then add the NP suspension. If the NPs are exposed to salt alone or too high salt without dilution of extra liquid, this may cause irreversible aggregation of the NPs. Also, mixing depletant and salt first will allow the micelles to assume their thermodynamically stable form in that ionic strength, prior to acting on the NPs via depletion.

12. Aging of photo-DISA samples

When in a suspension of dispersed nanoparticles (NPs), azoTAB tends to crystallize into large, thin, semi-rectangular crystals, typically as long and wide as several microns, easily visible under an optical microscope. This likely occurs because the NPs act as nucleation sites for azoTAB crystallization. Visible azoTAB crystals form within about 6 hours, and continue to grow over several days. It is always best to use and characterize a NP-azoTAB sample within three hours, to avoid excessive azoTAB crystallization that would change the effective free depletant concentration, and that could affect the nucleation and growth of the assemblies (**Figure 27**).

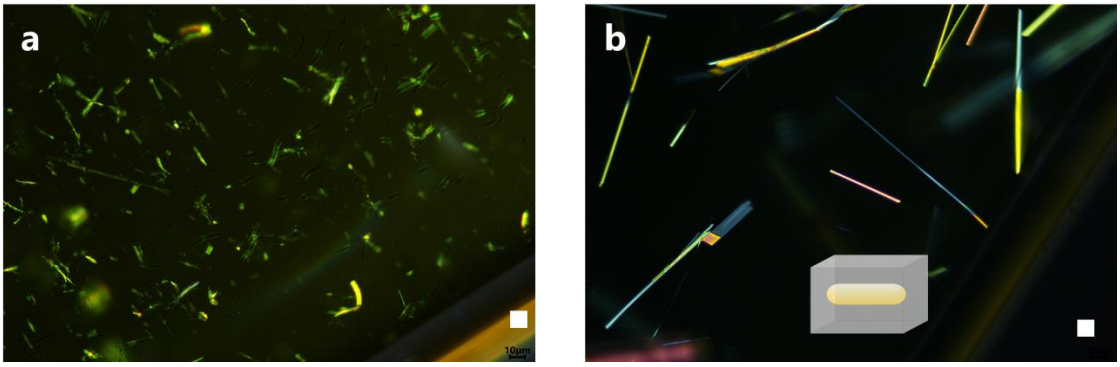

Figure 27. *AzoTAB crystals seen in by optical microscopy in transmission:* ***(a)*** *concentrated aqueous azoTAB (8A2, 400 mM, precipitates not separated from supernatant) with shorter surfactant crystals, and* ***(b)*** *an aged mixture of Au@Ag C4-NRs and azoTAB (8A2, 400 mM, precipitate not separated from supernatant), with larger and longer rectangular surfactant crystals seeded by the NRs.*

In cases of necessity, one can reverse the AzoTAB crystallization by sonicating the sample for about 30 min. However, this will also destroy any depletion-induced NP assemblies that may exist within.

13. Photo-DISA: Repeatable illumination of samples

Three things must be kept in mind when illuminating photo-DISA samples. First, always measure the irradiance of the light source used, converting power measurements from a photodiode to irradiance using the real surface area of the detector. When doing this, measure as well the distance between the lamp or light source and the sample, and the fraction of light landing on the sample or detector. Second, keep the power setting of the lamp consistent across all your experiments; it is hard to relate real irradiance with the power setting as they do not have a linear correlation. It is always good to measure your lamp's power with a photodiode set to the right wavelength to detect. Third, avoid irradiating a series of many

samples (e.g., arranged in a line) as they will each receive a different light irradiance or flux, and the azoTABs will undergo different degrees of isomerization in each one. Fourth, always remember and mark the areas where you are directly irradiating the sample, so that you can characterize the same areas before and after via optical microscopy, SAXS, or another technique.

3.5. References

(1) Blayo, C.; Houston, J. E.; King, S. M.; Evans, R. C. Unlocking Structure–Self-Assembly Relationships in Cationic Azobenzene Photosurfactants. *Langmuir* **2018**, *34* (34), 10123–10134. https://doi.org/10.1021/acs.langmuir.8b02109.

(2) Jones, B. E.; Greenfield, J. L.; Cowieson, N.; Fuchter, M. J.; Evans, R. C. Light-Driven Hexagonal-to-Cubic Phase Switching in Arylazopyrazole Lyotropic Liquid Crystals. *J. Am. Chem. Soc.* **2024**, *146* (18), 12315–12319. https://doi.org/10.1021/jacs.4c02709.

(3) Lekkerkerker, H. N. W.; Tuinier, R. *Colloids and the Depletion Interaction*; Lecture Notes in Physics; Springer Science+Business Media B.V: Dordrecht, 2011.

(4) Hotton, C.; Trazo, J. G.; Modin, E.; Bardouil, A.; Kutalia, N.; Marcone, J.; Nag, R.; Goldmann, C.; Paineau, E.; Chuvilin, A.; Impéror-Clerc, M.; Bizien, T.; Constantin, D.; Hamon, C. Evaporation-Induced Phase Transitions in Free-Standing Plasmonic Nanoparticle Assemblies. *Nano Lett.* **2026**, acs.nanolett.6c01619. https://doi.org/10.1021/acs.nanolett.6c01619.

(5) Tsourtou, F. D.; Peroukidis, S. D.; Peristeras, L. D. The Phase Behaviour of Cetyltrimethylammonium Chloride Surfactant Aqueous Solutions at High Concentrations: An All-Atom Molecular Dynamics Simulation Study. *Soft Matter* **2022**, *18* (7), 1371–1384. https://doi.org/10.1039/D1SM01639C.

(6) Chen, Z.; Greaves, T. L.; Fong, C.; Caruso, R. A.; Drummond, C. J. Lyotropic Liquid Crystalline Phase Behaviour in Amphiphile–Protic Ionic Liquid Systems. *Phys. Chem. Chem. Phys.* **2012**, *14* (11), 3825. https://doi.org/10.1039/c2cp23698b.

(7) Aswal, V. K.; Kohlbrecher, J.; Goyal, P. S.; Amenitsch, H.; Bernstorff, S. Counterion Condensation on Charged Micelles in an Aqueous Electrolyte Solution as Studied with Combined Small-Angle Neutron Scattering and Small-Angle x-Ray Scattering. *J. Phys.: Condens. Matter* **2006**, *18* (50), 11399–11410. https://doi.org/10.1088/0953-8984/18/50/001.

(8) Hansen, J.-P.; Hayter, J. B. A Rescaled MSA Structure Factor for Dilute Charged Colloidal Dispersions. *Molecular Physics* **1982**, *46* (3), 651–656. https://doi.org/10.1080/00268978200101471.

(9) Hayter, J. B.; Penfold, J. An Analytic Structure Factor for Macroion Solutions. *Molecular Physics* **1981**, *42* (1), 109–118. https://doi.org/10.1080/00268978100100091.

(10) Berr, S.; Jones, R. R. M.; Johnson, J. S. Effect of Counterion on the Size and Charge of Alkyltrimethylammonium Halide Micelles as a Function of Chain Length and Concentration as Determined by Small-Angle Neutron Scattering. *J. Phys. Chem.* **1992**, *96* (13), 5611–5614. https://doi.org/10.1021/j100192a075.

(11) Aliyah, K.; Lyu, J.; Goldmann, C.; Bizien, T.; Hamon, C.; Alloyeau, D.; Constantin, D. Real-Time *In Situ* Observations Reveal a Double Role for Ascorbic Acid in the Anisotropic Growth of Silver on Gold. *J. Phys. Chem. Lett.* **2020**, *11* (8), 2830–2837. https://doi.org/10.1021/acs.jpclett.0c00121.

(12) Goldmann, C.; Chaâbani, W.; Hotton, C.; Impéror-Clerc, M.; Moncomble, A.; Constantin, D.; Alloyeau, D.; Hamon, C. Confinement Effects on the Structure of Entropy-Induced Supercrystals. *Small* **2023**, 2303380. https://doi.org/10.1002/smll.202303380.

(13) Park, K.; Koerner, H.; Vaia, R. A. Depletion-Induced Shape and Size Selection of Gold Nanoparticles. *Nano Lett.* **2010**, *10* (4), 1433–1439. https://doi.org/10.1021/nl100345u.
(14) Scarabelli, L.; Coronado-Puchau, M.; Giner-Casares, J. J.; Langer, J.; Liz-Marzán, L. M. Monodisperse Gold Nanotriangles: Size Control, Large-Scale Self-Assembly, and Performance in Surface-Enhanced Raman Scattering. *ACS Nano* **2014**, *8* (6), 5833–5842. https://doi.org/10.1021/nn500727w.
(15) Miyazaki, K.; Schweizer, K. S.; Thirumalai, D.; Tuinier, R.; Zaccarelli, E. The Asakura–Oosawa Theory: Entropic Forces in Physics, Biology, and Soft Matter. *The Journal of Chemical Physics* **2022**, *156* (8), 080401. https://doi.org/10.1063/5.0085965.
(16) Wuttke, J. Numerically Stable Form Factor of Any Polygon and Polyhedron. *J Appl Crystallogr* **2021**, *54* (2), 580–587. https://doi.org/10.1107/S1600576721001710.
(17) Marcone, J.; Trazo, J. G.; Nag, R.; Goldmann, C.; Ratel-Ramond, N.; Hamon, C.; Impéror-Clerc, M. Form Factor of Prismatic Particles for Small-Angle Scattering Analysis. *J Appl Crystallogr* **2025**, *58* (2), 543–552. https://doi.org/10.1107/S1600576725000676.
(18) Trazo, J. G.; Marcone, J.; Nag, R.; Goldmann, C.; Kutalia, N.; Bizien, T.; Pansu, B.; Impéror-Clerc, M.; Hamon, C. Colloidal Tunable Metasurfaces via Depletion-Induced Self-Assembly of Plasmonic Nanorods. *ACS Appl. Mater. Interfaces* **2025**, *17* (45), 62349–62359. https://doi.org/10.1021/acsami.5c17436.
(19) Kutalia, N.; Trazo, J. G.; Marchand, S.; Goldmann, C.; Ratel-Ramond, N.; Dozov, I.; Bizien, T.; Constantin, D.; Impéror-Clerc, M.; Davidson, P.; Hamon, C. Plasmonic Nanorods Form Reconfigurable Liquid Crystalline Assemblies. May 21, 2026. https://doi.org/10.26434/chemrxiv.15003689/v1.
(20) Qin, F.; Zhang, H.; Tan, T.; Wang, J.; Liu, H.; Wang, C. Three-Step, Seed-Mediated Synthesis of Ultrathin AgNWs in Aqueous Solution. *Chem. Mater.* **2022**, *34* (10), 4613–4620. https://doi.org/10.1021/acs.chemmater.2c00468.
(21) Scarabelli, L.; Sánchez-Iglesias, A.; Pérez-Juste, J.; Liz-Marzán, L. M. A "Tips and Tricks" Practical Guide to the Synthesis of Gold Nanorods. *J. Phys. Chem. Lett.* **2015**, *6* (21), 4270–4279. https://doi.org/10.1021/acs.jpclett.5b02123.
(22) *Plasmonics: From Basics to Advanced Topics*; Enoch, S., Bonod, N., Eds.; Springer Series in Optical Sciences; Springer Berlin Heidelberg: Berlin, Heidelberg, 2012; Vol. 167. https://doi.org/10.1007/978-3-642-28079-5.
(23) Hamley, I. W. *Small-Angle Scattering: Theory, Instrumentation, Data, and Applications*, 1st ed.; Wiley, 2021. https://doi.org/10.1002/9781119768364.
(24) Zhang, F.; Ilavsky, J.; Long, G. G.; Quintana, J. P. G.; Allen, A. J.; Jemian, P. R. Glassy Carbon as an Absolute Intensity Calibration Standard for Small-Angle Scattering. *Metall Mater Trans A* **2010**, *41* (5), 1151–1158. https://doi.org/10.1007/s11661-009-9950-x.
(25) Yang, P.-W.; Thoka, S.; Lin, P.-C.; Su, C.-J.; Sheu, H.-S.; Huang, M. H.; Jeng, U.-S. Tracing the Surfactant-Mediated Nucleation, Growth, and Superpacking of Gold Supercrystals Using Time and Spatially Resolved X-Ray Scattering. *Langmuir* **2017**, *33* (13), 3253–3261. https://doi.org/10.1021/acs.langmuir.6b04319.
(26) Young, K. L.; Jones, M. R.; Zhang, J.; Macfarlane, R. J.; Esquivel-Sirvent, R.; Nap, R. J.; Wu, J.; Schatz, G. C.; Lee, B.; Mirkin, C. A. Assembly of Reconfigurable One-Dimensional Colloidal Superlattices Due to a Synergy of Fundamental Nanoscale Forces. *Proc. Natl. Acad. Sci. U.S.A.* **2012**, *109* (7), 2240–2245. https://doi.org/10.1073/pnas.1119301109.
(27) Sung, B.; Wensink, H. H.; Grelet, E. Depletion-Driven Morphological Transitions in Hexagonal Crystallites of Virus Rods. *Soft Matter* **2019**, *15* (46), 9520–9527. https://doi.org/10.1039/C9SM01207A.
(28) Nag, R.; Rouvière, N.; Trazo, J. G.; Marcone, J.; Kutalia, N.; Goldmann, C.; Impéror-Clerc, M.; Alloyeau, D.; Constantin, D.; Hamon, C. Depletion-Induced Tunable Assembly of Complementary Platonic Solids. *Nano Lett.* **2024**, *24* (51), 16368–16373. https://doi.org/10.1021/acs.nanolett.4c04923.

(29) Atkins, P. W.; de Paula, J.; Keeler, J. J. *Atkins' Physical chemistry*, 11. Aufl.; Oxford Univ. Press: Oxford, 2018.
(30) Zang, S.; Paul, S.; Leung, C. W.; Chen, M. S.; Hueckel, T.; Hocky, G. M.; Sacanna, S. Direct Observation and Control of Non-Classical Crystallization Pathways in Binary Colloidal Systems. *Nat Commun* **2025**, *16* (1), 3645. https://doi.org/10.1038/s41467-025-58959-0.
(31) García-Lojo, D.; Modin, E.; Gómez-Graña, S.; Impéror-Clerc, M.; Chuvilin, A.; Pastoriza-Santos, I.; Pérez-Juste, J.; Constantin, D.; Hamon, C. Structure and Formation Kinetics of Millimeter-Size Single Domain Supercrystals. *Adv. Funct. Mater.* **2021**, *31* (27), 2101869. https://doi.org/10.1002/adfm.202101869.
(32) Gómez-Graña, S.; Fernández-López, C.; Polavarapu, L.; Salmon, J.-B.; Leng, J.; Pastoriza-Santos, I.; Pérez-Juste, J. Gold Nanooctahedra with Tunable Size and Microfluidic-Induced 3D Assembly for Highly Uniform SERS-Active Supercrystals. *Chem. Mater.* **2015**, *27* (24), 8310–8317. https://doi.org/10.1021/acs.chemmater.5b03620.
(33) Bian, T.; Gardin, A.; Gemen, J.; Houben, L.; Perego, C.; Lee, B.; Elad, N.; Chu, Z.; Pavan, G. M.; Klajn, R. Electrostatic Co-Assembly of Nanoparticles with Oppositely Charged Small Molecules into Static and Dynamic Superstructures. *Nat. Chem.* **2021**, *13* (10), 940–949. https://doi.org/10.1038/s41557-021-00752-9.
(34) Impéror-Clerc, M. HDR: Etude Structurale de Fluides Complexes. **2007**. https://doi.org/10.13140/RG.2.2.21312.84483.
(35) Boström, M.; Deniz, V.; Franks, G. V.; Ninham, B. W. Extended DLVO Theory: Electrostatic and Non-Electrostatic Forces in Oxide Suspensions. *Advances in Colloid and Interface Science* **2006**, *123–126*, 5–15. https://doi.org/10.1016/j.cis.2006.05.001.
(36) Cheng, Z.; Jones, M. R. Assembly of Planar Chiral Superlattices from Achiral Building Blocks. *Nat Commun* **2022**, *13* (1), 4207. https://doi.org/10.1038/s41467-022-31868-2.

Chapter 4

TUNABLE METASURFACES VIA DEPLETION-INDUCED SELF-ASSEMBLY (DISA) OF NANORODS

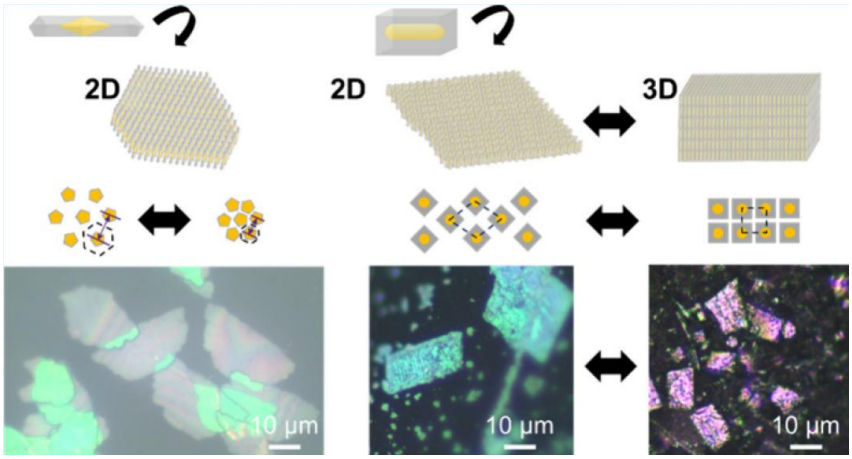

J. G. Trazo, et al. **Colloidal Tunable Metasurfaces via Depletion-Induced Self-Assembly of Plasmonic Nanorods.** *ACS Appl. Mater. Interfaces.* 2025, 17(45).

https://doi.org/10.1021/acsami.5c17436

Article Text in Annex

4.1. Introduction

Metamaterials, Anisotropy, and Self-Assembly

Many fundamental models of self-assembly deal with the organization of predominantly isotropic objects with relatively unbroken symmetries, such as spheres and cubes which pack into 3D superstructures[1,2]. However, emerging technologies in opto-electronics, catalysis, and biomedicine rely more and more on nanostructured arrays with limited uni-dimensionality (1D) or bi-dimensionality (2D) like *metasurfaces*, to achieve peculiar optical, mechanical, or electronic properties not found in conventional materials like bulk metals or classical glass-based optics. Among these properties are nano-porosity, elastic anisotropy, optical transparency, negative or fractional refractive index, high surface reactivity, surface plasmon resonance and so on[3] (**Figure 1**). Photonic or electromagnetic metamaterials are particularly

interesting because of their ability to manipulate light due to subwavelength periodicity in their structure. On the other hand, diffractive plasmonic metasurfaces, often noble metal arrays with lattice parameters in the UV-visible to near IR wavelength range, exhibit very sharp surface lattice resonances (SLR) determined by their lattice periodicity, which are promising for many optical applications[4,5]. While they possess unique optical properties, these metamaterials are typically made by complex top-down approaches like e-beam lithography, photolithography, or laser ablation on a substrate, which results in static material properties, as noted in Chapter 1. Their fabrication often requires multi-step depositions, chemical treatments, or high-temperature exposure[5,6] (**Figure 2**).

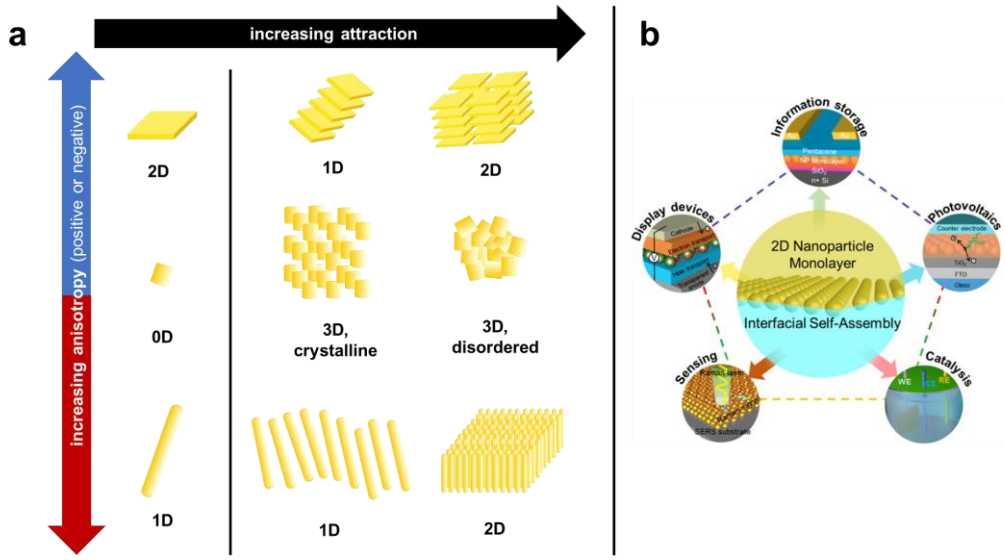

Figure 1. Design of metamaterials. (a) *'Metamaterials' with dimensionality control via anisotropy transfer in nanoparticle self-assembly, such as via depletion forces.* ***(b)*** *General applications of 2D plasmonic metasurfaces[7].*

In this regard, recent research has proposed the *tunable self-assembly* of anisotropic building blocks as a bottom-up way to construct finely structured 1D or 2D superstructures, acting as colloidal or 'liquid' metamaterials. This colloidal approach has the advantage of the building blocks being reconfigurable in suspension, and of the construction being generally cheaper.

By inducing the preferential self-assembly of anisotropic rod or plate-like nanoparticles (NPs) between their larger facets, an *anisotropy transfer* from the NP shape to the micron-scale superstructure shape can occur. NPs can be passively or actively directed to spontaneously self-organize into *self-limited structures* (often found in biological systems), growing in limited directions as a 1D or 2D superstructure if a directional attractive force, like polymer patches,

engineered DNA ligands, or depletion, exists between the NPs (**Figure 1**)[8]. In such self-limited assembly, one avoids 3D superstructures that have low surface-to-volume ratio which is disadvantageous for certain catalytic, sensing, or optical applications. *In situ* self-assembly can also be done in water, which is advantageous for biomedical or bio-inspired devices. Lastly, unlike nanostructures made by lithography or printing, colloidal self-assembly can be made active, i.e., changing NP position or orientation in response to a stimulus, allowing one to make switchable metamaterials (**Figure 2**)[9].

In this chapter, taking inspiration from these examples, we investigate the possibility of creating *dynamic, reversible, and colloidal* 1D/2D plasmonic metamaterials using in situ depletion-induced self-assembly (DISA) of anisotropic metal nanorods (NRs). Here, we chose depletion for its two main advantages. First, the relatively low magnitude of the depletion attraction, a few kT, ensures ease of reversibility of the assembly versus other forces like electrostatics. Second, depletion forces are stronger between the larger facets of anisotropic NPs[10]. Depletion will be compared with other self-assembly methods in the next sections.

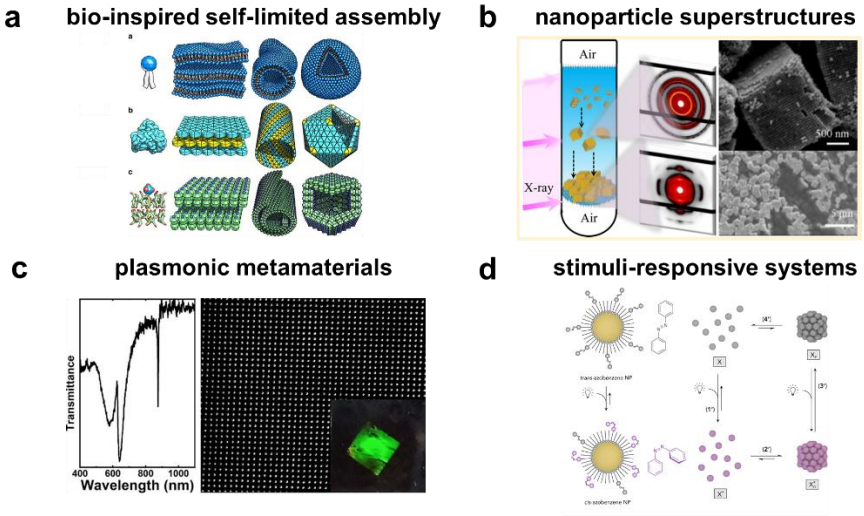

Figure 2. Key examples and inspirations in nanoscale self-assembly. (a) *Self-limited assembly in lipid and protein membranes in biological systems[11]. **(b)** 3D colloidal Au nanocube superstructures by depletion[12]. **(c)** Template-made diffractive Au metasurface with collective surface lattice resonance[4]. **(d)** Active photoinduced self-assembly of AuNPs via solvophobic/dissipative interactions of azobenzene ligands[13].*

Colloidal Self-Assembly of Nanoparticles: State-of-the-Art and Challenges

Let us now look briefly at the existing strategies for creating colloidal plasmonic superstructures via NP self-assembly, and identify challenges that could be addressed by the DISA technique. More broadly, plasmonic superstructures can be either (1) dry/substrate-based, or (2) wet/colloidal. Among dry, substrate-based strategies, electron-beam or photolithography on a metal or dielectric remains a gold standard in making nanostructured lattices with defined symmetry, high uniformity, and structural precision to as small as 5-10 nm, especially for more intricate repeating unit shapes[3,6]. More recently, PDMS mold/template-assisted stamping of a NR suspension onto a substrate has also become common method for making noble metal metasurfaces (**Figure 3a**)[4,14]. This technique has the advantage of ease and lower cost, and has been used to make a variety of metasurface patterns, including ones exhibiting circular dichroism[15]. In template-assisted stamping, NPs gather, self-assemble, and dry in wells in the PDMS templates. Other researchers have made metasurfaces by depositing monolayer NP arrays onto plasma-treated glass substrates, leading to ultra-uniform NP spatial distribution but without any long-range lattice order, leading to metasurface-like properties such as narrow collective plasmon resonances (**Figure 3b**). Such systems often exhibit ultra-uniformity due to NP-NP and NP-substrate electrostatic interactions. These metasurfaces were made by either immersion or dip-coating of the treated glass substrate into a NP suspension, followed by a washing and drying step[16]. However, precise engineering and predictive modeling of such surfaces can more difficult than with regular lattices. Furthermore, all three substrate-based strategies give only static metasurface properties.

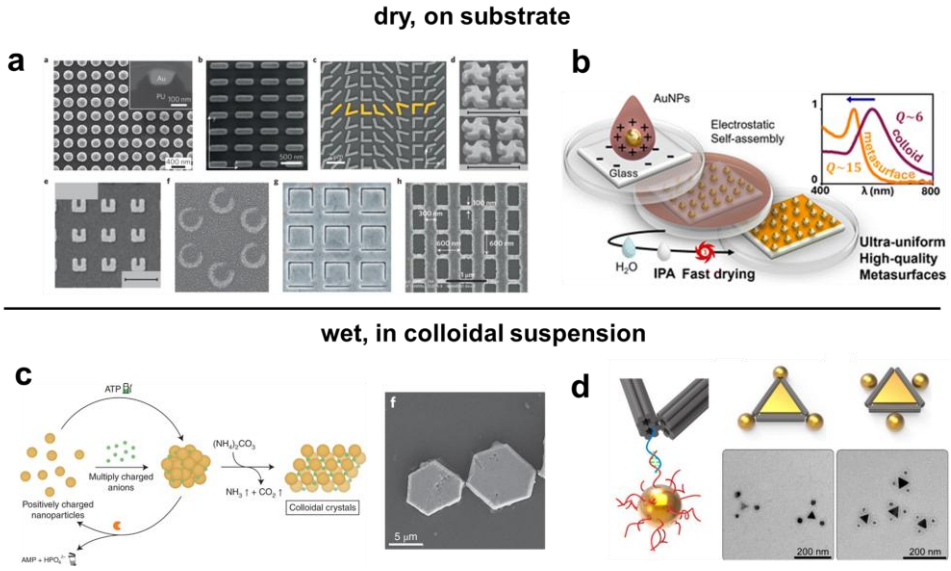

Figure 3. Existing dry vs. wet strategies for creating plasmonic metasurfaces. (a) *Substrate-based metasurfaces made by lithography or templates[3]. **(b)** Ultra-uniform metasurface made by electrostatic adsorption of AuNPs onto a charged glass surface[16]. **(c)** Coulombic co-assembly of AuNPs and multiply charged ions[17]. **(d)** Precise colloidal clusters of plasmonic NPs assembled by DNA origami[18].*

Among common wet self-assembly strategies, there are *electrostatic, solvophobic, and DNA-based* approaches. Various electrostatic or Coulombic self-assembly strategies have been employed, either by functionalizing NPs with complementary positively and negatively charged ligands[17], and/or by using polycations and polyanions[13]. Since electrostatic interactions are quite strong, they can initially yield more amorphous NP structures, which need to be transformed into larger crystalline domains via some type of recrystallization or annealing. The literature on such electrostatic assembly is predominantly on spherical gold NPs, with limited data on metal nanorods or plates. Finally, the strength of Coulombic forces (e.g. versus van der Waals or depletion forces) renders electrostatic assemblies difficult to reverse and practically non-reconfigurable; a large input of energy is required to disassemble them (**Figure 3c**)[13,17]. NP assembly may also be induced by solvophobic effects, where appropriate NP ligands like polymer chains or other large molecules can attract one another and stick the NPs together upon a change of solvent polarity. However with this method, 1D or 2D structures are hard to realize without selective 'patchy' ligand functionalization of the NPs only on certain areas[19,20]. Meanwhile, assembly by DNA or oligonucleotide ligands – via base-pair matching of complementary DNA strands on the NP surfaces – is a well-developed and precise method for making intricate NP assemblies in liquid, or for attaching NPs onto

precisely engineered positions on a substrate grid[21]. However, the preparation of the DNA ligands can be tedious, and the length and flexibility of the ligands can alter the effective shape of the NPs in the supercrystal[22]. On the other hand, using DNA origami alone (i.e., using nanoscale folding DNA as arbitrarily shaped 2D or 3D templates for NPs), one can only make assemblies with a limited number of particles, often dimers or trimers (**Figure 3d**)[18,23,24]. DNA is also restricted by its sensitivity to conditions like pH or salt concentration, depending on the desired application[18]. In general, these wet strategies require additional ligand exchanges or surface chemistry modifications that could be incompatible with certain NP compositions or geometries, add cost, or reduce the NP colloidal stability.

In response to these challenges, we propose DISA as an alternative wet self-assembly strategy that is ligand-free and chemically-universal. Instead, a chemically-inert stimulus, in the form of native CTAC or CTAB micelles as *depletant*, is used in combination with precise *anisotropic NR* shape engineering, in order to promote precise self-limited superstructures.

Controlling 'anisotropic' depletion-induced self-assembly

Having outlined the motivation of our study, we now review the idea of using depletion-induced self-assembly (DISA), briefly introduced earlier in this report, to design anisotropic 1D and 2D superstructures in colloidal aqueous suspension with plasmonic metaproperties. Given previous literature, we hypothesize that with long gold core – silver shell (Au@Ag) NRs, depletion can act as a pseudo-directional attractive force to favor side-by-side NR assembly into 1D chains or 2D metasurfaces[25–27] In this project, Au@AgNRs with varying anisotropy will be the building blocks for the tunable metasurfaces, while aqueous CTAC micelles will be used as the depletant (**Figure 4**).

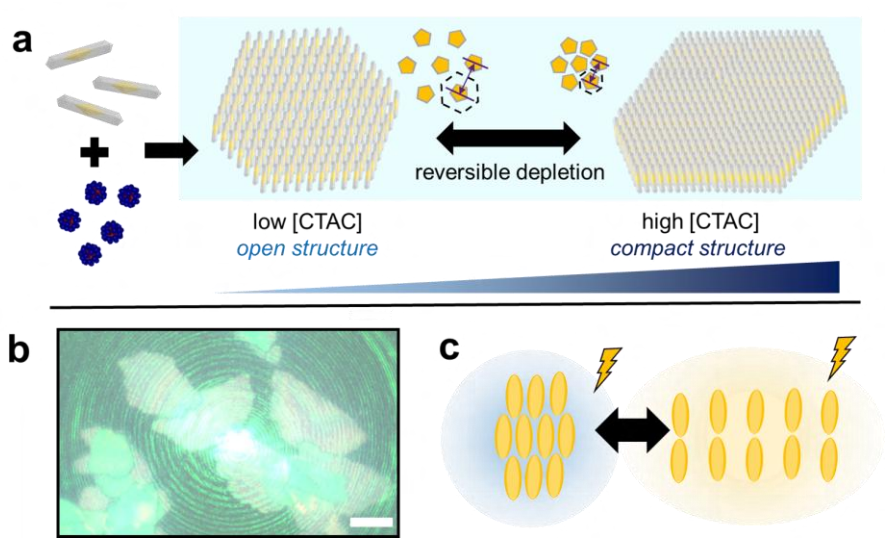

Figure 4. Scheme of designing dynamic and colloidal plasmonic metasurfaces via DISA: (a) *Process of metasurface formation by tunable side-by-side self-assembly of gold-core silver-shell nanorods (Au@Ag NRs).* ***(b)*** *in situ analyte sensing via surface-enhanced Raman scattering (SERS) with the NR metasurfaces.* ***(c)*** *Illustration of tunable plasmon resonance and plasmonic enhancement via NR DISA.*

Fine-tuned control of this DISA system requires the control of three parameters: (1) the NR size and shape (i.e., aspect ratio and cross-section symmetry), (2) the depletant concentration over time, and (3) the speed of assembly/crystallization. Note that all three of these factors have been observed to yield superstructures of different dimensionality and lattice symmetry in other systems like *fd* virus rods, gold nanocubes, or charged colloidal spheres[12,28,29]. To close, there are three open questions that motivate this investigation of DISA:

First, is it possible to tune the dimensionality of colloidal assemblies of NRs made via depletion, by tuning the NP anisotropy or depletion strength? Is it possible to stabilize highly-extended (few to 100s of microns wide) 2D monolayer lattices with high surface-to-volume ratio and tunable inter-NR gaps? What about 1D or 3D assemblies? What are the possible lattice symmetries in each case? What is the typical range of inter-NR gap distances possible, and what is the precision of control with the DISA method?

Second, is depletion-induced self-assembly of NRs into metasurfaces reversible by rediluting the surfactant, whether low or high depletant concentration was used for assembly? Given that depletion is an entropic process, is the assembly fully cyclable, or is there kinetic trapping

leading to hysteresis? What is the timescale of assembly as a function of depletant concentration, and the commutation time for a full assembly-disassembly cycle? What is the crystallization mechanism for NR self-assemblies by depletion? Is it an equilibrium self-assembly, and is it classical crystallization?

Third, how do the surface plasmon resonances (SPR) of the NRs interact, shift, or couple as a function of assembly dimensionality, domain size, orientation, and inter-NR gaps as we change depletant concentration? How does plasmonic enhancement change? Are such SPR changes reversible? What applications could exploit such modulable SPRs or plasmonic enhancement?

4.2. Perspectives

Kinetics and reversibility of DISA

Following our studies on slow versus fast DISA (**article SI**), mathematical modelling of DISA kinetics for cyclic assembly-disassembly is the next step in this project. A deeper study on the DISA hysteresis is also recommended, as it is highly probable that the metasurface assembly and disassembly pathways are different with fast redilution of CTAC depletant. More investigation into the structure and formation of kinetically-trapped aggregates in fast DISA is needed. Additionally, other factors like finite volume or confinement, surface effects, and sedimentation appear to have effects on the colloidal metasurface formation and structure, and these need to be disentangled from the main parameters of depletant concentration NR aspect ratio (AR).

Fast vs. slow DISA kinetics: 1D needles vs. 2D platelets

We currently maintain that C5-NRs predominantly form 2D metasurfaces due to their sharp tips and higher ARs, hindering tip-to-tip NR stacking, but a systematic comparison of NR assemblies with varied cross-sections but with the same lengths and widths remains to be done. In the course of this study, we serendipitously discovered the existence of long '1D needle' assemblies of NRs which undulate via Brownian motion (**Figure 5**) under certain depletions. These mainly form when long NRs are put in contact with low depletant concentrations, and/or with fast mixing of depletant. These needles are seen to either coexist

with the 2D platelet-like metasurfaces when assembling short or medium C8 or C5-NRs (AR 5 to 10), or exist as the sole form of assembly in the case of C5-NRs with high aspect ratios, typically above 10. These needles occur only very rarely with square C4-NRs, though we hypothesize this is due to the lower ARs tested.

It was initially thought that these NRs could be stacked assemblies of small platelets, stacked along the long axis of the rods as in previous studies on the depletion of virus rods[28,30]. This is because, geometrically, there is no apparent reason for rods to self-organize along only one axis. However, though LCTEM and POM with micron-long C5-NRs, we directly observed that these objects are side-by-side assemblies, with rapid fluctuations in rod position along the NR z-axis, akin to wormlike motion. SAXS data also showed that the center-to-center distance between the NRs can reach as high as 80 to 90 nm, and that the needles have a thickness of a few side-by-side chains stacked on top of each other. The high center-to-center distance and the wormlike motion in the needles suggests that the attractive depletion force between the NRs inside is very weak, in contrast to strong depletion forces needed to form tip-to-tip columnar fibrils of rods (e.g., in the case of *fd* virus rods[28]); this corroborates with our observation of needles mostly at low depletant concentration. Nonetheless, small populations of needles were found to exist even at high depletant concentrations, up to 500 mM CTAC, suggesting that these assemblies may have seeded early and remained kinetically trapped.

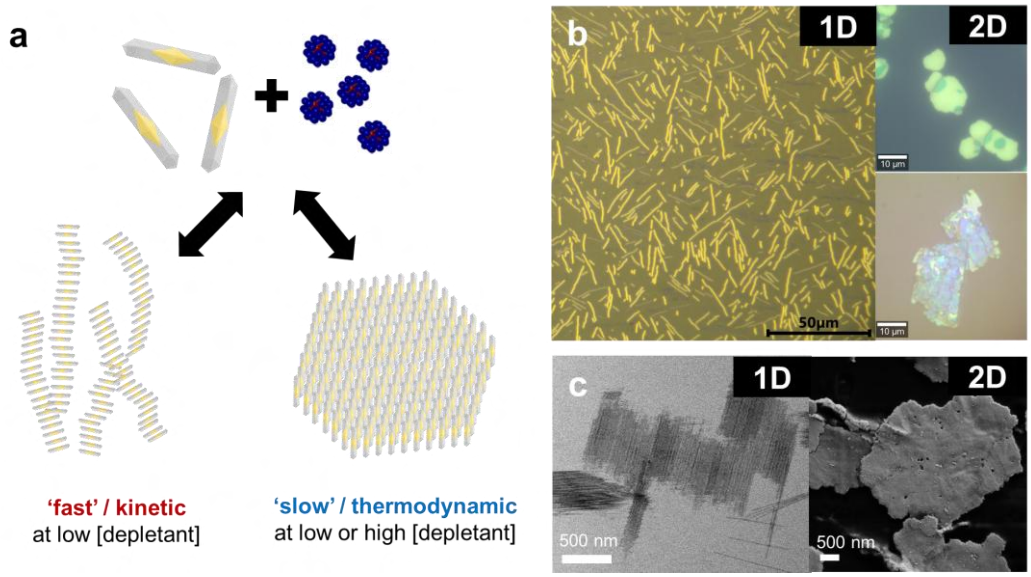

Figure 5. Dynamic 1D needle assemblies of long plasmonic NRs. (a) *Scheme of 1D needle vs. 2D platelet formation. 1D vs. 2D colloidal assemblies of long NRs seen via* ***(b)*** *optical microscopy (reflection mode), and* ***(c)*** *electron microscopy (left: liquid cell TEM; right: SEM).*

Currently, we propose that the needles are a *metastable kinetic product* of DISA, as they predominantly appear in fast addition of depletant, and in the case of C8-NRs (AR = 5), needles were directly observed to *transform into 2D metasurfaces*, more thermodynamically stable, over the course of two to three hours. It is probable that needle formation occurs by monomer-by-monomer addition, either because surface energy is highest at the needle tips, or because of a steric effect. In any case, confinement does not appear to be the main driving factor as the needles form even in wide capillaries. Interestingly, according to some simulation studies, the self-assembly of ill-fitting particles, such as irregular or strained polygons, tend to form 1D fiber assemblies regardless of specific shapes and across a wide range of attractive forces[29,31,32]. It is unclear how directly this applies our system of C5-NRs, but in any case, the correlation between rod cross-section and the dimensionality of assemblies must be investigated further.

Ultra-slow DISA kinetics: a zoo of nanostructures

One notable strategy for studying the kinetics of concentration-induced colloidal self-assembly, like DISA, is capillary dialysis (**Figure 6a,b**) such as in one recent study on ionic colloidal crystallization[29]. To perform this with our NR DISA system, a capillary with the nanoparticles is immersed in a bath to create a slow-moving concentration gradient of CTAC depletant, allowing one to perform 'ultra-slow' DISA, with each point along the capillary also acting as different kinetics curves of differing speeds over time. In theory, such slow self-assembly would result in larger, well-ordered superstructures. More details on this pseudo-dialysis or immersion experiment are recounted in Chapter 3.

Having tested such ultra-slow DISA in preliminary experiments with long C5-NRs, we also explored using this technique to assemble a wide range of anisotropic NP structures, to see what kinds of crystal shapes could be formed. Remarkably, a real zoo of different supercrystal structures was observed (**Figure 6c-f**).

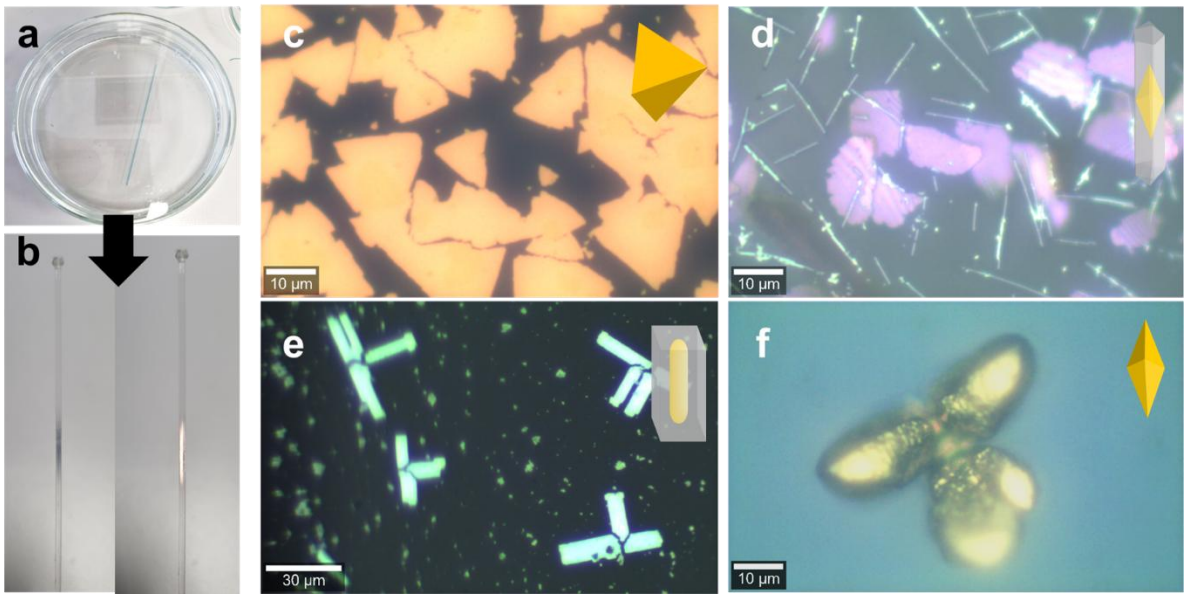

Figure 6. Ultra-slow depletion-induced self-assembly via capillary immersion / pseudo-dialysis. ***(a)*** *Immersion of a NR-filled capillary in a CTAC depletant bath.* ***(b)*** *Large lustrous assemblies formed after two weeks, among them, via in situ optical microscopy (reflection):* ***(c)*** *triangular platelets from Au nano-tetrahedra,* ***(d)*** *thin metasurfaces and needles from long Au@Ag C5-NRs,* ***(e)*** *rectangular prismatic supercrystals of Au@Ag C4-NRs, and* ***(f)*** *three or four-fold 3D bipyramid flowers from Au bipyramids.*

Three main observations were noted from this ultra-slow DISA experiment. First, while anisotropy transfer remains and crystal habits resemble the shape of the individual rods, dimensionality is primarily 2D (e.g. for tetrahedra and nanorods) – verified by adjusting the microscope focus and tilting the sample, unless the symmetry of the individual NP strongly prohibits it in the case of bipyramidal NPs which formed 3D flower-like supercrystals. Second, variations in assembly speed, due to gradients in depletant and NP concentration along the capillary, change the overall size and correlation length of the assemblies. Smaller assemblies are found close to the open end of the capillary where depletant entered earlier and faster. Finally, defects and nucleation sites appear to play a crucial role in the final shapes of the assemblies.

While this ultra-slow DISA study needs to be developed further, current results show its potential in unveiling the crystallization mechanism of rods, among other particles, into 2D superstructures over a long period of time, even up to several weeks. It may also help us build up a fuller phase diagram, including kinetic or metastable states, of the possible depletion-induced assemblies of different NRs.

Optimization of colloidal SERS

The technique of in situ SERS using colloidal DISA metasurfaces as substrates, though promising, still has two potential drawbacks. First, the variance of the Raman signal measured in a single sample is very high, reaching a relative standard deviation (RSD) of 50%. Even with the same metasurfaces measured multiple times, the Raman count remains quite variable, suggesting that Brownian motion and variable orientation of the assemblies affects the Raman scattering. However, even in the dried state (i.e. via EISA), the Raman count RSD is still 60% of that in liquid. This implies that variation in assembly size and low surface homogeneity of the substrate decrease the signal repeatability, as hypothesized in literature[33,34]. To further study this, it is also recommended to do a SERS series with metasurfaces of different size or crystallinity. This can be done by self-assembling the NRs with different speeds of depletant addition. Supplementary studies for our recent article already showed a different trend in Raman counts with fast versus slow DISA, which may support the idea that crystalline domain size is the major factor influencing SERS enhancement (**Figure 7**). On the other hand, further tests on sedimented metasurfaces should be done, which in theory could eliminate the effect of Brownian motion and variable orientation of the assemblies. It would also be interesting to test whether the Raman enhancement of the 1D needle assemblies is dependent on the needle orientation with respect to the laser polarization, in the case of polarized SERS. Second, it is still unknown why green (532 nm) versus red (633 nm) excitation produces near opposite trends in Raman signal, as noted in our article. Numerical simulations of the colloidal metasurfaces excited by green versus red light may help explain this effect. It is also worth noting that one study has found that close-packed side-by-side assembly of anisotropic metal NPs (e.g. Au NRs) can reduce ensemble-averaged SERS signal once certain assembly sizes are reached, due to destructive interference of the radial component of the NR SPRs[35], which may partly rationalize our findings here.

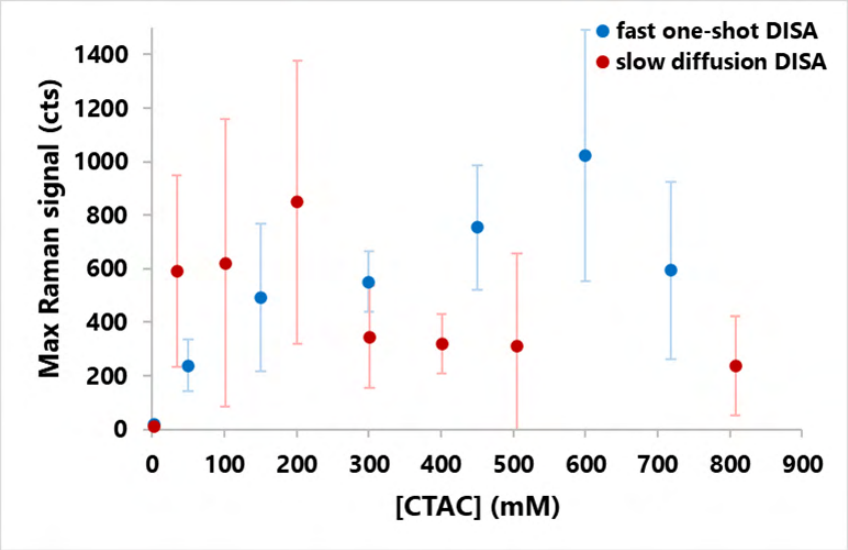

Figure 7. In-situ surface-enhanced Raman scattering (SERS) with colloidal metasurfaces of C5-S assemblies: *Comparison of one-shot versus slow diffusion DISA, attaining maximum SERS counts at different depletant concentrations.*

Finally, it is necessary to test our SERS system with a variety of other analytes of different chemical makeup and molecular size. For more information on this, we detail one promising development of our SERS project in Chapter 6 on photoswitchable DISA.

Colloidal plasmonic liquid crystals of anisotropic nanorods

A big breakthrough during the course of this DISA project was the accidental discovery of aqueous colloidal liquid crystals (LCs) of plasmonic NRs in close collaboration with our fellow PhD student Nika Kutalia in LPS, who subsequently led this new offshoot project. More information can be found in our recent ChemRxiv preprint: *Plasmonic nanorods form reconfigurable liquid crystalline assemblies* (N. Kutalia, J. Trazo, et al.: doi.org/10.26434/chemrxiv.15003689/v1)[36]. This discovery has given more insight into anisotropy transfer and entropic effects in self-organizing systems of colloidal nanorods, as well as plasmonic properties manifested in a LC phase.

It was found that at sufficiently high NR concentration, for sufficiently NR high aspect ratios above 15, and at low depletant strength (< 2 mM CTAC where depletion forces are negligible), Au@Ag NRs dispersed in water transition from an isotropic phase to a nematic (N) phase, self-organizing into a LC with orientational order but no positional order. This transition can be theoretically rationalized by the Onsager hard-rod model accounting for net entropy

maximization[37]. The nematic phases exhibited the typical optical properties of LCs, such as Schlieren and threaded textures and global birefringence under polarized optical microscopy (POM). Upon further increase in NR concentration, the nematic phase transitions to a smectic B (SmB) phase, where the rods self-organize into distinct fluid layers of side-by-side rods with 2D hexagonal intralayer order, but with no interlayer order. For Au@Ag NRs with an aspect ratio of 35, the SmB phase exhibited a mosaic grainy texture, with interlayer period of around 1300 nm, corresponding to the length of one NR plus an interlayer gap (**Figure 8**).

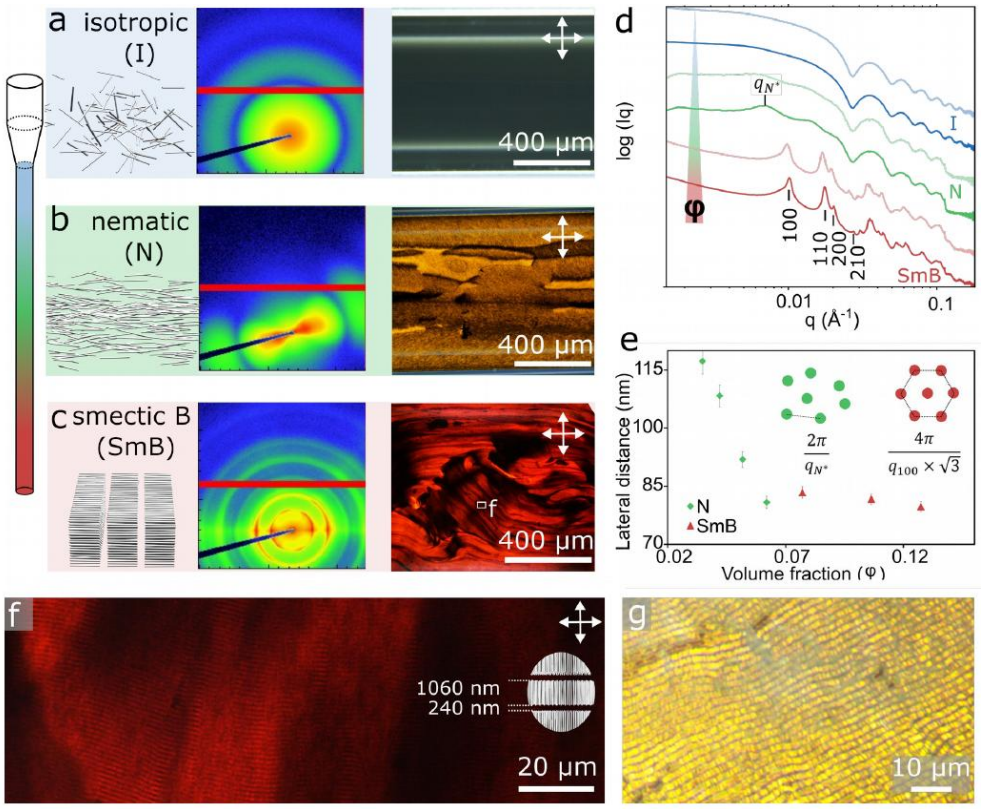

Figure 8. Liquid crystal phases of aqueous colloidal suspensions of plasmonic NRs[36]. (a-c) *Sequential phases of colloidal Au@Ag NRs in water at high NR concentration and low depletion strength, showing schemes, 2D SAXS diffractograms, and polarized optical microscopy (POM) images in transmission.* ***(d)*** *1D SAXS radial profiles for the three phases, at increasing NR concentration.* ***(e)*** *Evolution of average lateral distance between the NRs at increasing NR concentration.* ***(f-g)*** *Layered grainy textures of the smectic B phase seen by POM, in transmission and dark field reflection mode respectively.*

Most remarkably, these LCs were multi stimuli-responsive, with reversible structural changes in response to light (which likely induces anisotropic plasmonic heating), temperature, AC electric field, magnetic field, and also depletants (CTAC micelles) as a chemical stimulus. For all stimuli, the typical commutation time ranged from 1 to 5 s to about 5 min. By controlling depletion strength, either by changing the depletant concentration or the temperature, one

could reversibly switch between the LC phase dominated by inter-NR repulsion, and the colloidal superstructure phase dominated by depletion-induced inter-NR attraction. In this case, the superstructures were predominantly 1D needle assemblies, with the same 2D hexagonal symmetry as the SmB LC phase, but with much shorter inter-NR gap distances versus the LC phase (**Figure 9**). Using the capillary pseudo-dialysis technique mentioned earlier, a continuous transition between the LC and superstructure phases could be observed along the length of the capillary (**Figure 10**). With further development, this LC-superstructure transition could be leveraged for optical switching applications. More studies into the optical properties of these LCs are also ongoing, in light of the possible use of this system in prototype optoelectronic devices. At ultra-low ionic strength, these LC phases can also exhibit brilliant structural color, as will be discussed in the next section.

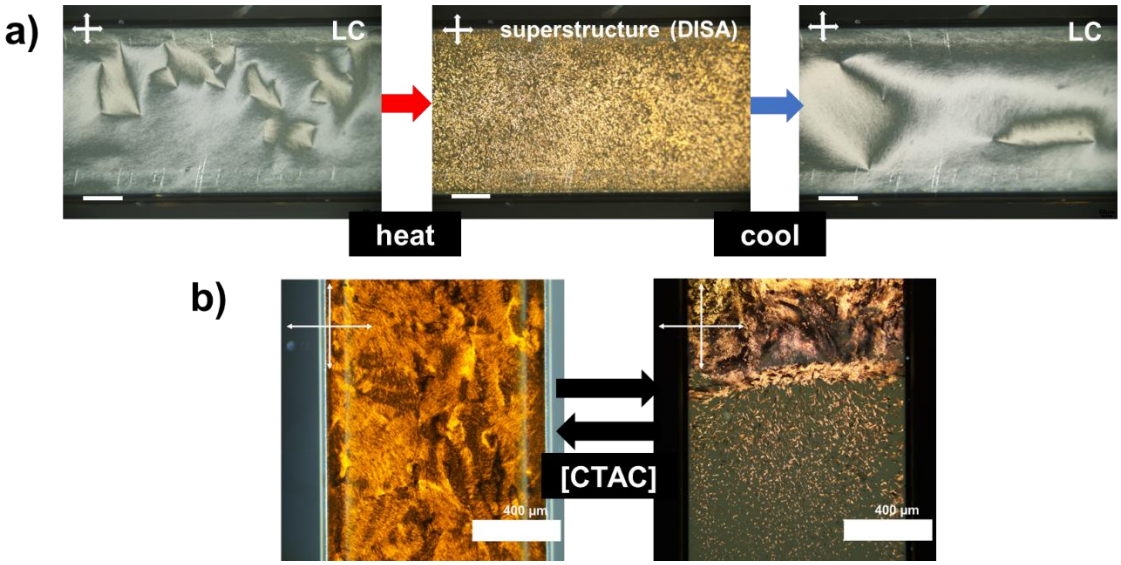

Figure 9. Reversible depletion-induced phase transitions in plasmonic NR liquid crystals: (a) *temperature-stimulus 'freezing by heating' and* ***(b)*** *chemical-stimulus.*

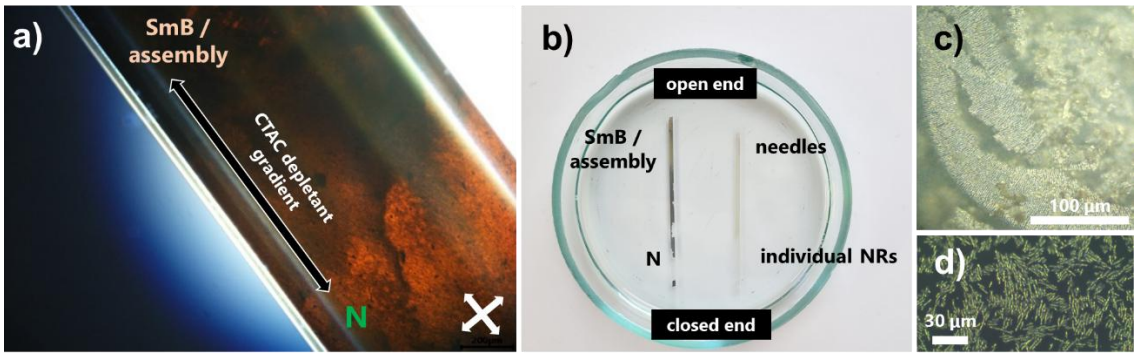

Figure 10. Ultra-slow DISA by diffusion (pseudo-dialysis) in the case of micron-long Au@Ag NRs. ***(a)*** *Polarized optical microscopy image: Gradual transition from nematic liquid crystal phase to depletion-induced assembly or smectic B phase of the long NRs.* ***(b)*** *Capillaries filled with long NRs immersed in a bath of 15 mM CTAC.* ***(c)*** *Smectic-like bundles of NR sheets, and* ***(d)*** *looser needles of side-by-side NRs seen by optical microscopy in reflection mode.*

Towards diffractive colloidal metasurfaces

Finally, let us touch briefly on the possibility of creating diffractive metasurfaces in the near UV- to visible to near-IR range using our colloidal DISA method. Diffractive metasurfaces can exhibit sharp surface lattice resonances (SLRs) which can be used for many photonic or opto-electronic applications. In this chapter, it was noted that a maximum of about 70 nm in center-to-center lattice parameter can be attained in our colloidal 2D metasurfaces of metal NRs. Theoretically, this limit is dictated by the range of electrostatic repulsion between the NRs, balanced by the range of attractive depletion which is dictated by the effective hydrodynamic size of the depletants. It is this hydrodynamic size that determines the maximum exclusion volume between NRs where depletion will be nonzero. There are thus two ways of increasing the lattice parameter: (1) reduce electrostatic screening – by lowering ionic strength as much as possible, and (2) use larger depletants, e.g. physically larger micelles. This however is very difficult to do when using charged CTAC micelles as depletant.

One could use longer surfactant molecules that form bigger micelles in aqueous medium, which increases the range of the depletion interaction. One could also use neutral, uncharged depletants like polymer nanoparticles (e.g. PEG, dextran) which do not add ionic strength to the system, increasing the Debye length and thus the effective size of the depletants and the effective range of depletion. Moreover, functionalizing the NRs with longer ligands or multiply charged ligands might extend the range of electrostatic repulsion[10,38,39].

Still, even from preliminary experiments with our current micron long C5-NRs, we observed the formation of thin 2D platelet assemblies at high NR concentration, low surfactant concentration (i.e., low ionic strength, less than 10^{-3} M), and under confinement, where the NRs were expected to typically form liquid crystal phases (**Figure 11a-c**). On the other hand, at very low ionic strength (> 10^{-5} M), these long rods assemble into extremely vivid colored fluid phases which exhibited photonic structural color as confirmed by SAXS and reflectance spectroscopy, rather plasmonic color (due to LSPRs). The photonic color emerges from light diffraction due to the side-by-side hexagonal lattice of the can be tuned from red to violet by simply increasing the NR concentration. While these structurally colored phases are promising, these are still strictly a type of liquid crystal, specifically either a columnar or smectic B phase, and not a colloidal crystalline monolayer. Still, these phases have rich optical metaproperties in the liquid state that are worth continued investigation (**Figure 11d**).

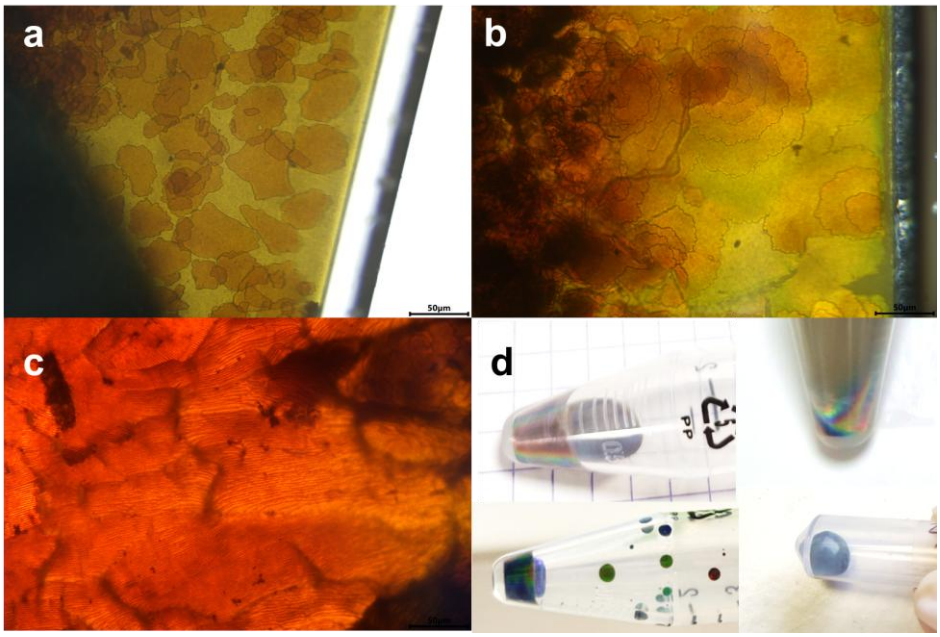

Figure 11. Preliminary results towards ultra-open and diffractive metasurfaces. (a-c) *Scintillating metasurface platelets of micron-long Au@Ag NRs formed form a liquid crystal of the same rods (30 wt.% Ag, 1 mM MUTAB in H_2O).* ***(d)*** *Tunable, visible-wavelength photonic structural colors in colloidal suspensions of micron-long Au@Ag NRs in a liquid crystal phase.*

4.3. Take-home message

We have shown that highly-extended 2D metasurfaces can be formed via *in situ* depletion-induced self-assembly (DISA) of Au@Ag NRs in liquid. In this process, long round-tipped C5-NRs are assembled by slow diffusion of CTAC depletant into a NR suspension. By decreasing

the speed of depletant diffusion, one can create thin metasurfaces from about 10 to 100 μm across. On the other hand, lower aspect ratio C5-NRs or flat-tipped C4-NRs form either 2D or 3D assemblies depending on the depletant concentration. By controlling the amount of depletant added, one can fine tune inter-NR gaps in the 2D assemblies, resulting in either open or closed metasurfaces with compacities ranging from 21% to 80%.

Second, this DISA process was found to be reversible, but only fully cyclable (up to five cycles) via slow redilution of the depletant via diffusion of water. Fast redilution appears to result in kinetically-trapped aggregates. Higher depletant concentration or mechanical agitation increases the speed of self-assembly but also decreases crystalline domain sizes. The duration of DISA can be controlled anywhere from one minute to two weeks; micron-sized crystals are formed by slowing down depletant diffusion to at least one to three hours. In addition, the formation of the metasurfaces appears to proceed by non-classical crystallization, not exclusively proceeding via monomer-by-monomer addition.

Third, the formation of metasurfaces induces tunable plasmonic enhancement via hotspots between the side-by-side NRs, allowing the assemblies to be used as a colloidal SERS platform in liquid. The evolution of SERS enhancement vs. depletant concentration was non-monotonic, as seen by evolution of SERS counts of 4ATP analyte adsorbed onto the metasurfaces. It is concluded that crystalline domain size is a primary determiner of overall SERS enhancement. Moreover, the SPRs of the NRs were found to either blue-shifted or red-shifted depending on the depletant concentration, linked to either dominantly side-by-side only (2D) or side-by-side plus tip-to-tip NR interaction.

In perspective, the mechanisms and depletion kinetics of the metasurface formation need to be further elucidated. To increase the viability of DISA as a SERS platform, new strategies to reduce the variation in SERS counts must be found. Finally, in order to create highly open and diffractive metasurfaces, we propose using depletants of different charge densities, or even neutral depletants, as well as longer NR ligands to shift the balance of electrostatic repulsion and attractive depletion, thus increasing lattice parameters to the visible wavelength range, to hopefully achieve functional properties like SLRs or structural colors.

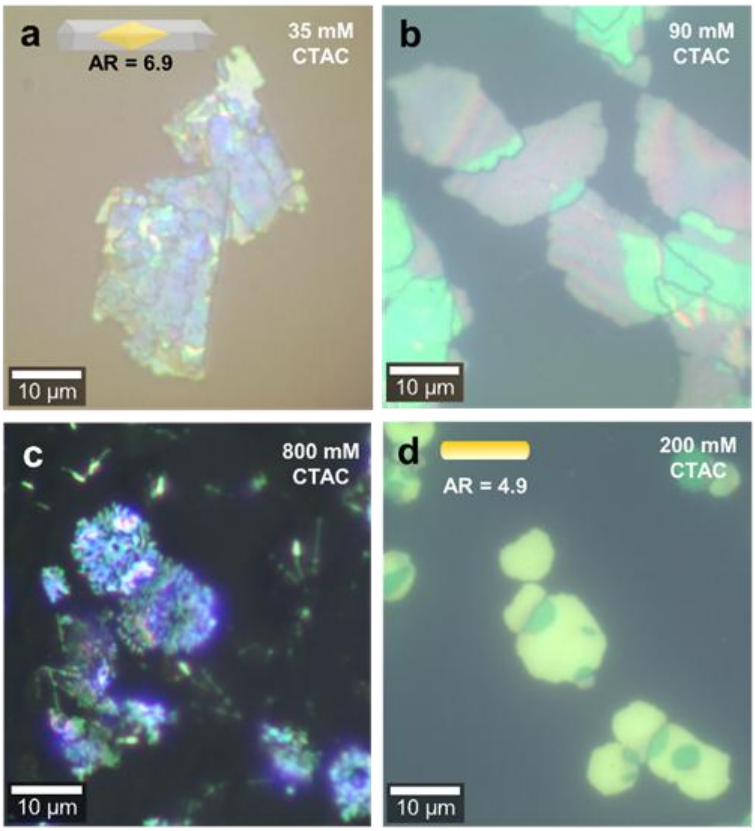

Figure 12: Typical appearance of 2D colloidal metasurfaces via DISA of long metal NRs. *In situ optical microscopy (reflection mode) images of colloidal metasurfaces of* ***(a-c)*** *Au@Ag C5-S NRs (l = 188.9 ± 12.5 nm; w = 27.2 ± 1.8 nm) assembled in varying CTAC concentrations, and of* ***(d)*** *small monocrystalline Au NRs (l = 74.3 ± 4.1 nm; w = 14.9 ± 1.3 nm) assembled in 200 mM CTAC.*

4.4. References

(1) Nag, R.; Rouvière, N.; Trazo, J. G.; Marcone, J.; Kutalia, N.; Goldmann, C.; Impéror-Clerc, M.; Alloyeau, D.; Constantin, D.; Hamon, C. Depletion-Induced Tunable Assembly of Complementary Platonic Solids. *Nano Lett.* **2024**, *24* (51), 16368–16373. https://doi.org/10.1021/acs.nanolett.4c04923.

(2) Marcone, J.; Chaâbani, W.; Goldmann, C.; Impéror-Clerc, M.; Constantin, D.; Hamon, C. Polymorphous Packing of Pentagonal Nanoprisms. *Nano Lett.* **2023**, *23* (4), 1337–1342. https://doi.org/10.1021/acs.nanolett.2c04541.

(3) Meinzer, N.; Barnes, W. L.; Hooper, I. R. Plasmonic Meta-Atoms and Metasurfaces. *Nature Photon* **2014**, *8* (12), 889–898. https://doi.org/10.1038/nphoton.2014.247.

(4) Qi, X.; Pérez, L. A.; Alonso, M. I.; Mihi, A. High *Q* -Factor Plasmonic Surface Lattice Resonances in Colloidal Nanoparticle Arrays. *ACS Appl. Mater. Interfaces* **2024**, *16* (1), 1259–1267. https://doi.org/10.1021/acsami.3c08617.

(5) Kuznetsov, A. I.; Brongersma, M. L.; Yao, J.; Chen, M. K.; Levy, U.; Tsai, D. P.; Zheludev, N. I.; Faraon, A.; Arbabi, A.; Yu, N.; Chanda, D.; Crozier, K. B.; Kildishev, A. V.; Wang, H.; Yang, J. K. W.; Valentine, J. G.; Genevet, P.; Fan, J. A.; Miller, O. D.; Majumdar, A.; Fröch, J. E.; Brady, D.; Heide, F.; Veeraraghavan, A.; Engheta, N.; Alù, A.; Polman, A.; Atwater, H. A.; Thureja, P.; Paniagua-Dominguez, R.; Ha, S. T.; Barreda, A. I.; Schuller, J. A.; Staude, I.; Grinblat, G.; Kivshar, Y.; Peana, S.;

Yelin, S. F.; Senichev, A.; Shalaev, V. M.; Saha, S.; Boltasseva, A.; Rho, J.; Oh, D. K.; Kim, J.; Park, J.; Devlin, R.; Pala, R. A. Roadmap for Optical Metasurfaces. *ACS Photonics* **2024**, *11* (3), 816–865. https://doi.org/10.1021/acsphotonics.3c00457.

(6) Su, V.-C.; Chu, C. H.; Sun, G.; Tsai, D. P. Advances in Optical Metasurfaces: Fabrication and Applications [Invited]. *Opt. Express* **2018**, *26* (10), 13148. https://doi.org/10.1364/OE.26.013148.

(7) Li, W.; Liu, J.; Tang, K.; Mao, X.; Jin, S.; Deng, R.; Zhu, J. Functional Materials of 2D Self-Assembled Nanoparticle Monolayers: Preparation and Application. *Chem. Mater.* **2024**, *36* (19), 9279–9298. https://doi.org/10.1021/acs.chemmater.4c01157.

(8) Li, S.; Guo, X.; Sun, M.; Qu, A.; Hao, C.; Wu, X.; Guo, J.; Xu, C.; Kuang, H.; Xu, L. Self-Limiting Self-Assembly of Supraparticles for Potential Biological Applications. *Nanoscale* **2021**, *13* (4), 2302–2311. https://doi.org/10.1039/D0NR08001B.

(9) Grzelczak, M.; Liz-Marzán, L. M.; Klajn, R. Stimuli-Responsive Self-Assembly of Nanoparticles. *Chem. Soc. Rev.* **2019**, *48* (5), 1342–1361. https://doi.org/10.1039/C8CS00787J.

(10) Lekkerkerker, H. N. W.; Tuinier, R. *Colloids and the Depletion Interaction*; Lecture Notes in Physics; Springer Science+Business Media B.V: Dordrecht, 2011.

(11) Yang, S.; Yan, Y.; Huang, J.; Petukhov, A. V.; Kroon-Batenburg, L. M. J.; Drechsler, M.; Zhou, C.; Tu, M.; Granick, S.; Jiang, L. Giant Capsids from Lattice Self-Assembly of Cyclodextrin Complexes. *Nat Commun* **2017**, *8* (1), 15856. https://doi.org/10.1038/ncomms15856.

(12) Yang, P.-W.; Thoka, S.; Lin, P.-C.; Su, C.-J.; Sheu, H.-S.; Huang, M. H.; Jeng, U.-S. Tracing the Surfactant-Mediated Nucleation, Growth, and Superpacking of Gold Supercrystals Using Time and Spatially Resolved X-Ray Scattering. *Langmuir* **2017**, *33* (13), 3253–3261. https://doi.org/10.1021/acs.langmuir.6b04319.

(13) Weißenfels, M.; Gemen, J.; Klajn, R. Dissipative Self-Assembly: Fueling with Chemicals versus Light. *Chem* **2021**, *7* (1), 23–37. https://doi.org/10.1016/j.chempr.2020.11.025.

(14) Chaâbani, W.; Lyu, J.; Marcone, J.; Goldmann, C.; Ten Veen, E. J. M.; Dumesnil, C.; Bizien, T.; Smallenburg, F.; Impéror-Clerc, M.; Constantin, D.; Hamon, C. Prismatic Confinement Induces Tunable Orientation in Plasmonic Supercrystals. *ACS Nano* **2024**, *18* (13), 9566–9575. https://doi.org/10.1021/acsnano.3c12799.

(15) Qi, X.; Pérez, L. A.; Mendoza-Carreño, J.; Garriga, M.; Alonso, M. I.; Mihi, A. Chiral Plasmonic Superlattices from Template-Assisted Assembly of Achiral Nanoparticles. *Nat Commun* **2025**, *16* (1), 1687. https://doi.org/10.1038/s41467-025-56999-0.

(16) Acunzo, A.; De Luca, M.; Marra, D.; Della Ventura, B.; Offenhäusser, A.; Mayer, D.; Velotta, R. Ultra-Uniform High-Quality Plasmonic Metasurfaces through Electrostatic Self-Assembly of Gold Nanoparticles on Chemically Unmodified Glass. *Nanoscale* **2025**, *17* (23), 14125–14133. https://doi.org/10.1039/D5NR01116G.

(17) Bian, T.; Gardin, A.; Gemen, J.; Houben, L.; Perego, C.; Lee, B.; Elad, N.; Chu, Z.; Pavan, G. M.; Klajn, R. Electrostatic Co-Assembly of Nanoparticles with Oppositely Charged Small Molecules into Static and Dynamic Superstructures. *Nat. Chem.* **2021**, *13* (10), 940–949. https://doi.org/10.1038/s41557-021-00752-9.

(18) Liu, W.; Gupta, P.; Zhang, Y.; Thapa, K.; Singamaneni, S.; Wang, R. DNA Origami-Assisted Regioselective Organization of Anisotropic Gold Nanotriangle Clusters. *ACS Appl. Opt. Mater.* **2025**, *3* (3), 514–519. https://doi.org/10.1021/acsaom.4c00086.

(19) Fava, D.; Winnik, M. A.; Kumacheva, E. Photothermally-Triggered Self-Assembly of Gold Nanorods. *Chem. Commun.* **2009**, No. 18, 2571. https://doi.org/10.1039/b901412h.

(20) Choueiri, R. M.; Galati, E.; Klinkova, A.; Thérien-Aubin, H.; Kumacheva, E. Linear Assembly of Patchy and Non-Patchy Nanoparticles. *Faraday Discuss.* **2016**, *191*, 189–204. https://doi.org/10.1039/C6FD00057F.

(21) Zheng, C. Y.; Palacios, E.; Zhou, W.; Hadibrata, W.; Sun, L.; Huang, Z.; Schatz, G. C.; Aydin, K.; Mirkin, C. A. Tunable Fluorescence from Dye-Modified DNA-Assembled Plasmonic Nanocube Arrays. *Advanced Materials* **2019**, *31* (41), 1904448. https://doi.org/10.1002/adma.201904448.

(22) Zhou, W.; Li, Y.; Je, K.; Vo, T.; Lin, H.; Partridge, B. E.; Huang, Z.; Glotzer, S. C.; Mirkin, C. A. Space-Tiled Colloidal Crystals from DNA-Forced Shape-Complementary Polyhedra Pairing. *Science* **2024**, *383* (6680), 312–319. https://doi.org/10.1126/science.adj1021.
(23) Sikeler, C.; Haslinger, F.; Martynenko, I. V.; Liedl, T. DNA Origami-Directed Self-Assembly of Gold Nanospheres for Plasmonic Metasurfaces. *Adv Funct Materials* **2024**, *34* (42), 2404766. https://doi.org/10.1002/adfm.202404766.
(24) Ryssy, J.; Natarajan, A. K.; Wang, J.; Lehtonen, A. J.; Nguyen, M.; Klajn, R.; Kuzyk, A. Light-Responsive Dynamic DNA-Origami-Based Plasmonic Assemblies. *Angew Chem Int Ed* **2021**, *60* (11), 5859–5863. https://doi.org/10.1002/anie.202014963.
(25) Young, K. L.; Jones, M. R.; Zhang, J.; Macfarlane, R. J.; Esquivel-Sirvent, R.; Nap, R. J.; Wu, J.; Schatz, G. C.; Lee, B.; Mirkin, C. A. Assembly of Reconfigurable One-Dimensional Colloidal Superlattices Due to a Synergy of Fundamental Nanoscale Forces. *Proc. Natl. Acad. Sci. U.S.A.* **2012**, *109* (7), 2240–2245. https://doi.org/10.1073/pnas.1119301109.
(26) Goldmann, C.; Chaâbani, W.; Hotton, C.; Impéror-Clerc, M.; Moncomble, A.; Constantin, D.; Alloyeau, D.; Hamon, C. Confinement Effects on the Structure of Entropy-Induced Supercrystals. *Small* **2023**, 2303380. https://doi.org/10.1002/smll.202303380.
(27) Sharma, P.; Ward, A.; Gibaud, T.; Hagan, M. F.; Dogic, Z. Hierarchical Organization of Chiral Rafts in Colloidal Membranes. *Nature* **2014**, *513* (7516), 77–80. https://doi.org/10.1038/nature13694.
(28) Sung, B.; Wensink, H. H.; Grelet, E. Depletion-Driven Morphological Transitions in Hexagonal Crystallites of Virus Rods. *Soft Matter* **2019**, *15* (46), 9520–9527. https://doi.org/10.1039/C9SM01207A.
(29) Zang, S.; Paul, S.; Leung, C. W.; Chen, M. S.; Hueckel, T.; Hocky, G. M.; Sacanna, S. Direct Observation and Control of Non-Classical Crystallization Pathways in Binary Colloidal Systems. *Nat Commun* **2025**, *16* (1), 3645. https://doi.org/10.1038/s41467-025-58959-0.
(30) Gibaud, T.; Constantin, D. Direct Liquid to Crystal Transition in a Quasi-Two-Dimensional Colloidal Membrane. *J. Phys. Chem. Lett.* **2018**, *9* (15), 4302–4307. https://doi.org/10.1021/acs.jpclett.8b01524.
(31) Le Roy, H.; Terzi, M. M.; Lenz, M. Collective Deformation Modes Promote Fibrous Self-Assembly in Deformable Particles. *Phys. Rev. X* **2025**, *15* (1), 011022. https://doi.org/10.1103/PhysRevX.15.011022.
(32) Lenz, M.; Witten, T. A. Geometrical Frustration Yields Fibre Formation in Self-Assembly. *Nature Phys* **2017**, *13* (11), 1100–1104. https://doi.org/10.1038/nphys4184.
(33) Mercedi, A.; Cardoni, F.; Toffanello, F.; Reguera, J.; Meneghetti, M.; Litti, L. Reliable Methodology for Measuring SERS Enhancement Factor on Colloidal and Solid Substrates: A Practical Guide. *J Raman Spectroscopy* **2025**, *56* (9), 835–849. https://doi.org/10.1002/jrs.6776.
(34) Kao, Y.-C.; Han, X.; Lee, Y. H.; Lee, H. K.; Phan-Quang, G. C.; Lay, C. L.; Sim, H. Y. F.; Phua, V. J. X.; Ng, L. S.; Ku, C. W.; Tan, T. C.; Phang, I. Y.; Tan, N. S.; Ling, X. Y. Multiplex Surface-Enhanced Raman Scattering Identification and Quantification of Urine Metabolites in Patient Samples within 30 Min. *ACS Nano* **2020**, *14* (2), 2542–2552. https://doi.org/10.1021/acsnano.0c00515.
(35) Lee, A.; Ahmed, A.; Dos Santos, D. P.; Coombs, N.; Park, J. I.; Gordon, R.; Brolo, A. G.; Kumacheva, E. Side-by-Side Assembly of Gold Nanorods Reduces Ensemble-Averaged SERS Intensity. *J. Phys. Chem. C* **2012**, *116* (9), 5538–5545. https://doi.org/10.1021/jp3010597.
(36) Kutalia, N.; Trazo, J. G.; Marchand, S.; Goldmann, C.; Ratel-Ramond, N.; Dozov, I.; Bizien, T.; Constantin, D.; Impéror-Clerc, M.; Davidson, P.; Hamon, C. Plasmonic Nanorods Form Reconfigurable Liquid Crystalline Assemblies. May 21, 2026. https://doi.org/10.26434/chemrxiv.15003689/v1.
(37) Vroege, G. J.; Lekkerkerker, H. N. W. Phase Transitions in Lyotropic Colloidal and Polymer Liquid Crystals. *Rep. Prog. Phys.* **1992**, *55* (8), 1241–1309. https://doi.org/10.1088/0034-4885/55/8/003.
(38) Hunter, R. J. *Foundations of Colloid Science*, 2. ed., reprinted.; Oxford Univ. Press: Oxford, 2009.
(39) Cheng, Z.; Jones, M. R. Assembly of Planar Chiral Superlattices from Achiral Building Blocks. *Nat Commun* **2022**, *13* (1), 4207. https://doi.org/10.1038/s41467-022-31868-2.

Chapter 5

CHIRALITY AND TUNING THE FRUSTRATED SELF-ASSEMBLY OF NANORODS

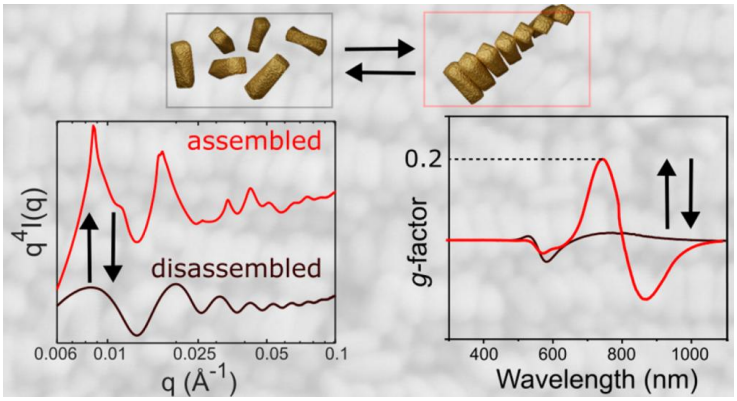

J. G. Trazo, A. Serrano-Frejeiro, M. Mychinko, N. Kutalia, M. Impéror-Clerc, *S. Bals, L.M. Liz-Marzán, J. Pérez-Juste, I. Pastoriza-Santos, C. Hamon*. **Tunable Plasmonic Circular Dichroism of Hierarchical Chiral Assemblies.** *Chem. Mater.* 2025, 37(16).

https://doi.org/10.1021/acs.chemmater.5c00909

Article Text in Annex

This chapter will focus on using DISA to create tunable chiral gold nanostructures tp achieve plasmonic circular dichroism (PCD). This project is a collaboration with colleagues from three different institutions: CINBIO (Universidade de Vigo, Spain), EMAT (Universiteit Antwerpen, Belgium), and CIC biomaGUNE (San Sebastián, Spain). The Spanish teams developed the chiral gold nanorod (cGNR) synthesis and performed circular dichroism (CD) spectroscopy, while the Belgian team specialized in electron microscopy, including 3D tomography and cryo-TEM for *in situ* observation of the chiral assemblies. In LPS, our own task was the development of the DISA assembly-disassembly protocol, structural analysis, kinetics of assembly growth, and in situ optical plus scanning electron microscopy (SEM).

5.1. Introduction

In **Chapter 4**, we have explored how the control of depletion strength, nanorod (NR) aspect ratio, as well as cross-section symmetry, influences the 2D vs. 3D dimensionality of colloidal superstructures formed by self-assembly of these NRs via in situ depletion (DISA). This interplay between individual NR shape and collective dimensionality is one characteristic feature of the DISA method where interparticle attraction is greater between the larger facets of the particles. One may call this feature an *anisotropy transfer* from the long NRs to the micron scale of 1D needle-shaped or 2D disk-shaped assemblies[1–3].

Other geometric parameters of the NR building blocks can also be played with in order to achieve emergent plasmonic superstructures with more variety in their form, including twisting or screwlike symmetries, just by tuning the shapes of the NRs. In particular, producing chiral assemblies (i.e., left- or right-handed structures with non-superimposable mirror images) is of great interest for plasmonic systems, in terms of both structural properties (e.g. viral capsids and cell flagella[4]) and optical properties (e.g. in biological and plasmonic catalysis)[5]. *Chirality transfer* across different length scales is a ubiquitous phenomenon in nature and is key to understanding many biological and physical phenomena[6,7]. At present, however, the connection between the chirality of molecular or nanoscale building blocks and the emergent chiroptical or chiral-structural properties of ensembles is not yet well understood in many systems[7]. Still, much recent research has focused on the role and the propagation of *frustration* in chirality transfer, leading to self-assembly into a wide variety of hierarchical superstructures, including ones where chirality influences their structural and optical properties (**Figure 1**)[4,8].

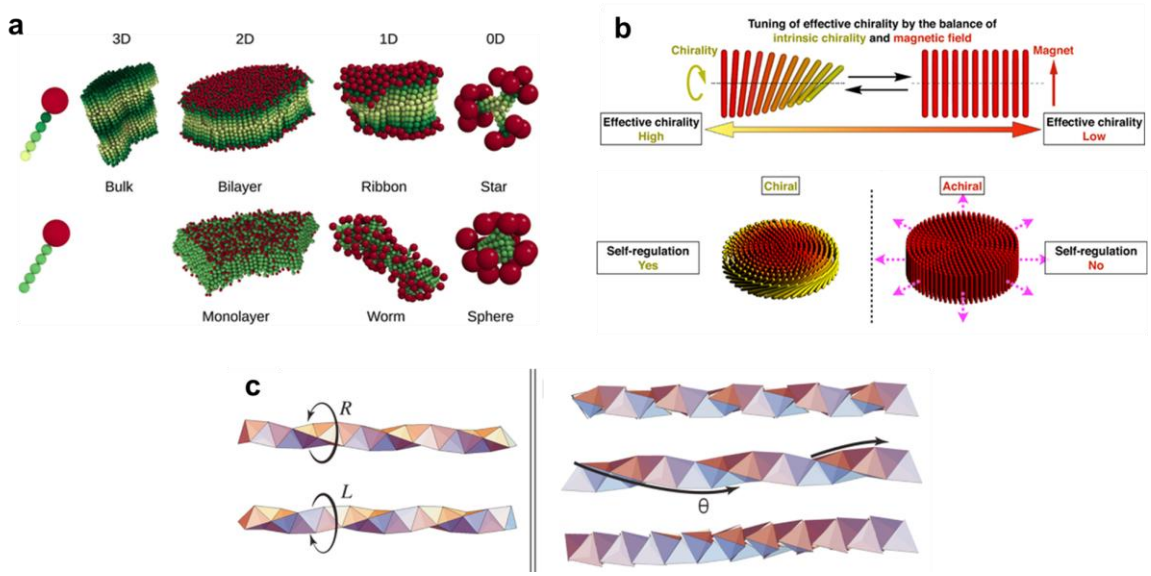

Figure 1. *Frustration propagation in various self-assembled systems:* ***(a)*** *different superstructure dimensionalities based on head versus tail size in lipid-like NPs[9],* ***(b)*** *active tuning of chirality in 2D assemblies of M13 bacteriophage rods via magnetic field [10],* ***(c)*** *frustration-driven chiral structures in the modelled self-assembly of nano-tetrahedra[4].*

Study of Chirality: Background, Research Directions, Applications

The first documented discovery of molecular chirality was made by Louis Pasteur, via his observation of the crystallization of a racemic mix of L and D enantiomers of tartaric acid in a dish, yielding left and right-handed crystal geometries. Pasteur hypothesized that this handedness of crystal geometries arose from a similar handedness of the tartaric acid molecule at the smaller scale[11]. In the following decades, with the development of stereochemistry, the chirality of more and more biological and pharmaceutical compounds was studied. For example, carvone and limonene stereoisomers have distinct smells. It was also discovered that all known life on earth exhibited homochirality with its fundamental building blocks (nucleic acids, peptides, sugars). In the 1950s and 60s, the notorious thalidomide drug scandal revealed the extreme importance of understanding activity and increasing purity of S versus R isomers for medicinal applications. More recently, bio-physical studies have also tested possible theories of the origin of homochirality in life (**Figure 2**)[11,12].

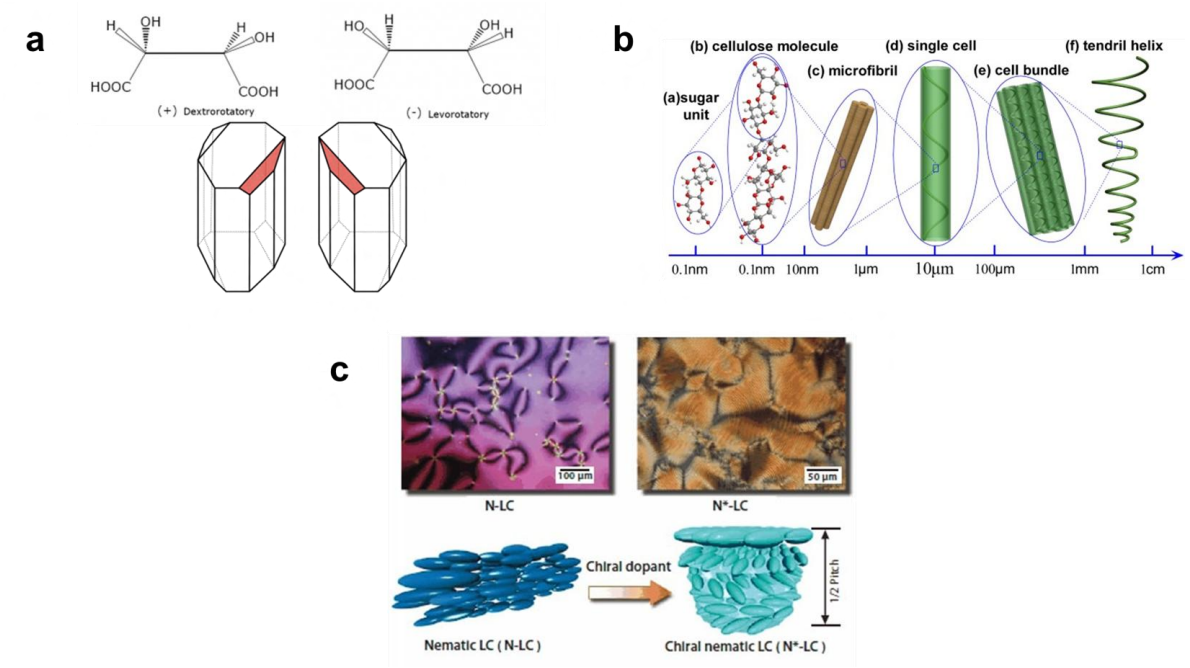

Figure 2. Historical background and study of chirality in different fields: (a) *crystals of D vs. L-tartaric acid[11]. **(b)** biological chirality transfer from sugar handedness as the origin of helicity in plant tendrils[13]. **(c)** seeding of chirality in molecular liquid crystals by adding small amounts of chiral dopants[14].*

In quantum physics, recent studies explored the connection between chirality and the origin of matter and the variety and symmetry in fundamental particles and forces[15]. Other papers have discussed the origin and transfer of hierarchical order at different length scales, for instance in the chirality of plant tendrils or of animal shells, or curvature in liposomes[13]. Several mechanisms for the emergence of hierarchical chirality have been proposed, using model systems like cholesteric liquid crystals – where chiral inducer molecules are added to 'dope' an achiral system[14], the self-assembly of cellulose nanocrystals (CNC)[6], and the assembly of colloids like *fd* virus rods, where the handedness of the assembly may or may not correspond to the handedness of the individual NPs, depending on the screw angle between consecutive particles in the assembly[8,16] (**Figure 2**). To date, there has been limited information on hierarchical chirality transfer in colloidal plasmonic NP systems.

Enhancing Plasmonic Circular Dichroism: State-of-the-art and challenges

Chirally-structured materials can achieve additional geometrical degrees of freedom, which endow them with unique mechanical and optoelectronic properties. For example, such structures, often with 1D symmetries, could act as tough yet flexible, re-contractable systems.

Other bio-inspired chiral functional materials could also be designed for optics, enantioselective catalysis, biomedical use, and information encoding, particularly with plasmonic NP systems, which exhibit differential absorption of left versus right circularly polarized (LCP/RCP) light, a behavior called plasmonic circular dichroism (PCD)[5,17]. The circular dichroism (CD) of individual molecules is on average much weaker than that of chiral plasmonic particles – with a dissymmetry g-factor of around 10^{-5} and is in the UV range, rather than the visible or near-IR wavelengths. Meanwhile, chiral Au NPs have g-factors up to about 0.5 in the red to near-IR range. Such chiral NPs are especially prized for their easily tunable surface plasmon resonances (SPR) which exhibit CD, and for their general biocompatibility[18–20]. In the field of plasmonic nanoscience, two strategies exist for tunable PCD[5] (**Figure 3**). The first is the use of individual, *intrinsically* chiral NPs, which requires a good synthesis protocol using a chiral inducer molecule like cysteine or a peptide[18]. The second case is the assembly of individually achiral NPs into chiral superstructures, achieving an *extrinsic* geometric chirality, often done with chiral ligands or linkers like DNA origami, with templating media or host matrices like cholesteric liquid crystals, including cellulose nanocrystals[21,22].

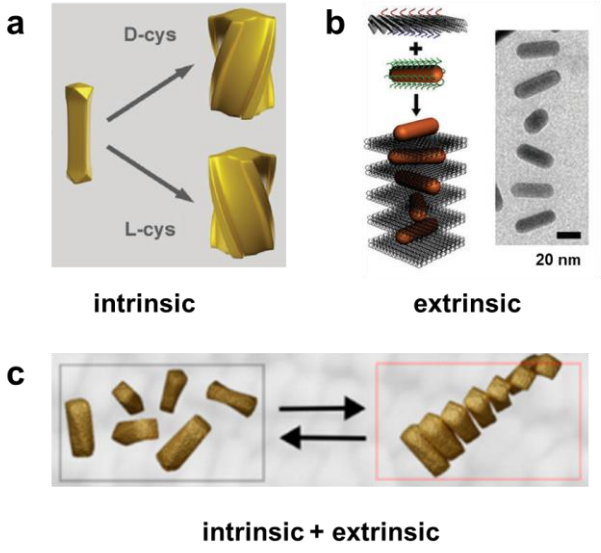

Figure 3. Strategies for achieving plasmonic circular dichroism (PCD): (a) *intrinsic chirality with individual fourfold twisted gold nanorods (cGNRs)[17,18]. **(b)** extrinsic chirality by assembling gold nanorods with DNA origami helices[21]. **(c)** combined intrinsic-extrinsic PCD via depletion-induced self-assembly (DISA) with cGNRs of tuned aspect ratio, twist, and inter-NR gap for tunable propagation of frustration.*

A vast majority of published findings use either only intrinsic or only extrinsic chirality to create tunable PCD response. Interestingly, recent studies on assembly, including by 'tip-to-tip' chiral

NP welding, yielded either only low-to-medium CD enhancement, or loss of the CD signal entirely, or to a mere spectral shift in the CD resonance[23]. Other methods such as dried template-assisted chiral assemblies or metasurfaces (e.g. templated spiral and gammadion arrays, chiral nanorod 1D chains, or Au NR trimers on deformable PDMS substrates[24–26]) or electrostatic assembly using achiral citrate salts have yielded high g-factor assemblies, but with limited reconfigurability[27] (**Figure 4**). By contrast, in this project, we combine these two strategies by self-assembling intrinsically chiral nanorods into extrinsically chiral twisting superstructures by reversible depletion, relying on the controlled and tunable propagation of frustration to achieve tunable PCD. Specifically, we formed in situ and reversible colloidal assemblies of fourfold twisted chiral gold nanorods (cGNRs) using CTAC-mediated DISA. In this case, there are three major advantages of using DISA. First, achieving chiral assembly does not require specific ligand or NP surface chemistry, or adding a secondary template material (e.g. liquid crystals, DNA origami) and is thus valence-free and applicable to the assembly of other kinds of NPs. Second, the attractive forces causing assembly are reversible and modulable depending on depletant concentration[1,2], as noted in the previous chapter, presumably allowing the on/off switching and tuning of PCD directly in suspension. Third, this approach is substrate-free, bottom-up, and exists as a 'fluid metamaterial', eliminating problems of surface effects and orientation bias when using the system.

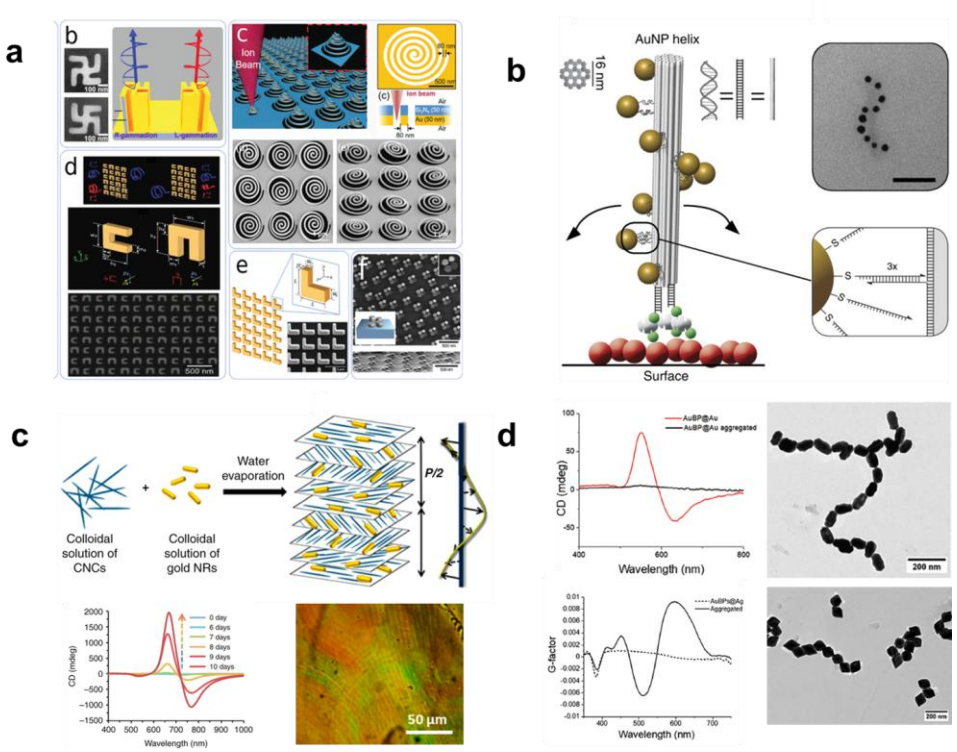

Figure 4. State-of-the-art in fine-tunable chiral assemblies and metamaterials: (a) *various designs for chiral metasurfaces using both Au and different semiconductor compounds[25]. **(b)** AuNP helices with switchable CD using DNA bundles anchored to a substrate[28]. **(c)** templated chiral assembly of AuNRs using cellulose liquid crystals[29]. **(d)** CD enhancement or loss via tip-to-tip welding of anisotropic chiral Au or Au@Ag NPs[23].*

To test whether one can indeed attain tunable PCD enhancement via frustration or chirality transfer from chiral Au NRs (cGNRs) to chiral assemblies using depletion, two key questions or themes must be explored. Note that for this study, we selected cGNRs with an aspect ratio of about 1.7, with a twisting C4 or square section, and varying degrees of twist, controlled by selective oxidation with a Au(III) oxidant.

First, do cGNRs form extrinsically chiral (e.g., twisting) colloidal superstructures when self-assembled by depletion? What lattice symmetries result from assembling cGNRs versus similar achiral NRs? Could the assembly geometry in fact cancel rather than enhance the chirality of the system? Is the cGNR self-assembly reversible? How does controlled increase or decrease of the depletion force affect degrees of twist and frustration in these colloidal assemblies?

Second, does the depletion-induced self-assembly (DISA) of cGNRs cause an enhancement of the plasmonic circular dichroism (PCD) signal? If yes, what is the physical origin of this enhancement? How does changing depletion force tune the chiroptical response or plasmonic

circular dichroism (PCD) of the assemblies? Can the PCD be repeatedly switched on and off by cyclic assembly-disassembly by depletion? Can the PDC amplitude be controlled over time? What is the wavelength range of the PCD for the colloidal cGNR assemblies?

5.2. Perspectives

Supplementary study on cGNR self-assembly

PCD enhancement mechanism and role of [CTAC]

Further investigation of this cGNR-DISA system must focus on verifying the origin and mechanism of PCD enhancement, and the exact quantification of extrinsic chirality of the cGNR assemblies as a function of depletant concentration, as there is still debate as to the relative contributions of simple plasmonic coupling (i.e. inter-NR face-to-face gaps or d_{gap}) versus domain size versus the dimensionality of the cGNR clusters to the PCD. In any case, the evolution of maximum CD vs. [CTAC] is non-monotonic, which suggests d_{gap} is not the only major factor in the enhancement (**Article Figure S11**). One may argue that very high depletion strength, while increasing plasmonic coupling due to stronger depletion forces between NRs, also yields smaller side-by-side chiral clusters due to faster nucleation and growth. However, in *fast mixing* of cGNRs and CTAC, the main method used for our CD kinetics, the cluster (monodomain size) is almost equal for 90 mM and 500 mM CTAC (**Article Figure S9-S10**). This is not the case, however, for *slow mixing*, where the cluster size is about 1.6 times larger at 60 mM versus at 500 mM CTAC. We conclude it possible, therefore, that the speed of CTAC addition, while likely not changing the general cluster symmetry, could change the cluster size and 1D vs. 3D (aggregated) dimensionality, which strongly contributes to the CD enhancement. More experiments taking the CD spectra of cGNR assemblies by very slow depletant diffusion are also recommended. We also propose to conduct further cryo-TEM imaging on the colloidal cGNR assemblies at a wider range of [CTAC] to properly study their helicity (**Article Figure S13**).

Molecular dynamic simulations of the colloidal cGNR clusters of varying size and dimensionality could also shed more light on the PCD enhancement mechanism, supplementing our TEM and SAXS data. These simulations can be done for all three cGNR

helicities, as decreasing helicity was seen to lead to lower maximum CD signal (**Figure 5**), suggesting that the frustration-driven attainment of extrinsic chirality is quite sensitive to minor changes in the NR surface twist. In the future, the chemical synthesis of these cGNRs also ought to be refined to increase their monodispersity in size and twist degree, either directly in the synthesis protocol or in a post-synthesis purification step.

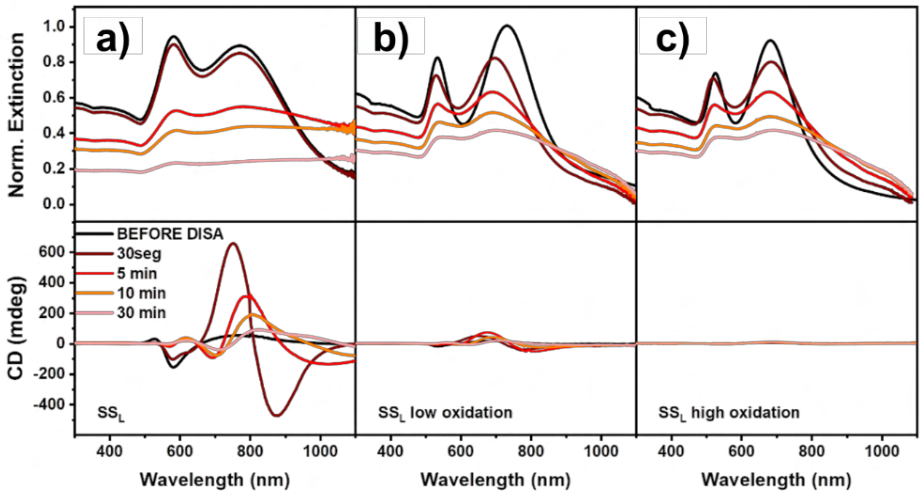

Figure 5. *Self-assembly kinetics of* ***(a)*** *cGNR_1,* ***(b)*** *cGNR_2(D), and* ***(c)*** *cGNR_3 in 70 mM CTAC monitored by UV-vis-NIR extinction (top) and CD (bottom) spectroscopies.*

Additionally, the dynamics and cyclability of the cGNR self-assembly/disassembly should be studied further, particularly the amount of hysteresis after multiple dilution cycles. More interestingly, we also observed that the cGNR clusters at low [CTAC] near the depletion threshold (around 60 to 90 mM CTAC) could be disassembled by *gentle agitation* of the solutions, signaled by the recovery of the plasmonic color of dispersed cGNRs, followed by fast recovery of the assemblies after about 3 min, again signaled by a color change (**Figure 6**). This result could be a first step towards a mechanically-responsive chiral sensor in suspension.

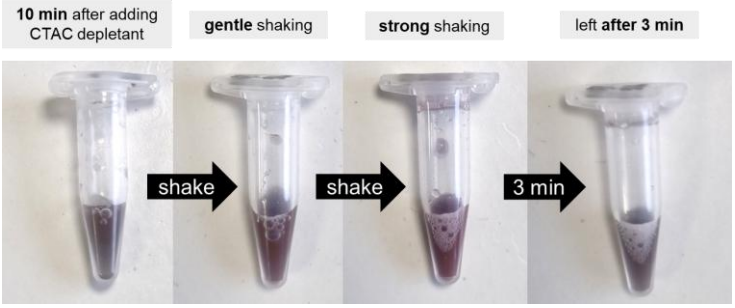

Figure 6. Temporally-dynamic recovery of loose cGNR DISA assemblies by mechanical agitation.

Various curved superstructures via ultra-slow DISA

In the article, we noted that while fast DISA results in PCD enhancement, the overall shape of the superstructures is small and faceting of the superstructures is minimal and irregular. Slow crystallization of the cGNRs by EISA over about two to three days (i.e., by slow diffusion of CTAC depletant), by contrast, yielded rounded superstructures with varying curvature, with greater long-range order and presumably higher CD enhancement. In our supplementary experiments, we discovered that larger and more unique superstructures can be obtained with DISA by greatly slowing down the speed of depletant diffusion into the cGNR suspension using the immersion or pseudo-dialysis method noted in Chapters 3 and 4. This prolonged the self-assembly over a period of almost two weeks, yielding a plethora of curved and twisting structures along different sections of the capillary, moving from the capillary mouth towards the center (**Figure 7**). There was an apparent increase of dimensionality and curvature of the assemblies towards the open end of the capillary (e.g., 1D/2D assemblies far from the open end, to 3D curved surfaces near the open end), where contact with the depletant was earliest and DISA proceeded fastest. Based on our preliminary findings and on other diffusion-controlled assembly studies[30], we currently infer that a combination of NR concentration and assembly kinetics, which proceeds at different speeds at different points along the capillary, is an additional knob for tuning hierarchical chirality transfer if DISA is allowed to proceed very slowly.

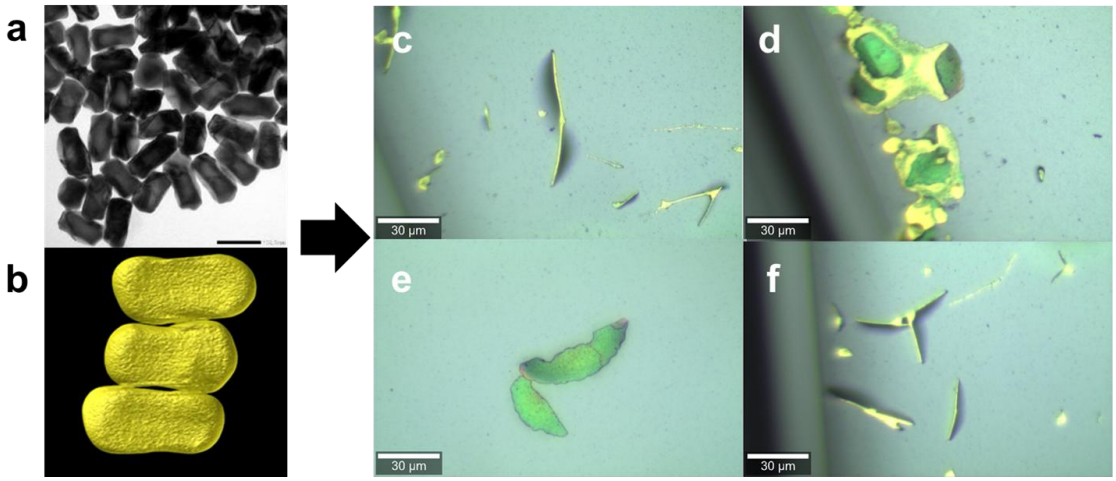

Figure 7. Zoo of highly-extended curved and twisting structures made by cGNR_1 (a-b) self-assembly by ultra-slow DISA with capillary immersion in a 25 wt.% aqueous CTAC bath: (c) *curved standing 1D/2D assemblies,* ***(d)*** *highly curved surfaces in 3D,* ***(e)*** *half-moon assemblies, and* ***(f)*** *multi-arm structures, occurring predominantly in specific regions along the length of the capillary.*

Assembly behavior of long chiral nanoscrews

In the course of this cGNRs project, an additional perspective of assembling much longer chiral AuNRs was explored in collaboration with Kevin (Tsz-Him) Chow and Luis Liz-Marzán from CIC biomaGUNE. It was hypothesized that higher aspect ratio gold nanoarrows and nanoscrews[26,31] could form more elongated 1D-like objects via DISA (versus 2D/3D assemblies), as noted in the last chapter, and such objects could have symmetries that are more desirable for chiral plasmonic superstructures. The pitch of the nanoscrew (NS) grooves could be tuned by using different chiral growth inducers at different concentrations, like L vs. D-cysteine typically yielding wider grooves (named NS1, **Figure 8b,d,f,g, Figure 9a-d**), or helical micelles made with CTAC doped with (R) or (S)-binamine, a chiral naphtol compound, typically yielding finer grooves (named NS2, **Figure 9e-f**)[32]. These nanoscrews were then assembled by fast one-shot mixing with different concentrations of CTAC depletant, which yielded either straight side-by-side needle-like assemblies for high aspect ratio (AR = 12 to 14) NSs, and *curved or distorted needle-like assemblies* for lower aspect ratio NSs (AR = 7), while long achiral rods always formed straight needles as expected (**Figure 8a-f**). At the time of writing, however, no PCD enhancement has been reported for these nanoscrew assemblies upon fast depletion-induced self-assembly (DISA) at several CTAC concentrations. Our preliminary conclusion is that an optimal groove pitch-to-nanorod length ratio is required for chirality transfer to the colloidal assembly geometry, and thus attain PCD enhancement. It is possible that a very small pitch (i.e. fine grooves) induces a strong turning of the NSs that is sterically incompatible with the NR length. It is also possible that the steric effect (or shape self-matching of assembling NSs) with such a small pitch cannot be transmitted via depletion force except at very high depletant concentration, when the assembling NSs have the minimum possible gap. Twisting nanoscrew clusters have been observed in the literature via other methods, but often with much lower AR of 3 to 4[33].

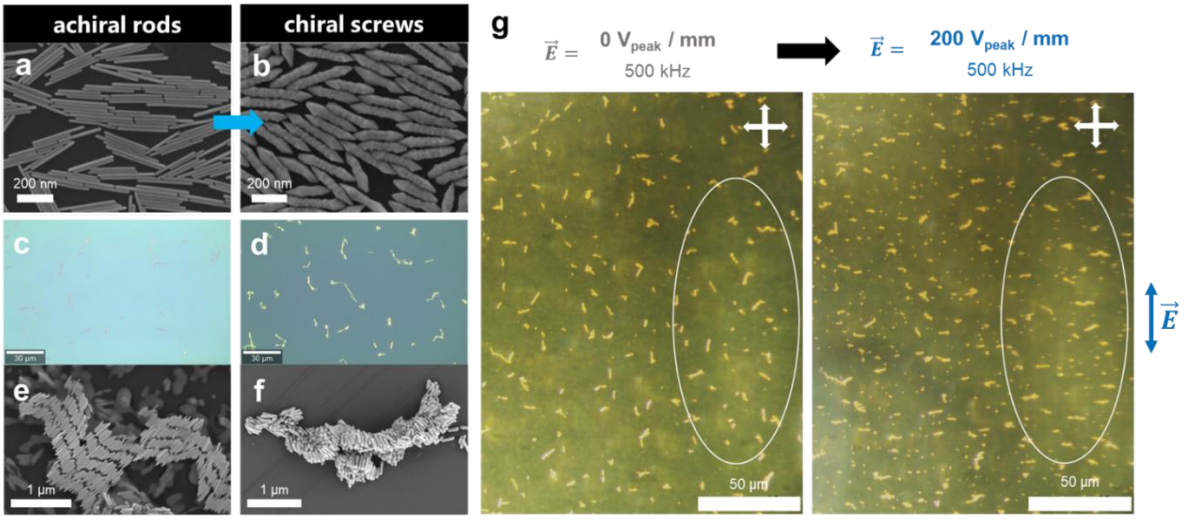

Figure 8. Formation of curved needle or thread-like assemblies of Au nanoscrews via DISA. *Comparison of self-assembling achiral pentatwinned rods versus chiral nanoscrews (NS1) with similar lengths:* ***(a, b)*** *SEM images of the individual NPs,* ***(c, d)*** *colloidal depletion-induced assemblies of the NPs observed by in situ optical microscopy (reflection mode),* ***(e, f)*** *SEM images of the same colloidal assemblies after fast drying.* ***(g)*** *Alignment of colloidal nanoscrew assemblies by AC electric field, observed by in situ optical microscopy under crossed polarizers.*

The fact that longer NSs self-assemble into straight needles may also be due to larger inter-NR gaps between the rods – as their CTAC assembly threshold at lower depletion force due to their bigger size, preventing them from sensing each other's grooved surfaces. To remedy this, we tried to add a small amount of NaCl into the assembly mixture to screen the interparticle electrostatic repulsion and shorten the interparticle gap. This resulted in more twisted and dendritic assemblies, however with somewhat less crystallinity – where amorphous and crystalline regions coincide. At higher CTAC and NaCl concentrations, however, there are be very few truly helical structures, and disordered aggregates dominate in suspension (**Figure 9**).

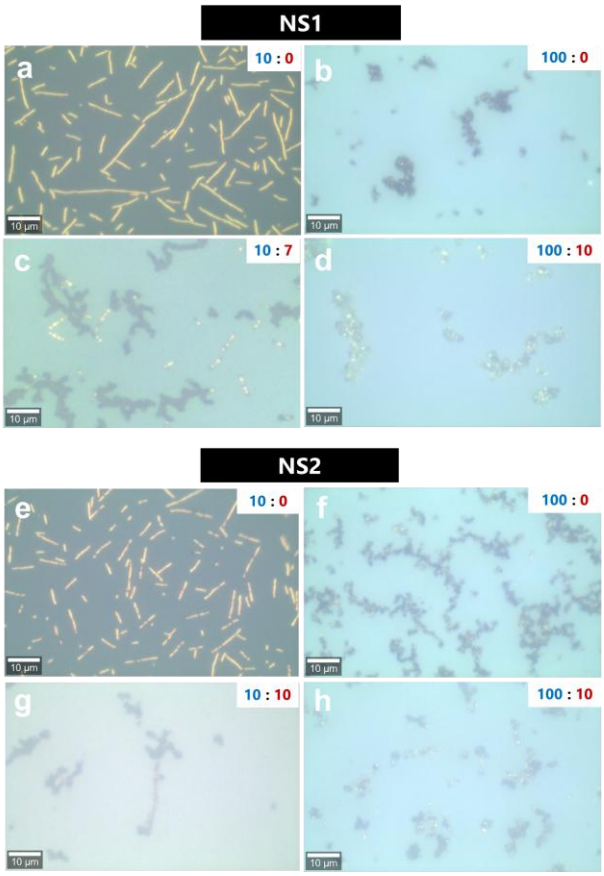

Figure 9. Forcing and tuning needle curvature by addition of NaCl during DISA. *Comparing NS1* ***(a-d)*** *with wider groove pitch versus NS2* ***(e-h)*** *with finer groove pitch, self-assembled at different depletant and salt concentrations. The numbers at the top-right of each image represent the [CTAC]:[NaCl] molarities respectively.*

In terms of application, these curved and distorted NS needles were tested for potential use as stimuli-responsive reversibly deformable nano-objects, akin to actuating elastic bands. To test this possible deformation, we exposed suspensions of these needles to an AC electric field of increasing voltages. The needles were observed in situ by optical microscopy under crossed polarizers, to check any birefringence in the assemblies – that is, variable light refraction (i.e., different refractive indices) with different directions of incident light, which hints at the collective orientation of the rods in the superstructures. At high field values close to 200 V/mm, there was indeed realignment and partial stretching of the needles, due to the NS alignment and polarizability. Nonetheless, the high voltage required to achieve this deformation is still too high for practical and prolonged use, partially due to charge screening because of the high ionic strength from free CTAC micelles required for depletion-induced self-assembly. The NS dimensions likely need to be optimized, to have a high enough interaction area to achieve

more flexible curved structures at lower CTAC, while maintaining minimal NR length for an optimal length to groove pitch ratio. In addition, the CTAC ligand on the NS surfaces replaced by a shorter amphiphilic thiol like MUTAB, which would form a shorter bilayer, and decrease the average gap between the rods in the needle assemblies, to improve the sensing of the chiral grooves of the NSs. Playing with both NaCl addition and MUTAB ligand exchange could also be a good strategy for stabilizing possible cholesteric liquid crystals of these NSs that we have recently begun to study.

Seeding chirality in achiral systems and binary assemblies

Inspired by the use of helical CTAC:binamine (CB) micelles to induce chiral growth of grooved or helical Au NPs employed in previous studies[26,32], we also studied the possibility of inducing chiral self-assembly of achiral nanorods using the same helical CB micelles as a templating agent (**Figure 10a**). One can liken these micelles to chiral dopants or templates which can seed the propagation of chirality in a colloidal superstructure, as in the case of molecular liquid crystals or cellulose nanocrystals (CNCs) for example[6]. This part of the thesis project remains very preliminary. However, a few mixed results have been noted for DISA of long pentagonal rods (C5-NRs) with CB as depletant. Via *in situ* optical microscopy, some promising results include seeing partially distorted or curved '1D needle' assembles of C5-NRs at certain CB concentrations (**Figure 10b,c**). Another method of seeing chirality into an assembly of achiral rods could be the inducing DISA in a mixture of chiral and achiral NRs with similar length and depletion threshold. We have not yet tested this with a pair of rods with matching depletion threshold, but this is certainly an avenue to explore in the near future.

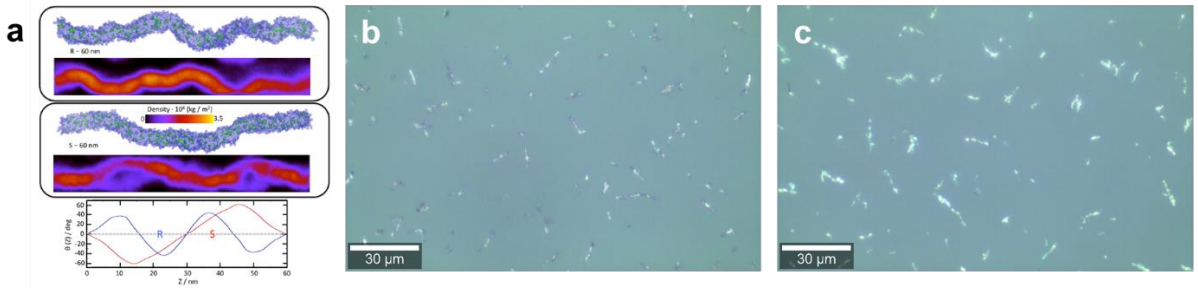

Figure 10. Inducing chiral assembly with helical wormlike micelles: (a) *Molecular dynamics simulations of the CTAC/BINAMINE (CB) helical micelle system[32]. **(b)** Distorted needle assemblies of pentagonal nanorods (C5-NRs, L = 190 nm, W = 30 nm) in 30 mM CTAC : 0.75 mM binamine **(c)** Distorted needle assemblies of pentagonal nanorods (C5-NRs, L = 1000 nm, W = 30 nm) in 90 mM CTAC : 2.25 mM binamine.*

5.3. Take-home message

The spontaneous and dynamic self-organization of intrinsically chiral plasmonic nanoparticles into extrinsically chiral superstructures is a promising strategy for making tunable colloidal platforms for chiral optoelectronics, sensing, and catalysis.

By combining the fine-tuning of twist in chiral fourfold gold nanorods (cGNRs) via controlled oxidative etching, with in situ depletion-induced self-assembly (DISA) in liquid suspension, one obtains hierarchical chiral assemblies of cGNRs due to chirality transfer, with the interparticle gaps being tunable by depletant concentration. As the cGNRs decrease in helicity due to etching, the lattices of their corresponding assemblies transition from 1D-symmetric twisting clusters, to 2D rhombic assemblies, to 2D hexagonal platelet assemblies, as we determined by in situ SAXS, optical microscopy, and SEM. These cGNRs can be repeatedly assembled and disassembled over many cycles by simple depletant addition and redilution.

These cGNR clusters act as a platform for the reversible, spectrally-tunable, and temporally-dynamic enhancement of plasmonic circular dichroism (PCD) directly in liquid colloidal suspension, with the optical g-factor increasing up to two orders of magnitude, according to cyclic CD kinetics studies done by our collaborators. It was also found that decreasing the intrinsic cGNR helicity greatly decreases the maximum PCD amplitude upon DISA. This also demonstrates that the PCD comes from the NPs directly, and not from any ligands or remaining chiral molecules on the NP surfaces.

Notably, our approach requires no special chemical modification or ligand exchange of the nanoparticle. Our study of cGNRs of varying twist suggests a high sensitivity of PCD and extrinsic chirality to small changes in NR helicity, which is an object of further study.

In perspective, the exact mechanism of PCD enhancement needs to be clarified with structural experiments and numerical simulations. The optimal range of NP helicity or groove pitch and NP length / width for the highest PCD enhancement (i.e., most efficient chirality transfer) must also be determined experimentally. Finally, using stimuli-responsive depletants could greatly shorten the commutation time of the reversible cGNR assembly, versus using typical surfactants like CTAC.

5.4. References

(1) Trazo, J. G.; Marcone, J.; Nag, R.; Goldmann, C.; Kutalia, N.; Bizien, T.; Pansu, B.; Impéror-Clerc, M.; Hamon, C. Colloidal Tunable Metasurfaces via Depletion-Induced Self-Assembly of Plasmonic Nanorods. *ACS Appl. Mater. Interfaces* **2025**, *17* (45), 62349–62359. https://doi.org/10.1021/acsami.5c17436.

(2) Young, K. L.; Jones, M. R.; Zhang, J.; Macfarlane, R. J.; Esquivel-Sirvent, R.; Nap, R. J.; Wu, J.; Schatz, G. C.; Lee, B.; Mirkin, C. A. Assembly of Reconfigurable One-Dimensional Colloidal Superlattices Due to a Synergy of Fundamental Nanoscale Forces. *Proc. Natl. Acad. Sci. U.S.A.* **2012**, *109* (7), 2240–2245. https://doi.org/10.1073/pnas.1119301109.

(3) Lekkerkerker, H. N. W.; Tuinier, R. *Colloids and the Depletion Interaction*; Lecture Notes in Physics; Springer Science+Business Media B.V: Dordrecht, 2011.

(4) Serafin, F.; Lu, J.; Kotov, N.; Sun, K.; Mao, X. Frustrated Self-Assembly of Non-Euclidean Crystals of Nanoparticles. *Nat Commun* **2021**, *12* (1), 4925. https://doi.org/10.1038/s41467-021-25139-9.

(5) Brissaud, C.; Jain, S.; Henrotte, O.; Pouget, E.; Pauly, M.; Naldoni, A.; Comesaña-Hermo, M. Plasmonic Chirality Meets Reactivity: Challenges and Opportunities. *J. Phys. Chem. C* **2025**, *129* (7), 3361–3373. https://doi.org/10.1021/acs.jpcc.4c08454.

(6) Parton, T. G.; Parker, R. M.; Van De Kerkhof, G. T.; Narkevicius, A.; Haataja, J. S.; Frka-Petesic, B.; Vignolini, S. Chiral Self-Assembly of Cellulose Nanocrystals Is Driven by Crystallite Bundles. *Nat Commun* **2022**, *13* (1), 2657. https://doi.org/10.1038/s41467-022-30226-6.

(7) Parker, R. M.; Guidetti, G.; Williams, C. A.; Zhao, T.; Narkevicius, A.; Vignolini, S.; Frka-Petesic, B. The Self-Assembly of Cellulose Nanocrystals: Hierarchical Design of Visual Appearance. *Advanced Materials* **2018**, *30* (19), 1704477. https://doi.org/10.1002/adma.201704477.

(8) Zhang, Z.; Grelet, E. Tuning Chirality in the Self-Assembly of Rod-like Viruses by Chemical Surface Modifications. *Soft Matter* **2013**, *9* (4), 1015–1024. https://doi.org/10.1039/C2SM27264D.

(9) Tomazic, F.; Muttathukattil, A.; Nabiyan, A.; Schacher, F.; Engel, M. Geometric Frustration Directs the Self-Assembly of Nanoparticles with Crystallized Ligand Bundles. *J. Phys. Chem. B* **2024**, *128* (45), 11258–11266. https://doi.org/10.1021/acs.jpcb.4c04562.

(10) Wang, S.; Kang, L.; Salamon, P.; Wang, X.; Uchida, N.; Araoka, F.; Aida, T.; Dogic, Z.; Ishida, Y. Stimuli-Responsive Self-Regulating Assembly of Chiral Colloids for Robust Size and Shape Control. *Nat Commun* **2024**, *15* (1), 9891. https://doi.org/10.1038/s41467-024-54217-x.

(11) Sevin, A. Pasteur and Molecular Chirality. *bibnum* **2015**. https://doi.org/10.4000/bibnum.459.

(12) Clayden, J.; Greeves, N.; Warren, S. *Organic Chemistry*, 2nd ed.; Oxford university press: Oxford, 2012.

(13) Wang, J.-S.; Wang, G.; Feng, X.-Q.; Kitamura, T.; Kang, Y.-L.; Yu, S.-W.; Qin, Q.-H. Hierarchical Chirality Transfer in the Growth of Towel Gourd Tendrils. *Sci Rep* **2013**, *3* (1), 3102. https://doi.org/10.1038/srep03102.

(14) Akagi, K. Asymmetric Polymerization in Chiral Liquid Crystals. https://www.sigmaaldrich.com/FR/fr/technical-documents/technical-article/materials-science-and-engineering/polymer-synthesis/asymmetric-polymerization.

(15) Pati, J. C.; Salam, A. Lepton Number as the Fourth "Color." *Phys. Rev. D* **1974**, *10* (1), 275–289. https://doi.org/10.1103/PhysRevD.10.275.

(16) Grelet, E.; Tortora, M. M. C. Elucidating Chirality Transfer in Liquid Crystals of Viruses. *Nat. Mater.* **2024**, *23* (9), 1276–1282. https://doi.org/10.1038/s41563-024-01897-x.

(17) Serrano-Freijeiro, A.; Renero-Lecuna, C.; Obelleiro-Liz, M.; Martín, V. F.; Dey, D.; Taboada, J. M.; Schatz, G. C.; Pastoriza-Santos, I.; Pérez-Juste, J.; Liz-Marzán, L. M. Wavelength-Dependent Differential Amplification of Raman Scattering by Chiral Gold Nanorods for Multiplexed Encoding. *Adv Funct Materials* **2025**, e07076. https://doi.org/10.1002/adfm.202507076.

(18) Ni, B.; Mychinko, M.; Gómez-Graña, S.; Morales-Vidal, J.; Obelleiro-Liz, M.; Heyvaert, W.; Vila-Liarte, D.; Zhuo, X.; Albrecht, W.; Zheng, G.; González-Rubio, G.; Taboada, J. M.; Obelleiro, F.; López, N.; Pérez-Juste, J.; Pastoriza-Santos, I.; Cölfen, H.; Bals, S.; Liz-Marzán, L. M. Chiral Seeded Growth of

Gold Nanorods Into Fourfold Twisted Nanoparticles with Plasmonic Optical Activity. *Advanced Materials* **2023**, *35* (1), 2208299. https://doi.org/10.1002/adma.202208299.
(19) Visheratina, A.; Kumar, P.; Kotov, N. Engineering of Inorganic Nanostructures with Hierarchy of Chiral Geometries at Multiple Scales. *AIChE Journal* **2022**, *68* (1), e17438. https://doi.org/10.1002/aic.17438.
(20) Santiago, E. Y.; Irfan, M.; Ávalos-Ovando, O.; Govorov, A. O.; Correa-Duarte, M. A.; Besteiro, L. V. Light-to-Matter Chirality Transfer in Plasmonics. *Mater. Horiz.* **2025**, *12* (14), 4940–4969. https://doi.org/10.1039/D5MH00179J.
(21) Probst, P. T.; Dong, Y.; Zhou, Z.; Aftenieva, O.; Fery, A. Bottom-Up Assembly of Inorganic Particle-Based Chiroptical Materials. *Advanced Optical Materials* **2024**, *12* (5), 2301834. https://doi.org/10.1002/adom.202301834.
(22) Liu, Q.; Kuzyk, A.; Endo, M.; Smalyukh, I. I. Colloidal Plasmonic DNA-Origami with Photo-Switchable Chirality in Liquid Crystals. *Opt. Lett.* **2019**, *44* (11), 2831. https://doi.org/10.1364/OL.44.002831.
(23) Carone, A.; Mariani, P.; Désert, A.; Parola, S. Colloidal Assemblies of Chiral Plasmonic Nanoparticles Induce Tunable Circular Dichroism Response. *Advanced Optical Materials* **2023**, *11* (18), 2300119. https://doi.org/10.1002/adom.202300119.
(24) Lin, H.-T.; Hsu, Y.-Y.; Cheng, P.-J.; Wang, W.-T.; Chang, S.-W.; Shih, M.-H. *In Situ* Tunable Circular Dichroism of Flexible Chiral Metasurfaces Composed of Plasmonic Nanorod Trimers. *Nanoscale Adv.* **2022**, *4* (11), 2428–2434. https://doi.org/10.1039/D2NA00144F.
(25) Lininger, A.; Palermo, G.; Guglielmelli, A.; Nicoletta, G.; Goel, M.; Hinczewski, M.; Strangi, G. Chirality in Light–Matter Interaction. *Advanced Materials* **2023**, *35* (34), 2107325. https://doi.org/10.1002/adma.202107325.
(26) Chow, T. H.; Jo, S.; Lu, Y.; Rivilla, I.; Mychinko, M.; Bals, S.; Mihi, A.; Liz-Marzán, L. M. Intrinsic and Extrinsic Circular Dichroism in Linear Arrays of Anisotropic Chiral Nanoparticles. *Nano Lett.* **2026**, *26* (4), 1394–1402. https://doi.org/10.1021/acs.nanolett.5c05530.
(27) Zhang, N.-N.; Mychinko, M.; Gao, S.-Y.; Yu, L.; Shen, Z.-L.; Wang, L.; Peng, F.; Wei, Z.; Wang, Z.; Zhang, W.; Zhu, S.; Yang, Y.; Sun, T.; Liz-Marzán, L. M.; Bals, S.; Liu, K. Self-Matching Assembly of Chiral Gold Nanoparticles Leads to High Optical Asymmetry and Sensitive Detection of Adenosine Triphosphate. *Nano Lett.* **2024**, acs.nanolett.4c03782. https://doi.org/10.1021/acs.nanolett.4c03782.
(28) Schreiber, R.; Luong, N.; Fan, Z.; Kuzyk, A.; Nickels, P. C.; Zhang, T.; Smith, D. M.; Yurke, B.; Kuang, W.; Govorov, A. O.; Liedl, T. Chiral Plasmonic DNA Nanostructures with Switchable Circular Dichroism. *Nat Commun* **2013**, *4* (1), 2948. https://doi.org/10.1038/ncomms3948.
(29) Querejeta-Fernández, A.; Chauve, G.; Methot, M.; Bouchard, J.; Kumacheva, E. Chiral Plasmonic Films Formed by Gold Nanorods and Cellulose Nanocrystals. *J. Am. Chem. Soc.* **2014**, *136* (12), 4788–4793. https://doi.org/10.1021/ja501642p.
(30) Zang, S.; Paul, S.; Leung, C. W.; Chen, M. S.; Hueckel, T.; Hocky, G. M.; Sacanna, S. Direct Observation and Control of Non-Classical Crystallization Pathways in Binary Colloidal Systems. *Nat Commun* **2025**, *16* (1), 3645. https://doi.org/10.1038/s41467-025-58959-0.
(31) Wang, Q.; Wang, Z.; Li, Z.; Xiao, J.; Shan, H.; Fang, Z.; Qi, L. Controlled Growth and Shape-Directed Self-Assembly of Gold Nanoarrows. *Sci. Adv.* **2017**, *3* (10), e1701183. https://doi.org/10.1126/sciadv.1701183.
(32) González-Rubio, G.; Mosquera, J.; Kumar, V.; Pedrazo-Tardajos, A.; Llombart, P.; Solís, D. M.; Lobato, I.; Noya, E. G.; Guerrero-Martínez, A.; Taboada, J. M.; Obelleiro, F.; MacDowell, L. G.; Bals, S.; Liz-Marzán, L. M. Micelle-Directed Chiral Seeded Growth on Anisotropic Gold Nanocrystals. *Science* **2020**, *368* (6498), 1472–1477. https://doi.org/10.1126/science.aba0980.
(33) Wang, S.; Zheng, L.; Chen, W.; Ji, L.; Zhang, L.; Lu, W.; Fang, Z.; Guo, F.; Qi, L.; Liu, M. Helically Grooved Gold Nanoarrows: Controlled Fabrication, Superhelix, and Transcribed Chiroptical Switching. *CCS Chem* **2021**, *3* (9), 2473–2484. https://doi.org/10.31635/ccschem.020.202000472.

Chapter 6

ACTIVE LIGHT-CONTROLLED ASSEMBLY BY PHOTOTUNABLE DEPLETION

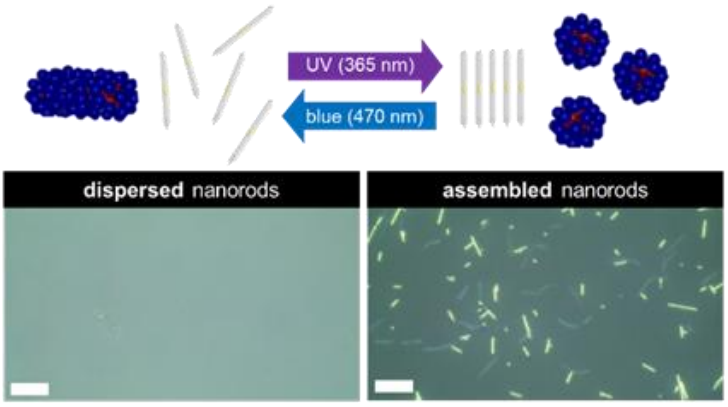

J. G. Trazo, et al. **Active light-controlled colloidal assembly by phototunable depletion.** *Article in preparation.* (Scale bars are 10 μm.)

6.1. Introduction

Towards active and programmable metamaterials

One important goal in materials science is the development of *programmable* materials, whose properties can be controlled not only in space (i.e., their structure and function) but also reconfigured in time, being able to react or adapt to time-evolving stimuli or programming their properties at certain time delays[1–3]. Metamaterials are sought to not only have novel properties, but have dynamic properties which are *stimuli-responsive*[4,5]. Often inspired by biological systems, there are four notable recent trends in nanomaterials development. First, there is a trend towards *self-regulating or adaptive materials*, where a system can exhibit periodic oscillatory behavior or re-adjust its properties towards a stable 'homeostasis' in response to a stimulus[6]. This is similar to out-of-equilibrium homeostasis in living organisms which respond and self-regulate with respect to their environment. Second, there is a trend towards *multi-stimuli-responsiveness*, where a nanomaterial can respond to various stimuli with orthogonal control (e.g., light, electric field, heat), whose effects can be coupled in interesting and functional ways[7,8]. Third, again mimicking biology, there is a search for *continuously modulable properties*, aside from mere on-off switching. Fourth, there is also a

trend towards *universal* or *valence-free* processes in nanomaterials, where no surface treatment or ligand functionalization is required, and the process can applied to materials regardless of their chemistry or scale; the depletion interaction is one such valence-free process[9–11]. In this way, nano-systems (e.g. nano-reactors, self-assembling systems[12]) can be more modular, with methods and materials becoming more cross-compatible, less limited by NP or ligand chemistry. In this way, metamaterials are becoming more 'life-like', programmable, and 4D, with dynamic control in time, as well as in control in spatial structure. Various examples of such programmable metamaterials in the broad sense are shown below (**Figure 1**), like adaptive, flexible Au/PET gap plasmon resonance devices for substrates for surface-enhanced Raman scattering (SERS)[13], bio-inspired self-assembled block copolymer particles for magnetically switchable structural colors[14], or multi-stimuli-responsive photo-patternable hydrogels for information encoding[15].

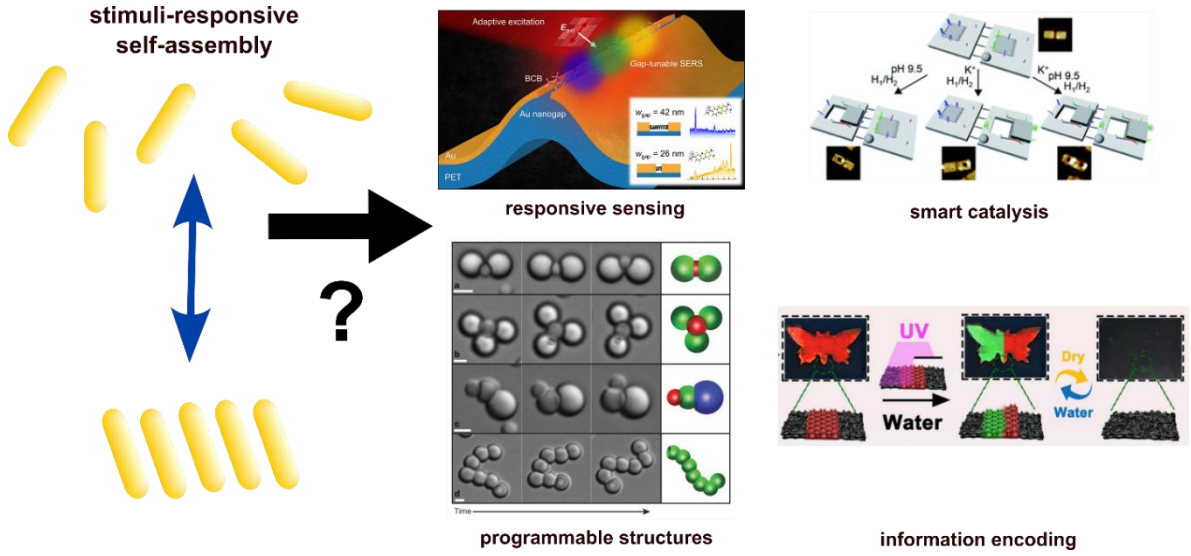

Figure 1. Active and programmable metamaterials as inspiration for using stimuli-responsive self-assembly. ***(a)*** *Adaptive Au gap-tunable surface-enhanced Raman spectroscopy (SERS) using mechanical and optical control[13].* ***(b)*** *Stimuli-responsive catalysis in nanocavities by mechanically-unlocking DNA origami tiles in response to chemical stimuli[16].* ***(c)*** *Programmable lock-and-key self-assembly of colloids by depletion[9].* ***(d)*** *Smart and multi-stimuli-responsive hydrogels with light-induced chemical crosslinkers for information security applications[15].*

One strategy of designing programmable metamaterials is using stimulus-driven (or stimulus-tunable) self-assembly at the nano and microscale. In fact, spontaneous self-assembly has been used as a model system to better understand and develop such metamaterials[17–19]. Various papers have reported the use of stimulus-driven assembly in different applications: (1)

as a chemical reaction factories for applications like smart catalysis (*e.g., reversible trapping of reactants in 'nanoflasks' by light-induced colloidal assembly*)[12,16], (2) as sensors for detection or self-regulation (*e.g., cyclable H_2 gas detection using self-assembled core-shell Au@Pd nanoarray)*[20], (3) as ways to create programmable structures (*e.g., DNA ligands to create programmable NP assemblies*) [2,3,9,17,21], as active optical or plasmonic devices (*e.g., gold nanoarrow or nanoscrew assemblies for chiroptical switching*[22]) and (5) as means for complex or dynamic information encoding (*e.g., re-erasable image writing in hydrogels*)[15,23].

Understanding the dynamics of various stimuli-driven nanoscale processes is key to designing smart and programmable metamaterials. One of the biggest challenges in dynamic self-assembly is how to render certain NP systems stimuli-responsive and reversible, which is often a challenge of finding the right NP or ligand functionalization chemistry. This is because, to date, most stimuli-responsive self-assembly strategies rely on specific ligand functionalization or surface treatment of the NPs to create *active particles*. Each ligand or NP chemistry is often designed to respond to specific stimuli with precise control, such as temperature, light, dipole interactions, or chemical stimuli[7,24]. Here we enumerate several notable examples of stimuli-responsive self-assembly in recent publications. Azobenzene-based ligands have been used to induce photoswitchable solvophobic self-organization of Au NPs in an sPMMA gel, leading to tunable plasmonic colors for image writing. This solvophobic effect and other kinds of NP self-assembly can also be driven by chemical fuels (e.g., in dissipative self-assembly), including enzyme activity, or changes in pH in the case of ionizable ligands[23,25–27]. Organic molecules, such as thermotropic liquid crystals or thermoresponsive polymers, have been attached to Ag NP surfaces to reversibly assemble these particles into 1D or 2D arrays by heating/cooling between[28]. Finally, electric fields (direct or alternating current) and magnetic fields have been used to induce the self-assembly of various NP types such as polymer (PS, PMMA) colloids, thiol-coated Au or Ag NPs, and superparamagnetic (SPM) NPs, with or without additional surface functionalization[7,29–31] (**Figure 2**).

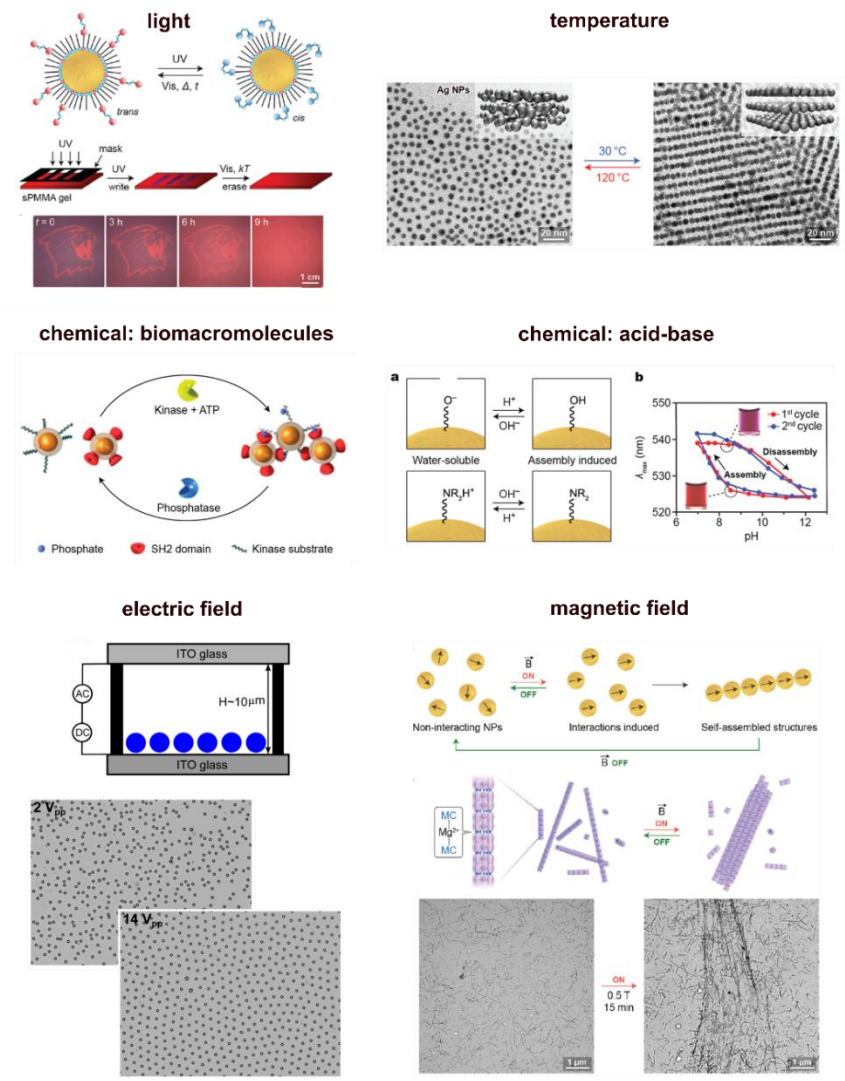

Figure 2. Various strategies for stimuli-responsive metamaterials by self-assembly[7]. (a) *Self-erasing images made by gold NP (AuNP)-embedded gels, with NPs functionalized with light-sensitive azobenzene ligands[23]. **(b)** Thermally tunable silver NP (AgNP) metamaterial, using liquid crystal molecular ligands on the AgNPs[28]. **(c)** Superparamagnetic Fe_3O_4 NPs dynamically self-assembled by kinase and phosphatase enzymes[32]. **(d)** pH-controlled reversible aggregation of AuNPs functionalized with ionizable FMP thiol ligands[26]. **(d)** Electric-field assisted self-assembly of micrometric polystyrene (PS) spheres[29]. **(e)** Reversible magnetic self-assembly of superparamagnetic iron oxide nanoparticles (SNPs) jacketed in nanotubular proteins[30].*

While these stimuli have been investigated and applied in proof-of-concept systems, few of them have featured multi-stimuli response, and much less valence-free interactions. In the case of ligand functionalization, which is very powerful, one is limited by chemical or physical grafting of the ligand to the base NPs. Therefore, we propose use an *active medium* rather than *active particles* (i.e., NPs rendered active by ligands/surface chemistry) as a more valence-free strategy of stimuli-responsive self-assembly, relying instead on assembling agents

suspended in solution. Classic depletion-induced self-assembly (DISA) is one example of medium based self-assembly, yet the depletion interaction itself is not directly stimuli-responsive (excepting the depletant itself as a 'chemical stimulus', or micellar depletants which can change size depending on temperature), nor is depletion self-regulating nor time-evolving in its strength[9,10,33]. Therefore, in this chapter, we investigate whether or not DISA can be rendered directly or indirectly active, so that depletion can be used to create an active (e.g., phototunable) medium, versus using ligand-equipped active particles.

Light-controlled self-assembly and disassembly: state-of-the-art and challenges

Light is arguably the best candidate for creating truly active and programmable metamaterials. Light stimuli can also be delivered nearly instantaneously and *in situ* with *precise spatiotemporal control*, without the need for disturbing or opening one's system. It can be delivered selectively in *many wavelengths or polarizations* for different responses of different materials. Lastly, light can enable *multi-stimuli responsiveness* and *self-regulation* due to light-matter interactions / coupling of light with heating, electric, magnetic effects. It is also particularly interesting from the chemist's perspective as photoinduced processes often proceed in a *different kinetic pathway* than thermal ones, potentially uncovering previously inaccessible phenomena. In recent literature, there have been many studies on the photo-induction (i.e., on/off switching) of self-assembly, but *full light control or modulation* of the assembly strength or degree has been more rarely reported[2,7,17,34]. This thesis project aims to advance one of the first examples of full light modulation of colloidal self-assembly, including the attainment of intermediate or metastable states.

The sensitivity of many materials, particular organic molecules, to various wavelengths of light means that light-controlled self-assembly can proceed by very different mechanisms. For instance, upon irradiation with the appropriate color of light, photoacids based on merocyanine/spiropyran compounds release H^+ ions in solution, changing the pH and ionic strength of the system on demand, which can be used to trigger or tune electrostatic assembly of charged colloidal NPs with not just temporal but also spatial precision[17,35]. The same photoacids have been used to tune the folding of DNA origami connecting and templating the orientation of Au NR dimers, creating switchable 'chiral metamolecules' in suspension[36,37].

Meanwhile, azobenzene-derived alcohols, which change their conformation and effective size upon UV/blue irradiation, can be used as additives in colloidal cellulose-based liquid crystals (LCs), where they can sterically control the pitch of the LC according to their isomerization state, leading to tunable structural color[38] (**Figure 3**).

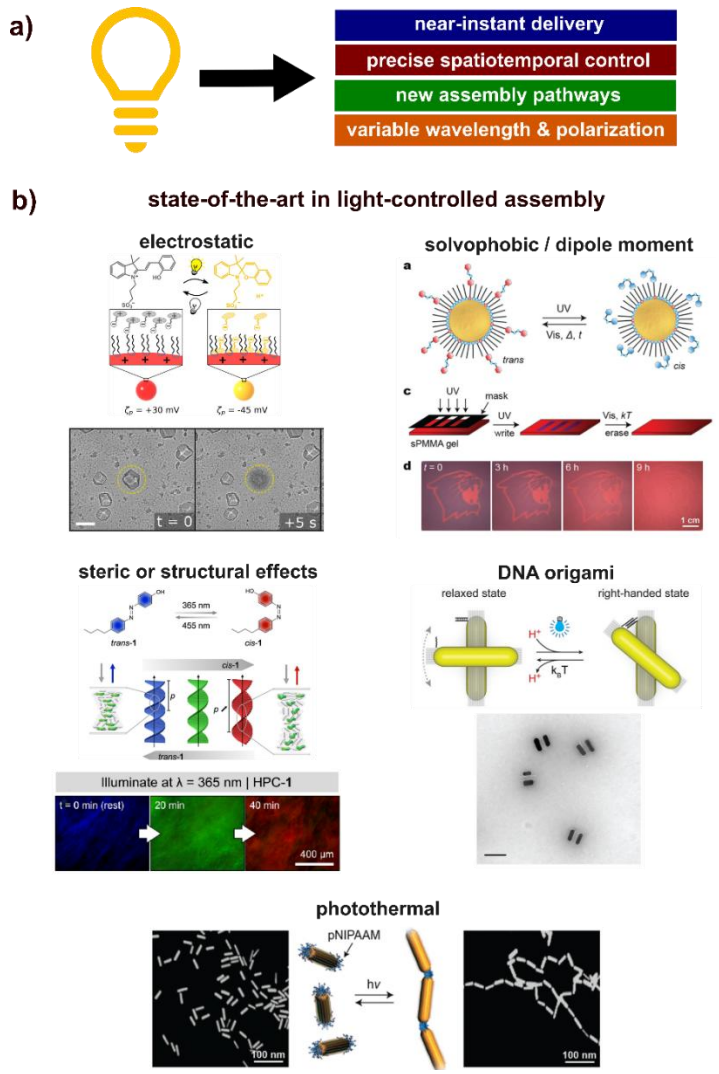

Figure 3. Light-controlled NP self-assembly. ***(a)*** *Key advantages and principles of light-induced modulation in nanomaterials.* ***(b)*** *State-of-the-art of light-induced NP assembly and photoswitchable matter: Light control of* ***electrostatic*** *co-assembly of colloids using a merocyanine/spiropyran photoacid[17];* ***solvophobic*** *self-assembly of AuNPs coated with azobenzene-based ligands[23];* ***steric/structural*** *tuning of the structural color of cholesteric liquid crystals using an azobenzene-based alcohol as a photoresponsive 'switch'[38];* ***DNA-origami****-based light-switchable dimers of Au nanorods (NRs) in a photoacid solution[36];* ***photothermal*** *triggering of Au NR self-assembly using the reversible thermal contraction of pNIPAAM ligands[39].*

Nonetheless, the majority of these methods are not valence-free. In addition, they have found limited application in assemblies of very anisotropic particles, or of binary and multi-component mixtures (e.g. different nanoparticle sizes), or metastable and intermediate states of assembly. Another challenge is the chemical development of newer, more stable, or more polyvalent photoswitchable moieties/compounds apart from traditional azobenzene or spiropyran. The development of chemical photoswitches in the IR range is also an open field. For gold and silver NPs, it is still unclear as to how to integrate plasmonic properties directly into the photo-switchability, where the light-responsive moiety can couple with the SPRs of the system. Also, azobenzene and spiropyran-based compounds have been used many times to create active particles by chemical functionalization of the particle surfaces, but have not yet been extensively used to create an active and valence-free medium for self-assembly[7,17,40,41].

Given these challenges, we now turn to azobenzene-based surfactants like *azoTABs as light-sensitive depletants* as candidates for creating phototunable active media for NP self-assembly. Azobenzene-based compounds exist in two configurations, the thermodynamically stable *trans isomer*, stable in dark conditions or under blue/visible light, and the *cis isomer*, stable under UV light. When dispersed in water, azoTABs and other similar surfactants self-organize into micelles whose curvature, and thus size and shape, depends drastically on whether the molecules are in the trans or cis form (**Figure 4**). Such change in micellar size and shape changes the number concentration of the micelles upon light irradiation, changing the effective osmotic pressure and thus the attractive depletion force exerted by these micelles on larger dispersed NPs. In this project, we shall call this phenomenon phototunable depletion-induced self-assembly (photo-DISA).

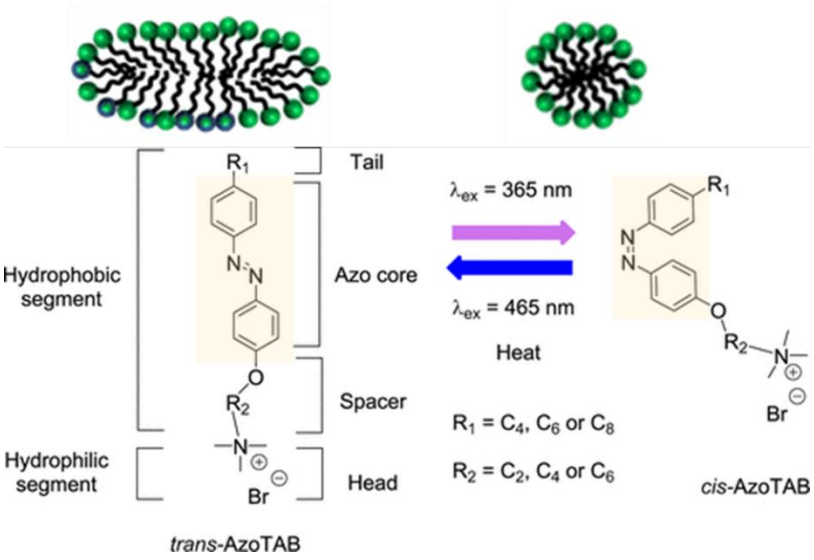

Figure 4. Reversible change in micelle shape and size upon azoTAB photoisomerization. *Adapted from C. Blayo, et al[40].*

Before proceeding to a describe our photo-DISA system and the challenges it must tackle, let us take a brief overview of the current applications of azobenzene and other similar photosensitive organic compounds in materials science. So far, these photosensitive compounds have been used to achieve three notable cases of photoswitchable material properties. First, they were used to switch *optical or plasmonic properties* in nanoparticle systems, specifically absorbance and colors of nanoparticle mixtures, films, or gels, which have been employed in self-erasing images, sensors, or information encoding[23,25]. Second, they have been used as switchable *mechanophores* to achieve light switching of the mechanical properties (e.g. stiffness and fracture behavior) of gels[42]. Third, they have been used to induce *structural phase transitions*, when combined with gels or co-surfactants. Such transitions include fluid-to-gel transitions, which yields a photoswitchable rheological control, and a permeable to non-permeable membrane transition in high concentration arylazopyrazole photosurfactants (AAP-PS), which was exploited to control gas diffusion on demand[38,43] (**Figure 5**). While these applications of photosensitive organic compounds are impressive, and give some inspiration for creating valence-free active media for self-assembly, there is yet to be reported a use of such compounds for creating extended and well-ordered 1D or 2D metamaterials, nor has there been cited a direct use of these compounds as photosensitive depletants.

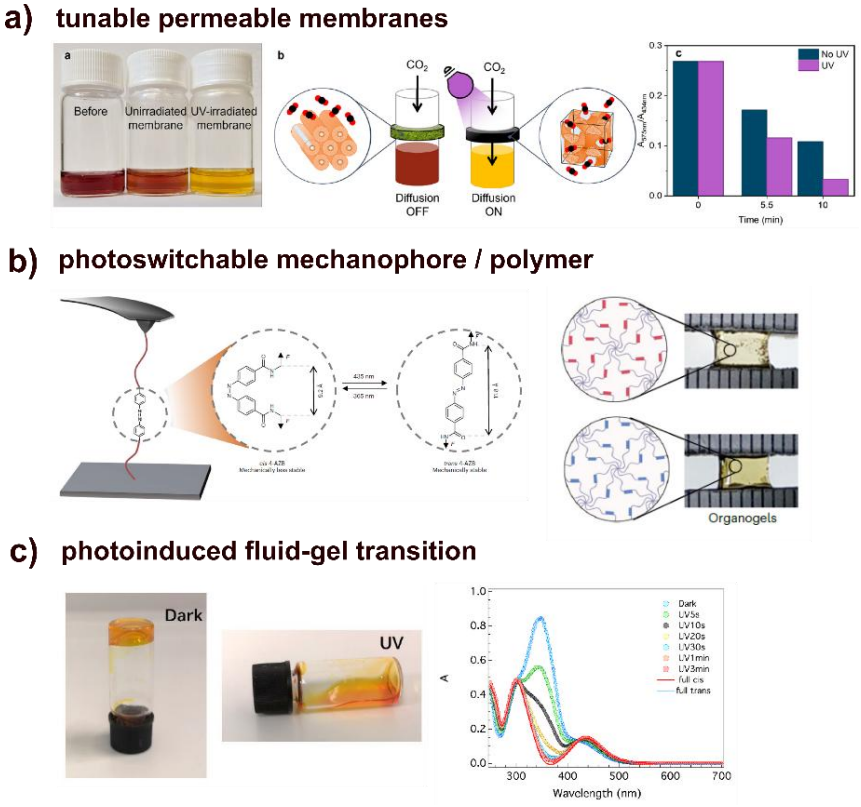

Figure 5. Current applications of azobenzene or other photosensitive compound based-materials. ***(a)*** *Gel membrane made with liquid crystalline arylazopyrazole photosurfactant (AAP-PS), exhibiting light-tunable CO_2 gas permeability*[41]. ***(b)*** *Azobenzene used as a photoswitchable mechanophore applied for light control of polymer network fracturing*[42]. ***(c)*** *UV/blue irradiation induces fluid-gel transitions in photosurfactant-polyelectrolyte mixtures forming wormlike micelle networks*[43].

How to design and control photo-DISA?

We propose phototunable depletion (photo-DISA) as a new strategy of stimuli-responsive self-assembly methods. There are three primary motivations for our study of photo-DISA. First, it will be the first known example of *directly rendering the depletion interaction light-controllable.* This entails a new, universal, and valence-free method of self-assembly based on simple entropic effects by the Asakura-Oosawa (AO) model[10,44].

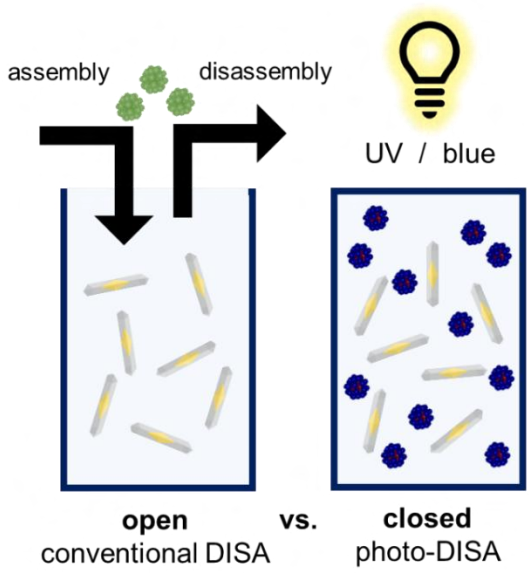

Figure 6. Classic 'open' DISA versus 'closed' photo-DISA.

Second, it will improve the *practicality of DISA* for use in *closed* active nano-systems. In conventional DISA, cycling between assembled and disassembled NP states typically requires concentration, sedimentation, and redilution of the colloidal sample to change the depletant concentration, which entails external addition or removal of liquid, rendering the system *open*, as noted in **Chapter 4**[11,45,46]. With photo-DISA, the concentration of depletant particles is controlled by an external light stimulus (i.e., the number of micellar depletants changes, while the number of surfactant molecules remains constant), keeping the system *closed* and decreasing its cycling time (**Figure 6**).

Third, using light will *increase the degrees of control* (e.g., spatial, temporal, wavelength, polarization) for DISA, allowing greater control and faster response time for potential photo-DISA based devices, and potentially uncovering new states, phases, or crystal structures of colloidal NP assemblies, including metastable or intermediate states via new kinetic pathways, as noted in the perspectives of **Chapters 4 and 5**.

From these aforementioned motivations, we list three open questions which we aim to answer:

First, how can one prove that the light irradiation of azoTABs will indeed cause photo-induced depletion leading to NP self-assembly (photo-DISA)? How can one prove it is really a depletion-based mechanism? Will there be other nanoscale forces that work together or

against the photo-DISA mechanism? And if it is indeed depletion-based, can other non-metallic NPs (e.g. polymer, ceramic, semiconductor particles) be assembled by photo-DISA?

Second, by how much can using azoTABs improve the cyclability and the switching rate of DISA? In terms of the practicality and robustness of the system, how many times can an azoTAB – NP mixture be cycled? Is the cyclability dependent on illumination conditions? How can we speed up or slow down the cycle time?

Third, given the additional temporal and spectral control of photo-DISA, can we stabilize metastable or intermediate states of NP assemblies, for example by rapidly switching between wavelengths (UV vs. blue) of illumination (*i.e., analogous to active stabilization in a Kapitza pendulum*), by changing the duration of illumination, or by mixing wavelengths with different irradiance? Can on achieve states between full assembly and full disassembly, or various inter-NP distances? Could one achieve different superstructure phases of assemblies, or different degrees of crystallinity with these control parameters?

6.2. Results and discussion

Preparing the azoTAB based photo-DISA System

To start our investigation of photo-DISA, we prepared *passive metal nanorods* as the assembly colloidal building blocks, and *active azoTAB photosurfactant* as the depletant to induce assembly. Different nanorod sizes and depletant chemistries were then screened.

For the building blocks, Au@Ag C5-NRs were prepared with differing length but constant width and cross-section, to investigated the effect of aspect ratio (AR), according to our aforementioned protocol (**Chapter 2 on achiral C5 nanorods**). Meanwhile, four different azoTAB compounds were synthesized in-house by the LPS chemistry service (Claire Goldmann, see **Chapter 3**) with differing carbon chain lengths for tail and the spacer beside the azobenzene moieties. Based on previous literature, it is known that the change in azoTAB micelle size and shape – and thus the change in effective depletion force – is generally maximized when the length difference between the tail and spacer carbon chains is greatest[40,43]. On the other hand, based prior results in this thesis (**Chapter 4**), it is known that higher AR NRs assemble at lower depletant concentrations, which is also good for using azoTABs which have relatively poorer

solubility versus other surfactants[40,43]. At such lower concentrations, the diffusion of depletant is slower and inter-NP gaps are greater, which generally improved the cyclability of their assembly/disassembly[11,33]. Therefore, we aimed to (1) use NRs with the highest possible ARs to minimize their depletion threshold, and to (2) use depletants with the largest change in micellar size/shape upon photoisomerization (*typically with highest tail vs. spacer length difference*) while remaining soluble enough to not excessively crystallize in water. As such, we focused on three pentatwinned gold core – silver shell (Au@Ag) NRs with 6, 8, or 32 equivalents of silver versus gold, termed PR6, PR8, and PR32 respectively, synthesized according to the protocols in **Chapter 2** on classic achiral C5 nanorods. (**Figure 7**). Note that for most experiments, PR6 and PR8 exhibited similar self-assembly behavior due to their similar lengths. Their dimensions were determined by TEM, and their experimental self-assembly thresholds determined by fast DISA (i.e., one-shot mixing of NRs and azoTAB depletant), showing that the rods do self-assemble using azoTAB as a depletant (**Table 1**). Further proof of NR self-assembly using azoTAB depletant (e.g., SAXS, optical microscopy) is discussed later. Basic characterization of both the passive C5-NRs was performed as noted in **Chapters 2 and 3** for the methods, and **Chapter 4 (Article SI)** for the typical results.

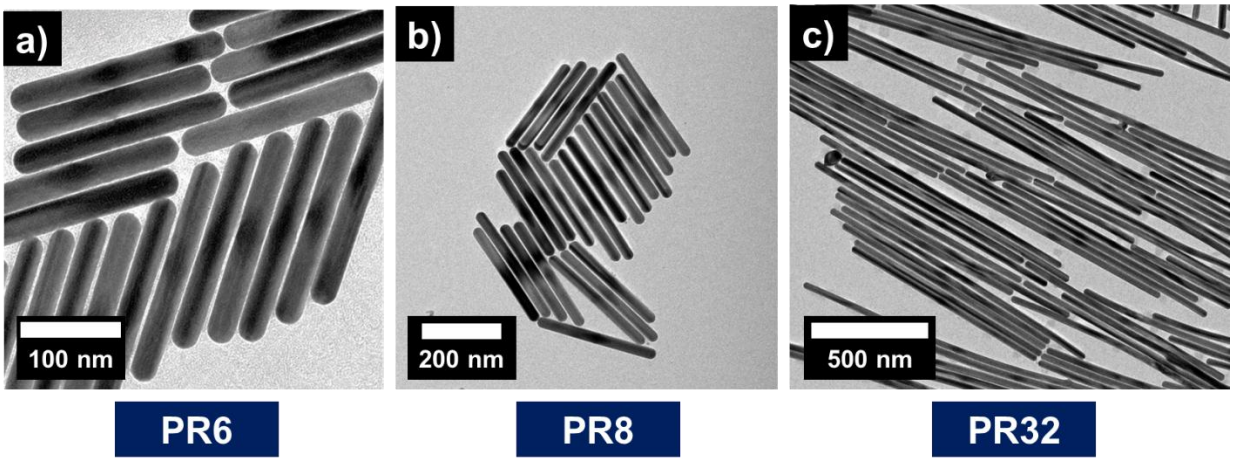

Figure 7. Preparation of photo-DISA components: passive metal NRs of varying length. (a) *PR6 (AuBP@Ag6eq.),* ***(b)*** *PR8 (AuBP@Ag8eq.),* ***(c)*** *PR32 (AuBP@Ag32eq.).*

Table 1. Dimensions and self-assembly threshold in [AzoTAB] of the representative pentatwinned NRs batches used for photo-DISA.

NR	equivalents of Ag	NR length	NR width	aspect ratio (AR)	*dark* experimental self-assembly threshold (*8A2, trans*)	*UV* experimental self-assembly threshold (*8A2, cis*)
PR32	**32**	1060 ± 230 nm	30.6 ± 1.6 nm	34.6 ± 0.4	6 mM	2 mM
PR8	**8**	299 ± 26 nm	27.1 ± 1.5 nm	11.0 ± 1.1	50 mM	20 mM
PR6	**6**	259.1 ± 15.7 nm	30.6 ± 1.0 nm	8.47 ± 0.7	85 mM	40 mM

Among the four different azoTABs, C_8AzoOC_2 (8A2) and C_2AzoOC_2 (2A2) were prioritized for photo-DISA experiments, since the other compounds C_4AzoOC_6 (4A6) and C_6AzoOC_4 (6A4) were too poorly soluble in water from 15-50 °C, and often yielded turbid mixtures with solid azoTAB precipitate in suspension especially above 100 mM, meaning that the real molar concentration of azoTAB in the form as micellar depletants was low, and differed much from the total azoTAB concentration in the mixture, with such in the form of undissolved precipitates or crystals. 2A2 also served as a good control for 8A2, in order to compare the effect of a high tail vs. spacer length difference, from the case of 2A2 which was inferred to adopt nearly spherical micelles in both the trans and cis state[40,43]. As noted previously (**Chapter 3**), the azoTABs were characterized by ^{1}H-NMR, SAXS, UV-vis-NIR extinction spectroscopy, and gravimetric analysis (i.e., weight fractions of azoTAB in supernatant vs. precipitate) in both the trans and cis isomers, to verify their chemical structure and purity, probe their micellar structure, and make sure they properly photoisomerize as expected when exposed to UV or blue light (**Figure 8**). By ^{1}H-NMR, the 8A2 batch was found to be 83% pure, while the 2A2 batch was about 91% pure. In spite of this impurity however, the experimental and theoretical depletion thresholds using these azoTABs were still in good agreement, suggesting that the impurities do not appreciably affect the number concentration of micellar depletants in suspension. Finally, we also note that, as the trans-cis photoisomerization is a *dynamic equilibrium*, light irradiation can never obtain either a system of 100% trans or 100% cis azoTAB. Rather, for a set of irradiation conditions (e.g., light intensity or irradiance, wavelength), for a certain azoTAB concentration, and for each azoTAB's absorption spectrum, the system evolves toward a photostationary state (PS), a steady state where the fraction of trans vs. cis isomers stops changing, as evidenced by a steady state UV-vis absorption spectrum. Under the irradiation conditions used in this project, the PS is reached in around 2

to 3 min for UV light reaching around 80 to 90% cis vs. 20 to 10% trans composition, according to known literature. On the other hand, an azoTAB solution left in the dark will thermally relax towards a nearly 100% trans composition, with a characteristic time dependent on the azoTAB tail and spacer lengths[40,43,47].

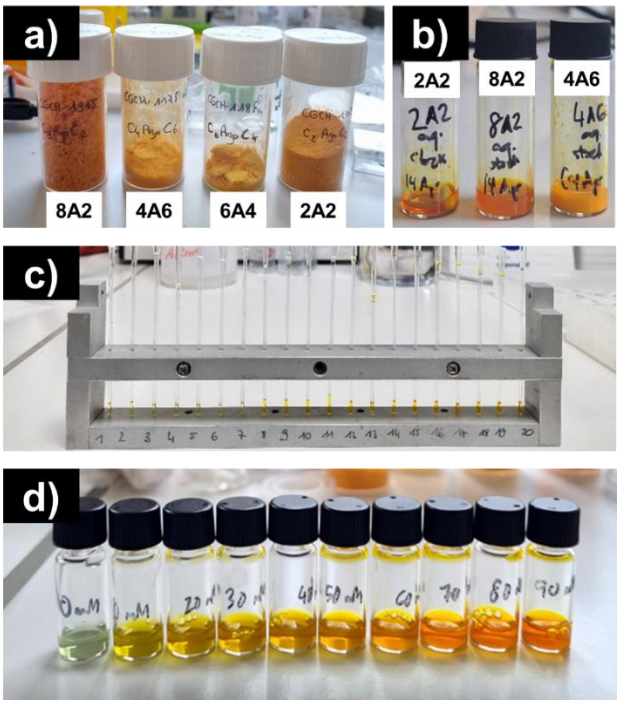

Figure 8. Preparation of photo-DISA components: active azoTAB photosurfactant. ***(a)*** *Solid powders of purified azoTABs, synthesized in-house.* ***(b)*** *Concentrated aqueous stock solutions (400 mM) of 2A2, 8A2, and 4A6 azoTABs, with varying amounts of undissolved solids.* ***(c)*** *SAXS analysis preparation: round glass capillaries filled with aqueous 2A2 and 8A2 solutions of increasing concentrations.* ***(d)*** *Screening of NR (PR8) depletion self-assembly threshold with 8A2 in the dark state, with increasing [8A2] left to right, 0 to 90 mM.*

By doing both fitting of 1D SAXS radial profiles of 8A2 azoTAB solutions in dark and in UV (**Figure 9**), and NR assembly test series (by *fast DISA via one-shot mixing of NRs and azoTAB*, **Figure 8d**) at increasing azoTAB concentrations for 8A2 and 2A2, we could estimate the shape anisotropy and size of the micelles acting as depletant. The full fitting results for 2A2 are not yet complete, as the current SAXS data does not go far enough into the high q-range to fully see and fit the micellar form factor oscilaltions. Still, it was discovered that in general, 8A2 micelles adapt an oblate ellipsoid geometry with an anisotropic shell (i.e., the shell radius is larger near the equator than at the poles), with greater anisotropy in the trans state versus

2A2. Note that in our model, the core and shell are defined by their contrast in X-ray scattering length densities (SLD). This means that the core is comprised of the aliphatic tail, while the shell contains the rest of the azoTAB molecule – the azobenzene moiety, the charged trimethylammonium head, the condensed Br^- counterions, and absorbed water molecules in the shell region (**Figure 9a**).

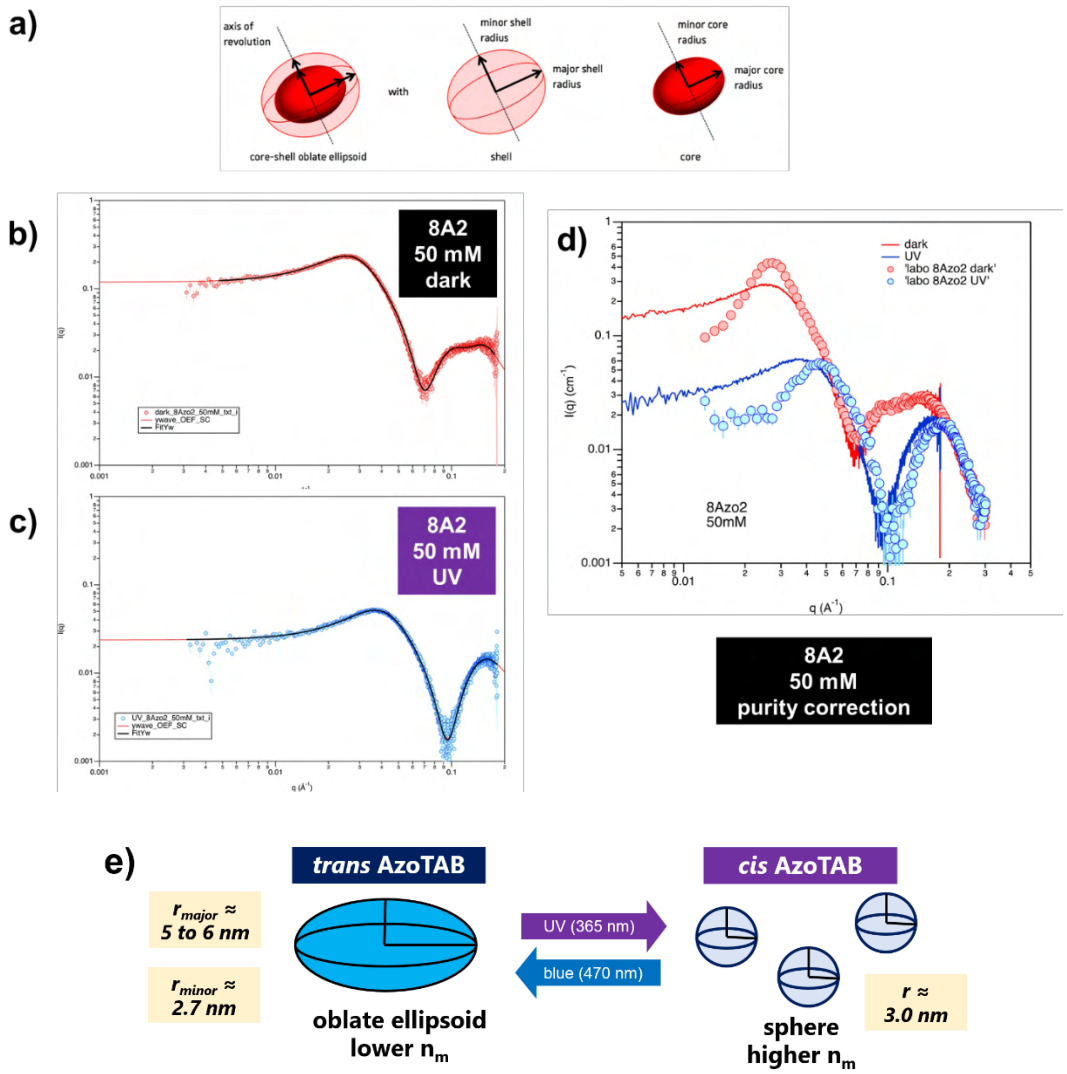

Figure 9. Studying the structure of azoTAB micelles by SAXS fitting. ***(a)*** *Core-shell oblate ellipsoid structure of the 8A2 azoTAB micelle.* ***(b)*** *SAXS fitting of 8A2 50 mM in the trans photostationary state (dark) and* ***(c)*** *the same sample in the cis photostationary state (UV) using a* ***core-shell oblate ellipsoid form factor****, and a* ***Hayter MSA structure factor****.* ***(d)*** *Correction factor for purity of 8A2. Fitting was done by our collaborator J. Combet (ICS Strasbourg).* ***(e)*** *Scheme of the change in azoTAB micelle size, shape, and number density in trans versus cis isomers.*

The fitting results for 8A2 micelles at two [azoTAB] concentrations are laid out in **Table 2**. Three major findings must be noted from this fitting. First, in agreement with literature, the trans 8A2 micelles (form in the dark state) grow 'fatter', preferentially along the equatorial axis as azoTAB concentration is increased. Note that the number of micelles also increases with increasing [azoTAB], evidenced by increasing intensity at low q and a growing structure factor. Still, the average micelle size and aggregation number also grows. The dimensions for 8A2 micelles in the range of 20, 50, and 100 mM matches the range of values in previous publications[40,43]. Second, the cis micelles (form under UV) are much smaller in volume, and closer to a spherical shape. Quantitatively, there is an approximately threefold decrease in aggregation number ($N_{agg,dark}$ / $N_{agg,UV}$) (i.e., the number of surfactant molecules per micelle) and in micelle volume, and thus a *threefold increase in the number concentration* of micelles, meaning a similar increase in depletion force. This agrees well with our experimental depletion threshold screening of the NRs in 8A2, where *the threshold in dark (trans) is about two to three times more than in UV (cis)* (**Table 1**). Third, the experimental azoTAB curves in absolute scaling roughly confirmed the known degree of impurity of our 8A2 samples, as the magnitude was slightly less compared to previously known pure 8A2 and 2A2 samples made in ICS Strasbourg.

Table 2. Geometric parameters of azoTAB micelles in water from 1D SAXS data fitting: *comparing 20 mM and 100 mM azoTAB in the dark and UV irradiated states.*

20 mM

8A2, 20 mM | trans (dark)			
	$radius_{core}$ (Å)	V_{core} (Å³)	$N_{agg} = V_{core} / V_{tail}$
major	43.2	93807	387
minor	12.0		
	$radius_{micelle}$ (Å)	$V_{micelle}$ (Å³)	$N_{agg} = V_{core} / V_{8A2}$
major	52.9	323526	513
minor	27.6		

8A2, 20 mM | cis (UV)			
	$radius_{core}$ (Å)	V_{core} (Å³)	$N_{agg} = V_{core} / V_{tail}$
major	28.7	41403	171
minor	12.0		
	$radius_{micelle}$ (Å)	$V_{micelle}$ (Å³)	$N_{agg} = V_{core} / V_{8A2}$
major	36.3	128605	204
minor	23.3		

$N_{agg, dark}$ / $N_{agg, UV}$	
core	2.26
micelle	2.51

100 mM

8A2, 100 mM | trans (dark)			
	$radius_{core}$ (Å)	V_{core} (Å³)	$N_{agg} = V_{core} / V_{tail}$
major	51.8	134874	556
minor	12.0		
	$radius_{micelle}$ (Å)	$V_{micelle}$ (Å³)	$N_{agg} = V_{core} / V_{8A2}$
major	60.5	410285	650
minor	26.8		

8A2, 100 mM | cis (UV)			
	$radius_{core}$ (Å)	V_{core} (Å³)	$N_{agg} = V_{core} / V_{tail}$
major	29.1	42565	175
minor	12.0		
	$radius_{micelle}$ (Å)	$V_{micelle}$ (Å³)	$N_{agg} = V_{core} / V_{8A2}$
major	34.4	118469	188
minor	23.9		

$N_{agg, dark}$ / $N_{agg, UV}$	
core	3.18
micelle	3.46

Interestingly, as will be discussed in the next sections, while both 8A2 and 2A2 could induce DISA of C5-NRs, only 8A2 induced a detectable increase in depletion force upon isomerization to the *cis* form upon UV irradiation, due to the greater initial anisotropy of the 8A2 micelles[40,43]. This was determined via SAXS, measuring the average side-by-side inter-NR gap in colloidal '1D needle' assemblies of PR32. As seen in **Figure 10**, the lattice parameters using 8A2 are consistently larger at all [azoTAB] versus 2A2, suggesting an overall larger effective micelle size, accounting for its hydrodynamic size due to electrostatic repulsion. The overall larger size of 8A2 molecules means both a longer range of depletion force, and a larger minimum inter-NR gap distance at high [azoTAB]. More on the differences between 8A2 and 2A2 as active depletants will be discussed in the next section.

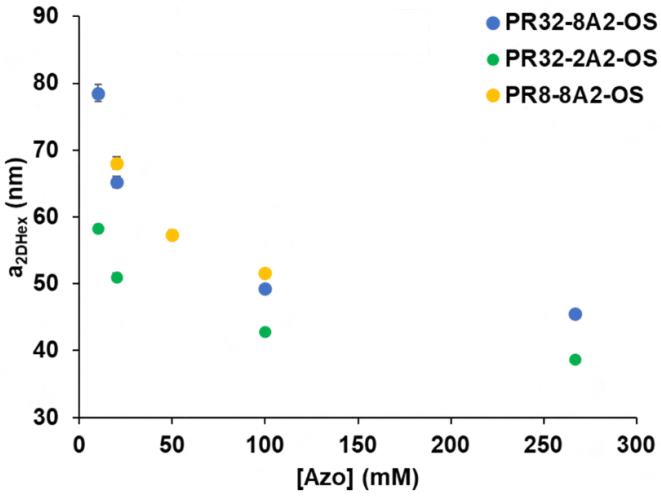

Figure 10. Trend in inter-NR gap in C5-NR assemblies with different azoTABs (8A2 vs. 2A2): [azoTAB] series.

Reversible light-controlled assembly into 1D 'needles'

After studying the basic characteristics of the C5-NR + azoTAB photo-DISA system, we then proceeded to investigate its behavior under UV (365 nm) and under blue (470 nm) light irradiation, whether and in what way photo-DISA could be induced. To test the induction of photo-DISA, we prepared C5-NR – azoTAB aqueous mixtures at different [azoTAB], injected them into optical capillaries, and exposed them to UV or blue LED light at the highest power

setting; the full procedure for sample preparation and irradiation is found in the methodology (**Chapter 2**). Following UV irradiation of samples above the [azoTAB] 'UV' depletion threshold but below the 'dark' depletion threshold (**Table 1**), the formation of micron-sized and Brownian 1D needle-like structures was observed within 2 to 5 min. When the [azoTAB] is close to the UV depletion threshold, blue light irradiation then induces disassembly of these structures within 1 to 5 min, slightly faster than the assembly. By optical microscopy, UV-vis-NIR absorption, and SAXS, we confirmed that these needles are indeed side-by-side assemblies of the C5-NRs. Interestingly, for both PR8 and PR32, and for both 8A2 and 2A2, only 1D needles were formed, and no 2D platelet-like assemblies were observed, except in very rare instances of ultra-slow addition of azoTAB or bizarre confinement conditions (**Figure 11**). This is inferred to be an effect of the fast DISA kinetics, in turn due to the fast increase in depletion force because of the azoTAB photoisomerization completed in around 3 min (**see Chapter 4, Perspectives**).

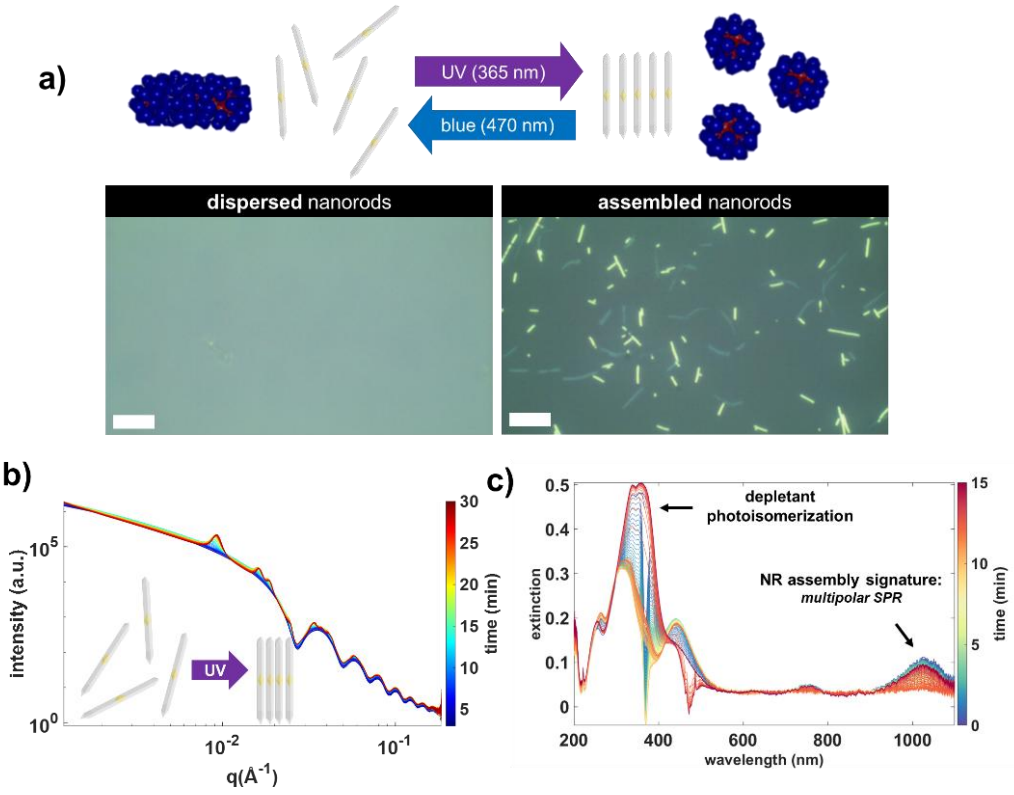

Figure 11. Light control of depletion: Reversible phototunable depletion-induced self-assembly (photo-DISA). (a) *Scheme of photo-DISA and in situ optical microscopy images of a C5-NR (PR8) – azoTAB (8A2) suspension before and after photo-DISA.* ***(b)*** *SAXS kinetics of photo-DISA upon UV irradiation: Progressive self-assembly of PR32 (in 8A2 2 mM) into needles of stacked side-by-side NRs.* ***(c)*** *UV-vis-NIR extinction kinetics of photo-DISA (PR8 + 8A2 20 mM) upon UV then blue irradiation: Self-assembly (t = 0 to 10 min) then disassembly (t = 10 to 15 min).*

For each NR size, we experimentally noted two critical concentrations of azoTAB. The lower UV depletion threshold, as noted in the previous section, is the minimum [azoTAB] to have no NR assembly in the dark or after blue exposure, and assemblies after UV exposure. The higher dark depletion threshold is the minimum [azoTAB] to already have NR assemblies without UV exposure, and where UV exposure simply decreases the interparticle gaps in the assemblies. These concentrations are a direct function of the effective interaction areas of the lateral face of the NRs. We found that between the lower and higher thresholds is the [azoTAB] regime for cyclable *assembly-disassembly*, while above the higher threshold is the regime for cyclable *contraction-expansion* of the side-by-side assemblies, due to further modulation of the depletion force acting on existing NR assemblies.

By SAXS data, these 1D needles were found to be assemblies of side-by-side C5-NRs, evidenced by the transition over time from the NR form factor to sharp Bragg peaks corresponding to a 2D hexagonal lattice of NRs. The existence of a 2D lattice implies that the needles are in fact thicker stacks of several side-by-side chains, rather than single 1D chains. However, the exact stacking of side-by-side NR chains into thicker structures is not yet fully known, given that the thin needles often exhibit a 2D hexagonal symmetry by SAXS. Additionally, by in situ optical microscopy, these needles exhibit very dynamic behavior, often breaking and reforming or joining with other needles. This suggests that they assemble by a non-classical assembly crystallization mechanism, and that the strength of the depletion force holding them together is only slightly above that of thermal agitation (4-5 kT)[19,21,33]. Snapshots of this dynamic needle behavior, including the UV/blue induced assembly-disassembly are shown in **Figure 12**.

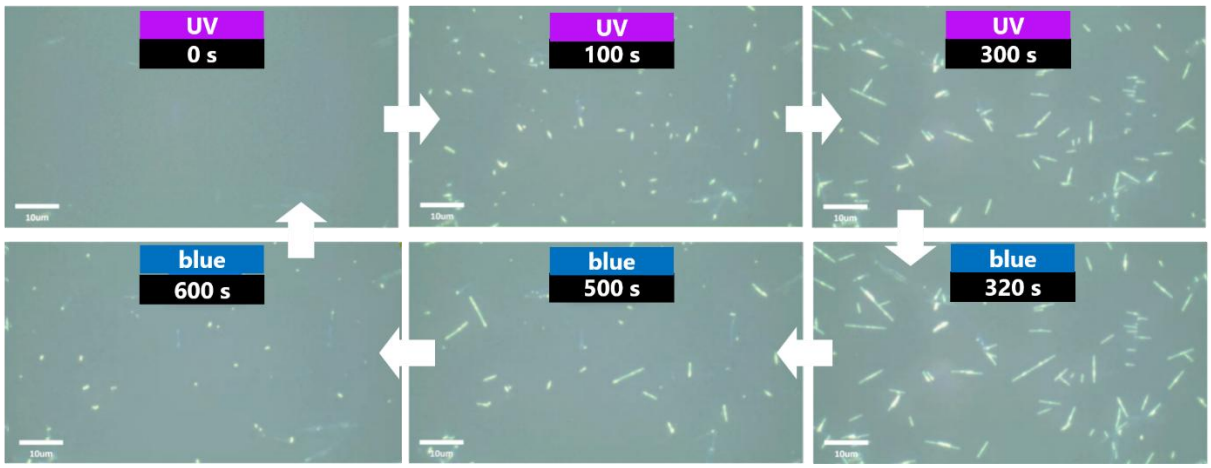

Figure 12. Optical microscopy in reflection: *Video snapshots of progressive photo-induced 'needle' assembly and disassembly of PR6 NRs in 40 mM 8A2 azoTAB, upon illumination with UV (365 nm, 5 min) and blue (470 nm, 5 min) light respectively. This experiment done by our master's intern Phuong-Lan Dao*

Further discussion of both cyclic assembly-disassembly and cyclic contraction-expansion of the 1D needles follows in the next sections. Interestingly, it was found that only the 8A2 surfactant could induce detectable modulation of the inter-NR gap in the needles, while no modulation was observed using 2A2 (**Figure 13**). We conclude then that 2A2 photo-isomerization does not appreciably increase the overall number of micelles (i.e., depletant particles), while 8A2 does. This agrees with previous literature that a greater difference in tail vs. spacer length causes a greater curvature change upon photo-isomerization[40,43,48]. Also, as noted earlier, depletion with 2A2 yields shorter inter-NR gaps versus 8A2, due to the smaller effective micelle size. Such shorter gaps could make 2A2-induced assemblies more susceptible to kinetic trapping when the attractive depletion forces are too 'sticky' and harder to reverse[11,49].

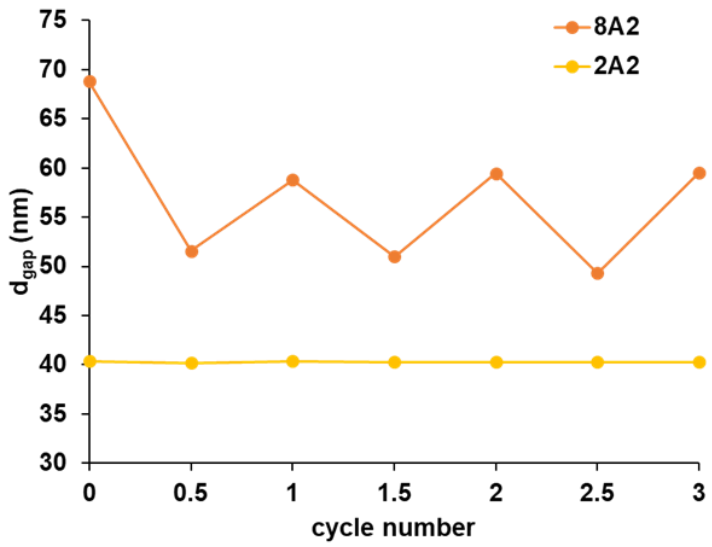

Figure 13. Cycling of inter-NR gap in needle assemblies of PR32: *8A2 versus 2A2 azoTAB.*

Controlling, modelling, and verifying the photo-depletion mechanism

At this point, it is not yet proven that the reversible light-controlled NR assembly into needles is directly due to a depletion-induced mechanism (i.e., because of a change in depletion force of free micellar depletants in suspension) and not due to some other light-induced effect.

To test that the formation of the needles is due to photo-depletion *specifically due to UV-induced azoTAB isomerization*, we first decided to rule out the two most likely competing mechanisms: (1) solvophobic / polarity effects due to azoTAB adsorption onto the metal NR surface, or (2) photothermal heating leading to aggregation, due to some unverified mechanism. To perform these tests, a special batch of C5-NRs was prepared where the typical CTAC ligand bilayer protecting the rods was replaced by a monolayer strongly-binding thiol surfactant called MUTAB, a close analog of CTAB, which would passivate the NR surfaces by sterically hindering the adsorption of azoTAB (**see Chapter 2**). Then, various mixtures of these 'thiolated' rods (NR-MUTAB) would be subjected to the same photo-DISA assembly protocol, making aqueous NR + azoTAB mixtures and irradiating with light. In these tests, two parameters were varied, the depletant (*with azoTAB, or without azoTAB, or with CTAC as a passive depletant*) and the wavelength of light irradiation (*UV or red*), with the non-azoTAB and red irradiated samples serving as control conditions. Among these conditions, only the simultaneous presence of azoTAB and UV irradiation induced the formation of any assemblies,

specifically needles. This positive result proves that the assembly is indeed a wavelength-specific phenomenon due to azoTAB photo-isomerization, and as the NR surfaces were passivated by MUTAB, the assembly was not due to solvophobic or polarity effects (**Figure 14**). To rule out photothermal effects as the cause of the needle formation, we are currently conducting both temperature measurements of our photo-DISA samples at illuminated by LEDs (365 nm, 470 nm, 660 nm) at varying irradiance, and also directly heating up PR + azoTAB mixtures from around 30 to 50 °C to check for any self-assembly. No definitive results have yet to come from these ongoing experiments, but it is expected that there would be negligible sample heating from LED irradiation, even at close sample-to-LED distances of a few mm.

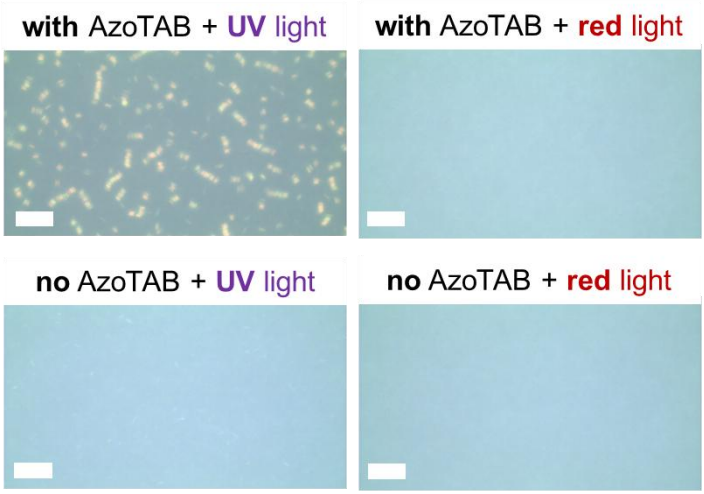

Figure 14. Photo-DISA control experiments: *Verifying a depletion-induced mechanism of self-assembly due to azoTAB isomerization under UV light. Scale bars are 10 µm.*

UV-vis-NIR absorption provided additional supporting evidence that the formation of C5-NR assemblies is casually linked to the light-induced photoisomerization of the azoTAB. The azo isomerization can be followed by changes in azobenzene moiety absorbance in the 250 to 550 nm range, while the NR assembly is followed by the broadening and disappearance of the multipolar longitudinal SPR modes at around 1050 nm and 770 nm[43,50,51]. The start of the disappearance of the multipolar SPRs is delayed by about 30 s to 1 min versus the change in the azobenzene absorbance, suggesting causality. Nonetheless, as discussed in the next section, further control experiments are required to establish causality and ascertain that the mechanism is induced by photo-depletion (**Figure 15a**). However, as will be reported later, via SAXS, no delay was observed in the case of cycling between *contracted-expanded* states. The

delay in the case of assembled-disassembled cycling suggests that this process requires some initial activation energy to start, or that it has a degree of hysteresis.

In agreement with previous studies on azoTAB-based and similar systems[23,52], by fitting our UV-vis-NIR kinetics data – following both the azoTAB absorbance at 441 nm and the NR multipolar mode (at 847 nm for the PR6 multipolar M_2 SPR mode), we conclude that both the azoTAB photoisomerization and the NR SPR decay in our photo-DISA system follows first-order kinetics, fitted with a single-exponential model, which is also the known kinetics for azoTAB isomerization. This result reinforces a clear causal link between the two, and that the rate-limiting step of this photo-DISA is the photoisomerization, and is not NR or depletant diffusion, nor is photo-DISA limited by some other physical process. This marks an interesting result in that both solvophobic and depletion-induced assembly, when both induced by azo-isomerization, follow similar rate laws.

It was found that the azoTAB trans-to-cis and cis-to-trans photoisomerizations had half-lives of 81.0 s and 21.4 s, respectively, in agreement with other studies on azoTABs[47,53,54]. Additionally, both the NR assembly and disassembly processes followed by the PR6 M_2 mode were well described by a first-order single-exponential model yielding coefficients of determination of R^2=0.996 and 1.000, respectively. The extracted characteristic relaxation times were $\tau_{assembly}$ = 649.3s and $\tau_{disassembly}$ = 468.5s, corresponding to half-lives of 450.1 s and 324.8 s, respectively (**Figure 15b,c**).

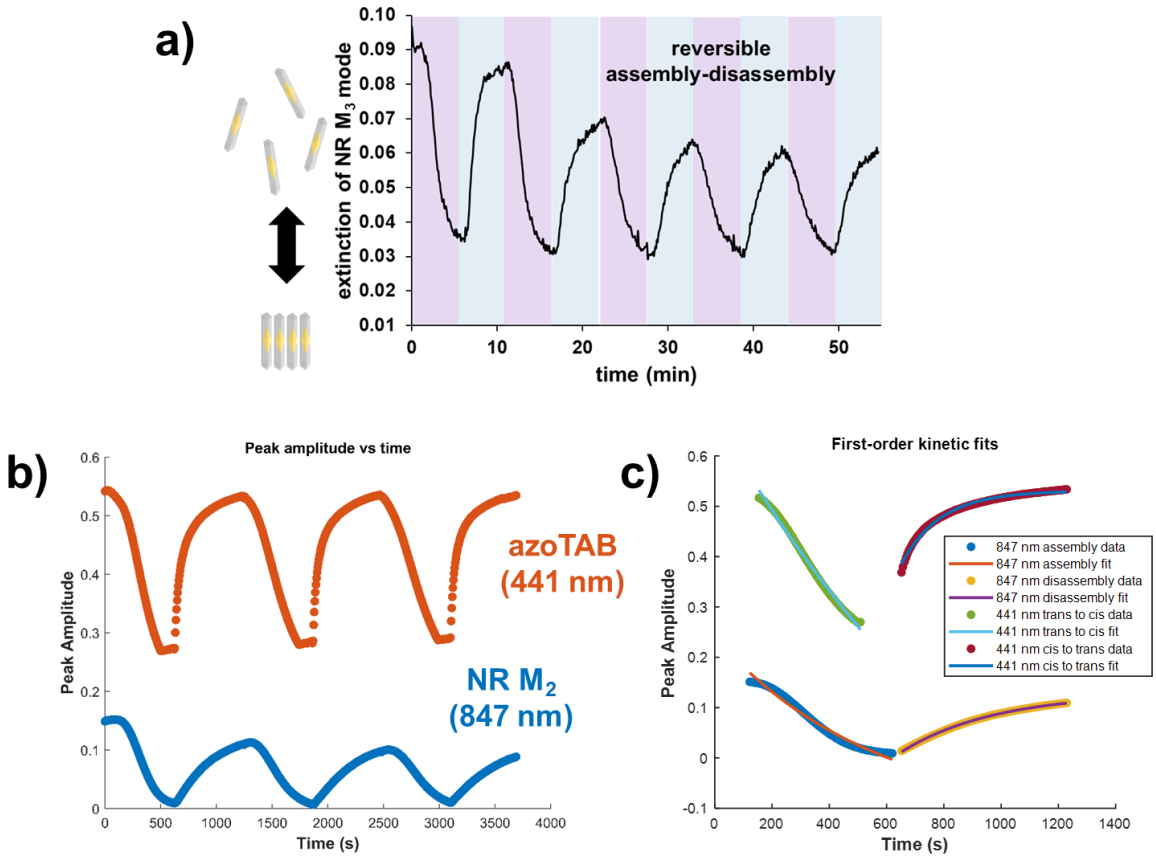

Figure 15. Kinetics and causality of the photo-DISA process: (a) *Simultaneous monitoring via UV-vis-NIR kinetics of the 8A2 azoTAB isomerization and C5-NR (PR8) self-assembly, showing temporal correlation.* ***(b)*** *The same UV-vis-NIR kinetics monitoring but for PR6 self-assembly.* ***(c)*** *Exponential fitting (first-order) of the time-evolving extinction of the 8A2 azoTAB isomerization and PR6 self-assembly after UV (assembly) and blue (disassembly) illumination.*

To further check our photo-depletion mechanism, we compared the experimental inter-NR gap distance (d_{gap}) in the needle assemblies versus the theoretical d_{gap} calculated as the potential well minimum via the DLVO/AO model (**see Chapter 3**), simplifying the rods as parallel plates of silver in a suspension of spherical Brownian micelles broadly modelling the azoTAB micelles. In this model, we consider three forces acting on the particles: van der Waals forces, electrostatic repulsion, and attractive depletion, as used in **Chapter 4** on DISA-based metasurfaces[11,55,56]. Here, we assume that due to the minimal eccentricity of the trans azoTAB micelles compared to their hydrodynamic size and mean free path, the ellipsoidal shape of the micelles can be ignored in their contribution to these three forces, and can instead be modelled as spheres with an appropriate effective radius, typically around 5 nm for the trans azoTAB micelles, and 2 nm for the cis case. Compared to Chapter 4, in comparing the potentials in the 'dark/blue' trans and 'UV' cis states, we switch out only the effective radius.

Doing the DLVO calculation, one finds that, in the *assembly-disassembly regime*, there is an appearance of one or two negative potential wells (about 2 to 5 kT deep) after UV irradiation where there was no well initially. In the *contraction-expansion regime*, there is a shift of the depletion-dominated well position towards shorter gap distances after UV irradiation, with good agreement between d_{gap} determined by SAXS and that calculated by DLVO (**Figure 16**).

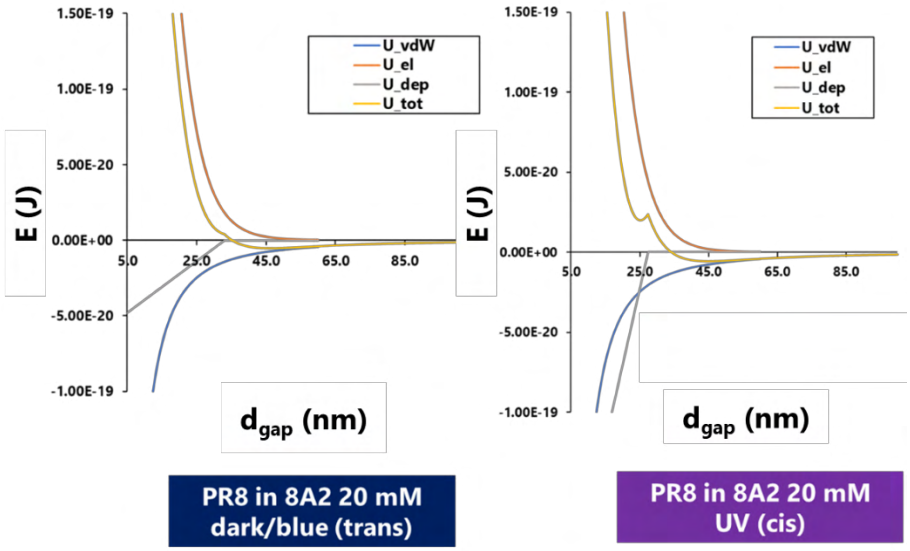

Figure 16. Theoretical DLVO depletion potential between two C5-NRs (PR8). (a) *PR8 in 8A2 20 mM, trans isomer in dark/blue,* ***(b)*** *PR8 in 8A2 20 mM, cis isomer in UV.*

Nonetheless, there still exists some minor discrepancies in the well minima between model and experiment, often within the range of 1-3 nm. An accurate comparison of the depletion model d_{gap} and the experimental d_{gap} is still limited by remaining uncertainty in the purity of our synthesized azoTAB, despite the range of purity known by ^{1}H-NMR and SAXS fitting, and uncertainty in the fractional charge of the azoTAB micelles, which is not well-known in the literature, and could only be crudely estimated with our previously mentioned SAXS fitting, particularly with the Hayter MSA structure factor model.

Cyclable behavior of the assemblies

Next, we consider the robustness of the cyclability of our photo-DISA system. We will also touch on some interesting and unexpected effects of repeated UV/blue irradiation on the structure of the C5-NR assemblies and the azoTAB phase. The main experiments were

conducted with the help of our master's intern Phuong-Lan Dao, and done with a homemade programmable illumination setup (PhotoSwitch) made with the instrumentation team of our laboratory in LPS. The PhotoSwitch setup consists of two LEDs, UV (365 nm) and blue (470 nm) whose light is collimated and directed into an exit hole into which an optical fiber can be connected, to locally direct the LED light to a desired region of a sample. The LED switching and power is run by a control box which can be remotely controlled through a PC via an ethernet connection, allowing precise pre-programmed illumination profiles in time and power (**Figure 17**, **Chapter 3**).

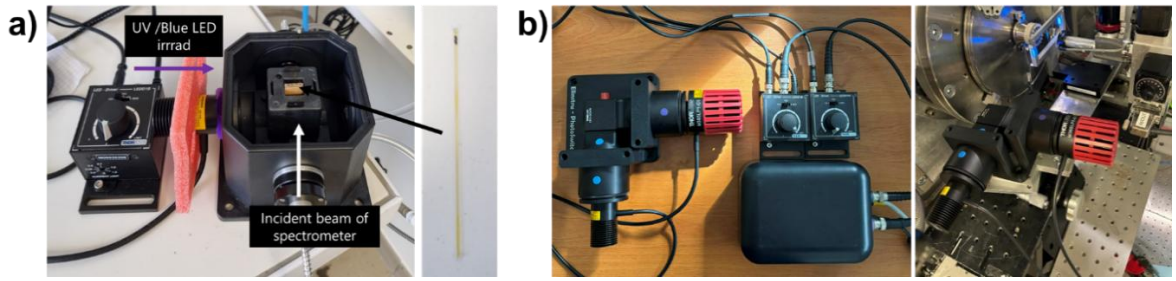

Figure 17. Photo-DISA illumination setups. (a) *Initial LED irradiation and spectrometry setup for UV-vis-NIR kinetics for in situ study of the photo-DISA process.* ***(b)*** *Completed remote-controlled 'PhotoSwitch' illumination used for in situ photo-DISA during SAXS measurements.*

Armed with this setup, we investigated both cyclic assembly-disassembly and cyclic contraction-expansion for PR6 or PR8, and for PR32 C5-NRs, especially with SAXS to probe real time structural changes in the needle assemblies in response to light. Four major findings were noted. First, cyclability of both assembly-disassembly and contraction-expansion was observed only close to the lower (UV) and higher (dark) critical self-assembly threshold values of [azoTAB], where depletion forces were low enough to allow for structural changes in the needles. The fully cyclability of assembly-assembly was observed by SAXS, as evidenced the sequential appearance of Bragg peaks during UV illumination, implying the existence of long-ranged ordered superstructures of NRs, followed by the disappearance of the Bragg peaks during blue illumination (**Figure 18**).

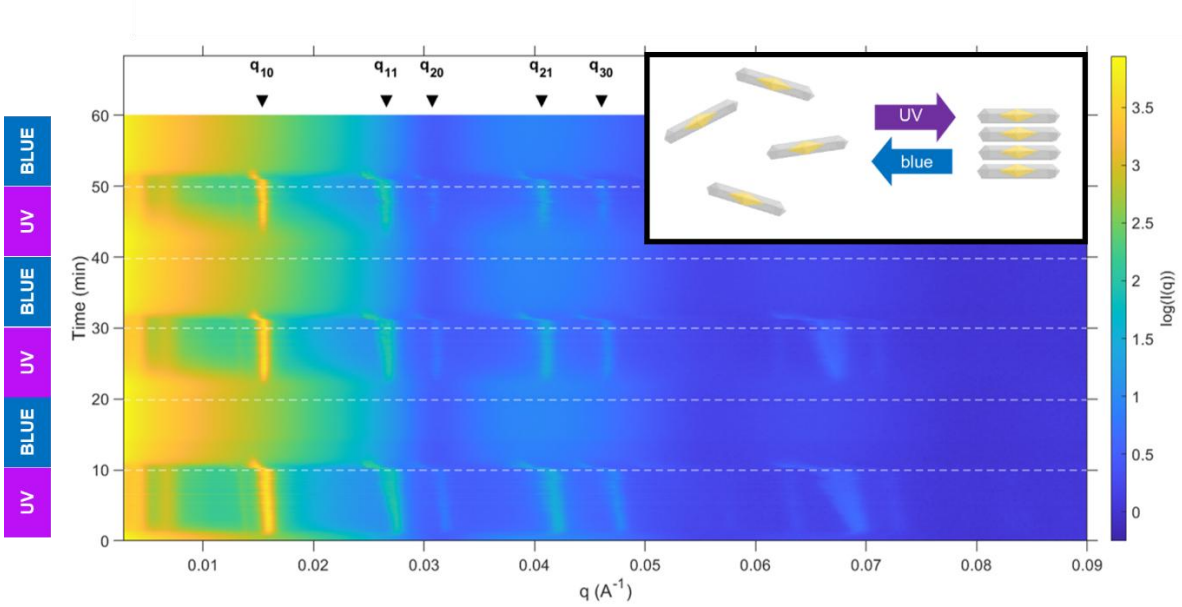

Figure 18. *Heat map of 1D radial SAXS profiles: Fully reversible and cyclic assembly-disassembly of PR6 NRs in 40 mM 8A2 upon UV and blue illumination.*

At much higher [azoTAB], no cycling in assembly degree or inter-NR gaps was observed, even when the real depletion force would change. This can be explained by two connected factors. First, the inter-NR gap does not change very much at very high [azoTAB] (**Figure 10**). Second, when the system is close to the critical [azoTAB], the attractive potential wells experienced by the nanorods are quite shallow, close to 4-5 kT, while at higher [azoTAB], the deeper potential wells cause kinetic trapping of the system[11,19,33,57]. Second, both assembly-disassembly and contraction-expansion were reversible for at least five cycles when close to the aforementioned UV and dark thresholds. Specifically, one can recover up to around 90% of either the original lattice parameter or X-ray scattering intensity in five cycles. This good cyclability supports the case of photo-DISA for use in active and programmable assemblies (**Figure 19**).

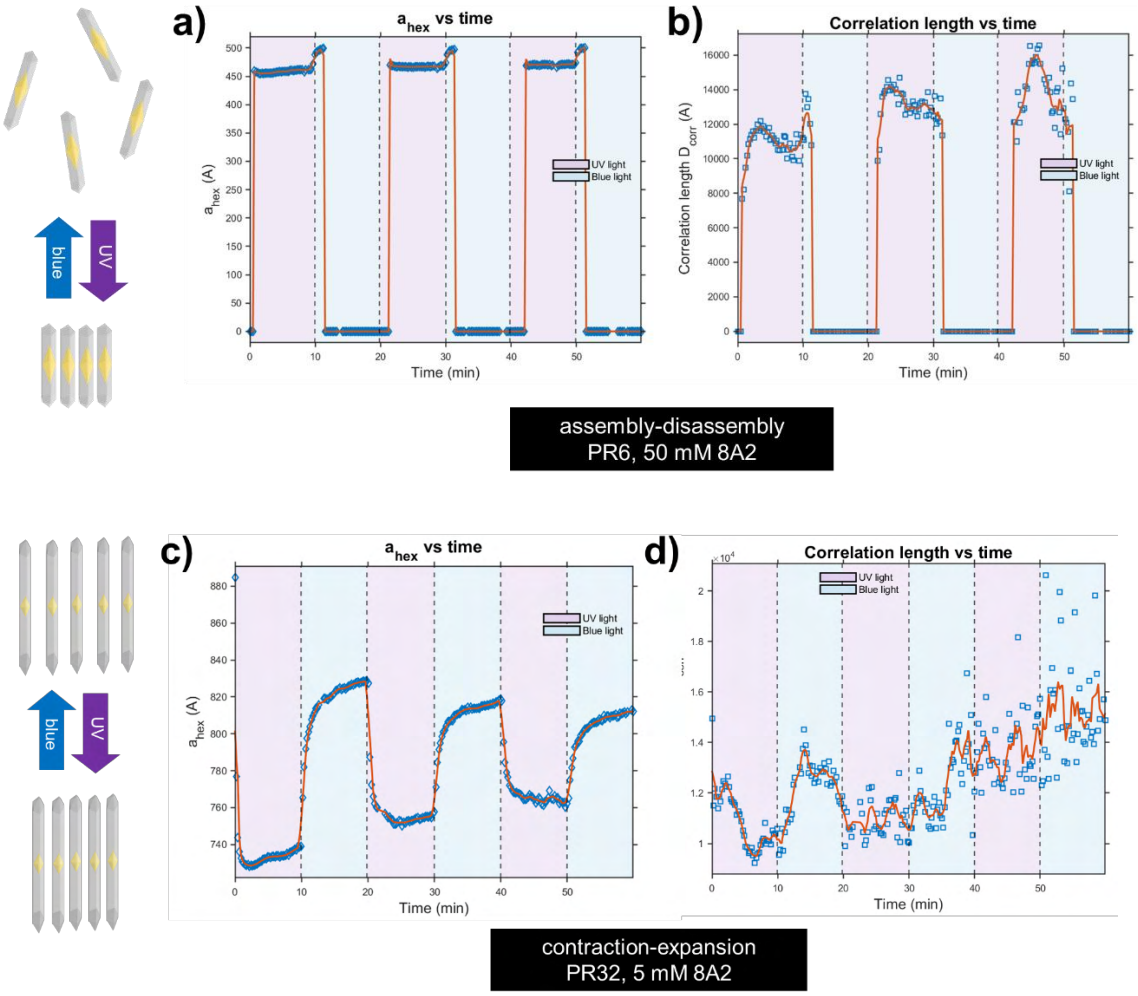

Figure 19. Cycling behavior of the photo-DISA system monitored by the assembly lattice parameter (a_{hex}) and correlation length (domain size): (a-b) *Assembly-disassembly (PR6, 50 mM 8A2),* ***(c-d)*** *Contraction-expansion (PR32, 5 mM 8A2).*

Third, there is an approximate 1 min delay in assembly-disassembly onset after UV or blue irradiation respectively, while there is no appreciable delay in contraction-expansion. As noted similarly before on the UV-vis-NIR extinction kinetics, this implies that there is some activation energy threshold of depletion strength required to initiate assembly and disassembly, or that there is some kinetic trap causing this delay, which may be linked to the entropic nature of depletion. Fourth, repeated cycling of both assembly-disassembly and contraction-expansion causes a slow increase and greater spread in crystalline domain size (*correlation length*) of the colloidal needles. Fast cycling between states of high and low depletion force, with full cycles lasting from 10-20 min, appears to increase the entropy in the system. Interestingly, repeated changing of inter-NR gap caused the d_{gap} in the trans and cis states to approach each other, towards an equilibrium d_{gap}, akin to a 'pendulum dampening' effect (**Figure 19c**). Similarly, as

noted earlier, repeated assembly-disassembly causes the multipolar SPRs of the NRs to approach an equilibrium extinction, with a similar dampening effect. It is notable that this dampening occurs despite the relatively long UV/blue full cycling time (10-20 min) compared to the speed of azoTAB isomerization to the photostationary (PS) state (1-2 min), or the attainment of the stable assembly structure in the UV or blue PS states (3-5 min)[43,53]. This observation is due to either some kinetic or hysteresis effects due to the UV/blue cycling, or could be due to partial X-ray bleaching of the azoTABs during the prolonged SAXS measurements. Preliminary studies have already been done comparing fast (5 min full cycle) versus slow (30 min full cycle) UV/blue cycling times, but no conclusive results have yet been drawn.

Interestingly, it was discovered that our photo-DISA system is very sensitive to small changes in ionic strength. By adding small amounts of salt such as NaCl, one can tune both the speed of assembly/disassembly, as well as the extent of reversibility of this assembly. In general, increasing ionic strength decreased both the assembly and disassembly speed. Small additions of salt can also enable reversibility of assembly that is normally irreversible at a certain [azoTAB] (**Figure 20**). We have tried to rationalize this effect via theoretical DLVO calculation of the inter-NR potential well. At low added salt concentrations, the potential well is sometimes smoothened and widened, which could explain increased reversibility. Physically speaking, this can be explained by increased charge screening, or by changes in the surface charge of the NRs[55,58]. It is important to note that first, salt addition also changes the size and shape of the azoTAB micelles, and second, a full theory explaining this salt effect cannot yet be proposed here. However, additional information will be gained from ongoing further studies.

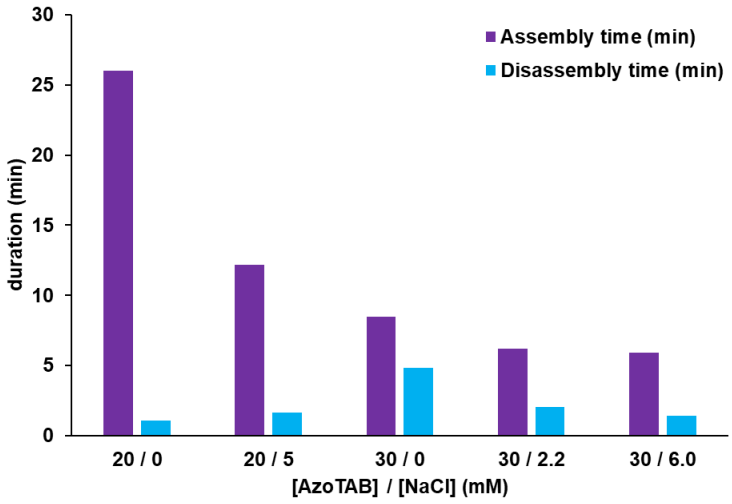

Figure 20. Tuning assembly and disassembly time with ionic strength: *PR8 assembled by photo-DISA in varying [8A2] and [NaCl].*

Active plasmonics: Light-controlled SERS for analyte detection

As a proof of concept for light-controlled plasmonic detection, we then tested photo-DISA as a means of modulating the degree of surface-enhanced Raman scattering (SERS) of analyte molecules (e.g., organic dyes or pollutants) between or on metal nanoparticles, to achieve light-modulable detection. The hypothesis is that by photo-switching between either assembled-disassembled or contracted-expanded needle states, one can use light to control the plasmonic enhancement between the side-by-side metal NRs, and thus modulate the SERS signal of a compound close to or adsorbed onto the NR surfaces. Similarly to the previous chapter, a mixture of C5-NRs and depletant, in this case PR8 and 8A2, was put into an optical capillary and probed with Raman microscopy. Here, we probed two main analytes: 4-aminothiophenol (4ATP) using a 633 nm red excitation laser, and methylene blue (MB) using a 532 nm green laser. In both cases, a low concentration solution of the analyte was directly injected into the PR8 – 8A2 mixture, without its direct grafting or functionalization onto the NR surface (**Figure 21a**).

Two main questions were posed regarding light-controlled SERS. First, does photo-induced cycling of assembly-disassembly or of contraction-expansion induce a notable change in SERS counts of an analyte. Second, if yes, is this change fully reversible and cyclable? Does the

cycling cause a hysteresis in the SERS behavior? Or does the cycling SERS signal get dampened and approach an equilibrium value?

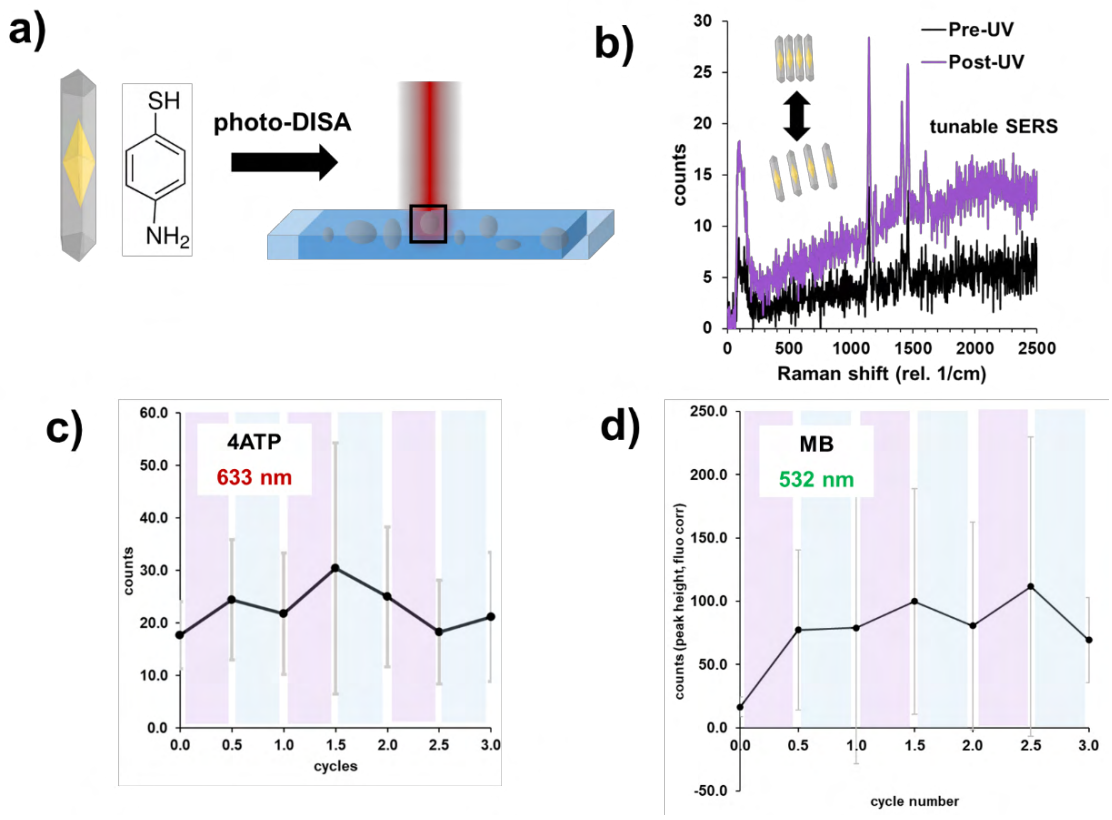

Figure 21. Cyclable SERS detection via reversible photoswitchable contraction of PR8 assemblies. ***(a)*** *Scheme of in situ colloidal SERS with assemblies tunable by photo-DISA.* ***(b)*** *Change in SERS spectrum of methylene blue (MB) upon UV-induced contraction of PR8 assemblies (PR8 in 80 mM 8A2). Measurement of 10^{-5} M MB, 532 nm excitation at 0.1 mW laser power, 10 acquisitions of 1 s integration time.* ***(c)*** *Cyclable SERS signal of 4ATP (10^{-5} M) in PR8, 70 mM 8A2; measured with 633 nm excitation at 0.1 mW laser power, 5 acquisitions of 1 s integration time.* ***(d)*** *Cyclable SERS signal of MB (10^{-3} M), with fluorescence correction, in PR8, 70 mM 8A2; measured with 532 nm excitation at 0.1 mW laser power, 10 acquisitions of 1 s integration time.*

In the case of cyclic needle contraction-expansion near the UV threshold in [azoTAB], both 4ATP and MB showed cyclable SERS counts at maximum Raman shifts of 1081 rel. cm^{-1} and 1629 rel. cm^{-1} (i.e., the tallest peaks) respectively. By photo-DISA, a 20% to 30% change in SERS counts with respect to the dark state) can be attained, coinciding with a d_{gap} change of around 5 nm in the case of PR8 in 70 mM 8A2 as the NR assembly contracts and expands. Generally, the SERS counts can be fully cycled for at least three times. On the other hand, SERS experiments using cyclic needle assembly-disassembly are still ongoing, and are expected to yield greater differences in SERS counts of the analytes in solution (**Figure 21b-d**).

So far, in these light-controlled SERS experiments, two critical observations must be noted. First, as with conventional DISA, the relative standard deviation (RSD) of the max SERS counts is typically 50% which is very high, and this RSD increases as the SERS counts increase. As noted in **Chapter 4**, this spread can be rationalized as an effect of Brownian motion of the in situ colloidal needles, or of variations in needle size, orientation, and crystallinity[11,59]. Second, on average, the SERS signal using azoTAB-based depletion is lower and less stable over time than that using CTAC-based depletion, suggesting that the depletion force exerted by azoTAB micelles is on average weaker than that for CTAC micelles. In fact, by three or four full UV-blue cycles, the needles become much more unstable when exposed to the excitation laser, and start to partially disassemble after 3 to 5 seconds of exposure at 0.100 mW power, for a 1 μm wide laser beam. Such instability of the assembly could be also linked to photo-degradation of the azoTAB, thus weakening the effective depletion forces, due over repeated laser and LED irradiation. It may also be caused by partial azoTAB adsorption onto the NR surfaces, or by partial crystallization in solution, as thin micron-sized azoTAB crystals become more abundant after multiple UV-blue cycles, as evidenced by both polarized optical microscopy and by SAXS. Further investigation into this instability of the assemblies must be done.

In perspective, light-controlled SERS using cyclic assembly-disassembly should be prioritized in the future, as we expect a greater change in SERS counts in this type of cycling, with non-overlapping error bars for counts in the assembled and disassembled states. Next, it must be tested whether the rate of UV-blue cycling or the light irradiance affects the cycling of the SERS signal. Slower cycling rates and lower LED power – leading to slower azoTAB isomerization – could be required to 'relax' a greater proportion of the assemblies towards their equilibrium state after irradiation, or to also induce more size-monodisperse assembly of needles, perhaps improving the spread of the SERS signal. Finally, it would also be good to study the evolution of SERS signal as a function of needle orientation with respect to laser polarization[59,60].

Intermediate and metastable states via photo-DISA

Another major goal of the photo-DISA project is the stabilization of intermediate and metastable assembly states with light control, either by partial isomerization of the azoTAB, by

simultaneous UV and blue illumination, or by rapid switching between UV and blue illumination. The last case is a type of dynamic stabilization, akin to a Kapitza pendulum mechanism, where a normally inaccessible or transient state (under normal irradiation conditions / in the UV or blue photostationary state) can be prolonged over time[19,61]. With this in mind, we used the PhotoSwitch setup to irradiate suspensions of C5-NR with 8A2 in a 'Kapitza irradiation' experiment, using rapidly alternating UV and blue light, switching in the range of a few seconds to ten seconds, trapping the azoTAB in a state between the UV and blue photostationary states, and in theory, in a state with intermediate depletion strength. In this state, it is unclear whether the azoTABs tend to adopt a micelle size and shape in between the fully cis and trans states in a unimodal distribution, or whether there is a very polydisperse mixture of micelle sizes and shapes.

Below is shown the data for the Kaptiza experiment of PR32 in 5 mM 8A2, just above the dark threshold in [azoTAB]. In situ SAXS measurements revealed that, under rapid UV/blue 'Kapitza' switching, the lattice parameter (or equivalently the inter-NR gaps) of the needle assemblies of PR32 could be kept at values in between those obtained for pure UV or blue irradiation. By shifting the ratio of UV versus blue duration, one could quickly shift the lattice parameter to larger distances with longer bursts of blue illumination, or shorter distances with longer UV bursts. It was concluded that Kapitza switching at a specific UV/blue duration ratio creates a new dynamic equilibrium lattice parameter, rather than simply slowing down the approach (i.e., kinetics) to the pure UV or pure blue equilibrium states. Therefore, we show that continuous photo-modulation of the attractive depletion force, and of assembly lattices is possible using our system (**Figure 22**). Current efforts are now focused on extending this Kapitza concept to cyclic assembly-disassembly systems, where rapid UV/blue switching may stabilize amorphous nonequilibrium structures and other transient assembly states, just as rapid stimuli changes have been observed to induce bizarre structures in the self-assembly of other kinds of colloids[17,21,62]. Lastly, the stabilization of intermediate states by fast irradiation (i.e., partial azoTAB isomerization) must be investigated. In this latter case, it is unclear how long these states would last without constant light input, as thermal relaxation of the azoTAB to the trans isomer proceeds over several hours[40,43,47].

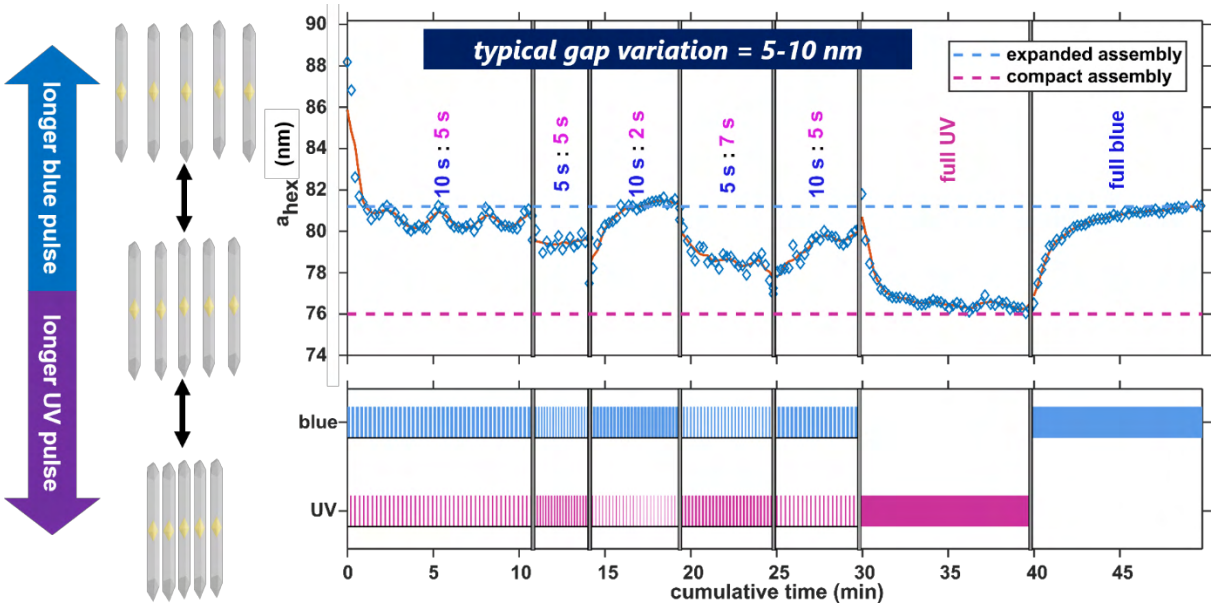

Figure 22. Kapitza pendulum stabilization: Setup and evolution of the assembly lattice parameter. *PR32 in 5 mM 8A2, in a sequence of the following ratios of rapidly switching UV:blue illumination: 5s:10s → 5s:5s → 2s:10s → 7s:5s → 5s:10s.*

Photo-patterned self-erasing images

Finally, we tried to implement the photo-DISA method in information encoding, specifically for photo-patterned self-erasing or rewritable images. The development of such images is one common test employed to know the degree of spatiotemporal control and the robustness of a photoresponsive system. Here, we aimed to investigate three aspects of our photo-patterned system.

First, can the photo-DISA induced formation of needles make an image with high enough visual contrast, and be sufficiently spatially selective to create *defined images*? As shown in **Figure 23**, we found that clear images can indeed be made using a paper or cardboard cutout as a photomask, where areas exposed to UV light form assemblies appearing lustrous gold to orange by eye. Various masks were tested, from simple bars and shapes to complex letters in logos. The approximate resolution of the borders between assembled and non-assembled regions ranges from 100 to 200 µm. The image contrast was optimal when the C5-NR concentration is above 100 mM M^0, that is in total reduced metal.

Second, is this photo-patterning reversible, that is, *self-erasing* when exposed to blue light? What is the characteristic writing and erasing time? It was observed that these photo-

patterned images could be generated within 3 to 10 min, depending on the UV LED irradiance. Blue light exposure also erases the produced images. However, completely erasure is possible only when the azoTAB concentration is very close to the UV threshold, for instance 15-20 mM 8A2 in the case of PR8 NRs (**Figure 23**). Preliminary results also suggest that thiol passivation of the NR surface with 4ATP may increase the reversibility (i.e., degree of disassembly) upon blue irradiation, perhaps due to surface charge effects. More tests will be done to check this hypothesis.

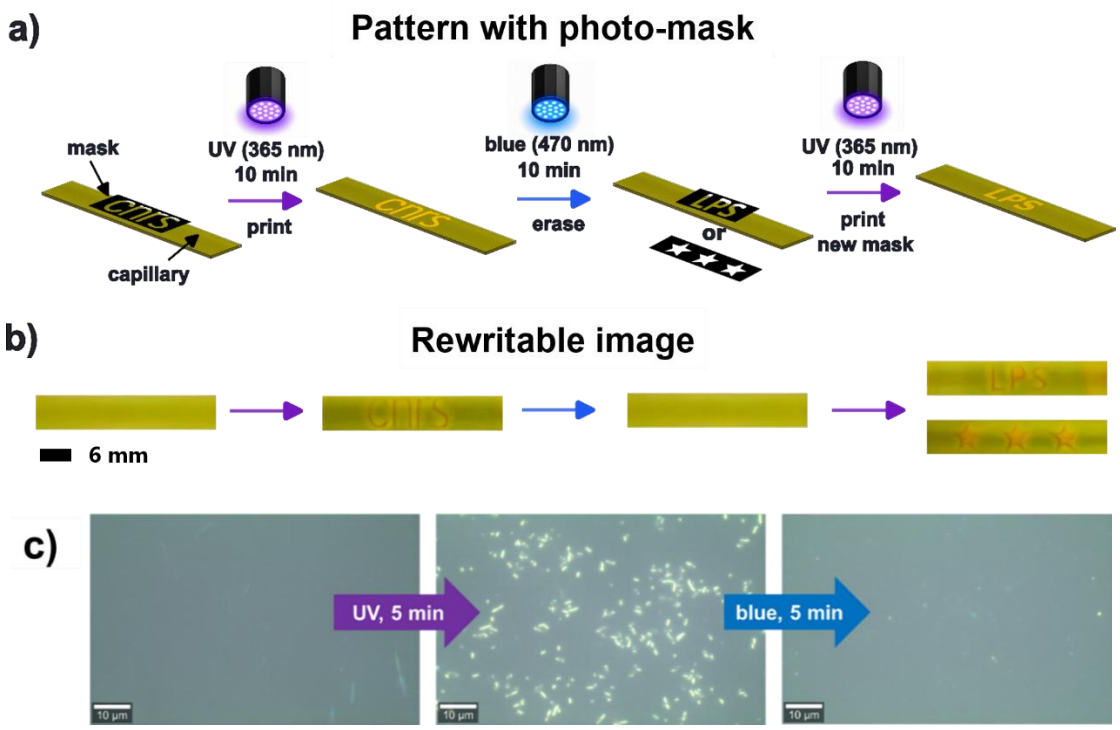

***Figure 23. Re-erasable photopatterned images via photo-DISA: PR8 in 15 mM 8A2**. **(a)** Scheme of reversible photopatterning an image in a colloidal NR suspension by UV irradiation with a mask. **(b)** Resulting images due to photo-DISA. Images taken by optical microscopy (transmission). **(c)** High-magnification zoom in optical microscopy (reflection) showing the assembly and disassembly of the PR8 NRs resulting in the re-erasable images.*

Third, can intermediate states of assembly be used to obtain *controlled lightness-darkness* in the images? Through POM and SAXS, it was noted that varying [azoTAB] or irradiation time within a certain range can change the number density and size of the needle assemblies, as well as the apparent color. The contrast of the image could also be controlled by printing different thicknesses of ink onto a clear photomask, changing the effective degree of irradiation. While we have not yet investigated this effect experimentally, it remains a good perspective. Interestingly, when using a clear cellulose acetate photomask with black inkjet

printer ink for the mask, we obtain *inverse images* where the clear areas of the photomask have little to no needle assemblies, while the black ink-covered areas have high density of assemblies. One preliminary explanation is that the cellulose acetate film causes strong absorption and scattering of UV light, which is altered or mitigated by the presence of a black ink layer, causing this image inversion. Thus, to obtain direct images with our photo-DISA setup, other photomask materials must be used, apart from paper cutouts.

Similar to the light-controlled SERS experiments, we also conjecture that a gentler irradiation of the NR-azoTAB mixtures at low irradiance (~0.05 mW/mm^2 for UV and blue, or power 3 out of 6 on the ThorLabs LED T-cube control) could induce more gradual change in depletion forces and prevent kinetic trapping of the assemblies. Interestingly, such prolonged UV irradiation at low irradiance yielded mixtures of 1D needle and 2D platelet assemblies. This is similar to how slow diffusion of CTAC depletant in conventional DISA leads to full reversibility, versus fast depletant addition and redilution.

6.3. Perspectives

Kinetics, reversibility, and assembly dimensionality

In this discussion, it has been noted a few times that more comprehensive kinetics experiments are needed to have a better understanding of the mechanism of photo-DISA, of the variables that affect the reversibility and speed of the self-assembly and disassembly, and the origins of any kinetic trapping or hysteresis. An important variable to check is the light irradiance and switching rate, which could have important kinetic effects on the size, dimensionality, and crystallinity of the colloidal assemblies. Preliminary results have shown that very low UV irradiance just above the UV threshold in [azoTAB], or slow diffusion of depletant above the dark threshold, both induce partial formation of 'metasurfaces' or 2D platelets of side-by-side NRs (**Figure 24**). It still remains to be seen whether shorter metal nanorods (and other metal NP shapes like bipyramids, platelets, or spheres) preferentially form 1D or 2D superstructures by UV-triggered photo-DISA. A second important perspective is the development of new photosurfactant compounds, even outside of azobenzene moieties – instead using arylazopyrazole, etc.) with greater solubility in water and more maximized change in micelle

curvature and size upon exposure to light stimulus. Also, the effect of salts and polyelectrolytes on the azoTAB-driven photo-DISA must be studied further[41,43,47].

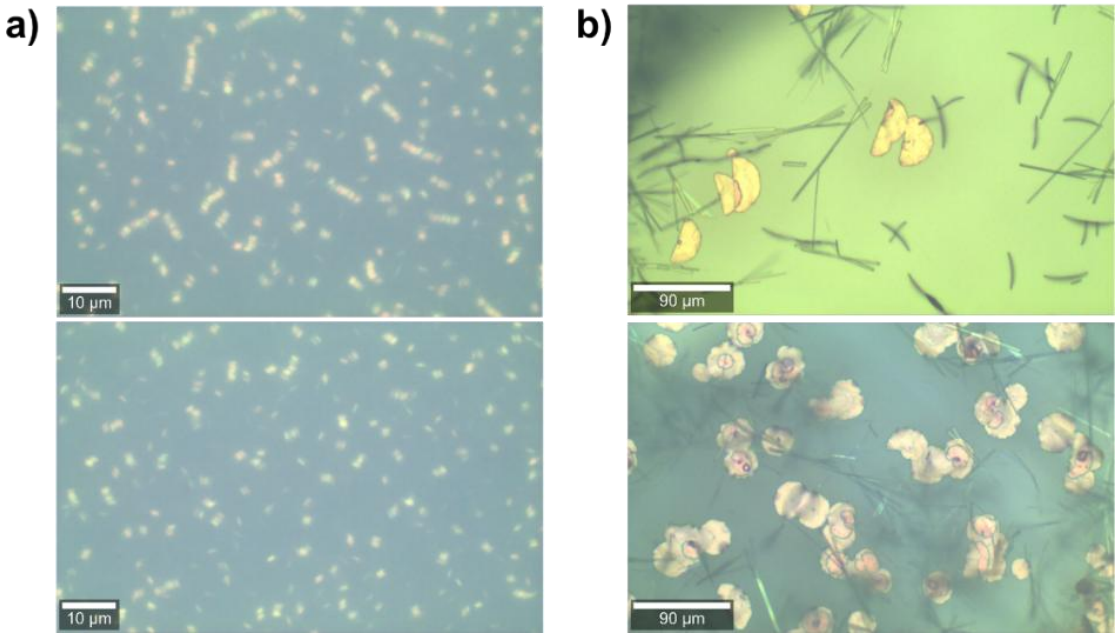

Figure 24. AzoTAB depletant induces long NR self-assembly into different dimensionalities: (a) *1D 'needles' with fast photo-DISA upon UV illumination, or* ***(b)*** *2D 'platelets' with ultra-slow diffusion of AzoTAB, without UV illumination.*

Valence-free assembly with non-metallic particles

Next, it is important to apply the photo-DISA strategy to other non-metallic particles with different compositions and ligand chemistries, to test the hypothesis that photo-DISA is indeed a more universal valence-free method of colloidal assembly. To this effect, preliminary experiments are underway to use photo-DISA to self-assemble different NPs like goethite nanorods (GT NRs) (a type of iron (III) oxide-hydroxide mineral), micron-sized silica spheres, or polymer NPs. Below is shown one ongoing experiment on the self-assembly of colloidal GT NRs in water, where the nanorods are approximately 300 nm long and 20 nm wide. By in situ polarized optical microscopy (POM), it was found that CTAC induced GT NR self-assembly into semi-elongated superstructures, with regions of coherent GT NR alignment as seen under crossed polarizers with the quarter wave plate. Meanwhile, when a suspension of GT NRs in 8A2 was irradiated with UV light for 5 min, very small colloidal objects started to appear, but these are not yet definitely proven to be colloidal assemblies of the rods (**Figure 25**). In any

case, when performing DISA or photo-DISA with non-metallic NPs, one must verify that there are no effects like depletant ad-/absorption onto or into the NPs which may interfere with the DISA mechanism.

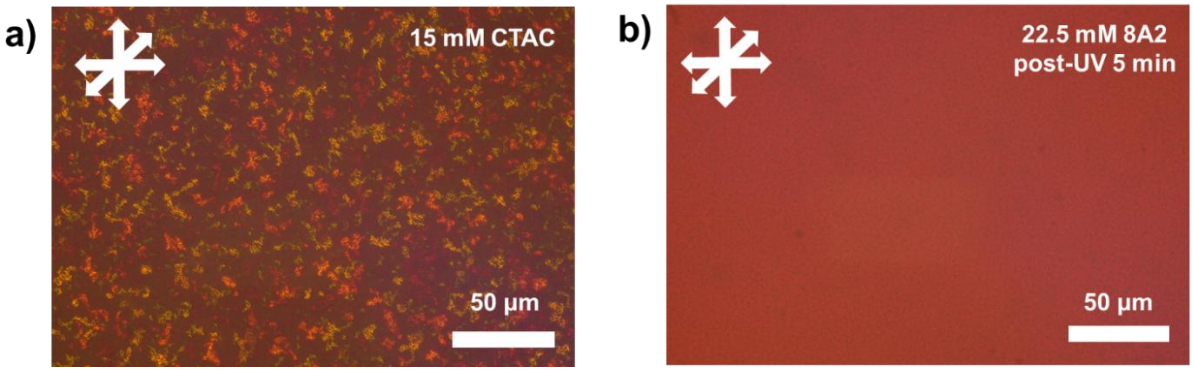

Figure 25. Depletion with non-plasmonic nano-objects: DISA with suspensions of goethite (GT) nanorods as building blocks. (a) *in 15 mM CTAC (classic DISA).* ***(b)*** *in 22.5 mM 8A2, after 5 min of UV irradiation (photo-DISA).*

Photo-DISA in other forms of soft matter

Finally, photo-DISA can be applied to other types of matter beyond typical colloidal NP assemblies. Light control of depletion could be exploited to tune the structure, and thus the optical or mechanical properties of various forms of soft matter, like gels, liquid crystals, foams, and certain biological systems. In the Perspectives section of **Chapter 4**, we briefly mentioned our discovery of photonic structural color in colloidal liquid crystals (LCs) of long metal NRs. This structural color only appears at low ionic strength, where the inter-NR lattice parameters are comparable to visible light, causing diffraction of visible wavelengths. One could imagine a system where a photo-acid is introduced into such a structurally colored LC, where irradiation of the system causes the photo-acid to release H^+ ions in solution, change the surface charge of the NRs, and increase the ionic strength. This should cause a weakening or total disappearance of the structural colors, thus making photo-DISA a viable tool for switching photonic properties.

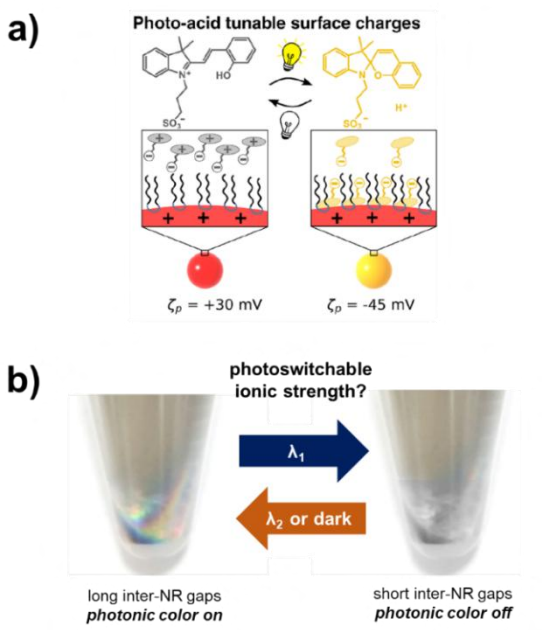

***Figure 26. Proposed photoswitchable photonic structural color via photo-DISA**. **(a)** Tuning NP surface charges and ionic strength using a merocyanine / spiropyran photo-acid in solution. Adapted from van Kesteren, et al.[17] **(b)** Proposed scheme of photoswitchable photonic color in colloidal liquid crystals (LCs) of metal NRs: Photonic color exists only at long inter-NR gaps, which exists at low ionic strength.*

6.4. Conclusion and take-home message

In this chapter, we have demonstrated for the first time direct and modulable light-control of depletion forces, to induce phototunable depletion-induced self-assembly (photo-DISA) of passive metal NPs using active azoTAB photosurfactant in aqueous medium. It was proven that this phototunable NP self-assembly proceeds by a depletion mechanism, due to a change in the number concentration of azoTAB micelles which change shape and size upon azobenzene photoisomerization under UV/blue light. This was shown by control experiments with surface-passivated metal NRs, excluding solvophobic mechanisms.

This light-controlled photo-DISA allows for reversible assembly-disassembly or contraction-expansion of metal NR (C5-NR) assemblies by UV/blue light exposure up to ten cycles, with switching rate (i.e., a full cycle) as fast as 3 to 5 min. By photo-DISA, high aspect ratio metal NRs predominantly form colloidal and dynamic 1D needle-like assemblies of side-by-side NRs due to fast assembly kinetics. Modulation of depletion is only achieved when the tail and spacer length of the azoTAB is sufficiently different, as in the case of 8A2 (C_8AzoOC_2TAB) as opposed to 2A2. Both the azoTAB photoisomerization and the NR assembly-disassembly can be separately followed by UV-vis-NIR extinction, and the two were found to have strong

temporal correlation. Also, the values of the inter-NR gaps in the assemblies, determined by SAXS, were consistent with the attractive forces due to depletion induced by azoTAB micelles. By varying the azoTAB concentration and changing the intensity of UV or blue irradiation, or by rapidly switching between these two wavelengths, one can achieve continuous modulation of attractive depletion forces beyond simple 'on-off' states. Specifically, by rapid UV/blue switching, one can stabilize a range of intermediate inter-NR gaps in the needles, resembling the dynamic stabilization of a Kapitza pendulum. This photo-DISA method has three key advantages: (1) it is valence-free, meaning compatible with many NP types (e.g., metal NRs, mineral or metal oxide NPs, polymer colloids) and not requiring specific ligand chemistry or NP surface treatment; (2) it directly renders DISA phototunable in a closed system, speeding up the switching rate and practicability of the method; (3) it enables good spatiotemporal control of depletion-induced NR self-assembly as shown by the cyclability and photo-patterned image applications of this method. We also showed that photo-DISA can be applied to active functional devices. Light contraction-expansion of the needles can be used for light-controlled modulation of *in situ* surface-enhanced Raman scattering (SERS) of analytes like 4-aminothiophenol (4ATP) or methylene blue (MB). On the other hand, photo-DISA can be used to create photo-patterned, self-erasing images using a photomask, which enables spatial information encoding not only optically but potentially by SERS.

In perspective, four main points can be addressed to further improve the photo-DISA method. First, the design, chemical synthesis, and purification of azoTABs must be improved to increase their solubility in water, minimize crystallization, and maximize the change in micelle curvature and size upon UV/blue irradiation for greater ability to modulate depletion. Second, the use of photo-DISA to induce attraction or self-assembly between other types of particles / materials, especially polymeric, semiconductor, or biobased particles would be an exciting possibility. Third, our understanding of the cyclability and hysteresis of photo-DISA still leaves many open questions. The irradiance (i.e., power per unit area) of UV/blue light used appears to play a role in the degree of cyclability that is not yet well understood. Fourth, the stabilization of intermediate and metastable states by photo-DISA, either by rapid 'Kapitza' switching or partial irradiation, remains to be explored, and its mechanism still not well understood.

6.5. References

(1) Amyar, H.; Ceratti, D. R.; Benisty, H.; Cattoni, A.; Besbes, M.; Faustini, M. Self-Regulating and Self-Oscillating Metal-Organic Framework Hybrid Plasmonic Metasurfaces. *Nat Commun* **2025**, *16* (1), 10392. https://doi.org/10.1038/s41467-025-65338-2.

(2) Thorimbert, F.; Odziomek, M.; Chateau, D.; Parola, S.; Faustini, M. Programming Crack Patterns with Light in Colloidal Plasmonic Films. *Nat Commun* **2024**, *15* (1), 1156. https://doi.org/10.1038/s41467-024-45365-1.

(3) Jones, M. R.; Seeman, N. C.; Mirkin, C. A. Programmable Materials and the Nature of the DNA Bond. *Science* **2015**, *347* (6224), 1260901. https://doi.org/10.1126/science.1260901.

(4) Wang, P.; Nasir, M. E.; Krasavin, A. V.; Dickson, W.; Jiang, Y.; Zayats, A. V. Plasmonic Metamaterials for Nanochemistry and Sensing. *Acc. Chem. Res.* **2019**, *52* (11), 3018–3028. https://doi.org/10.1021/acs.accounts.9b00325.

(5) Kuzyk, A.; Schreiber, R.; Zhang, H.; Govorov, A. O.; Liedl, T.; Liu, N. Reconfigurable 3D Plasmonic Metamolecules. *Nature Mater* **2014**, *13* (9), 862–866. https://doi.org/10.1038/nmat4031.

(6) Byun, C.; Ceratti, D. R.; Mimoso, C.; Boissière, C.; Faustini, M. A Homeostatic Photonic Device Integrating Vapor-Regulated Thermo-Optical Feedback Mechanisms. *Adv Funct Materials* **2025**, *35* (24), 2424453. https://doi.org/10.1002/adfm.202424453.

(7) Grzelczak, M.; Liz-Marzán, L. M.; Klajn, R. Stimuli-Responsive Self-Assembly of Nanoparticles. *Chem. Soc. Rev.* **2019**, *48* (5), 1342–1361. https://doi.org/10.1039/C8CS00787J.

(8) Kutalia, N.; Trazo, J. G.; Marchand, S.; Goldmann, C.; Ratel-Ramond, N.; Dozov, I.; Bizien, T.; Constantin, D.; Impéror-Clerc, M.; Davidson, P.; Hamon, C. Plasmonic Nanorods Form Reconfigurable Liquid Crystalline Assemblies. May 21, 2026. https://doi.org/10.26434/chemrxiv.15003689/v1.

(9) Sacanna, S.; Irvine, W. T. M.; Chaikin, P. M.; Pine, D. J. Lock and Key Colloids. *Nature* **2010**, *464* (7288), 575–578. https://doi.org/10.1038/nature08906.

(10) Lekkerkerker, H. N. W.; Tuinier, R. *Colloids and the Depletion Interaction*; Lecture Notes in Physics; Springer Science+Business Media B.V: Dordrecht, 2011.

(11) Trazo, J. G.; Marcone, J.; Nag, R.; Goldmann, C.; Kutalia, N.; Bizien, T.; Pansu, B.; Impéror-Clerc, M.; Hamon, C. Colloidal Tunable Metasurfaces via Depletion-Induced Self-Assembly of Plasmonic Nanorods. *ACS Appl. Mater. Interfaces* **2025**, *17* (45), 62349–62359. https://doi.org/10.1021/acsami.5c17436.

(12) Zhao, H.; Sen, S.; Udayabhaskararao, T.; Sawczyk, M.; Kučanda, K.; Manna, D.; Kundu, P. K.; Lee, J.-W.; Král, P.; Klajn, R. Reversible Trapping and Reaction Acceleration within Dynamically Self-Assembling Nanoflasks. *Nature Nanotech* **2016**, *11* (1), 82–88. https://doi.org/10.1038/nnano.2015.256.

(13) Moon, T.; Joo, H.; Das, B.; Koo, Y.; Kang, M.; Lee, H.; Kim, S.; Chen, C.; Suh, Y. D.; Kim, D.-S.; Park, K.-D. Adaptive Gap-Tunable Surface-Enhanced Raman Spectroscopy. *Nano Lett.* **2024**, *24* (12), 3777–3784. https://doi.org/10.1021/acs.nanolett.4c00289.

(14) Mazzotta, G.; Bertucci, S.; Mendoza-Carreño, J.; Mihi, A.; Lova, P.; Comoretto, D.; Steiner, U.; Lattuada, M.; Dodero, A. Bio-Inspired Magnetically Tunable Structural Colors from Elliptical Self-Assembled Block Copolymer Microparticles. *Adv Funct Materials* **2026**, *36* (38), e28686. https://doi.org/10.1002/adfm.202528686.

(15) Guo, X.; Li, Y.; Hanif, F.; Zhu, L.; Kong, M.; Zhang, S.; Zhang, Y.; Tang, B. Information Security with Smart Hydrogels: Photo-Patterning and Multi-Stimuli Responsive Structural Color. *Nano-Micro Lett.* **2026**, *18* (1), 311. https://doi.org/10.1007/s40820-026-02130-x.

(16) Wang, J.; Zhou, Z.; Li, Z.; Willner, I. Programmed Catalysis within Stimuli-Responsive Mechanically Unlocked Nanocavities in DNA Origami Tiles. *Chem. Sci.* **2021**, *12* (1), 341–351. https://doi.org/10.1039/D0SC04108D.

(17) Van Kesteren, S.; Smina, N.; Zang, S.; Leung, C. W.; Hocky, G. M.; Sacanna, S. Light-Controlled Colloidal Crystallization. *Chem* **2026**, 102917. https://doi.org/10.1016/j.chempr.2025.102917.

(18) Bishop, K. J. M.; Wilmer, C. E.; Soh, S.; Grzybowski, B. A. Nanoscale Forces and Their Uses in Self-Assembly. *Small* **2009**, *5* (14), 1600–1630. https://doi.org/10.1002/smll.200900358.
(19) Whitelam, S.; Jack, R. L. The Statistical Mechanics of Dynamic Pathways to Self-Assembly. *Annu. Rev. Phys. Chem.* **2015**, *66* (1), 143–163. https://doi.org/10.1146/annurev-physchem-040214-121215.
(20) Tang, J.; Chen, Q.; Shao, H.; Tang, C.; Wang, D.; Fan, M. Self-Assembled Core–Shell Au@Pd Nanoparticle Arrays for Optical Hydrogen Sensing. *ACS Appl. Nano Mater.* **2025**, *8* (8), 3804–3814. https://doi.org/10.1021/acsanm.4c06416.
(21) Zang, S.; Paul, S.; Leung, C. W.; Chen, M. S.; Hueckel, T.; Hocky, G. M.; Sacanna, S. Direct Observation and Control of Non-Classical Crystallization Pathways in Binary Colloidal Systems. *Nat Commun* **2025**, *16* (1), 3645. https://doi.org/10.1038/s41467-025-58959-0.
(22) Wang, S.; Zheng, L.; Chen, W.; Ji, L.; Zhang, L.; Lu, W.; Fang, Z.; Guo, F.; Qi, L.; Liu, M. Helically Grooved Gold Nanoarrows: Controlled Fabrication, Superhelix, and Transcribed Chiroptical Switching. *CCS Chem* **2021**, *3* (9), 2473–2484. https://doi.org/10.31635/ccschem.020.202000472.
(23) Klajn, R.; Wesson, P. J.; Bishop, K. J. M.; Grzybowski, B. A. Writing Self-Erasing Images Using Metastable Nanoparticle "Inks." *Angew. Chem. Int. Ed.* **2009**, *48* (38), 7035–7039. https://doi.org/10.1002/anie.200901119.
(24) Li, Z.; Fan, Q.; Yin, Y. Colloidal Self-Assembly Approaches to Smart Nanostructured Materials. *Chem. Rev.* **2022**, *122* (5), 4976–5067. https://doi.org/10.1021/acs.chemrev.1c00482.
(25) Weißenfels, M.; Gemen, J.; Klajn, R. Dissipative Self-Assembly: Fueling with Chemicals versus Light. *Chem* **2021**, *7* (1), 23–37. https://doi.org/10.1016/j.chempr.2020.11.025.
(26) Wang, D.; Kowalczyk, B.; Lagzi, I.; Grzybowski, B. A. Bistability and Hysteresis During Aggregation of Charged Nanoparticles. *J. Phys. Chem. Lett.* **2010**, *1* (9), 1459–1462. https://doi.org/10.1021/jz100406w.
(27) Kundu, P. K.; Samanta, D.; Leizrowice, R.; Margulis, B.; Zhao, H.; Börner, M.; Udayabhaskararao, T.; Manna, D.; Klajn, R. Light-Controlled Self-Assembly of Non-Photoresponsive Nanoparticles. *Nature Chem* **2015**, *7* (8), 646–652. https://doi.org/10.1038/nchem.2303.
(28) Lewandowski, W.; Fruhnert, M.; Mieczkowski, J.; Rockstuhl, C.; Górecka, E. Dynamically Self-Assembled Silver Nanoparticles as a Thermally Tunable Metamaterial. *Nat Commun* **2015**, *6* (1), 6590. https://doi.org/10.1038/ncomms7590.
(29) Gong, J.; Wu, N. Electric-Field Assisted Assembly of Colloidal Particles into Ordered Nonclose-Packed Arrays. *Langmuir* **2017**, *33* (23), 5769–5776. https://doi.org/10.1021/acs.langmuir.7b00547.
(30) Sim, S.; Miyajima, D.; Niwa, T.; Taguchi, H.; Aida, T. Tailoring Micrometer-Long High-Integrity 1D Array of Superparamagnetic Nanoparticles in a Nanotubular Protein Jacket and Its Lateral Magnetic Assembling Behavior. *J. Am. Chem. Soc.* **2015**, *137* (14), 4658–4661. https://doi.org/10.1021/jacs.5b02144.
(31) Chovnik, O.; Balgley, R.; Goldman, J. R.; Klajn, R. Dynamically Self-Assembling Carriers Enable Guiding of Diamagnetic Particles by Weak Magnets. *J. Am. Chem. Soc.* **2012**, *134* (48), 19564–19567. https://doi.org/10.1021/ja309633v.
(32) von Maltzahn, G.; Min, D. -H.; Zhang, Y.; Park, J. -H.; Harris, T. J.; Sailor, M.; Bhatia, S. N. Nanoparticle Self-Assembly Directed by Antagonistic Kinase and Phosphatase Activities. *Advanced Materials* **2007**, *19* (21), 3579–3583. https://doi.org/10.1002/adma.200701183.
(33) Young, K. L.; Jones, M. R.; Zhang, J.; Macfarlane, R. J.; Esquivel-Sirvent, R.; Nap, R. J.; Wu, J.; Schatz, G. C.; Lee, B.; Mirkin, C. A. Assembly of Reconfigurable One-Dimensional Colloidal Superlattices Due to a Synergy of Fundamental Nanoscale Forces. *Proc. Natl. Acad. Sci. U.S.A.* **2012**, *109* (7), 2240–2245. https://doi.org/10.1073/pnas.1119301109.
(34) Ercole, F.; Davis, T. P.; Evans, R. A. Photo-Responsive Systems and Biomaterials: Photochromic Polymers, Light-Triggered Self-Assembly, Surface Modification, Fluorescence Modulation and Beyond. *Polym. Chem.* **2010**, *1* (1), 37–54. https://doi.org/10.1039/B9PY00300B.

(35) Bian, K.; Schunk, H.; Ye, D.; Hwang, A.; Luk, T. S.; Li, R.; Wang, Z.; Fan, H. Formation of Self-Assembled Gold Nanoparticle Supercrystals with Facet-Dependent Surface Plasmonic Coupling. *Nat Commun* **2018**, *9* (1), 2365. https://doi.org/10.1038/s41467-018-04801-9.
(36) Ryssy, J.; Natarajan, A. K.; Wang, J.; Lehtonen, A. J.; Nguyen, M.; Klajn, R.; Kuzyk, A. Light-Responsive Dynamic DNA-Origami-Based Plasmonic Assemblies. *Angew Chem Int Ed* **2021**, *60* (11), 5859–5863. https://doi.org/10.1002/anie.202014963.
(37) Kuzyk, A.; Urban, M. J.; Idili, A.; Ricci, F.; Liu, N. Selective Control of Reconfigurable Chiral Plasmonic Metamolecules. *Sci. Adv.* **2017**, *3* (4), e1602803. https://doi.org/10.1126/sciadv.1602803.
(38) Hassan, F.; Chan, C. L. C.; Parton, T. G.; Wang, Z.; Shen, Q.; Li, R.; Frka-Petesic, B.; Parker, R. M.; Vignolini, S. Tuning the Circularly Polarized Reflection from Cholesteric Hydroxypropyl Cellulose Using Molecular Photoswitches. *Angew Chem Int Ed* **2026**, *65* (1), e20839. https://doi.org/10.1002/anie.202520839.
(39) Fava, D.; Winnik, M. A.; Kumacheva, E. Photothermally-Triggered Self-Assembly of Gold Nanorods. *Chem. Commun.* **2009**, No. 18, 2571. https://doi.org/10.1039/b901412h.
(40) Blayo, C.; Houston, J. E.; King, S. M.; Evans, R. C. Unlocking Structure–Self-Assembly Relationships in Cationic Azobenzene Photosurfactants. *Langmuir* **2018**, *34* (34), 10123–10134. https://doi.org/10.1021/acs.langmuir.8b02109.
(41) Jones, B. E.; Greenfield, J. L.; Cowieson, N.; Fuchter, M. J.; Evans, R. C. Light-Driven Hexagonal-to-Cubic Phase Switching in Arylazopyrazole Lyotropic Liquid Crystals. *J. Am. Chem. Soc.* **2024**, *146* (18), 12315–12319. https://doi.org/10.1021/jacs.4c02709.
(42) Li, Y.; Xue, B.; Yang, J.; Jiang, J.; Liu, J.; Zhou, Y.; Zhang, J.; Wu, M.; Yuan, Y.; Zhu, Z.; Wang, Z. J.; Chen, Y.; Harabuchi, Y.; Nakajima, T.; Wang, W.; Maeda, S.; Gong, J. P.; Cao, Y. Azobenzene as a Photoswitchable Mechanophore. *Nat. Chem.* **2024**, *16* (3), 446–455. https://doi.org/10.1038/s41557-023-01389-6.
(43) Liu, Y. Photo-Responsive Systems in Aqueous Solution : From Model Polyelectrolytes to Polyelectrolyte-Surfactant Complexes. Doctorat ès Chimie physique, PhD, Strasbourg, 2021. https://doi.org/10.70675/c68ea144z8422z42ebz9333ze4c721ab008c.
(44) Miyazaki, K.; Schweizer, K. S.; Thirumalai, D.; Tuinier, R.; Zaccarelli, E. The Asakura–Oosawa Theory: Entropic Forces in Physics, Biology, and Soft Matter. *The Journal of Chemical Physics* **2022**, *156* (8), 080401. https://doi.org/10.1063/5.0085965.
(45) Yang, P.-W.; Thoka, S.; Lin, P.-C.; Su, C.-J.; Sheu, H.-S.; Huang, M. H.; Jeng, U.-S. Tracing the Surfactant-Mediated Nucleation, Growth, and Superpacking of Gold Supercrystals Using Time and Spatially Resolved X-Ray Scattering. *Langmuir* **2017**, *33* (13), 3253–3261. https://doi.org/10.1021/acs.langmuir.6b04319.
(46) Goldmann, C.; Chaâbani, W.; Hotton, C.; Impéror-Clerc, M.; Moncomble, A.; Constantin, D.; Alloyeau, D.; Hamon, C. Confinement Effects on the Structure of Entropy-Induced Supercrystals. *Small* **2023**, 2303380. https://doi.org/10.1002/smll.202303380.
(47) Sharma, A.; Bekir, M.; Lomadze, N.; Santer, S. Photo-Isomerization Kinetics of Azobenzene Containing Surfactant Conjugated with Polyelectrolyte. *Molecules* **2020**, *26* (1), 19. https://doi.org/10.3390/molecules26010019.
(48) Blayo, C.; Kelly, E. A.; Houston, J. E.; Khunti, N.; Cowieson, N. P.; Evans, R. C. Light-Responsive Self-Assembly of a Cationic Azobenzene Surfactant at High Concentration. *Soft Matter* **2020**, *16* (40), 9183–9187. https://doi.org/10.1039/D0SM01512A.
(49) Kruse, J.; Merkens, S.; Chuvilin, A.; Grzelczak, M. Kinetic and Thermodynamic Hysteresis in Clustering of Gold Nanoparticles: Implications for Nanotransducers and Information Storage in Dynamic Systems. *ACS Appl. Nano Mater.* **2020**, *3* (9), 9520–9527. https://doi.org/10.1021/acsanm.0c02249.
(50) *Plasmonics: From Basics to Advanced Topics*; Enoch, S., Bonod, N., Eds.; Springer Series in Optical Sciences; Springer Berlin Heidelberg: Berlin, Heidelberg, 2012; Vol. 167. https://doi.org/10.1007/978-3-642-28079-5.

(51) Otomalo, T. O.; Di Mario, L.; Hamon, C.; Constantin, D.; Do, K.; O'Keeffe, P.; Catone, D.; Paladini, A.; Palpant, B. Sharp Spectral Variations of the Ultrafast Transient Light Extinction by Bimetallic Nanoparticles in the Near-UV. *Adv. Optical Mater.* **2021**, *9* (8), 2001778. https://doi.org/10.1002/adom.202001778.
(52) Gu, R.; Lamas, J.; Rastogi, S. K.; Li, X.; Brittain, W.; Zauscher, S. Photocontrolled Micellar Aggregation of Amphiphilic DNA-Azobenzene Conjugates. *Colloids and Surfaces B: Biointerfaces* **2015**, *135*, 126–132. https://doi.org/10.1016/j.colsurfb.2015.07.010.
(53) Titov, E.; Sharma, A.; Lomadze, N.; Saalfrank, P.; Santer, S.; Bekir, M. Photoisomerization of an Azobenzene-Containing Surfactant Within a Micelle. *ChemPhotoChem* **2021**, *5* (10), 926–932. https://doi.org/10.1002/cptc.202100103.
(54) Arya, P.; Jelken, J.; Lomadze, N.; Santer, S.; Bekir, M. Kinetics of Photo-Isomerization of Azobenzene Containing Surfactants. *The Journal of Chemical Physics* **2020**, *152* (2), 024904. https://doi.org/10.1063/1.5135913.
(55) Cheng, Z.; Jones, M. R. Assembly of Planar Chiral Superlattices from Achiral Building Blocks. *Nat Commun* **2022**, *13* (1), 4207. https://doi.org/10.1038/s41467-022-31868-2.
(56) Nag, R.; Rouvière, N.; Trazo, J. G.; Marcone, J.; Kutalia, N.; Goldmann, C.; Impéror-Clerc, M.; Alloyeau, D.; Constantin, D.; Hamon, C. Depletion-Induced Tunable Assembly of Complementary Platonic Solids. *Nano Lett.* **2024**, *24* (51), 16368–16373. https://doi.org/10.1021/acs.nanolett.4c04923.
(57) Scarabelli, L.; Coronado-Puchau, M.; Giner-Casares, J. J.; Langer, J.; Liz-Marzán, L. M. Monodisperse Gold Nanotriangles: Size Control, Large-Scale Self-Assembly, and Performance in Surface-Enhanced Raman Scattering. *ACS Nano* **2014**, *8* (6), 5833–5842. https://doi.org/10.1021/nn500727w.
(58) Boström, M.; Deniz, V.; Franks, G. V.; Ninham, B. W. Extended DLVO Theory: Electrostatic and Non-Electrostatic Forces in Oxide Suspensions. *Advances in Colloid and Interface Science* **2006**, *123–126*, 5–15. https://doi.org/10.1016/j.cis.2006.05.001.
(59) Langer, J.; Jimenez De Aberasturi, D.; Aizpurua, J.; Alvarez-Puebla, R. A.; Auguié, B.; Baumberg, J. J.; Bazan, G. C.; Bell, S. E. J.; Boisen, A.; Brolo, A. G.; Choo, J.; Cialla-May, D.; Deckert, V.; Fabris, L.; Faulds, K.; García De Abajo, F. J.; Goodacre, R.; Graham, D.; Haes, A. J.; Haynes, C. L.; Huck, C.; Itoh, T.; Käll, M.; Kneipp, J.; Kotov, N. A.; Kuang, H.; Le Ru, E. C.; Lee, H. K.; Li, J.-F.; Ling, X. Y.; Maier, S. A.; Mayerhöfer, T.; Moskovits, M.; Murakoshi, K.; Nam, J.-M.; Nie, S.; Ozaki, Y.; Pastoriza-Santos, I.; Perez-Juste, J.; Popp, J.; Pucci, A.; Reich, S.; Ren, B.; Schatz, G. C.; Shegai, T.; Schlücker, S.; Tay, L.-L.; Thomas, K. G.; Tian, Z.-Q.; Van Duyne, R. P.; Vo-Dinh, T.; Wang, Y.; Willets, K. A.; Xu, C.; Xu, H.; Xu, Y.; Yamamoto, Y. S.; Zhao, B.; Liz-Marzán, L. M. Present and Future of Surface-Enhanced Raman Scattering. *ACS Nano* **2020**, *14* (1), 28–117. https://doi.org/10.1021/acsnano.9b04224.
(60) Lyu, J.; Chaâbani, W.; Modin, E.; Chuvilin, A.; Bizien, T.; Smallenburg, F.; Impéror-Clerc, M.; Constantin, D.; Hamon, C. Double-Lattice Packing of Pentagonal Gold Bipyramids in Supercrystals with Triclinic Symmetry. *Advanced Materials* **2022**, *34* (21), 2200883. https://doi.org/10.1002/adma.202200883.
(61) Kapitza, P. L. Маятник с вибрирующим подвесом. *Успехи физических наук* **1951**, *44* (5), 7–20. https://doi.org/10.3367/UFNr.0044.195105b.0007.
(62) Bian, T.; Gardin, A.; Gemen, J.; Houben, L.; Perego, C.; Lee, B.; Elad, N.; Chu, Z.; Pavan, G. M.; Klajn, R. Electrostatic Co-Assembly of Nanoparticles with Oppositely Charged Small Molecules into Static and Dynamic Superstructures. *Nat. Chem.* **2021**, *13* (10), 940–949. https://doi.org/10.1038/s41557-021-00752-9.

CONCLUSION AND PERSPECTIVES

In this doctoral project, inspired by advances in nanochemistry and in bioinspired materials, we have explored and further developed in situ depletion-induced self-assembly (DISA) of anisotropic metal nanoparticles (NPs) as a strategy of creating ***colloidal metamaterials in liquid***, particularly highly-ordered, tunable, low-dimensionality (1D or 2D), and stimuli-responsive systems capable of reversible assembly and disassembly.

This DISA method was investigated through a model system of colloidal metal nanorods (NRs) as building blocks and cationic surfactant (passive CTAC or active azoTAB) micelles as depletants in aqueous medium. This thesis was motivated by two scientific questions: First, how can one leverage ***anisotropy*** *or* ***frustration*** in NP geometries to create low-dimensional, anisotropic, or chiral superstructures, thus achieving anisotropic metaproperties? How can such transfer of anisotropy or frustration be mediated by depletion forces, which are stronger between larger NP facets? Second, can one achieve fine ***spatiotemporal light control of DISA*** by using photoswitchable surfactants like azoTAB as a depletant? What is the mechanism of such light-controlled NP assembly? Is this assembly reversible and is the attractive force continuously modulable as a function of irradiation conditions?

In the beginning of this project, we designed and characterized the two components of our model system: anisotropic (high aspect ratio) gold (Au) or gold core-silver shell (Au@Ag) NRs, and CTAC or azoTAB micelles. New protocols for controlled seed-mediated synthesis of such NRs up to 1 µm long were developed, allowing the direct observation of their colloidal self-assembly by optical microscopy. Moreover, new insights into CTAC phase behavior and the ellipsoidal structure of CTAC and azoTAB micelles at a wide range of concentrations were uncovered, notably probing their varying micelle eccentricity and charge, and creating a calibration tool for in situ depletant concentration with small-angle X-ray scattering (SAXS) data. More information is found in our article: ***C. Hotton, J. G. Trazo, et al. Nano Lett. 2026, 26(25).***

Using this two-component DISA system, we tested various protocols for achieving well-ordered colloidal plasmonic NR assemblies suspended in water, with the aim of having dynamic reconfigurable superstructures as opposed to dried, static superstructures by evaporation. During this process, we made four notable advancements: First, we noted that

anisotropy transfer occurs from the individual high aspect ratio NRs to their assemblies. Fast depletant introduction often yields *1D needle* assemblies of side-by-side NRs due to assembly kinetics, while slow introduction yields micron-sized *2D platelet* or *metasurface* assemblies of standing NRs, as the particles prefer to interact through their lateral facets. C5-NRs also preferentially form 2D metasurfaces versus C4-NRs, which tend to make 3D or loose stacks of 2D superstructures. The metasurfaces varied in 2D compacity as a function of depletant concentration and NR aspect ratio, ranging from 21% to 80%. More generally, interparticle gaps can be tuned over a wide range of distances by DISA. Second, we noted that the speed of depletant introduction into the colloidal system greatly influences the reversibility of DISA. DISA is fully reversible for up to five cycles or more but only with a slow change of depletant concentration by diffusion. Third, DISA can be directly monitored in situ by optical microscopy, revealing the formation of dynamic, Brownian 2D or 1D superstructures of NRs. By conducting DISA with ultra-slow diffusion (pseudo-dialysis) of CTAC into a long capillary, one can probe assembly simultaneously at different kinetic rates, and obtain crystalline assemblies up to 100 µm wide or larger. Fourth, we showed that dilute analyte detection can be done by using these metasurfaces as colloidal substrates for surface-enhanced Raman scattering (SERS). Using 4-aminothiophenol (4ATP) as a Raman marker, it was discovered that the SERS counts increase greatly upon assembly, but then follows a non-monotonic trend as depletant continues increasing. It is theorized that SERS enhancement strongly depends on the crystalline domain size of the metasurfaces. These results on colloidal metasurfaces via DISA are presented in our published article: ***J. G. Trazo, et al. ACS Appl. Mater. Interfaces. 2025, 17(45)***.

In the case of self-assembling twisted chiral gold NRs (cGNRs), we showed that depletion can induce their reversible and cyclable assembly into frustrated side-by-side colloidal structures with extrinsic chirality due to shape-induced frustration and chirality transfer. These colloidal structures were typically cGNR clusters with 1D symmetry. By addition-redilution of CTAC depletant, *spectrally-tunable and time-evolving plasmonic circular dichroism (PCD)* of the cGNRs is attained in suspension, with *reversible enhancement of the chiroptical signal or g-factor in suspension by nearly 100 times*. Decreasing the degree of twist of the cGNRs by controlled oxidative *NR etching changes the corresponding assembly's lattice symmetry*, from 1D to 2D rhombic or 2D hexagonal, and also decreases the maximum g-factor enhancement.

Based on current results, we hypothesize that there is an optimal NR length to groove pitch ratio to achieve the highest g-factor enhancement upon self-assembly. The kinetics of cGNR DISA, particularly at ultra-slow regime, leading to bizarre 1D to 3D curved surfaces, remains to be elucidated. We share the in-depth results in our recent article: ***J. G. Trazo, et al. Chem. Mater. 2025, 37(16).***

Finally, by combining passive (non-stimuli-responsive) NRs with active azobenzene-based photosurfactants (azoTAB) as depletants, we demonstrated spatiotemporal control of colloidal NP assembly with UV/blue light irradiation. Thus, to our knowledge, *direct photoswitchability of the depletion force* has been achieved for the first time, finding several proofs of a depletion-driven self-assembly mechanism. This photo-DISA technique can be applied as a *valence-free* self-assembly mechanism for other NPs, meaning that it works regardless of NP composition or surface/ligand chemistry. *Cyclic assembly-disassembly or expansion-contraction* of 1D or 2D NR assemblies can be triggered by alternate UV/blue irradiation. Remarkably, *intermediate or metastable states* could be attained by rapid UV/blue switching at the timescale of < 10 s, with stabilization analogous to a Kapitza pendulum mechanism. This photo-DISA process was proved to be spatially selective with resolution in the 0.1 mm range, allowing the creation of *photopatterned images* using a suspension of NRs with an image mask. Moreover, by controlling the structure of plasmonic NR assemblies, photo-DISA can be used to do in situ *light-modulable SERS detection* of analytes like 4ATP or methylene blue (MB).

In conclusion, by playing with the precise engineering of particle shape and with depletion strength, one can achieve tunable, valence-free, and stimulus-driven control of NP self-assembly by DISA, where anisotropy and frustration can be propagated to create dynamic, low-dimensional, or chiral assemblies, including some metastable states, which can act as colloidal metamaterials in liquid. By SERS, UV-vis-NIR spectroscopy, and CD spectroscopy, it was shown that the tunable structure of these assemblies is correlated with their tunable plasmonic properties. Many new questions and perspectives have been opened by this thesis, particularly on anisotropy transfer and on dynamic colloidal crystallization. A fuller kinetic model and mechanism of reversible DISA or photo-DISA, especially for the formation of 1D and 2D superstructures, and accounting for possible kinetic trapping, remains to be proposed. Methods for the direct observation of colloidal NP self-assembly via optical microscopy is ripe

for further development. Glass capillary or PDMS micro- to millifluidic setups are in development in our team for in situ SAXS and microscopy measurements. Ultra-slow DISA can also be further improved to grow single crystals greater than 100 µm in characteristic dimensions. On photo-DISA, the stabilization of intermediate assembly states by both partial photo-isomerization or 'Kapitza' wavelength switching must be explored more. Another interesting perspective is the use of (passive or photosensitive) surfactant or polymer depletants with different sizes or charges, to probe the effects of depletion with different ranges of attraction balanced by electrostatic repulsion of varying magnitudes. Finally, the correlations of SERS signal counts and standard deviation with the average lattice parameter, crystalline domain size, and assembly dimensionality is yet to be fully ascertained.

In broader perspective, our advancements in DISA can expand to three notable applications. First, as DISA is valence-free, it could be used to reversibly assemble a *wide range of other particles* like mineral, polymer, or biological nano or micron-sized colloidal particles. Second, it can be used to *dynamically stabilize or tune states of soft matter* such as liquid crystals (LCs) and gels, including the colloidal LCs of long Au@Ag NRs which we discovered during this project. Third, by engineering NP ligands and playing with the depletant chemistry, the interparticle distances in depletion-induced assemblies could be increased to obtain *diffractive or photonic metamaterials* with resonances in the visible to near-IR range (e.g., structural colors, collective lattice resonances). Currently, we already have confirmed the existence of photonic structural colors in columnar/smectic LCs of long metal NRs. Fourth, combinations of *multiple active or passive depletants* could be used to obtain multi-stimuli responsive assemblies that respond to more than one light wavelength or trigger, which is desired for fine-tuned and orthogonal control of material properties.

In the quest towards active metamaterials by self-assembly, this thesis has leveraged *tunable and stimuli-responsive depletion forces to attain* '***living colloidal crystals***': *reconfigurable plasmonic assemblies in liquid, with modulable functional properties.* Further developments in the chemical synthesis of depletants, particularly photo-depletants, more comprehensive DISA kinetics studies, and new experimental techniques for self-assembly and its in situ observation at both short and long timescales are needed to further advance DISA towards greater versatility and spatiotemporal control.

ANNEX: PUBLISHED ARTICLES

Colloidal Tunable Metasurfaces via Depletion-Induced Self-Assembly of Plasmonic Nanorods

Jaime Gabriel Trazo,[1] Jules Marcone,[1] Rahul Nag,[1] Claire Goldmann,[1] Nika Kutalia,[1] Thomas Bizien,[2] Brigitte Pansu,[1] Marianne Impéror-Clerc,[1] and Cyrille Hamon[1]*

[1] *Laboratoire de Physique des Solides, Université Paris-Saclay, CNRS, Orsay 91405, France.*

[2] *SWING beamline, SOLEIL Synchrotron, 91190 Gif-sur-Yvette, France.*

ABSTRACT

Self-assembly offers a scalable approach to creating nanostructures with tunable properties, particularly for plasmonic materials. Conventional self-assembly often produces dense 3D supercrystals, which restrict light and analyte accessibility. By contrast, directing assembly into 2D metasurfaces increases active surface area and promotes collective optical responses, making them highly promising for sensing and photocatalysis. While metasurfaces are typically immobilized on interfaces, here we introduce the concept of "colloidal metasurfaces", which are liquid-dispersed and reconfigurable assemblies. Specifically, we exploit depletion-induced self-assembly (DISA) to reversibly organize anisotropic plasmonic nanorods (Au@Ag) into colloidal metasurfaces. By tuning the depletion strength, we achieve dimensional control between 2D and 3D arrangements and modulate the compacity of the colloidal assemblies from 21% to 80%. Assemblies of nanorods with different cross-sections reveal shape-dependent reconfigurability: pentagonal rods maintain hexagonal lattice symmetry, whereas square rods undergo symmetry shifts from rhombic to square. These colloidal metasurfaces support multiple assembly–disassembly cycles without loss of optical function and enable modulation of Raman scattering through lattice parameter tuning. Together, this work establishes a functional, reconfigurable colloidal platform for plasmonic metasurfaces using shape-directed DISA.

Keywords: *self-assembly, depletion, plasmonic metasurface, nanorods, small-angle X-ray scattering (SAXS), surface-enhanced Raman scattering (SERS)*

INTRODUCTION

Self-assembly offers a powerful and cost-effective approach to constructing technologically relevant structures at the nanoscale, enabling the bottom-up design of materials with tunable properties that are unattainable through standard methods like lithography or printing. In particular, plasmonic nanoparticles (NPs) can be assembled into supercrystals that exhibit novel and enhanced optical functionalities due to their subwavelength structuration.[1] NP self-assembly generally yields to such large 3D nanostructures because the interactions between the building blocks are isotropic. This can restrict functionality to the surface of the supercrystal, as molecules and light may not easily penetrate its volume.[1-4] In contrast, directed self-assembly into 2D structures, or "metasurfaces," represents a promising route toward metamaterials with collective plasmonic properties and a high surface-to-volume ratio that would be particularly advantageous for applications in sensing and photocatalysis.[5, 6] In nature, precise and anisotropic assemblies such as viral capsids or fibers are common,[7] but engineering inorganic nanostructures with complex and well-defined architectures that can enhance light matter-interaction remains a significant challenge.

A common directional assembly approach involves engineering chemical patches, such as polymers, DNA, or proteins, on the surface of NPs.[8-10] These patches enable selective interactions beyond close-packed configurations, allowing the formation of exotic architectures such as colloidal diamonds,[11-13] Kagome lattices,[14, 15] colloidal polymers,[16-19] or colloidal molecules.[20, 21] Metasurfaces can also be achieved by assembling NPs at liquid interfaces, where a variety of structural arrangements can emerge.[22-25] Confinement strategies provide another route to control dimensionality and access complex architectures.[26-29] Alternatively, scaffolds such as DNA origami can direct NP assembly with spatial and temporal control, though typically limited to small clusters.[30-32] Finally, combining particle shape anisotropy with surface functionalization offers additional control over self-organization, enabling complex or dimensionally tailored structures.[14, 33-35] In summary, ligand-based strategies have been developed to introduce directional interactions, typically by functionalizing specific facets or regions of the NP surface. However, achieving such regioselective functionalization becomes increasingly difficult for anisotropic NPs with multiple crystallographic facets, as local variations in exposed facets and curvature strongly influence ligand adsorption. Here, we explore a directed self-assembly approach capable of orienting anisotropic NPs into large-scale assemblies without the need for surface functionalization or external fields.

Depletion-induced self-assembly (DISA) is an emerging strategy for creating tunable NP assemblies in colloidal suspensions. It typically involves adding small macromolecular species, such as polymers or surfactant micelles, as depletants to a NP suspension.[36-40] Faceted NPs preferentially stack along their larger facets to maximize entropy, thereby minimizing the system's free energy and achieving assemblies with long-range order. Various crystal structures have been realized by assembling various NP morphologies (e.g., rods, polyhedra, and plates), leading to 3D or self-limited assemblies.[37, 39, 41-47] Previously, it was observed that platelets typically formed 1D assemblies,[41] while rods can pack into smectic phases (layered structures without interlayer registry) or crystals (with interlayer registry).[37, 48, 49] Interestingly, equilibrium interparticle distances can be tuned by carefully balancing competing interactions, especially attractive depletion forces and repulsive electrostatic forces. In a recent study, we incidentally observed the formation of 2D structures with no detectable interlayer stacking.[43] However, more work is needed to understand how the dimensionality of the assemblies depends on the detailed shape of the NPs and their interaction, as well as investigate their collective plasmonic properties.

In this work, plasmonic nanorods (gold core–silver shell, Au@Ag NRs) with square or pentagonal cross-sections and varying aspect ratios were self-assembled using DISA. We investigate how to stabilize 3D or 2D structures depending on the shape of the NPs and the depletion strength in the medium. While the 2D hexagonal lattice symmetry remained consistent for the pentagonal nanorods, a shift in symmetry from 2D rhombic to 3D tetragonal was observed for the square nanorods. In both cases, the lattice parameters could be finely tuned, resulting in compacities as low as 21%. Moreover, the assembly process was fully reversible, with up to five assembly–disassembly cycles performed without significant loss of their extinction properties. Finally, we demonstrate that the Raman scattering of a probe molecule can be modulated by adjusting the lattice parameters. Overall, these colloidal metasurfaces represent reconfigurable nanostructures whose properties are governed by tunable colloidal interactions, opening up new opportunities for *in situ* plasmonics.

RESULTS AND DISCUSSION

A central motivation of this work was to create 2D layered colloidal structures of nanorods, referred to as metasurfaces throughout the manuscript. Inspired by previous studies showing that rod-like colloids, such as viruses,[50-52] can form 2D assemblies due to depletion-induced side-to-side alignment, we hypothesized that similar colloidal assemblies in water could be

achieved with plasmonic nanorods. In particular, we investigated whether tuning the nanorod shape and the strength of the depletion interaction could stabilize such planar architectures. To investigate the parameters governing self-assembly, we tested two types of prismatic Au@Ag NRs made by seed-mediated growth, with either a square (C4) or a pentagonal (C5) cross section (**Figure 1a**) and of three different sizes termed S, M, or L (small, medium, large respectively).

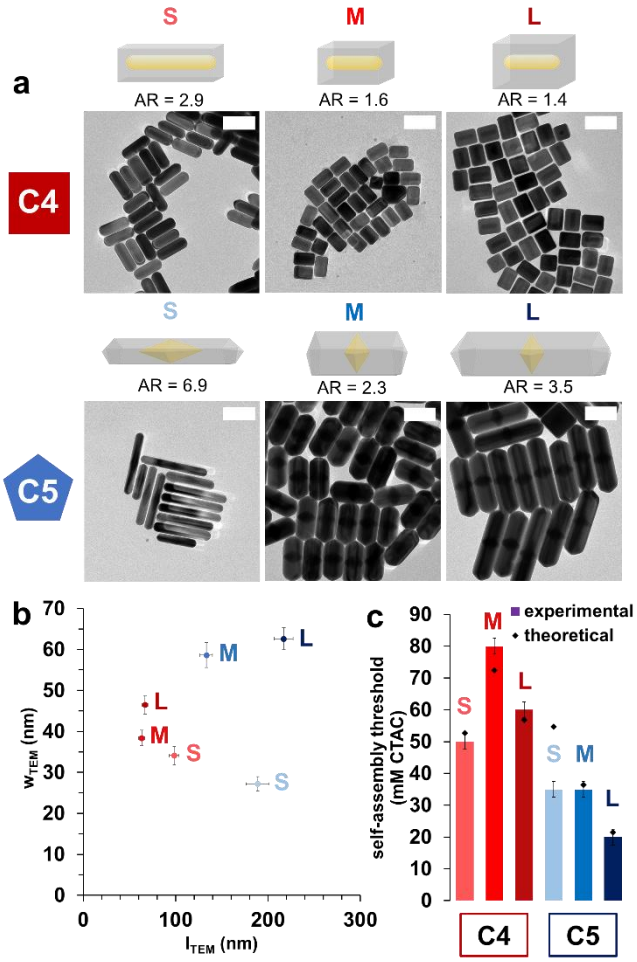

Figure 1: Metal nanorods (NRs) of varying shape anisotropy for depletion-induced self-assembly (DISA). a) TEM micrographs and corresponding illustrations of Au@Ag NRs with varying size/anisotropy (S, M, L) and cross-section symmetry (C4 or C5). Scale bars are 100 nm. **b)** Size distribution of the NRs determined by TEM image analysis. **c)** Experimental and calculated thresholds of CTAC depletant concentration to induce DISA of the various C4 and C5-NRs.

The dimensions of the NRs were determined by transmission electron microscopy (TEM) and by using a recent methodology based on the modeling of Small Angle X-ray Scattering (SAXS) form factor of nanoprisms.[53] Advantages of using SAXS are to confirm the nature of the cross section of the nanorods while increasing the statistical significance of the size distribution analysis compared to TEM. Dimensions of the different nanoparticles are reported in **Figure 1b** and in **Table S1**, and **Figures S1-S4**. For each NR system, we varied the concentration of cetyltrimethylammonium chloride (CTAC) over a wide concentration range (3 mM to 808 mM) to induce DISA. The CTAC addition was typically done via slow diffusion of surfactant solution in NR suspension (**Figure S5**).[54]

Upon addition of CTAC into the NR suspensions, DISA was observed above a threshold CTAC concentration, which was found to be inversely proportional to the surface area of the nanorods' lateral facets (**Figure 1c, Figure S1**). The attractive depletion force between two NRs can be estimated with the Asakura-Oosawa-Vrij model,[41, 55, 56] by the product of the osmotic pressure $\Pi = n_m kT$ exerted by spherical depletants (of radius r_m and number density n_m) and the overlap volume of depletion zones $V_{exc} = 2r_m A$, where A is the area overlap between the NRs.

$$U_{dep} = -\Pi V_{exc} = -2r_m\, A\, n_m\, kT \qquad \textbf{(1)}$$

In the case of micellar depletants, n_m is proportional to the molar concentration $c - cmc$ of surfactant molecules (**Equation 2**), where N_0 is Avogadro's number, c is the total molar concentration of surfactant, cmc is the critical micellar concentration of the surfactant, and N_{agg} is the micelle aggregation number:

$$n_m = \frac{N_0(c-cmc)}{N_{agg}} \qquad \textbf{(2)}$$

Experimental values of this self-assembly threshold agrees very well with **Equation 1**, as DISA typically occurred when $|U_{dep}| > 5$ kT (**Figure 1c**).[57] This model is valid for the CTAC concentration range investigated in this study but becomes inaccurate at higher concentrations, where micelles change in size and shape and the osmotic pressure no longer scales linearly with micelle concentration. A larger discrepancy is observed for C5-S, where the experimental CTAC threshold (35 mM) is significantly lower than the theoretically predicted value of 55 mM. This deviation arises because the end facets contribute to the effective length of the nanorods, whereas our model treats them as continuous structures.

The aspect ratio (AR) of the pentagonal C5-NRs ranged from 2.3 to 6.9 (C5-S, M, L). Across all these sizes, DISA induced self-assembly of C5-NRs into colloidal metasurfaces over a broad range of CTAC concentrations (**Figure 2a-b, Figure S6-S9**). SAXS and SEM analyses revealed

a 2D hexagonal lattice symmetry, with the long axes of the nanorods oriented perpendicular to the assembly plane (**Figure 2b-d**). Given the pentagonal cross-section of the NRs, this configuration results in no preferential in-plane orientation, leading to the formation of a plastic crystal, characterized by positional order without orientational order. The 2D nature of the assemblies is evidenced in the SAXS patterns by radially extended Bragg spots at low q, consistent with the form factor of 2D platelets, where the spot elongation reflects the small thickness. These diffraction features are consistent with 2D platelets made of a few loosely stacked layers (typically less than 5 layers), with no 3D ordering between adjacent layers (**Figure 2c-d**). While interlayer stacking is minimal, the intralayer 2D hexagonal order is well-defined at all [CTAC], as shown by sharp peaks and multiple harmonics (peaks (10), (11), (20), etc…), corresponding to up to 1500 NRs per crystalline domain.

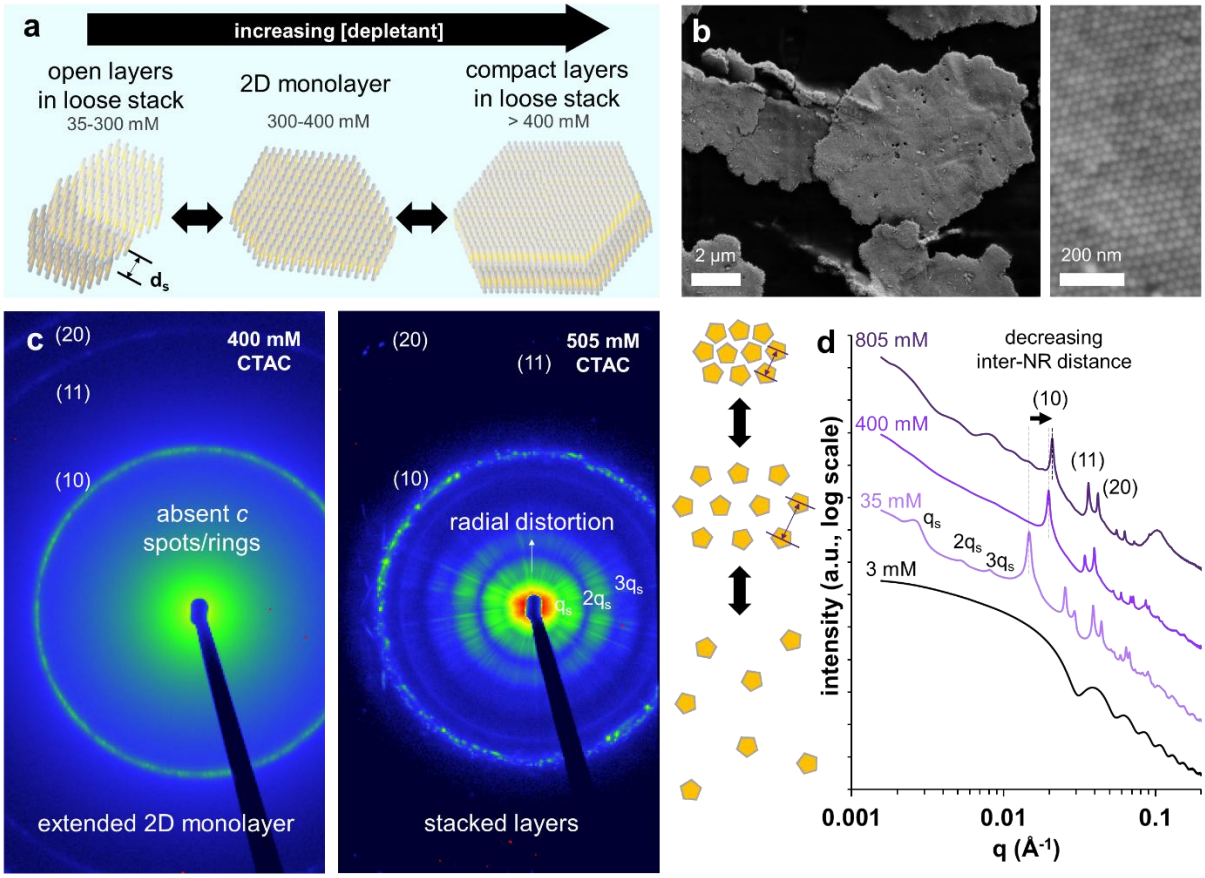

Figure 2: Colloidal metasurfaces with tunable interparticle gaps via DISA of C5-NRs. a) Illustration of the formation of C5-S NRs metasurfaces at varying depletant concentration; $d_s = 2\pi/q_s$ the average interlayer distance in the stacks. **b)** SEM images of the dried 2D assemblies (C5-S), showing their platelet shape and their in-plane structure. **c)** Representative 2D SAXS

patterns and **d)** series of 1D SAXS radial profiles of the colloidal metasurfaces (C5-S) prepared at varying depletant concentrations. Graphs were shifted vertically for clarity.

With the square-section C4-NRs, DISA induces preferential self-assembly into 3D colloidal supercrystals (**Figure 3a-c, Figure S10-S11**), across a wide range of depletant concentrations. The C4-NRs predominantly formed 3D supercrystals with primitive tetragonal lattice symmetry from 300 mM CTAC and higher, which corresponds to the close-packed arrangement. Below 250 mM, assemblies corresponded to lamellar stacks of metasurfaces without interlayer registry (**Figure 3a-d, Figure S11**). In this case, the 2D lattice symmetry is centered rectangular (oc), meaning that standing NRs are organized into monolayers with a rhombic lattice. Under optical microscopy in solution, macroscopic assemblies with a rhombus shape were observed, reminiscent of their crystal symmetry (**Figure S10**). Similar symmetry transition has been observed in superball assemblies,[58-61] which represent an intermediate shape between a sphere and a cube. Although the C4-NRs are prismatic in shape, the slight rounding of their lateral edges likely accounts for the observed phase transition under varying osmotic pressure.
SAXS data analysis revealed that the stabilization of the metasurface depended on the aspect ratio of the C4-NRs, with the occurrence of metasurface formation decreasing in the order C4-L > C4-M > C4-S. For assemblies of both C4-S and C4-M, a specific CTAC concentration of around 300 mM was identified as a sweet spot where few-layer to monolayer metasurfaces formed, as indicated by the absence (for C4-S) or near absence (for C4-M) of distinct diffraction peaks at low q values (**Figure 3c-d, Figure S7, S9**). Below 300 mM CTAC, the lattice symmetry is rhombic but becomes tetragonal at higher [CTAC]. Interestingly, for C4-S, the tetragonal crystal domains still resemble thin platelets comprising up to approximately 1600 NRs in the plane and a thickness of about 10 NRs (**Figure S11**). The C4-NR aspect ratio strongly determined the range of depletant concentration in which the rods could self-assemble into 3D tetragonal supercrystals. For low to medium aspect ratio NRs (C4-S and C4-M), long-range tetragonal order is observed at high [CTAC]. In the case of C4-M, there is also a region where 2D and 3D order coexist. On the other hand, low aspect ratio C4-L assemblies always exhibit 2D lattice order across all [CTAC], even if the colloidal objects are 3D in the larger scale. Overall, these results strengthen the hypothesis that higher AR and low depletant concentration favors anisotropic self-assembly into 2D structures.

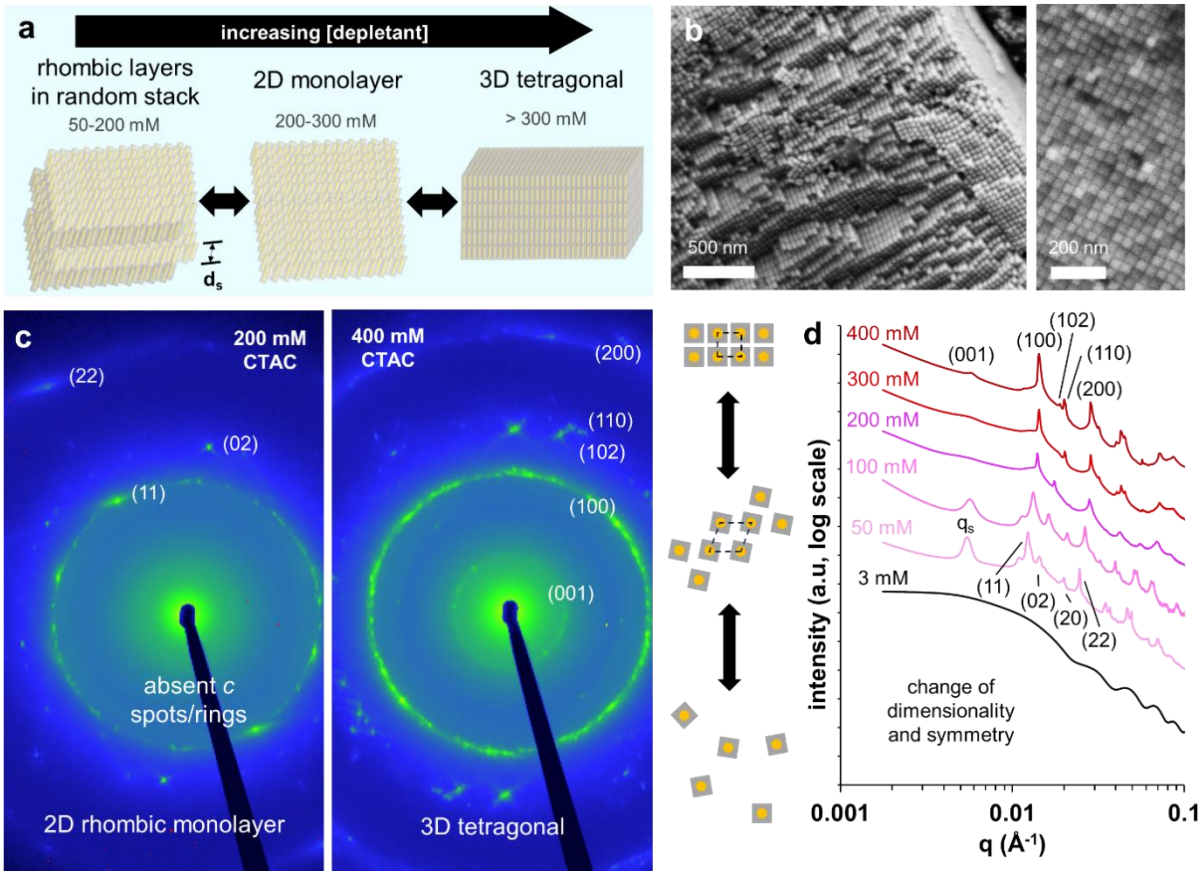

Figure 3: Colloidal metasurfaces with tunable interparticle gaps and dimensionality via DISA of C4-NRs. a) Illustration of the formation of C4-S NRs metasurfaces at varying depletant concentration; $d_L = 2\pi/q_L$ the average interlayer distance in the stacks. **b)** SEM images of the dried assemblies (C4-M), showing its tetragonal (tP) lattice. **c)** Typical 2D SAXS patterns and **d)** a series of 1D SAXS radial profiles of the colloidal assemblies of C4-S prepared at varying depletant concentrations; 2D centered rectangular (rhombic) lattice symmetry is in pink while 3D tetragonal is in red. Graphs were shifted vertically for clarity.

By comparing the two types of nanorods, it was shown that both C5-NRs and C4-NRs formed metasurfaces with various symmetries, but the CTAC concentration range over which metasurfaces could be obtained was narrower for C4-NRs. C4-NRs are enclosed by six {100} facets on both their sides and ends, while C5-NRs are pentatwinned and enclosed by five {100} side facets and five {111} facets at each tip.[62] As a result, C5-NRs have pointed tips, whereas C4-NRs have flat tips that are more likely to align through depletion interactions. This subtle difference in tip geometry helps explain the more limited conditions for metasurface formation in the case of C4-NRs. In line with this, monocrystalline AuNRs with rounded tips (l_{TEM} = 74.3

± 4.1 nm; w_{TEM} = 14.9 ± 1.3 nm), were also found to yield thin and sharply-faceted platelet metasurfaces with a 2D hexagonal lattice by DISA (**Figure S6**).

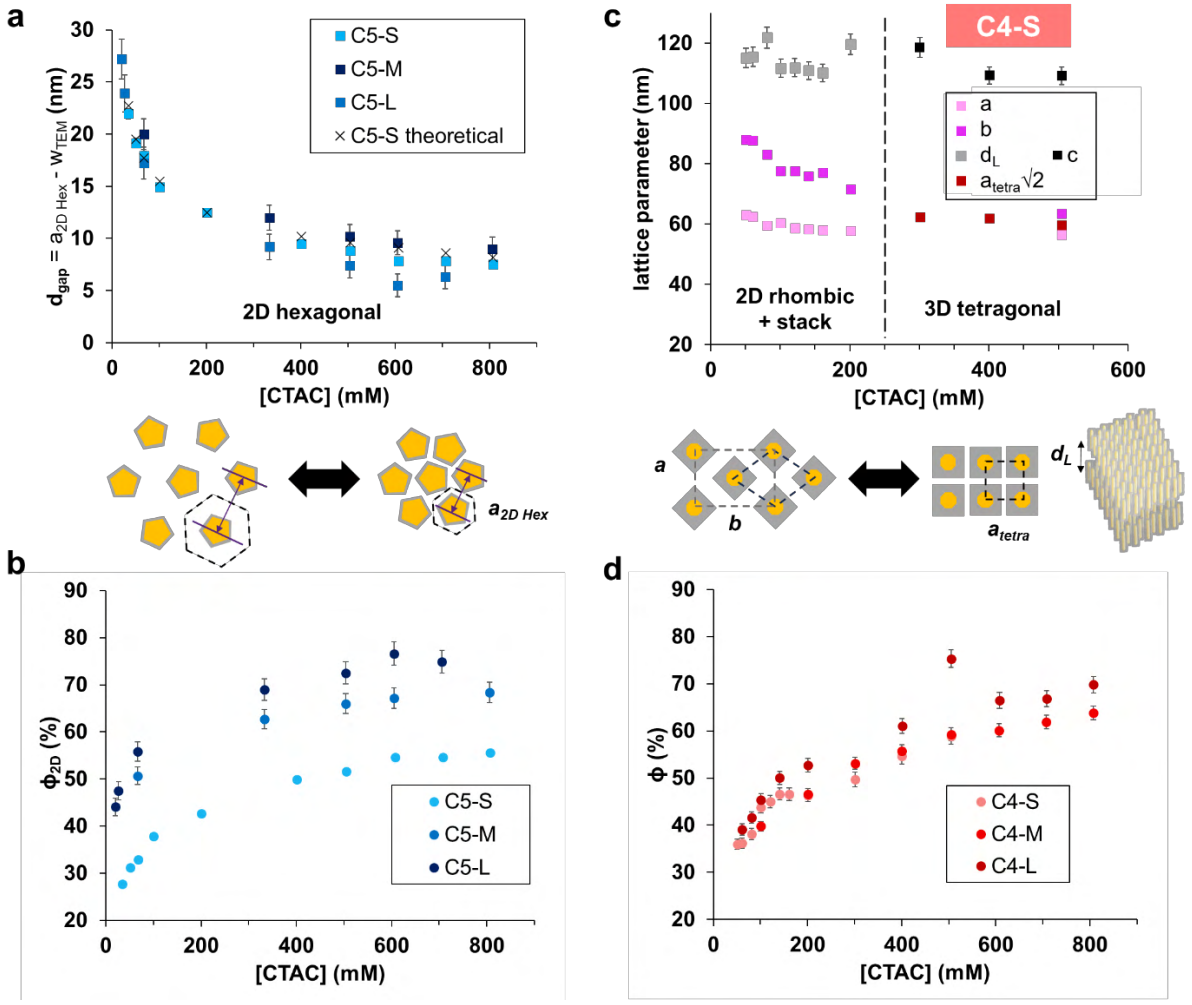

Figure 4: Tunable inter-NR gap distances and compacities in C5-NR and C4-NR colloidal metasurfaces. a-b) Plot of the inter-NR gap (dgap) and compacities against CTAC concentration for three sizes of C5-NRs. **c)** Plot of the lattice parameters of C4-S metasurfaces against CTAC concentration; *a* and *b* are the lattice parameters for the 2D centered rectangular (oc, rhombic) symmetry and *dL* is the average interlayer distance of the loosely-stacked rhombic layers; a_{tetra} and *c* are the lattice parameters for a primitive tetragonal (tP) lattice. **d)** Plot of the compacities against CTAC concentration for three sizes of C4-NRs.

These 2D nanorod metasurfaces exhibit tunable inter-NR gaps (d_{gap}) that depend on the CTAC concentration in the medium (**Figure 4a-b**). As [CTAC] increases, d_{gap} decreases. For example, d_{gap} ranging from 27 ± 2 nm to 6 ± 1 nm was observed as [CTAC] increased from 35 mM to

800 mM, respectively for C5-L (**Figure 4a**). The minimum d_{gap} corresponds to the thickness of two CTAC bilayers (≈6 nm) coating the NRs.[63] This variation in inter-NR gap arises from the balance between the attractive depletion force and the repulsive electrostatic interactions due to the positively charged CTAC bilayers, with some contribution of attractive Van der Waals forces as well. The observed trend in d_{gap} agrees with theoretical predictions (**Figure 4a, Figure S12**). As a consequence of this modulable d_{gap}, the C5-NRs metasurfaces exhibited a remarkably wide range of compacities (ϕ_{2D}), ranging from very 'open' metasurfaces (ϕ_{2D} = 28%) that are mostly filled with solvent, to compact metasurface (ϕ_{2D} = 77%) (**Figure 4b, S8**). Similarly, the colloidal supercrystals formed by C4-NRs showed adjustable inter-NR gaps and 3D compacities, ranging from 39% to 70%, depending on the depletant concentration in the surrounding medium (**Figure 4c-d**). These compacity values are significantly lower than those reported for dry supercrystals, and also fall below the theoretical packing limits for crystallization of hard particles, which are 92% for 2D pentagons,[64] 100% for 2D square and 74% for spheres in fcc arrangement. Under optical microscopy in solution, distinct colors were observed in both reflection and transmission modes, as a consequence of tunable plasmonic coupling (**Figures S6, S10**). Further increasing the aspect ratio of C5-NRs, beyond C5-L, enabled the formation of even more open metasurfaces, with compacities as low as 21% (**Figure S8**).

We then conducted time-resolved SAXS and extinction measurements to monitor the assembly and disassembly kinetics of C4-NRs (**Figure 5**). These processes were controlled by the slow diffusion of either a concentrated CTAC solution or pure water into the NR suspension, to induce assembly and disassembly respectively (**Figure S13**). In these conditions, assembly/disassembly processes took about 1h (**Figure 5a-b**), although the growth of crystalline domains continues beyond this time. These experiments show that the rhombic symmetry appeared as a transient state during the self-assembly process, bridging the transition from individually dispersed NRs to the final 3D tetragonal supercrystal as [CTAC] gradually diffused into the NR suspension (**Figure 5a**). It is proposed that the formation of C4-NR metasurfaces arises from preferential depletion interactions between the lateral faces of the nanorods at lower [CTAC], where the depletion force between the tip faces remains too weak to overcome thermal Brownian motion.

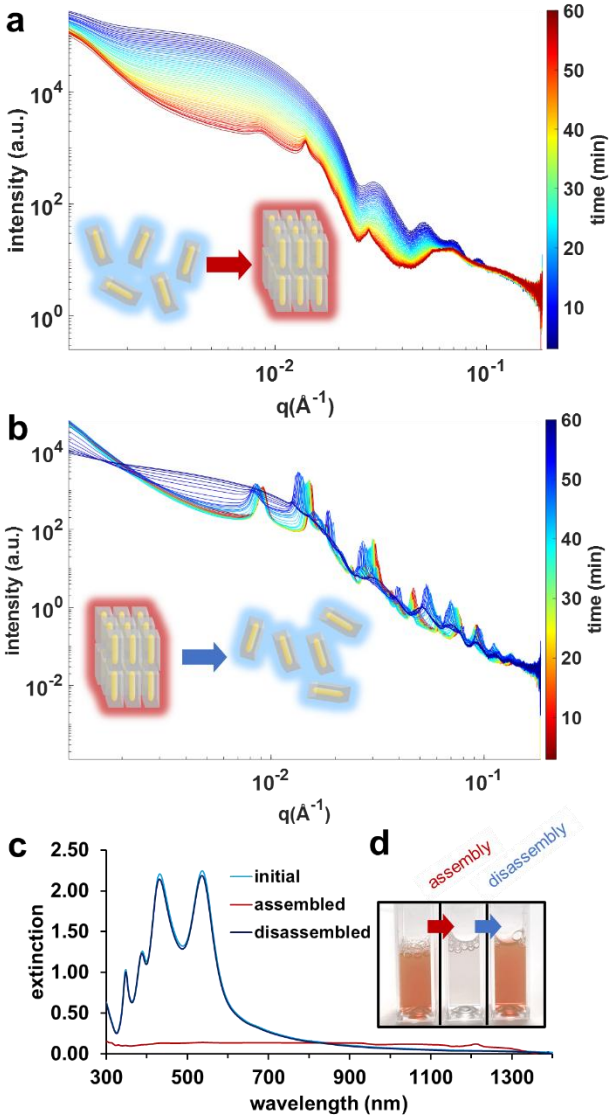

Figure 5: Reversible C4-NR assembly and disassembly using depletion. a) SAXS kinetics of C4-NR assembly by slow diffusion of depletant (t = 3 to 60 min) into the NR dispersion. **b)** SAXS kinetics of C4-NR disassembly by slow diffusion of water (t = 3 to 60 min) into the NR assembly suspension. **c)** UV-visible-NIR extinction spectra of C4-M after self-assembly and disassembly. Assembly was performed at 200 mM CTAC; **d)** Corresponding photographs of the cuvettes.

It was found that the depletion-induced interactions were fully reversible as the SAXS curve and extinction spectra of individual C4-M NR could be retrieves over multiple assembly-disassembly cycles (**Figure 5c-d, Figure S13**). Under slow DISA, nearly complete recovery of the original optical density (OD) was achieved after one to three full cycles, with the maximum longitudinal SPR blue-shift remaining below 1 nm (**Figure 5c, Figures S13-S15**). In contrast

when disassembly was triggered by one-shot dilution, the optical properties of the individual C4-NRs were not fully restored. A persistent blue shift of up to 21 nm and a recovery of only ~70% of the OD were observed, indicating partial aggregation of the nanorods (**Figure S14**). This outcome is attributed to rapid dilution, driving the system into kinetically trapped, small aggregates. Notably, the irreversibility of self-assembly becomes more pronounced at higher CTAC concentrations, where inter-NR gaps are smaller. Consequently, equilibrium structures are more likely to form at moderate CTAC concentrations and under slow self-assembly kinetics. These results should be considered in the context of a recent publication by our group, in which the assembly and disassembly of chiral NRs could be achieved under fast kinetics without any loss of optical activity.[65] Beyond the difference in NP shape, a key distinction lies in the size of the assemblies: in the previous work, assemblies typically consisted of only 3–4 NRs on average, whereas the metasurfaces presented here comprise thousands of NRs. This highlights the greater susceptibility of larger assemblies to kinetic trapping and irreversible aggregation under non-equilibrium conditions.

Finally, we investigated how the plasmonic properties of the metasurfaces could be tuned by varying the CTAC concentration. To this end, surface-enhanced Raman scattering (SERS) spectroscopy was performed on colloidal C5-S NR metasurfaces assembled at different CTAC concentrations (**Figure 6a-c**). Measurements were conducted in aqueous phase on a population of individual metasurfaces with a distribution of sizes and which undergo Brownian motion, both of which account for the large standard deviation in SERS counts. Since CTAC exhibits a low Raman scattering cross-section, the C5-S NRs were functionalized with a Raman reporter molecule, 4-aminothiophenol (4ATP), prior to their self-assembly via DISA. Upon excitation with either red (633 nm) or green (532 nm) lasers, self-assembly into metasurfaces led to an enhancement in the Raman signal of 4ATP by approximately two orders of magnitude compared to dispersed NRs (**Figure 6c**). While individual NPs contribute to the measured SERS signal through the lighting rod effect,[66] a noticeable 40 nm blue shift of the longitudinal plasmon band was readily observed at low CTAC concentration (**Figure S17**). These observations indicate that SERS enhancement arises both from the formation of plasmonic hotspots due to plasmonic coupling and from the increasing density of nanorods within the laser excitation area. Surprisingly, further increasing the CTAC concentration, thereby reducing d_{gap}, did not result in a continuous increase in SERS intensity, as might be expected from increased plasmonic coupling.[67] Instead, a non-monotonic dependence was observed, with a maximum Raman

enhancement occurring at d_{gap} = 11.0 ± 0.3 nm (at 200 mM CTAC) for 633 nm excitation and d_{gap} = 13.8 ± 0.3 nm (at 100 mM CTAC) for 532 nm (**Figure 6d-e**). This result aligns with the formation of metasurfaces featuring larger monodomains, where up to 1500 NRs were counted within the metasurface plane at an intermediate CTAC concentration (**Figure 6e, Figure S9**). While SERS enhancement is inherently localized, it can also benefit from increased spatial coherence and surface area of the metasurface. Beyond the optimal CTAC concentration, the Raman signal decreased and eventually reached a plateau. This steady-state, spanning a broad CTAC concentration range (200–800 mM), coincides with the stabilization of d_{gap} around 5.3 ± 0.2 nm. Overall, these experiments demonstrate that the size of the monodomains are important for SERS performance, potentially having a greater impact than d_{gap}.

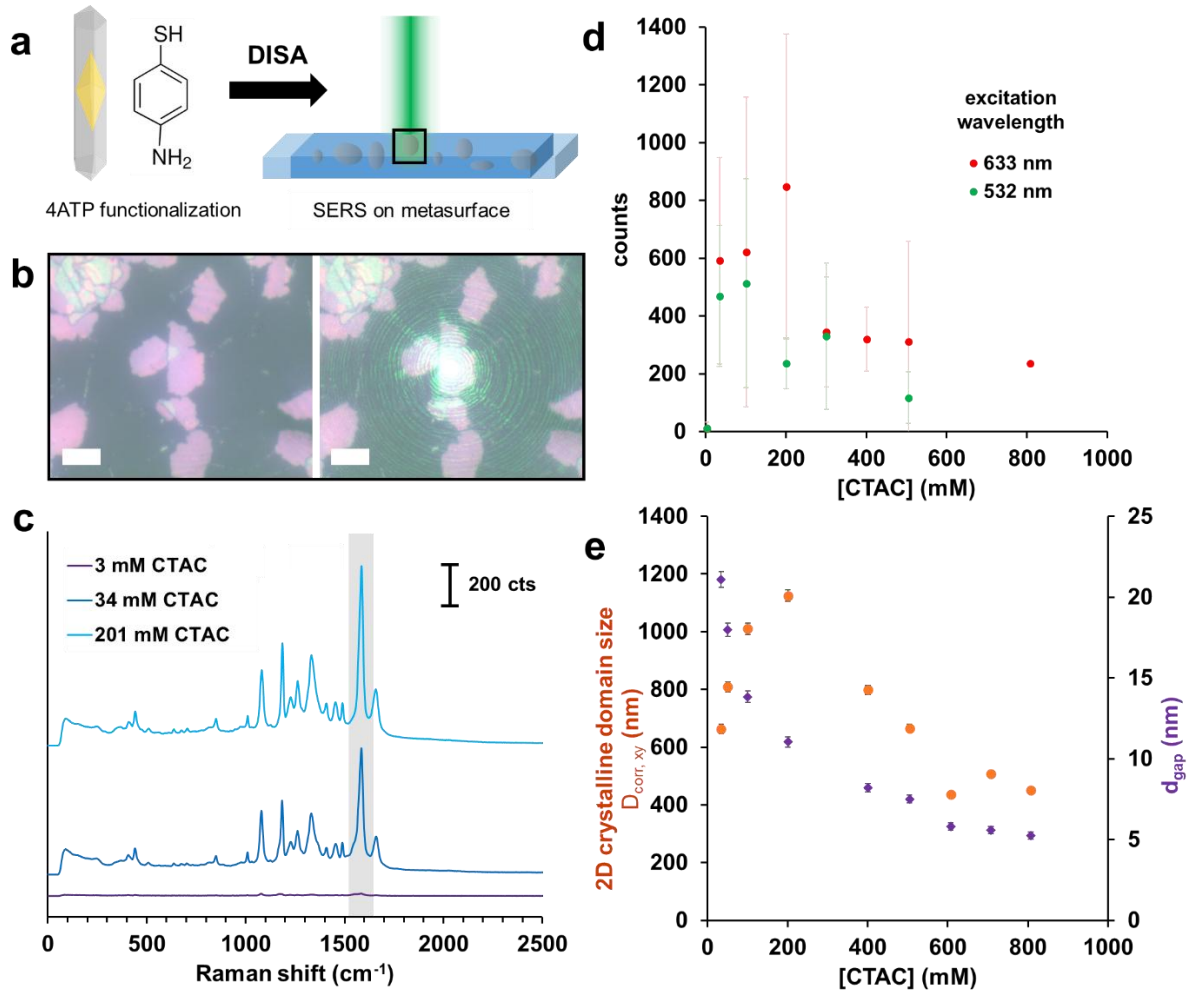

Figure 6: Tunable plasmonic response via SERS on colloidal DISA-based metasurfaces. **a)** Scheme of the 4ATP molecule that was used to coat C5-S NRs before assembly and subsequent SERS measurements at varying CTAC. **b)** Optical microscopy image of a

metasurface, before and during irradiation with a green 532 nm laser. Scale bars are 10 μm. **c)** Representative SERS spectra of 4ATP measured on C5-S at varying CTAC concentration. At 3mM, the measurement was performed on dispersed NRs. Each measurement was taken at excitation wavelength 633 nm, laser power 0.1 mW, averaging 10 acquisitions of 1 s integration time each. **d**) Plot of the mean SERS intensity at 1585 cm^{-1} of C5-S@4ATP metasurfaces at varying CTAC concentration at two excitation wavelength (633 nm and 532 nm). Spectra were averaged over 15 metasurface at each [CTAC] and the laser power was 0.1 mW at each wavelength. **e)** Comparison of the 2D crystalline domain size ($D_{corr,\ xy}$) of C5-S@4ATP metasurfaces and of their inter-NR face-to-face gaps (d_{gap}) as a function of the concentration of CTAC.

CONCLUSION

While metasurfaces are conventionally understood as nanoparticle assemblies immobilized on solid interfaces, this work introduces the concept of colloidal metasurfaces, where nanoparticles self-assemble into reconfigurable two-dimensional structures in liquid. The structural characteristics of these metasurfaces, including dimensionality, lattice symmetry, and packing density, can be precisely tuned by controlling the addition of CTAC micelles. By adjusting the depletant concentration, the inter-NR distances within the metasurfaces can be modulated, enabling compacities ranging from as low as 21% to as high as 80%. We found that metasurface formation occurs predominantly at intermediate CTAC concentrations and depends critically on the NR cross-section and anisotropy. Specifically, C4-NRs form extended metasurfaces with rhombic symmetry within a narrow CTAC concentration window, whereas C5-NRs, assemble into metasurfaces with hexagonal symmetry over a broader concentration range because of a subtle difference in tip geometry. Moreover, these DISA-induced metasurfaces can be reversibly assembled and disassembled for at least four cycles without significant loss of optical properties. Finally, *in situ* SERS measurements on these colloidal metasurfaces reveal a direct link between the tunability of the assembly structure and the resulting plasmonic response. This underscores the potential of DISA as a versatile and controllable strategy for fabricating adjustable plasmonic metasurfaces.

EXPERIMENTAL SECTION

Materials. The chemicals were purchased from Sigma-Aldrich and VWR. They were used without further purification: hexadecyltrimethylammonium bromide (CTAB, ≥99%, VWR), hexadecyltrimethylammonium chloride (CTAC, 25 wt.% in H_2O, 90%, Sigma-Aldrich), sodium borohydride ($NaBH_4$, ≥96%, Sigma-Aldrich), L-ascorbic acid (AA, ≥ 99%, Sigma-Aldrich), hydrogen tetrachloroaurate trihydrate ($HAuCl_4 \cdot 3H_2O$, ≥99.9%, Sigma-Aldrich), silver nitrate ($AgNO_3$, ≥99.0%, Sigma-Aldrich), hydrochloric acid (HCl, 37%), benzyldimethylhexadecylammonium chloride (BDAC, 99%, Sigma-Aldrich). Milli-Q water (18.2 MΩ cm) was used in all the synthesis and characterizations measurements.

Synthesis of metal nanorods of varying anisotropy.

Gold core - silver shell nanorods (Au@AgNRs) were synthesized by seed-mediated growth in aqueous solution as described previously in literature.[43, 62, 64, 68, 69]

C4 (square section) Au@Ag nanorods or cuboids. This synthesis required three steps: the fabrication of monocrystalline gold seeds, followed by a first seed-mediated growth to obtain gold nanorods, and finally a second seed-mediated growth of silver to obtain the C4-NRs. For small C4-NRs (C4-S), the gold cores were higher aspect ratio AuNRs. For medium and large C4-NRs (C4-M and C4-L), lower aspect ratio AuNRs served as the gold cores.

3) ***C4-S.*** To make long AuNRs for the C4-S gold core, first, the monocrystalline gold seeds were obtained from a solution of CTAB (50 mM) and decanol (14 mM) in H_2O (7 mL), to which was added $HAuCl_4$ (140 µL, 25 mM), AA (35 µL, 100 mM) and $NaBH_4$ (280 µL, 20 mM). The mixture was stirred at room temperature for 1 h. The gold nanorods were obtained from 100 mL of a similar CTAB/decanol/water solution, to which was added $AgNO_3$ (800 µL, 10 mM), HCl (7 mL, 1 M), $HAuCl_4$ (2 mL, 25 mM), AA (1.3 mL, 100 mM) and 6 mL of the previously prepared seeds solution. The mixture was stirred at 28°C for 4 h, before being centrifuged at 15000 rcf for 1 h and washed with water twice. Finally, the Au@Ag C4-NRs were obtained from a solution of 250 mL of a similar CTAB/decanol/water solution, to which was added $AgNO_3$ (500 µL, 100 mM), $HAuCl_4$ (5 mL, 25 mM), AA (2 mL, 100 mM), HCl (25 mL, 1 M) and the previously prepared nanorod solution (650 µL, $[Au^0]$ = 8.75 mM). The final Au@Ag C4-NRs were obtained by Ag growth onto these high AR AuNRs. Here, the AuNRs, $AgNO_3$ solution, and ascorbic acid solution were added into an aqueous CTAC solution to achieve a final

gold concentration [Au^0] of 0.25 mM, CTAC concentration of 10 mM, with a Ag^+:Au^0 molar ratio of 8:1 and a Ag^+:AA molar ratio of 4:1 for C4-S This mixture was stirred at 70 °C for 2h. After synthesis, the C4-NRs were collected and washed by two rounds of centrifugation, and then purified using CTAC-induced depletion.

4) ***C4-M and C4-L.*** To obtain lower AR AuNRs as the gold core, first, monocrystalline seeds were obtained from a solution of CTAB (100 mM, 4.7 mL) mixed with $HAuCl_4$ solution (25 mM, 50 μL) at 30°C. After mixing, freshly prepared $NaBH_4$ (300 μL, 10 mM) solution was injected with vigorous stirring. This seed solution was aged at 30°C for at least 30 min before adding it into the growth solution. Next, the growth solution to synthesize AuNRs was prepared by mixing aqueous CTAB (250 mL, 100 mM), 5-bromosalicylic acid (450 mg, 5-BrSA), and water (240 mL). This mixture was sonicated until all the solids dissolved. Then, aqueous $AgNO_3$ (476 μL, 100 mM) and aqueous $HAuCl_4$ solution (10 mL, 25 mM) were added to the mixture to begin Au^{3+} prereduction. The progress of prereduction was monitored by UV-vis spectroscopy; prereduction was allowed to continue until the absorbance at 396 nm reached 0.7 (with an optical path of 1 cm), at which ascorbic acid solution (1250 μL, 100 mM) was injected under vigorous stirring, followed quickly by adding 800 μL of previously synthesized seed solution with stirring. The mixture was then kept stirring at 30°C for 4 h. After synthesis, the AuNRs were collected and washed by two rounds of centrifugation. The final Au@Ag C4-NRs were obtained by Ag growth onto these AuNRs. Here, the AuNRs, $AgNO_3$ solution, and ascorbic acid solution were added into a CTAC aqueous solution to achieve a final gold concentration [Au^0] of 0.25 mM, CTAC concentration of 10 mM, with a Ag^+:Au^0 molar ratio of 8:1 and a Ag^+:AA molar ratio of 4:1 for C4-M, and a Ag^+:Au^0 molar ratio of 12:1 and a Ag^+:AA molar ratio of 4:1 for C4-L. This mixture was stirred at 70 °C for 2h. After synthesis, the C4-NRs were collected and washed by two rounds of centrifugation, and then purified using CTAC-induced depletion.

C5 (pentagonal section) Au@Ag nanorods. This synthesis required three steps: the fabrication of pentatwinned gold seeds, followed by a first seed-mediated growth to obtain either gold pentagonal bipyramids (AuBPs) for C5-S and other thin C5-NRs or gold decahedra (AuDh) for C5-M and C5-L, and then a second seed-mediated growth of silver to obtain C5-NRs. The seeds were synthesized in a solution of CTAC (60 mM) in water (33 mL) to which

was added trisodium citrate (4 mL, 50 mM) at 30°C. The mixture was left at 30°C for 30 min before adding $NaBH_4$ (1 mL, 25 mM). After stirring for 30 s, the mixture was left for 5 days in an oven at 40°C to obtain pentatwinned seeds.

3) ***C5-S*** To prepare AuBPs as cores for C5-S NRs, first, a growth solution was prepared by successive addition of aqueous CTAB (200 mL, 100 mM), $AgNO_3$ (200 µL, 100 mM), $HAuCl_4$ (4 mL, 25 mM), HCl (4 mL, 1 M), and finally with vigorous stirring, first ascorbic acid solution (1600 µL, 100 mM), and then the pentatwinned seeds solution (3600 µL) after the mixture turned colorless. The mixture was left stirring at 30°C for 4 h. After synthesis, the particles were collected and washed by two rounds of centrifugation. Further purification of the BPs was done by BDAC-induced depletion. For this, in a 15 mL tube, concentrated 450 mM BDAC surfactant solution and water was added to 1 mL of concentrated BP solution ($[Au^0]$=100 mM, [CTAC] = 1 mM), to achieve a total mixture volume of 10 mL and a final BDAC concentration of 350 mM. This suspension was mixed, and then allowed to stand vertically and separate overnight, with the purified PRs sedimenting as a precipitate. This BP precipitate was separated from the supernatant; then, the purified BPs were washed with 1 mM CTAC in one centrifugation step at 8000 rpm for 10 min. Finally, all the precipitate was redispersed into 1 mM CTAC for storage. The final thin Au@Ag C5-NRs were obtained by Ag growth onto these AuBPs. Here, the AuBPs, $AgNO_3$ solution, and ascorbic acid solution were added into a CTAC aqueous solution to achieve a final gold concentration $[Au^0]$ of 0.25 mM, CTAC concentration of 10 mM, with a Ag^+:Au^0 molar ratio of 4:1 and a Ag^+:AA molar ratio of 4:1 for C5-S. For other lengths of thin C5-NRs (**Figure S8**), the Ag^+:Au^0 molar ratio can be varied from 2:1 to 8:1, keeping a Ag^+:AA molar ratio of 4:1. This mixture was stirred at 70 °C for 2h. After synthesis, the C5-NRs were collected and washed by two rounds of centrifugation, and then purified using CTAC-induced depletion.

4) ***C5-M, C5-L.*** To prepare AuDhs as cores for C5-M and C5-L NRs, first, a growth solution was prepared from a solution of BDAC (100 mM) in water (400 mL) to which was added $HAuCl_4$ (8 mL, 25 mM) and AA (3 mL, 100 mM). A portion of the same pentatwinned seed solution (1200 µL, [Au] = 0.3 mM) was added under fast stirring. The mixture was subsequently left under slow stirring at 30°C for 30 min. The

decahedra were then centrifuged for 10 min at 6000 rpm and washed with water, before being stored in 5 mL of 5 mM CTAC. The final Au@Ag C5-NRs were made by silver growth onto these AuDhs. Here, the AuDhs, $AgNO_3$ solution, and ascorbic acid solution were added into a CTAC aqueous solution to achieve a final gold concentration [Au^0] of 0.25 mM, CTAC concentration of 10 mM, with a Ag^+:Au^0 molar ratio of 5:1 and a Ag^+:AA molar ratio of 4:1 for C5-M, and with a Ag^+:Au^0 molar ratio of 8:1 and a Ag^+:AA molar ratio of 4:1 for C5-L. This mixture was stirred at 70 °C for 2h. After synthesis, the C5-NRs were collected and washed by two rounds of centrifugation, and then purified using CTAC-induced depletion.

Preparation of C5-S NRs for SERS. C5-S NRs were functionalized with 4-aminothiophenol (4ATP). Into a round bottom flask, an aqueous 40 mL solution of CTAC (2.5 mM), hydrochloric acid (3.3 mM, targeting a pH of 2.5 to 3.0), 4ATP (15 µM by adding 60 µL of 10 mM 4ATP ethanol solution), and C5-S NRs (0.5 mM in Au^0 + Ag^0) was prepared. The mixture was stirred at 60 °C for 3 h. Afterwards, the functionalized C5-NRs were collected and washed by two rounds of centrifugation, and stored in aqueous 2.5 mM CTAC.

Methods

Transmission electron microscopy. TEM was performed at Imagerie-Gif (I2BC CNRS, Gif-sur-Yvette, France) using a JEOL JEM-1400 microscope operating at 120 kV with a filament current of ≈55 µA.

UV-visible-NIR extinction spectroscopy. Extinction spectra of the cGNR suspensions were obtained by a Cary 5000 UV-vis-NIR spectrophotometer (Agilent) in polystyrene cuvettes with an optical path length of 1 cm. Au^0 concentrations of pure Au NR suspensions were estimated using their measured extinction at 400 nm, taking a NP concentration of 0.5 mM in Au0 for a sample absorbance of 1.2.[70, 71]

Optical microscopy. Optical microscopy images were obtained by a WITec Alpha300 Access microscope in reflection mode.

Scanning electron microscopy. SEM images were obtained with a Zeiss Supra55VP, operating at an acceleration voltage of 3 kV. We used two strategies, yielding similar results, to retrieve assemblies for SEM, both aimed at minimizing evaporation-induced self-assembly:

1) Fast drying: The suspension is dried under a gentle air flow.

2) Quenching with ethanol: The suspension is prepared in a vial with a Si wafer at the bottom where the assemblies sediment. After at least 12 h of DISA, most of the supernatant is removed, and the pellet is washed with ethanol to limit further assembly.

Small-Angle X-ray Scattering. SAXS measurements were performed on the SWING beamline of the SOLEIL synchrotron (Saint-Aubin, France) at a beam energy of 16 keV with a sample-to-detector distance of 6.22 m, resulting in a q range of 0.001 to 0.24 $Å^{-1}$. Exposure times were 1000 ms per measurement. The beam size was approximately 500 × 200 μm^2 (horizontal × vertical). All measurements were performed at room temperature (295 K). The scattered signal was recorded by an Eiger 4M detector (Dectris Ltd, Switzerland) with a pixel size of 75 μm. Preliminary data treatment (angular averaging and normalization) was done using the software Foxtrot developed at the beamline (https://www.synchrotron-soleil.fr/fr/lignes-de-lumiere/swing), which yielded the intensity as a function of the scattering vector magnitude I(q) in absolute units. Subsequent SAXS data modeling and analysis was done either with homemade Python codes (https://pypi.org/project/prismformfactors/) or with SasView 6.0.0 (https://www.sasview.org/).[53] The positions (q-values) of the Bragg peaks in the 1D SAXS radial profiles of each sample were manually fitted using a homemade Python code to determine the lattice symmetry and parameters of the different NR colloidal metasurfaces. 3D compacities of the colloidal assemblies were calculated by dividing the volume of one metallic NR with the volume of the corresponding 3D primitive unit cell of the assembly at the specific CTAC concentration. Similarly, 2D compacities of colloidal metasurfaces were calculated by dividing the cross-sectional area of one NR with the area of the corresponding 2D primitive unit cell of the assembly at the specific CTAC concentration. Note that only the metallic volume or area of the NR is considered in this calculation, and not the CTAC ligand bilayer around the NR. The shapes of the Bragg peaks in the 1D SAXS radial profiles of each sample were fitted in SasView Version 6 using a pseudo-Voigt model (https://marketplace.sasview.org/models/127/), which is a weighted sum of a Gaussian and a Lorentzian peak model. The full width at half maximum (FWHM) value from the fit is taken to calculate the Debye-Scherrer correlation length (D_{corr}) in either the xy plane or the z-axis of the NR assemblies with the z-axis taken along the normal of a metasurface, as follows:

$$D_{corr} = \frac{2\pi\, n}{FWHM}$$

where n is a constant, equal to 1.05 for $D_{corr, xy}$, and 0.89 for $D_{corr, z}$, different from unity due to the anisotropy of the shapes of the NR assemblies, which causes elongations of the Bragg spots in different directions depending on which *hkl* reflection they correspond to.

Surface Enhanced Raman Scattering. SERS microscopy was done using a WITec Alpha300 Access microscope and C5-S functionalized with 4-ATP. For each batch of metasurfaces made at a specific CTAC concentration, the Eppendorf tube containing NR metasurfaces was gently agitated, and 5 µL of suspension was taken up into an optical capillary (0.05 mm × 1 mm section). The capillary is then sealed and set on the microscope stage for SERS. For each capillary, measurements are taken on 15 metasurfaces randomly chosen along the whole length of the capillary. For each metasurface measurement, an average of 10 spectrum acquisitions each acquired in 1 s, with the 100x objective and at optimal focus for maximum SERS counts. Measurements are done with both red laser (633 nm) and green laser (532 nm) excitation, with 0.1 mW laser power, with the 100x objective.

Depletion-induced self-assembly. Two procedures were tested for DISA, resulting in slow or fast self-assembly kinetics, as described in the following.

3) Slow kinetics*:* This procedure is adapted from[72]. Into a round glass capillary (diameter = 1.5 mm), 10 µL of aqueous NR suspension (~100 mM Ag^0, at 2.51 mM CTAC) is injected with a syringe near the bottom of the capillary, leaving a 1 cm deep air pocket below. Then, 20 µL of aqueous CTAC solution of the selected concentration was slowly deposited on top of the NR phase with a syringe, ensuring a sharp and well-defined interface between the two phases. Finally, the capillaries were sealed using a glue gun and left undisturbed for at least 24 h to allow diffusion, self-assembly, and equilibration before characterization of the colloidal sample by SAXS or optical microscopy.
4) Fast kinetics*:* Into a 0.5 mL Eppendorf tube, 10 µL of aqueous NR suspension (~100 mM Ag^0, at 2.5 mM CTAC) was rapidly and evenly mixed within a few seconds with 20 µL of aqueous CTAC solution of the selected concentration. The mixture was allowed to stand, self-assemble, and equilibrate for either 1 h or 24 h before characterization by SAXS or optical microscopy. The colloidal one-shot sample is transferred to a glass capillary prior to SAXS characterization.

ACKNOWLEDGMENTS

The CNRS is acknowledged for funding and support. J.G.T acknowledges financial support from the 2MIB Doctoral School of Université Paris-Saclay (Programme Blanc GS Chimie). J.M. acknowledges financial support by the ANR NIMROD project (ANR-21-CE09-0019) for his Ph.D. R.N. acknowledges financial support by the ANR METATRAP project (ANR-22-CE09-0011) for his postdoctoral position. N.K. acknowledges financial support by the ANR CODENAME project (ANR-23-CE09-0032) for his Ph.D. The authors acknowledge SOLEIL for the provision of synchrotron radiation facilities (experiments 20231786). The authors thank Stéphan Rouzière for the use of the MORPHEUS platform. The present work had benefited from the electronic microscopy facility of Imagerie-Gif, (http://www.i2bc.parissaclay.fr), member of IBiSA (http://www.ibisa.net), supported by "France-BioImaging" (ANR10-INBS-04-01), and the Labex "Saclay Plant Science" (ANR-11-IDEX-0003-02).

Supporting Information Available

The supporting information contains: TEM image analysis of the NRs, SAXS analysis of the assemblies obtained by DISA, optical microscopy images of the self-assembled systems, additional optical characterization of the assemblies by extinction spectroscopy.

REFERENCES

(1) Garcia-Lojo, D.; Nunez-Sanchez, S.; Gomez-Grana, S.; Grzelczak, M.; Pastoriza-Santos, I.; Perez-Juste, J.; Liz-Marzan, L. M. Plasmonic Supercrystals. *Acc. Chem. Res.* **2019**, *52*, 1855–1864.

(2) Meinzer, N.; Barnes, W. L.; Hooper, I. R. Plasmonic Meta-Atoms and Metasurfaces. *Nat. Photonics* **2014**, *8*, 889–898.

(3) Pileni, M. P. 2D Superlattices and 3D Supracrystals of Metal Nanocrystals: A New Scientific Adventure. *J. Mater. Chem.* **2011**, *21*, 16748–16758

(4) Kasani, S.; Curtin, K.; Wu, N. A Review of 2D and 3D Plasmonic Nanostructure Array Patterns: Fabrication, Light Management and Sensing Applications. *Nanophotonics* **2019**, *8*, 2065–2089.

(5) Hamon, C.; Novikov, S. M.; Scarabelli, L.; Solis, D. M.; Altantzis, T.; Bals, S.; Taboada, J. M.; Obelleiro, F.; Liz-Marzan, L. M. Collective Plasmonic Properties in Few-Layer Gold Nanorod Supercrystals. *ACS Photonics* **2015**, *2*, 1482–1488.

(6) Herran, M.; Juergensen, S.; Kessens, M.; Hoeing, D.; Köppen, A.; Sousa-Castillo, A.; Parak, W. J.; Lange, H.; Reich, S.; Schulz, F.; et al. Plasmonic Bimetallic Two-Dimensional Supercrystals for H2 Generation. *Nat. Catal.* **2023**, *6*, 1205–1214.

(7) Hagan, M. F.; Grason, G. M. Equilibrium Mechanisms of Self-Limiting Assembly. *Rev. Mod. Phys.* **2021**, *93*, 025008.

(8) Ofir, Y.; Samanta, B.; Rotello, V. M. Polymer and Biopolymer Mediated Self-Assembly of Gold Nanoparticles. *Chem. Soc. Rev.* **2008**, *37*, 1814–1825.

(9) Kostiainen, M. A.; Hiekkataipale, P.; Laiho, A.; Lemieux, V.; Seitsonen, J.; Ruokolainen, J.; Ceci, P. Electrostatic Assembly of Binary Nanoparticle Superlattices Using Protein Cages. *Nat. Nanotechnol.* **2013**, *8*, 52–56.

(10) Laramy, C. R.; Lopez-Rios, H.; O'Brien, M. N.; Girard, M.; Stawicki, R. J.; Lee, B.; de la Cruz, M. O.; Mirkin, C. A. Controlled Symmetry Breaking in Colloidal Crystal Engineering with DNA. *ACS Nano* **2019**, *13*, 1412–1420.

(11) He, M.; Gales, J. P.; Ducrot, E.; Gong, Z.; Yi, G. R.; Sacanna, S.; Pine, D. J. Colloidal Diamond. *Nature* **2020**, *585*, 524–529.

(12) Liu, W.; Tagawa, M.; Xin, H. L.; Wang, T.; Emamy, H.; Li, H.; Yager, K. G.; Starr, F. W.; Tkachenko, A. V.; Gang, O. Diamond Family of Nanoparticle Superlattices. *Science* **2016**, *351*, 582–586.

(13) Kalsin, A. M.; Fialkowski, M.; Paszewski, M.; Smoukov, S. K.; Bishop, K. J.; Grzybowski, B. A. Electrostatic Self-Assembly of Binary Nanoparticle Crystals with a Diamond-Like Lattice. *Science* **2006**, *312*, 420–424.

(14) Li, Z.; Lim, Y.; Tanriover, I.; Zhou, W.; Li, Y.; Zhang, Y.; Aydin, K.; Glotzer, S. C.; Mirkin, C. A. DNA-Mediated Assembly of Au Bipyramids into Anisotropic Light Emitting Kagome Superlattices. *Sci. Adv.* **2024**, *10*, eadp3756.

(15) Chen, Q.; Bae, S. C.; Granick, S. Directed Self-Assembly of a Colloidal Kagome Lattice. *Nature* **2011**, *469*, 381–384.

(16) Liu, K.; Nie, Z.; Zhao, N.; Li, W.; Rubinstein, M.; Kumacheva, E. Step-Growth Polymerization of Inorganic Nanoparticles. *Science* **2010**, *329*, 197–200.

(17) Nie, Z.; Fava, D.; Kumacheva, E.; Zou, S.; Walker, G. C.; Rubinstein, M. Self-Assembly of Metal-Polymer Analogues of Amphiphilic Triblock Copolymers. *Nat. Mater.* **2007**, *6*, 609–614.

(18) Klinkova, A.; Therien-Aubin, H.; Choueiri, R. M.; Rubinstein, M.; Kumacheva, E. Colloidal Analogs of Molecular Chain Stoppers. *Proc. Natl. Acad. Sci. U.S.A.* **2013**, *110*, 18775–18779.

(19) Liu, K.; Lukach, A.; Sugikawa, K.; Chung, S.; Vickery, J.; Therien-Aubin, H.; Yang, B.; Rubinstein, M.; Kumacheva, E. Copolymerization of Metal Nanoparticles: A Route to Colloidal Plasmonic Copolymers. *Angew. Chem., Int. Ed.* **2014**, *53*, 2648–2653.

(20) Duguet, E.; Desert, A.; Perro, A.; Ravaine, S. Design and Elaboration of Colloidal Molecules: An Overview. *Chem. Soc. Rev.* **2011**, *40*, 941–960.

(21) Yi, C.; Liu, H.; Zhang, S.; Yang, Y.; Zhang, Y.; Lu, Z.; Kumacheva, E.; Nie, Z. Self-Limiting Directional Nanoparticle Bonding Governed by Reaction Stoichiometry. *Science* **2020**, *369*, 1369–1374.

(22) Shevchenko, E. V.; Talapin, D. V.; Kotov, N. A.; O'Brien, S.; Murray, C. B. Structural Diversity in Binary Nanoparticle Superlattices. *Nature* **2006**, *439*, 55–59.

(23) Talapin, D. V.; Shevchenko, E. V.; Bodnarchuk, M. I.; Ye, X.; Chen, J.; Murray, C. B. Quasicrystalline Order in Self-Assembled Binary Nanoparticle Superlattices. *Nature* **2009**, *461*, 964–967.

(24) Marcone, J.; Juergensen, S.; Barrios-Capuchino, J.; Li, X.; Goldmann, C.; Koppen, A.; Pfeiffer, W.; Lehmkuhler, F.; Parak, W. J.; Kociak, M.; et al. Plasmonic Polymorphs by Combining Shape Anisotropy and Soft Interactions in Bipyramid Thin Films. *Small* **2025**, *21*, e2500389.

(25) Udayabhaskararao, T.; Altantzis, T.; Houben, L.; Coronado-Puchau, M.; Langer, J.; Popovitz-Biro, R.; Liz-Marzán, L. M.; Vuković, L.; Král, P.; Bals, S.; et al. Tunable Porous Nanoallotropes Prepared by Post-Assembly Etching of Binary Nanoparticle Superlattices. *Science* **2017**, *358*, 514–518.

(26) de Nijs, B.; Dussi, S.; Smallenburg, F.; Meeldijk, J. D.; Groenendijk, D. J.; Filion, L.; Imhof, A.; van Blaaderen, A.; Dijkstra, M. Entropy-Driven Formation of Large Icosahedral Colloidal Clusters by Spherical Confinement. *Nat. Mater.* **2015**, *14*, 56–60.

(27) Jedrych, A.; Pawlak, M.; Gorecka, E.; Lewandowski, W.; Wojcik, M. M. Light-Responsive Supramolecular Nanotubes-Based Chiral Plasmonic Assemblies. *ACS Nano* **2023**, *17*, 5548–5560.

(28) Wan, S.; Xi, X.; Zhang, H.; Ning, J.; Zheng, Z.; Zhang, Z.; Long, Y.; Deng, Y.; Fan, P.; Yang, D.; et al. Shape-Mediated Oriented Assembly of Concave Nanoparticles under Cylindrical Confinement. *ACS Nano* **2022**, *16*, 21315–21323.

(29) Chaabani, W.; Lyu, J.; Marcone, J.; Goldmann, C.; Ten Veen, E. J. M.; Dumesnil, C.; Bizien, T.; Smallenburg, F.; Imperor-Clerc, M.; Constantin, D.; et al. Prismatic Confinement Induces Tunable Orientation in Plasmonic Supercrystals. *ACS Nano* **2024**, *18*, 9566–9575.

(30) Peil, A.; Zhan, P.; Duan, X.; Krahne, R.; Garoli, D.; Liz-Marzan, L. M.; Liu, N. Transformable Plasmonic Helix with Swinging Gold Nanoparticles. *Angew. Chem., Int. Ed.* **2023**, *62*, e202213992.

(31) Kuzyk, A.; Schreiber, R.; Zhang, H.; Govorov, A. O.; Liedl, T.; Liu, N. Reconfigurable 3D Plasmonic Metamolecules. *Nat. Mater.* **2014**, *13*, 862–866.

(32) Kuzyk, A.; Urban, M. J.; Idili, A.; Ricci, F.; Liu, N. Selective Control of Reconfigurable Chiral Plasmonic Metamolecules. *Sci. Adv.* **2017**, *3*, e1602803.

(33) Zhong, Y.; Moore, T. C.; Dwyer, T.; Butrum-Griffith, A.; Allen, V. R.; Chen, J.; Wang, Y.; Cheng, F.; Glotzer, S. C.; Ye, X. Engineering and Direct Imaging of Nanocube Self-Assembly Pathways. *Nat. Chem. Eng.* **2024**, *1*, 532–541.

(34) Zhou, W.; Li, Y.; Je, K.; Vo, T.; Lin, H.; Partridge, B. E.; Huang, Z.; Glotzer, S. C.; Mirkin, C. A. Space-Tiled Colloidal Crystals from DNA-Forced Shape-Complementary Polyhedra Pairing. *Science* **2024**, *383*, 312–319.

(35) Lin, H.; Lee, S.; Sun, L.; Spellings, M.; Engel, M.; Glotzer, S. C.; Mirkin, C. A. Clathrate Colloidal Crystals. *Science* **2017**, *355*, 931–935.

(36) Vo, T.; Glotzer, S. C. A Theory of Entropic Bonding. *Proc. Natl. Acad. Sci. U.S.A.* **2022**, *119*, e2116414119.

(37) Young, K. L.; Personick, M. L.; Engel, M.; Damasceno, P. F.; Barnaby, S. N.; Bleher, R.; Li, T.; Glotzer, S. C.; Lee, B.; Mirkin, C. A. A Directional Entropic Force Approach to Assemble Anisotropic Nanoparticles into Superlattices. *Angew. Chem., Int. Ed.* **2013**, *52*, 13980–13984.

(38) van Anders, G.; Klotsa, D.; Ahmed, N. K.; Engel, M.; Glotzer, S. C. Understanding Shape Entropy through Local Dense Packing. *Proc. Natl. Acad. Sci. U.S.A.* **2014**, *111*, E4812–E4821.

(39) Nag, R.; Rouviere, N.; Trazo, J. G.; Marcone, J.; Kutalia, N.; Goldmann, C.; Imperor-Clerc, M.; Alloyeau, D.; Constantin, D.; Hamon, C. Depletion-Induced Tunable Assembly of Complementary Platonic Solids. *Nano Lett.* **2024**, *24*, 16368–16373.

(40) Lekkerkerker, H. N. W.; Tuinier, R.; Vis, M. Depletion Interaction. In *Colloids and the Depletion Interaction*; Springer International Publishing: Cham, 2024; pp 67–120.

(41) Young, K. L.; Jones, M. R.; Zhang, J.; Macfarlane, R. J.; Esquivel-Sirvent, R.; Nap, R. J.; Wu, J.; Schatz, G. C.; Lee, B.; Mirkin, C. A. Assembly of Reconfigurable One-Dimensional

Colloidal Superlattices Due to a Synergy of Fundamental Nanoscale Forces. *Proc. Natl. Acad. Sci. U.S.A.* **2012**, *109*, 2240–2245.

(42) Kim, J.; Song, X.; Ji, F.; Luo, B.; Ice, N. F.; Liu, Q.; Zhang, Q.; Chen, Q. Polymorphic Assembly from Beveled Gold Triangular Nanoprisms. *Nano Lett.* **2017**, *17*, 3270–3275.

(43) Goldmann, C.; Chaabani, W.; Hotton, C.; Imperor-Clerc, M.; Moncomble, A.; Constantin, D.; Alloyeau, D.; Hamon, C. Confinement Effects on the Structure of Entropy-Induced Supercrystals. *Small* **2023**, *19*, e2303380.

(44) Cheng, Z.; Jones, M. R. Assembly of Planar Chiral Superlattices from Achiral Building Blocks. *Nat. Commun.* **2022**, *13* (1), 4207.

(45) Wan, S.; Xia, X.; Gao, Y.; Zhang, H.; Zhang, Z.; Wu, F.; Wu, X.; Yang, D.; Li, T.; Li, J.; et al. Curvature-Guided Depletion Stabilizes Kagome Superlattices of Nanocrystals. *Science* **2025**, *387* (6737), 978–984.

(46) Chiu, C.-Y.; Chen, C.-K.; Chang, C.-W.; Jeng, U. S.; Tan, C.-S.; Yang, C.-W.; Chen, L.-J.; Yen, T.-J.; Huang, M. H. Surfactant-Directed Fabrication of Supercrystals from the Assembly of Polyhedral Au–Pd Core–Shell Nanocrystals and Their Electrical and Optical Properties. *J. Am. Chem. Soc.* **2015**, *137* (6), 2265–2275.

(47) Baranov, D.; Fiore, A.; van Huis, M.; Giannini, C.; Falqui, A.; Lafont, U.; Zandbergen, H.; Zanella, M.; Cingolani, R.; Manna, L. Assembly of Colloidal Semiconductor Nanorods in Solution by Depletion Attraction. *Nano Lett.* **2010**, *10* (2), 743–749.

(48) Zheng, J.; Cheng, X.; Zhang, H.; Bai, X.; Ai, R.; Shao, L.; Wang, J. Gold Nanorods: The Most Versatile Plasmonic Nanoparticles. *Chem. Rev.* **2021**, *121* (21), 13342–13453.

(49) Scarabelli, L.; Hamon, C.; Liz-Marzán, L. M. Design and Fabrication of Plasmonic Nanomaterials Based on Gold Nanorod Supercrystals. *Chem. Mater.* **2017**, *29* (1), 15–25.

(50) Gibaud, T.; Barry, E.; Zakhary, M. J.; Henglin, M.; Ward, A.; Yang, Y.; Berciu, C.; Oldenbourg, R.; Hagan, M. F.; Nicastro, D.; et al. Reconfigurable Self-Assembly through Chiral Control of Interfacial Tension. *Nature* **2012**, *481* (7381), 348–351.

(51) Sung, B.; Wensink, H. H.; Grelet, E. Depletion-Driven Morphological Transitions in Hexagonal Crystallites of Virus Rods. *Soft Matter* **2019**, *15* (46), 9520–9527.

(52) Barry, E.; Dogic, Z. Entropy Driven Self-Assembly of Nonamphiphilic Colloidal Membranes. *Proc. Natl. Acad. Sci. U.S.A.* **2010**, *107* (23), 10348–10353.

(53) Marcone, J.; Trazo, J. G.; Nag, R.; Goldmann, C.; Ratel-Ramond, N.; Hamon, C.; Imperor-Clerc, M. Form Factor of Prismatic Particles for Small-Angle Scattering Analysis. *J. Appl. Crystallogr.* **2025**, *58* (Pt 2), 543–552.

(54) Yang, C. W.; Chiu, C. Y.; Huang, M. H. Formation of Free-Standing Supercrystals from the Assembly of Polyhedral Gold Nanocrystals by Surfactant Diffusion in the Solution. *Chem. Mater.* **2014**, *26* (16), 4882–4888.

(55) Asakura, S.; Oosawa, F. On Interaction between Two Bodies Immersed in a Solution of Macromolecules. *J. Chem. Phys.* **1954**, *22* (7), 1255–1256.

(56) Vrij, A. Polymers at Interfaces and the Interactions in Colloidal Dispersions. *Pure Appl. Chem.* **1976**, *48* (4), 471–483.

(57) Park, K.; Koerner, H.; Vaia, R. A. Depletion-Induced Shape and Size Selection of Gold Nanoparticles. *Nano Lett.* **2010**, *10* (4), 1433–1439.

(58) Zhang, Y.; Lu, F.; van der Lelie, D.; Gang, O. Continuous Phase Transformation in Nanocube Assemblies. *Phys. Rev. Lett.* **2011**, *107* (13), 135701.

(59) Rossi, L.; Soni, V.; Ashton, D. J.; Pine, D. J.; Philipse, A. P.; Chaikin, P. M.; Dijkstra, M.; Sacanna, S.; Irvine, W. T. M. Shape-Sensitive Crystallization in Colloidal Superball Fluids. *Proc. Natl. Acad. Sci. U.S.A.* **2015**, *112* (17), 5286–5290.

(60) Batten, R. D.; Stillinger, F. H.; Torquato, S. Phase Behavior of Colloidal Superballs: Shape Interpolation from Spheres to Cubes. *Phys. Rev. E* **2010**, *81* (6), 061105.

(61) Meijer, J.-M.; Pal, A.; Ouhajji, S.; Lekkerkerker, H. N. W.; Philipse, A. P.; Petukhov, A. V. Observation of Solid–Solid Transitions in 3D Crystals of Colloidal Superballs. *Nat. Commun.* **2017**, *8* (1), 14352.

(62) Gómez-Graña, S.; Goris, B.; Altantzis, T.; Fernández-López, C.; Carbó-Argibay, E.; Guerrero-Martínez, A.; Almora-Barrios, N.; López, N.; Pastoriza-Santos, I.; Pérez-Juste, J.; et al. Au@Ag Nanoparticles: Halides Stabilize {100} Facets. *J. Phys. Chem. Lett.* **2013**, *4* (13), 2209–2216.

(63) Gomez-Grana, S.; Hubert, F.; Testard, F.; Guerrero-Martinez, A.; Grillo, I.; Liz-Marzan, L. M.; Spalla, O. Surfactant (Bi)layers on Gold Nanorods. *Langmuir* **2012**, *28* (2), 1453–1459.

(64) Marcone, J.; Chaabani, W.; Goldmann, C.; Imperor-Clerc, M.; Constantin, D.; Hamon, C. Polymorphous Packing of Pentagonal Nanoprisms. *Nano Lett.* **2023**, *23* (4), 1337–1342.

(65) Trazo, J. G.; Freijeiro, A. S.; Mychinko, M.; Kutalia, N.; Impéror-Clerc, M.; Bals, S.; Liz-Marzán, L. M.; Pérez-Juste, J.; Pastoriza-Santos, I.; Hamon, C. Tunable Plasmonic Circular Dichroism of Hierarchical Chiral Assemblies. *Chem. Mater.* **2025**, *37* (16), 6237–6245.

(66) Jackson, J. D. *Classical Electrodynamics*, 3rd ed.; Wiley: New York, 1998.

(67) Langer, J.; Jimenez de Aberasturi, D.; Aizpurua, J.; Alvarez-Puebla, R. A.; Auguie, B.; Baumberg, J. J.; Bazan, G. C.; Bell, S. E. J.; Boisen, A.; Brolo, A. G.; et al. Present and Future of Surface-Enhanced Raman Scattering. *ACS Nano* **2020**, *14* (1), 28–117.

(68) Sanchez-Iglesias, A.; Winckelmans, N.; Altantzis, T.; Bals, S.; Grzelczak, M.; Liz-Marzan, L. M. High-Yield Seeded Growth of Monodisperse Pentatwinned Gold Nanoparticles through Thermally Induced Seed Twinning. *J. Am. Chem. Soc.* **2017**, *139* (1), 107–110.

(69) González-Rubio, G.; Kumar, V.; Llombart, P.; Díaz-Núñez, P.; Bladt, E.; Altantzis, T.; Bals, S.; Peña-Rodríguez, O.; Noya, E. G.; MacDowell, L. G.; et al. Disconnecting Symmetry Breaking from Seeded Growth for the Reproducible Synthesis of High Quality Gold Nanorods. *ACS Nano* **2019**, *13* (4), 4424–4435.

(70) Scarabelli, L.; Sánchez-Iglesias, A.; Pérez-Juste, J.; Liz-Marzán, L. M. A "Tips and Tricks" Practical Guide to the Synthesis of Gold Nanorods. *J. Phys. Chem. Lett.* **2015**, *6* (21), 4270–4279.

(71) Hendel, T.; Wuithschick, M.; Kettemann, F.; Birnbaum, A.; Rademann, K.; Polte, J. In Situ Determination of Colloidal Gold Concentrations with UV–Vis Spectroscopy: Limitations and Perspectives. *Anal. Chem.* **2014**, *86* (22), 11115–11124.

(72) Yang, P. W.; Thoka, S.; Lin, P. C.; Su, C. J.; Sheu, H. S.; Huang, M. H.; Jeng, U. S. Tracing the Surfactant-Mediated Nucleation, Growth, and Superpacking of Gold Supercrystals Using Time and Spatially Resolved X-ray Scattering. *Langmuir* **2017**, *33* (13), 3253–3261.

Table of Contents Figure:

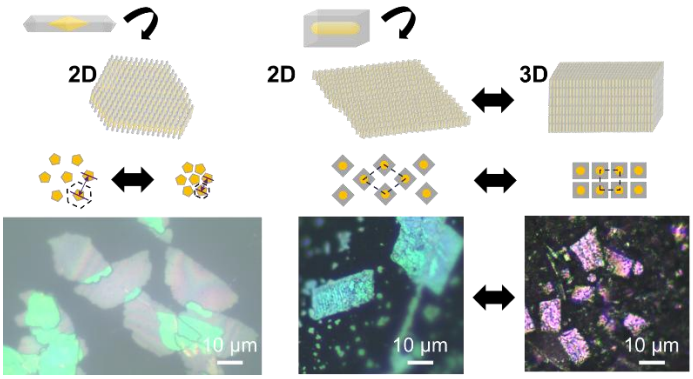

Supporting Information:

Colloidal Tunable Metasurfaces via Depletion-Induced Self-Assembly of Plasmonic Nanorods

Jaime Gabriel Trazo,[1] Jules Marcone,[1] Rahul Nag,[1] Claire Goldmann,[1] Nika Kutalia,[1] Thomas Bizien,[2] Brigitte Pansu,[1] Marianne Impéror-Clerc,[1] and Cyrille Hamon[1]*

[1] *Laboratoire de Physique des Solides, Université Paris-Saclay, CNRS, Orsay 91405, France.*

[2] *SWING beamline, SOLEIL Synchrotron, 91190 Gif-sur-Yvette, France.*

corresponding author's email address: cyrille.hamon@cnrs.fr

Table S1: Size distribution analysis of the Au@Ag NRs of varying shape, and their minimum DISA threshold.

	l_{TEM} (nm)	w_{TEM} (nm)	l_{SAXS} (nm)	w_{SAXS} (nm)	aspect ratio (AR_{TEM})	facet interaction area (A_{TEM}, 1000 nm^2)	experimental self-assembly threshold (mM CTAC)	theoretical self-assembly threshold (mM CTAC)
C4-S	**98.5 ± 5.4**	**34.1 ± 2.2**	78.3 ± 6.3	37.2 ± 3.0	2.9 ± 0.2	3.4 ± 0.3	50 ± 5	53 ± 5
C4-M	**63.2 ± 3.2**	**38.4 ± 1.9**	70.4 ± 9.2	41.8 ± 2.9	1.6 ± 0.1	2.4 ± 0.2	80 ± 5	72 ± 5
C4-L	**66.9 ± 3.0**	**46.5 ± 2.3**	76.4 ± 8.4	50.0 ± 3.0	1.4 ± 0.1	3.1 ± 0.2	60 ± 5	57 ± 5
C5-S	**188.9 ± 12.5**	**27.2 ± 1.8**	121.8 ± 7.3	26.4 ± 1.3	6.9 ± 0.6	3.2 ± 0.3	35 ± 5	55 ± 5
C5-M	**133.2 ± 6.6**	**58.6 ± 3.0**	111.7 ± 7.8	61.2 ± 6.1	2.3 ± 0.2	4.9 ± 0.4	35 ± 5	36 ± 3
C5-L	**217.1 ± 10.2**	**62.6 ± 2.7**	182.7 ± 7.3	60.0 ± 3.0	3.5 ± 0.2	8.5 ± 0.6	20 ± 5	22 ± 1

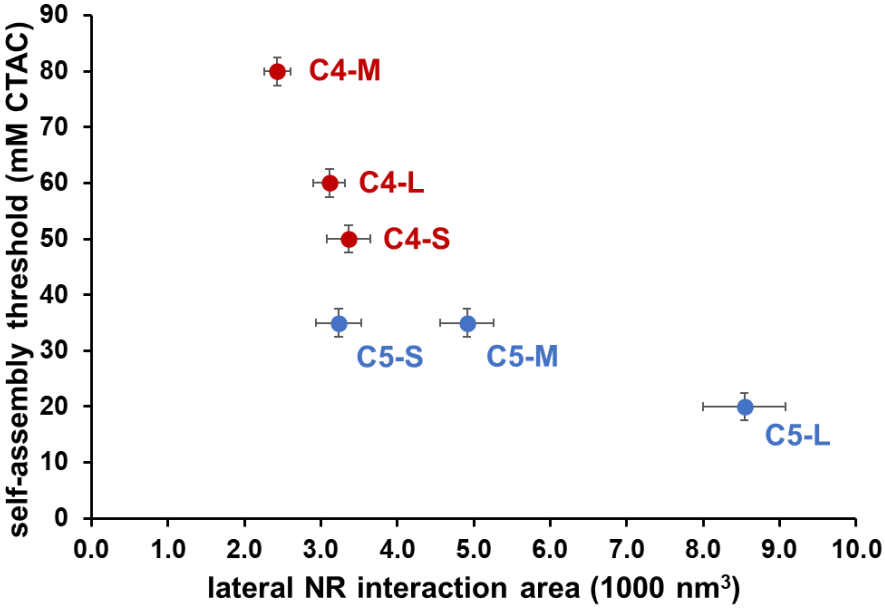

Figure S1: **Plot of the depletion interaction (lateral facet) areas of the C4-NRs and C5-NRs versus their experimental side-by-side self-assembly thresholds with CTAC.** Lateral NR facet areas *A* were determined using TEM image analysis: *For C4-NRs,* $A = l_{TEM} \times w_{TEM}$. *For C5-NRs,* $A = l_{TEM} \times a$, *where a is the edge length of the pentagonal section. Here, a is approximated as* $\pi w_{TEM} / 5$.

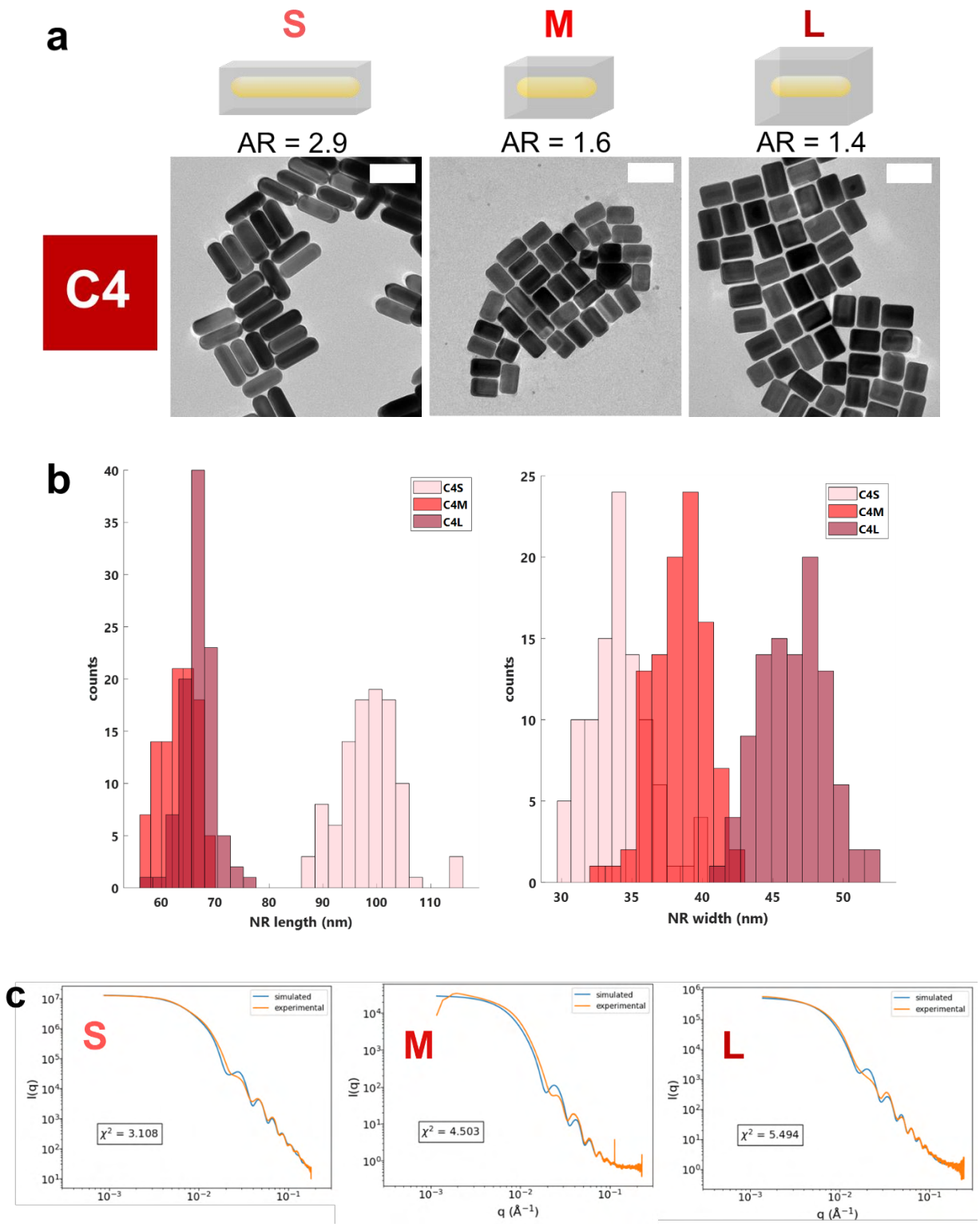

Figure S2: Size characterization of C4-NRs. a) TEM micrographs and corresponding illustrations of the NRs (Scale bars are 100 nm.) **b)** Histograms of length and width distributions determined from TEM image analysis. **c)** NR size analysis by SAXS form factor fitting.[1]

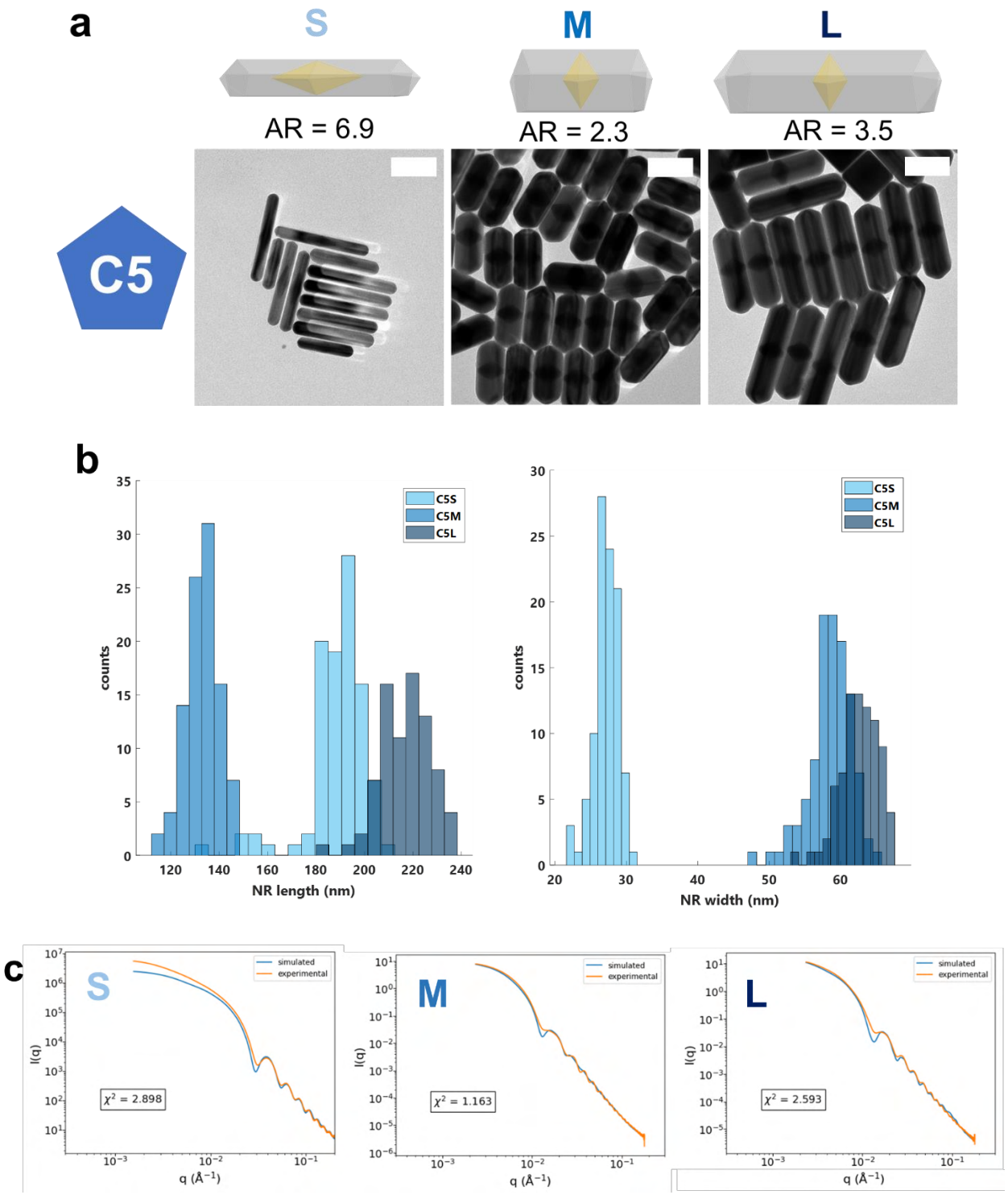

Figure S3: Size characterization of C5-NRs. a) TEM micrographs and corresponding illustrations of the NRs (Scale bars are 100 nm.) **b)** Histograms of length and width distributions by TEM image analysis. **c)** NR size analysis by SAXS form factor fitting. [1]

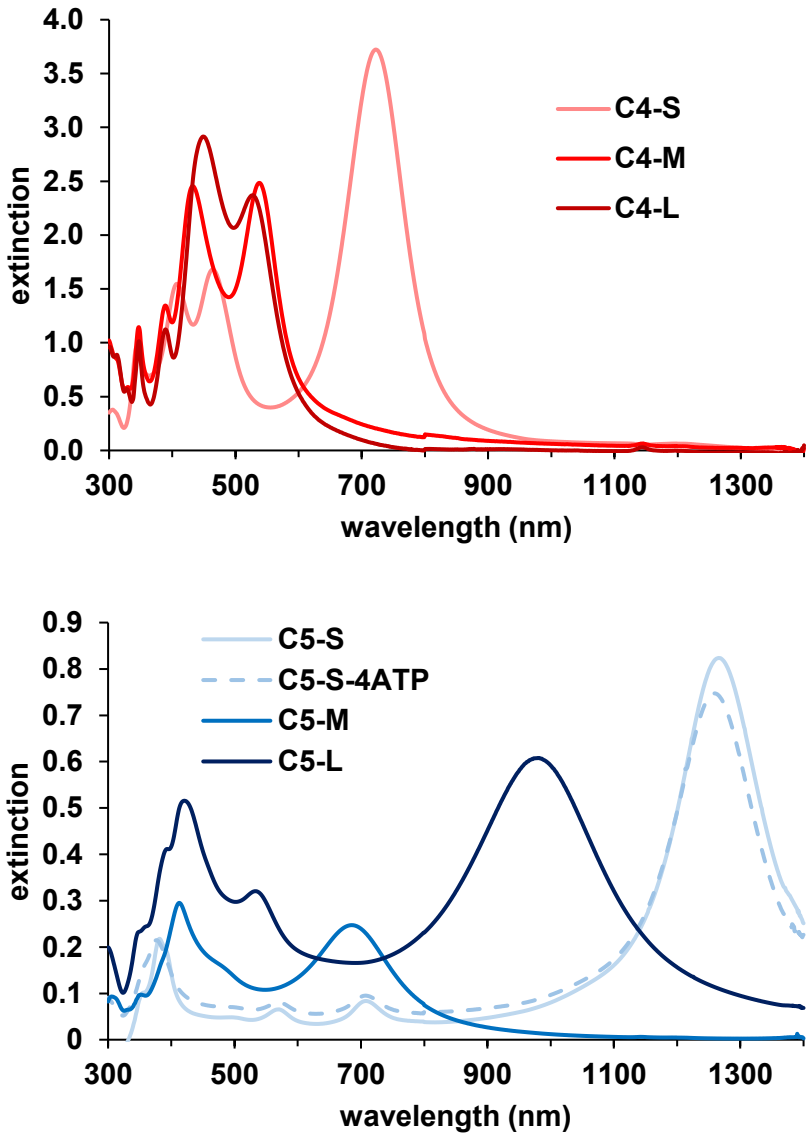

Figure S4: UV-vis-NIR extinction spectra of the C4-NRs and C5-NRs in aqueous suspension (2.5 mM CTAC). The blue dashed line corresponds to the C5-S-4ATP NRs used for SERS experiments, before self-assembly.

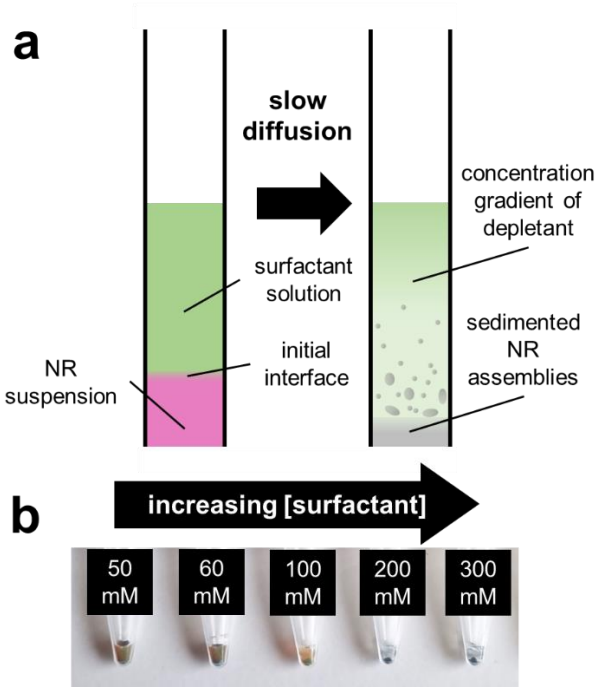

Figure S5: Depletion-induced self-assembly (DISA) of NRs in colloidal suspension by slow diffusion of CTAC. a) Scheme of slow-diffusion DISA in a capillary. **b)** Series of C4-M NR samples assembled at increasing CTAC concentration, with the color change signifying the formation of colloidal assemblies.

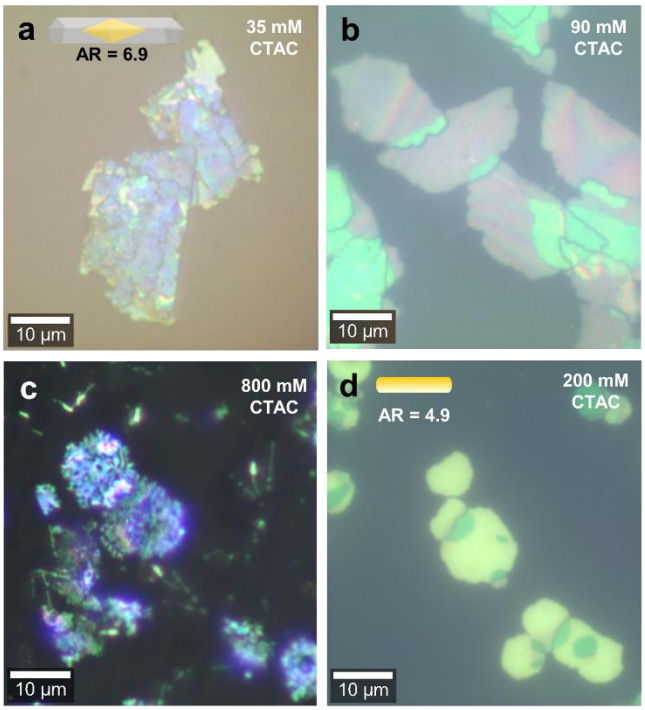

Figure S6: Visual inspection of 2D colloidal metasurfaces via DISA. In situ optical microscopy (reflection mode) images of colloidal metasurfaces of **a-c)** Au@Ag C5-S NRs assembled in varying CTAC concentrations, and of **d)** small monocrystalline Au NRs (l = 74.3 ± 4.1 nm; w = 14.9 ± 1.3 nm) assembled in 200 mM CTAC.

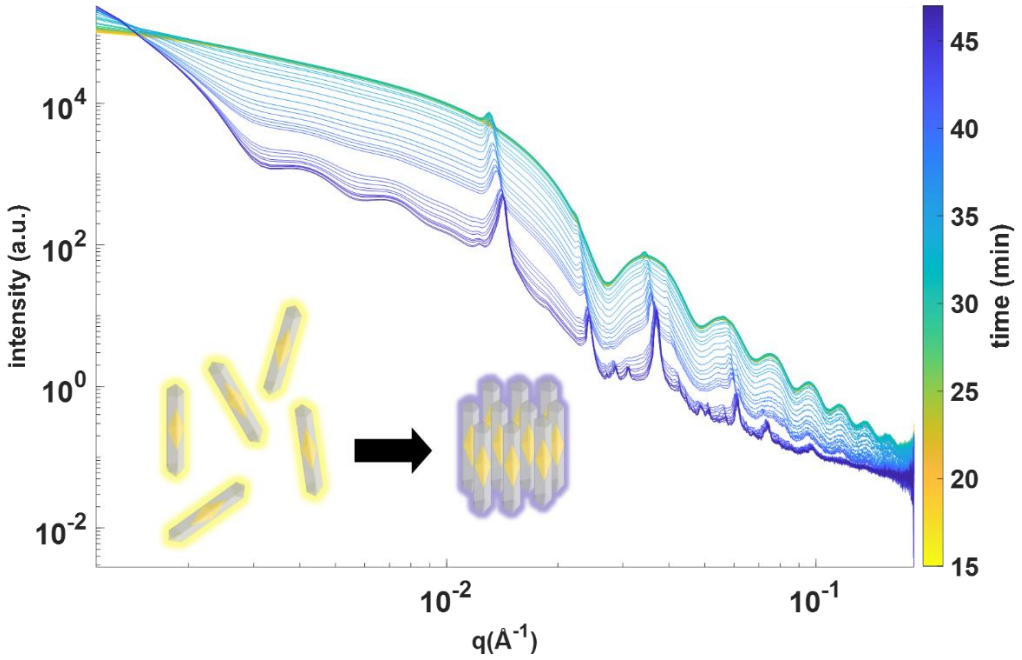

Figure S7: SAXS kinetics measurement of the self-assembly of C5-S NRs into 2D metasurface by slow diffusion. The NR suspension, initially containing 2.5 mM CTAC, was brought into contact with a 760 mM CTAC solution to initiate DISA.

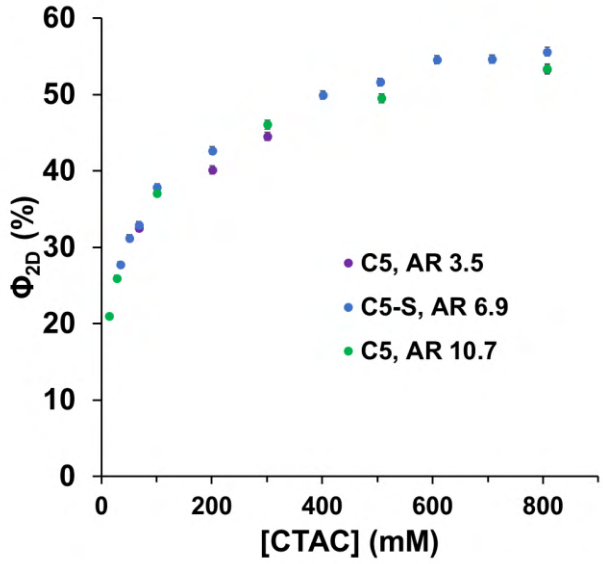

Figure S8: Comparison of 2D compacities in long metal C5-NR metasurfaces of differing aspect ratios. Error bars are too small to be visible.

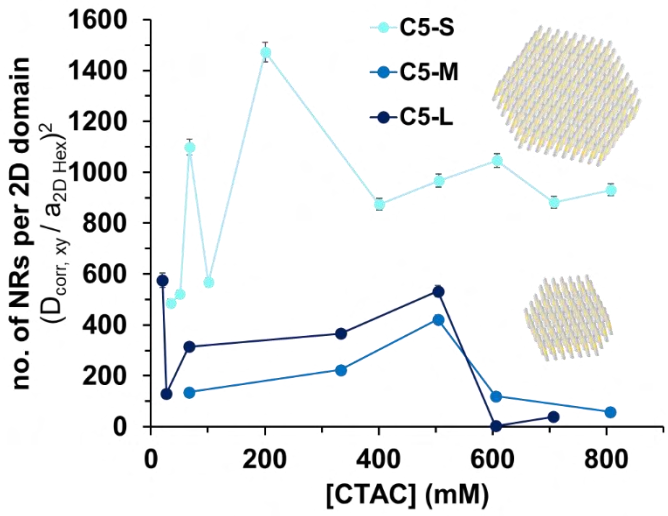

Figure S9: Variation in the 2D crystalline domain size, counted as the number of NRs, in C5-NR metasurfaces as a function of depletant concentration. For some points, error bars are too small to be visible.

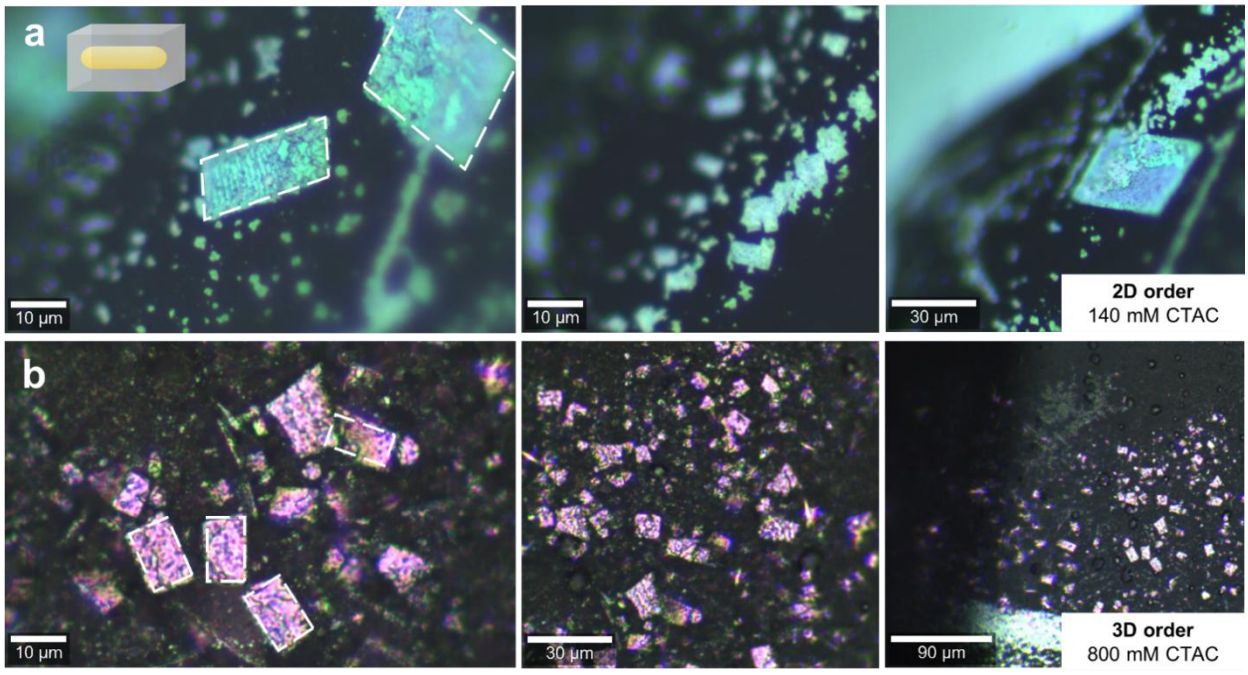

Figure S10: In situ optical microscopy (reflection mode) of colloidal C4-M NR assemblies, with 2D versus 3D lattice order. For some assemblies, the contours are highlighted, revealing rhombic shapes in (a) and prismatic shapes in (b).

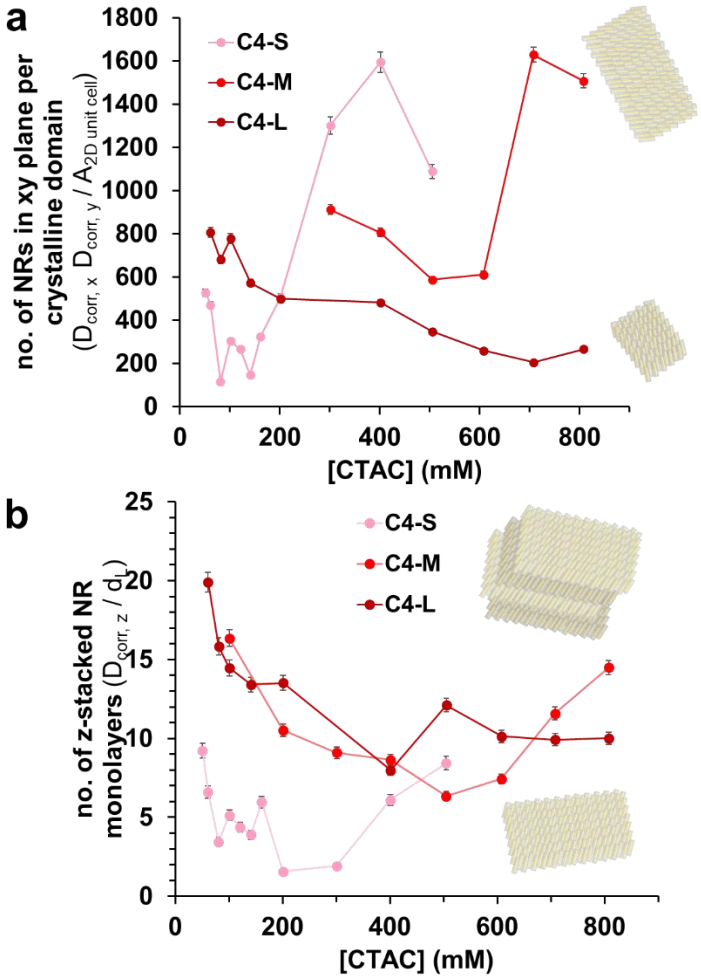

Figure S11: **Change in size and dimensionality of crystalline domains in 2D to 3D colloidal assemblies of C4-NRs.** Variation in the number of nanorods per domain in **a)** the xy-plane and **b)** the z-axis (i.e. number of stacked monolayers) in C4-S assemblies, as a function of depletant concentration. For some points, error bars are too small to be visible.

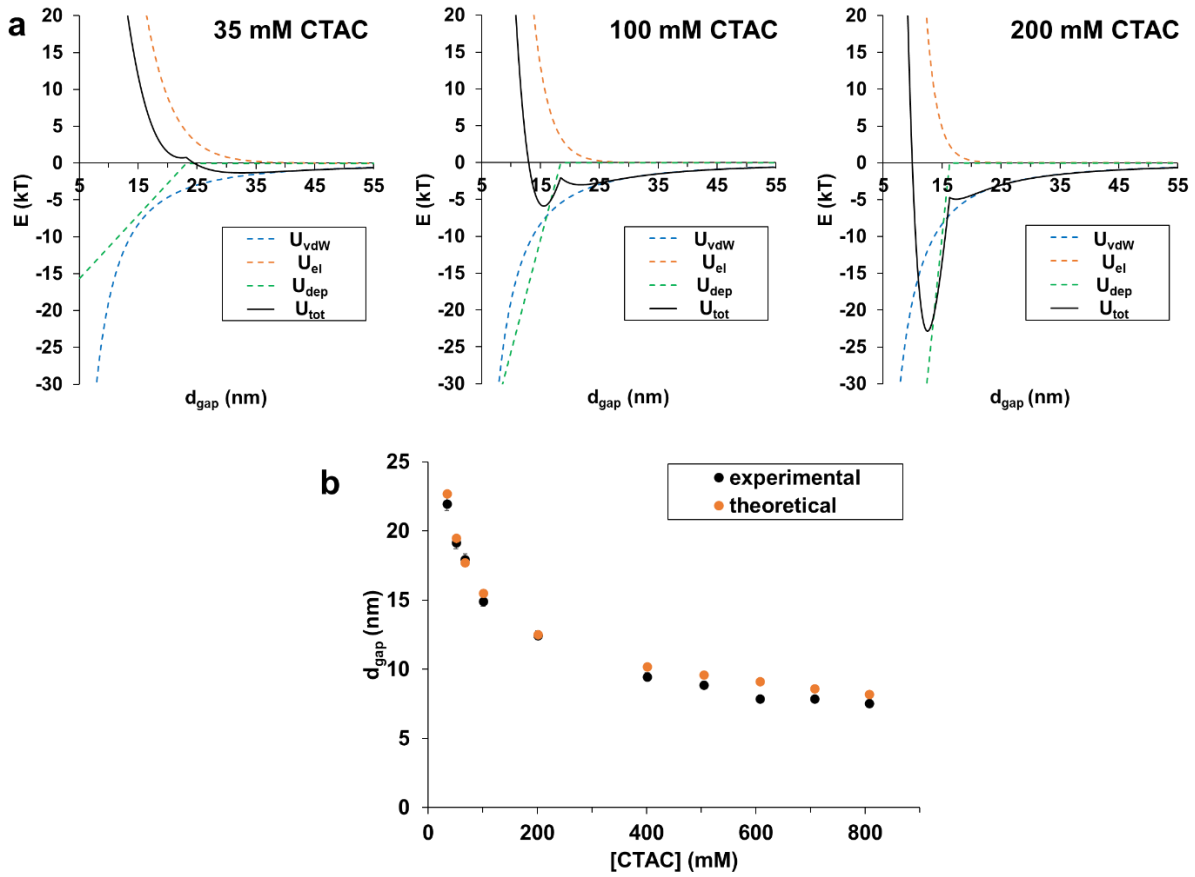

Figure S12: Calculation of theoretical inter-NR face-to-face gap distance (d_{gap}) for C5-S DISA assemblies. The interaction potentials between pairs of colloidal NRs were modeled as those between flat silver plates, accounting for the sum of van der Waals, electrostatic, and depletion forces. Equations were taken from reference.[2] A Hamaker constant of $H = 9 \times 10^{-20}$ J was used for the Ag–water–Ag geometry.[3] The theoretical equilibrium d_{gap} corresponds to the inter-NR gap at the minimum of the total potential well. a) Variation of the total potential with depletant concentration. b) Comparison between experimental and theoretical inter-NR gaps for C5-S metasurfaces.

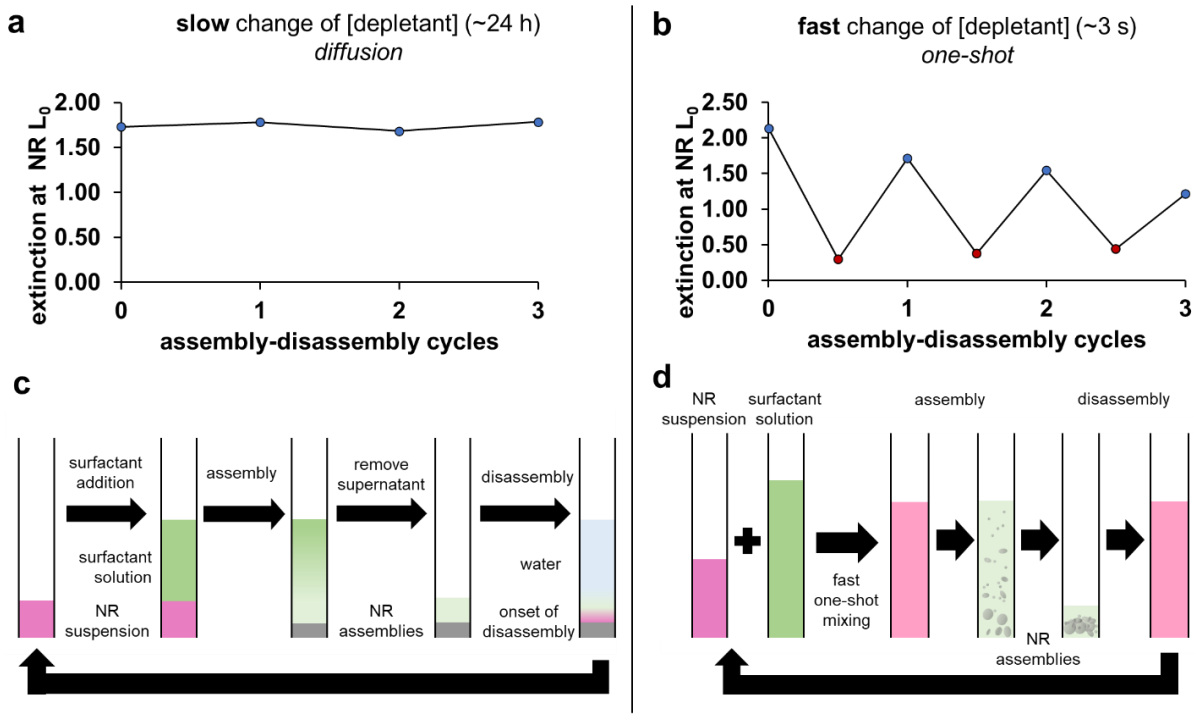

Figure S13: Cyclic reversibility of DISA by either slow (diffusion) or fast (one-shot mixing) change of depletant concentration, showing assembly-disassembly of C4-M NRs. a) Full reversibility by slow diffusion monitored by UV-vis-NIR extinction after three cycles. **b)** Partial reversibility by fast one-shot mixing monitored by UV-vis-NIR extinction after three cycles. **c)** Scheme of cyclic assembly-disassembly by slow diffusion. **d)** Scheme of cyclic assembly-disassembly by one-shot mixing.

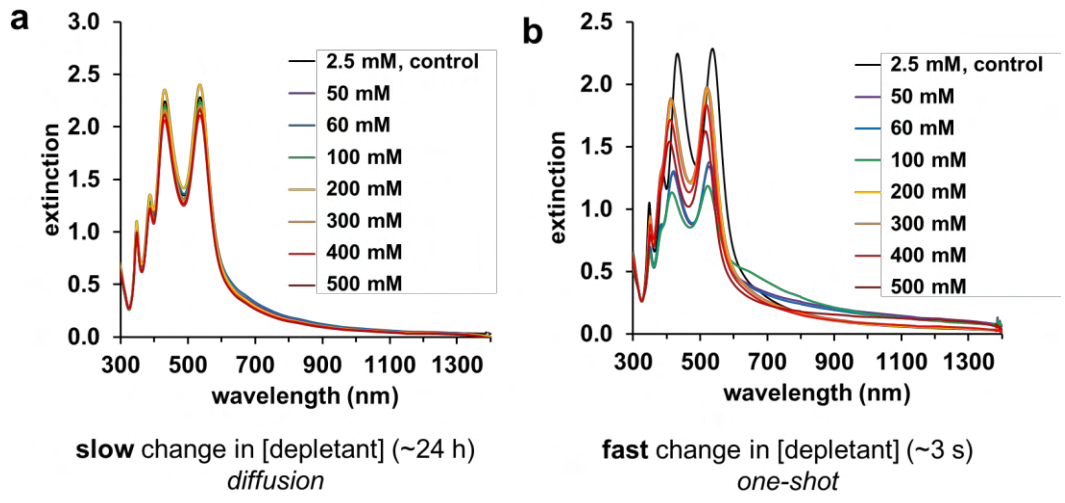

Figure S14: UV-vis-NIR extinction spectra of C4-M NRs after one cycle of depletion-induced assembly-disassembly, using different depletant (CTAC) concentrations, comparing: a) slow diffusion with near-full reversibility versus, **b)** fast one-shot mixing with partial reversibility, evidenced by the blue-shifts in the NR localized SPR peaks.

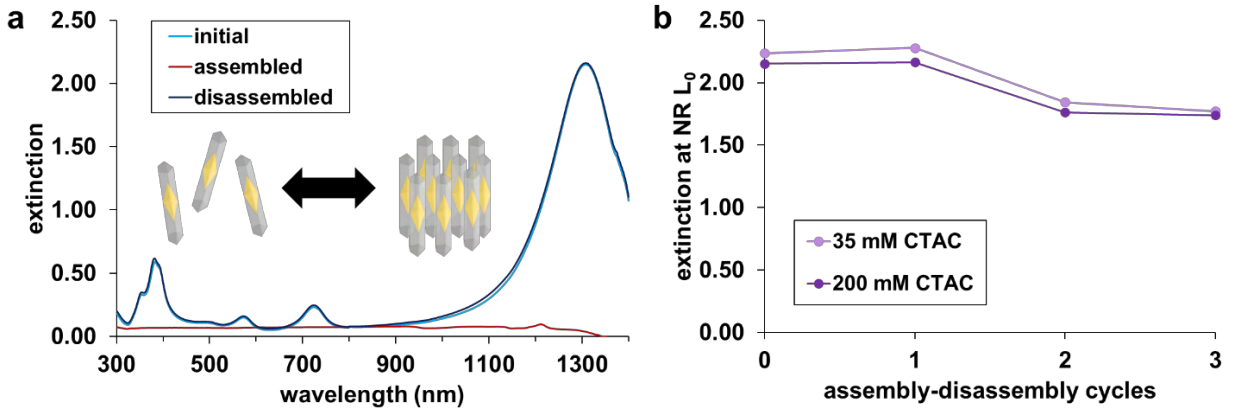

Figure S15: Reversible assembly-disassembly of C5-S NRs by slow diffusion of depletant probed by UV-vis-NIR absorption spectroscopy. a) Spectra for assembly at 200 mM CTAC and disassembly at 10 mM CTAC. **b)** Cyclic reversibility of slow DISA at lower versus higher depletion strength.

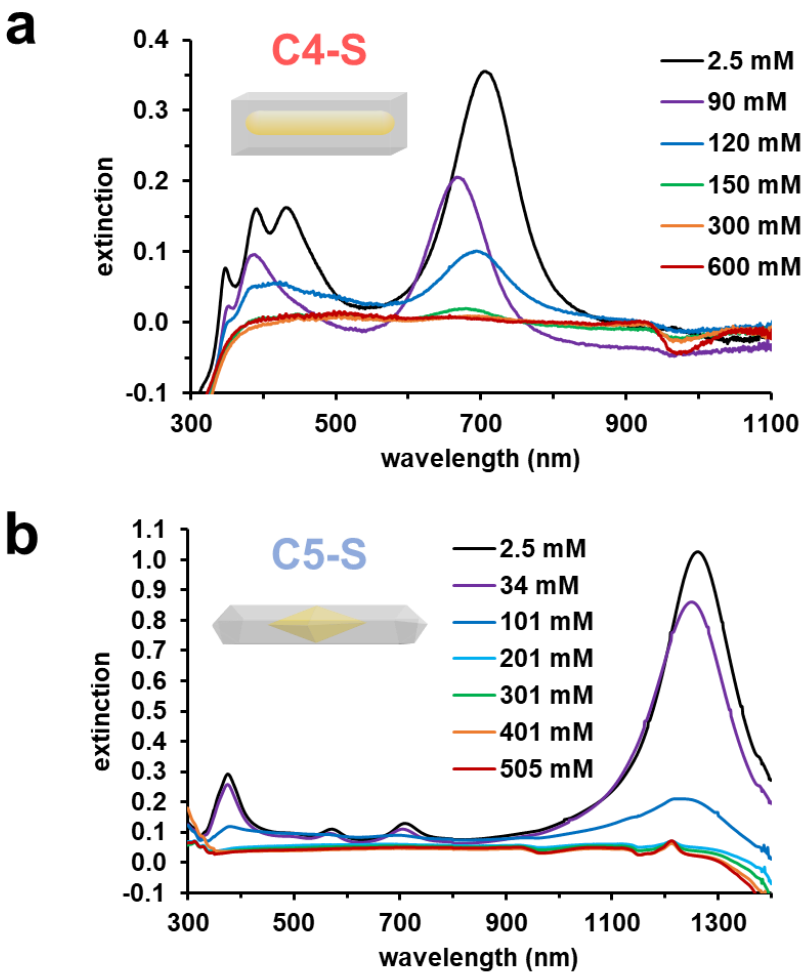

Figure S16: UV-vis-NIR extinction spectra of a) C4-S and b) C5-S NRs at different depletant (CTAC) concentrations, showing changes in LSPR peaks due to side-by-side and/or tip-to-tip plasmonic coupling upon fast DISA.

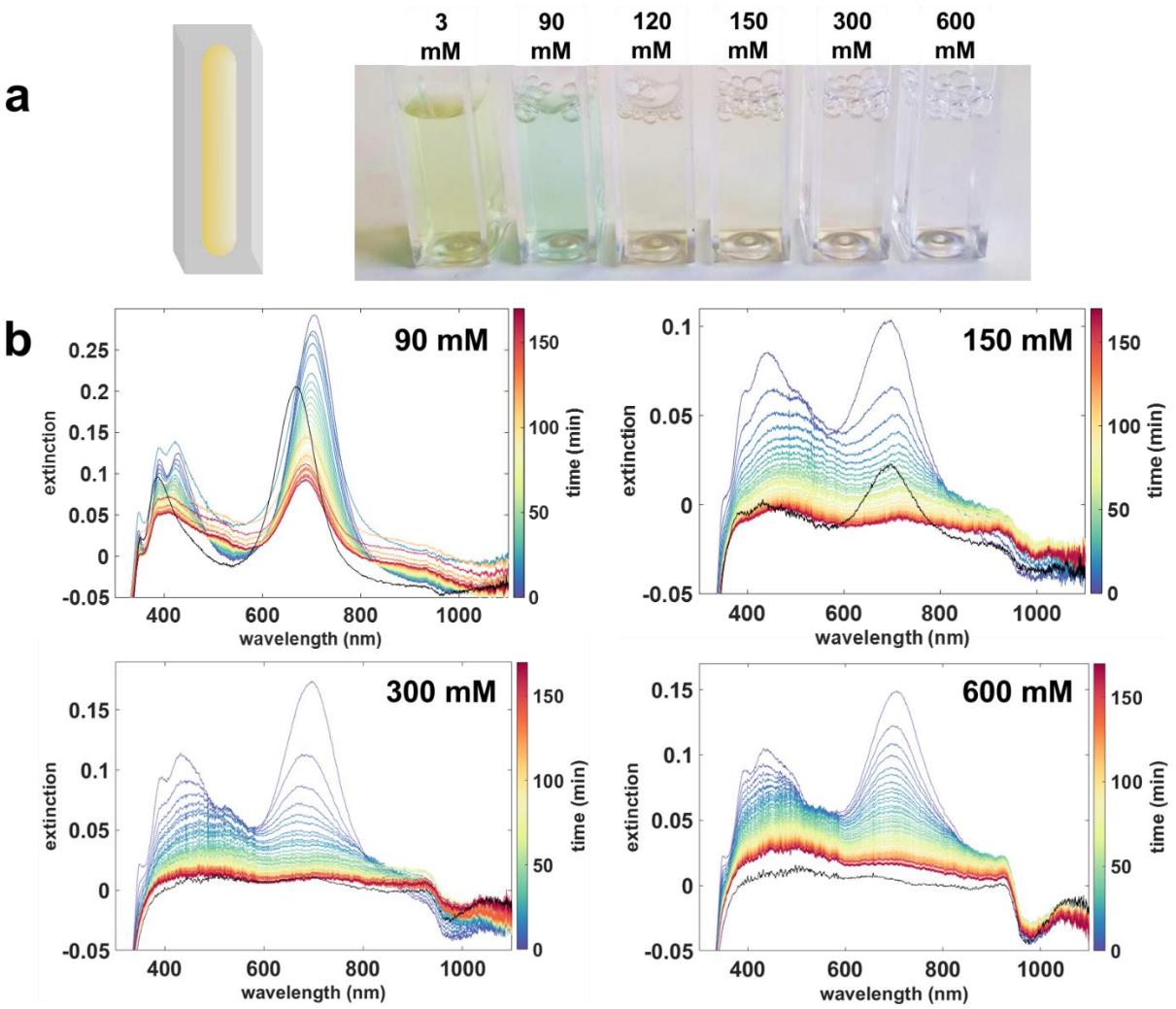

Figure S17: UV-vis-NIR kinetics of DISA by fast one-shot mixing in different CTAC concentrations. a) Cuvettes of C4-S NR suspensions at varying [CTAC], showing a change in color or eventual disappearance due to sedimentation. **b)** Time-resolved UV-vis-NIR extinction spectra, taken from 0 to 170 min post-depletant addition. Spectra in black were taken after 3 days post-depletant addition.

References

(1) Marcone, J.; Trazo, J. G.; Nag, R.; Goldmann, C.; Ratel-Ramond, N.; Hamon, C.; Imperor-Clerc, M. Form factor of prismatic particles for small-angle scattering analysis. *J. Appl. Crystallogr.* **2025**, *58* (Pt 2), 543-552.

(2) Cheng, Z.; Jones, M. R. Assembly of planar chiral superlattices from achiral building blocks. *Nat Commun* **2022**, *13* (1), 4207.

(3) Jiang, K.; Pinchuk, P. Temperature and size-dependent Hamaker constants for metal nanoparticles. *Nanotechnology* **2016**, *27* (34), 345710.

CHEMISTRY OF MATERIALS

pubs.acs.org/cm

Article

Tunable Plasmonic Circular Dichroism of Hierarchical Chiral Assemblies

Jaime Gabriel Trazo,[¶] Andrés Serrano Freijeiro,[¶] Mikhail Mychinko, Nika Kutalia, Marianne Impéror-Clerc, Sara Bals, Luis M. Liz-Marzán, Jorge Pérez-Juste,* Isabel Pastoriza-Santos,* and Cyrille Hamon*

Cite This: https://doi.org/10.1021/acs.chemmater.5c00909

Read Online

ACCESS | Metrics & More | Article Recommendations | Supporting Information

ABSTRACT: Plasmonic circular dichroism (PCD) is a powerful approach for enhancing chiroptical effects at the nanoscale with promising applications such as optical information processing, sensing, and catalysis. However, a key challenge remains in achieving both strong and tunable optical responses. While most strategies use either intrinsically chiral nanoparticles (NPs) or achiral NPs arranged into chiral assemblies, combining both offers a promising route to amplify chiral optical responses. Here, 4-fold-twisted gold nanorods (cGNRs) were assembled by depletion-induced self-assembly (DISA) into chiral superstructures with tunable PCD properties. By reducing cGNR helicity via chemical etching, we study how building block helicity affects hierarchical structure formation. Whereas static helical supercrystals were obtained on substrates upon evaporation-induced self-assembly (EISA), DISA allowed us to dynamically modulate the interparticle distance in solution from 13 ± 1.2 nm to 6.9 ± 1.0 nm. The assembly/disassembly process was found to be fully reversible, thereby enabling a modulation of the *g*-factor by 2 orders of magnitude with a switching rate of approximately 1 h. Beyond achieving high dissymmetry factors of 0.2, our approach establishes a reconfigurable PCD platform that is free from ligand exchange constraints and compatible with different NP shapes. Though response times remain too slow for optical computing, these findings are relevant for the development of optical modulators and memory devices based on dynamic chiral metafluids.

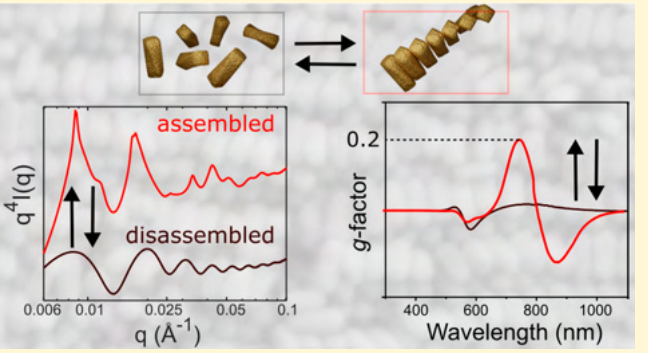

INTRODUCTION

Plasmonic circular dichroism (PCD) is emerging as a powerful tool for amplifying chiroptical effects at the nanoscale, which can be driven by various mechanisms.[1−4] Here, we focus on a combination of optical activity arising from geometrical chirality, which can be observed in colloidal nanoparticles (NPs) lacking mirror and inversion symmetry, with the assembly of colloidal NPs into chiral superstructures. Colloidal PCD materials enable energy-selective, dissymmetric interactions with circularly polarized light, opening potential applications in chiral sensing, enantioselective catalysis, and optical information processing.[5−11] Various synthetic protocols have been developed to produce chiral plasmonic NPs, often involving chiral molecules or micelles,[12,13] while different strategies have also been employed for the assembly of achiral NPs into chiral structures.[14−17] Although these two approaches have evolved independently, a few recent studies propose combining them to obtain materials with high and tunable dissymmetry factors.[18−22] Some of these recent works have focused on assembling chiral NPs into achiral structures to induce a tunable PCD response, but no significant increase in the PCD amplitude was reported. Instead, different outcomes were observed: either a loss of the PCD response[20] or a spectral shift in the PCD signal due to plasmonic coupling.[21,22] PCD enhancement appears to depend critically on hierarchical chirality, as shown in another work,[18] where the assembly of 4-fold twisted chiral gold nanorods (cGNRs) into helical superstructures led to enhanced PCD compared to individual cGNRs.[18] In the latter work, the assembly process was driven by the irreversible aggregation of colloids upon electrostatic screening. We hypothesized that introducing depletion forces in such systems would offer greater versatility in tuning the interactions between cGNRs, thereby enabling active control over the PCD response.

Depletion-induced self-assembly (DISA) is driven by an entropic attraction between colloids upon introduction of smaller particles, because bringing the colloids closer together

Received: April 15, 2025
Revised: August 7, 2025
Accepted: August 7, 2025

Downloaded via UNIVERSITE PARIS-SACLAY on August 15, 2025 at 11:03:44 (UTC).
See https://pubs.acs.org/sharingguidelines for options on how to legitimately share published articles.

© XXXX The Authors. Published by American Chemical Society

increases the free volume available to the depletants (typically polymers or surfactant micelles).[23−26] The range of accessible interparticle distances is given by the size of the depletant, whereas the strength of the interaction increases with the osmotic pressure and, hence, with the depletant concentration.[26] In the plasmonic NP field, DISA has been primarily used for shape purification and for the formation of assemblies on substrates in conjunction with evaporation-induced self-assembly (EISA). Recent works have demonstrated that DISA can be used for the reversible assembly of plasmonic NPs in suspension into well-defined structures with tunable lattice parameters.[25,27−29] In this process, there is no need for ligand exchange because the same surfactant used during NP synthesis can also be used for DISA, where the micelles serve as effective depletants. Although various anisotropic NP shapes have been successfully assembled using DISA, the self-assembly of chiral NPs via this method remains unexplored.

Reconfigurable PCD materials offer precise control over spectral and dynamic aspects of the PCD response, which is essential for developing responsive chiral nanodevices.[30,31] While PCD can be manipulated by applying external stimuli (e.g., chemical, electrical, mechanical, or electromagnetic) to NPs attached onto a substrate,[31] their structural conformation remains largely unchanged. In contrast, chiral assemblies dispersed in solution offer a promising alternative because colloids can be assembled, disassembled, and rearranged into tailored structures to modulate the PCD response. Beyond being fundamentally different from substrate-based strategies, such "metafluids" are isotropic, thereby avoiding the dependence of excitation incidence angle, and their ability to reconfigure in volume can be advantageous for chiral sensing and catalysis, by facilitating interactions between target molecules and NPs. Typically, existing reconfigurable systems rely on soft matter templates, like liquid crystals or DNA origami, to control the orientation of achiral plasmonic NPs.[31−35] However, these template-based approaches impose limitations on versatility and scalability, requiring processing steps such as ligand exchange and template design, which constrain the NP shape, size, and achievable assemblies. Moreover, the assembly of chiral NPs into higher-order chiral nanostructures is yet to be demonstrated by these methods. In contrast, DISA offers a template-free approach that can simply consist of modulating the concentration of the surfactant used during NP synthesis to drive their assembly. Here, we show that DISA can be used to assemble higher-order chiral structures with dynamically tunable chiroptical properties. This represents a significant step toward the creation of active chiral fluids capable of controlling light's amplitude, frequency, and polarization in real time.

We report the reconfigurable assembly of cGNRs into hierarchical chiral structures. We synthesized cGNRs and controlled their helicity through precise chemical etching, resulting in nanostructures with varying lattice symmetries. Using EISA with the same cGNRs, we obtained supercrystals with a helical structure, whereas DISA allowed for tunable inter-NP distances by adjusting the depletant concentration, ranging from 13 to 7 nm. The *g*-factor of the assembled cGNRs was enhanced by 2 orders of magnitude compared to the isolated cGNRs measuring at the same wavelength, with these assemblies reaching a highest value around 0.2. Furthermore, the PCD response could be dynamically adjusted in solution by cGNR assembly and disassembly. This work demonstrates that DISA enables the formation of template-free, reconfigurable chiral materials with tunable chiroptical properties.

RESULTS AND DISCUSSION

4-Fold-twisted cGNRs were synthesized by seeded growth on achiral single-crystalline GNR seeds, in the presence of a molecular chiral inducer—namely, L-cysteine.[36] To systematically adjust the helicity of the resulting cGNRs, controlled chemical etching was performed using Au^{3+} as an oxidant, which resulted in a gradual transformation of the twisted cGNRs into achiral nanorods with rounded edges (Figure 1a).

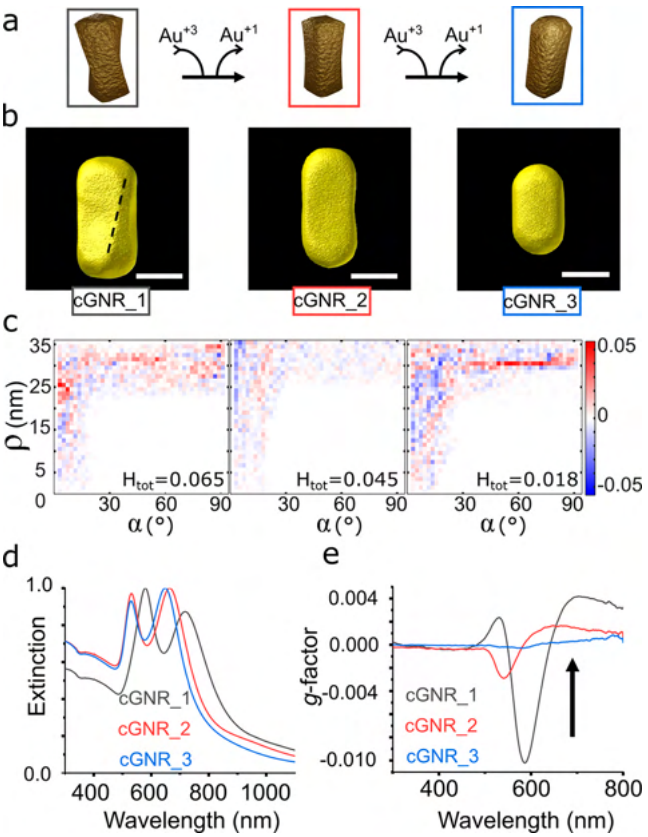

Figure 1. Reducing the helicity of twisted gold nanorods by controlled etching. (a) Scheme of the etching process to gradually reduce the helicity of cGNRs. (b) Electron tomography reconstructions of cGNRs with decreasing helicity. Scale bar is 50 nm for all images. (c) Corresponding plots of the helicity function $H(\rho,\alpha)$ for each cGNR. (d,e) Extinction and *g*-factor spectra, respectively, for the different cGNR samples.

Our study focused on three GNR batches: as-synthesized chiral nanorods (cGNR_1), partially oxidized nanorods (cGNR_2) obtained by etching for 3 h, and fully oxidized nanorods (cGNR_3) obtained by extended etching for 24 h. The dimensions of the resulting nanoparticles, determined by transmission electron microscopy (TEM), in terms of length (L) and width (W) were as follows: cGNR_1 (L = 114 ± 11 nm, W = 59 ± 4 nm); cGNR_2 (L = 104 ± 10 nm, W = 55 ± 3 nm); and cGNR_3 (L = 89 ± 10 nm, W = 61 ± 3 nm) (Figure S1). Representative cGNRs from each sample were investigated by electron tomography (ET), and the 3D reconstructions evidenced that the degree of twisting decreased in the order cGNR_1 > cGNR_2 > cGNR_3 (Figure 1b). This trend was confirmed by quantitative analysis

https://doi.org/10.1021/acs.chemmater.5c00909
Chem. Mater. XXXX, XXX, XXX−XXX

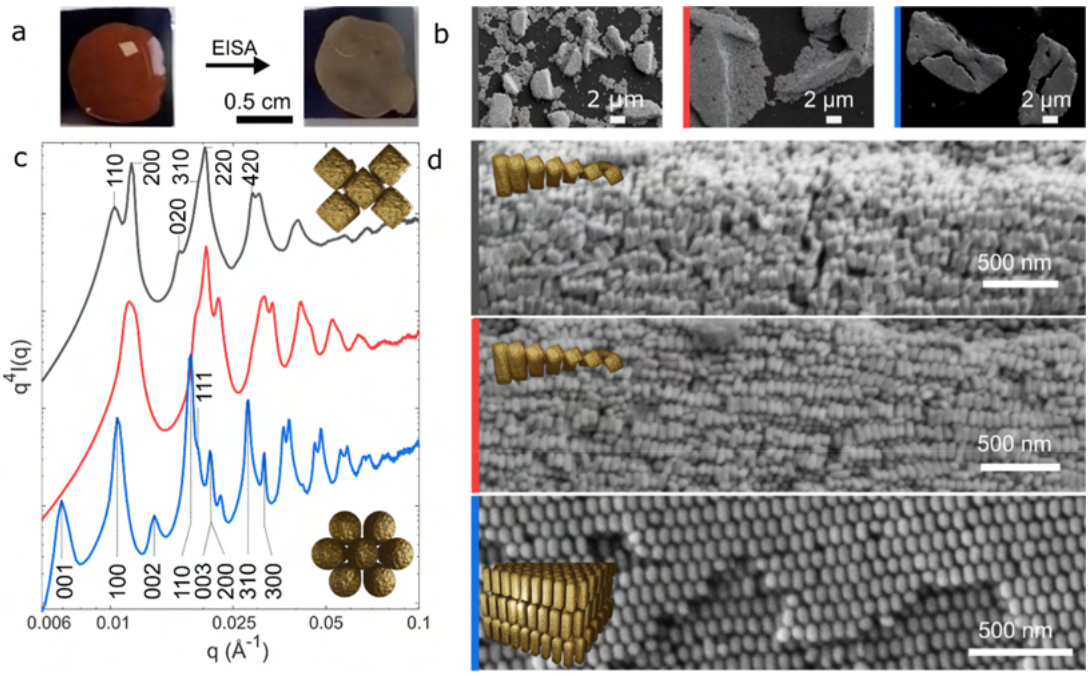

Figure 2. Self-assembly of cGNRs with varying helicity into supercrystals. (a) Photograph of a sessile droplet containing cGNR_1 before (left) and after (right) drying on a silicon substrate. (b) SEM micrographs at low magnification, corresponding to cGNR_1 (black), cGNR_2 (red), and cGNR_3 (blue) supercrystals. (c) SAXS-integrated diffractograms collected on dry supercrystals for cGNR_1 (black), cGNR_2 (red), and cGNR_3 (blue) and corresponding indexation for a 2D rectangular lattice (top) and a 3D hexagonal lattice (bottom). (d) SEM micrographs, high magnification, corresponding to cGNR_1 (black), cGNR_2 (red), and cGNR_3 (blue) supercrystals.

of the twisted morphology through computation of the helicity function H(ρ,α) from the 3D reconstructions as recently reported (Figures 1c, see Supporting Information for details on the quantification).[37] Indeed, total helicity values of H_{tot} of 0.065, 0.045, and 0.018 were determined for cGNRs obtained at increasing etching times. The positive sign of the helicity measure indicates a right-handedness of the nanorods, as expected from seed-mediated growth in the presence of L-cysteine. As etching progressed, a blue shift of the longitudinal plasmon band was observed (Figure 1d), along with a reduction in circular dichroism (Figure 1e), indicating the loss of plasmonic chirality due to cGNR etching.

All three cGNR colloids were then self-assembled by using two methods: EISA on a substrate and DISA in solution. For the dried assemblies, the resulting nanostructures were analyzed via *in situ* small-angle X-ray scattering (SAXS) and scanning electron microscopy (SEM) (Figure 2).

We studied the self-assembly of cGNRs into supercrystals by EISA. A droplet of each cGNR sample in a 2.5 mM cetyltrimethylammonium chloride (CTAC) solution was allowed to evaporate slowly on a silicon substrate (Figure 2a). Upon complete drying, supercrystals with semielliptical shapes and of varying sizes were analyzed by SEM (Figures 2b,d and S4−S6). The average size of the supercrystals increased as the helicity of the rods decreased, ranging from 5.3 ± 2.5 μm^2 for cGNR_1, to 38.1 ± 14.4 μm^2 for cGNR_2, and 30.3 ± 10.7 μm^2 for cGNR_3 (Figure S2). These results suggest that the packing frustration for cGNR_1 is more likely to introduce lattice defects than that for cGNR_3, which in turn causes the supercrystals to break at smaller sizes. For complementary structural analysis, we collected 2D SAXS images and processed the data to generate the integrated diffractograms shown in Figure 2c. In SAXS, the beam footprint measured approximately 175 × 300 μm^2, which is significantly larger than that of a single supercrystal. As a result, each measurement represents an average over multiple supercrystals, providing a broader structural overview that complements the local observations obtained through SEM. For both cGNR_1 and cGNR_2, SEM micrographs revealed a layered helical structure (Figure 2d), which was indexed as a rectangularly centered (rhombic) lattice by SAXS (Figure 2c). This structure consists of stacked twisted layers of cGNRs, where each individual layer has a centered rectangular lattice. On the other hand, a hexagonal lattice structure was identified for cGNR_3 (Figure 2c). We also collected SAXS diffractograms at different positions on the sample, because the structure could vary between the edge and the center due to the coffee ring effect (Figure S3).[38−40] While the structure of cGNR_2 supercrystals remained consistent across the substrate, cGNR_1 supercrystals were more extended at the edges of the deposit. Additionally, the orientation of cGNR_3 gradually shifted from horizontal (long axis parallel to the substrate) at the edges to vertical (long axis perpendicular to the substrate) toward the center. Variation in nanorod orientation across the sample and semielliptical supercrystal shapes were observed across a range of nanorod systems with differing shapes and surface chemistries,[41−43] suggesting that the underlying mechanism is independent of these specific parameters. Although the coffee-ring effect is known to generate gradients in NP and surfactant concentrations during evaporation,[38,40] the precise role of these gradients in directing the formation and symmetry of supercrystals is not yet fully understood. Further studies are required to disentangle the contributions of evaporation dynamics, interparticle forces, and interfacial effects to the final superstructure morphology. Overall, our experiments demonstrate that supercrystals with hierarchical chirality can be achieved through EISA for

https://doi.org/10.1021/acs.chemmater.5c00909
Chem. Mater. XXXX, XXX, XXX−XXX

building blocks with geometrical helicity. However, since the structures are dried, they are nonreconfigurable.

Our second approach involved the self-assembly of cGNRs in solution through DISA.[26,29] As CTAC micelles act as effective depletants, the cGNRs were exposed to various CTAC concentrations to induce the formation of colloidal assemblies (Figure 3a).

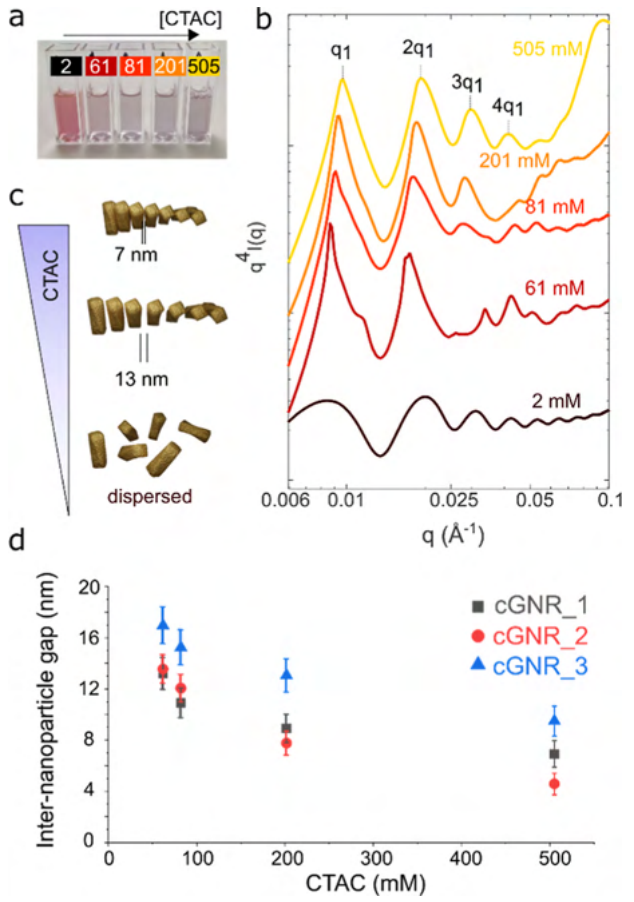

Figure 3. cGNRs assembled by DISA in solution. (a) Photograph of five cuvettes containing cGNR_1 at 2 mM, 61 mM, 81 mM, 201 mM, and 505 mM CTAC concentrations, from left to right. (b) SAXS-integrated diffractograms collected in solution for cGNR_1 at the same CTAC concentrations. (c) Schematic illustration of how variations in CTAC concentration modulate inter-NP distance. (d) Plot of inter-NP gap distance (face-to-face) as a function of CTAC concentration.

At 2.5 mM CTAC, the SAXS curves correspond to the form factor of noninteracting isolated NPs, indicating stable dispersions (Figure 3b). At CTAC concentrations above 60 mM, Bragg peaks emerge, indicating the formation of colloidal cGNR assemblies. The peak indexation revealed different structures depending on the nanorod helicity. The cGNR_1 sample exhibited a 1:2:3:4 peak progression, corresponding to the formation of one-dimensional (1D) nanostructures with an internal side-by-side nanorod alignment (Figure 3b). In comparison, cGNR_2 and cGNR_3 assemble in solution into 2D nanostructures, consistent with their EISA counterpart. While cGNR_2 assembles into 2D centered rectangular lattices (Figure S7a), the cGNR_3 lattice is hexagonal (Figure S7b). Debye−Scherrer analysis[44] revealed that the extension of the lattices was consistently smaller for cGNR_1, compared to cGNR_3 (Figure S8). These trends align with the size analysis obtained for EISA supercrystals (Figure S2), yet the smaller size of assemblies formed in solution compared to those formed upon drying suggests that the slow drying process promotes the development of higher-order structures. Although lattice symmetries were similar between EISA and DISA samples, the inter-NP gap distances differed significantly between the two strategies. The inter-NP distance averaged 2.6 ± 0.9 nm in the EISA samples, whereas it ranged from 13.2 ± 1.2 nm to 6.9 ± 1.0 nm in DISA for cGNR_1 as the CTAC concentration in the colloidal dispersion was varied (Figure 3c,d). This shifting equilibrium distance results from the balance between attractive forces (depletion and van der Waals) and repulsive electrostatic interactions.[27] At around 500 mM in CTAC, the inter-NP spacing approaches the thickness of the two surfactant bilayers coating adjacent cGNRs (≈6.4 nm).[45] Overall, SAXS experiments indicate that the assemblies of cGNRs formed by DISA correspond to the helical assemblies formed by EISA in terms of lattice symmetry (but not inter-NP distance). To complement SAXS results, we carried out liquid-phase TEM (LPTEM) and cryo-TEM to image the assemblies of cGNR_1 in the direct space (Figures S9, S10). In both cases, a side-to-side arrangement was evidenced, supporting the formation of 1D nanostructures in solution. This set of experiments allowed us to confirm a larger inter-NP distance for assemblies obtained via DISA, compared to EISA, with approximately 10 nm observed in solution (Figure S10), versus 2.5 nm in the dried state, in good agreement with SAXS diffractograms. Although LPTEM and cryo-TEM confirmed the presence of large interparticle distances, they did not allow us to estimate the twist angles. This limitation stems from the tendency of such assemblies to reorganize, especially in confined environments where NPs align with the interfaces. We have previously studied this effect and demonstrated that assemblies formed via DISA can undergo rearrangement before and during TEM observation, mainly due to radiolysis effects.[46]

We now turn our focus to the PCD response of the colloidal assemblies mediated by DISA (Figure 4a). As a control experiment, tests were conducted at a low CTAC concentration (10 mM), where no assemblies were observed, so both extinction and CD spectra remained unaltered (Figure 4b).

At CTAC concentrations above 50 mM, DISA induced a significant enhancement of the chiroptical response of the cGNR suspensions (Figures 4c and S11). Kinetic experiments were conducted by monitoring the CD signal throughout the self-assembly process. As shown in Figure 4c for 70 mM CTAC, assemblies formed rapidly within 30 s and continued to grow over the following 30 min. Kinetic SAXS experiments confirmed that the assemblies formed within 2 min (Figure S12). At the earlier stages of DISA, enhanced CD responses compared to individual cGNRs were recorded, together with a reversal of the bisignate peak of the assemblies compared to the individual NPs (Figures 4c and S11). For instance, the cGNR_1 assemblies achieved an optical asymmetry *g*-factor of 0.2 at 740 nm, which was 2 orders of magnitude higher than that of individual c-GNRs (0.0016 at the same wavelength). We infer that chiral amplification may arise from the formation of clusters rather than requiring extended order,[18] as supported by SAXS experiments. Moreover, the inversion in chirality can be attributed to a gain in compactness when the cGNRs of a given helicity self-assemble into structures with opposite handedness.[18] At later stages of the DISA process, the CD

https://doi.org/10.1021/acs.chemmater.5c00909
Chem. Mater. XXXX, XXX, XXX−XXX

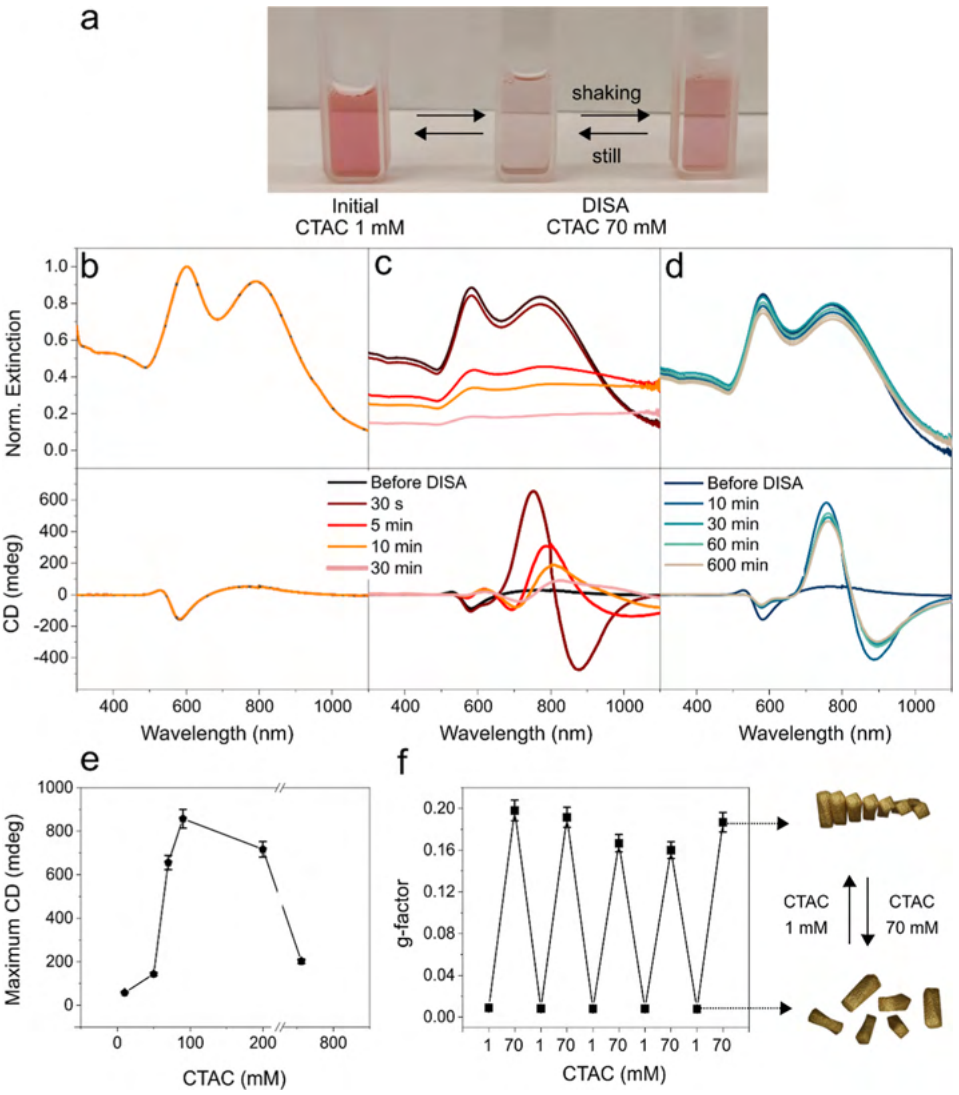

Figure 4. Reconfigurable PCD assembly of cGNR_1 via DISA. (a) Photograph of three cuvettes containing, from left to right: cGNR_1 in 1 mM CTAC; cGNR_1 in 70 mM CTAC after 30 min of sedimentation; and cGNR_1 in 70 mM CTAC after redispersion of the precipitate. (b-d) Self-assembly kinetics of cGNR_1 in 10 mM (b) and 70 mM (c) CTAC monitored by extinction (top) and CD (bottom) spectroscopies. (d) Extinction (top) and CD (bottom) spectra of cGNR_1 dispersion in 70 mM CTAC recorded at different times. Before optical measurements, the colloidal dispersion was manually shaken. (e) Maximum CD response as a function of CTAC concentration. (f) Reconfigurable *g*-factor, calculated at 740 nm, as a function of CTAC concentration cycles. Schemes illustrating the concept of reconfigurable PCD response.

signal red-shifted and decreased in amplitude, likely due to the formation of larger assemblies that sedimented at the bottom of the cuvette (Figure 4a). Similar results were obtained for CTAC concentrations ranging from 50 to 756 mM (Figure S11). It should be noted that the decrease in the CD signal at CTAC concentrations above 100 mM is due to the extremely fast depletion and sedimentation of the particles, which does not allow for a reliable measurement of the CD response of the assembly. Interestingly, at any stage of the process, the assemblies sedimented in the cuvette could be redispersed, restoring a CD signal close to its initial maximum value, even after 10 h (Figure 4d). Analyzing the extinction and CD band during the self-assembly revealed a gradual red shift due to plasmon coupling between neighboring NPs (Figures 4c and S11).[47] Since side-to-side NP coupling would result in a blue shift of the resonance modes,[18] the red shift here suggests the formation of self-assembled structures with multiple coupling modes, including both side-to-side and end-to-end interactions. Interestingly, plotting the maximum CD as a function of CTAC concentration revealed a maximum when particles were dispersed in 90−200 mM CTAC (Figures 4e, S11).

From the SAXS analysis, we can conclude that the overall size of the assemblies did not change significantly with the added CTAC concentration (Figure S13), counting 3−4 cGNRs per assembly and with inter-NP distances varying between 10.9 ± 1.2 and 8.9 ± 1.1 nm within the 90−200 mM CTAC range. Therefore, the variation of the CD response with CTAC concentration could be ascribed to the assembly of cGNRs. Similar experiments were carried out with cGNR_2 and cGNR_3 at 70 mM CTAC. As shown in Figure S14, self-assembly led to an enhanced CD signal for cGNR_2, whereas the increment was lower than that for cGNR_1. In contrast, no significant CD response was detected for cGNR_3. LPTEM and Cryo-TEM analyses of the assemblies confirmed the presence of a ladder-type assembly with relatively large interparticle distances (see Figures S9, S10), but, unfortu-

https://doi.org/10.1021/acs.chemmater.5c00909
Chem. Mater. XXXX, XXX, XXX−XXX

nately, these techniques did not allow us to obtain a reliable estimate of the twist angle. Recently, Liu et al. reported finite difference time domain (FDTD) simulations for assemblies comprising cGNRs with a similar morphology to those presented in our study.[18] The authors studied in detail the effect of the number of particles forming the assembly, the gap distance between particles, and the rotation angle between adjacent particles. The results indicate the highest CD signal for assemblies containing 3−5 chiral nanorods, with gap distances of 3−6 nm and rotation angles between 20° and 30° (see Figure 4 in ref 18). Interestingly, the reported FDTD simulations are in good agreement with our experimental spectra. Therefore, even though the limitations of the DISA approach do not allow an *in situ* determination of the rotation angle, we propose that the FDTD simulations reported in ref 18 sufficiently explain our experimental data.

We then leveraged the tunability of the depletion interactions to actively adjust the PCD response of these assemblies. Initially, cGNR_1 was self-assembled via DISA at 70 mM CTAC, and the resulting sediment was subsequently redispersed in a 1 mM CTAC solution inside the same cuvette (Figures 4f and S15). This cycle was repeated multiple times, leading to reversible *g*-factor variations spanning 2 orders of magnitude (from 0.0016 to 0.2 measured at 740 nm) as the system switched between disassembled and assembled states. Notably, at higher wavelengths (e.g., 880 nm), the dispersed cGNRs display almost no display chiroptical activity (*g*-factor around 0.001), whereas the assemblies display a high *g*-factor of 0.1. This demonstrates that integrating chirality across different length scales is a promising strategy for designing materials with strong chiroptical properties over a broad spectral range. Additionally, our approach enables modulation of the *g*-factor in solution, achieving a two-orders-of-magnitude change with a switching rate of approximately 1 h, which can be accelerated by centrifugation for 5 min at 2240 rcf.

CONCLUSIONS

This work demonstrates that cGNRs can be assembled into hierarchical chiral nanostructures via DISA, exhibiting enhanced, spectrally tunable, and temporally dynamic PCD responses. Gold nanorods with a gradual degree of helicity were obtained by colloidal synthesis combined with chemical etching, allowing us to investigate how the chirality of the building blocks influences the construction of higher-order chiral structures by self-assembly. Different hierarchical structures, ranging from smectic to centered rectangular, were obtained by EISA, notably forming extended helical supercrystals on the substrates. In solution, the cGNRs can be reversibly assembled by DISA, resulting in a wide tunability of the PCD response. In these experiments, the inter-NP gap distance could be tuned from 13 ± 1.2 nm to 6.9 ± 1.0 nm by adjusting the CTAC concentration. The reversible process of assembling and disassembling the NPs could be repeated multiple times inside the same cuvette, leading to variations of the *g*-factor by 2 orders of magnitude when switching between the disassembled and assembled states. This work shows that DISA can be used to form nanostructures with hierarchical chirality displaying enhanced, spectrally tunable, and temporally evolving PCD responses. Besides achieving a remarkably high *g*-factor, we demonstrate reconfigurable PCD response with a switching rate of about 1 h. While these rates are still too slow for display technologies or optical computing,[48,49] they open new possibilities for optical modulators and memory devices. Overall, DISA offers a promising pathway to achieve hierarchical chirality in plasmonic NPs, with the added advantage over purely electrostatic strategies of greater versatility, enabling reconfigurability and tunable optical responses.

EXPERIMENTAL SECTION

Chemicals. All of the starting materials were obtained from Sigma-Aldrich and used without further purification: hexadecyltrimethylammonium bromide (CTAB for molecular biology, ≥ 99%), hexadecyltrimethylammonium chloride (CTAC, 95% w/w aqueous solution), 1-decanol (n-decanol, 98%), hydrogen tetrachloroaurate trihydrate ($HAuCl_4 \cdot 3H_2O$, ≥ 99.9%), silver nitrate ($AgNO_3$, ≥ 99.0%), L-ascorbic acid (≥99%), hydroquinone (HQ, ≥ 99%), sodium borohydride ($NaBH_4$, 99%), D-cysteine (D-cys, 99%), and L-cysteine (L-cys, 99%). Milli-Q-grade water (resistivity 18.2 MΩ cm at 25 °C) was used in all experiments. All reagents were used as received without further purification.

Characterization. TEM and low-magnification TEM images were obtained on a JEOL JEM-1400PLUS transmission electron microscope operating at an acceleration voltage of 120 kV. For UV−vis−NIR spectroscopy, extinction spectra were recorded using a Jasco V-750 spectrophotometer. Regarding circular dichroism spectroscopy, spectra were recorded using a Jasco V-1700 CD-spectrophotometer. For the characterization of colloidal dispersions, quartz cuvettes with an optical path of 5 mm were used for the extinction and CD equipment. Au^0 concentrations of the cGNR suspensions were estimated using their measured extinction at 400 nm, taking a NP concentration of 0.5 mM in Au^0 for a sample absorbance of 1.2.[50]

Synthesis of cGNRs. cGNRs were prepared by a five-step seed-mediated growth approach that can be described as follows: (1) the synthesis of 1−2 nm gold seeds, (2) synthesis of small anisotropic seeds, (3) synthesis of "minirods", (4) synthesis of larger achiral rods, and (5) synthesis of the cGNRs. Steps 1−4 were adapted from González-Rubio et al.[51] with minor modifications, and step 5 was described by Bing Ni et al.[36] with slight modifications.

(1) Synthesis of 1−2 nm gold seeds: in a 50 mL glass beaker, 50 μL of NaOH 0.5 M was added to 20 mL of an aqueous solution containing 50 mM CTAB and 13.5 mM *n*-decanol at 27 °C to adjust the pH to 7.6. Then, 200 μL of a 50 mM $HAuCl_4$ solution was added, obtaining a yellowish solution. Immediately after, 800 μL of fresh 20 mM $NaBH_4$ was added under strong magnetic stirring (1000−1100 rpm). The reduction was allowed to proceed under stirring for 2 min until the solution turned brownish yellow. The solution was then left undisturbed for at least 1 h at 27 °C prior to use.

(2) Synthesis of anisotropic seeds: in a 500 mL Erlenmeyer flask, 200 mL of an aqueous solution containing 50 mM CTAB and 13.5 mM *n*-decanol at 27 °C was prepared. Subsequently, 1.6 mL of 10 mM $AgNO_3$, 14 mL of 1 M HCl, 2 mL of 50 mM $HAuCl_4$, and 2.6 mL of 0.1 M ascorbic acid were added at 25 °C. Next, 12 mL of the previously prepared seed solution was added under stirring, and the mixture was allowed to age for at least 4 h until it turned dark brown. After that time, the longitudinal LSPR band should be centered around 730 nm. The obtained particles were centrifuged at 23140 rcf for 45 min in 2 mL tubes and redispersed in 5.5 mL of 10 mM CTAB, yielding a final Au^0 concentration of 10 mM.

(3) Synthesis of "minirods". In a 500 mL Erlenmeyer flask, a 200 mL solution of CTAB 50 mM and n-decanol 13.5 mM was prepared. Then, 1.6 mL of $AgNO_3$ (10 mM), 14 mL of HCl (1 M) (HCl volume must be adjusted as specified in [1]), 2 mL of $HAuCl_4$ (50 mM), and 2.6 mL of ascorbic acid (0.1 M) were subsequently added at 25 °C. Then, 12 mL of the previously prepared seed solution was added under stirring, and the mixture was left for aging for at least 4 h until it turned dark brown. After that time, longitudinal plasmon should peak at 730 nm, and the final particles were centrifuged at 15000

https://doi.org/10.1021/acs.chemmater.5c00909
Chem. Mater. XXXX, XXX, XXX−XXX

rpm for 45 min in 2 mL tubes and dispersed in 5.5 mL of CTAB 10 mM for a final Au^0 concentration of 10 mM.

(4) Synthesis of achiral AuNRs: first, 174 mL of an aqueous solution containing 50 mM CTAB and 11 mM n-decanol was prepared. Then, 2 mL of 50 mM $HAuCl_4$ was added, and the resulting yellowish solution was left undisturbed for 10 min at 16 °C. Afterward, 3 mL of 10 mM $AgNO_3$, 20 mL of 1 M HCl, 1.6 mL of 0.1 M ascorbic acid, and 400 μL of 10 mM Au "minirods" were sequentially added. The resulting mixture was left undisturbed for 5 h to allow complete anisotropic growth. Then, the particles were centrifuged at 5750 rcf for 20 min in 50 mL tubes and redispersed in 5 mL of 1 mM CTAB, yielding a final Au^0 concentration of 5 mM. The LSPR maximum was at 1150 nm.

(5) Chiral gold nanoparticles. Typically, 200 μL of HAuCl4 (10 mM) was dispersed in 10 mL of a 10 mM CTAC solution and incubated at 40 °C for 8−10 min. Then, for the chiral nanoparticles with a larger aspect ratio, 200 μL of L-ascorbic acid (0.1 M), 40 to 60 μL of L-/D-cysteine (20 μM), and 12 μL of achiral gold nanorods with LSPR at 1150 nm (5 mM) were added sequentially. For chiral particles with a smaller aspect ratio, 200 μL of L-ascorbic acid (0.1 M), 120 μL of L-/D-cysteine (20 μM), and 14 μL of achiral gold nanorods with LSPR at 1040 nm (5 mM) were added instead. The particles were then centrifuged (10 min at 3980 rcf) and dispersed in 1 mM CTAC twice.

Oxidation of cGNRs. cGNRs with different degrees of oxidation were prepared by a procedure described by Jessica Rodríguez-Fernández et al.'s report[52] with slight modifications. 2.5 mL of 2 mM cGNRs dispersed in CTAC 1 mM was added to a 20 mL solution of CTAB (50 mM). Subsequently, 100 μL of $HAuCl_4$ (50 mM) was added with stirring (500 rpm). The oxidation was then stopped by centrifugation (10 min at 4700 rcf twice, dispersing the particles in 1 mM CTAC) at different times to yield cGNR_2 and cGNR_3 after 3 h and 24 h, respectively.

Self-Assembly by EISA. A 10 μL drop of cGNRs (30 mM Au^0, 2.5 mM CTAC) was drop-cast onto a substrate (either a silicon wafer or a glass coverslip) and allowed for around 48 h. Whereas Si wafers were preferred for SEM characterization, glass coverslips were preferred for SAXS characterization. Throughout the drying process, the sample was placed in a covered container with added water droplets to maintain saturated humidity, thereby slowing down evaporation.

Self-Assembly by DISA. Two procedures were tested for DISA, resulting in slow or fast self-assembly kinetics, as described in the following. This was tested because slow kinetics are known to induce more extended assemblies, including in DISA.[53] While the results displayed in Figure S13 show an effect of the self-assembly kinetics, the shape of the cGNRs induced more notable effects on the size of the assemblies.

(1) Slow kinetics. This procedure was adapted from ref 53. Into a round glass capillary (diameter = 1.5 mm), 10 μL of the cGNR suspension (35 mM Au^0 in cGNRs, 1 mM CTAC) was injected with a syringe near the bottom of the capillary, leaving an air pocket below of several millimeters from the bottom. Then, 20 μL of an aqueous cetyltrimethylammonium chloride (CTAC) solution (at varying CTAC concentration) was carefully deposited on top with a syringe, ensuring a sharp and well-defined interface between the two phases. Finally, the capillaries were sealed using a glue gun and left undisturbed for at least 24 h to allow diffusion and equilibration before characterization by SAXS.

(2) Fast kinetics. Into a polystyrene cuvette (optical path length = 1 cm), 10 μL of the cGNRs suspension (35 mM Au^0 in cGNRs, 1 mM CTAC) was rapidly mixed with 1990 μL of aqueous CTAC (at a chosen surfactant concentration).

Reconfigurable PCD. In a 10 mL centrifuge tube, 2 mL of CTAC 87.5 mM and 500 μL of cGNRs were added for a final concentration of 70 mM CTAC. The CD and extinction spectra were immediately measured one after another in order to calculate the *g*-factor at the optimal assembly stage. Then, the sample was either left undisturbed until total sedimentation of the nanoparticles or centrifuged at 2240 rcf for 5 min to accelerate the sedimentation process, yielding the same result. The supernatant was then carefully removed, and the remaining NPs were dispersed in 2.5 mL of 1 mM CTAC. The CD and extinction spectra were then measured again, followed by another centrifugation at 3980 rcf for 10 min. The supernatant was discarded, and the precipitates at the bottom of the tube were dispersed with CTAC 70 mM, completing one cycle as shown in Figure 4G.

Small-Angle X-ray Scattering. SAXS data was collected at the SWING beamline of the SOLEIL Synchrotron (Saint-Aubin, France), using a beam energy of 12 keV and a sample-to-detector distance of 6.22 m. Each measurement had an exposure time of 1000 ms. The beam size was approximately 500 × 200 μm^2 (horizontal × vertical). For colloidal samples in capillaries, a z-scan of the capillary was performed, while for dried samples prepared via EISA on a glass substrate, a radial scan of the droplet was conducted, measuring multiple points from the edge to the center. All measurements were performed at room temperature (295 K). The scattered signal was recorded using an Eiger 4 M detector (Dectris Ltd., Switzerland) with a pixel size of 75 μm. Preliminary data treatment, including angular averaging and normalization, was performed using Foxtrot, the dedicated software developed at the beamline (https://www.synchrotron-soleil.fr/fr/lignes-de-lumiere/swing). The processed data yielded intensity as a function of scattering vector I(q) in absolute units. Further SAXS data modeling and analysis were conducted using either custom Python scripts or SasView 6.0.0.

Transmission Electron Microscopy, Electron Tomography, and Helicity Measurements. Scanning transmission electron microscopy (STEM) and electron tomography experiments (ET) were performed using a "cubed" Thermo Fisher Scientific Themis Z instrument operated at 300 kV in high-angle annular dark field STEM (HAADF-STEM) mode. Electron tomography (ET) series were acquired over an angular range of ± 75°, with a tilt increment of 3°, and were used as an input for SIRT reconstruction using the Astra Toolbox 1.8 for MATLAB R2019A.[54] Visualization of the 3D reconstructions was performed using Amira 5.4.0 software. The helical morphology of cGNRs was quantitatively characterized using an updated version of our previously reported method.[37] Liquid and cryostudies of assemblies of chiral NPs were performed using a single-use sealable sample holder (K-KIT) and a 2550 Cryo Transfer Tomography Holder (Fischione Instruments), respectively.

■ ASSOCIATED CONTENT

Supporting Information

The Supporting Information is available free of charge at https://pubs.acs.org/doi/10.1021/acs.chemmater.5c00909.

TEM image analysis of the cGNRs, SEM image analysis of the supercrystals, SAXS analysis of the supercrystals obtained by DISA and EISA, additional SEM images of the self-assembled systems, electron tomography reconstruction images of the assemblies, and additional optical characterization of the assemblies by CD and extinction spectroscopy (PDF)

■ AUTHOR INFORMATION

Corresponding Authors

Jorge Pérez-Juste − *CINBIO, Departamento de Química Física, Universidade de Vigo, 36310 Vigo, Spain;* orcid.org/0000-0002-4614-1699; Email: juste@uvigo.gal

Isabel Pastoriza-Santos − *CINBIO, Departamento de Química Física, Universidade de Vigo, 36310 Vigo, Spain;* orcid.org/0000-0002-1091-1364; Email: pastoriza@uvigo.gal

https://doi.org/10.1021/acs.chemmater.5c00909
Chem. Mater. XXXX, XXX, XXX−XXX

Cyrille Hamon − *Université Paris-Saclay, CNRS, Laboratoire de Physique des Solides, 91405 Orsay, France;* orcid.org/0000-0001-9529-9102; Email: cyrille.hamon@cnrs.fr

Authors

Jaime Gabriel Trazo − *Université Paris-Saclay, CNRS, Laboratoire de Physique des Solides, 91405 Orsay, France*

Andrés Serrano Freijeiro − *CINBIO, Departamento de Química Física, Universidade de Vigo, 36310 Vigo, Spain*

Mikhail Mychinko − *EMAT and NANOlab Center of Excellence, University of Antwerp, 2020 Antwerp, Belgium;* orcid.org/0000-0002-7630-9245

Nika Kutalia − *Université Paris-Saclay, CNRS, Laboratoire de Physique des Solides, 91405 Orsay, France*

Marianne Impéror-Clerc − *Université Paris-Saclay, CNRS, Laboratoire de Physique des Solides, 91405 Orsay, France;* orcid.org/0000-0002-0269-7556

Sara Bals − *EMAT and NANOlab Center of Excellence, University of Antwerp, 2020 Antwerp, Belgium;* orcid.org/0000-0002-4249-8017

Luis M. Liz-Marzán − *CINBIO, Departamento de Química Física, Universidade de Vigo, 36310 Vigo, Spain; CIC BiomaGUNECIC biomaGUNE, Basque Research and Technology Alliance (BRTA), 20014 Donostia-San Sebastián, Spain; Centro de Investigación Biomédica en Red de Bioingeniería, Biomateriales y Nanomedicina (CIBER-BBN), 20014 Donostia-San Sebastián, Spain; Ikerbasque, Basque Foundation for Science, 48009 Bilbao, Spain;* orcid.org/0000-0002-6647-1353

Complete contact information is available at: https://pubs.acs.org/10.1021/acs.chemmater.5c00909

Author Contributions

¶J.G.T. and A.S.F. contributed equally to this paper.

Notes

The authors declare no competing financial interest.

■ ACKNOWLEDGMENTS

The CNRS is acknowledged for funding and support. C.H. acknowledges financial support from the ANR CODENAME project (ANR-23-CE09-0032). The authors acknowledge SOLEIL for the provision of synchrotron radiation facilities (experiment 20231786), and they would like to thank Thomas Bizien for assistance in using beamline SWING. The authors thank Stéphan Rouzière for the use of the MORPHEUS platform. The present work benefited from the electronic microscopy facility of Imagerie-Gif (http://www.i2bc.parissaclay.fr), a member of IBiSA (http://www.ibisa.net), supported by "France-BioImaging" (ANR10-INBS-04-01), and the Labex "Saclay Plant Science" (ANR-11-IDEX-0003-02). M.M. and S.B. acknowledge financial support by the European Research Council (ERC CoG No. 815128 REALNANO). I.P.-S. and J.P.-J. acknowledge the support from MICIU/AEI/10.13039/501100011033 and ERDF/EU (Grant Number: PID2022-138724NB-I00) and the Xunta de Galicia/ERDF (grant GRC ED431C 2020/09). I.P.-S., J.P.-J., L.M.L.-M., and A.S.-F. acknowledge the use of scientific and technical services of Centro de Apoio Científico e Tecnolóxico á Investigación (CACTI-Universidade de Vigo). L.M.L.-M. and S.B. acknowledge funding from the European Research Council (ERC Synergy Grant #101166855 CHIRAL-PRO).

■ REFERENCES

(1) Cho, N. H.; Guerrero-Martínez, A.; Ma, J.; Bals, S.; Kotov, N. A.; Liz-Marzán, L. M.; Nam, K. T. Bioinspired chiral inorganic nanomaterials. *Nat. Rev. Bioengineer.* **2023**, *1* (2), 88−106.

(2) Ávalos-Ovando, O.; Santiago, E. Y.; Movsesyan, A.; Kong, X.-T.; Yu, P.; Besteiro, L. V.; Khorashad, L. K.; Okamoto, H.; Slocik, J. M.; Correa-Duarte, M. A.; et al. Chiral Bioinspired Plasmonics: A Paradigm Shift for Optical Activity and Photochemistry. *ACS Photonics* **2022**, *9* (7), 2219−2236.

(3) Hentschel, M.; Schäferling, M.; Duan, X.; Giessen, H.; Liu, N. Chiral plasmonics. *Sci. Adv.* **2017**, *3* (5), No. e1602735.

(4) Goerlitzer, E. S. A.; Puri, A. S.; Moses, J. J.; Poulikakos, L. V.; Vogel, N. The Beginner's Guide to Chiral Plasmonics: Mostly Harmless Theory and the Design of Large-Area Substrates. *Adv. Opt. Mater.* **2021**, *9* (16), 2100378.

(5) Kim, R. M.; Huh, J. H.; Yoo, S.; Kim, T. G.; Kim, C.; Kim, H.; Han, J. H.; Cho, N. H.; Lim, Y. C.; Im, S. W.; et al. Enantioselective sensing by collective circular dichroism. *Nature* **2022**, *612* (7940), 470−476.

(6) Negrin-Montecelo, Y.; Movsesyan, A.; Gao, J.; Burger, S.; Wang, Z. M.; Nlate, S.; Pouget, E.; Oda, R.; Comesana-Hermo, M.; Govorov, A. O.; et al. Chiral Generation of Hot Carriers for Polarization-Sensitive Plasmonic Photocatalysis. *J. Am. Chem. Soc.* **2022**, *144* (4), 1663−1671.

(7) Both, S.; Schaferling, M.; Sterl, F.; Muljarov, E. A.; Giessen, H.; Weiss, T. Nanophotonic Chiral Sensing: How Does It Actually Work? *ACS Nano* **2022**, *16* (2), 2822−2832.

(8) Warning, L. A.; Miandashti, A. R.; McCarthy, L. A.; Zhang, Q.; Landes, C. F.; Link, S. Nanophotonic Approaches for Chirality Sensing. *ACS Nano* **2021**, *15* (10), 15538−15566.

(9) Im, S. W.; Ahn, H. Y.; Kim, R. M.; Cho, N. H.; Kim, H.; Lim, Y. C.; Lee, H. E.; Nam, K. T. Chiral Surface and Geometry of Metal Nanocrystals. *Adv. Mater.* **2020**, *32* (41), No. e1905758.

(10) Kumar, J.; Eraña, H.; López-Martínez, E.; Claes, N.; Martín, V. F.; Solís, D. M.; Bals, S.; Cortajarena, A. L.; Castilla, J.; Liz-Marzán, L. M. Detection of amyloid fibrils in Parkinson's disease using plasmonic chirality. *Proc. Natl. Acad. Sci. U.S.A.* **2018**, *115* (13), 3225−3230.

(11) Tadgell, B.; García-Astrain, C.; Henriksen-Lacey, M.; Martín, V. F.; Obelleiro-Liz, M.; Liz-Marzán, L. M. Monitoring of the Local Extracellular Environment Using Chiral Gold Nanoparticles. *J. Am. Chem. Soc.* **2025**, *147* (3), 2860−2870.

(12) Lee, H.-E.; Ahn, H.-Y.; Mun, J.; Lee, Y. Y.; Kim, M.; Cho, N. H.; Chang, K.; Kim, W. S.; Rho, J.; Nam, K. T. Amino-acid- and peptide-directed synthesis of chiral plasmonic gold nanoparticles. *Nature* **2018**, *556* (7701), 360−365.

(13) González-Rubio, G.; Mosquera, J.; Kumar, V.; Pedrazo-Tardajos, A.; Llombart, P.; Solís, D. M.; Lobato, I.; Noya, E. G.; Guerrero-Martínez, A.; Taboada, J. M.; et al. Micelle-directed chiral seeded growth on anisotropic gold nanocrystals. *Science* **2020**, *368* (6498), 1472−1477.

(14) Chen, W.; Bian, A.; Agarwal, A.; Liu, L.; Shen, H.; Wang, L.; Xu, C.; Kotov, N. A. Nanoparticle Superstructures Made by Polymerase Chain Reaction: Collective Interactions of Nanoparticles and a New Principle for Chiral Materials. *Nano Lett.* **2009**, *9* (5), 2153−2159.

(15) George, J.; Thomas, K. G. Surface Plasmon Coupled Circular Dichroism of Au Nanoparticles on Peptide Nanotubes. *J. Am. Chem. Soc.* **2010**, *132* (8), 2502−2503.

(16) Guerrero-Martínez, A.; Auguié, B.; Alonso-Gómez, J. L.; Džolić, Z.; Gómez-Graña, S.; Žinić, M.; Cid, M. M.; Liz-Marzán, L. M. Intense Optical Activity from Three-Dimensional Chiral Ordering of Plasmonic Nanoantennas. *Angew. Chem., Int. Ed.* **2011**, *50* (24), 5499−5503.

(17) Lu, J.; Xue, Y.; Bernardino, K.; Zhang, N.-N.; Gomes, W. R.; Ramesar, N. S.; Liu, S.; Hu, Z.; Sun, T.; de Moura, A. F.; et al. Enhanced optical asymmetry in supramolecular chiroplasmonic assemblies with long-range order. *Science* **2021**, *371* (6536), 1368−1374.

(18) Zhang, N. N.; Mychinko, M.; Gao, S. Y.; Yu, L.; Shen, Z. L.; Wang, L.; Peng, F.; Wei, Z.; Wang, Z.; Zhang, W.; et al. Self-Matching Assembly of Chiral Gold Nanoparticles Leads to High Optical Asymmetry and Sensitive Detection of Adenosine Triphosphate. *Nano Lett.* **2024**, *24* (41), 13027−13036.
(19) Wang, S.; Zheng, L. H.; Chen, W. J.; Ji, L. K.; Zhang, L.; Lu, W. S.; Fang, Z. Y.; Guo, F. C.; Qi, L. M.; Liu, M. H. Helically Grooved Gold Nanoarrows: Controlled Fabrication, Superhelix, and Transcribed Chiroptical Switching. *Ccs Chemistry* **2021**, *3* (9), 2473−2484.
(20) Carone, A.; Mariani, P.; Désert, A.; Parola, S. Colloidal Assemblies of Chiral Plasmonic Nanoparticles Induce Tunable Circular Dichroism Response. *Adv. Opt. Mater.* **2023**, *11* (18), 2300119.
(21) Yao, C.; He, H.; Kong, W.; Hu, L.; Shen, X.; Tao, J.; Sang, Y.; Nie, Z. Polymer-Driven Co-Assembly of Achiral and Chiral Nanoparticles into Plasmonic Nanoclusters with Quantitatively Modulated Optical Chirality. *Adv. Sci.* **2025**, No. e04850.
(22) Maniappan, S.; Dutta, C.; Solís, D. M.; Taboada, J. M.; Kumar, J. Surfactant Directed Synthesis of Intrinsically Chiral Plasmonic Nanostructures and Precise Tuning of their Optical Activity through Controlled Self-Assembly. *Angew. Chem., Int. Ed.* **2023**, *62* (21), No. e202300461.
(23) Frenkel, D. Order through entropy. *Nat. Mater.* **2015**, *14* (1), 9−12.
(24) Vo, T.; Glotzer, S. C. A theory of entropic bonding. *Proc. Natl. Acad. Sci. U S A* **2022**, *119* (4), No. e2116414119.
(25) Young, K. L.; Personick, M. L.; Engel, M.; Damasceno, P. F.; Barnaby, S. N.; Bleher, R.; Li, T.; Glotzer, S. C.; Lee, B.; Mirkin, C. A. A directional entropic force approach to assemble anisotropic nanoparticles into superlattices. *Angew. Chem., Int. Ed.* **2013**, *52* (52), 13980−13984.
(26) Lekkerkerker, H. N. W.; Tuinier, R.; Vis, M. Phase Behaviour of Colloidal Platelet−Depletant Mixtures. In *Colloids and the Depletion Interaction*; Lekkerkerker, H. N. W., Tuinier, R., Vis, M., Eds.; *Lecture Notes in Physics*, Springer International Publishing, 2024; pp 285−317.
(27) Young, K. L.; Jones, M. R.; Zhang, J.; Macfarlane, R. J.; Esquivel-Sirvent, R.; Nap, R. J.; Wu, J.; Schatz, G. C.; Lee, B.; Mirkin, C. A. Assembly of reconfigurable one-dimensional colloidal superlattices due to a synergy of fundamental nanoscale forces. *Proc. Natl. Acad. Sci. U S A* **2012**, *109* (7), 2240−2245.
(28) Chiu, C.-Y.; Chen, C.-K.; Chang, C.-W.; Jeng, U. S.; Tan, C.-S.; Yang, C.-W.; Chen, L.-J.; Yen, T.-J.; Huang, M. H. Surfactant-Directed Fabrication of Supercrystals from the Assembly of Polyhedral Au−Pd Core−Shell Nanocrystals and Their Electrical and Optical Properties. *J. Am. Chem. Soc.* **2015**, *137* (6), 2265−2275.
(29) Nag, R.; Rouviere, N.; Trazo, J. G.; Marcone, J.; Kutalia, N.; Goldmann, C.; Imperor-Clerc, M.; Alloyeau, D.; Constantin, D.; Hamon, C. Depletion-Induced Tunable Assembly of Complementary Platonic Solids. *Nano Lett.* **2024**, *24* (51), 16368−16373.
(30) Urban, M. J.; Shen, C.; Kong, X.-T.; Zhu, C.; Govorov, A. O.; Wang, Q.; Hentschel, M.; Liu, N. Chiral Plasmonic Nanostructures Enabled by Bottom-Up Approaches. *Annu. Rev. Phys. Chem.* **2019**, *70*, 275−299.
(31) Neubrech, F.; Hentschel, M.; Liu, N. Reconfigurable Plasmonic Chirality: Fundamentals and Applications. *Adv. Mater.* **2020**, *32* (41), No. e1905640.
(32) Kuzyk, A.; Schreiber, R.; Zhang, H.; Govorov, A. O.; Liedl, T.; Liu, N. Reconfigurable 3D plasmonic metamolecules. *Nat. Mater.* **2014**, *13* (9), 862−866.
(33) Bagiński, M.; Tupikowska, M.; González-Rubio, G.; Wójcik, M.; Lewandowski, W. Shaping Liquid Crystals with Gold Nanoparticles: Helical Assemblies with Tunable and Hierarchical Structures Via Thin-Film Cooperative Interactions. *Adv. Mater.* **2020**, *32* (1), 1904581.
(34) Jedrych, A.; Pawlak, M.; Gorecka, E.; Lewandowski, W.; Wojcik, M. M. Light-Responsive Supramolecular Nanotubes-Based Chiral Plasmonic Assemblies. *ACS Nano* **2023**, *17* (6), 5548−5560.
(35) Liu, N.; Liedl, T. DNA-Assembled Advanced Plasmonic Architectures. *Chem. Rev.* **2018**, *118* (6), 3032−3053.
(36) Ni, B.; Mychinko, M.; Gomez-Grana, S.; Morales-Vidal, J.; Obelleiro-Liz, M.; Heyvaert, W.; Vila-Liarte, D.; Zhuo, X.; Albrecht, W.; Zheng, G.; et al. Chiral Seeded Growth of Gold Nanorods Into Fourfold Twisted Nanoparticles with Plasmonic Optical Activity. *Adv. Mater.* **2023**, *35* (1), No. e2208299.
(37) Heyvaert, W.; Pedrazo-Tardajos, A.; Kadu, A.; Claes, N.; González-Rubio, G.; Liz-Marzán, L. M.; Albrecht, W.; Bals, S. Quantification of the Helical Morphology of Chiral Gold Nanorods. *ACS Mater. Lett.* **2022**, *4* (4), 642−649.
(38) Han, W.; Lin, Z. Learning from "Coffee Rings": Ordered Structures Enabled by Controlled Evaporative Self-Assembly. *Angew. Chem., Int. Ed.* **2012**, *51* (7), 1534−1546.
(39) Marín, Á. G.; Gelderblom, H.; Lohse, D.; Snoeijer, J. H. Order-to-Disorder Transition in Ring-Shaped Colloidal Stains. *Phys. Rev. Lett.* **2011**, *107* (8), 085502.
(40) Deegan, R. D.; Bakajin, O.; Dupont, T. F.; Huber, G.; Nagel, S. R.; Witten, T. A. Capillary flow as the cause of ring stains from dried liquid drops. *Nature* **1997**, *389* (6653), 827−829.
(41) Xie, Y.; Guo, S.; Ji, Y.; Guo, C.; Liu, X.; Chen, Z.; Wu, X.; Liu, Q. Self-Assembly of Gold Nanorods into Symmetric Superlattices Directed by OH-Terminated Hexa(ethylene glycol) Alkanethiol. *Langmuir* **2011**, *27* (18), 11394−11400.
(42) Marcone, J.; Chaabani, W.; Goldmann, C.; Imperor-Clerc, M.; Constantin, D.; Hamon, C. Polymorphous Packing of Pentagonal Nanoprisms. *Nano Lett.* **2023**, *23* (4), 1337−1342.
(43) Gómez-Graña, S.; Pérez-Juste, J.; Alvarez-Puebla, R. A.; Guerrero-Martínez, A.; Liz-Marzán, L. M. Self-Assembly of Au@Ag Nanorods Mediated by Gemini Surfactants for Highly Efficient SERS-Active Supercrystals. *Adv. Opt. Mater.* **2013**, *1* (7), 477−481.
(44) Li, T.; Senesi, A. J.; Lee, B. Small Angle X-ray Scattering for Nanoparticle Research. *Chem. Rev.* **2016**, *116* (18), 11128−11180.
(45) Gomez-Grana, S.; Hubert, F.; Testard, F.; Guerrero-Martinez, A.; Grillo, I.; Liz-Marzan, L. M.; Spalla, O. Surfactant (bi)layers on gold nanorods. *Langmuir* **2012**, *28* (2), 1453−1459.
(46) Goldmann, C.; Chaabani, W.; Hotton, C.; Impéror-Clerc, M.; Moncomble, A.; Constantin, D.; Alloyeau, D.; Hamon, C. Confinement Effects on the Structure of Entropy-Induced Supercrystals. *Small* **2023**, *19* (44), No. e2303380.
(47) Halas, N. J.; Lal, S.; Chang, W.-S.; Link, S.; Nordlander, P. Plasmons in Strongly Coupled Metallic Nanostructures. *Chem. Rev.* **2011**, *111* (6), 3913−3961.
(48) Gu, T.; Kim, H. J.; Rivero-Baleine, C.; Hu, J. J. Reconfigurable metasurfaces towards commercial success. *Nat. Photonics* **2023**, *17* (1), 48−58.
(49) Neubrech, F.; Duan, X.; Liu, N. Dynamic plasmonic color generation enabled by functional materials. *Sci. Adv.* **2020**, *6* (36), No. eabc2709.
(50) Scarabelli, L.; Sánchez-Iglesias, A.; Pérez-Juste, J.; Liz-Marzán, L. M. A "Tips and Tricks" Practical Guide to the Synthesis of Gold Nanorods. *J. Phys. Chem. Lett.* **2015**, *6* (21), 4270−4279.
(51) González-Rubio, G.; Kumar, V.; Llombart, P.; Díaz-Núñez, P.; Bladt, E.; Altantzis, T.; Bals, S.; Peña-Rodríguez, O.; Noya, E. G.; MacDowell, L. G.; et al. Disconnecting Symmetry Breaking from Seeded Growth for the Reproducible Synthesis of High Quality Gold Nanorods. *ACS Nano* **2019**, *13* (4), 4424−4435.
(52) Rodríguez-Fernández, J.; Pérez-Juste, J.; Mulvaney, P.; Liz-Marzán, L. M. Spatially-Directed Oxidation of Gold Nanoparticles by Au(III)−CTAB Complexes. *J. Phys. Chem. B* **2005**, *109* (30), 14257−14261.
(53) Yang, P. W.; Thoka, S.; Lin, P. C.; Su, C. J.; Sheu, H. S.; Huang, M. H.; Jeng, U. S. Tracing the Surfactant-Mediated Nucleation, Growth, and Superpacking of Gold Supercrystals Using Time and Spatially Resolved X-ray Scattering. *Langmuir* **2017**, *33* (13), 3253−3261.
(54) van Aarle, W.; Palenstijn, W. J.; De Beenhouwer, J.; Altantzis, T.; Bals, S.; Batenburg, K. J.; Sijbers, J. The ASTRA Toolbox: A platform for advanced algorithm development in electron tomography. *Ultramicroscopy* **2015**, *157*, 35−47.

https://doi.org/10.1021/acs.chemmater.5c00909
Chem. Mater. XXXX, XXX, XXX−XXX

Tunable Plasmonic Circular Dichroism of Hierarchical Chiral Assemblies

Jaime Gabriel Trazo,[1$] Andrés Serrano Freijeiro,[2$] Mikhail Mychinko,[3] Nika Kutalia,[1] Marianne Impéror-Clerc,[1] Sara Bals,[3] Luis M. Liz-Marzán,[2,4,5,6] Jorge Pérez-Juste,[2*] Isabel Pastoriza-Santos,[2*] and Cyrille Hamon[1*]

[1] Laboratoire de Physique des Solides, Université Paris-Saclay, CNRS, Orsay 91405, France.

[2] CINBIO, Universidade de Vigo, Departamento de Química Física, Campus Universitario As Lagoas, Marcosende, Vigo 36310, Spain

[3] EMAT and NANOlab Center of Excellence, University of Antwerp, 2020 Antwerp, Belgium.

[4] CIC biomaGUNE, Basque Research and Technology Alliance (BRTA), 20014 Donostia-San Sebastián, Spain;

[5] Centro de Investigación Biomédica en Red de Bioingeniería, Biomateriales y Nanomedicina (CIBERBBN), 20014 Donostia-San Sebastián, Spain;

[6] Ikerbasque, Basque Foundation for Science, 48009 Bilbao, Spain;

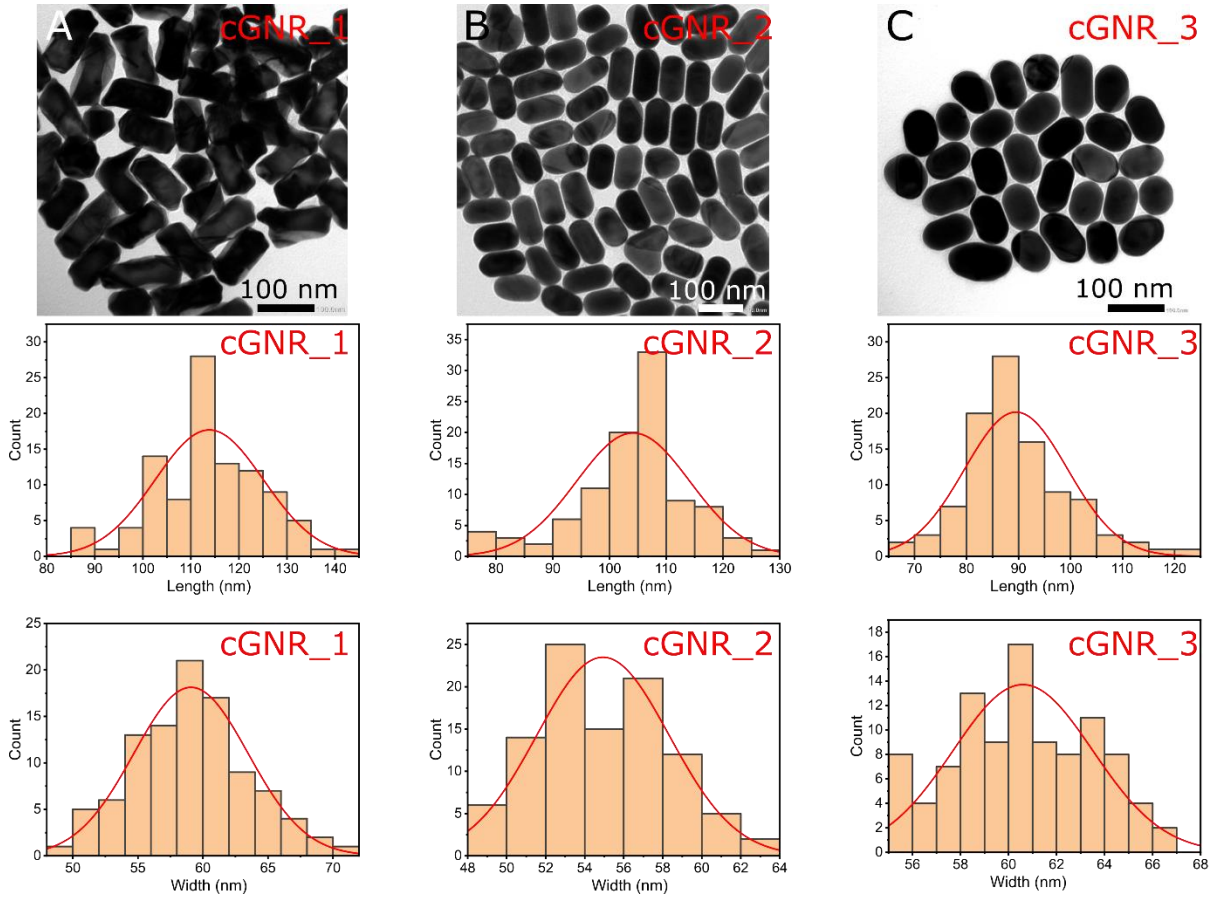

Figure S1: A-C) TEM images and corresponding size distribution analysis of cGNR_1, cGNR_2 and cGNR_3 respectively. The resulting NPs had lengths (L) and widths (W) as follows: cGNR_1 (L = 113.8 ± 11.3 nm, W = 59.1 ± 4.4 nm), cGNR_2 (L = 104.2 ± 10.0 nm, W = 54.9 ± 3.4 nm), and cGNR_3 (L = 89.5 ± 9.9 nm, W = 60.6 ± 2.9 nm).

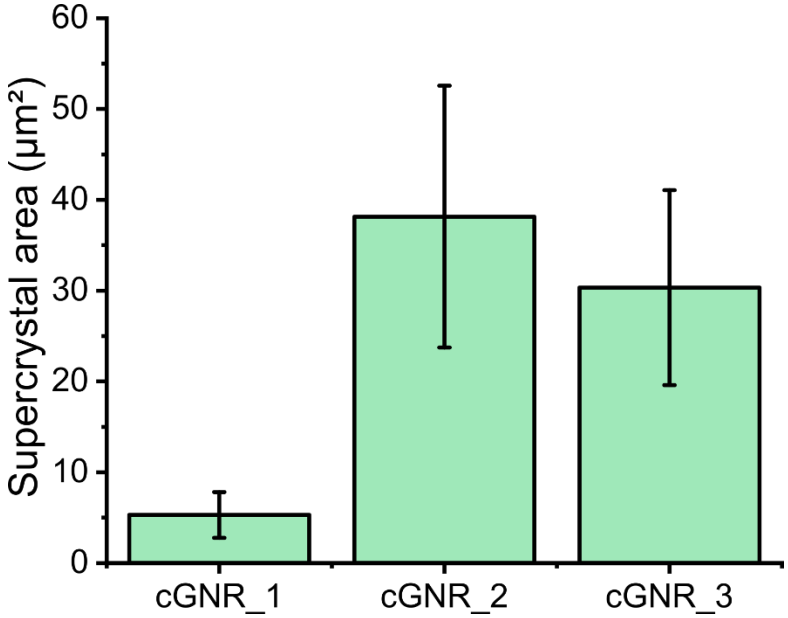

Figure S2: Size analysis of the supercrystals obtained by the self-assembly of cGNRs by **EISA**.

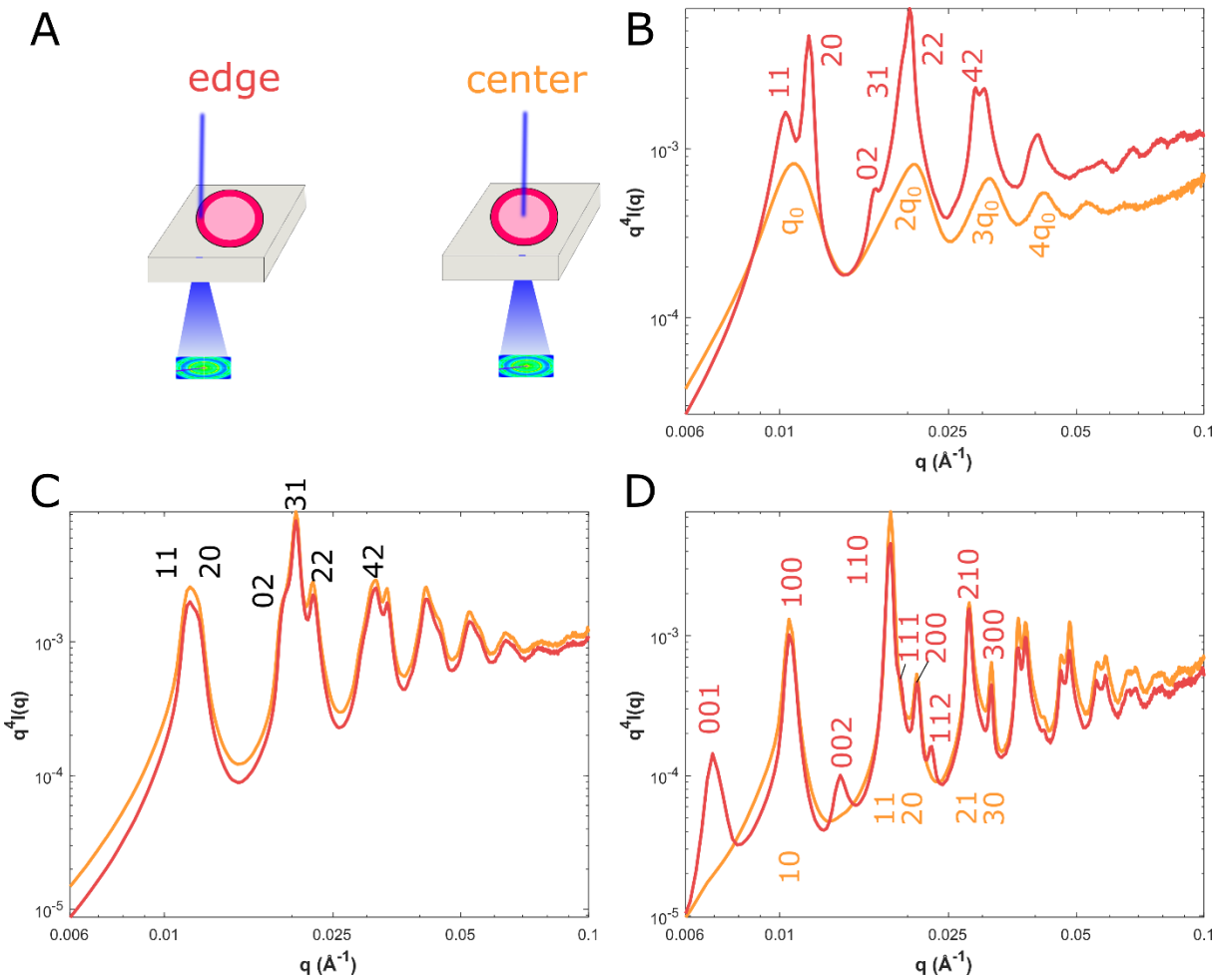

Figure S3: SAXS analysis at the edge and center of the different GNR **films obtained by EISA**. A) Illustration of the SAXS measurement method, depicting one measurement at the coffee ring (red) and another at the center (orange). B) Representative integrated diffractograms for cGNR_1, indexed as 2D centered rectangular. The clear difference between the curves indicates that the domains are more extended at the edge (red) compared to the center (orange). C) Representative integrated diffractograms for cGNR_2, indexed as 2D centered rectangular. The lack of difference between the curves indicates that the supercrystal structure is the same at the edge and center. D) Representative integrated diffractograms for cGNR_3, indexed as 2D hexagonal (orange) and 3D hexagonal (red). The clear difference between the curves suggests a shift in the orientation of cGNRs 3 supercrystals from horizontal at the edge to vertical toward the center.

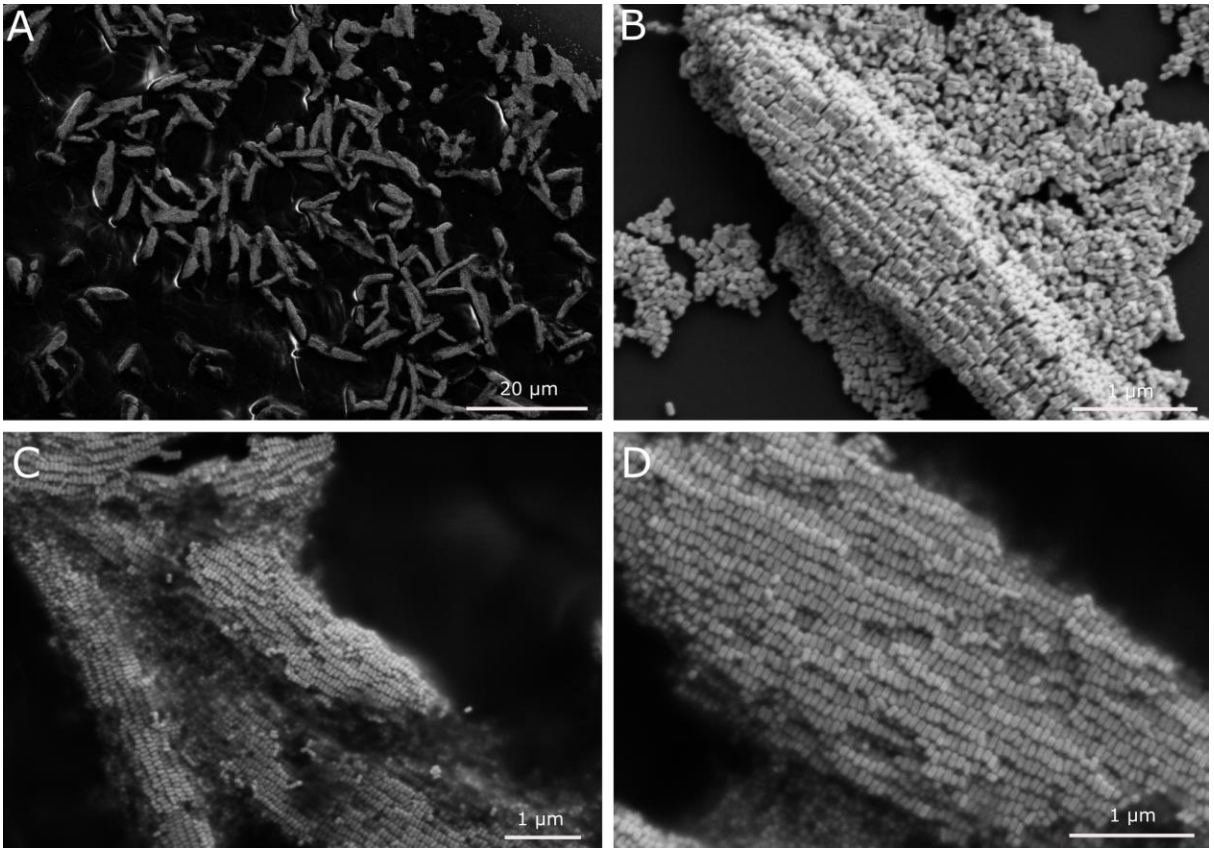

Figure S4: Additional SEM images of the cGNR_1 supercrystals at different magnifications.

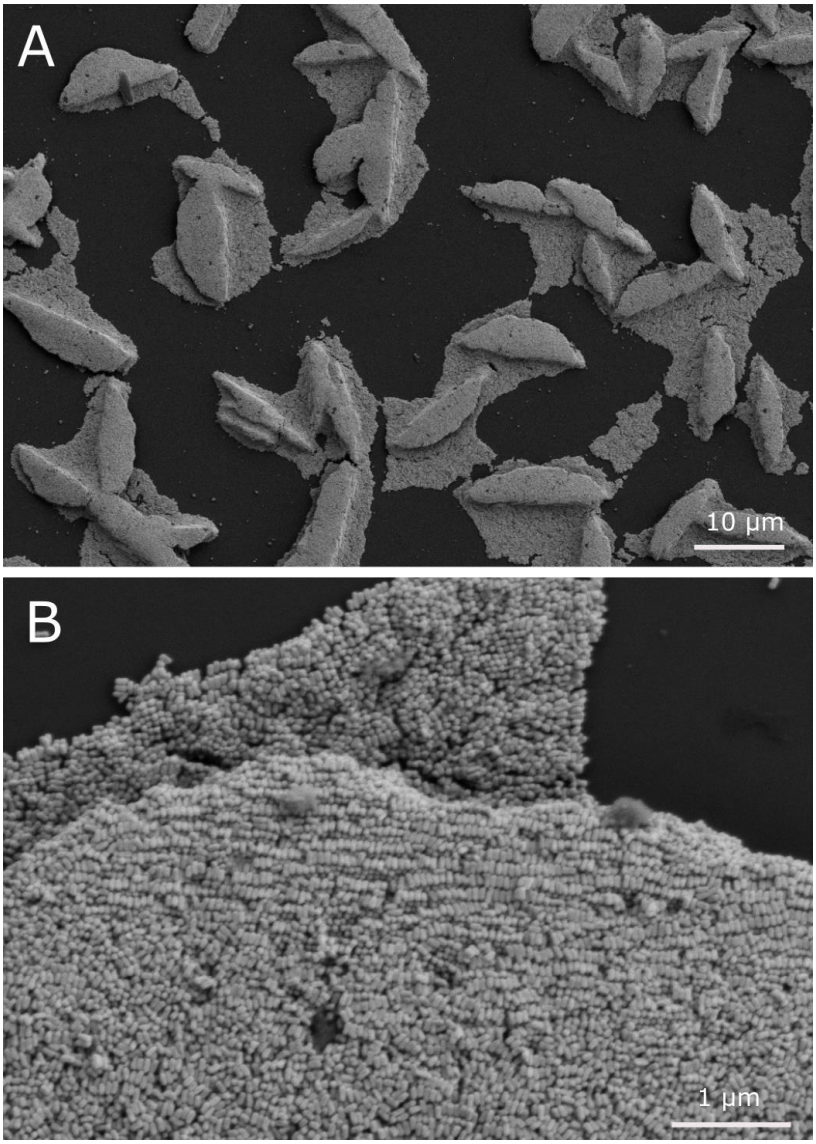

Figure S5: Additional SEM images of the cGNR_2 supercrystals at different magnifications.

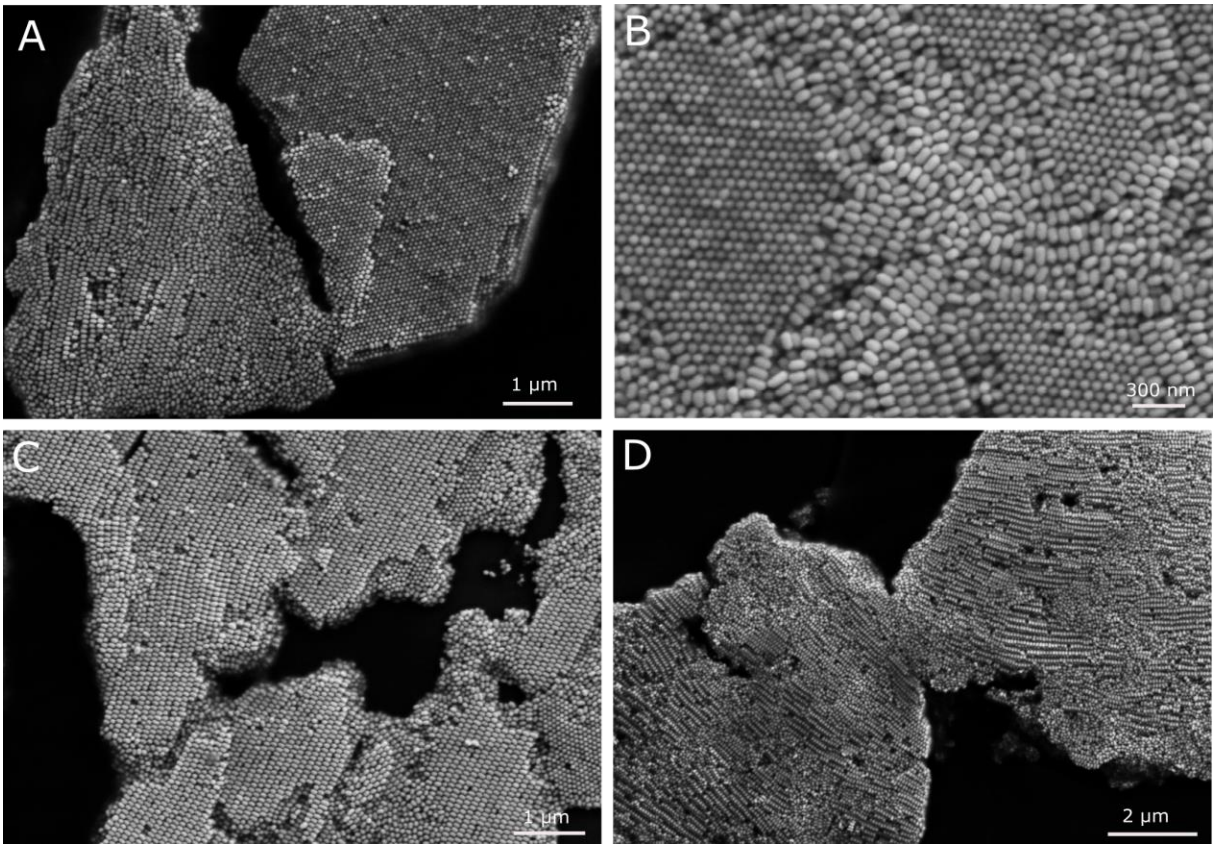

Figure S6: Additional SEM images of the cGNR_3 supercrystals at different magnifications

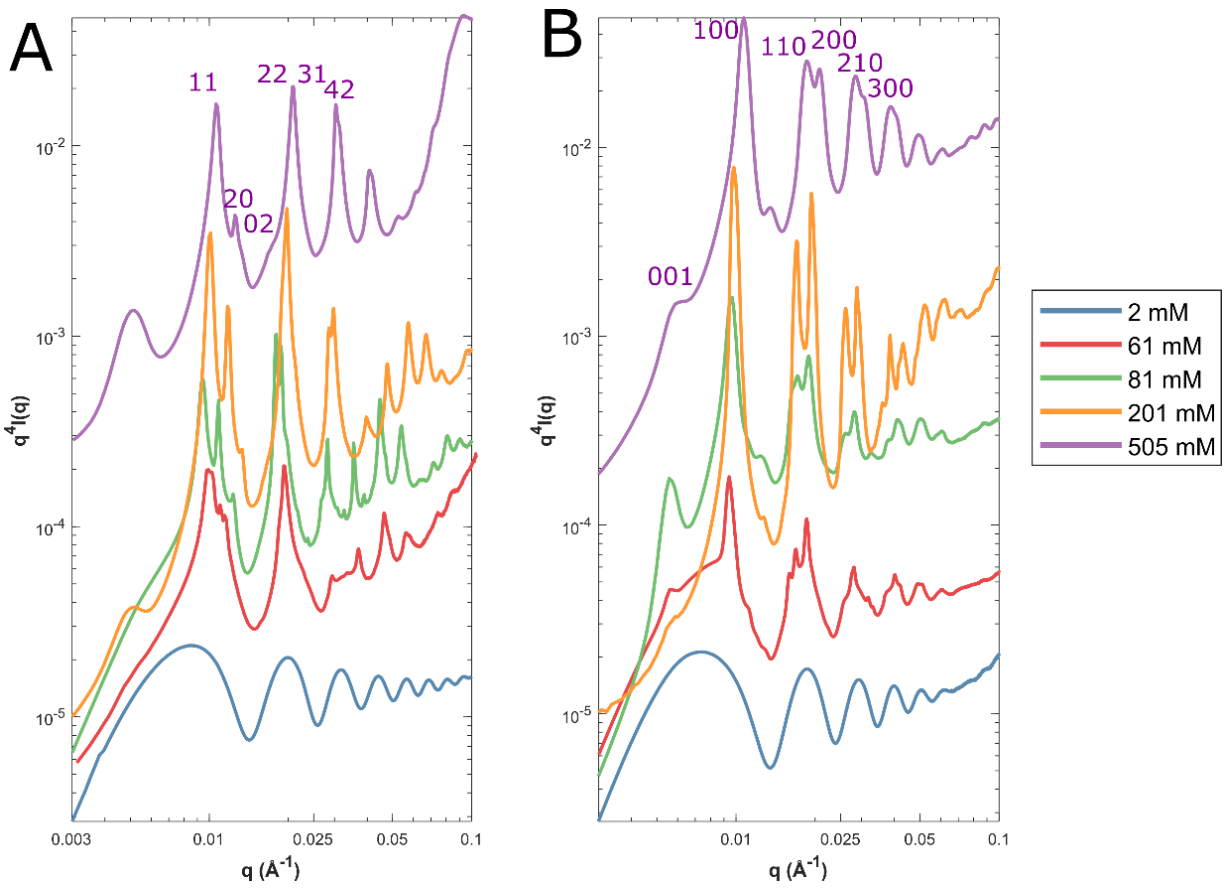

Figure S7: SAXS analysis of colloidal assemblies by DISA as a function of CTAC concentration. A-B) SAXS-integrated diffractograms collected in solution for cGNR_2 and cGNR_3 as a function of CTAC concentrations. In (A), the indexation corresponds to a 2D centered rectangular lattice, while in (B), it corresponds to a 2D hexagonal lattice.

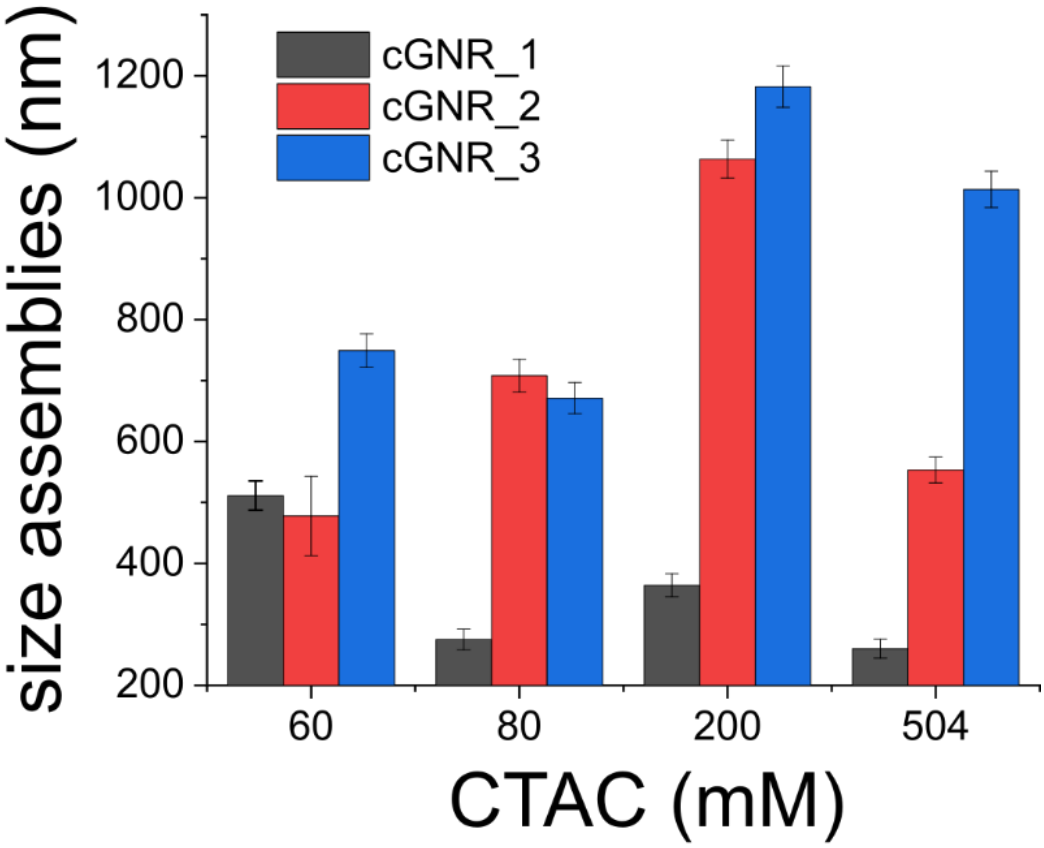

Figure S8: Size analysis of colloidal assemblies by DISA as a function of CTAC concentration. Evolution of the crystallite size in the assemblies for cGNR_1, cGNR_2 and cGNR_3 as a function of CTAC concentration. The size was determined using Debye-Scherrer analysis on the 11 peak for cGNR_1 and cGNR_2 and 100 peak for cGNR_3.

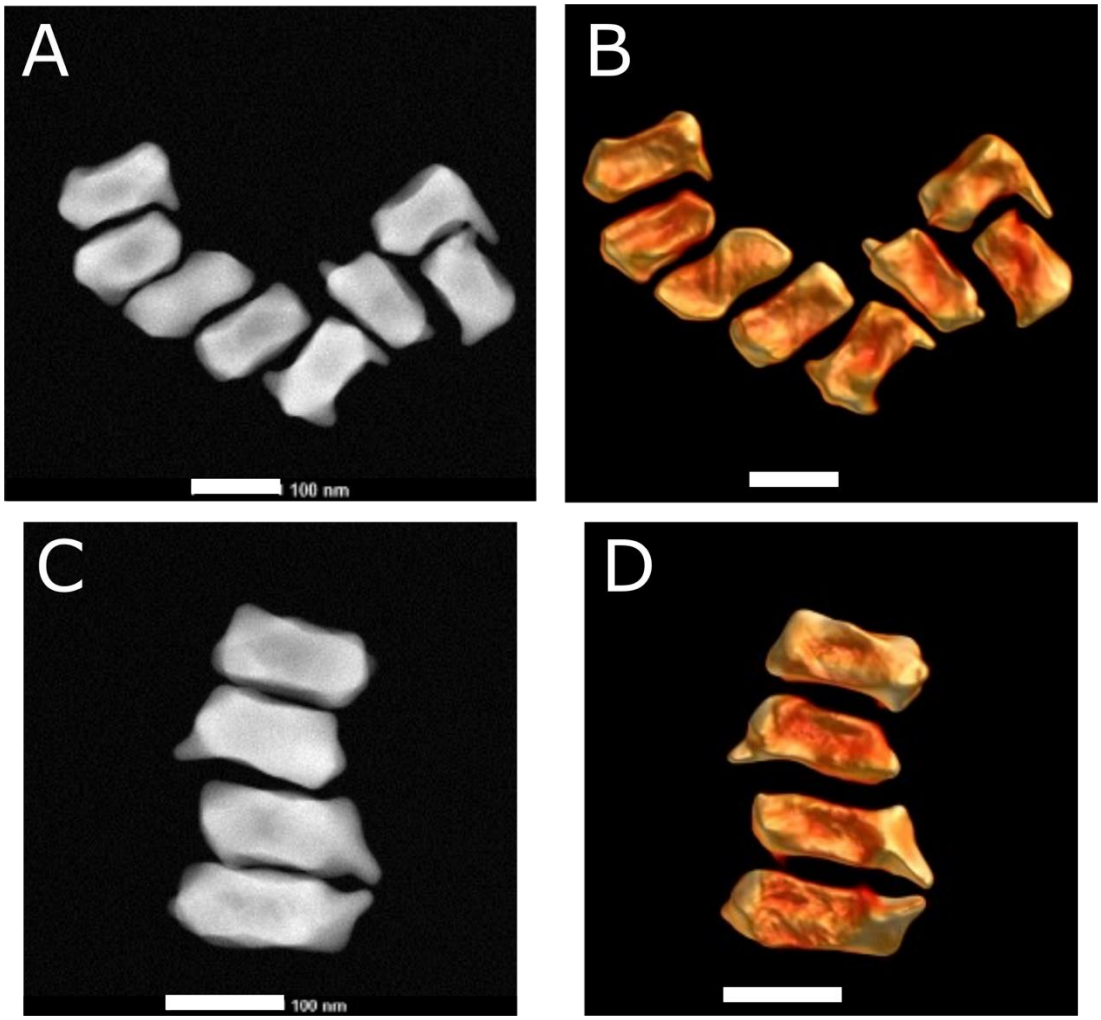

Figure S9: In situ characterization of cGNR assemblies formed via DISA using liquid-phase TEM. A, C) STEM-HAADF images of two cGNR assemblies. B, D) Corresponding ET reconstruction. Scale bar in all images is 100 nm.

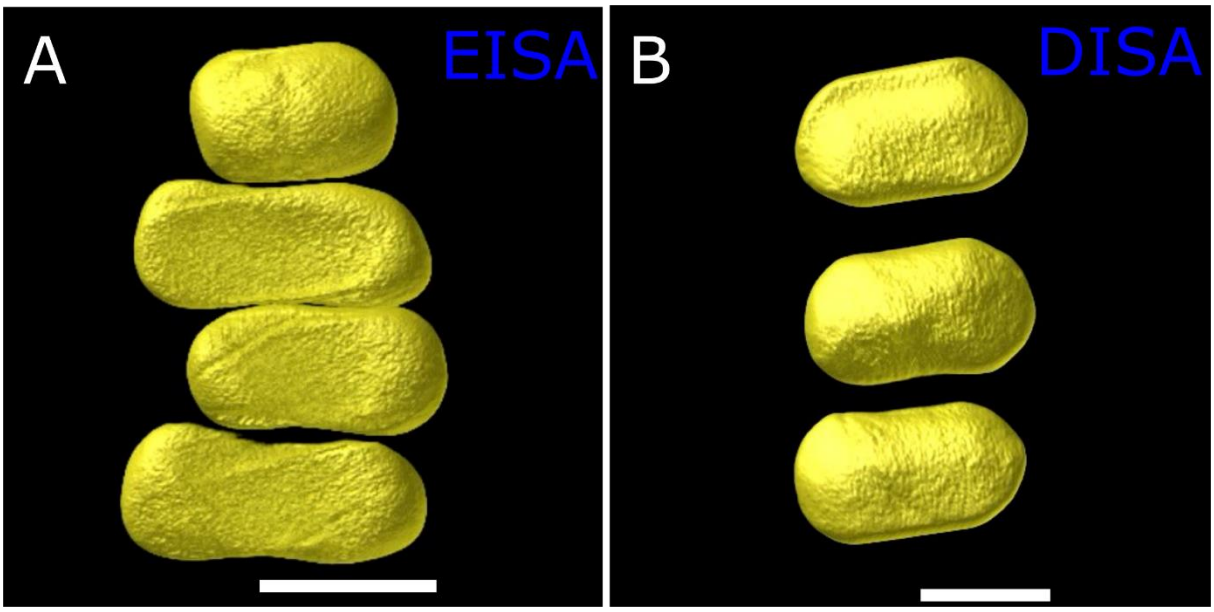

Figure S10: In situ characterization of the cGNR assemblies by Cryo-TEM. A-B) In situ characterization of the assemblies by cryo-TEM for EISA (dry, A) and DISA (in solution, B). In EISA, the interparticle distance is 2.5 ± 1.2 nm, whereas in DISA, it is 10.1 ± 2.7 nm. Scale bar in both images is 50 nm.

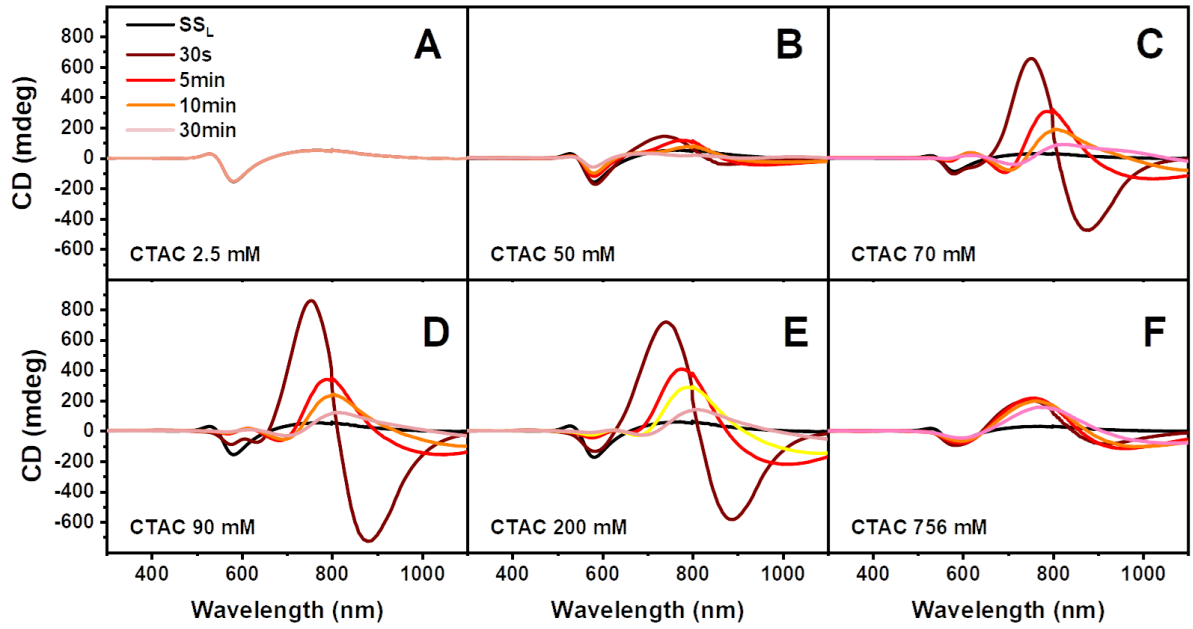

Figure S11: Kinetics of the PCD assembly of cGNR_1 as a function of CTAC concentration via DISA. A-F) Time-resolved CD spectra of cGNR_1 dispersions in the presence of CTAB at different concentrations: 2.5 mM (A), 50 mM (B), 70 mM (C), 90 mM (D), 200 mM (E) and 756 mM (F).

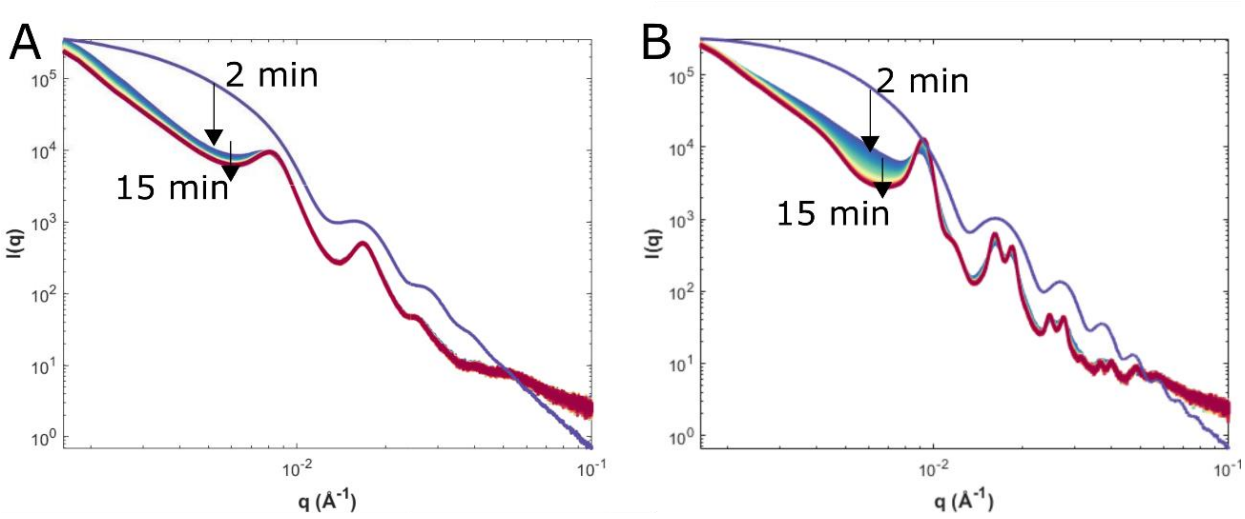

Figure S12: Time-resolved SAXS analysis of the cGNR_1 and cGNR_3 self-assembly. A-B) SAXS integrated diffractograms collected along the self-assembly of cGNR_1 (A) and cGNR_3 (B). The first blue curve represents the SAXS signal before self-assembly, corresponding to the form factor of non-interacting NPs. The NPs were then rapidly mixed with a concentrated CTAC solution to reach a final concentration of 90 mM CTAC. The two-minute arrow accounts for the dead time required to load the capillary and initiate the first SAXS acquisition after the self-assembly process began. SAXS images were subsequently acquired for 15 minutes with a temporal resolution of 3 seconds. These results indicate that the assemblies formed within the first two minutes. The slight evolution of the signal after this time suggests that the structures continue to grow slightly over time.

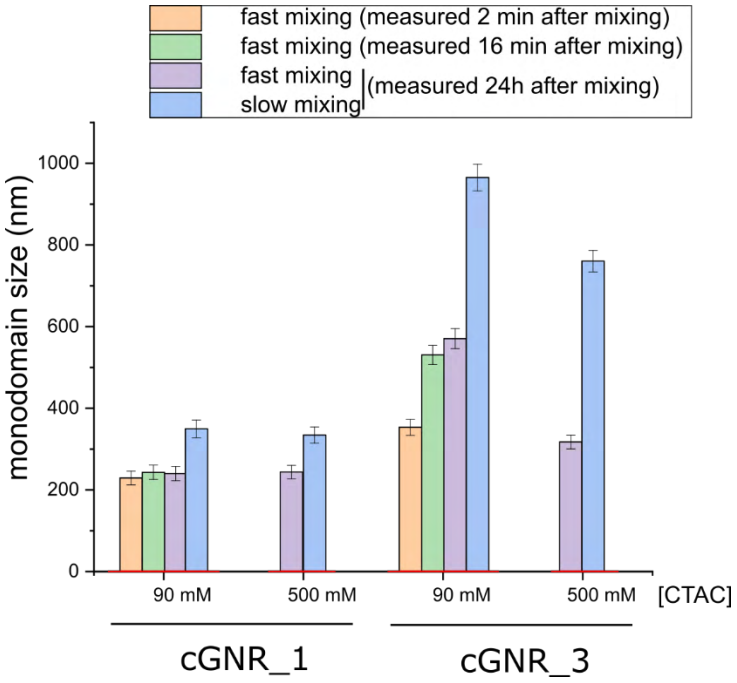

Figure S13: Evolution of the assembly size for cGNR_1 and cGNR_3 as a function of mixing conditions and CTAC concentration. The influence of two different mixing methods for the depletant and cGNR solutions was analyzed using Debye-Scherrer analysis of SAXS diffractograms. Mixing times of approximately 1 second (fast) and 24 hours (slow) correspond to one-shot mixing and slow diffusion in SAXS capillaries, respectively. The orange and green bars represent the analysis of selected SAXS curves shown in Figure S12. Overall, the results show that both the shape of the cGNRs and the mixing time influence the crystallite size, whereas the depletant concentration used during self-assembly has a limited effect.

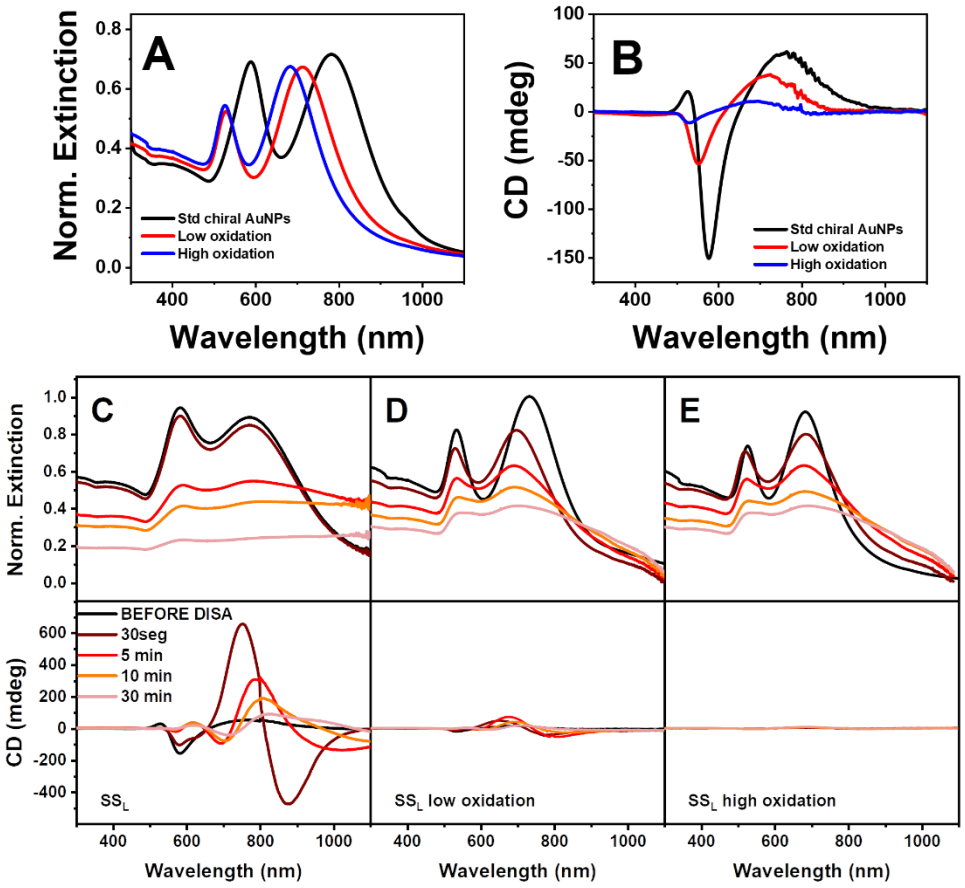

Figure S14: Extinction (A) and CD (B) spectra of c-GNR_1 (black), cGNR_2 (red) and cGNRs_3 (blue). Self-assembly kinetics of cGNR_1 (C), cGNR_2(D), cGNR_3 (E) in 70 mM CTAC monitored by extinction (top) and CD (bottom) spectroscopies.

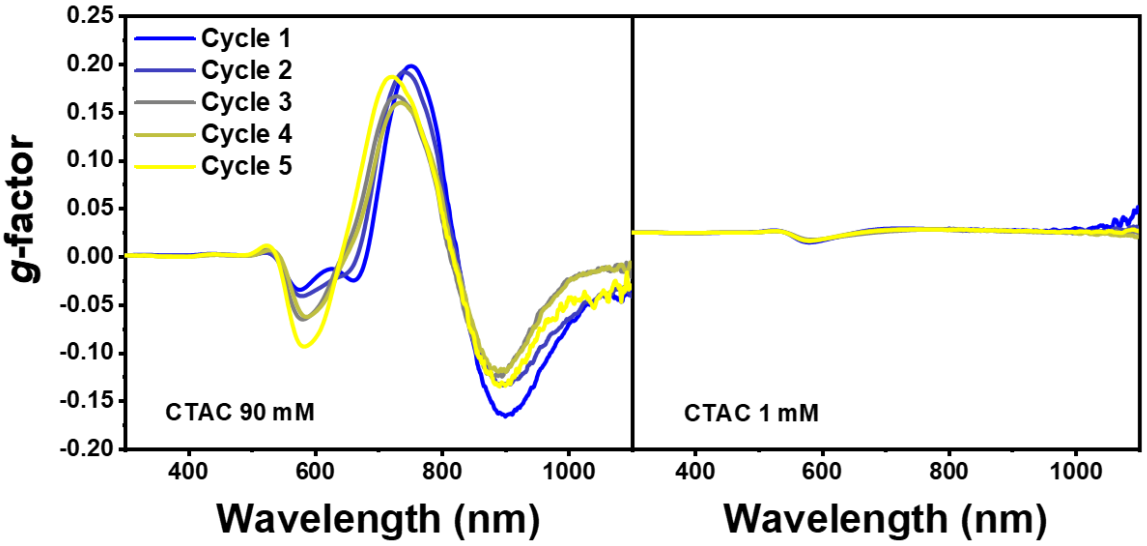

Figure S15: *g*-factor spectra of reconfigurable assembles of chiral GNRs at 70 mM CTAC, (left) and 1 mM CTAC (right) repeated during 5 reversibility cycles for cGNR_1.